UNIVERSIDADE DE LISBOA

FACULDADE DE CIÊNCIAS

Strain partitioning and the seismicity distribution within a transpressive plate boundary: SW Iberia-NW Nubia

Doutoramento em Geologia

Geodinâmica Interna

Sónia Dulce Manzoni Martins Ferreira da Silva

Tese orientada por:

Professor Doutor Pedro António Gancedo Terrinha e Professor Doutor Luís Manuel Henriques Marques Matias

Documento especialmente elaborado para a obtenção do grau de doutor

2017

UNIVERSIDADE DE LISBOA

FACULDADE DE CIÊNCIAS

Strain partitioning and the seismicity distribution within a transpressive plate boundary: SW Iberia-NW Nubia

Doutoramento em Geologia

Geodinâmica Interna

Sónia Dulce Manzoni Martins Ferreira da Silva

Tese orientada por:

Professor Doutor Pedro António Gancedo Terrinha e Professor Doutor Luís Manuel Henriques Marques Matias

Júri:

Presidente:

- Doutor César Augusto Canêlhas Freire de Andrade

Vogais:

- Doutor Nevio Zitellinii
- Doutor Luís Filipe Fuentefria de Menezes Pinheiro
- Doutor Mourad Bezzeghoud
- Doutor João Manuel Lopes Cardoso Cabral
- Doutor Pedro António Gancedo Terrinha

Documento especialmente elaborado para a obtenção do grau de doutor

Este trabalho foi financiado pela Fundação para a Ciência e Tecnologia (SFRH/BD/46227/2008)

2017

To my little boy, David

“Eu amo o Longe e a Miragem,

Amo os abismos, as torrentes, os desertos...”

José Régio

in Cântico Negro

Abstract

The Gulf of Cadiz offshore SW Iberia is an area linked with episodic destructive seismic and tsunamigenic events, such as the M~8.8, 1st November 1755 Lisbon earthquake among others. The association of active faults to this kind of high magnitude event has been extensively studied specially due to the contribution of several international projects for more than two decades. However, the meaning of the persistent small to intermediate magnitude seismicity recognized in this region is still particularly not fully understood. This is, at least, related to the lack of an accurate hypocenter location of these events resulting from an asymmetrical geographical distribution of the permanent seismic network.

One of the main purposes of the NEAREST project (Integrated observation from NEAR shore sourcES of Tsunamis: towards an early warning system GOCE, contract n. 037110) was the identification and characterization of seismogenic and tsunamigenic structures in the Gulf of Cadiz area, source region of the Lisbon 1755 earthquake and tsunami. To address this problem 24 broadband Ocean Bottom Seismometers (OBS) and a seafloor multiparametric station GEOSTAR (Geophysical and Oceanographic Station for Abyssal Research) acquired between August 2007 and July 2008 passive seismic data in this region. The results delivered a detailed record of the local seismicity, revealing 3 main clusters of earthquakes, two of them coinciding with the location of the 3 larger instrumental earthquakes in the area: i) the 28th February 1969 (Mw~8.0); ii) the 12th February 2007 (Mw=6.0) and iii) the 17th December 2009 (Mw=5.5). Focal mechanisms show a mixed pattern, mostly strike-slip and reverse dip-slip with a very few normal mechanisms. The results show that of the recorded events are located in the mantle (at depths between 30 and 60 km). This implies the existence of tectonically active structures located much deeper than the ones mapped by Multichannel seismic reflection.

A thorough analysis shows that the seismicity clusters are offset with respect to the upper crustal active thrusts. The wide-range solutions of focal mechanisms also imply that the related source processes are complex. This can reflect the interaction of different active geological features, such as faults and rheological boundaries. To understand these new results in the context of the seismo-tectonics of the Gulf of Cadiz a review of some available geophysical data (reflection and refraction seismic profiles interpretation) in this area is presented as well as novel work on seismic reflection profile IAM GB1 across a rheologic boundary and seismicity cluster.

Our study shows that the seismicity clusters are located at faults intersections mapped at the seafloor and shallow crust, suggesting that the crustal tectonic faults are replicated in the lithospheric mantle. These fault interferences are

associated with boundaries of lithospheric domains prone to localize stress and seismic strain.

Active crustal faults are either locked or move through slow aseismic slip. Frictional slip in crustal faults is probably limited to high magnitude earthquakes. Serpentinization probably induces tectonic decoupling limiting micro-seismicity to depths below the serpentinized layer. It is expected that during high-magnitude events seismic rupture is favored by weakening mechanisms and propagates upwards through the serpentinized layer up to the surface.

The results obtained in this work improve our knowledge about the local seismicity and related active faults in the Gulf of Cadiz area, giving a new contribution to access to the seismic hazard in the Nubia-Iberia plate boundary in the Northeast Atlantic Region.

Keywords: *Nubia-Iberia plate boundary; micro-seismicity; serpentinization; strain partitioning; high-magnitude earthquakes*

Resumo

O Golfo de Cádis é uma região com uma sismicidade moderada embora se conheça, tanto no registo histórico como instrumental, eventos de elevada magnitude. O sismo de 1 de Novembro de 1755 é um exemplo paradigmático com uma magnitude estimada de 8.8 e um tsunami associado com Mt = 8.5.

Já o sismo de 28 de Fevereiro de 1969, é o mais importante registado instrumentalmente, teve uma Ms de 7.9, ao qual esteve associado um pequeno tsunami. Mais recentemente, salientam-se os sismos de 12 de Fevereiro de 2007, com Mw=6.0 e o de 17 de Dezembro de 2009, com Mw =5.5 (EMSC-European-Mediterranean Seismological Centre). No entanto, a sismicidade nesta região é descrita como de magnitude baixa a intermédia, com uma distribuição em profundidade acima dos 60 km.

Correlacionar esta sismicidade com potenciais estruturas sismogénicas no Golfo de Cádis constituiu um dos objectivos do projecto NEAREST (Integrated observation from NEAR shore sourcES of Tsunamis: towards an early warning system GOCE, contract n. 037110). Neste contexto, foram necessárias uma caracterização e localização mais precisas dos eventos sísmicos ocorridos nesta região, até agora limitadas pelos constrangimentos inerentes à distribuição geográfica das estações permanentes terrestres. Por isso, foi desenvolvida uma campanha de aquisição de dados contínuos utilizando uma rede de sismómetros de fundo do mar.

A rede sísmica NEAREST operou de modo contínuo num período de 11 meses, entre Agosto de 2007 Julho de 2008, integrando 24 sismómetros de fundo do mar (OBS) e uma estação multiparamétrica- GEOSTAR. Durante as campanhas de colocação e recuperação dos instrumentos, as manipulações dos OBS e GEOSTAR estiveram a cargo do Alfred Wegener Institute for Polarand Marine Research e do Istituto Nazionale di Geofisica e Vulcanologia – INGV, respectivamente.

Os OBS foram construídos pela K.U.M. Umwelt- und Meerestechnik Kiel GmbH, Germany e incorporavam sismómetros de banda larga Güralp CMG-40T e um hidrofone. A GEOSTAR é um observatório que integra diversos equipamentos para a recolha de dados geofísicos e oceanográficos em contínuo. Nesta estação estão incluídos um sismómetro de banda larga com 3 componentes e um hidrofone usados nesta campanha.

As estações terrestres estão a cargo do Instituto Português do Mar e da Atmosfera (IPMA) e Instituto Dom Luiz (IDL) correspondendo a sismómetros de banda larga também com 3 componentes. Os registos nestas estações foram apenas utilizados para constranger as soluções dos mecanismos focais. Em trabalhos futuros, prevê-se a sua inclusão na localização dos eventos identificados pela rede NEAREST. Durante o período de aquisição foram

registados na rede terrestre, para a área delimitada pela rede NEAREST, cerca de 270 sismos locais.

Durante o período de funcionamento da rede NEAREST foram identificados cerca de 750 eventos observados em mais de 3 estações. Deste total 590 sismos estavam localizados na área da rede NEAREST. A localização hipocentral foi testada usando diferentes metodologias e modelos de velocidades: a) inversão conjunta das posições hipocentrais e correcções de estações; b) o método das diferenças duplas e c) a inversão conjunta do modelo de velocidades-localizações hipocentrais e correcções de estações.

O catálogo final inclui 443 eventos identificados em mais de 6 estações e localizados na área da rede NEAREST. De um modo geral, a maioria dos hipocentros estão localizados a mais de 30 km de profundidade, portanto no manto. As magnitudes locais variam entre 1.2 e 4.8.

As localizações epicentrais e hipocentrais baseadas na rede NEAREST divergem das soluções conhecidas para a rede terrestre (providenciadas pelo IPMA), estando deslocadas para SW e sendo mais profundas. A diferença de profundidade pode atingir os 40 km. A campanha do projecto NEAREST permitiu a identificação de uma grande quantidade de eventos não detectada pela rede terrestre.

Esta campanha permitiu ainda uma redefinição da distribuição da sismicidade na região, até então considerada difusa. Destes resultados foi possível reconhecer 3 enxames de sismicidade, dois destes coincidentes com 3 dos maiores eventos observados no registo instrumental. Tanto os sismos de 28 de Fevereiro de 1969 (*Mw~8.0*) como 12 de Fevereiro de 2007 (*Mw=6.0*) na proximidade da Falha da Ferradura e 17 de Dezembro de 2009 (*ML=6.0*) na região do canhão de São de Vicente. Os mecanismos focais do catálogo NEAREST são consistentes com estes eventos bem como com soluções de tensores de momento publicadas para esta região.

No enxame do canhão de São Vicente é onde estão localizados a maioria dos eventos. Os hipocentros encontram-se a profundidades entre os 20 e os 55 km. A distribuição dos epicentros apresenta um alinhamento ≈ NE-SW ao longo do canhão de São Vicente e prolongando-se para o limite NE da Falha da Ferradura. Os mecanismos focais dominantes são de desligamento e oblíquos, combinando movimento de desligamento com uma menor contribuição de movimento inverso. Foram ainda registados raros eventos em falha normal. A compressão máxima é aproximadamente sub-paralela ao SHmax, com uma direcção ≈NW-SE.

Os epicentros localizados no enxame a SW da Falha da Ferradura, tem um alinhamento aproximadamente NW-SE, sub-paralelo à direcção de SHmax regional. Neste enxame os hipocentros são mais profundos localizando-se entre os 30 e os 55km. Os mecanismos focais são na sua maioria de

desligamento puro existindo alguns eventos em falha inversa e também raras soluções em falha normal. Importa salientar que as soluções de desligamento apresentam frequentemente um plano subparalelo à orientação das falhas de desligamento SWIM (≈WNW-ESE a E-W). A compressão máxima é aproximadamente NW-SE e NNW-SSE, a W e E do enxame de sismicidade, respectivamente. As direcções de SHmax são mais uma vez coincidentes com a direção de compressão máxima.

No enxame do Banco do Gorringe maioria dos sismos estão localizados no bordo SW deste relevo submarino, sub-paralelos à falha do Gorringe. Os eventos são menos profundos quando comparados com os outros dois enxames, na sua maioria acima dos 40 km. Os mecanismos focais são na sua maioria de desligamento e em falha inversa. Também neste enxame foram registados alguns sismos em falha normal. A direcção de compressão máxima e o SHmax são NNW-SSE.

O facto de estes eventos se localizarem predominantemente no manto constitui um dos principais resultados deste trabalho. Neste contexto, tendo em consideração a profundidade dos eventos sísmicos, a correlação da sismicidade com as estruturas sismogénicas na região do Golfo de Cádis é particularmente complexa. Esta comparação foi desenvolvida com base nos dados de sísmica de reflexão e refração disponíveis.

Do nosso estudo resulta que a sismicidade parece estar concentrada em zonas de interferência de falhas localizadas no manto subcrustal litosférico. Estas deverão ser uma replicação do padrão observado a níveis crustais e parecem ser coincidentes com transições entre diferentes domínios litosféricos. Estas zonas de interferência de falhas deverão ser áreas favoráveis à acumulação de tensões e deformação sísmica.

As falhas activas crustais deverão estar ou bloqueadas ou movimentar-se de modo assísmico. A movimentação sísmica pode estar associada apenas a sismos de maior magnitude. A existência de níveis serpentinizados no Golfo de Cádis é suportada por dados de sísmica refracção e furos de sondagens profundas. Estes podem funcionar como planos de descolamento para as grandes falhas inversas, acomodando a movimentação asísmica e impedindo a micro-sismicidade de se propagar aos níveis crustais. Durante os sismos de elevada magnitude estes níveis serpentinizados deverão funcionar como zona enfraquecida, de baixo atrito, favorecendo a propagação da ruptura sísmica até à superfície.

Os resultados obtidos neste trabalho melhoram o nosso conhecimento sobre a sismicidade e a sua relação com as falhas activas na região do limite de placas litosféricas no Golfo de Cádis, contribuindo para o estudo do risco sísmico associada a sismos devastadores.

Palavras-chave: *fronteira de placas Núbia-Ibéria; micro-sismicidade; serpentinização; partição da deformação; sísmos de elevada magnitude*

Acknowledgements

The work presented here was not possible without the support of many people to whom I would like to thank.

I start to acknowledge the support of my supervisors, Pedro Terrinha and Luis Matias: for suggesting the thesis topic, help me pursue my goals and reviewing this manuscript.

To Wolfram Geissler by having received me in the Alfred Wegener Institute Helmholtz Centre for Polar and Marine Research for processing of the NEAREST OBS data (as part of the *FCT* and the Deutscher Akademischer Austauschdienst (*DAAD*) Agreement for Cooperation in Science for Portuguese and German research teams).

To Nevio Zitellini for including me in the NEAREST project as well as the collaboration and discussion on the thesis topic.

To Cesar Ranero, for the participation in the MCS reflection campaign in the Gulf of Cadiz and Alboran, as part of the TOPOMED (ESF-EUROCORE Programme) project. Also for teach me the fundamental steps for MCS processing in GLOBE Claritas, during my visit to Barcelona Center for Subsurface Imaging from the Instituto Cientifico del Mar. Also to Ivan, Naira, Agnese, Savitri and Alejandra for helping me during both the campaign and visit to Barcelona.

Christian Hensen and Marianne Nuzzo for including me in the COST Action ES1301 -Impact of Fluid circulation in old oceanic Lithosphere on the seismicity of transfOrm-type plate boundaries: neW solutions for early seismic monitoring of major European Seismogenic zones (FLOWS). Ingo Grevemeyer for the participation in the OBS recovery campaign from TOPOMED (ESF-EUROCORE Programme) project.

To Fernando Carrilho and Dina Vales, for patiently explaining me the details of the IPMA seismic network.

To Nuno Dias for helping me with my first incursions into the VELEST application. To Martin Romsdorf for collaborate in the initial processing of the NEAREST data.

To Filipe Rosas for introducing me to marine geology and Gulf of Cadiz geological thematic. I would also like to thank my colleagues from Marine Geology and Geo-resources division/IPMA: Carlos Ribeiro, Cristina Roque, Débora Duarte, Joana Santos, João Noiva, Luis Batista, Manuel Teixeira, Margarida Henriques, Marisa Loureiro, Marta Neres, Pedro Brito, Sara Rodrigues, Susana Muinos e Vitor Magalhães. As well as, support from my former colleagues from Marine Geology and Geo-resources division/IPMA and Marine Geology Department/LNEG: Vasco Valadares, Tiago Cunha, João Duarte, Rui Quartau, Gabriela Carrara, Ana Fernandes, Henrique Duarte and

Ruben Borges.

Special thanks to Marianne Nuzzo who also reviewed some parts of the manuscript.

To my colleagues from the geophysical Division/IPMA: Dina Vales, Rachid Omira, Alice Cunha, Patricia Silva and Paulo Alves, I would like to thank for all the support.

To my GeoArte group: Sónia, Cristina and Inês: I am very grateful for all the talks, coffee and teas…

To all my friends and family without whom I couldn't have finished this journey. Thank you for all the patience and endless support. My special thanks to Nuno and to my son, David (my little boy), to whom I dedicate this work.

This work was benefit from the support of several projects:

EMODnet-Geology Project coordinated by the Natural Environment Research Council – British Geological Survey (NERC-BGS).

MODELINK (from April 2014-present): "Modeling the tectonic missing link between the active Gloria and SWIM fault systems along the (Atlantic) Eurasia-Nubia plate boundary"; Project coordinator: Filipe M. Rosas (University of Lisbon, IDL)

SWIMGLO (from 2010-2013):"The Gloria-SWIM plate boundary Faults connection and its importance on the propagation of tectonic deformation and deep water ecosystems along the Azores-Gibraltar Plate Boundary"; Project coordinator Pedro Terrinha (Instituto Nacional de Engenharia, Tecnologia e Inovação (INETI), Portugal).

TOPOMED (2008-2012) "Plate re-organization in the western Mediterranean: lithospheric causes and topographic consequences" – A Collaborative Research Project for the ESF-EUROCORE Programme – 4D Topography Evolution in Europe: Uplift, Subsidence and Sealevel Change (TOPO-EUROPE).

The NEAREST project was funded by the financial EU Specific Programme "Integrating and Strengthening the European Research Area", Sub-Priority 1.1.6.3, "Global Change and Ecosystems", contract n. 037110.

ALMOND (2008-2011): "Modelação multi-escala da deformação do Golgo de Cádis"; Project coordinator Maria da Conceição Neves (University of Algarve, Portugal).

I acknowledge a Ph.D. scholarship (SFRH/BD/46227/2008) of Fundação para a Ciência e Tecnologia (FCT), and research grant from MINEPLAT (ALT20030145FEDER000013).

I acknowledge the support by Landmark Graphics Corporation via the Landmark University Grant program and GMT (Wessel & Smith 1998) used in many of figure plotting. I also acknowledge IPMA and IDL for the data from land

seismic networks.

I would like to thank the host institutions: Marine Geology and Geo-resources division/ Instituto Português do Mar e da Atmosfera (IPMA), Instituto Dom Luiz (IDL) and the University of Lisbon, Department of Geology

Figures index

Table index

Table of contents

I.Introduction

The seismicity in the Gulf of Cadiz region has been classified as diffuse with respect to the distribution of the epicentres and intermediate in what respects frequency and magnitude of the events, although occasionally the area is stricken by strong and mega-earthquakes. Examples of these are, i) the 1st November of 1755 earthquake which had estimated magnitude of 8.8 (Richter, 1958 and Johnston, 1996) that generated a large tsunami on the coast of Portugal, SW Spain and NW Morocco and ii) the instrumentally recorded 28th February 1969 earthquake that had a surface magnitude (Ms) of 7.9 (Fukao, 1973) and a small tsunami associated with.

In the last decades, research focussed on the mapping of seismogenic and tsunamigenic sources in this area through acquisition of swath bathymetry, multi-seismic reflection, wide-angle and refraction seismic surveys, analogue and numerical modelling. A remarkable improvement on the understanding of the tectonic activity resulted from the processing and interpretation of these data. However, there is still an unclear relation between the seismicity and the active faults identified. The accurate location of seismicity is hampered by the fact that the onshore seismic stations network is positioned around a semi-circle across south Portugal, southwest Spain and northwest Morocco. As a result earthquakes locations are poorly constrained, particularly for low to intermediate magnitude events.

One of the main goals of the NEAREST project was the characterization of potential seismogenic and tsunamigenic sources located near shore in the Gulf of Cadiz area was. To ensure accurate seismicity identification, 24 ocean bottom seismometers (LOBSTER- **L**ongterm **O**cean **B**ottom **S**eismometer for **T**sunami and **E**arthquake **R**esearch) and a multiparametric station – GEOSTAR were deployed in this area to register, in continuous, passive seismic data for one year. This dataset is a unique opportunity to achieve accurate earthquakes locations and seismic sources. Accordingly, the main objectives of this project are:

i) characterize the micro-seismicity in the study area;

ii) identify and characterize the mechanisms that control seismicity distribution in the area;

iii) understand the slip distribution in the active faults, in detail the faults interference and strain partitioning mechanisms;

iv) contribute to the definition of the plate boundary in the SW Iberia-NW Morocco region, improve rheological models and define the limits of the seismogenic zone.

I.1. Geodynamic setting of the study area

The Gulf of Cadiz is located in the Eastern termination of the Azores-Gibraltar Fracture Zone (AGFZ), west of the Gibraltar orogenic arc and oceanic slab (Figure I.1). Here, the plate boundary zone between Eurasia (Iberia) – Africa (Nubia) has been described as diffuse because the tectonic deformation spreads across a broad area (Sartori et al., 1994, Zitellini et al 2009). The plate boundary is itself a matter of discussion because it appears that two types of plate boundary are present, i) a subduction zone under the Gibraltar arc (Gutscher et al., 2002) and ii) a transform type boundary accommodated by the SWIM dextral strike-slip faults (Zitellini et al., 2009). According to recent data the central part is floored by Late Jurassic to Early Cretaceous oceanic lithosphere (Figure I.1). This new finding is supported by seismicity distribution pattern, tomography as well as refraction and wide-angle seismic profiles:

- Preliminary results from NEAREST OBS experiment presented in Geissler et al. (2010). According to these authors, the depth distribution of the seismicity shows a pronounced pick at 50 km coherent with the 600°C isotherm in Late Jurassic to Early Cretaceous oceanic lithosphere (McKenzie *et al.,* 2005). This limit would mark the base of brittle deformation and the seismogenic layer;
- Monna et al., (2012) presented a three-dimensional P wave upper-mantle tomography model for the southwest Iberian margin (and Alboran Sea) based on teleseismic arrival time recorded by Iberian and Moroccan land stations and by the NEAREST OBS network. Because this study included a long-term instrumental coverage at sea, it resulted in a better resolve of upper-mantle structure. A clear high-velocity anomaly is imaged under the NEAREST array underlying the Horseshoe Abyssal Plain. The thickness of this anomaly (≈80–150 km) is compatible with an old oceanic lithosphere (~140 Ma, McKenzie *et al.,* 2005) as speculated in Geissler et al. (2010).
- New refraction and wide-angle seismic reflection data were acquired within the NEAREST project to study the crustal structure of the SW Iberian margin. The P2 profile, roughly N-S, is a 340 km long profile across from the central Gulf of Cadiz to the Variscan continental margin in the Algarve, Southern Portugal (see Figure I.1 for location and Figure I.2). The seismic velocity and crustal geometry model obtained in Sallarès et al.,(2011) reveal three distinct crustal domains: a 28–30 km-thick continental crust in the north; an abrupt transition zone and a last domain ≈150 km-wide, with a ≈7 km-thick crust of oceanic nature (>140 m.y.-old). In this last domain, absolute velocities in the bottom layer are lower than excepted probably due to fault related rock fracturing, alteration and mantle serpentinization (Sallarès et al., 2011). Local low

upper mantle velocities, between 7.8-7.9 km/s, were also identified in wide-angle multichannel seismic reflection profile by Gonzalez et al. (1996) in **I**berian **A**tlantic **M**argin project (details on the project in chapter II).

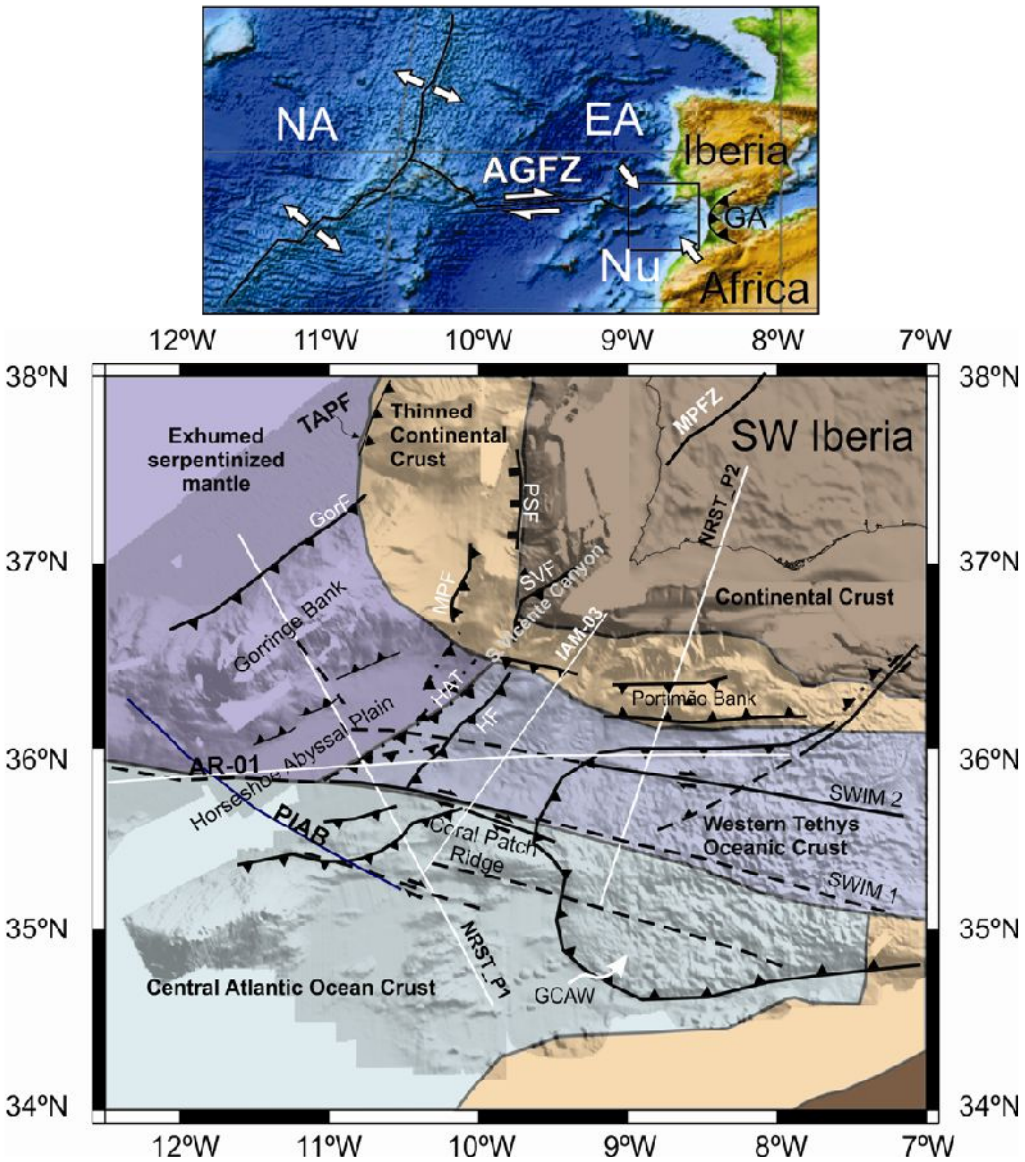

Figure I.1- Geodynamic setting of the studied area. On top is the location in the context of the present plate tectonic model (AGFZ- Azores Gibraltar Fracture Zone; EU-Eurasia, Nu-Nubia and NA-North America, the base is National Oceanic and Atmospheric Administration (NOAA),ETOPO1 Global Relief Model). On the bottom is a simplified tectonic map and the lithospheric domains in the Gulf of Cadiz (tectonic structures adapted from Duarte et al., 2013, lithospheric domains from NEAREST refraction profile P1 and schematic map in Martinez-Loriente et al, 2013, NEAREST refraction P2 in Sallàres et al., 2011, AR-01 Multichannel seismic (MCS) profile from Rovere et al, 2004 and IAM-03 MCS profile from Gonzalez et al, 1996). Abbreviations- GCAW- Gulf of Cadiz Accretionary Wedge; HAT- Horseshoe Abyssal plain Thrust HF-Horseshoe Fault; GorF-Gorringe Fault; MPF-Marquês de Pombal Fault; SVF-São Vicente Fault; Pereira de Sousa Fault and MPFZ- Messejana Plasencia Fault Zone, TAPF-Tagus Abyssal Plain Thrust and PIAB- Paleo Iberia-Africa plate Boundary (from Rovere et al., 2004)

This fragment of old oceanic crust is a remnant of a narrow oceanic basin of the western Alpine Tethys ocean, a transtensional corridor connecting the Tethyan and the Boreal seas from Jurassic to Cretaceous times. Accordingly, the first evidences for tectonic rifting in the area remount to Triassic times and extended to the early Cretaceous.

The Mesozoic continental extension was largely controlled by late Variscan inherited NE-SW extensional faults bounding rifting segments and future abyssal plains in the Southwest Iberia (Pereira and Alves, 2013). The 500 km long Messejana–Plasencia Fault zone (see Figure I.1) is intruded by a ~200 My doleritic dyke (Youbi et al., 2003). Offshore this fault merges with the São Vicente Fault and plays an important role in the recorded micro-seismicity (Terrinha et al., 2009, Pereira and Alves, 2013).

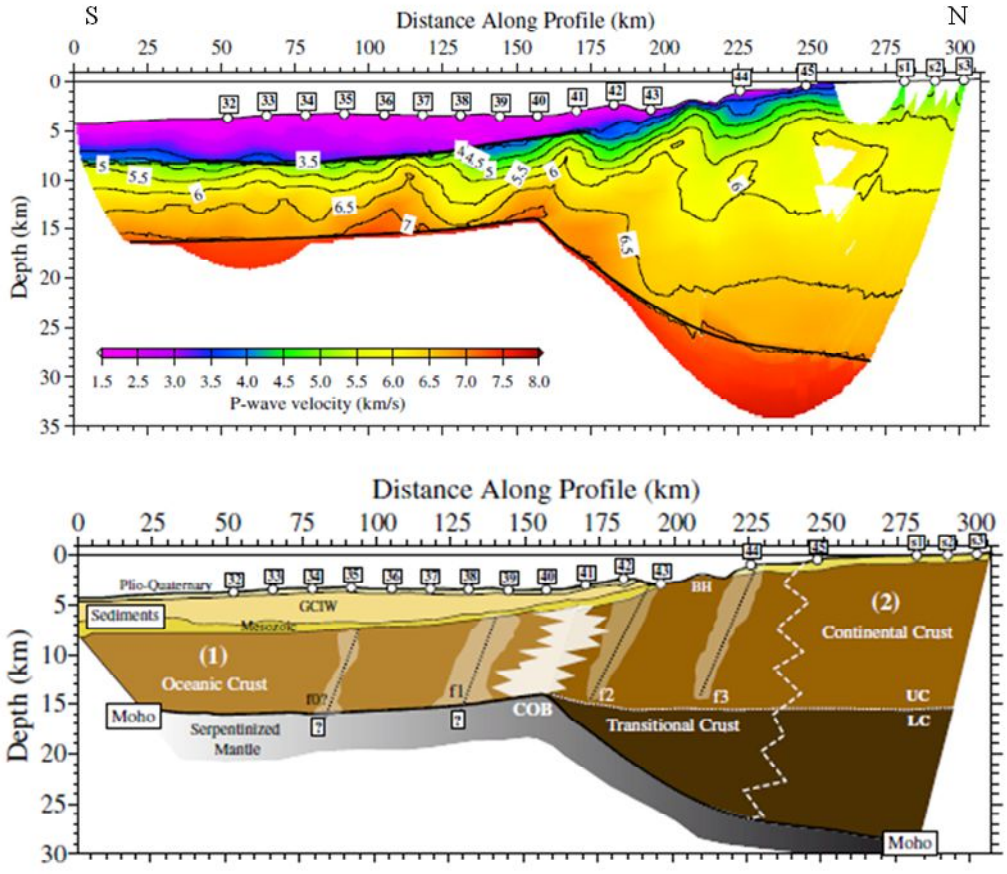

Figure I.2- NEAREST P2 Wide-angle and refraction profile, cutting across the central Gulf of Cadiz and extending to the Variscan continental margin in the Algarve, Southern Portugal (see location on Figure I.1). The top image shows the refraction profile and the bottom image is a schematic interpretation of the different crustal domains. Note that according to the obtained velocities model the ocean –continental transition is abrupt, around km 160. To the S, the profile revealed crustal seismic velocities probably defining a Jurassic oceanic Tethys realm. On top, a thick sediment cover related to the Gulf of Cadiz Accretionary Wedge (in the referenced work refered as imbricated wedge, Sallarès et al., 2011). To North, upper and lower crusts define the continental domain. Low upper mantle velocities in the profile were related to serpentinization.

To the South, in the Horseshoe Abyssal plain, the Horseshoe Abyssal plain Thrust (HAT - Martinez-Loriente et al, 2013, see Figure I.3) separates a band of

exhumed mantle (Sallarès et al., 2013) of the Gorringe Bank and Tagus Abyssal Plain from the Western Tethys Basin. Serpentinization in this region is in agreement with the refraction data results on upper mantle velocities between 7.2–7.4 km/s of Purdy (1986).

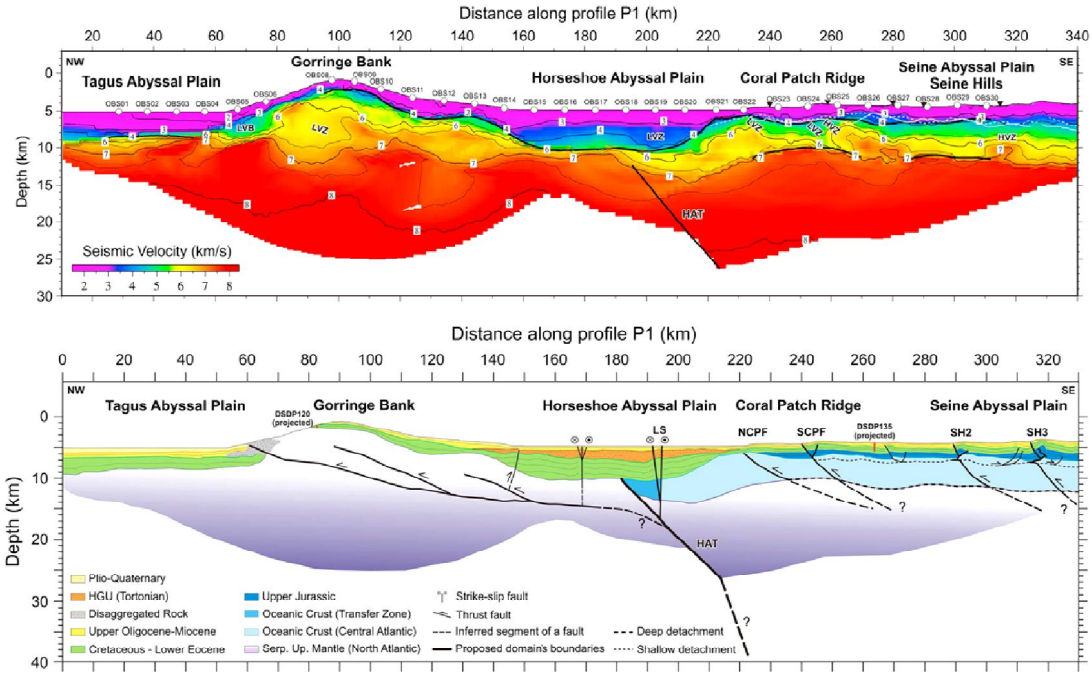

Figure I.3- NEAREST P1 Wide-angle and refraction profile, roughly NW-SE. cutting across the Tagus Abyssal Plain (TAP), the Gorringe Bank (GB), the Horseshoe Abyssal Plain (HAP), the Coral Patch Ridge (CPR) and ending at the Seine Abyssal Plain (SAP, Figure I.1 for location, Martinez-Loriente et al., 2013). The top image shows the refraction profile and the bottom image is a schematic interpretation of the different crustal domains. According to Sallarès et al. (2013), NW sector of is an area of exhumed serpentinized upper mantle related to the opening of the North Atlantic Ocean (from TAP to HAP). To the SE, from the HAP to the SAP was identified an Oceanic domain. The transition between the two domains is marked by the HAT -Horseshoe Abyssal plain Thrust.

Between rifting episodes, the Gulf of Cadiz area is marked by several inversion episodes, well described in the Algarve basin, lower Jurassic, middle Jurassic to upper Jurassic transition and upper Jurassic to early Cretaceous (Terrinha et al., 2002). These transient geodynamic setting was explained by combined processes: thermal subsiding episodes, local inversion of the oblique transtensional tectonics and ridge push compression (idem).

From Late Cretaceous-Paleogene to Miocene, the convergence between Africa and Iberia was accommodated by a South Iberia subduction. Srivastava et al (1990) proposed subduction of oceanic crust beneath Iberia in Miocene times based on palinspastic reconstructions of the oceanic magnetic anomalies. Lonergan and White (1997) and Gutscher et al. (2002, 2006) proposed for this region an east-dipping subduction slab below the Gibraltar Arc based on geometric constraints of the final consumption of the Tethyan ocean in the west Mediterranean and on tomography, respectively.

Duarte et al. (2013), based on a new tectonic map, proposed ongoing subduction propagation west of the Gibraltar oceanic slab into the Atlantic

Ocean resulting from the propagation of compressive stresses from the Gibraltar Arc and stresses related to the large-scale Africa-Eurasia convergence (see Figure I.4). Zitellini et al. (2009) mapped a 600 km long WNW-ESE striking dextral strike-slip faults (SWIM Faults, Figure I.1), connecting the Gloria Fault oceanic plate boundary to the Rif-Tell Fault Zone in northern Africa, proposing that this could constitutes the present day precursor of a transcurrent plate boundary in the region (Figure I.5). However, Cunha et al. (2012) based on thin-shell models for the lithosphere investigated the neotectonics of the Gulf Cadiz and concluded that models dominated by long SWIM faults (600km) would not reproduce the known deformation on the NE-SW, thrust system (e.g Horseshoe and Gorringe Faults). Neres et al. (2016) presented a neotectonic model comprising the area from the West Mediterranea across the Gloria Fault. This model confirms the Cunha et al (2012) results and favors the existence of an independent Alboran microplate.

Present day kinematic models for the Eurasia (Iberia) – Africa (Nubia) Plate Boundary, in the region of the Gulf of Cadiz, estimate a convergence of 4-5 mm/yr (Argus et al., 1989, DeMets et al., 1994, Nocquet and Calais, 2004, Stich et al., 2006), with an approximate WNW-ESE to NW-SE horizontal motion (DeMets et al., 1994, Calais et al., 2003 Fernandes et al., 2007 and Serpelloni et al. 2007). The average horizontal compression is defined as NW-SE, solution based on borehole, focal mechanisms and moment tensor analysis (Ribeiro et al. 1996, Borges et al., 2001, Stich et al., 2010, Heidbach et al,. 2008). Stress is accommodated in main active faults (see detailed descrition in section I.2) and major lithospheric transitions.

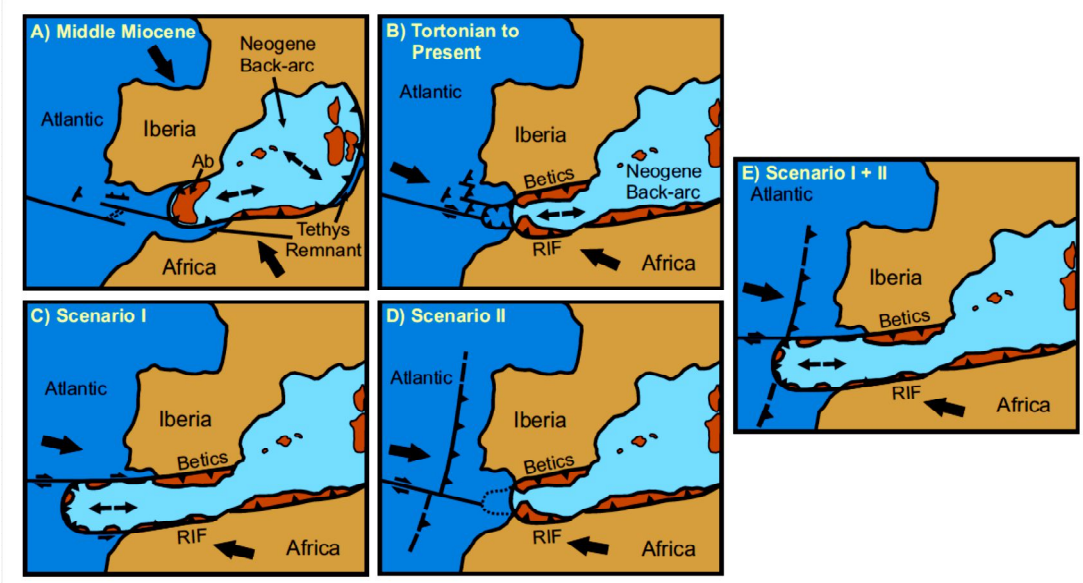

Figure I.4- Evolution of the Gulf of Cadiz (Duarte et al, 2013) from the Middle Miocene to present day (A-B) and three possible evolution scenarios (C-E).

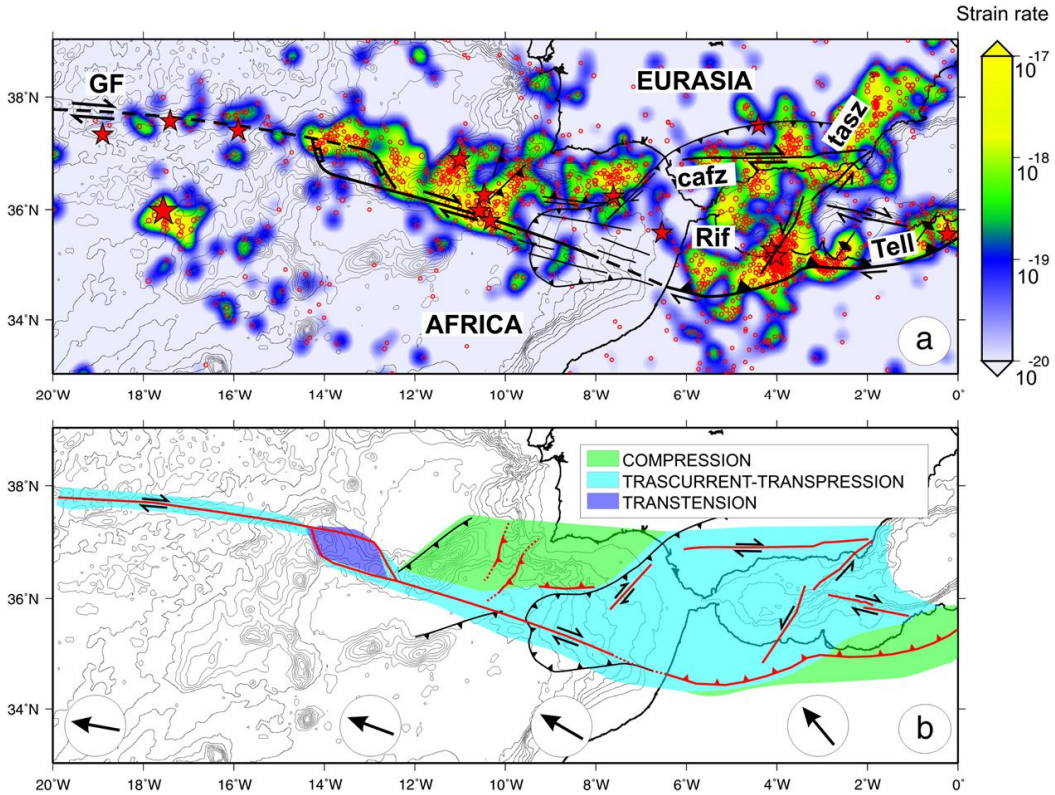

Figure I.5- Present Africa–Europe Plate Boundary proposed in Zitellini et al. (2009). a) The proposed plate boundary on top of seismic strain rate derived from the seismic events (red circles and stars). b) Main geodynamic domains and relative motion of Africa with respect to Eurasia (black arrows).

I.2.Main fault systems

The main active faults in the area were described in several studies trying to identify the main seismogenic and tsunamigenic sources in SW Iberia (e.g Zitelini et al. 2001, Gutscher et al., 2002; Gràcia et al.2003, Terrinha et al. 2003, Zitellini et al., 2004, Stich et al, 2007, Terrinha et al., 2009). Three main systems are presented (Figure I.1): the accretionary wedge and subduction slab; the N-S to NE-SW striking thrusts system (e.g. Marquês de Pombal Fault and Horseshoe Fault) and the WNW-ESE striking dextral strike-slip faults (SWIM fault system). An outline of these structures is presented next and resumed in the Table I.1.

Table I.1- A resume of the dimensions and average slip along the fault estimations for some of main active faults in the Gulf of Cadiz (data compiled from previous works).

Fault	Length (km)	Width (km)	Dip (max)	Area (km2)	slip (m)	Reference
SWIM 2 (LN)	130	50	90°	6500	6.3	Bartolome et al,. 2012
SWIM 1 (LS)	180	50	90°	9000	4.5	Bartolome et al,. 2012
HSF	150	120	45°	18031	10	Matias et al., 2013 (references therein)
GF	200	80	40°	16000	12	Matias et al., 2013 (references therein)
SVF	50	140	45°	7050	10	Matias et al., 2013 (references therein)
MPF	60	120	45°	7012	10	Matias et al., 2013 (references therein)
AW	180	210	6.5°	37800	10	Gutscher et al., 2009

The Accretionary wedge:

The accretionary wedge is a major westward directed shallow dipping thrust system, related to an active (or recently inactive) subduction zone under the Gibraltar Arc. In bathymetry is described as U-shaped west dipping morphology (e.g. Duarte et al, 2013). Internally, it is constituted by w-verging thrusts, stacking a sequence of deformed sediments on top of a package of underformed sediments, gently dipping towards the east (Figure I.6). According to Gutscher et al., (2002) this is tectonically driven (subduction related) rather than by gravity sliding along a west-dipping surface (e.g. Maldonado et al., 1999; Torelli et al., 1997).

The N-S to NE-SW striking thrusts system

The N-S to NE-SW thrust faults are related to prominent escarpments and root deep into the basement, possibly extending into the upper mantle (Figure I.6, Duarte et al., 2011).

The Marquês de Pombal Fault (MPF) is a thrust fault with a trace >50 km, with maximum uplift of 1100 m and the related deformed area is described as at least 100 km in length (e.g. Zitellini et al, 2001). The MPF, combined with a Back-Thrust Fault (BTF), were described as good candidates for the 1755 earthquake source in Zitellini et al. (2001). In the same study, a depth conversion of the AR-10 profile is presented (Figure I.7), showing that the geometry of the MPF-BTF system is consistent with a layer of hypocenters distribution between 16 and 18 km in depth, marking a weakness in the crust with a rupture area with the same order of magnitude as the 1755 event. In alternative, the HF has been proposed as an additional source area which combined with MPF, could explain the 1755 earthquake (Ribeiro et al., 2006). These two main tectonic structures would be connected by a transfer fault, striking WNW-ESE.

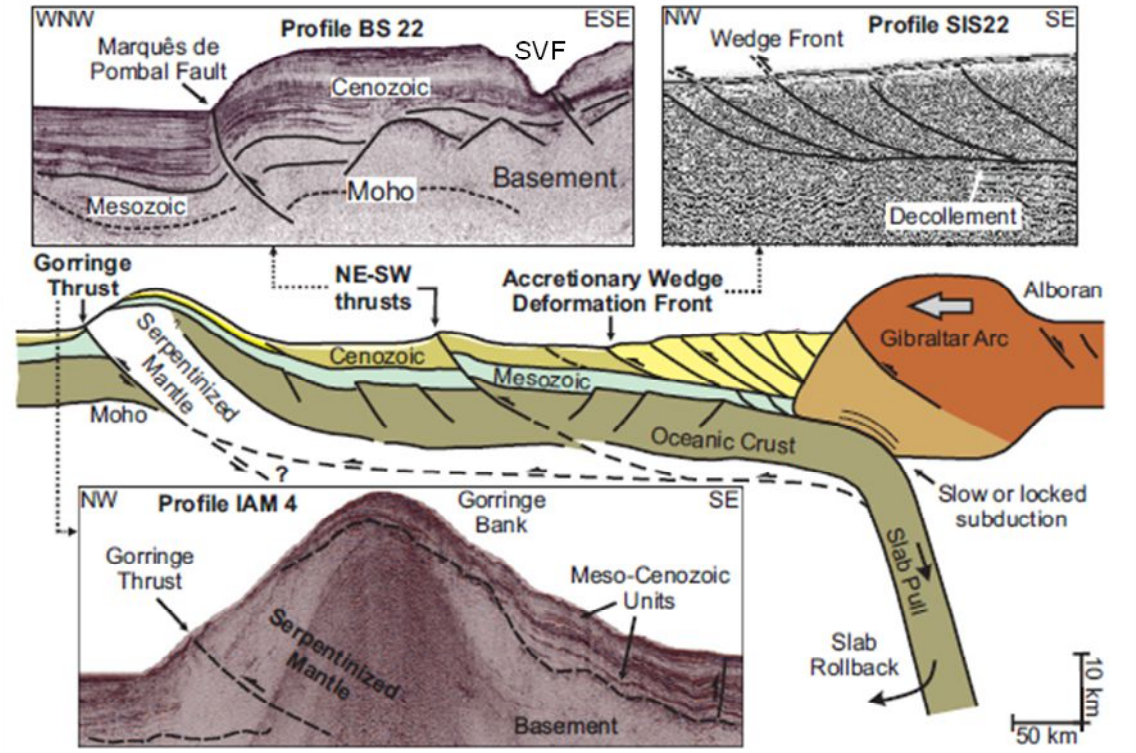

Figure I.6- NE-SW thrust fault system in the Gulf of Cadiz, including Gorringe, Horseshoe and Marquês de Pombal faults as well as the Accretionary Wedge. A schematic profile shows the relations between these structures and an east-dipping subduction zone (Profiles interpretation and schematic profile from Duarte et al., 2013).

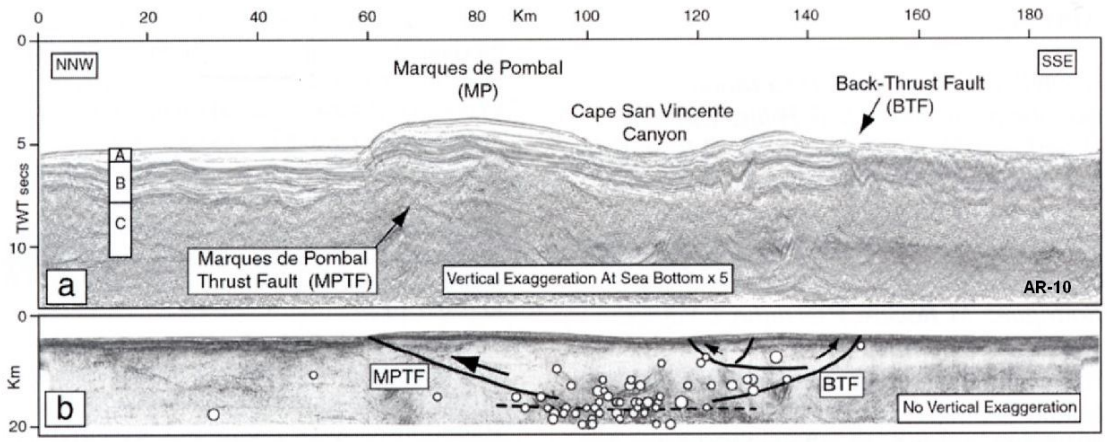

Figure I.7- AR-10 multichannel seismic profile (image from Zitellini *et al.*, 2001)-a) with post-stack time migration; b) Depth converted; A- syn-compression sediments, B- pre-compression sediments and C-acoustic basement defined as continental crust thinned during Eurasia-North Atlantic Mesozoic rift; Seismicity is from land network records from 1995 to 2000 (for details see figures 1-2 in Zitellini et al., 2001).

The Horseshoe Fault (HF) is a NE-SW striking thrust fault, deeply-rooted, cutting through the basement down to the Moho (?) (see Figure I.8, Martinez-Loriente et al., 2016) and displacing the seafloor (Terrinha et al., 2009; Duarte, 2011; Rosas et al., 2012, in appendix VI and Duarte et al., 2013). To the NE, the fault scarp has a maximum height of 1000m decreasing gradually towards the SW, the interference zone with the SWIM fault. In this particular area, new faults were identified referred as corner structures. These faults have a dominant oblique movement, mainly dextral transcurrent movement (Figure I.9, Rosas et al, 2012, in appendix VI).

The São Vicente Fault (SVF) strikes ≈NE-SW steeply dipping to the SE flanking the São Vicente Canyon (Figure I.6) with a reverse kinematic component. Pereira and Alves (2013) depict in detail the offshore extension of the Messejana-Plasencia Fault Zone (MPFZ, see Figure I.1), which comprehends the SVF. The onshore part of this fault is more than 500km long, cuts across Paleozoic folds and contains a tholeiitic basic dyke of ~200 Ma of age that can exceed 80m in width; these features attest for the deep origin of this fault, possibly cutting across the Moho.

The Gorringe Bank (GB) is a 5 km high seamount with a 9 m positive geoid anomaly and an elastic lithosphere thickness of 35km (Hayward et al., 1999, Jiménez-Munt et al., 2010 and references within). Girardeau et al. (1998) considered that the Gorringe Bank comprises a lithosphere composition mainly composed of serpentinized peridotites locally with a sheet-like gabbro intrusion, rare tholeiitic dikes and pillow-lavas. The present day structure, according to Jiménez-Munt et al. (2010), is controlled by a major NW verging, sub-crustal thrust fault - the Gorringe Fault (GorF in Figure I.1 and Figure I.6) with a ramp and flat geometry with at least 20 km shortening in 5-10 Ma (Late-middle

Miocene). Tectonic and seismic activities are testified by major mass wasting processes. Lo Iacono et al. (2012) and Valadares (2012) identified several slumps, slide scarps and mass movements in the Gorringe bank flanks.

The Horseshoe Abyssal plain Thrust (HAT-Figure I.8) was defined by Martinez-Loriente et al., (2013). It is a NE-SW trending, NW-verging tectonic structure that establishes the boundary between domains of Cretaceous exhumed serpentinized mantle and Jurassic oceanic crust (Figure I.1). More recently Martinez-Loriente et al., (2016) refined the NE-SW to a NNE-SSW trend, which eventually may link to the MPF.

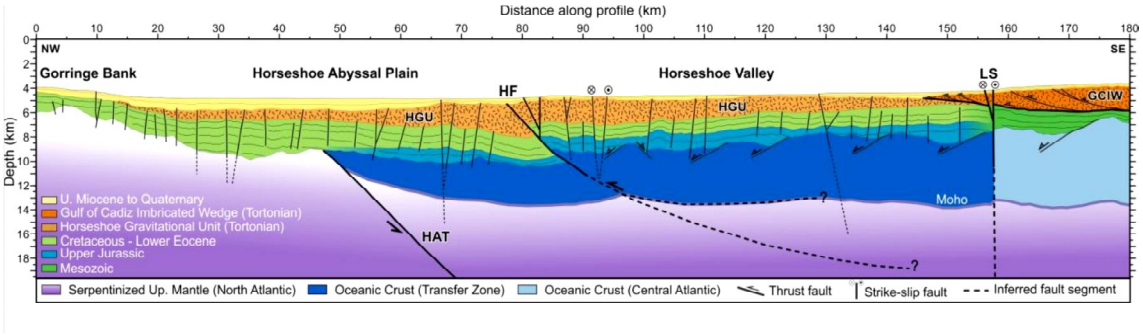

Figure I.8- Regional synthetic lithospheric cross-section from Martinez-Loriente et al., (2016) illustrating the HAT and HF in depth.

The SWIM faults

The SWIM Faults (SWIM stands for South West Iberia Margin) (Figure I.9) were firstly identified as WNW-ESE trending lineaments in MATESPRO swath bathymetry compilation (Terrinha et al, 2009 and Rosas et al., 2009) and later defined as vertical faults with the same trend in Zitellini et al., (2009). These faults host mud volcanoes and correspond to deep rooted dextral strike-slip faults, cutting through the Mesozoic basement, upper-Miocene sediments up to the sea floor present day sediments (Zitellini et al., 2009 and Rosas et al., 2009). In the basement these structures are, at least locally, related with pre-existent rift Mesozoic faults (Terrinha et al., 2009 and Duarte et al., 2011, in appendix VII). In both NEAREST refraction profiles P1 and P2, these structures are shown to extended into the oceanic crust (and possible into the upper mantle, Martínez-Loriente et al., 2013 and Sallarès et al., 2011). The SWIM faults bathymetric expression is clear to the East, to the north of the Coral Path Ridge, but become less prominent in the Horseshoe Abyssal Plain.

Neotectonic numerical modelling indicates that the SWIM faults should be regarded as discontinuous features (Cunha et al., 2012.) and not as mature lithospheric-scale features marking the present day plate boundary between Nubia and Eurasia as suggested by Zitellini et al. (2009).

According to analogue modelling in Duarte et al. (2011, in appendix VII) the intersection pattern of the SWIM faults with the Gulf of Cadiz Accretionary Wedge indicates that both tectonic structures are active in the Present.

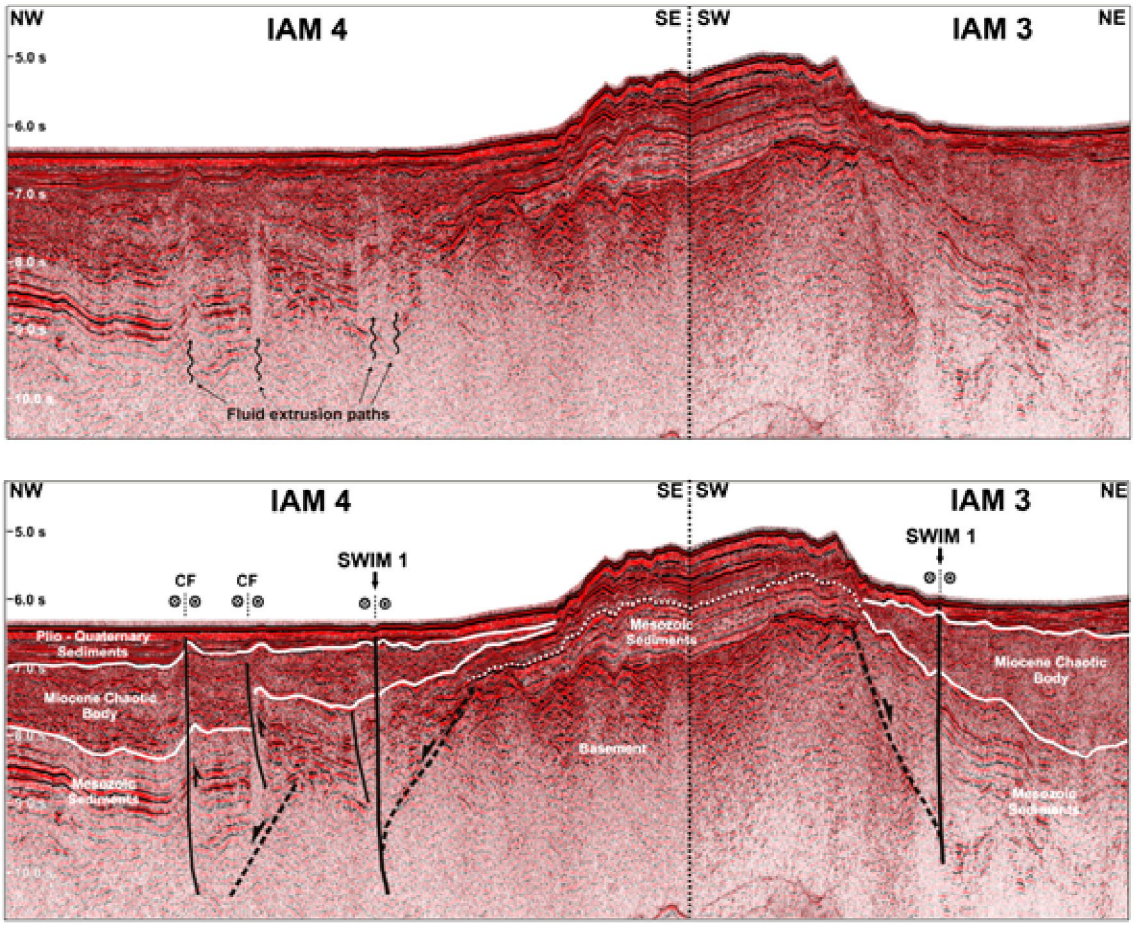

Figure I.9- SWIM 1 fault and corner faults interpretation from Rosas et al., (2012 in attachment).

I.3.Seismicity

I.3.1.Historical seismicity

The seismicity in the Gulf of Cadiz region is distributed, with events of low to intermediate magnitude, occasionally disturbed by strong earthquakes. An example is the 1st November 1755 earthquake (Figure I.10 and Figure I.11) which had estimated magnitude of 8.75 (Richter, 1958 and Johnston, 1996) or M=8.5 (Solares and Arroyo, 2004). This earthquake will be discussed with more detail in section I.3.1.

According to Carrilho et al. (2010) the historical period is considered until 1960. From that year on it was installed the World-Wide Standardized Seismograph Network. Within the historical seismicity few events are known until the medieval age as we can see in Figure I.10.

The 63 B.C. earthquake is the first known historical event in the area of the Gulf of Cadiz (Figure I.10 and Figure I.11). It affected mostly the Portugal and Galiza coasts and the estimated magnitude is 8.5 (Martins and Mendes Victor, 2001). An associated tsunami may have forced the population to escape from near coastal villages (Carrilho et al., 2010 and references therein). The 382 A.D earthquake with M≈7.0 (Martins and Mendes Victor, 2001) caused a large

destructive tsunami that is associated with the disappearing of an existing island (Baptista et al, 2007 and references therein). In 24th of August 1356, a large earthquake located in the Horseshoe Abyssal plain (M≈7.5, idem), was felt in all Iberian Peninsula. Reports of the damages are similar to the 1755 event; however no tsunami evidences were described (Carrilho et al., 2010).

In the 18th century, besides the 1755 earthquake, two other large earthquakes occurred in the area of the Algarve. The 6th of March 1719 earthquake was located in the area of Portimão. The estimated magnitude was 7.0 or lower according to Carrilho et al. (2010) and references therein, but the reported damages are restricted to Portimão and local villages. Also in Algarve, an earthquake struck Tavira on 27th December 1722. It was felt from the São Vicente cape to Spanish borders. It had a tsunami associated that flooded Tavira but had no significant effects in the other towns on the shore of Algarve. Baptista et al. (2007) based on numerical tsunami modelling and multichannel seismic profiles interpretation, estimated a magnitude ≈6.5 and the epicentre in the nearby submarine area, to the SSE of Tavira associated with NNE-SSW inverted thrust system, verging to WNW.

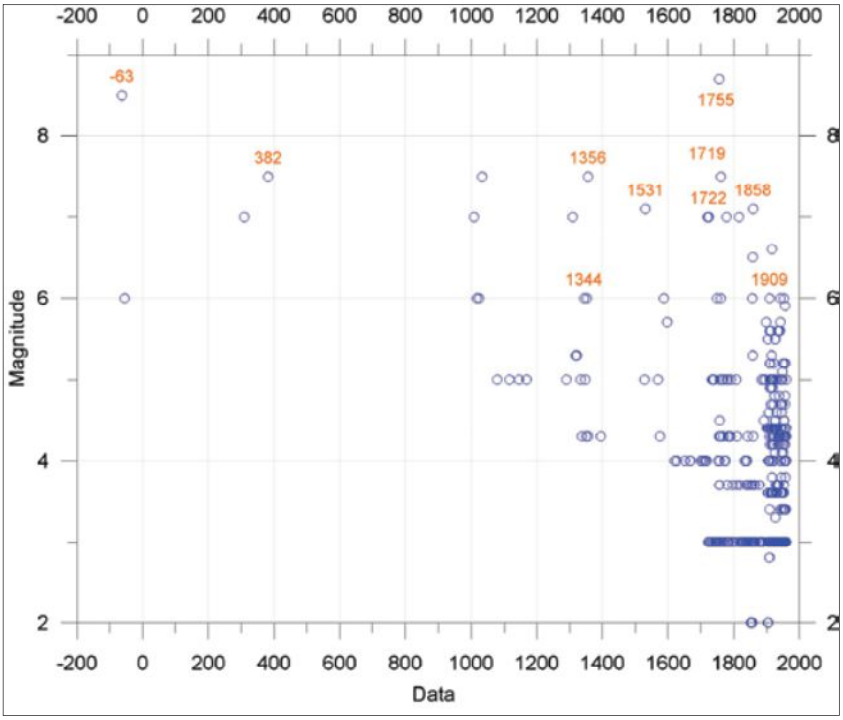

Figure I.10- Magnitudes distribution through time for historical earthquakes (from Carrilho et al., 2010)

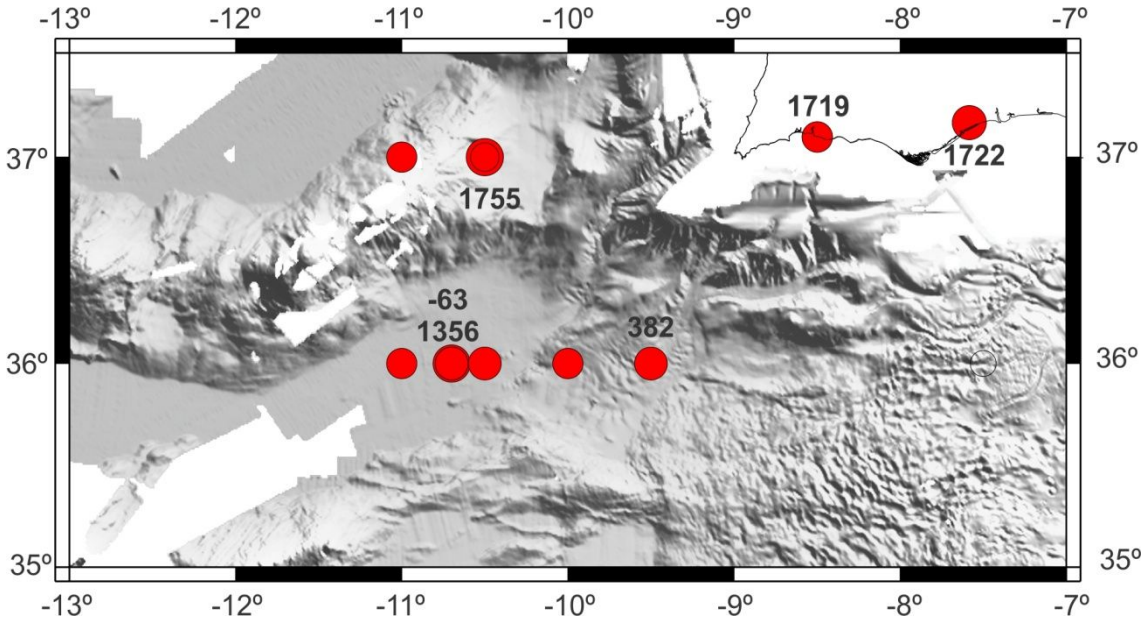

Figure I.11- Historical seismicity in the Gulf of Cadiz area. Events with M≥7, with both magnitude and "*locations"* from Martins and Mendes Victor (2001**)**

I.3.1.1.The 1st November 1755 earthquake and tsunami

The 1st November 1755 earthquake and tsunami was extensively studied over the years. There are several historical documents describing this event that was felt from Finland to the Azores and Cape Verde Islands. With estimated magnitudes ranging from 8.5 to 8.8, it is one of the most destructive earthquakes in the History of Europe. The tsunami invaded Lisbon downtown roughly 250m and 10-15m waves were reported in São Vicente Cape. Its effects were described in Madeira, Cadiz and Cornwall, with water agitation expressed in Scotland and Switzerland (Baptista and Miranda, 2009). Still, the tectonic source and mechanism of this event is a matter of discussion (see Figure I.12).

An estimation of the source characteristics were drawn by various authors in comparison with earthquakes from the instrumental record and/or based on event description and tsunami evidences. Johnston et al. (1996) suggested that the seismic source (based on isoseismal area, see Figure I.12) should have a fault length 180-200km, width 80 km and an average displacement of 10-14m. Accordingly, these authors proposed the northwestwards directed Gorringe fault (Figure I.1) as the possible seismogenic structure for this event. Gardin et al. (2007) based on simulation of ground motions also agree that the Gorringe bank should be the source area of this event. However, numerical models on tsunami propagation show incompatibility with this solution (Baptista et al, 1998).

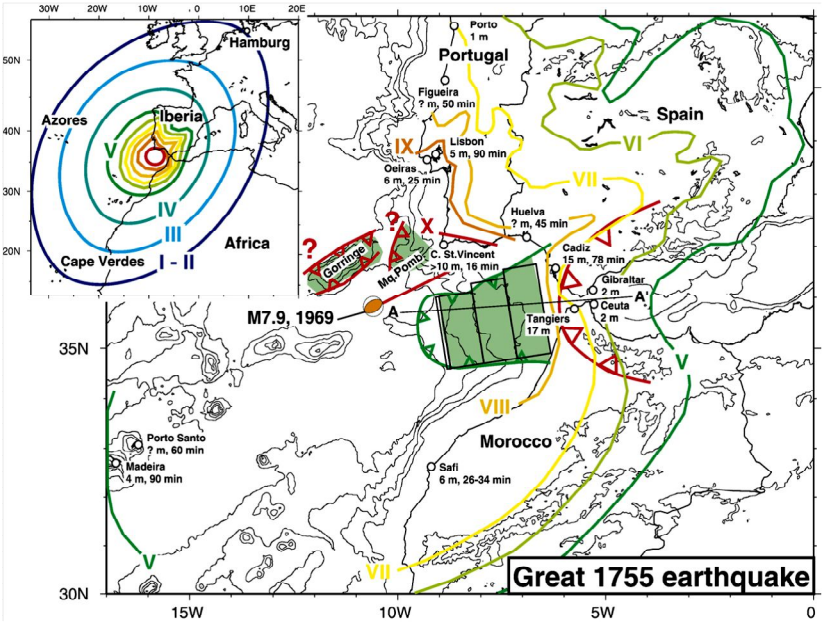

Figure I.12-The isoseismal lines for the 1755 earthquake and some of suggested source mechanism: *Marquês de Pombal* Thrust, Gorringe faults and east dipping subduction zone below Gibraltar arc. Also the location and focal mechanism of the 28th February 1969 earthquake (are from Gutscher et al, 2006).

The Marquês de Pombal Thrust fault -Back-Thrust system was also proposed by Zitellini et al (2001).The authors associated this system to the seismicity observed below the São Vicente Canyon. These events would mimic the rupture area of the 1755 Lisbon Earthquake (Figure I.7. and Figure I.12)

Ribeiro et al. (2006) discuss the different source solutions proposed for this event. Besides the limitations referred to the Gorringe Bank Fault solution, these authors point out that the MPF-BTF system does not fulfil rupture area requirements. It is described other possibilities adding complement source areas to this system: a) Horseshoe Fault (HsF); b) Pereira de Sousa- Principe de Avis Fault system; c) Guadalquivir bank Fault (also in Baptista et al., 2003). The authors favour the HsF-MPT solution based on the similar orientation and almost geometric continuity between both fault zones, which facilitate strain/displacement transfer between them. Other complex sources are described by Vilanova et al., (2004) including the Lower Tagus Valley (LTV) fault near Lisbon. This fault is located in the Tagus River valley and would explain the strong motion in Lisbon. According to these authors the isoseismic pattern in Lisbon cannot be explained by an offshore source alone, arguing that the main offshore shock triggered an onshore rupture in the LTV fault.

Gutscher et al. (2002, 2004 and 2006) and Thiebot and Gutscher (2006) proposed that the seismogenic source is related with an east-dipping active subduction zone imaged on seismic tomography, below the Gibraltar Arc, also related with deep seismicity in Granada region. Gutscher et al. (2006) also suggested that besides the subduction zone that would explain the seismic moment associated with this event, an additional source located to the NW (in

the area of the Gorringe or northern Gulf of Cadiz) is needed to account for the tsunami descriptions.

Stich et al. (2007) scaled the source parameters of the 12th February 2007 to the 1755 event, suggesting a fault length of 230 to 315 km and an average slip of 8.5 to 11.7m, for a seismic moment between $7 \times 10^{21} Nm$ and $14 \times 10^{21} Nm$ for Mw= 8.5 and 8.7, respectively. The authors suggest that an active subduction is not mandatory to generate the 1755 earthquake and agree in a composite multi-fault rupture including the Horseshoe fault and any other fault (eg. Marquês de Pombal or São Vicente faults).

Matias et al. (2013) proposed an improved method to define fault models for tsunamigenic events in the Gulf of Cadiz. The authors point out that a Mw 8.5-8.75 earthquake, with a seismic moment of $7.16 \times 10^{21} Nm$ to $1.70 \times 10^{22} Nm$, the rupture length would be of 143 to 220 km, the width from 119 to 120 km and an average displacement of 6.44 and 9.90m, respectively. This is true for a source area in the Gulf of Cadiz but outside the accretionary wedge. Within the accretionary wedge the source dimensions are complex based on the parameters identified in subduction zones elsewhere. Accordingly the seismic source would vary between a length of 282-315 km, a width 79-105 km and an average displacement ranging from 7.8-10 m, for Mw 8.5 to 8.75, respectively. The source parameters in the accretionary wedge area are roughly in agreement with Sitch et al. (2007) calculations.

More recently, Zitellini et al. (2009) suggested an alternative source solution combining a 600km long active fault zone WNW-ESE dextral strike-slip with the Horseshoe fault. This solution would comprise a total rupture area of more than 400km, compatible with the expected parameters to the 1755 event.

I.3.2.Instrumental seismicity

In the instrumental record, the Gulf of Cadiz is the source area of the Ms≈8.0 28th February 1969 earthquake (Figure I.13). The hypocenter was located between 22-33 km depth (López-Arroyo & Udias, 1972 and Fukao, 1973) and the focal mechanism solutions point-out to a thrust with small strike-slip movement, striking NE-SW, parallel to the Gorringe fault and dipping either NW (Fukao, 1973) or SE (López-Arroyo & Udias, 1972). The aftershock sequence had one Mb≈5.5 event with similar fault plane solution but located 50 ± 5 km deep (Grimison et al., 1986) or 29 km (Buforn et al., 2004), in the upper mantle.

To the east is the location of the 12 February 2007, with Mw ≈ 6.0 and hypocenter at 40 km beneath the seafloor. The moment tensor inversion showed a thrust with small strike-slip movement. The preferred fault plane is discussed both in Stich et al. (2007) and Custódio at al. (2011) with contradicting results. Stich et al. (2007) indicate a NE-SW solution parallel to the Horseshoe Fault but located in the footwall of this fault and dipping in the opposite direction. However, Custódio et al. (2011) refer to a WNW-ESE

solution, dipping 46º SW. For all the above cases seismic activity diverges from the known active faults in the Gulf of Cadiz region. This event was also studied by Buforn et al, (2007) and selected the same preferred fault plane as Stich et al. (2007). Buforn et a. (2007) estimated Mw=5.9, a rupture area ≈160km^2, with 14 and 12.5 km in length and width, respectively. The maximum displacement is of 0.63m. Much smaller is Stich et al. (2007) calculated dimension: an average area of 54km^2, with fault length 8.2 and width 6.5km.

Other important events are the 29th July 2003 with Mw=5.3 at 40 km depth, in the same area of the 12 February 2007 event. Pro et al. (2012) calculated the source parameters: an area of 50 km^2 and an average displacement of 0.08m. The focal mechanism is also similar to the 12 February 2007 earthquake. Finally, more recently is the 2009, 17th December earthquake with Mw=5.5, with a rupture area of 113km^2 and an average slip of 0.08. The moment tensor corresponds to a dip-slip solution with a nearly NNE-SSW sub-vertical solution or a sub-horizontal plane NNW-SSE. The event was located in the São Vicente canyon, at a depth of 36 km (Pro et al., 2012).

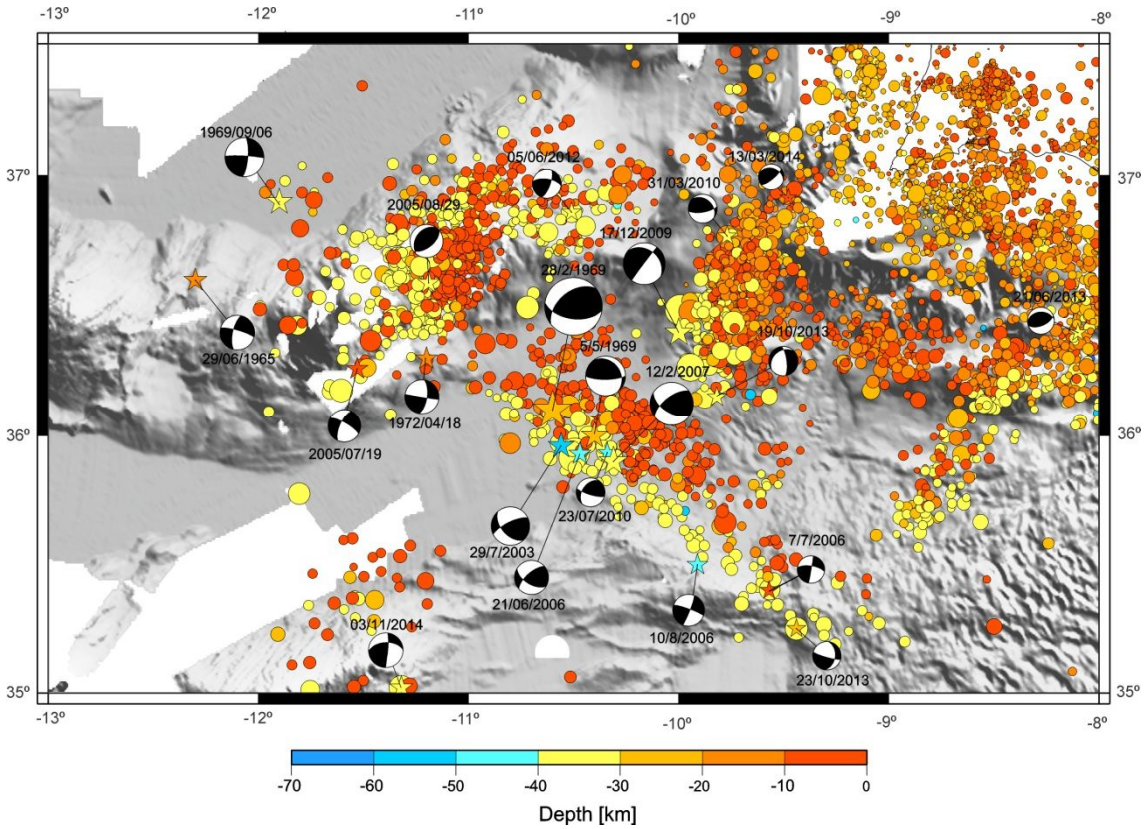

Figure I.13- Instrumental seismicity in the Gulf of Cadiz area (circles define low to intermediate magnitude earthquakes, 2000-2015, recorded by Instituto Português do Mar e da Atmosfera permanent seismic network, stars define the location of the highest instrumental events recorded in this area, from Borges et al., 2001 references within, Stich et al, 2010 and Custódio et al., 2016).

The seismic energy release during historical and instrumental periods (until 2003) is presented in Carrilho (2005). The author compiled the information from four different catalogues restricted to M≥4 earthquakes. We show just three in Figure I.14: In Figure I.14A is shown a catalogue from the beginning of the

seismic network, in the early 60's to middle 80's (sec XX). It is clear that released energy pattern in our study area is completely disturbed and dominated by M=8, 28th February 1969 earthquake. During the period shown in Figure I.14B no high magnitude earthquakes were recorded. In this case, we can observe a different pattern defined by the released seismic energy in the Gulf of Cadiz. NW-SE alignments, sub-parallel to SH-max and a roughly NE-SW pattern coincident with the Gorringe Bank. Both features are coincident with dense seismic activity in Figure I.13. In Figure I.14C, all events are included since the first historical earthquake until 2003. The pattern is completely saturated by the 1755 Lisbon earthquake.

The patterns observed in Figure I.14 are somehow biased because they result from monitoring off-shore seismic activity (in the Gulf of Cadiz) based on an on-shore land permanent network. Carrilho (2005) presents an important study on the seismicity in the Southwest Portugal Mainland. In his final remarks refers that limitation on events locations resulting from land-network geographical distribution can be overcome by ocean bottom stations network in Gulf of Cadiz.

Preliminary results from NEAREST OBS experiment were presented in Geissler *et al.* (2010). The study is centred in a catalogue with 36 earthquakes (ML 2.2 to 4.8). These events are concentrated at 40–60 km depth, near the base of the seismogenic layer and roughly align along two perpendicular directions, NNE-SSW and WNW-ESE striking structures. Each direction defines a hypocenters cluster, along the São Vicente canyon and the Horseshoe abyssal plain, respectively. The study points out the necessity to evaluate seismic activity by means of OBS networks, since detailed information can be gained on hypocenter locations and fault kinematics (Geissler *et al.*, 2010).

Custódio et al, (2015, 2016) also reported the existence of hypocentres clustering in the Gulf of Cadiz, in the Gorringe Bank, the Horseshoe abyssal plain, the São Vicente Canyon and in the Guadalquivir Bank. According to these authors, offshore seismicity shows intriguing features that can be better explored with more accurate depth estimates as well as better estimates of absolute epicentral locations. These would promote a more adequate dataset to envision the relation between offshore clusters and seismo-tectonic structures.

More recently Grevemeyer et al. (2016) reported the results of a temporary OBS network deployment in the area of the Portimão bank and the accretionary wedge. The experiment was 6 months long and resulted in a dataset with 86 events located in ≥6 stations. Most seismicity was located in the Portimão bank with depth between 15 and 40 km. If compared with Sallarès et al. (2011) P2-NEAREST refraction profile, these depth ranges correspond to lower continental crust or uppermost mantle. The existence of seismicity at these domains is rare. According to Grevemeyer et al. (2016), it might be caused by the specific geological setting, where deformation occurs in cool lithosphere of Mesozoic age, resulting in a strong lower crust and upper continental mantle.

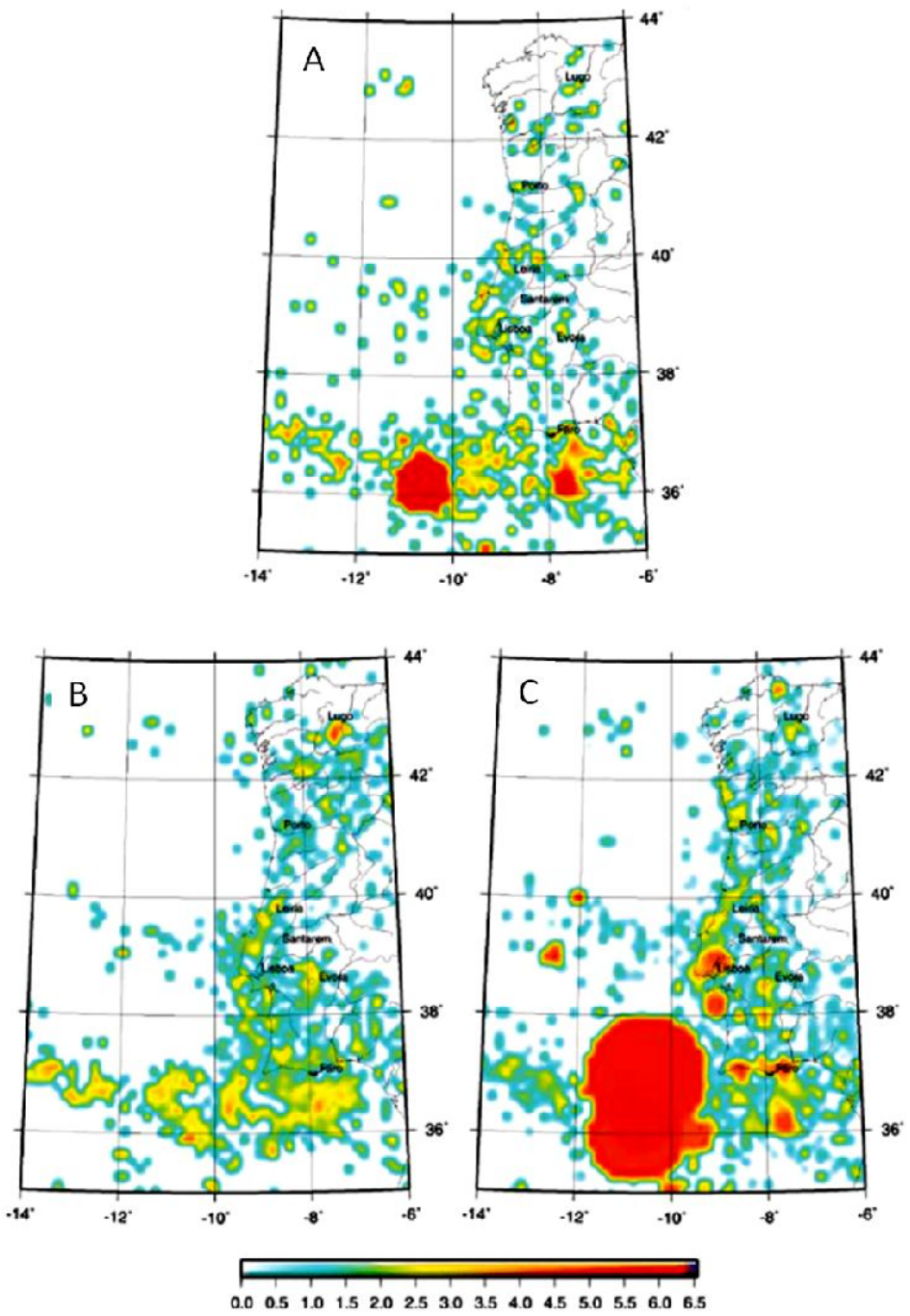

Figure I.14- Seismic energy release in Portugal and adjacent areas for events with M≥4: A-from 1961-1985; B-from 1995-2003; C- From 63 BC to 2003 (from Carrilho et al., 2010).

I.3.3.Fault rupture parameters for Mw≥4 events in the Gulf of Cadiz

Wells and Coppersmith (1994) is a classic work that uses empirical formulations that compare seismic events with fault rupture areas. However, this paper is based on a global dataset that included exclusively shallow-focus continental interplate or intraplate earthquakes of magnitudes greater than approximately 4.5 which are not comparable with the Gulf of Cadiz geodynamic setting. Instead, Matias et al., 2013 formulation was specifically conceived for the Gulf of Cadiz area, although for large magnitude events.

The relation between fault dimensional parameters and the seismic event is established by the seismic moment definition:

$$M_o = \mu A u$$

Where μ is the shear modulus, A is the fault rupture area (L*W) and u is the average slip along the fault. We can access the M_o from the moment magnitude M_w using the following relation:

$$M_w = \frac{\log M_o}{1.5} - 6.07,$$

with M_o in Nm (based on IASPEI recommendation).

So, for a given M_w we can calculate the seismic moment. Since we are working with NEAREST catalogue, we only have access to local magnitude estimations. There is no clear relation between this magnitude estimation and seismic moment. We will use the moment magnitude estimations for 3 common events reported in Stich et al. (2010). Also, we deduced the fault parameters for the larger earthquakes in the Gulf of Cadiz and the area linking to the Gloria fault system. For events rupturing in the crust we assumed a $\mu = 4.0 \times 10^{10}$ Pa, for crust and mantle rupture $\mu = 6.5 \times 10^{10}$ Pa and finally within the mantle $\mu = 7.0 \times 10^{10}$ Pa (based on Matias et al, 2013 and references within). We assume based on the available refraction data that the Moho depth is between 10km and 15km. To estimate fault rupture we used the following definitions based on Matias et al., 2013:

$$W = \frac{L}{1.2}$$

$$u = \frac{\alpha \times L}{4}$$

$$L = \sqrt[3]{\frac{M_o \times 4.8}{\mu \times \alpha}}$$

With $\alpha = 1.8 \times 10^{-5}$. The results for Mw≥4 earthquakes in the Gulf of Cadiz are presented in the Table I.2.

Table I.2-Fault rupture parameters for Mw≥4 earthquakes in the Gulf of Cadiz

Event	LAT	LONG	DEPTH	Mw	Mo	L (km)	W (km)	D (m)	D max (m)	A (km2)	Reference	Area
19-07-2005	36.260	-11.530	10	4.5	7.16E+15	1.62	1.35	0.07	0.15	2.18	Stich et al., 2010	Gulf of Cadiz
07-07-2006	35.400	-9.570	8	3.8	6.38E+14	0.72	0.60	0.03	0.07	0.44	Stich et al., 2010	Gulf of Cadiz
28-02-1969	36.100	-10.600	22	7.8	6.38E+20	63.97	53.31	2.88	5.76	3410	Fukao 1973	Gulf of Cadiz
05-05-1969	36.000	-10.400	29	5.5	2.26E+17	4.53	3.77	0.20	0.41	17.1	Buforn_et al.1988	Gulf of Cadiz
06-09-1969	36.900	-11.900	35	5.4	1.60E+17	4.04	3.36	0.18	0.36	13.6	Buforn_et al.1988	Gulf of Cadiz
29-07-2003	35.800	-10.600	30	5.3	1.13E+17	3.60	3.00	0.16	0.32	10.8	Pro_et al. 2013	Gulf of Cadiz
13-12-2004	36.300	-9.900	53	4.9	2.85E+16	2.21	1.85	0.10	0.20	4.09	Pro_et al. 2013	Gulf of Cadiz
29-08-2005	36.590	-11.190	40	4.6	1.01E+16	1.57	1.31	0.07	0.14	2.05	Stich et al., 2010	Gulf of Cadiz
21-06-2006	35.930	-10.470	50	4.7	1.43E+16	1.76	1.47	0.08	0.16	2.58	Stich et al., 2010	Gulf of Cadiz
10-08-2006	35.500	-9.910	50	4.4	5.07E+15	1.25	1.04	0.06	0.11	1.29	Stich et al., 2010	Gulf of Cadiz
12-02-2007	35.900	10.310	50	6.0	1.27E+18	8.05	6.71	0.36	0.72	54	Stich et al., 2010	Gulf of Cadiz
11-01-2008	36.490	-9.990	50	4.5	7.16E+15	1.40	1.16	0.06	0.13	1.63	Stich et al., 2010	Gulf of Cadiz
10-05-2008	35.970	-10.770	50	3.9	9.01E+14	0.70	0.58	0.03	0.06	0.41	Stich et al., 2010	Gulf of Cadiz
17-07-2008	36.240	-9.890	60	3.9	9.01E+14	0.70	0.58	0.03	0.06	0.41	Stich et al., 2010	Gulf of Cadiz
17-12-2009	36.500	-10.000	56	5.5	2.26E+17	4.53	3.77	0.20	0.41	17.1	Pro_et al. 2013	Gulf of Cadiz

I.4.Earthquakes dynamics and seismogenic limits

Faults move at different speeds, ranging from m/s during an earthquake to cm/year at tectonic plate rates. Accordingly, slip is accommodated by slow-slip creep, slow-slip seismic event and stick-slip. It is unclear how the transition between these slip mechanisms occurs (Peng and Gomberg, 2010). Nevertheless, it seems that slip is largely dependent on specific characteristics of fault zones, such as frictional proprieties (e,g Sholz, 1998, Rice and Cocco, 2005, Peng and Gomberg, 2010).

It appears that frictional stability in fault zones is a key element on earthquakes generation, since earthquakes will occur mostly in pre-existing fault zones or anisotropy planes and rarely at newly formed fault planes. Brace and Byerlee (1966) defined that the earthquake cycle results from a stick-slip frictional instability. The earthquake is the slip event and the stick period would explain interseismic elastic strain accumulation interval. The transition from one stage to another depends on the nature of friction in the faults.

Scholz (1998) explained that seismogenesis is determined by frictional stability and restricted to areas of unstable friction. This parameter was studied for different rocks through experimental tests, resulting in several friction laws. The following example is the one that best explains observation and it was given by the Dieterich-Ruina law (in Sholz, 1998).

I.4.1.Friction stability laws, aseismic and seismic slip

The rate and the state of friction law is given by

$$\tau_{ss} = (\sigma - p)[\mu_0 + (a - b)\ln(V/V_0)]$$

Where τ_{ss} is the steady–state frictional strength and dependent on the slip rate, V, effective normal stress $(\sigma - p)$, where σ is normal stress and p is the pore fluid pressure in the fault. The initial friction coefficient is given by μ_0 and the initial steady-state velocity is defined by V_0, a defines the direct frictional response to the increase of slip velocity increase while b describes the frictional response in reverse transition (fast to slow, see Figure I.15). For $(a - b) > 0$, the fault segment has velocity-strengthening behaviour, so remains stable (creep) at seismic slip velocities. While for $(a - b) < 0$, the fault segment has velocity-weakening behaviour which results in unstable and potentially seismogenic area. This parameter is primarily dependent on material proprieties, resulting that some lithologies would favour velocity weakening behaviour while others would have a velocity strengthening behaviour; seismic and aseismic, respectively.

The temperature has an essential control on the $(a - b)$ parameter. At low temperatures $(a - b)$ can be negative and progressively become positive with the increase of temperature. This transition is dependent in the mineral content

of the fault zone. For granite, as is exemplified in Sholz (1998), the temperature transition is 300ºC, coincident the onset of crystal plasticity of quartz. The depth in which this transition occurs depends on the local temperature gradient. According to the same author, this would explain the depth limit of earthquakes in the continental crust.

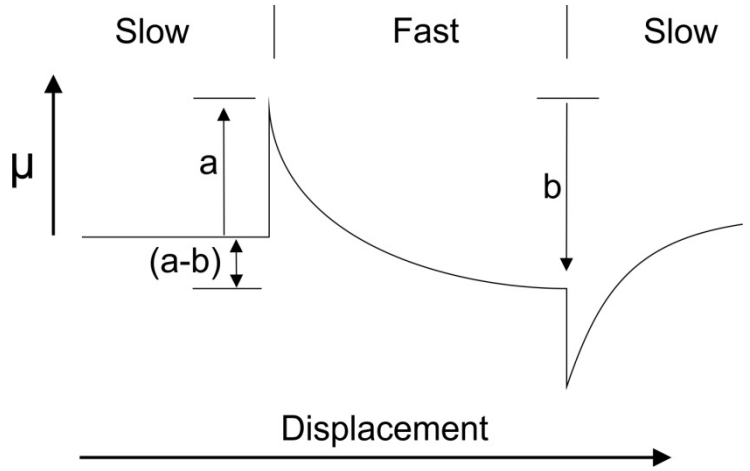

Figure I.15- A schematic representation of frictional (μ) response to variation on the velocity of displacement in a rock experimental test. Note that *a* defines the frictional response to slip rate increase while *b* describes an evolutionary response with velocity decrease. The difference between a-b defines the material response to changes in slip rate (for more details see text).Steady-state weakening.

I.4.2.Dynamic weakening of the fault zone and the transition between aseismic and seismic slip behavior

The transition between aseismic stable creep and unstable stick-slip behavior is not well understood and often assumed to be separated in space and to occur on two different types of fault segment (Noda and Lapusta, 2013).

These authors proposed a numerical model of a planar fault zone with heterogeneous rheology. In the model stable, creeping segments of a fault become unstable due to dynamic weakening. The rheological proprieties of the model was based on the laboratory measurements in samples from Mw 7.6 1999 Chi-Chi earthquake.

In detail the model included two patches. Patch A with small dynamic weakening, $(a-b)<0$, tending to seismic slip and Patch B, with $(a-b)>0$, prone to creeping, with lower permeability and therefore more susceptible co-seismic weakening due to thermal pressurization of pore fluids. The two patches were surrounding by steady area, moving at the representative plate rate. The model results show frequent earthquakes activity in patch A. Only large earthquakes reach Patch B. In this last case, slip is larger in patch B. During the experiments, Patch B showed complex rheological behaviour: creeping at tectonic strain rates, seismic slip contaminated by large events originated from Patch A, and locked.

Complex rupture patterns were also observed resulting from the interaction between the two patches. In a simulation of the Tohoku-Oki earthquake (Mw=9)

the slip was firstly propagated mostly to the Patch A. Next, thermal pressurization of Patch B promoted large local slip. This rupture increased stress concentration in Patch A causing re-rupture of the area.

The authors conclude that fluids can cause stable fault segments to accumulate great amounts of slip, due to thermal fluid pressurization during high slip rates. Understanding the possible contribution of aseismic slip segments during co-seismic slip is fundamental to evaluate seismic hazard of not only of subduction zones but also of large strike-slip faults.

I.4.2.1.Serpentinization as a weakening mechanism

Serpentinization is present at several geodynamic settings where water interacts with ultramafic rocks. Accordingly, it is common during continental extension in slow spreading centres; oceanic rifts and transform faults; in lithospheric scale strike-slip faults and in subduction zones. Serpentinites have a distinctive rheological behaviour that results in an effective control on tectonic processes. The role of serpentinization on strain localization, seismic slip and creep control at fault zones and of dehydration reaction on seismicity distribution in subduction zones has been broadly studied both by experimental and nature observations (Guillot et al., 2015).

One key finding is that slightly serpentinized rocks have the rheology of pure serpentinites. Based on mechanical data, Escartin et al. (2001) demonstrate that even for serpentine contents as low as 10 %, deformation is mostly accommodated along serpentinite bearing grain boundaries while olivine remains intact. Experiments demonstrated that serpentinization in fault zones, even if in lower percentage, will weaken and promote strain localization.

Amiguet et al. (2013) studied the deformation mechanism and rheology of serpentinites (lizardite and antigorite) in experiments and nature. Lizardite is described as one of the most common serpentinite minerals at low temperatures. It is stable at temperatures <320°C and at pressures <0.7 GPa above these values starts the transition to antigorite. At natural strain rates Lizardite shows brittle behavior and move towards a transition state at relative shallow depths and a shear stress > 100 MPa. Down to the deeper part of the crustal faults, lizardite is ductile by plastic flow: glide and/or dissolution precipitation. Also, lizardite has frictional proprieties with coefficient of internal friction (μ_F) ≈0.35, below most rocks (0.5 <μ_F < 0.8) resulting in lower frictional strength than expected based on Beyerlee law. Subsequently, the presence of lizardite in oceanic transform faults could explain the weakness of these faults. Antigorite is the high temperature serpentine mineral. Ductile behavior starts at roughly 30km in depth and a pressure of 1GPa, extending down to ≈90km deep (or at >700°C) where dehydration starts.

Another shallow depth serpentinite species is chrysotile. This mineral is less common than lizardite, but it is more stable at high water/rock ratios. Moore and

Lockner (2004) evaluated experimentally the variation of this mineral μ_F with effective normal stress and temperature variation. At temperatures below 100ºC and low stress (<50 MPa), μ_F=0.1; at high normal stress and temperature (≈281ºC and 200MPa) the frictional strength or μ_F is maximum ≈0.55. It is worthwhile noticing that at temperatures below 100ºC, chrysotile shows velocity strengthening at all strain-rates, and velocity weakening, in all experiments, at 281ºC. At intermediate temperatures, the authors reported a combination of the two behaviours. This pattern is in agreement with the seismic and creep observation in large strike-slip faults such as Hayward Fault, aseismic at shallow depth but probably locked bellow 5km depth, nevertheless associated with large earthquakes (Moore and Lockner, 2004).

High velocity friction experiments disclose dynamic weakening of serpentinite at seismic slip rates. According to Kohli et al. (2011) serpentinite displays velocity-strengthening behaviour at plate tectonic slip rates but dynamic weakening at seismic slip velocities. The experiments indicate that only a few millimeters of slip may be required at near-seismic velocities to achieve a weakened frictional state. Permanent frictional weakening may be related with Antigorite dehydration into talc, olivine and water (Kohli et al, 2011). Co-seismic dehydration of serpentinite, during large earthquakes, would lead to thermal pressurization and consequent weakening of the fault zone (Lin et al, 2013).

I.4.3.The depth limit of the seismogenic zone

The strength of the lithosphere is a function of composition, crustal thickness, and geotherm (Ranalli and Murphy, 1987). Accordingly, these variables will also control the depth limit of the seismogenic zone.

The rheological model of the oceanic lithosphere is defined by a strong brittle upper cover overlying a soft ductile layer (e.g. Mckenzie et al., 2005). The brittle strength will increase as pressure increases with depth and ductile strength will decrease drastically as temperature increases. The brittle-ductile transition (BDT) matches with the 600ºC isotherm and defines the depth limit of the earthquakes. It is also noteworthy that the 600ºC isotherm coincides with the transition between the velocity weakening to velocity strengthening of the olivine (Boettcher et al., 2007).

In the continental lithosphere rheology is more complex. According to some authors the seismogenesis is almost restricted to the crustal layer and there are little evidences for upper mantle earthquakes (Maggi et al., 2000). If restricted to the upper crustal levels, then quartz is generally the phase controlling the bulk rheology of the upper continental crust (e.g Afonso and Ranalli, 2004, references therein). Earthquakes in the mantle are rare and also limited to the temperatures below the 600ºC.

At continental margins, in the continent –ocean transition zone, lithospheric rheology reflects a compositional transition between oceanic and continental

domains. Accordingly, seismicity may be found at depths below from what is expected at continental domains but above or at the limit of the adjacent oceanic domain (Craig et al, 2011).

I.5.Thesis outline

The current chapter, chapter I, introduces the study case: background concepts and geodynamic setting.

Chapter II –Introduces the geophysical data and a background on the applied methodologies.

Chapter III- Describes the seismological studies: 1) processing NEAREST network experiment data; 2) Events location using both VELEST for simultaneous inversion of hypocenter location, stations corrections and an initial velocity mode and HypoDD for double-difference location methods; 3) Focal mechanism determination based on P-phase polarities; 4) stress tensor inversion using focal mechanism solutions.

Chapter IV- Presents the seismotectonic interpretation of the area by combining micro-seismicity information that resulted from the NEAREST experiment with the interpretation of multichannel seismic reflection profiles and available refraction, seismicity and bathymetric data.

Chapter V- Summarizes the principal findings in this project and points out future work ideas.

II.Data and methods

In this chapter, it is first described the acquisition of the seismological data and of the multichannel seismic reflection profiles used in this study. A short review of the most recent refraction and bathymetric data available is also provided. The methods used for processing (and interpretation) of the data are then presented, along with a summary of the fundamental background theory. The application details are developed in chapters III and IV dedicated to the seismological and geological interpretations, respectively.

II.1.Seismic network and instrument characterization

As part of the NEAREST project, 24 ocean bottom seismometers (OBSs) and the multi-parametric station GEOSTAR were deployed at the seafloor across the Gulf of Cadiz for the acquisition of passive seismicity data. The German DEPAS OBS instrument pool deployment was coordinated by the Alfred Wegener Institute (AWI) for Polar and Marine Research, and the experiment took place from August 2007 to August 2008. The network distribution is shown in Figure II.1, including land stations (from IPMA- Instituto Português do Mar e da Atmosfera and Instituto Dom Luiz-IDL) used in this work (Figure II.1).

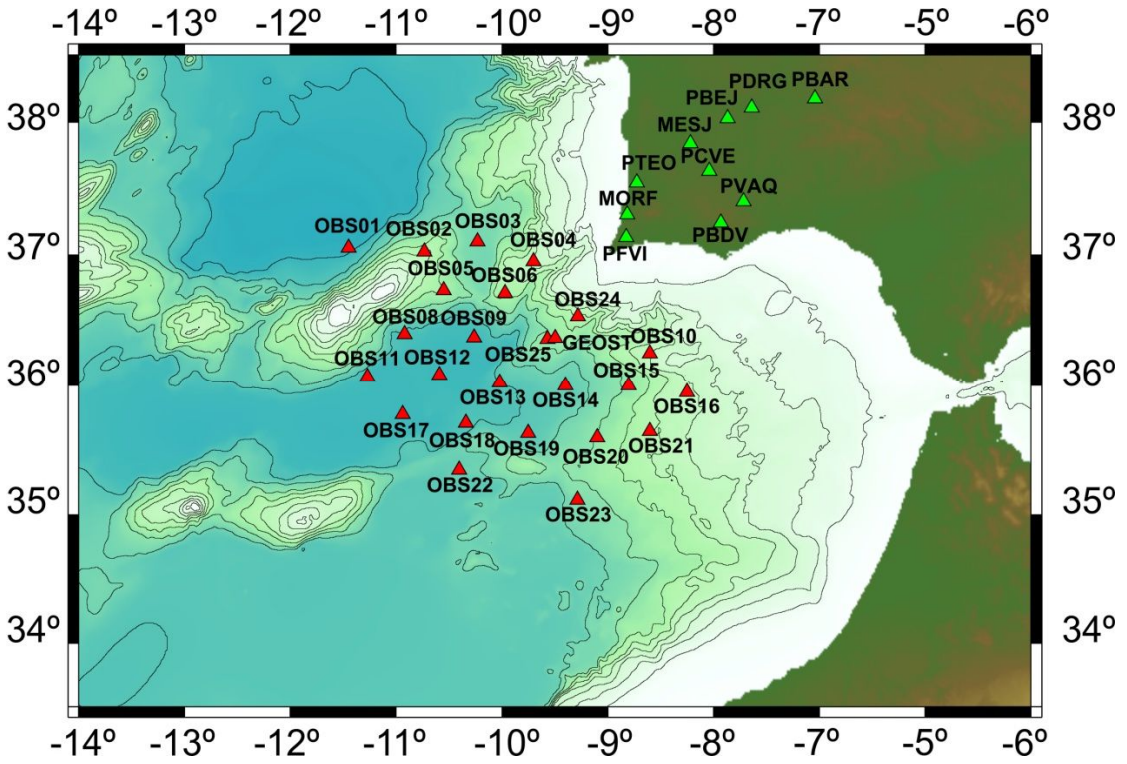

Figure II.1 NEAREST OBS network and permanent land network stations used in this work (*bathymetry from GEBCO-General Bathymetric Chart of the Oceans*).

II.1.1.LOBSTER network

The OBS specifically referred to as LOBSTER (Longterm Ocean Bottom Seismometer for Tsunami and Earthquake Research) were manufactured by K.U.M. Umwelt- und Meerestechnik Kiel GmbH, Germany. The deployment and recovery was coordinated by Wolfram Geissler from AWI.

All instruments were equipped with a Güralp CMG-40T broadband seismometer, incorporated in titanium pressure housing, a HTI-04-PCA/ULF hydrophone and a GEOLON MCS (Marine Compact Seismocorder) data logger from SEND GmbH Hamburg, Germany. The power supply both for seismometer and recorder was provided by 132 lithium power cells.

Each sensor channel was sampled at 100 Hz; preamplifier gain of the hydrophone channel was 4 and 1 for the three seismometer components (Figure II.2 and Table II.1). The total disk space of the stations was 20 GB covering a recording time of 11 to 12 months, depending on the seismic activity in the area. The clocks of the data loggers were synchronized by GPS time before deployment and synchronized again after recovery of the instruments using a SENDCOM-3 interface. The time difference was corrected linearly. The seismometers also incorporated a cardanic levelling mechanism, which started few hours after the OBS reached the seafloor and re-levelled every 15 days.

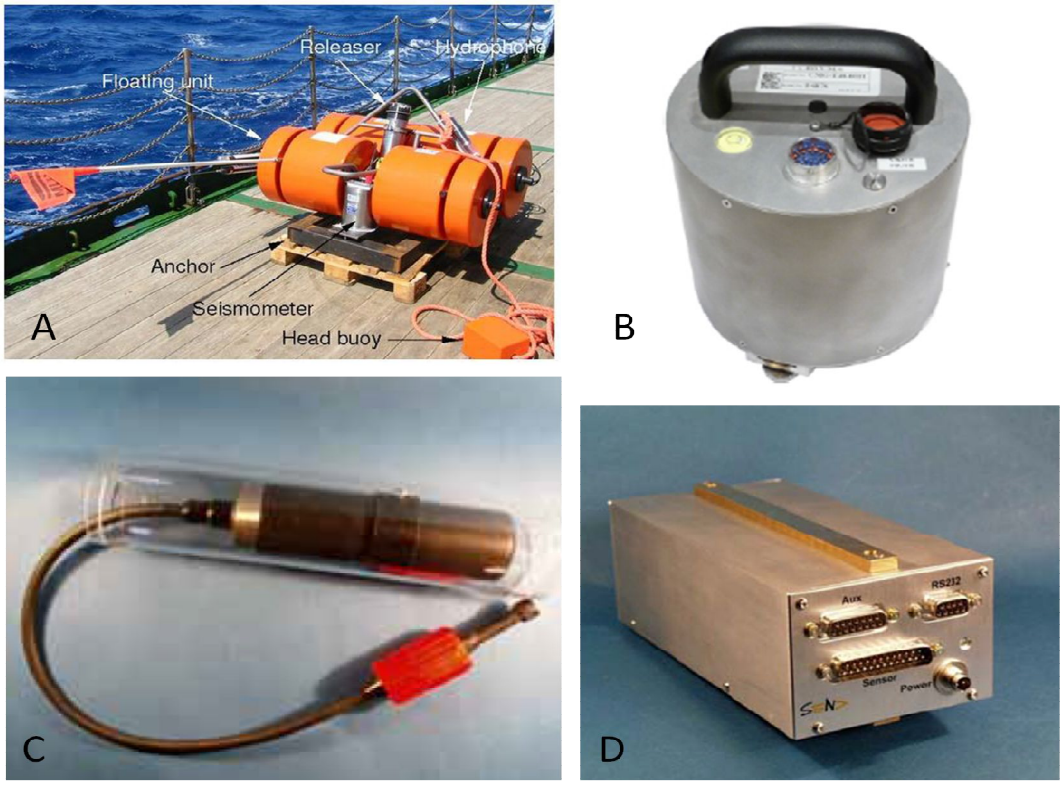

Figure II.2- A-LOBSTER system, B- Güralp CMG-40T broadband seismometer, C- HTI-04-PCA/ULF hydrophone and D- GEOLON MCS data recorder.

Table II.1- LOBSTER Seismic System (from NEAREST Deliverable 9).

Geophone:	Güralp CMG-40T, 60 sec - 50 Hz
Hydrophone:	HighTechInc HTI-04-PCA/ULF, 100 sec - 8 kHz
Digital data recording unit:	Send Geolon MCS, 24 bit, 1 - 1000 Hz, 20 GB

II.1.1.1.OBS calibration information

The metadata information was processed and gathered in dataless seed files by Carlos Corela (*Technical report on behalf of NEAREST project).* The dataless seed files were created using the PDCC software from IRIS. They contain all the standard information e.g. names of station, coordinates, network identifier or the start/end of acquisition and calibration information.

II.1.1.2.OBS quality check and pre-processing considerations

The quality control of the acquisition was done using the software SEISMIC HANDLER (http://www.seismic-handler.org) and SEISAN (Havskov & Ottemöller, 2011). Some problems were detected and reported: levelling, power, time correction and OBS orientation (from NEAREST Deliverable 9 report, 2009). In the table II.2 is a resume of the parameters check on-board.

The OBS 07 information is blank because this station was deployed for a test measurement (comparison with GEOSTAR) and recovered successfully during the 2007 deployment campaign. OBSs 24 and 25 were only deployed at November 27th, 2007 during another cruise with the fisher boat “Mario Luis” from Portimão (from NEAREST Deliverable 9 report, 2009).

The levelling problems

The seismometers incorporated a levelling system which was forced to start few hours after the deployment and was repeated every 15 days. Nine out of the twenty four OBS levelled correctly from the operation start, 2 started to level after one month (plus one after 6 months) and the 12 others did not level, at least one component (normally the X component), during the acquisition time (details in Table II.2).

Table II.2- Summary of the quality check applied on the LOBSTER network (acquisition period, components leveling, power level, disks space and time synchronization). Abbreviations: x, y and z indicate the component that were not working properly, BT- battery was low at the end of the operation; TODF- time was recorded correctly but the disk was full, TOSE- time was recorded correctly and recording stopped at the end of the operation, ns- time was not synchronized (from NEAREST Deliverable 9, 2009).

OBS nº			2007									2008													
			2-Aug	1-Sep	2-Sep	1-Oct	2-Oct	1-Nov	2-Nov	1-Dec	2-Dec	1-Jan	2-Jan	1-Feb	2-Feb	1-Mar	2-Mar	1-Apr	2-Apr	1-May	2-May	1-Jun	2-Jun	1-Jul	2-Jul	1-Aug
OBS01	BL	ns	x																						
0BS02	BL	ns	xz					z	xz	z				yz											
OBS03	BL	ns	x																						
OBS04	TODF		xyz																						
OBS05	BL	ns	x																						
OBS06	TODF		x																						
OBS07																									
OBS08	TOSE		x																						
OBS09	BL	ns	x																						
OBS10	TODF																								
OBS11	BL		xz																						
OBS12	TODF																								
OBS13	BL	ns	x																						
OBS14	TODF		x																						
OBS15	TODF		y																						
OBS16	TODF																								
OBS17	BL	ns	x																						
OBS18	TODF																								
OBS19	TODF																								
OBS20	TODF																								
OBS21	TODF																								
OBS22	BL	ns	x																						
OBS23	BL	ns	x																						
OBS24	TOSE																								
OBS25	TOSE																								

	all components okay	**BT**	battery low
	1 component dead	**TODF**	time okay, disk full
	2 component dead	**TOSE**	Time okay, stop by END
	3 component dead	**ns**	not synchronized

The power, memory use and time correction problems

At the time of recovery, 21 out of the 24 stations had already stopped recording because of lack of memory ("diskfull") and/or of power ("battery low") (details in Table II.2). These may be explained by the long duration of the acquisition period at a high sampling rate. The recording process stopped properly for the 11 stations with full disks, allowing time synchronization (Table II.3). The "battery low" message at 10 stations was unexpected, because the capacity of the 132 Li cells should have covered 12 month recording. The power lost was too severe (with only one exception- OBS11) stopping the recorders' internal clocks which unabled time synchronization.

Table II.3- Time drifts/year resulting from skew times measured onboard.

OBS	Drift s/year	skew (s)	OBS	Drift s/year	skew (s)
obs01	--,—	--,—	obs14	-3.89	-3.67
obs02	--,—	--,—	obs15	-0.09	-0.08
obs03	--,—	--,—	obs16	-4.56	-4.26
obs04	1.53	1.46	obs17	--,—	--,—
obs05	--,—	--,—	obs18	-2.77	-2.59
obs06	1.50	1.43	obs19	-3.58	-3.36
obs08	0.52	0.49	obs20	-3.46	-3.24
obs09	--,—	--,—	obs21	-2.67	-2.49
obs10	-0.12	-0.12	obs22	--,—	--,—
obs11	1.05	1.00	obs23	--,—	--,—
obs12	0.3	0.28	obs24	0.37	0.27
obs13	--,—	--,—	obs25	-0.1	-0.07

Another problem rose from the actual skew times measured onboard which revealed time drifts/year superior to the maximum expected drift of 1.46 seconds per year (for 8 out of 15 stations with synchronized time, see 30s-50 Hz). Three methods were used to estimate clock drifts for unsynchronized stations and to reproduce the skew times measured onboard: noise correlation functions, P-wave residuals and P-wave residuals double differences. The results from all methods showed coherency between them, with linear correlation ranging from 0.7 to 0.9 but none successfully reproduced time drifts higher than 1.5 seconds per year. Additional information from previous campaigns and also provided by Klaus Schleisiek from SEND pointed out that the skew times measured onboard may have an error of integer values.

P-wave arrivals residuals from the land stations and the P-wave residuals double difference were used as absolute time references to established final time corrections to onboard measured skew times and unsynchronized station. The final proposed set of clock drift and skew times applied to NEAREST AWI

OBS are provided in Table II.4 (from Luis Matias 2011, *Technical report on behalf of NEAREST project*).

Table II.4- Proposed set of clock drift and skew times applied to NEAREST AWI OBS.

OBS	Drift s/year	Skew s	OBS	Drift s/year	Skew s
OBS01	0.873	0.825	OBS14	0.348	0.329
OBS02	0.134	0.127	OBS15	-0.086	-0.081
OBS03	0.821	0.777	OBS16	-0.277	-0.258
OBS04	0.482	0.456	OBS17	-0.676	-0.638
OBS05	0.26	0.246	OBS18	-0.633	-0.593
OBS06	0.451	0.427	OBS19	0.688	0.643
OBS08	0.522	0.495	OBS20	0.816	0.761
OBS09	-0.265	-0.251	OBS21	0.542	0.505
OBS10	-0.123	-0.116	OBS22	1.283	1.208
OBS11	1.053	0.996	OBS23	-0.575	-0.541
OBS12	-0.761	-0.719	OBS24	0.377	0.267
OBS13	0.917	0.864	OBS25	-0.099	-0.071

OBS orientation problems

The orientation of the OBS on the seafloor is unknown and so the LOBSTER system was equipped with an electronic compass. However, the magnetic field around this equipment was dominated by the anchor system which conditioned any possible measurements. So, OBS orientations were estimated using P-phase polarization in teleseismic events (from NEAREST Deliverable 9, 2009). Corela (2014) also recovered OBS orientation using surface wave polarization in teleseismic events. He applied two different methods: Grigoli method and the Stachnik method (details on the procedure in Corela, 2014 and on the methods in Grigoli et al., 2011 as well as in Stachnik et al., 2012)

II.1.2.GEOSTAR

The GEOSTAR is a multidisciplinary observatory which comprises a set of geophysical and oceanographic sensors for continuous data acquisition. The GEOSTAR project is coordinated by the Istituto Nazionale di Geofisica e Vulcanologia –INGV. The GEOSTAR bottom station (Figure II.3B and Table II.5) is equipped with a GEOSTAR Guralp CMG-40T seismometer 30s-50 Hz (OBS), Guralp CMG-5T accelerometer DC-100Hz (ACC), OAS hydrophone DC-50 Hz (HYD), all with a sample rate of 100 Hz and a DM24 GURALP digitizer (24 bit) (from NEAREST Deliverable 9 report). Time synchronization is performed between a SERCEL rubidium clock and the GPS DM-24 channel.

Accurate and safe positioning at seafloor, re-entry and recovery capabilities of a Bottom Station are ensured by the dedicated cable suspended mobile docker – MODUS (Figure II.3A). The MODUS is an auxiliary module to deploy and

recovery the GEOSTAR bottom station (Figure II.3C). It is equipped with latch/release device, thrusters, video cameras, compass, sonar and altimeter that will help control deployment and recovery operations.

Table II.5- GEOSTAR seismic System.

Geophone:	Güralp CMG-40T, 30s-50 Hz
Hydrophone:	OAS DC-50 Hz, 0 sec - 5 kHz
Accelerometer	Guralp CMG-5T accelerometer DC-50Hz
Digital data recording unit:	GURALP DM-24 Digitizer , 24 bits

Figure II.3- GEOSTAR and deployment module (A-deployment module MODUS, B-GEOSTAR bottom station and C- MODUS and GEOSTAR.

II.1.2.1.GEOSTAR quality check and pre-processing considerations

Data quality check was performed using SAC software and included time and frequency domains. Three types of data disturbances were reported (From NEAREST Deliverable 9 report in http://nearest.bo.ismar.cnr.it/):

- A high amplitude disturbance (D1- Figure II.4) affecting all frequencies identified in all components both in geophone and accelerometer records. It was transversal to all acquisition periods with a recurrence time of 145s, lasting for 50s, and caused by anomalous re-levelling process;
- A high frequency disturbance (D2- Figure II.4) with 1Hz and affecting frequencies between 4-12 Hz;
- A loss of data disturbance resulting from periodical rebooting of the Seismometer Data- handling Unit (SDU).

The GEOSTAR group developed methods to correct disturbance D1 and D2 and results are displayed in Figure II.4. (from NEAREST Deliverable 9 report, 2009). However, in our study we used the uncorrected record.

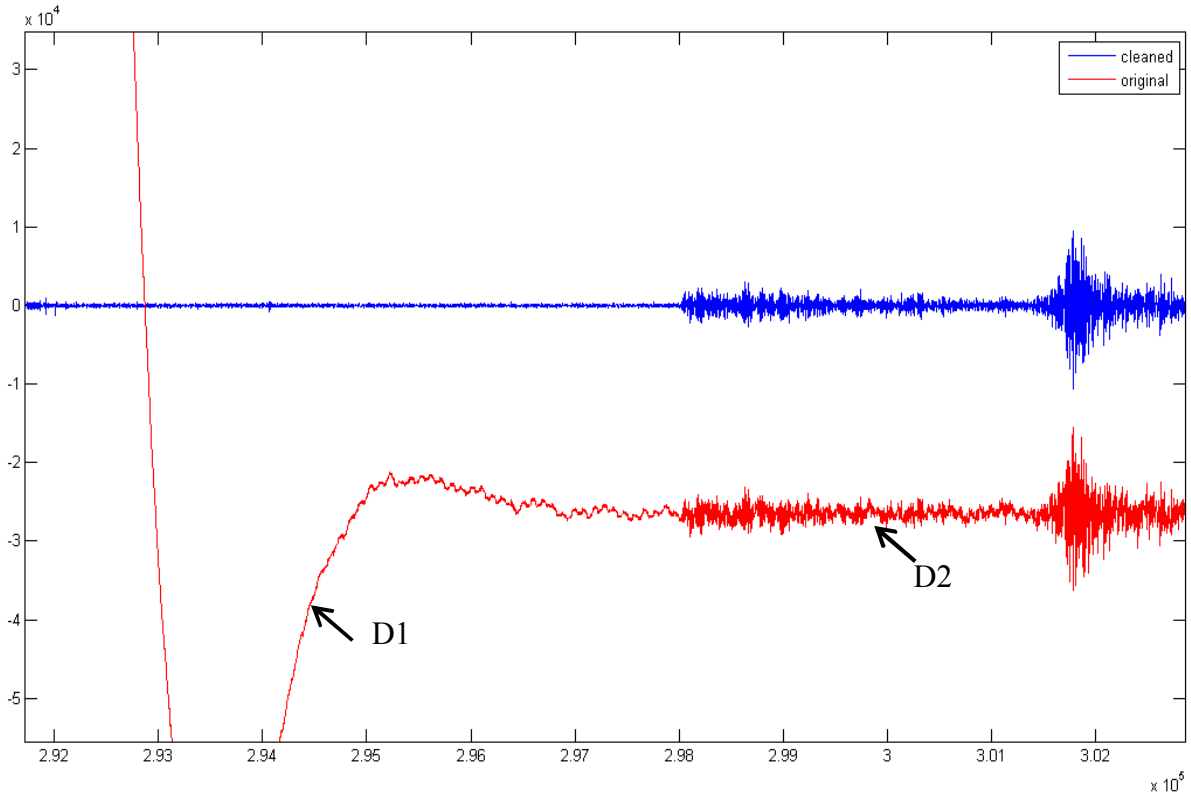

Figure II.4- Signal corrections for disturbances D1 and D2 (in red original signal and in blue corrected signal From NEAREST Deliverable 9 report in http://nearest.bo.ismar.cnr.it/).

Time corrections problem

The GEOSTAR data was distributed with a time-correction applied, having a total drift of 184 ms after 359 days. However during tests to solve the LOBSTER network synchronization problem, a 2s jump of the GEOSTAR clock close to the end of the deployment period was detected. To solve this unexpected observation GEOSTAR was corrected using clock drift estimated by the P-wave residuals double differences (as unsynchronized OBSs). A drift time correction of 1.925 in s/year and a skew time of 1.925 were therefore suggested (assuming that the acquisition time lasted exactly one year, information from Luis Matias, *Technical report on behalf of NEAREST project*).

II.1.3.Permanent Land network

The land stations are distributed in a seismic network coordinated by the Instituto Português do Mar e da Atmosfera (IPMA). The national seismic stations are owned by several institutions (see details on the land network in https://www.ipma.pt/pt/geofisica/).

During the acquisition period 275 earthquakes were detected by the land network within the deployment area (Figure II.5).The data recorded in this

network during the acquisition period was used as a preliminary reference for the earthquake events detected by NEAREST stations. Additionally, we used the data recorded in a selected group of stations (closer to the study area) to complement focal mechanism solutions. A description and localization of these stations are given in Table II.6 and Figure II.5.

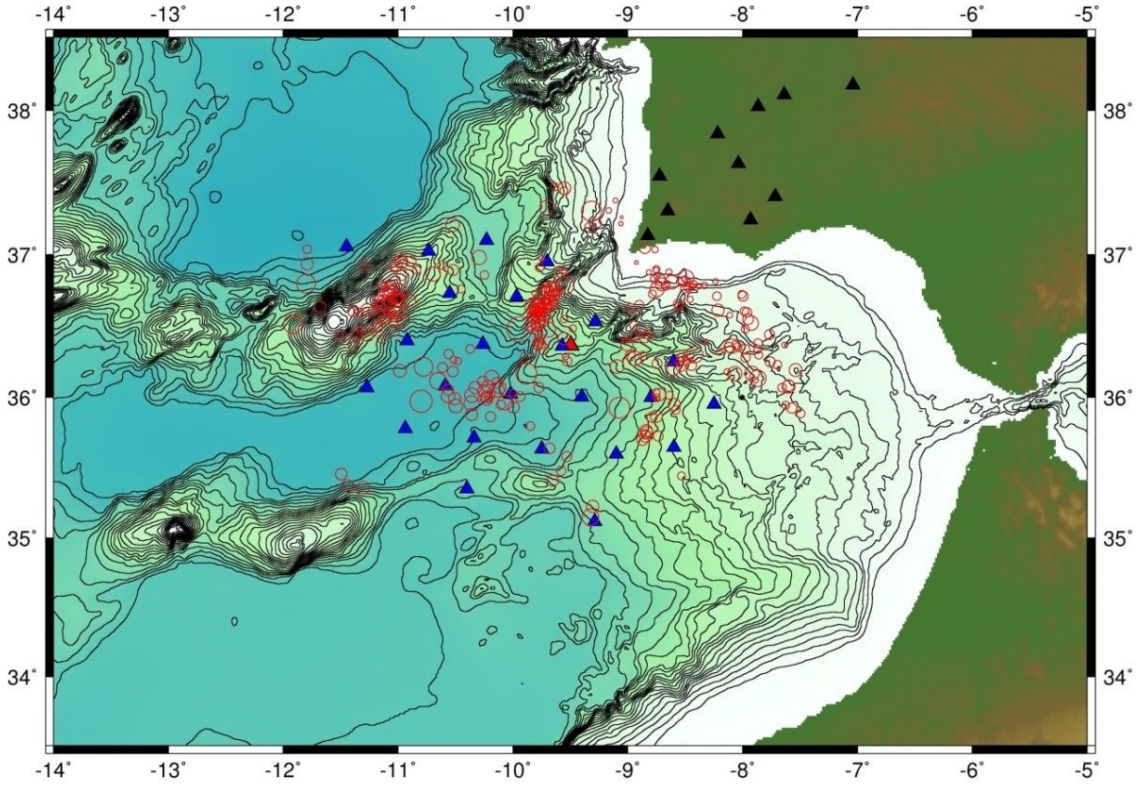

Figure II.5- Epicenters locations of the events detected by land stations (closer than 75 km to the nearest OBS) during NEAREST Project passive seismic acquisition experiment (blue triangles are AWI OBS network, red triangle is GEOSTAR, black triangles land network stations, red circles are earthquakes locations provided by the Instituto Português do Mar e da Atmosfera-IPMA*, bathymetry from GEBCO*).

Table II.6 – Details of the permanent land network seismic system (HH- High broadband, BH- Broad Band broadband, LH-Long period, HN- Accelerometer. Channel nomenclature is from seed format, details in http://www.fdsn.org/seed_manual/SEEDManual_V2.4.pdf. Stations MESJ and PDRG were installed in the frame of the NEAREST project).

Station	Sensor	Channels	Seismic data acquisition system	Data format and sampling rate	Institution
MORF	Guralp CMG-40T/30s	HH*,BH*,LH*	Reftek 130-01 24 bits	MiniSEED/100 sps (HH) /20 sps (BH)	IDL
MESJ	Streckeisen triaxial STS-2/120s	HH*,BH*,LH*	Reftek 130-01 24 bits	MiniSEED/100 sps (HH) /20 sps (BH)	IDL
PDRG	Streckeisen triaxial STS-2/120s	HH*,BH*,LH*	Reftek 130-01 24 bits	MiniSEED/100 sps (HH) /20 sps (BH)	IDL
PBAR	Guralp CMG 3ESPc-120s/5T	HH*,BH*,LH*,HN*	Guralp CGM DM24 24bits	Miniseed, 100 HZ	IPMA
PBEJ	Lennartz LE3D-5s/5T	EH*,SH*,HN*	Guralp CGM DM24 24bits	Miniseed, 62.5 HZ	IPMA
PCVE	Guralp CMG 3ESPc-120s/5T	HH*,BH*,LH*,HN*	Guralp CGM DM24 24bits	Miniseed, 100 HZ	IPMA
PTEO	Lennartz LE3D-5s/5T	HH*,BH*,LH*,HN*	Guralp CGM DM24 24bits	Miniseed, 62.5 HZ	IPMA
PVAQ	Guralp CMG 3T-120s/5T	HH*,BH*,LH*,HN*	Guralp CGM DM24 24bits	Miniseed, 100 HZ	IPMA
PBDV	Guralp CMG 3ESPc-120s/5T	HH*,BH*,LH*,HN*	Guralp CGM DM24 24bits	Miniseed, 100 HZ	IPMA
PFVI	Guralp CMG 3ESPc-120s/5T	HH*,BH*,LH*,HN*	Guralp CGM DM24 24bits	Miniseed, 100 HZ	IPMA

II.2. Bathymetry

The bathymetric map shown in Figure II.6 was used as the base for the seismotectonic interpretation of the passive seismic data resulting from NEAREST OBS experiment. This map was produced from a compilation of the high-resolution multibeam swath bathymetry data acquired in the Gulf of Cadiz. These data were processed by the ESF EuroMargins SWIM project "Earthquake and Tsunami hazards of active faults at the South West Iberian Margin: deep structure, high-resolution imaging and paleoseismic signature". The data were acquired during 19 surveys (Table II.7) totalling over 200 days of ship time, all performed between 1978 and 2006 by teams belonging to 14 research institutions from 7 European countries (Zitellini et al., 2009). The SWIM compilation comprises a mapping area of 180000 km^2, with a depth range from 30 to 5200 m and a 100 m cell size overall grid for the Gulf of Cadiz (Valadares, 2012).

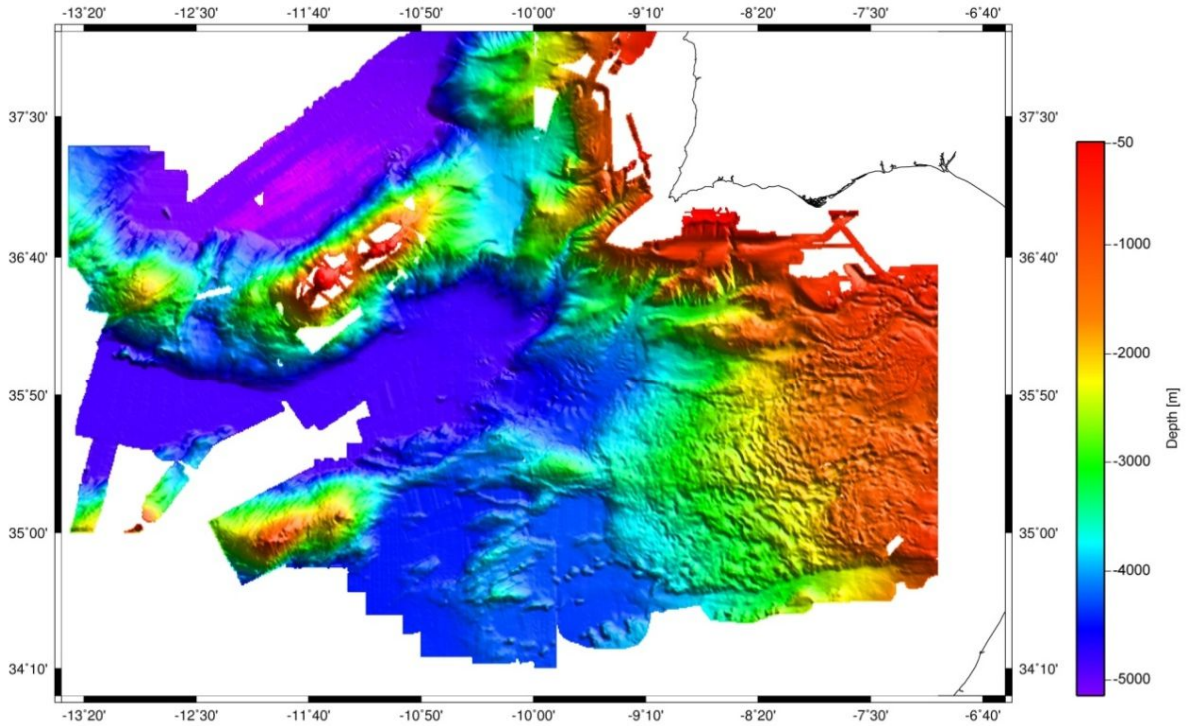

Figure II.6- SWIM compilation for the Gulf of Cadiz area plot.

Table II.7-Details on the surveys in SWIM bathymetry compilation (from Valadares, 2012).

Survey		Year	Institution	Vessel	Data
1	ESPICHEL	**1991**	IFREMER	R/V L'Atalante	Multibeam
2	TASYO	**2000**	IGME	R/V Hespérides	Multibeam
3	PARSIFAL	**2000**	CSIC-CMIMA	R/V Hespérides	Multibeam
4	CADISAR 1	**2001**	Univ. Bordeaux	R/V Le Suroît	Multibeam
5	HITS	**2001**	CSIC-CMIMA	R/V Hespérides	Multibeam
6	CADIPOR	**2002**	Ghent Univ.	R/V Belgica	Multibeam
7	GORRINGE	**2003**	IAMC-CNR	R/V Urania	Multibeam
8	TV-GIB	**2003**	UBO	R/V Le Suroît	Multibeam
9	PICABIA	**2003**	CSIC-CMIMA	R/V Marion Dufresne	Multibeam
10	GAP	**2003**	Bremen univ.	R/V Sonne	Multibeam
11	MATESPRO	**2004**	CGUL	R/V D. Carlos I	Multibeam, backscatter
12	CADISAR 2	**2004**	Univ. Bordeaux	R/V Le Suroît	Multibeam
13	DELILA	**2004**	IUEM/UBO	R/V D. Carlos I	Multibeam, backscatter
14	DELSIS	**2005**	IUEM/UBO	R/V Le Suroît	Multibeam
15	SWIM 2005	**2005**	ISMAR	R/V OGC Explora	Multibeam
16	HERMES	**2006**	NOC	R/V Charles Darwin	Multibeam
17	SWIM 2006	**2006**	CSIC-CMIMA	R/V Hespérides	Multibeam
18	EMEPC data	**2005**	EMEPC	R/V D. Carlos I	Multibeam
19	SISMER database	**1978**	IFREMER	R/V Jean Charcot	Multibeam
		1990	IFREMER	R/V L'Atalante	Multibeam

II.3.Multichannel seismic reflection and refraction profiles

The multichannel seismic profiles (MCS) studied in this work were selected from Academia surveys (Figure II.7). Our analysis of the MCS was specifically focused on the interpretation of passive seismicity results. Two main objectives were considered:

- Delimitate seismic units to support the interpretation of the velocity and stations correction derived during events location procedures (all available dataset, Figure II.7)
- Investigate the geological control on the seismicity distribution (selected profiles in Figure II.8).

We also completed the geological information with NEAREST and IAM wide-angle reflection/refraction profiles.

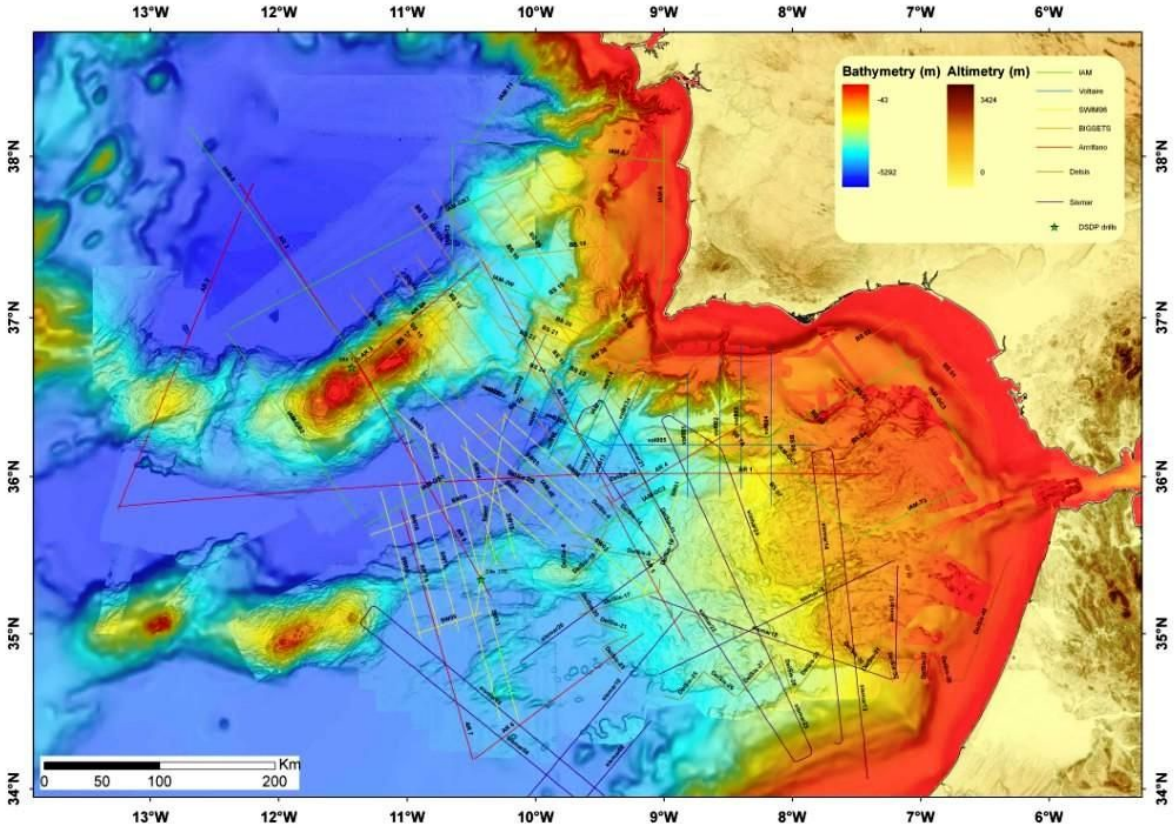

Figure II.7- All available multichannel seismic reflection and refraction profiles in the study area (except for NEAREST wide-angle reflection/refraction profiles depicted in the Figure II.8).

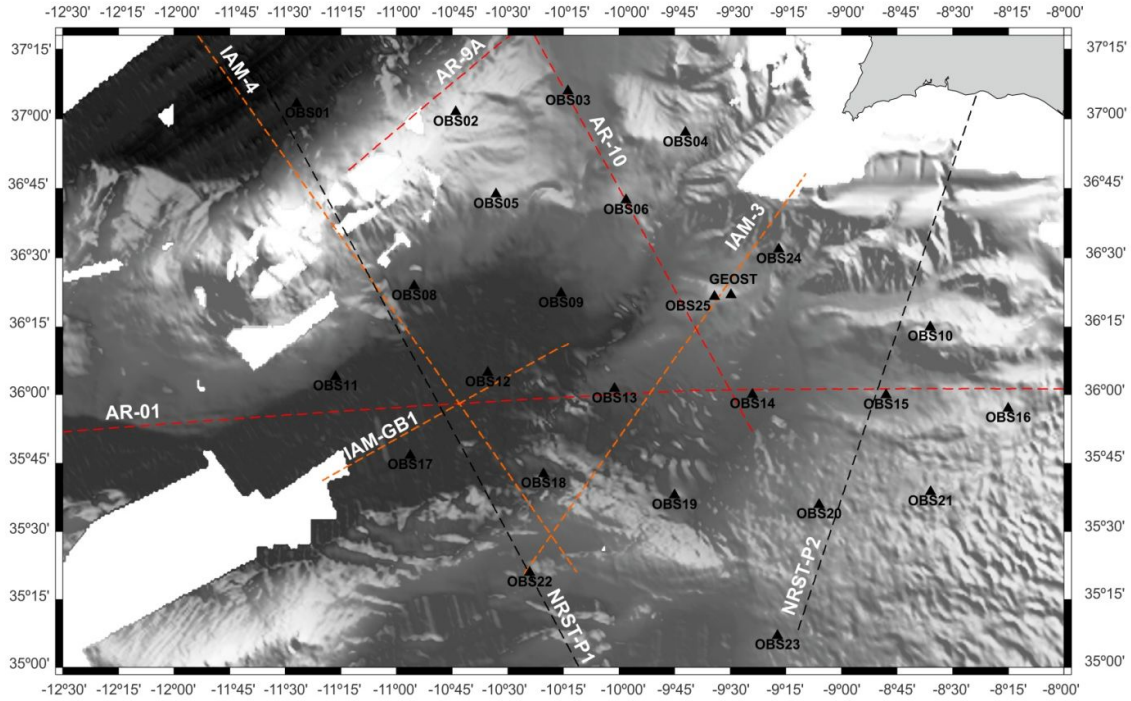

Figure II.8- Location of the selected MCS and refraction profiles and NEAREST OBS network (in red dashed lines ARRIFANO survey, in orange dashed lines is IAM Survey, and in black dashed lines NEAREST wide-angle reflection/refraction profiles).

II.3.1.ARRIFANO Survey

The ARRIFANO (**AR**c **RIFANO**) MCS survey was carried out in 1992 (AR92) onboard the R/V OGS-Explora as part of a research project funded by the Italian Consiglio Nazionale delle Recerche (Sartori et al., 1994). The acquisition equipment included 32 air guns array, with a volume of 80 L, a 3 km long streamer (with 120 receiver channels in 25 m groups). The shooting interval was 50 m, the sampling rate 2 ms and the record extended to 13 or 14s TWT.

Seismic processing was performed in the Istituto di Geologia Marina of Bologna and included resampling to 4ms, CDP (common depth point) gathering, spiking deconvolution, velocity analysis, normal moveout correction, stacking, spherical divergence correction, sum adjacent 12.5 CDPs, finite-difference wave-equation migration and time-variable filter. The time migration was made using stacking velocity with a reduction 10% (Sartori et al., 1994).

Afterwards, Rovere et al. (2004) reprocessed the 275km westernmost part of the AR01 profile (Figure II.8). The processing sequence included trace editing, amplitude balancing, normal moveout correction (NMO), common-midpoint stacking, predictive deconvolution, finite-difference time migration and time variant band-pass filtering. This section of the profile was pre-stack depth migrated. In Zitellini et al. (2001) is presented the AR-10 depth converted (location in Figure II.8).

II.3.2.BIGSET Survey

The **BIG S**ources of **E**arthquake and **T**sunami (BIGSET) survey was carried out on the RV/ Urania of the Italian Consiglio Nazionale delle Ricerche, in the area offshore the Cabo de São Vicente. The project was founded by the European Community (Zitellini et al., 2010).

The MCS reflection profiles were acquired using 4 SODERA-SSI GI-GUN air gun array, with a total volume ranging from 6.9 L to 8.2 L for deeper penetration survey. The high resolution survey was acquired using a single air gun with volume of 2.46 L. The pressure was set to 138 bar and 130-200 bars, for deep penetration and high resolution surveys, respectively. The streamer was 1200 m long, with 48 active channels in 25 m groups. The cable was at depth ranging between 6 to 10 m and near offset was set between 142 and 158 m. The shooting interval was variable between 25, 37.5, 50 and 100 m. A pre-amplified gain was set to 30 db, the sample rate was 1 ms and the data record length between 8 and 13 s. The primary navigation system was DGPS (Zitellini et al., 2010).

The data was recorded in SEG-D format. The procedure for MCS processing included: load geometry with CMP folding between 6 or 16 or 24 (100, 37.5, 25 m between shots); re-sampling to 4 ms; band-pass filter: 6-9-58-62.5Hz; edit traces; hand statics:-20ms; true amplitude recovery; gapped deconvolution: decon operator length 400 ms and prediction distance 24 ms; CMP sorting; interactive velocity analysis; NMO correction and stacking; top mute; finite-difference time migration; time and space variant Ormsby band pass filter and automatic gain control (Zitellini et al., 2010).

II.3.3.IAM Survey

The **I**berian **A**tlantic **M**argin (IAM) project was financed by the European Community Joule Program and coordinated by Enric Banda and Montserrat Torne from the Institute of Earth Sciences, Consejo Superior de Investigationes Cientificas (CSIC, Banda et al., 1995). This project explored the nature of the deep continental and oceanic crust in the Atlantic Iberia Margins. The acquisition campaign was designed to acquire near-vertical incidence reflection data complemented by on-shore and offshore wide-angle and refraction data on a few selected profiles, from the Cantabrian margin to the Gulf of Cadiz. In total 3700 km of MCS seismic data were acquired on 19 lines. 43 land stations and 19 OBS (Ocean Bottom Seismometers) were used for the acquisition of refraction and wide-angle reflection data. GECO-PRAKLA was in charge of the marine acquisition and it took place on board of the M/V GECO SIGMA, from August to September of 1993.

The IAM multichannel reflection seismic profiles were acquired using a 36 SWAG air-gun array with a total volume of 120 L and a pressure of 2000 psi. The source depth was of 15 m and the shot interval of 75 m. The receivers were

displayed in a streamer with 192 groups with an interval of 25 m, with five auxiliary channels. The cable was at a depth of 18m. The near offset defined in-line was 254 m. The streamer length, between the centre of the first and last receiver group, was 4775 m. The sample rate was 4ms and the record length 25 s. No low-cut filter was applied in the acquisition system only a high-cut filter at 92 Hz with a slope of 72 dB/oct and a gain constant of 24 dB. The primary navigation system was DGPS.

The acquisition format was SEG-D 20 bit binary, afterwards it was de-multiplexed and converted to SEG-Y in the pre-processing sequence. The available raw data was subdivided in five files in SEG-Y IBM floating point, Big Endian with headers in EBCDIC format. The 8 initial traces are auxiliary (test).

The processing sequence by Geco-Prakla comprised reformat from acquisition format SEG-D to SEG-Y, bandpass filter with low cut 6 Hz(36dB/oct) and an anti alias high cut 55Hz (130 dB/oct), temporal resampling to 8ms, trace edit, trace equalisation, spherical divergence correction using constant velocity function (1500m/s at 0ms and 6000m/s at 14000ms), least square predictive deconvolution, FK demultiple, Normal moveout correction, space variant front end and inner trace mute, spherical divergence compensation, stacking, noise attenuation F-K filter, Kirchhoff constant velocity (1700 m/s) time migration and time-space variant band-pass filtering**.** Jiménez-Munt et al. (2010) converted to depth the IAM-4 (Figure II.8) seismic profile using variable velocities of 1500 m/s for seawater, 2250 m/s to 3000 m/s for the sediment cover based on results proposed by Gónzalez et al. (1998).

In the present work we reprocessed and depth converted the IAM-GB1 profile (location in Figure II.8). The processing sequence included trace muting, in-line geometry trace editing, velocity analysis, NMO correction, predictive deconvolution, stacking, time migration and depth conversion. An overview on some of the processing background is presented in this chapter and details on processing parameters will be described in Appendix V.

II.3.4.NEAREST Wide-angle reflection/refraction profiles

The NEAREST project refraction profiles were acquired onboard of the Spanish research vessel R/V Hesperides in 2008. Two profiles were acquired (see Figure II.8):

1. Profile P1 is 340 km-long and resulted from a 30 OBS deployment array starting at the Tagus Abyssal plain and extending to Seine Abyssal plain (strike approximately NW-SE), crossing the Gorringe Bank topographic high;
2. Profile P2 is 260 km-long, resulting from an array of 15 OBS and 9 landstations, extending from South Portuguese zone and crossing the

Gulf of Cadiz accretionary wedge (to East of the Coral Patch Ridge) striking ≈N-S.

The instruments used in this experiment include 19 Ifremer MicrOBS models were provided by UBO-IUEM (**U**niversite de **B**retagne **O**ccidentale - **I**nstitut **U**niversitaire **E**uropeen de la **M**er), 17 short-period L2000s model from the Spanish UTM (**U**nitat de **T**ecnologia **M**arina) and 9 Hathor landstations also provide by UTM. The seismic source comprised two arrays with 7 Bolt airguns (model 1500 LL), providing a total volume of 70 L. The arrays were deployed at a depth of 12 m, and the shot interval was set to 90 s. The processing details and interpretation were published in Sallarès et al. (2013) and Martínez-Loriente et al. (2014) for profile P1 and Sallarès et al. (2011) for profile P2.

II.3.5.SWIM -2006 survey

The SWIM -2006 survey was carried out onboard the R/V Hesperides in 2006 as part of the Collaborative Research Project from European Science Foundation EuroMargins SWIM ("Earthquakes and Tsunami Hazards in the SouthWest Iberian Margin: High-resolution imaging of active faults and paleoseismic signature").

A total of 16 profiles were acquired with 8 air guns array at a depth of 6m, with a total volume of 17 L and a pressure of 2000 psi. The shooting interval was 25 m to 37.5 m. The streamer had an active section of 2400 m with 96 recording channels (in a group interval of 25 m). The near offset was 216 m and the cable was at 7 m depth. The sampling rate was 2 ms with a pre-amplified gain of 20 db, the record length ranged between 9 and 11s. The primary navigation system was DGPS

The processing work involved resampling to 4ms, trace editing, static recording delay correction, true amplitude recovery, top mute, F-K and bandpass frequency filter, predictive deconvolution, NMO correction (with constant velocity of 1700 m/s), stacking, spiking deconvolution, Stolt FK migration (1500 m/s) and final band-pass filtering. Final stacks and time migrated profiles were exported in SEG-Y format (Gràcia and Scientific-Party, 2006).

Pre-stack depth migrated and seismic interpretations of most of the SWIM profiles are published in Martínez-Loriente et al. (2013).

II.3.6.VOLTAIRE survey

The **V**aluation **O**f **L**arge **T**sunamis **A**nd **I**beria **R**isk for **E**arthquakes (VOLTAIRE) project was supported by Italian and Portuguese funding Agencies. The VOLTAIRE survey was carried out on/board of the RV/Urania. The research area was located on the SW margin of the Iberia, from the eastern border of the Tagus Abyssal Plain to the Guadalquivir Bank.

The VOLTAIRE MCS reflection profiles were acquired using a 2 SODERA-SSI GI-GUN air gun array, with a volume of 3.4 L. The shot interval was set to 50 m.

The receivers were displayed in a streamer with 48 groups with an interval of 12.5 m. The cable was at a depth of 9 m. The sample rate was 1 ms and the record length ≈12 s. The primary navigation system was DGPS.

The data was recorded in SEG-D format. The processing sequence included: re-sampling to 2 ms; edit traces; shot delay removal; true amplitude recovery; predictive deconvolution; CMP sorting; velocity analysis every 200 CMPs; NMO correction and stacking; band-pass filter and time migration using stacking velocity with a reduction 10% (Zitellini, Matias, Rovere and Scientific-Party, 2002).

II.4.Processing the seismological data

The processing sequence of the seismological data included the following steps express in the Figure II.9. Events detection and phase identification were made in collaboration with Martin Romsdorf from AWI (Romsdorf, 2010).

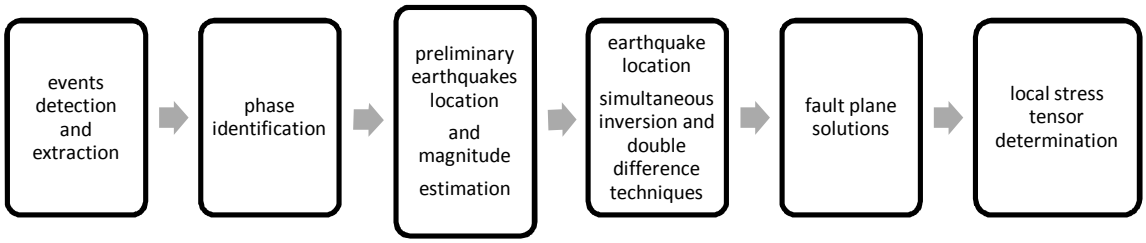

Figure II.9- Passive seismic data processing sequence.

II.4.1.Detection and extraction

The seismicity identification is based on the principle that we can distinguish an earthquake from the continuous ambient noise record in a seismogram. Local seismicity signal is characterized by an impulsive start, high frequency waves, an exponential amplitude envelope and a decrease in signal frequency in time. Another feature transversal to all type of seismic events (local, regional or teleseismic) is that the dominant wave period generally increases with time, starting from the moment of the first arrival, while other transient signals usually maintain the same dominant period throughout the duration of the events (Lee and Stewart, 1981). The identification of these events can be performed using different techniques; in our particular case we used spectrogram and automatic triggering analysis.

II.4.1.1.Spectrogram analysis

The spectrogram analysis consists of the examination of the average spectral content of the seismograms recorded in the vertical seismometer component. Daily spectrograms can be generated and converted into bitmap images, allowing the interpreter to visually identify spectral amplitude variations during seismic events by changes in a predefined colour palette. When stations in the

same area are plotted together, then an earthquake can be recognized as a linear alignment in the spectrogram.

To define the spectrogram, n spectral points are extracted (that must be a power of 2) and centred in each sample to be analysed. The Fast Fourier Transform (FFT) of that series is then computed. The FFT will transform the seismic signal from temporal into its frequency domain, needed to compute the spectrogram. There is no windowing applied to the data; only the linear trend is extracted. Ultimately, n/2 spectral amplitude points are produced. These amplitudes are averaged, decimated and plotted in the spectrogram (Figure II.10). The size of the sliding time-window, the averaging and plot limits define the frequency interval and the spectral window that is plotted.

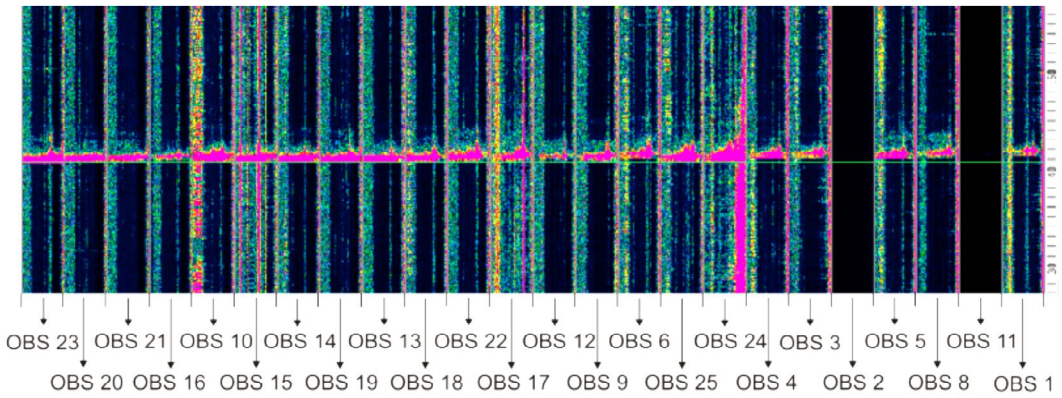

Figure II.10- Spectrogram of the vertical component in the NEAREST seismometers. An seismic events is observed as a linear disturbance common (in this example) to all stations (OBS 2 and 11 were not acquiring data).

II.4.1.2.Automatic triggering analysis

Different types of triggering algorithms are available, whether based on amplitude changes only or using more complex recognition systems. The 'short-time-average through long-time-average' (STA/LTA) trigger algorithm is the more commonly used.

The STA/LTA algorithm calculates the average values of the absolute amplitude of the seismic signal in two consecutive moving time windows. The short time window (STA) scans for a seismic event and the long-time window (LTA) defines the background amplitude of the seismic noise. When the ratio of STA /LTA (trigger ratio) reaches a pre-set value an event is declared. The event is considered finished when the STA /LTA ratio decreases to another pre-set value - detrigger ratio.

The length of the STA and LTA windows depend on the distance between the sensors and the average distance to a seismological active zone (Munro, 2004 and references within). The STA window must be defined for a period superior to the expected duration of the seismic event. However, it should not be significantly longer than the shortest event to be investigated. If the window is

very large, it no longer defines the envelope signal signature of the expected seismic event but the average amplitude of this event and the background seismic noise. Consequently, the sensitivity to detect small earthquake events (local events) is reduced. Hence the type (local vs distant) of events to be identified should be selected and prioritized. On the other hand, decreasing the STA window increases the sensitivity of the algorithm and this can induce triggering of false events. The LTA window should be a few periods longer than the typical irregular seismic noise variations. A typical LTA window is 60s.

The selection of the STA/LTA trigger threshold level is a crucial step because it determines which events will be extracted. High STA/LTA trigger threshold level decrease false triggering but could exclude a higher number of earthquakes. Defining a lower threshold level increases both false positives and events detection. In quiet seismic sites, the typical trigger threshold value is 4, but for stations located far from any man-made noise, such as deep marine environments, this value can be lower. The de-trigger threshold level determines the extension of the event detected. Very high levels prevent the extraction of long events while low levels include longer records with unnecessary data.

Another important parameter is the triggering pre-filter design. The filter is critical particularly for broadband seismometers with large response band (LOBSTER-60s-50Hz). The pre- triggering filter helps prioritize the frequencies to the dominant range of the seismic event of interest and attenuate or discard the effects of unwanted seismic background noise. Limiting the extraction of events when detected in a predefined number of seismic stations excludes earthquakes that cannot be located (details on the used triggering parameters are in the subchapter III.2.1).

II.4.2.Earthquake location

The earthquake location is defined by the hypocenter coordinates and origin in time. It can be determined from absolute or relative methods. In absolute techniques, events locations are referred to fix geographical and time systems while in relative methods earthquakes are located based in another event (master event) or relative to each other.

The determination of absolute earthquake locations depends on several factors including survey network geometry, seismic phase identification and accuracies of the arriving time readings. Another important factor is the influence of the velocity structure of the crust and mantle that are traversed by the seismic rays. The application of one dimensional velocity models to determine hypocenter location in a tri-dimensional variable space also creates limitations. This problem is particularly dominant when there is a high lateral variability in the lithospheric structure. To minimize the latter aspect, absolute location methods

can include station corrections or jointly determine velocities, hypocenters locations and station delays.

Relative location (e.g. double difference earthquake location algorithms) methods can also minimize errors resulting from tri-dimensional geological variability. Even when using simultaneous inversion techniques with stations corrections, improvements can still be made by using the double difference technique too. The double-difference method allows a precise earthquake location because it is based on the similitude between seismic events within the same cluster. A description of the main background concepts behind earthquake location is provided in the next section.

II.4.2.1.Stating the problem

The earthquake locations are determined based on the records registered in the seismometers located on the Earth's surface. Features, such as arrival time and amplitudes of the seismic waves are recorded by the seismic network. The location of the earthquake is then derived by matching an observed arrival time for seismic phases at the seismic stations and the calculated arrival times based on a hypothetical source location. Plausible velocity models are used to calculate theoretical arrival times. Hence, determining events location is an inverse problem where the observed data is arrival time and the unknowns are: spatial coordinates of the hypocenter, the origin time and velocity model. The forward problem is expressed mathematically by:

$$d = f\ (m, v)\ (1)$$

Where **d** is the arrival time, **m** is the location model and $\boldsymbol{v}$ denotes the velocity model. In the forward problem, changes in **d** derived from known modifications in $\boldsymbol{f}\ (\boldsymbol{m}, \boldsymbol{v})$ can be predicted**.** By contrast, the inverse problem involves solving the changes in $\boldsymbol{f}\ (\boldsymbol{m}, \boldsymbol{v})$ that yield the required data **d.** The best model is the one that produces the smallest misfit ($\mathbf{t_{res}}$) between the observed data ($\boldsymbol{t_{obs}}$) and the predicted data ($\boldsymbol{t_{cal}}$):

$$t_{res} = t_{obs} - t_{cal} (2)$$

For a source location $\mathbf{X_{src}}$ **(x)** and recording station coordinates $\mathbf{X_{sta}}$ **(x)**, the arrival time can be defined by:

$$t_{cal} = t_0 + T_{ij}^{cal} = t_0 + \int_{X_{src}}^{X_{sta}} u(x) ds\ (3)$$

Where $\mathbf{t_0}$ is the origin time, $\boldsymbol{u}$ is the model slowness (inverse of the seismic velocity) and $\boldsymbol{x}$ denotes a vector of spatial coordinates reproducing the ray path. Any change to the location results in the alteration of the ray path, and consequently of the seismic velocity. Similarly, changing the seismic velocity modifies the arrival time and therefore the earthquake location. This dependence is nonlinear and is referred as the coupled hypocenter-velocity problem. The hypocenter parameters, except for the origin time, are strongly

nonlinear and velocity parameters are moderately nonlinear (Kissling et al. 1994). Applying a first-order Taylor series expansion to (2, 3) yields a linear relationship between travel time residuals ($\mathbf{t_{res}}$) and adjustments in hypocentral ($\Delta \boldsymbol{h_k}$) and velocity ($\Delta \boldsymbol{m_i}$) parameters (e.g Kissling et al., 1994)

$$t_{res} = t_{obs} - t_{cal} = \sum_{k=1,4} \frac{\partial f}{\partial h_k} \Delta h_k + \sum_{i=1,n} \frac{\partial f}{\partial m_i} \Delta m_i \quad (4)$$

In matrix notation:

$$t = Hh + Mm \quad (5)$$

Where **t** is the vector of travel time residuals, **H** is the matrix of partial derivates of travel time with respect to hypocentral parameters (origin spatial coordinates and time) and **h** a vector with hypocentral parameters adjustments, **M** is the matrix of partial derivates of travel time with respect to velocity model parameters and **m** the vector of velocity model adjustments.

Assuming that the velocity model is known (based on previous seismological and refractions data), the location problem can be reduced to hypocentral parameters by removing the **Mm** from the *linearized* approximation. In that case:

$$t_{res} = t_{obs} - t_{cal} = \sum_{k=1,4} \frac{\partial f}{\partial h_k} \Delta h_k \quad (6)$$

And in detail for a station $\boldsymbol{i}$:

$$t_{res\,i} = \frac{\partial T_{cal}}{\partial x_i} \Delta x + \frac{\partial T_{cal}}{\partial y_i} \Delta y + \frac{\partial T_{cal}}{\partial z_i} \Delta z + \Delta t_o \quad (7)$$

Or in the matrix notation:

$$t_{res\,i} = Hh \quad (8)$$

The formulation of the earthquake location problem in this linear form is known as the Geiger method. However, ignoring the velocity parameter in the earthquake location problem introduces systematic errors to our solutions (Kissling et al., 1994). A successful solution can only be reached by constraining the initial velocity model based on dense geophysical data. The Geiger method (and modified versions) is used in several location programs including the HYPOCENTER 3.2 (details on Lienert, 1994) integrated in the SEISAN 9.01 package (Havskov and Ottemöller, 2011) used for the preliminary location of earthquakes in our study.

Once an adequate velocity model has been established, the location is constrained by the hypocentre parameters which represent 4 unknowns (the hypocenter coordinates and their origin in time). A solving equation is devised for each arrival time. The system can be determined using three seismic stations with four phase picking. However, a seismic network commonly has considerably more observations and the problem is *overdetermined,* meaning that a unique solution cannot be obtained. However, using a higher number of

recording stations allows to constrain redundancy errors in arrival times related to phase picking, clock synchronization, reading errors and systematic discrepancies between real velocity structure and velocity model.

An iterative approximation starting with a trial hypocenter solution (derived from the closest station) is used to solve the system with iterative corrections applied until the best solution is reached, minimizing the difference between observed and calculated arrival times in **M** stations. For most locations, programs use root mean square approximation to define the best solution:

$$RMS = \sqrt{\frac{1}{M}\sum_{J=1}^{M}\left(r_{ij}\right)^2} \quad (9)$$

Where $\boldsymbol{r_{ij}}$ is the temporal difference between the $\boldsymbol{t_{obs}}$ and $\boldsymbol{t_{cal}}$ (for a station $\boldsymbol{j}$ and a event source $\boldsymbol{i}$).

II.4.2.2.Joint Hypocentral Determination (JHD)

Assuming that the 1 D velocity model is well constrained, station correction delays must also be applied to yield the correct location of the earthquakes. These corrections combine not only errors related to the record acquisition and processing but also associated with the tri-dimensional subsurface geological structure variability below the seismic network. The Joint Hypocentral Determination (JHD) technique uses the simultaneous location of a group of events and common station corrections determinations. According to Pujol (2000), the resulting stations corrections can be related to un-modeled lateral velocity variations.

The JHD is distinct from single-event location approaches because it includes a stations corrections term ($\boldsymbol{ds_i}$). Considering a group of earthquakes **M** recorded in **N** stations the JHD formulation is:

$$w_{ij}\ r_{ij} = (dT_j + \frac{\partial t}{\partial x}dx_j + \frac{\partial t}{\partial y}dy_j + \frac{\partial t}{\partial z}dz_j + ds_i) \quad (11)$$

With

i=1, N; j=1, M

and

$$r_{ij} = t_{ij}^{o} - (T_j + \tau_{ij} + s_i) \quad (12)$$

Where $\boldsymbol{t_{ij}^{o}}$ is the observed arrival time and the remaining terms of the equation refers to the calculated arrival time, $\boldsymbol{T_j}$ being the computed initial origin time, $\boldsymbol{\tau_{ij}}$ the travel time based on a hypothetical hypocentral location and $\boldsymbol{s_i}$ is the initial stations corrections. The term $\boldsymbol{w_{ij}}$ refers to quality weights in stations readings. The partial derivates elements are the adjustments that must be determined.

In matrix notations the equation can be written as:

$$W_j\,A_j dX_j + W_j ds = W_j r_j \quad j = 1, M \quad (13)$$

Where *W* is the stations weight matrix, *A* is the adjustments partial derivates, *dXj* is the earthquake locations corrections, *ds* the stations delays and *rj* is the residuals vector. The JHD problem must solve all the terms of the equation simultaneously (see Pujol, 2000 for further details).

An approximate JHD technique was introduced by Frolich (1979). It uses single-events location and average stations residuals (Pujol, 2000), and adopts the following processing sequence:

1. Determination of earthquake locations individually;
2. Determination of average individual station delays based on all earthquakes;
3. Determination of the individual locations of earthquakes using stations corrections from step 2;
4. Iteratively improvement of earthquake location by repeating steps 1-3.

This is equivalent to solving the different terms of equation 13 individually. Solving step 1 corresponds to solving equation 13 for *ds*=0 and step 2 without earthquake location term. The station residuals are defined by (Pujol, 2000):

$$ds_i = \frac{\sum_{j=1}^{M} w_{ij}^2 r_{ij}}{\sum_{j=1}^{M} w_{ij}^2} \quad (14)$$

An JHD approximation was applied in data investigated here by combining HYP2 (a modified version by Luis Matias of HYP application from SEISAN 9.2 package, Havskov and Ottemöller, 2011) which allowed individual stations delays for p and s readings.

II.4.2.3.Simultaneous inversion

An accurate constraint of the velocity structure of the crust and upper mantle for a determined region is very difficult to obtain. In particular, excluding velocity parameters from the coupled hypocentre-velocity formulation (eq. 5) can introduce systematic errors in earthquakes locations (Kissiling et al., 1994). In the simultaneous inversion method hypocentral, velocity and station correction are jointly determined. The formulation can be written in matrix notation as:

$$t = Hh + Mm + \mathrm{e} \quad (15)$$

Where **t** is the residuals between observed and calculated arrival times, **H** is the matrix of partial derivates of travel time with respect to hypocentral parameters, **h** is the vector of hypocentral parameters adjustments, **M** is the matrix of partial derivates of the travel time with respect to velocity model, **m** is the vector of velocity model adjustments and **e** is the vector of travel time errors, resulting from errors in observations (stations coordinates, in measurements), in the use of wrong hypocentral and velocity parameters and errors related to the linearization of the coupled hypocentre-velocity formulation.

This formulation is highly dependent on the parameterization of the problem. One of the limitations derives from the velocity model layers structure used as input. During processing steps, the velocity value of each layer can fluctuate to find a better solution for events location. On the contrary, the number of layers and its thickness remains fixed. Therefore the validity of the hypocentre-velocity formulation solution is dependent on the specific structure of the initial velocity model. One way to overcome this limitation is to use previous knowledge on interface depth (e.g. refraction-reflection seismic profiles) to limit interface depths distribution. In the absence of previous data, several layers structures should be tested without exaggerated complexity. Beyond a determined complexity, the model becomes unrealistic. Moreover, the earthquakes ray paths does not comply with the necessary constraints to solve the model variability and the problem becomes *underdeterminate*.

Other restrictions originate from hypocentral distribution if earthquakes have limited depth distributions. In this case, the velocity model converges rapidly to an optimum solution within these layers but may not achieve a constrained solution for depth intervals having low earthquakes distributions. The best solution is obtained in the layers common to most ray-paths between the source area and all the seismic stations. Consequently, less accuracy is expected in subsurface layers below seismic stations and below the depth limit of the distribution of the hypocenters. In our study we used the VELEST (details on the method in Kissiling, 1995) application to compute the velocity model, the locations and stations corrections (see chapter III.3.2).

II.4.2.4.Relative location methods based on double difference (HypoDD)

As referred before, one of the main constrains on earthquake location comes from using one dimensional velocity models (even if well known) to determine hypocenters locations in a tri-dimensional variable lithosphere. We can minimize this difficulty by using 3-D simultaneous inversion methods or, alternatively, double-difference techniques.

The double difference approximation for earthquake location is based on the assumption that if two events are recorded in the same station and the hypocentral distance between them is smaller than the events-station distance as well as the lateral variability of the velocity model then the ray-paths are similar along most of the distance linking events origin-recording station. So, the difference in travel times is related to the space offset in events sources and it is not necessary to use station corrections.

The accuracy between relative arrivals times can be improved by waveform cross-correlation, assuming that both events are related to the same source mechanism and therefore produce similar seismic signatures in a common recording station (Waldhouser and Ellsworth, 2000). The method can be used in cluster analysis but also in larger distances by cross-correlating pairs of events across the area (see Figure II.11). A minimum distance within pairs of events

must be respected as a condition. In these, the slowness component in equation 3 must be constant across ray-paths to the receiver station.

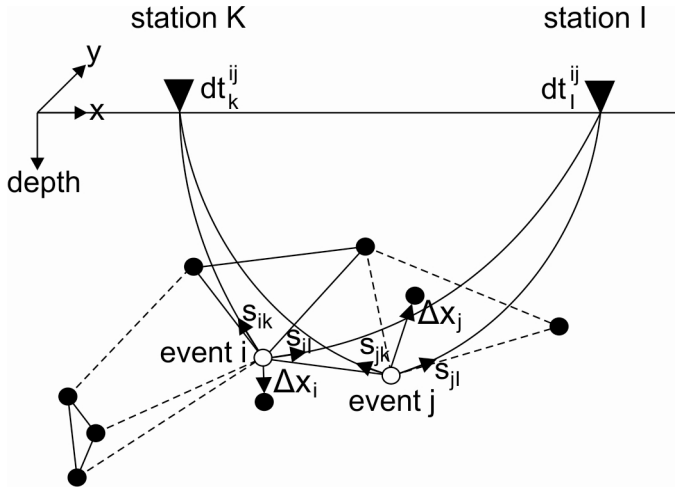

Figure II.11- Double difference method. Solid and open circles represent trial hypocenters that are linked to neighboring events by cross-correlation (solid lines) or catalog (dashed lines) data. For two events, *i* and *j*, the initial locations (open circles) and corresponding slowness vectors, s, with respect to two stations, *k* and *l*, are shown. Thick arrows (Δx) indicate the re-location vector for events *i* and *j* obtained with double difference method and *dt* is the travel-time difference between the events *i* and *j* observed at station *k* and *l*, respectively (from Waldhouser and Ellsworth, 2000).

Equation (6) can be rewritten for events ***i*** and ***j*** as:

$$\sum_{k=1}^{4} \frac{\partial t_k^{ij}}{\partial h_k} \Delta h_k^{ij} = dr_k^{ij} \quad (16)$$

Where $\Delta \boldsymbol{h_k^{ij}}$ is the difference relative hypocentral parameters for events ***i*** and ***j***, $\frac{\boldsymbol{\partial t_k^{ij}}}{\boldsymbol{\partial h_k}}$ are partial derivates of travel time between event source and receiver station (including a component of slowness). $\boldsymbol{dr_k^{ij}}$is the residual between observed and calculated arrival times between the two events:

$$dr_k^{ij} = (t_k^i - t_k^j)^{obs} - (t_k^i - t_k^j)^{cal} \quad (17)$$

To assure that the slowness vector across the raypaths is constant this difference can be written as:

$$\sum_{k=1}^{4} \frac{\partial t_k^i}{\partial h_k} \Delta h_k^i - \sum_{k=1}^{4} \frac{\partial t_k^j}{\partial h_k} \Delta h_k^j = dr_k^{ij} \quad (18)$$

Assuming a slowness vector and origin time for each event.

Solutions are found by iteratively adjusting the vector difference between nearby hypocentral pairs, with the locations and partial derivatives being updated after each iteration (Waldhauser, 2001). The double-difference residuals for pairs of earthquakes at each station are minimized by weighted least squares. We used *HypoDD* program package (Waldhauser, 2001) for relocating our dataset with the double-difference algorithm (details in chapter III.3.3).

II.4.3.Determine focal mechanisms and the regional stress tensor

II.4.3.1.Introduction

The way rocks react to stress depends on how large the stress is and for how long it is applied. Provided the applied stress remains below the yield stress (elastic limit) the short-term behaviour is elastic. An earthquake takes place when the elastic yield strength of the local rocks is exceeded and failure occurs. However, away from the rupture area the rocks' coherence is preserved. Seismic waves will therefore spread out by elastic deformation inducing ground motions reflecting the relative movement of the two sides of a source fault. These seismic waves are recorded in seismic stations. If earthquakes are caused by faulting then we can deduce the fault kinematics from an adequate set of seismograms and in turn the characteristics of the stress field acting on that region, as discussed below.

II.4.3.2.Focal mechanism

For most micro or local earthquakes networks, fault plane solutions are derived only from P-wave first motion polarity. Compared to waveform inversion methods, P-wave first motion polarities are still useful to constrain the source mechanisms for micro-seismicity studies, due to their waveform complexities that cannot be modelled by simple and smooth velocity structures. Figure II.12a shows the P-wave radiation pattern for a pure-strike slip fault. Since the radiation pattern of the seismic wave is dependent on the fault geometry and kinematics we can use it to work out the fault plane solution. If the radiation pattern induces the material to move away from the source fault area, then the first motion is compression. By contrast, if the material moves towards the fault source then the first motion is dilation. On the receiver stations, the seismograms record positive polarities, or upwards P-wave first motion, and negative polarities, or downwards P-wave first arrivals, respectively (see Figure II.12a).

The locations of compressions and dilatations leaving the fault zone are defined as points in a focal sphere. The first arrival polarities (observed at the receiver stations) are represented in the lower hemisphere and projected using the equal area stereographic representation. This is depicted in Figure II.12b. Each receiver station defines a polarity measure on the focal sphere (solid represents compression and open refers to dilatations -Figure II.12c). The first motions will delineate four quadrants, separated by two nodal planes (fault and auxiliary fault planes) along which there is no radiation of P-waves. The bisectrices of dilatation and compression quadrants are coincident in the maximum and minimum compression directions, respectively (Figure II.12d). The maximum stress is denoted by the P-axis while the minimum stress direction is defined as the T-axis. The B axis- indicates the intermediate stress and is perpendicular to both P and T axes. Note that from the radiation pattern in Figure II.12a it is

impossible to define which is the preferable fault plane. The solutions for both P and T axes define a force system that is defined as a "double-couple" (or DC). Non-DC sources, representative of complex rupture histories or including an "explosive" component, cannot be evaluated by the P-wave polarity method outlined here.

The focal mechanism solutions are defined by strike, dip and rake. Strike φ is measured between 0° and 360º. The convention for its measurement assumes that: the strike direction is defined by the horizontal line in the foot-wall of the fault-plane and its orientation is established by the *right-hand rule*. The dip δ is measured perpendicularly to the strike direction and the rake λ is the direction along the slip on the fault and is bounded between – 180° and 180°, where reverse fault is 0°<λ<180°, normal faults between -180° and 0° and right lateral strike-slip if λ=180° and left if λ=0° (Snoke, 2003). In this work two different methods (FOCMEC and FPFIT) were applied to estimate the focal mechanism solution. Both methods use a grid-search method to find the best fitting focal mechanism for the observed polarities.

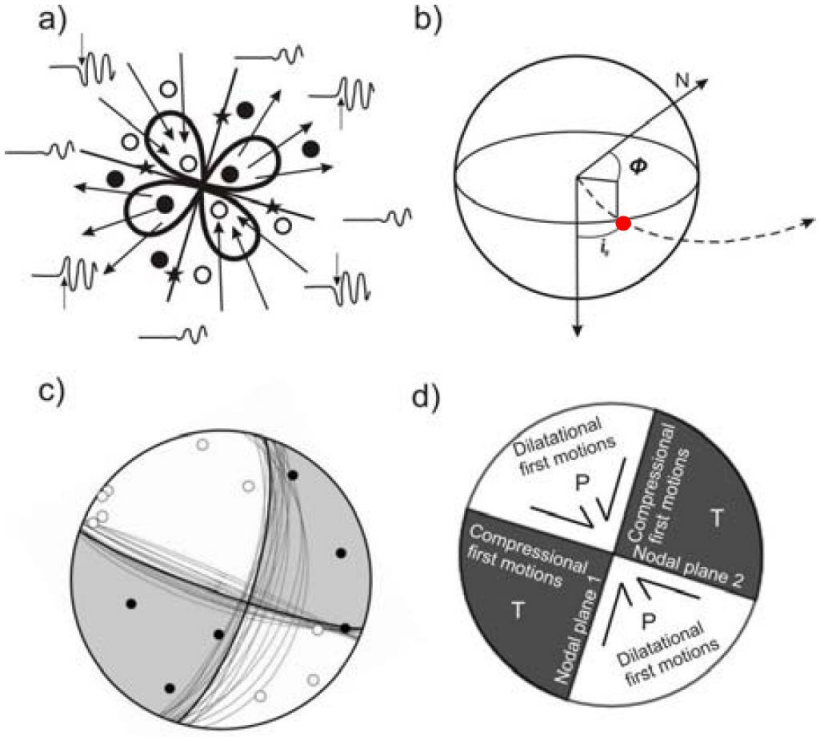

Figure II.12- Determining focal mechanism solution based on the polarity P-wave first motion a) P-wave radiation pattern (details in the text) b) ray-path and the focal sphere where φ is the strike and i_0 is the angle of emergence c) subdivision in quadrants and d) focal mechanism solution (adapted from World Stress Map Project guideline for focal mechanisms).

Cross-correlation and sequence analysis

Cross-correlation analysis is used to compare the P and/or S waves of closely related earthquakes that could result from the same seismic source. For closely related seismic activity it can be useful to define the location and geometry of

the seismogenic source zone. This is particularly reliable in seismic crisis, where seismic activity is highly concentrated both in time and space. Here, this analysis was applied to identify closely related events, re-locate them with JHD method and compute a composite focal mechanism. The cross-correlation function is defined by:

$$C(g,h,l) = \int_{-\infty}^{+\infty} g(t+l)h(t)dt \quad (19)$$

Where $g(t)$ and $h(t)$ are two seismic signals while l is the time lag between the two waveforms. For $l > 0$, $g(t)$ delayed with respect to $h(t)$ and vice-versa. In fact, two waveforms recorded at the same stations and related to events with similar/coincident locations are expected to have coherent phase picking. However, even for that particular scenario several aspects can impose discrepancies between the events picking:

1. Phase picking is a subjective procedure;
2. Variability in signal to noise ratio;
3. Events magnitude.

A normalised cross-correlation function is often used to reduce the influence of the waveform energy:

$$CN(g,h,l) = \frac{C(g,h,l)}{C(g,g)C(h,h)} \quad (20)$$

Where $C(g,g)$ and $C(h,h)$ defines the auto-correlation function.

The cross-correlation is performed by the multicorr application. It cross-correlates a given set of waveforms based on predefined parameters: the number of samples to compare, the time window and the correlation limits. Several indexes are obtained as outputs: compared events identification, cross-correlation value (1.0 for identical events), time lag of the waveforms and signal to noise ratio. The signal to noise ratio is computed by auto-correlating each event waveform in two time windows, one preceding and the other during the earthquake. Cross-correlation computation retrieves the average signal to noise ratio for the compared events. This parameter can be used to evaluate the reliability of the identified similarity. Multicorr outputs the index described above in individual files, identified by station component.

Events sequences are determined based on the output of multicorr. The application matrix-sup extracts the events that are defined as a sequences based on the following parameters:

1. A minimum correlation value;
2. A interval of signal to noise ratio to consider the above calculations;

For each sequence determined, files storing the events collection are created. The reliability of the results is tested by visual inspection of selected events

waveforms and by the proximity of events locations. Details on the cross-correlation and sequence analysis are presented in chapter III.4.2.1.

II.4.3.3.Determining the regional stress tensor

To determine the stress tensor based on focal mechanism data, P, B and T axes are considered good approximations to the principal stress directions σ_1 (maximum compression), σ_2 and σ_3, respectively. This is true for newly formed faults and ideal media without internal friction, where focal mechanism nodal planes match the maximum shear stress planes (Gephart and Forsyth, 1990a). However, in most geodynamic settings, the reactivation of pre-existing faults prevails since the stress needed to form new faults is considerably higher. In these cases, the directions of slip in a single fault (or in a limited number of faults) can diverge substantially from the regional principal maximum stress directions derived by the focal mechanism analysis. The direction of slip should be the one that coincides with the maximum shear stress direction on the fault plane. Additionally, the principal stress directions can be identified by considering the direction of slip in several faults for an area of uniform stress. In such a case, resulting focal mechanisms solutions are consistent with a limited number of common stress directions. By combining several observations, a range of matching solutions can be obtained for the local stress field.

Stress limits to pre-existing fault slip

The stress acting on a fault plane can be resolved in two components: the normal stress (σ_N) and the shear stress (σ_S), perpendicular and parallel to the plane, respectively. The σ_N inhibits sliding and σ_S promote it. In an isotropic medium a new fault will be formed if the applied stress exceeds the rocks strength. However, pre-existent faults have neither tensile nor cohesive strength; as a result failure occurs as long as frictional resistance to slip is overcome. The frictional resistance to slide is related to the normal stress acting on the surface, friction is directly proportional to the normal force. Other controlling factors are inherent to rock type and the fault surface. The roughness of the fault surface contradicts sliding, as the movement starts and promotes surface smoothness and decrease slide resistance.

Here, the Focal Mechanism Stress Inversion (FMSI) package from Gephart (1990) was used to define the best-fitting regional stress tensor compatible with the majority of observed earthquake focal mechanisms (for detailed aspects of the background theory see Gephart and Forsyth (1984) and Gephart (1990a, 1990b)). In Gephart and Forsyth (1984), the condition of slip on fault plane is defined according with the following assumptions: there is no shear slip perpendicular to the fault (in the direction of σ_N); and the maximum shear stress (σ_S) is in the direction of slip:

$$\sigma_N = \frac{\sigma_1+\sigma_3}{2} - \frac{\sigma_1-\sigma_3}{2}\cos 2\theta \quad (21)$$

$$\sigma_S = \frac{\sigma_1 - \sigma_3}{2} \sin 2\theta \quad (22)$$

Where θ is the angle between the fault plane and direction of maximum compression (.σ_1).

The inversion method

In the FMSI application the inversion process will find best fitting stress model to the focal mechanism data using a grid search approach and assuming a local uniform stress field. It is implicit that both the fault plane (two possibilities exist from the focal mechanism solution) and stress directions are unknown. Accordingly, a primary measure of the inversion model is the misfit between predicted and observed data (stress model and fault planes solutions).

The resulting stress model comprises the principal stress directions and additional a value **R**, the Stress Ratio, that is defined as:

$$R = \frac{(\sigma_2 - \sigma_1)}{(\sigma_3 - \sigma_1)} \quad (23)$$

R gives a measure of the relative magnitude of the stress, because of the assumption that $\sigma_1 \geq \sigma_2 \geq \sigma_3$, *R* is limited between 1 and 0. In the special case of hydrostatic stress R=0, in triaxial compressive domains *R* tends to 1 because $\sigma_1 \gg \sigma_2 \geq \sigma_3$, while in a tensile domain *R* tends to 0 with $\sigma_1 \geq \sigma_2 \gg \sigma_3$.

As mentioned before, the aim of the inversion process is to find the stress and *R* parameters that reduces the discrepancies between the observations and the predicted model. The misfit is the smallest rotation about any axis that brings one of the nodal focal mechanism planes and its slip direction/sense of slip into an orientation that is consistent with the stress model (Gephart and Forsyth, 1984). The discrepancies reflect not only relative rotations between the observations and model solutions but also errors in focal mechanism determinations and local stress variations (*idem*). If inconsistency between the inverted model and the observations result from stress variation it may be necessary to subdivide the initial dataset into subsets that sustain the assumption of uniformity. These subsets may be temporal or spatial limited. A focal mechanism with an inferred fault plane corresponding to a small value of shear stress must be considered suspect and can eventually be disregarded during the inversion procedure.

II.5.RE-processing IAM-GB1 multi-channel reflection profile

II.5.1.Introduction

This subchapter provides an overview of basic concepts of marine multichannel reflection profile acquisition and processing. Details of the acquisition of IAM-GB1 and of the re-processing parameters are presented Appendix V. Essential concepts on marine multi-channel seismic reflection acquisition system are presented first because of their importance for the processing stages.

The acquisition system is defined by the source model, the receiver sequence and the digital recording system. The source is a controlled artificial generated acoustic signal which result from explosions generated using different mechanisms: e.g. water steam (steam gun) or compressed air (airgun) injections or high electric pulses (sparker). Synchronized airguns arrays are the more common source for marine multi-channel acquisitions. The use of multiple airguns increases source energy and diminish bubble noise that affects data quality. The ideal source would produce a very short impulsive wavelet (Figure II.13a). However, isolated gas bubbles produced by an airgun oscillate and generate successive pulses (Figure II.13b) that cause source-induced noise. Airgun arrays can cause destructive interference of bubble pulses and alleviate the bubble noise using different volumes and towed at different depths (Figure II.13c).

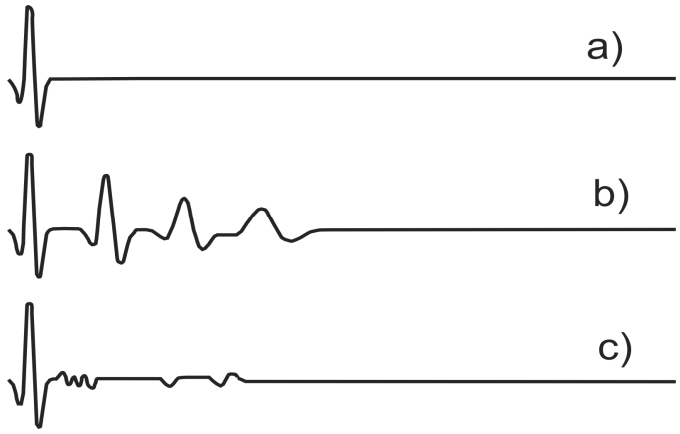

Figure II.13- A schematic example of ideal (a) and typical source-time functions produced by an airgun (b) and by an airgun array (c) in a marine experiment. In the airgun signal a series of bubble pulses are produced by pressure reverberations within the water which are attenuated with airgun combined array (from Shearer, 2009 and Sheriff and Geldart, 1995).

Another basic part of the marine acquisition system is the receiver station, which is most commonly a streamer (Figure II.14). The streamer is a buoyant surface marine cable that comprises an array of hydrophone groups (channels).

The hydrophones detect pressure changes induced by seismic waves' propagation following successive explosions generated from different sources and which are recovered from different points along the pre-defined profile. This analogue response is subsequently converted to a digital signal (pre-amplified

and pre-filtered) by an analogue-digital converter. The seismic signal is a continuous time function. The conversion into the digital domain (discrete record) is done using a fixed sample rate, typically between 1 and 4 ms for seismic reflection data. During digitalization the seismic signal would loses frequencies that are above a term defined as the Nyquist frequency, $f_N=(1/2\Delta t)$, Where Δt is the sampling rate, e.g. a sampling rate of 4ms will lose all the frequencies above 125Hz (Yilmaz, 1993). In fact, frequencies greater the Nyquist frequency will be converted into low frequencies and undistinguished from the original seismic signal. This phenomenon is defined frequency aliasing and is exemplified in Figure II.15. To avoid this contamination of the digital signal its applied a anti-aliasing filter. Normally, a high-cut filter with the cut-off frequency between ¾ to ½ of the Nyquist frequency.

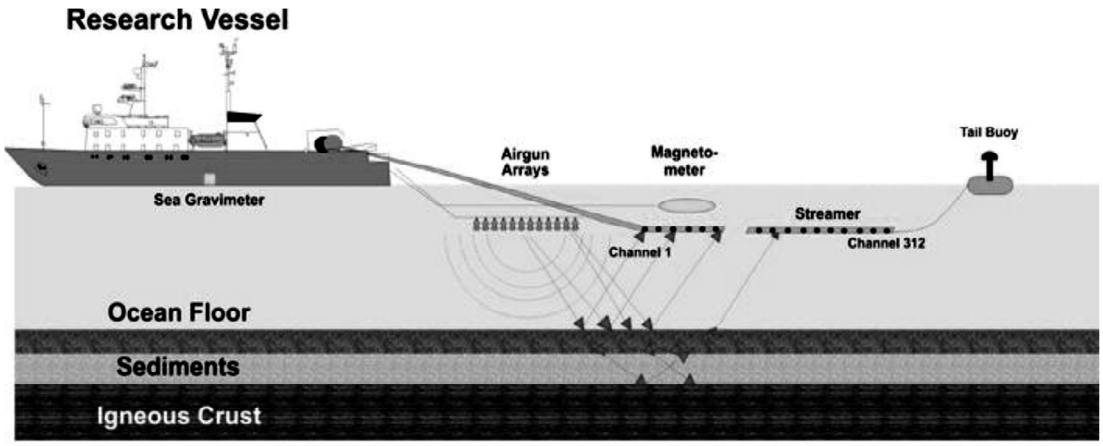

Figure II.14- Marine acquisition system (Adapted from www.bgr.bund.de).

The field geometry defined between the airgun array (as well explosion frequency), the streamer, the channel distribution within the streamer and the streamer extension depend on the scientific objectives of the acquisition campaign. The source and receiver spacing define a fundamental acquisition parameter: the fold. The marine multi-channel acquisitions operate in multiple cover system which consists in a multi-trace response observation (fold) of the same midpoint in a seismic profile, favouring an improved image of subsurface geology in that point: the common midpoint (CMP). Considering a sub-horizontal layered medium, then a common midpoint (CMP) is located at half distance (offset) between the receiver and the *shotpoint*. The method is exemplified in Figure II.16. For example if the shooting interval and receiver distance are both 25m (D in Figure II.16), then the **C**ommon **M**id-**P**oint (CMP, represented as P in Figure II.16) distance is 12.5m (half the distance between receivers, D/2 in Figure II.16); the fold is be defined by:

$$\frac{receivers\ distance}{2 \times shooting\ distance} \times n^{o} receivers$$

*f*or a streamer with 96 receivers groups it is 48. So, the same point in the seismic profile will be sampled by 48 different channels and imaged by 48 traces. This methodology is central to improve the signal to noise ratio, one of the main purpose of processing steps as discussed in the next subchapter.

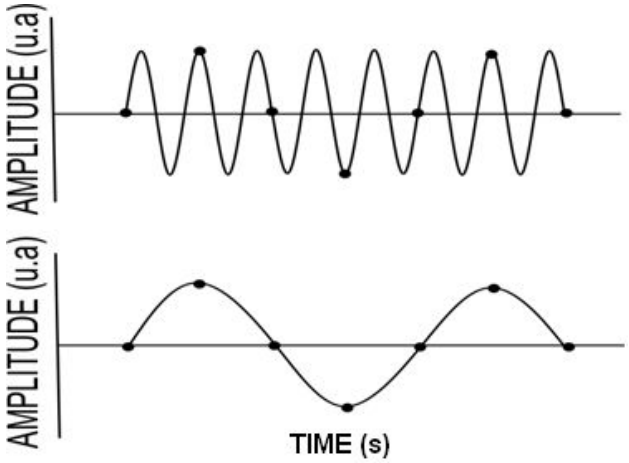

Figure II.15- Frequency aliasing. On top is an original high frequency signal and in the bottom is the interpolated, based on the sample rate (black dots), low frequency signal.

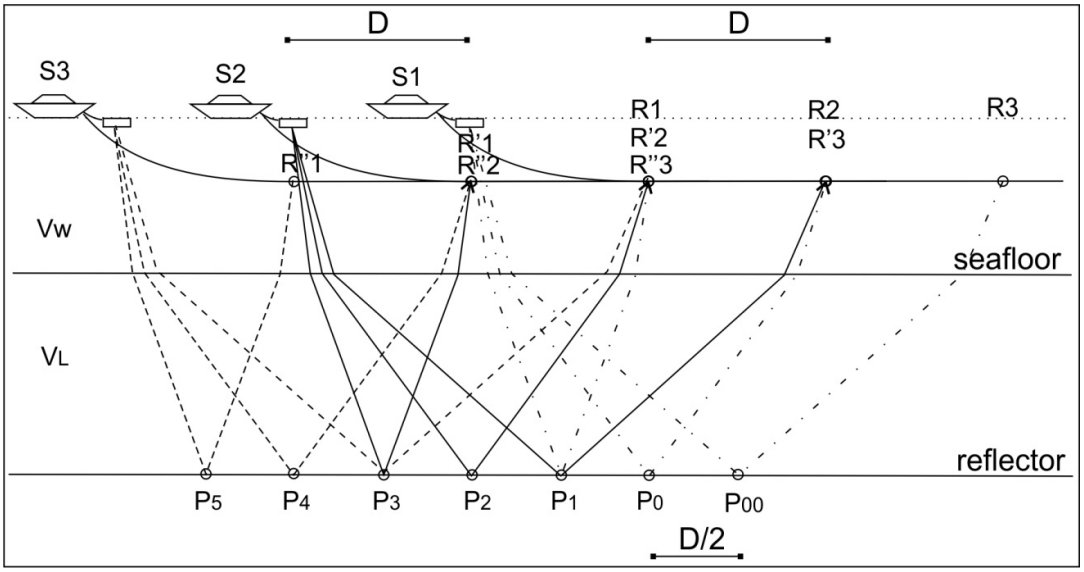

Figure II.16- Marine multiple cover system: SHOT1-3 define successive shooting positions; Rn, R'n, R''n are receivers at shoting positions S1, S2 and S3, respectively; Pn define covered positions in the reflector. D defines both shooting interval and receivers group distance, VW and VM are the water and first layer velocities, respectively dushed, full and point-dashed lines are ray path from source to Pn then reflected to receiver points in the streamer (from http://walter.kessinger.com/work/seisx_processing.html).

II.5.2.Processing sequence

The aim of marine seismic reflection data processing is to create an image of subsurface geology. This image results from the interaction between a relatively well- known artificial source with both the water and rock layers, and it is

recorded in arrays of receiver stations. The prime interest resides in the P-wave primary reflections; the remaining energy is considered noise. Noise can be the energy of direct, refracted, diffracted or multiple reflected waves (Figure II.17) but it can also result from sea swell (direct or movement induced in recording cable), from the vessel, fish bites or moreover from electrical spikes in the recording system. Increasing signal to noise is one of the main objectives of seismic processing steps. All energy in the seismic data departing from the signal of interest are considered as noise. It can be subdivided into coherent (e.g. direct, refracted or diffracted waves) and incoherent noise (e.g. instrument or cable noise). The coherent noise is consistent from trace to trace while incoherent or random noise lack of continuity between adjacent traces. These characteristics are fundamental to select which processing steps to be used to enhance the signal and attenuate the noise.

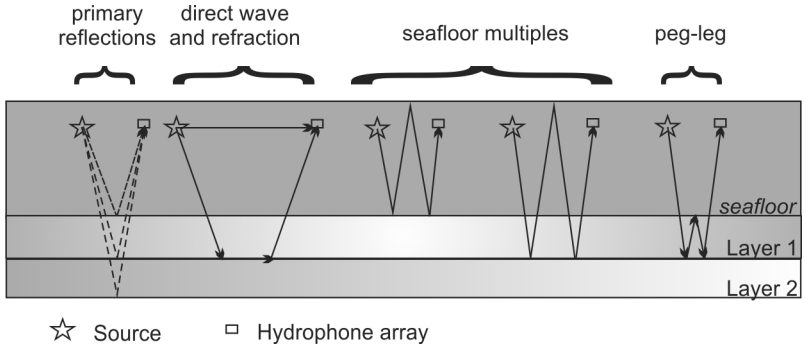

Figure II.17- Illustration of possible energy paths between the source and receivers arrays.

There are three fundamental steps in seismic reflection data processing: deconvolution, stacking and migration. However, defining the appropriate sequence and processing parameters is a critical task. It depends on several factors such as acquisition parameters (instrumental and external conditions) and the study adequacy. In this case, two main objectives were considered when reprocessing IAM-GB1 profile: firstly, to improve seismic attributes observations in the acoustic basement and secondly to obtain a depth converted profile.

II.5.2.1.Pre-processing steps

A typical processing sequence starts with some preliminary steps. First, the data acquisition format is identified. The field data are usually time-sequenced meaning that samples from the same time for all channels are packed together. The sample from a time x in the channel 1 is stored next to the same time sample from channel 2. However, in seismic processing steps it is convenient to have the data stored by channel. All the time samples from each channel are stored together followed by those in the next channels. This process is called de-multiplexing. The next pre-processing step engages a preliminary quality check of the acquired data. Auxiliary channels, noisy traces are deleted and a frequency analysis of the data is made. Accordingly, the dominant spectrum of

the recorded signal (and noise) is identified which will help to define which process and parameters are more adequate to attenuate undesirable noise.

Another step applied in the pre-processing stage is a preliminary amplitude correction to compensate energy lost due to wave propagation in the medium, resulting in two main effects:

1. Absorption resulting from the transformation of the elastic energy in heat during medium propagation. It will increase with depth and it will work as high-frequency filter. The correction can be applied based on time and space variant gain. Scattering also attenuates energy but its effect is like absorption and very difficult to separate. Both effects are considered and compensated together.
2. Spherical divergence resulting from the dispersion of energy in wavefront, as a function of the increasing distance between the shot and the receiver. This energy attenuation it is proportional to $1/r^2$ for a homogenous medium; where **r** is the radius of the spherical wavefront. In a stratified earth, the energy decay is proportional to the velocity in each layer. We can use a preliminary velocity estimation of each layer to apply the correction or we can just define a constant velocity and improve latter on based on more detailed velocity analysis needed for the stacking stage.

Finally, field geometry is taken into account based on the acquisition parameters. This step allow to short the data in CMP gathers and should precede any offset depend operation. Defining the correct geometry is fundamental for the reliability of remaining processing stages. Using wrong field parameters compromises the veracity of the final seismic image.

II.5.2.2.Deconvolution

The deconvolution aims at recovering the Earth signature in the seismic trace by eliminating the remaining noise and compressing the wavelet. Ideally, the seismic trace would only show the recorded earth response impulse (primary reflections) resulting from a spike wavelet source. However, the seismic trace comprises primary reflection plus a variety of multiples and noise from several sources, coherent and incoherent. Furthermore, the wavelet is not really a spike.

The seismic trace can be defined as the convolution between the source wavelet and the earth's response Yilmaz (2001):

$$x(t) = w(t) * e(t) + n(t)$$

Where $x(t)$ is the seismic record, $w(t)$ is the basic wavelet, $e(t)$ is the Earth's impulse response, $n(t)$ is the random ambient noise and * denotes convolution. This is defined as convolutional model (see Figure II.18). In theory if we know

the source wavelet form and succeed to eliminate the ambient noise then we could recover earth response.

If we could assume that we have low ambient noise than:

$$x(t) = w(t) * e(t)$$

This is the main goal of deconvolution, to design an operator/filter $a(t)$ that:

$$a(t) * x(t) = e(t)$$

If we combine the two last equations we would have:

$$x(t) = w(t) * a(t) * x(t)$$

Than by excluding $x(t)$

$$\delta(t) = w(t) * a(t)$$

With $\delta(t) = 1$ for t=0 and $\delta(t) = 0$ otherwise.

$$a(t) = 1 * w'(t)$$

Where $w'(t)$ is the inverse of the wavelet.

The seismic signal can be converted from time domain to frequency domain using forward Fast Fourier Transform (FFT). The seismic signal can be define in the frequency domain as a sum of sinusoids, each one with a unique frequency, amplitude and phase. This is one fundamental base to seismic data analysis and seismic processing. The backwards synthesis of all frequency components into time-dependent signal is done using inverse Fourier transforms. Note that convolution is equivalent to multiplication in the frequency domain while addition remains the same operation. So in the frequency domain:

$$A(\omega) = \frac{1}{W(\omega)}$$

Then the deconvolution operator or filter is the inverse of the wavelet.

The importance of this operation is that in the frequency domain the wavelet and the seismic trace have similar signatures as is shown in Yilmaz (2001, in figure 2.13, here see

Figure II.18). The same is also true for autocorrelation functions. In fact, wavelet and seismic trace autocorrelation functions are equal only where wavelet autocorrelation is non-zero (see

Figure II.18).

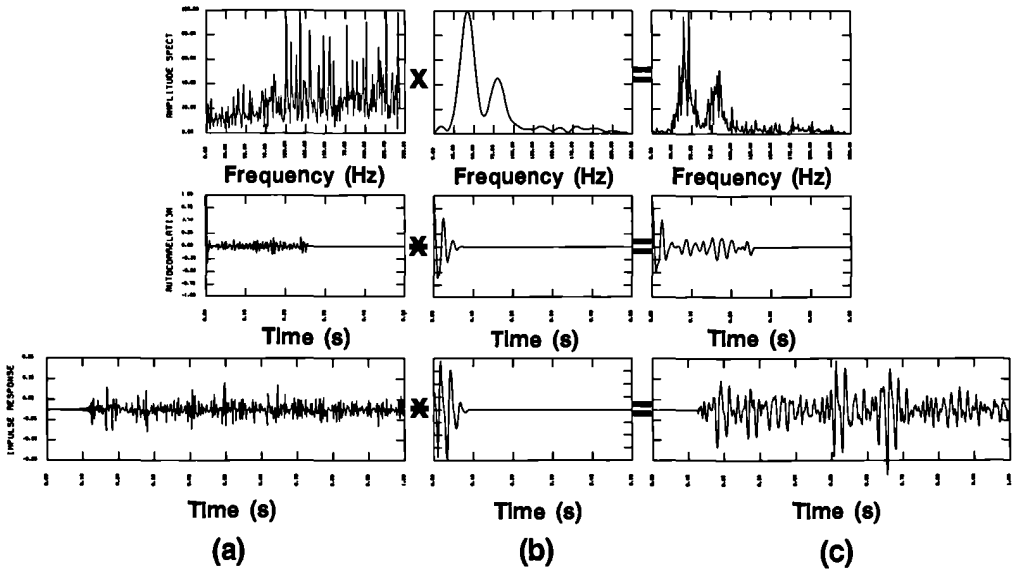

Figure II.18- The convolutional model. In the frequency spectrum and the autocorrelation functions of the wavelet (b) and the seismic trace (c) are similar (top and middle figures). Seismic trace is the convolution of t the earth impulse (a) response with a source wavelet in the time domain (bottom figure, from Yilmaz, 2001).

So, the fraction that is not similar should represent the impulse response of the Earth. This means that the wavelet trace can be found in the seismic record and the earth impulse extracted. This is the key for predictive deconvolution, and has been applied in the IAM-GB1 re-processing workflow.

II.5.2.3.CMP sorting, velocity analysis and stacking

The multi-channel seismic profiles acquisition is defined with a multi-fold coverage. As a result a CMP is covered by several traces (Figure II.19A). For an homogeneous layer the horizontal reflector defines an hyperbolic curve on a CMP gather (Figure II.19B). On the other hand, the direct wave defines a straight line in a two-way time (TWT) versus offset display. In order to increase the signal to noise ratio by stacking (Figure II.19D) the redundant observations available on the CMP gather, the hyperbolic curve must be corrected into a horizontal line (Figure II.19C). This process is the normal moveout (NMO) correction and is defined as follows (Yilmaz, 1993):

$$\Delta t_{NMO} = t(x) - t(0) = \sqrt{t^2(0) + \frac{x^2}{v_{NMO}^2}} - t(0)$$

Where $t(x)$ is the time between the shot-point, CMP and receiver while $t(0)$ is the time if the shot-point location was coincident with the receiver and the CMP was just below, at a point in a perpendicular line (Figure II.19a). For a homogeneous layer v_{NMO} is identical to the media seismic velocity. For a layered media with horizontal interfaces the travel-time curve of reflections is still

approximately hyperbolic and the NMO correction is still valid. For horizontal layering the CMP coincides with the CDP (Common Depth Point).

Note that if we consider that the reflector is not horizontal the CMP and CDP will be different (in fact there is no more a CDP) and the NMO correction is given by:

$$\Delta t_{NMO} = \sqrt{t^2(0) + \frac{x^2 cos^2 \phi'}{v_{NMO}^2}} - t(0)$$

Where $\phi'$is the apparent dip of the reflector (or the dip at the seismic section).

In a horizontally stratified medium, the travel time equation for a path between a source, a CMP at depth D and a receiver is (from Yilmaz, 1993):

$$t^2(x) = C_0 + C_1 x^2 \ldots + C_n x^{2n}$$

With $C_0 = t^2(0)$, $C_1 = 1/v_{RMS}^2$ and $C_n x^{2n}$ is a complex function that depends on layers velocity and thickness, where v_{RMS} is the velocity down at depth of the reflector D:

$$v_{RMS}^2 = \frac{1}{t(0)} \sum_{i=1}^{N} v_i^2 \Delta t_i(0)$$

Where v_i^2 is the interval velocity of the i^{th} layer. According to Yilmaz (1993) the travel time expression can be simplified if a small-spread approximation is considered, i.e. if the offset is smaller than the depth, then:

$$t^2(x) = t^2(0) + \frac{x^2}{v_{rms}^2}$$

For a horizontal layering v_{NMO} is equal to v_{rms}, the same assumption is applied for gentle dipping reflectors.

According to the above-described, three fundamental aspects control the NMO correction: the seismic velocity of the medium along the ray path, the shot-receiver distance and the reflectors depth. Hence, velocity analysis is an essential processing step that we will sum up next.

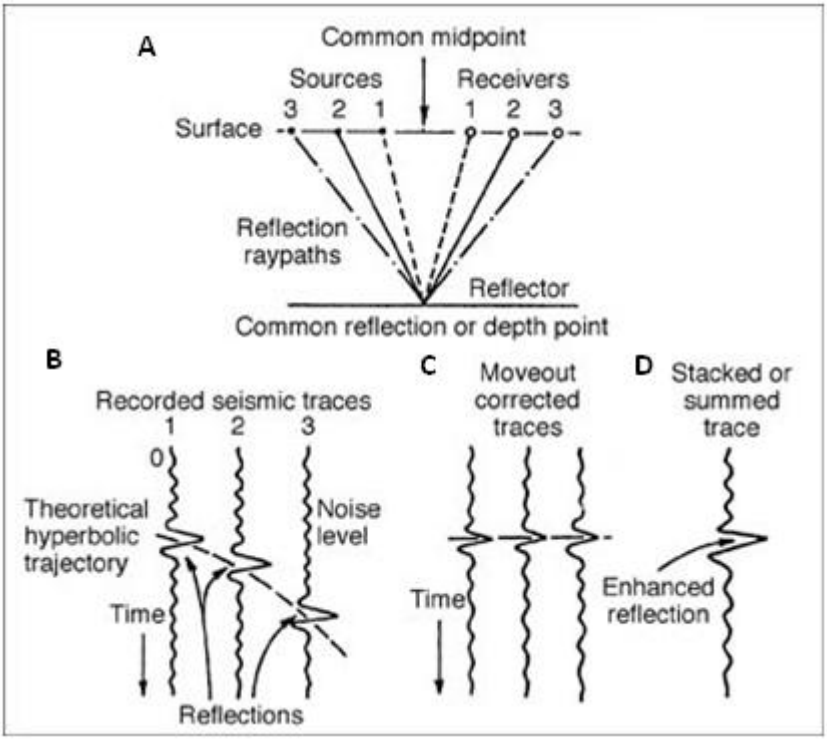

Figure II.19- Common Midpoint (A), common midpoint gather(B), NMO (C) and stacking (D) (adapted from http://www.glossary.oilfield.slb.com/Terms/c/common_midpoint.aspx).

The velocity analysis is an interactive processing procedure that enables an interpretation of the NMO (stacking) velocities. It can be done using different methods. However, here only the semblance analysis is shown (Figure II.20). The semblance measures the similarity between adjacent traces by evaluating its fit into a possible hyperbolic trajectory. The result is TWT vs velocity display with a similitude scale (see left display in Figure II.20). The interpreter selects the velocities with maximum semblance and simultaneously examines the result in:

1. CMP gather to verify the NMO correction of the reflectors (see centre display in Figure II.20);
2. In preliminary stack to assure the reflectors lateral coherency (see right display in Figure II.20).

These plots allow the interpreter to improve the NMO correction by correcting the stacking velocities to assure the horizontality of the reflectors. The final velocity model is used to generate the stacked section.

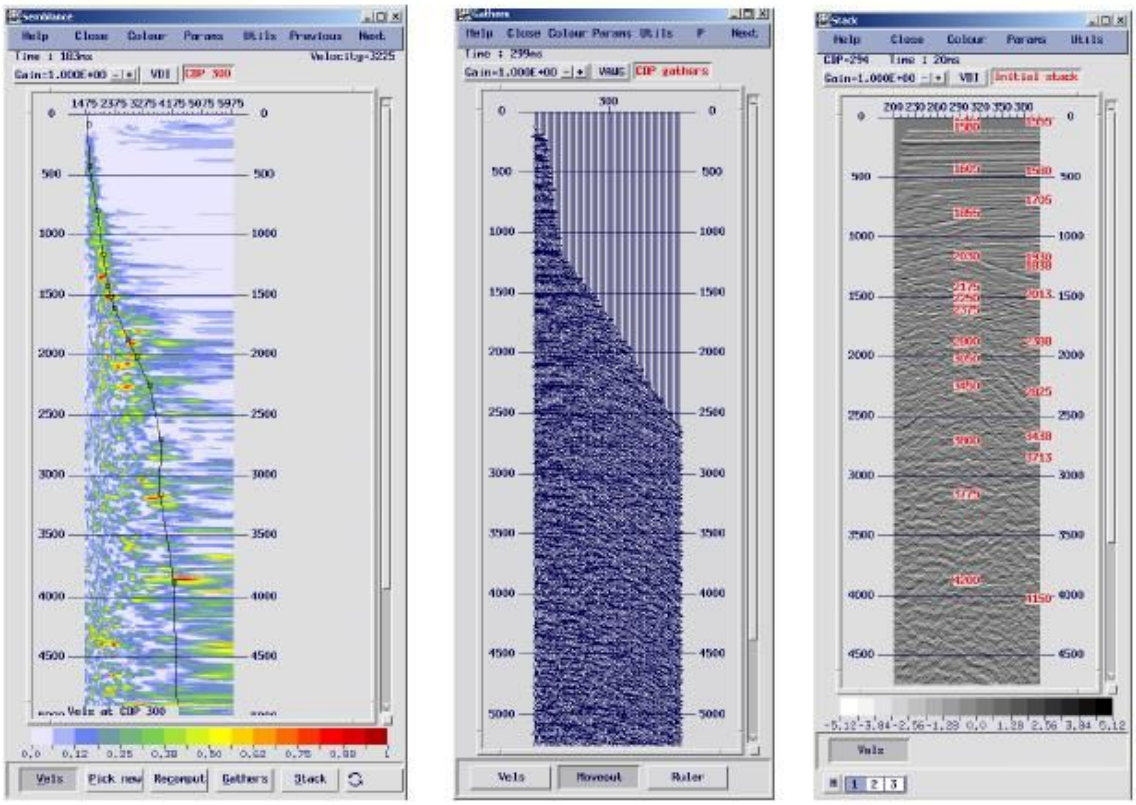

Figure II.20- Semblance analysis displays (to the left is semblance, in the center is a CMP gather and to the right is preliminary stack of CMP, image from Globe Claritas Marine Tutorial, version 5.4).

II.5.2.4.Time Migration and Depth Conversion

Migration relocates the dipping reflectors into its true position and collapse diffractions. Figure II.21 shows a schematic representation of the migration principles (from Yilmaz, 2001). The true geometry of geological feature that generates reflector CD is represented in a depth-distance profile (see Figure II.21a). In a zero-offset (or stacking) time section, vertical incidence of the ray generated at the reflector CD is assumed and recorded at the receivers AB. As a result the original reflector CD, dipping $\bar{\theta}$ is placed at position in C'D', dipping θ. Migration should position the C'D' into a position/geometry closer to CD. The quantitative analysis of this migration process is described in Figure II.22 (from Yilmaz, 2001). The relations between horizontal and vertical displacements on the migrated and unmigrated sections are defined by the following formulas (see definitions in Figure II.22).

$$dx = \frac{v^2 \Delta t}{4\Delta x}$$

$$dt = t\left[1 - \sqrt{1 - \left(\frac{v\Delta t}{2\Delta x}\right)^2}\right]$$

$$\frac{\Delta\tau}{\Delta x} = \frac{\Delta t}{\Delta x} \frac{1}{\sqrt{1 - \left(\frac{v\Delta t}{2\Delta x}\right)^2}}$$

Several observations are made by Yilmaz (2001) based on the described equations and Figure II.22:

The time dip at migrated sections are always greater than in stacking sections, i.e. $\frac{\Delta\tau}{\Delta x} > \frac{\Delta t}{\Delta x}$, or migration steepens reflectors;

In event E, the horizontal displacement Δx increases with time t;

Both horizontal and vertical displacements are dependent of the velocity selected for migration;

The steeper events imply higher horizontal and vertical displacement in migrated sections.

Time migration is an essential processing step to position observed seismic features closer to the geological reality. Several techniques are used for migration but all are based on the assumptions that:

1. Seismic section shows just primary reflections and diffractions;
2. The interval velocities along the ray-paths are known. Dix formulation is used to convert *rms* velocities into interval velocities:

$$V_i^2 = \frac{V_n^2 t_n - V_{n-1}^2 t_{n-1}}{t_n - t_{n-1}}$$

Where V_n is the *rms* velocity and t_n is the zero-offset arrival time corresponding to nth reflector (Sheriff and Geldart, 1995).

In practice, migration aims at solving the angle of incidence $\bar{\theta}$ (see Figure II.22) and track the ray path backwards to the reflecting point. The "Huygens' principle" is assumed, in which every point on a wavefront can be regarded as a new source. Each reflector is therefore seen as covered with point sources, all exploding at t=0 (Sheriff and Geldart, 1995). How this process is achieved allows distinguishing the different migration methods: e.g. Kirchhoff; finite-difference or frequency-wavenumber migrations.

A finite-difference method is used to reprocess the IAM GB1 MCS profile. This method allows to migrate dips up to 60°, produces less migration noise, is effective in low signal to noise areas and can accommodate lateral velocity variation (Sheriff and Geldart, 1995).

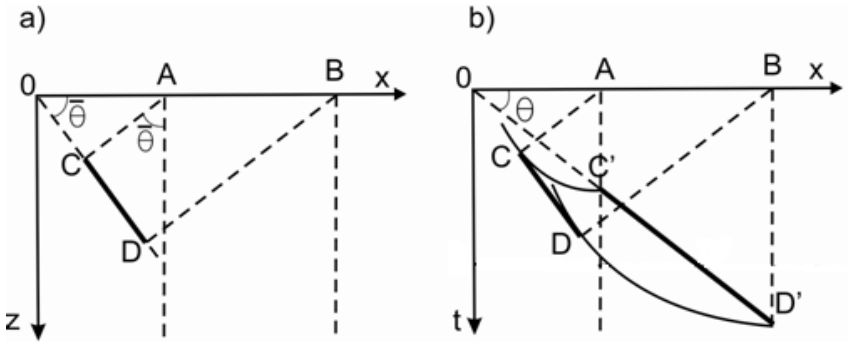

Figure II.21- Migration principles. a) Shows the true geometry of the reflector CD in a depth section, B) shows the same reflector in a stacking section (C'D') and the migrated back into position CD. It is clear that in the stacking section the reflector is less steep, deeper and longer than the original geological feature (image from Yilmaz, 2001).

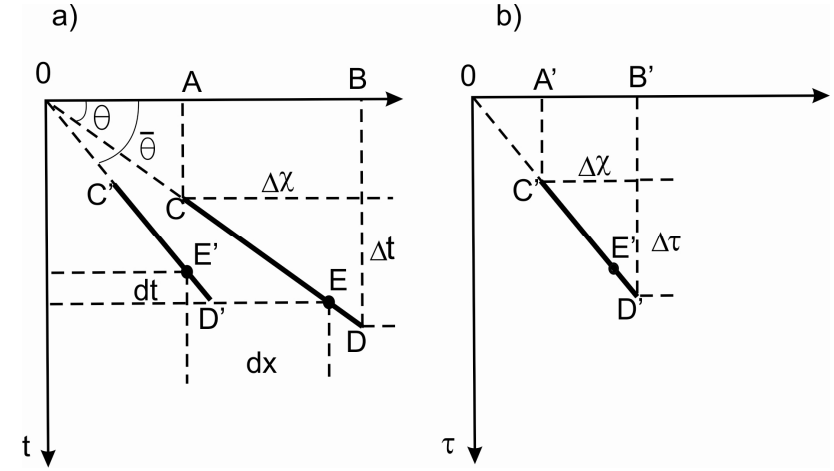

Figure II.22- Schematic representation of horizontal and vertical displacement in migrated sections. Note that reflector CD, in the unmigrated section, is moved to the C'D' position after migration. Event E and E' on the unmigrated and migrated section, respectively are used as reference for the amount of horizontal and vertical displacement (dt and dx).

The time migrated profile can be adjusted according to a vertical velocity function to obtain a linear in depth section. This depth conversion process differs from depth migration, which implies solving ray path in areas of high lateral velocity contrasts. Depth conversion is the process selected to obtain IAM-GB1 MCS profile in depth. What we obtained is a stretched version of the depth migrated profile, this approximation is particularly important in this work because it is helpful to relate geological structures with seismic activity. We selected this method because although this seismic section is located in the transition between different geodynamic domains, lateral velocity gradients are low as we will further discuss in chapter IV (and Appendix V).

II.6. Principles of seismic interpretation

Rocks are distinguished in seismology by seismic velocity and density. The product between density and velocity is the seismic impedance. The primary reflections recorded in the seismic trace result from seismic impedance contrasts that follow grossly the lithological bending or unconformities. As a result the primary reflectors have chronostratigraphic significance. It is worth

noticing that lateral *facies* transitions are too gradual to have any imprint at the seismic trace. These basic principles allow the correlation of reflectors of different areas and the link of the seismic signal with geological record.

Following the same principles, Mitchum et al., (1977) applied the stratigraphic concept of depositional sequence to the interpretation of seismic sections. A depositional sequence is "a stratigraphic unit composed of unconformable succession of genetically related strata and bounded at its top and base by unconformities or their correlated conformities". This definition is the bases of seismic stratigraphy and instructs the seismic interpretation as the study of the geometric pattern within a depositional sequence and of the surfaces separating it. The limiting boundaries can be:

- A hiatus defined by the nonexistence of an interval in geological record;
- An unconformity that is an erosional or a non-depositional surface and it marks a hiatus ;
- A conformity which separates sequences from different ages without evidences for a hiatus between it.

The concept is illustrated at Figure II.23. Seismic sequence is the depositional sequence in a seismic section and is subdivided in seismic units (numbers in Figure II.23). Seismic facies are the defining features that allow us to discriminate different seismic units. The essential parameters are summed up in Figure II.24

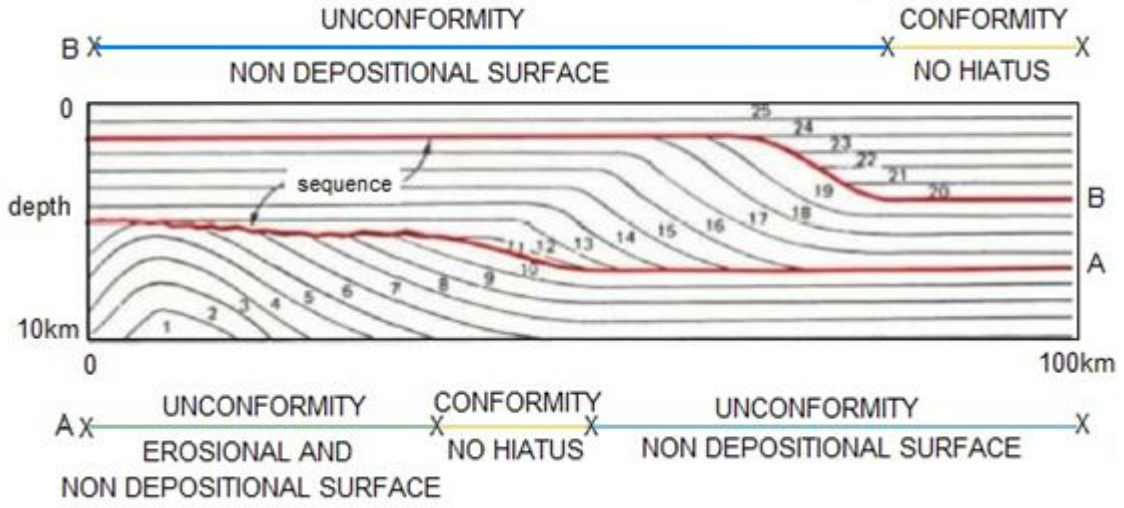

Figure II.23- Basic concepts of depositional sequence (from Roque, 2007 and references therein). Surfaces A and B define the base and the top of a seismic sequence. Both surfaces pass laterally from unconformities to conformities.

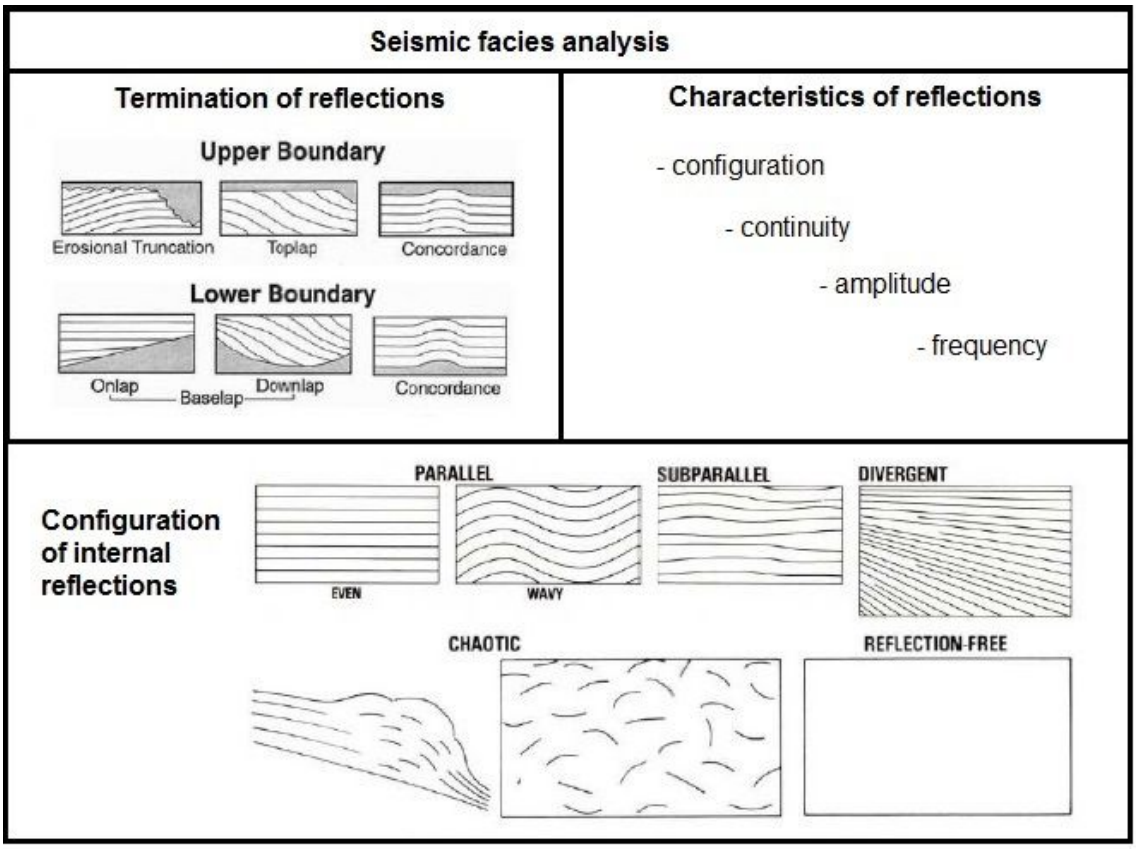

Figure II.24- Summary of parameters observed in seismic analysis (adapted from Valadares, 2012 and references therein).

III.NEAREST OBS experiment

In this chapter, we describe the results of the NEAREST seismic network experiment for local earthquakes monitoring in the Gulf of Cadiz region. It is subdivided in four sections. In the first section III.2, we describe pre-processing steps and preliminary results. We start by evaluating events detection and compare it with permanent land network data for the acquisition period. Next we describe the phase identification in LOBSTER OBS, GEOSTAR and land stations and local magnitudes estimation only from the OBS data. Finally, we present a preliminary earthquake location.

In the section III.3, we show the results on improving earthquakes location by applying Joint hypocenter determination, simultaneous inversion for hypocenter-velocity model and double-difference techniques. Fault-plane solutions and tensor analysis are described in section III.5 and III.6, respectively. In the last section we sum up and discuss the final results.

III.1.Pre-processing and preliminary results

III.1.1.Event detection and extraction

Since the NEAREST network acquired the passive seismic data in continuous, we tested two methods for earthquakes detection: spectrogram analysis and automatic trigger algorithm (details on both methods in chapter II).

The spectrogram image was created by using a routine package in FORTRAN code provided by Luís Matias. We started off by converting the originally waveform in seed format to ASCII using *rdseedasc* routine. In the next step, we used *len2bmp* application to generate spectrograms bitmaps (Figure III.1). This application uses an input file *len2bmp.in* with several user defined parameters (Figure III.2): the number of stations to output (nsta), the number sample points to compute the spectra (n_spectra); the instrument sample rate (sranom), the number of spectral frequencies to output (nfj), the number of frequencies to be averaged (n_sum), the time shift between spectra in s and the attenuation factor. Detected events were then extracted from each station waveform files (in seed format) using *rdmultiseed* routine and merged in events waveform files using *seisei* application (from SEISAN 9.0.1 package, Havskov and Ottemöller, 2011).

The second method uses an automatic REF-TEK trigger algorithm, STA/LTA (short time average/long time average). In this process, earthquakes are identified because absolute amplitude variations during these events are resolved from the background seismic noise. The effectiveness of this method depends mainly on trigger algorithm sensitivity and accuracy, determined by the adequacy of the selected trigger parameters (details in Table III.1Table III.2).

We only considered events that were identified simultaneously in more than 4 stations. An example is presented in Figure III.3 and Figure III.4.

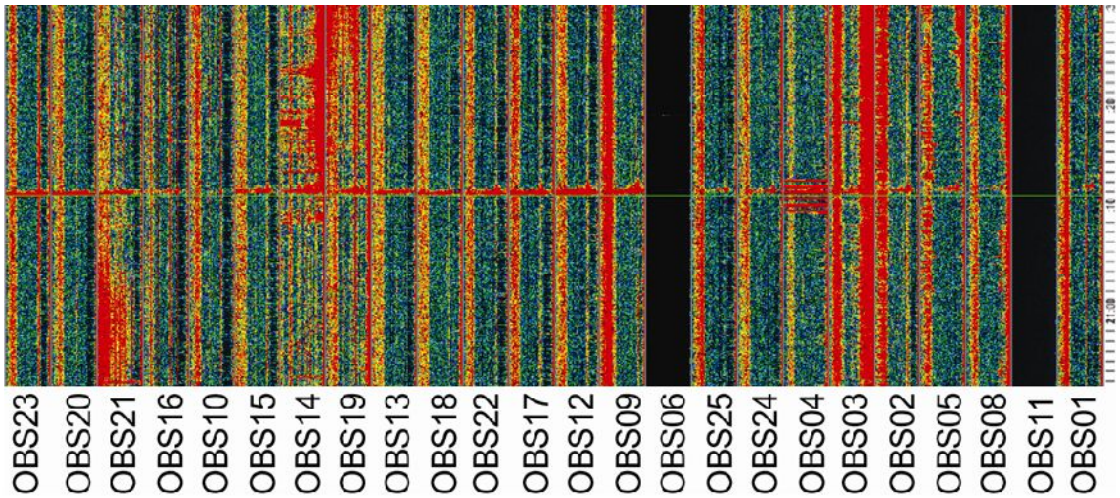

Figure III.1- A spectrogram for an event from January 12, 2008 21:21 detected in 22 LOBSTER OBS vertical component (OBS06 and OBS11 vertical were not acquiring). The horizontal linear disturbance marks the event allowing the observer to visually identify an earthquake. Afterwards, event detection is checked in respective seismograms.

```
&par
icol_new=3
bmpfil='20080810z.bmp'
spath='F:\2008-cruise\asc-bmp\obs16\20080110\n0716z.rs',
'F:\2008-cruise\asc-bmp\obs18\20080110\n0718z.rs',
'F:\2008-cruise\asc-bmp\obs19\20080110\n0719z.rs',
'F:\2008-cruise\asc-bmp\obs21\20080110\n0721z.rs',
'F:\2008-cruise\asc-bmp\obs22\20080110\n0722z.rs'
i_day=010
nsta=5
icomp_a=2
t_corr=0.,19*0.0
j_corr=0,19*0
sranom=100.
t_shift=5.
n_spec=1024
nfj=50
nf_sum=5
cptfil='seis.cpt'
a_fac=100.,100.,100.,100.,100.,100.,100.,100.,100.,100.,100.,100.,8*100.
h_legend=15
f_legend='bmp-legend.bmp'
eve_list='yes75km.cmp'
&end

c.....icol_new -> 1/0 generates or not the background file
c.....2 stops after generating the background
c.....a_fac  -> attenution factor
```

Figure III.2- An example of the *len2bmp* input file with defined parameters used to generate spectrograms bitmaps.

Table III.1- Triggering parameters to single OBS station.

Filter	Bandpass, 5 to 20 Hz
STA (short-time-average) window length	10 sec
LTA (long-time-average) window length	60 sec
Mean removal window length	200 sec
Trigger ratio	3.0
Detrigger ratio	0.7

Table III.2 -Triggering parameter for NEAREST network.

Network travel time (time which is allowed between first and last trigger inside the network)	15 sec
Minimum number of stations with same triggered event	4

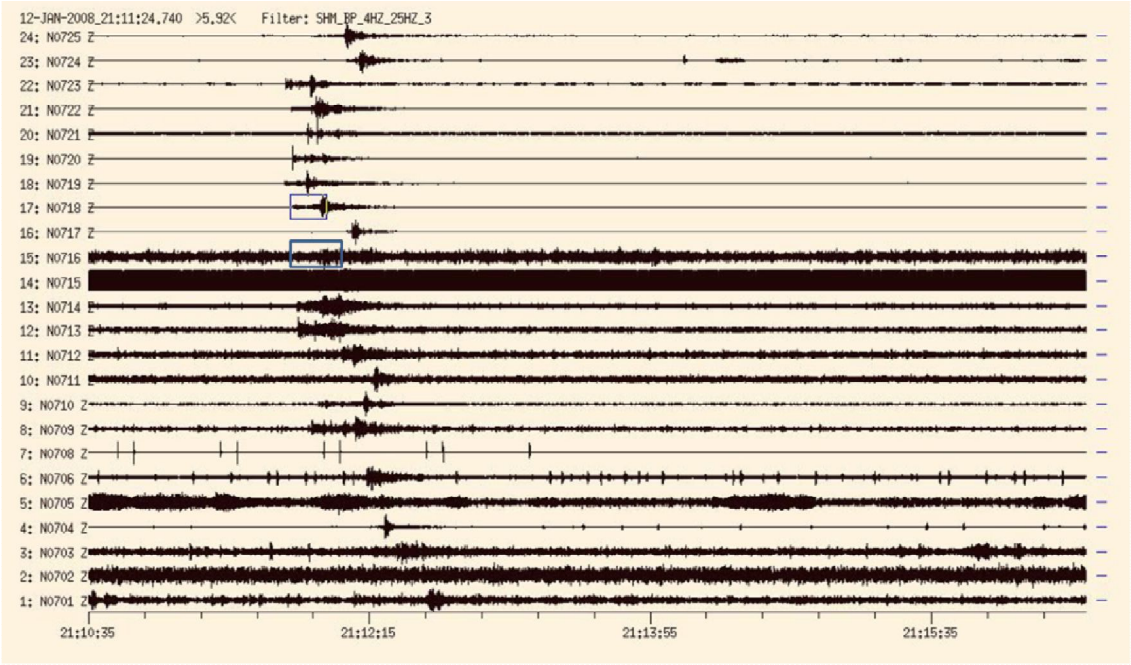

Figure III.3- The seismograms display for an event from January 12, 2008 21:21.

We compared the results from both techniques, for a reference month and recognized that 86 % were detected by the two methods. Most events restricted to spectrograms had low quality or could not be seen in the seismogram (false events). In this context, assuming that automatic REF-TEK trigger algorithm is a faster method, triggering it was the method chosen to extract events from the continuous data set.

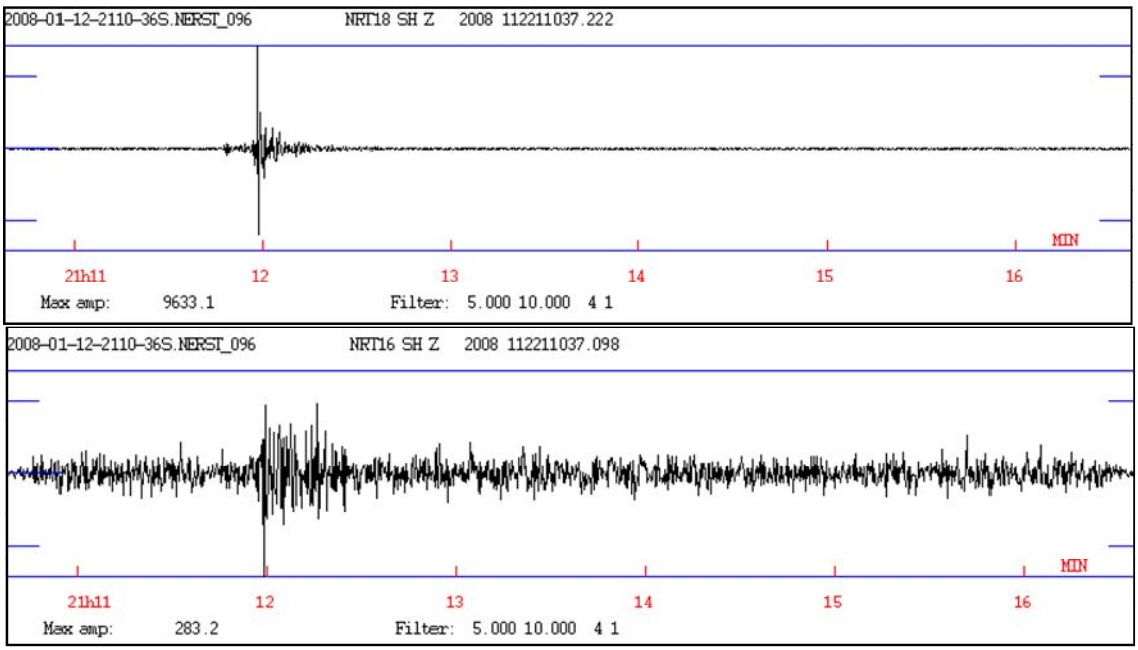

Figure III.4- Details on OBS18-OBS16 Z-component seismogram for January 12, 2008 21:21 event. Both stations show amplitude changes in during the event indentified in seismic spectrogram (fig.III.1). However the seismic event can only be clearly picked at OBS18 seismogram.

After running the triggering algorithm 1641 events were identified, 1322 of which were earthquakes (corresponding to 19% of false positives). To this dataset 32 events were added, detected only using spectrogram analysis (or detected by chance), producing a total 1354 events.

A quality control of the events was made using the categories defined in the Table III.3. As a result we obtained 52 events of best quality, 154 of high, 561 of medium and 587 of low. This means that 767 or 57% of the all events should be located. During the NEAREST network acquisition period, 422 earthquakes were recorded in landstations (data provided by Fernando Carrilho from IPMA-**I**nstituto **P**ortuguês do **M**ar e da **A**tmosfera, former IM-**I**nstituto de **M**etereologia, in *NEAREST 2008 Cruise Preliminary Report*) for the NEAREST network region. This means that the NEAREST Network added 345 to the events catalogue in the study area, i.e. these were not detected by the IPMA land stations. In contrast, only 58 events were undetected by the NEAREST OBS and reported in the land Network catalogue. Those events were located at NE of the NEAREST network, near the Algarve coast. In the Figure III.5 we plotted Land Network events located to a maximum of 75 km of the closest OBS station the region inside the black ellipse marks events not detected or poorly seen by NEAREST temporary network.

Table III.3- Quality check categories for earthquakes detection (from NEAREST Deliverable 9 report in http://nearest.bo.ismar.cnr.it/).

Best	Earthquakes visible, clear phases, with polarities in most OBS stations
High	Earthquakes visible, phases identifiable in most of the OBS
Medium	Earthquakes visible, phases identifiable on some of the OBS (minimum 3)
Low	Earthquakes visible, but phases vague or not identifiable

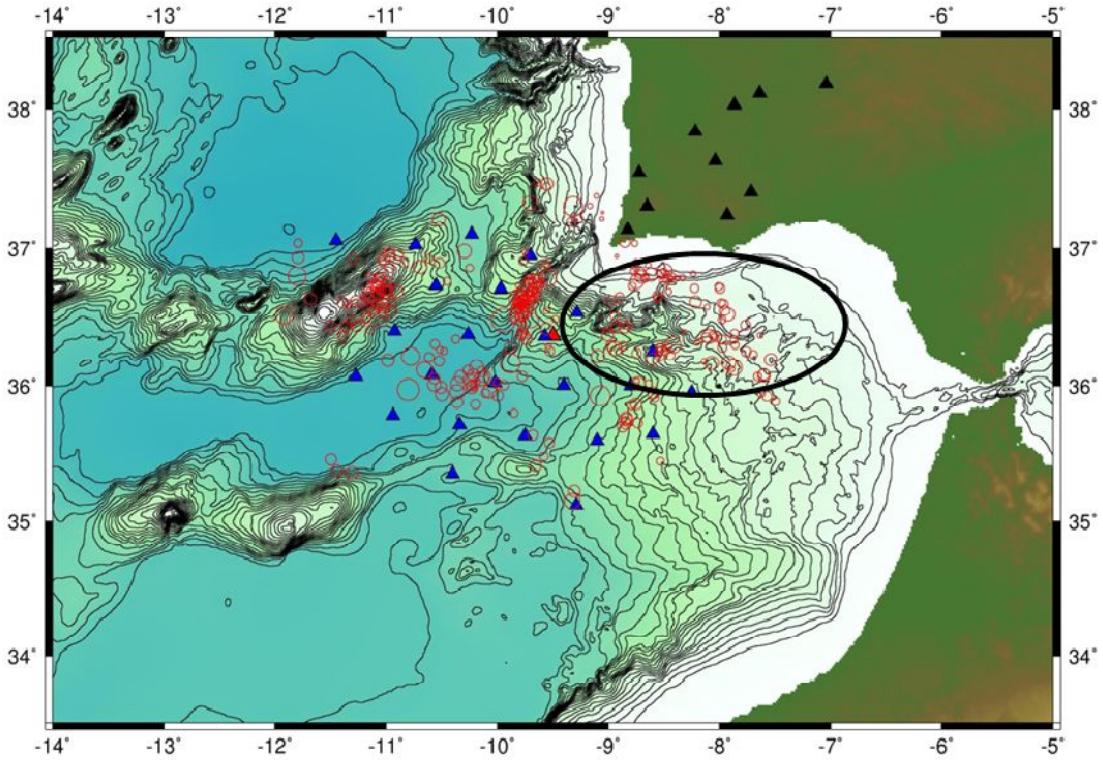

Figure III.5- Earthquakes (red circles) recorded by land permanent network at maximum of 75km of a NEAREST OBS. The seismic events within the black ellipse area were detected by land network and not visible by NEARE ST OBS stations (data provided by Fernando Carrilho from IPMA in *NEAREST 2008 Cruise Preliminary Report; bathymetry from GEBCO- General Bathymetric Chart of the Oceans*).

III.1.2.Phase identification and preliminary location

The seismic data analysis was carried out using SEISAN 9.0.1 Seismic Analysis package (Havskov and Ottemöller, 2011). For general plotting and signal analysis it was used the MULPLT program integrated in this package. All the events were manually picked for P and S waves' first arrivals, generally in the three components seismometer and in unfiltered signal (Figure III.6 and Figure III.7). When necessary band-pass filters were applied to improve signal to noise ratio and allow phases identification. One way band–pass filter with low-cut of 4Hz and high-cut of 25 Hz were applied to identify p-wave first arrival (Figure

III.8) and with low-cut of 2 Hz and high-cut of 4Hz for s-wave picking (Figure III.9).

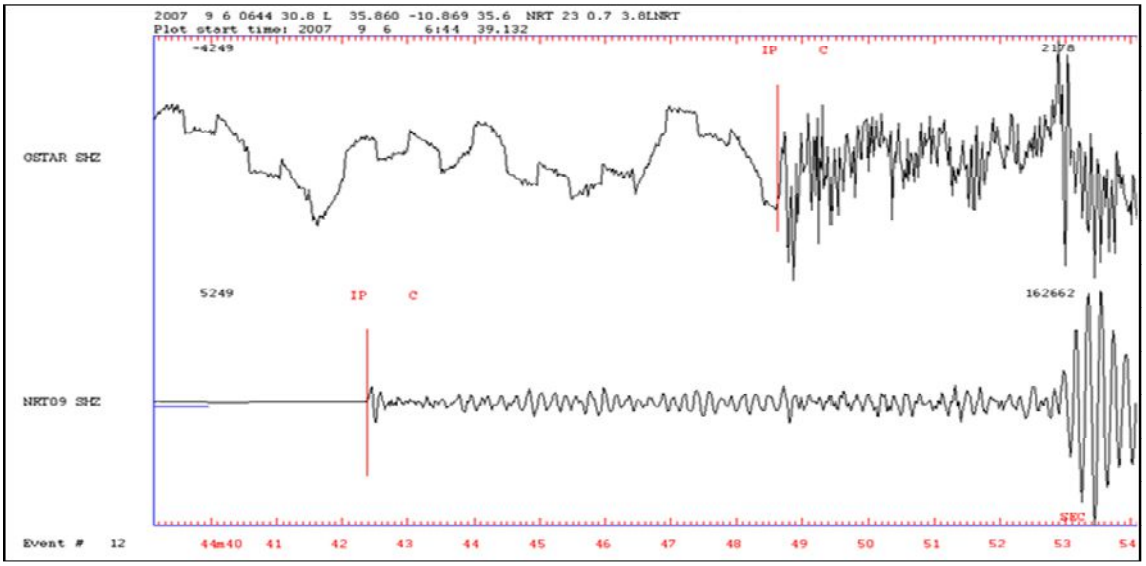

Figure III.6- Event recorded in GEOSTAR and OBS09 vertical component (no filter applied).

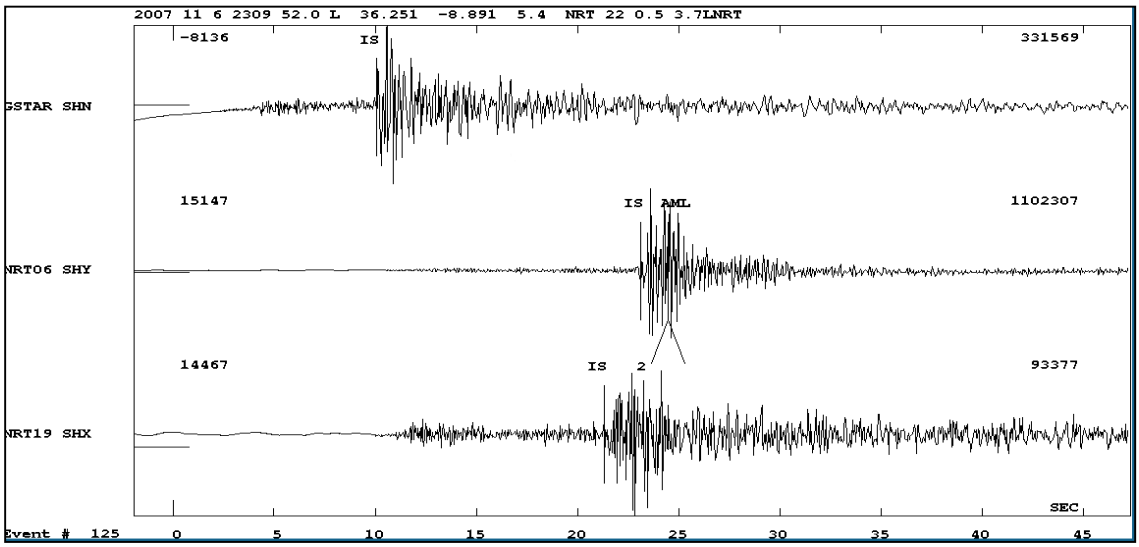

Figure III.7- Event recorded in GEOSTAR, OBS06 and OBS19 horizontal components (no filter applied).

P-wave first arrival polarities were read in unfiltered signal. In Figure III.10, we illustrate how misleading can be the use of filter signal to determine P-wave polarities. In this example we see that in unfiltered signal the P-wave first motion is up and in filter signal the polarity is reversed. To determine local magnitudes (M_L), we picked the maximum amplitude of the seismic events in Wood-Anderson seismogram of LOBSTER stations' horizontal components (Figure III.11).

The hydrophone record was used only as alternative for P wave picking (with high-pass 1Hz filter when required –Figure III.12) and polarity confirmations. In Figure III.12 is shown an example of hydrophone signal (note that polarities are

reversed). P-wave first arrival and polarity were picked on land stations signals exclusively to constrain focal mechanism solutions (Figure III.13).

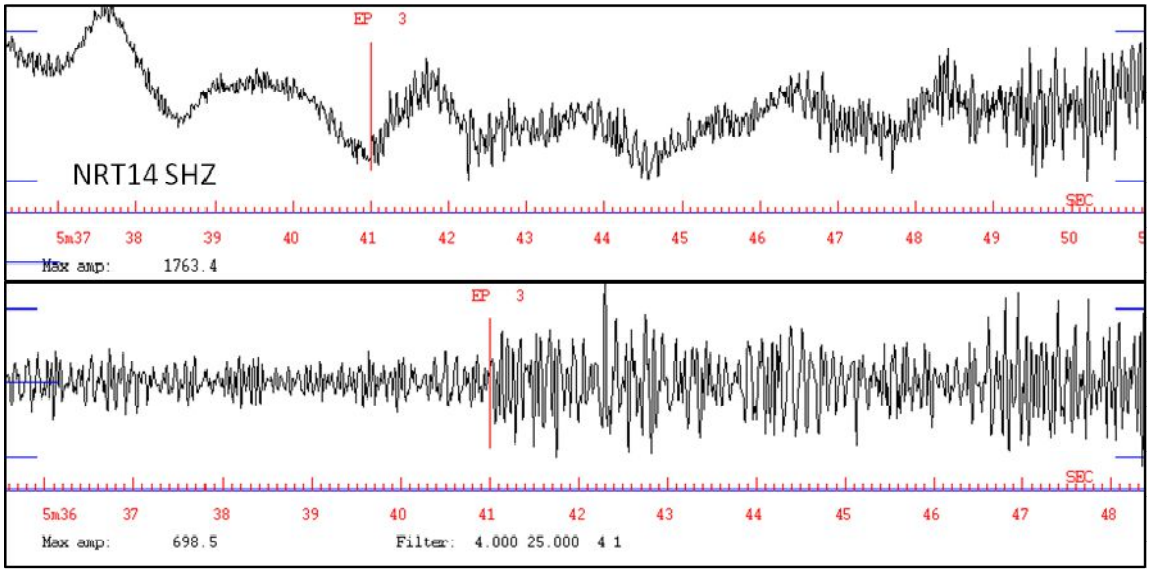

Figure III.8- Seismic event recorded in OBS14 vertical component (on top without filtering and the lower with band-pass filter of 4-25Hz).

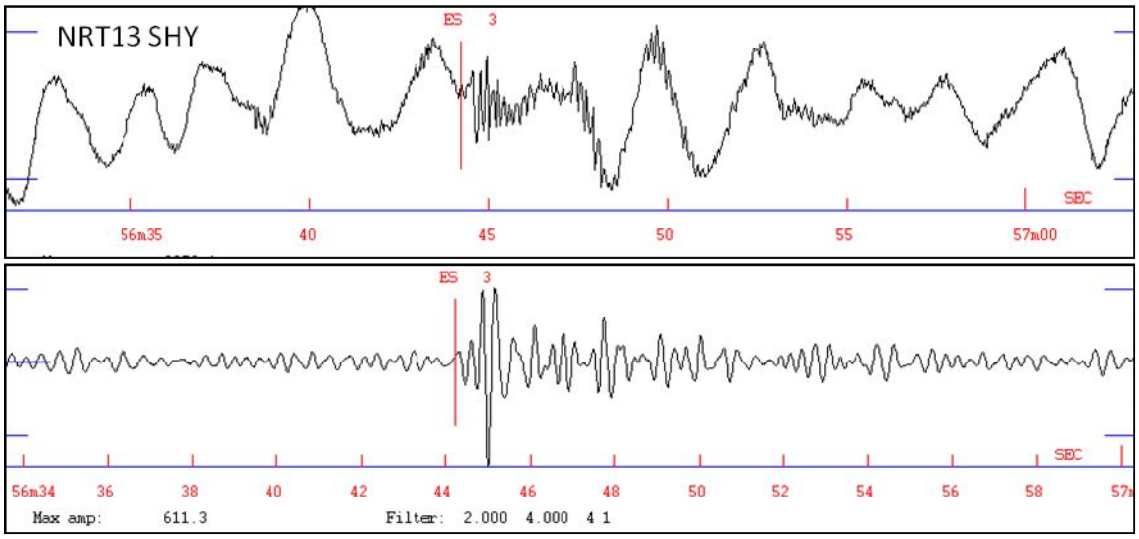

Figure III.9- Event recorded LOBSTER stations 13 horizontal component (on top without filtering and the lower with band-pass filter 2-4Hz).

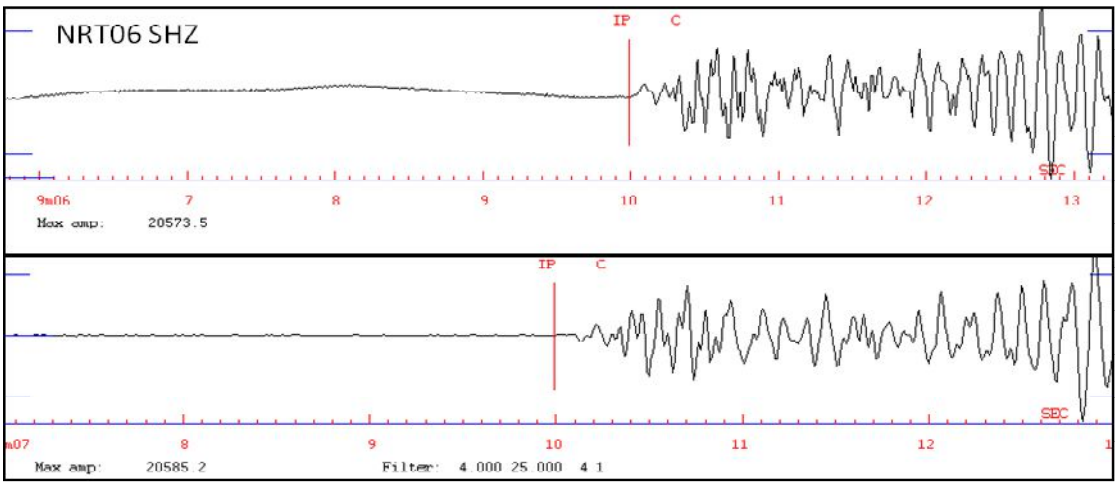

Figure III.10- Polarity picked in unfiltered (top) and filtered seismogram (bottom). We can recognize that using band pass-filter 4-25 Hz when picking for P-wave polarity can lead to wrong measurements. In unfiltered signal the P-wave polarity is clearly up and in filter is down.

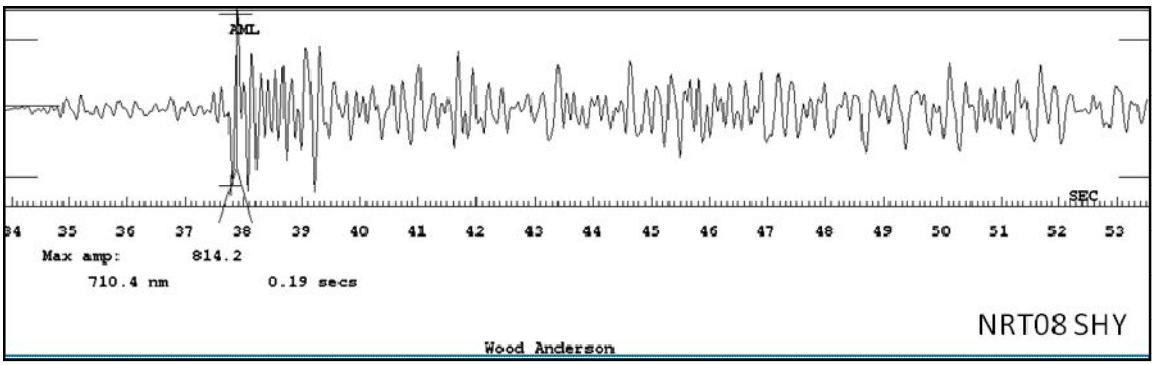

Figure III.11- Measurement of maximum amplitude in Wood-Anderson seismogram to compute the local magnitude.

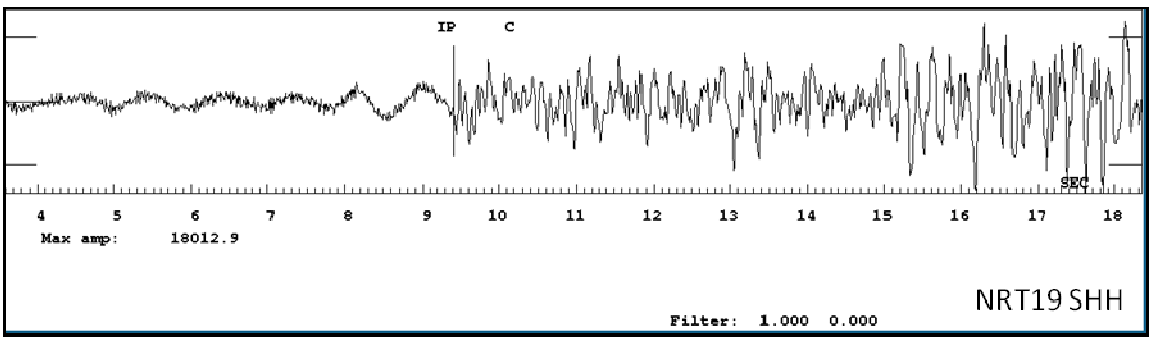

Figure III.12- Event recorded in the hydrophone of the LOBSTER station 19 (high-pass filter 1Hz).

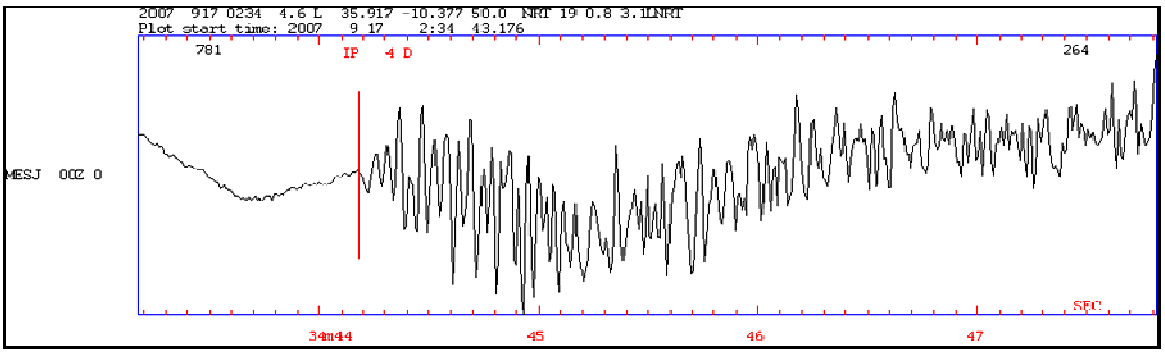

Figure III.13- Event recorded in land station MESJ on the vertical component (no filter).

Differential weighting was applied to all phases pickings based on reading uncertainty. A clear identification of first arrival was classified with weight 0 and poorly identified phase with weight 4. This weighting scheme is a fundamental pre-processing step to improve events locations solutions. It will define the relative quality of arrival time readings when computing earthquakes locations. All land stations picks were attributed with weight 4 to be excluded from earthquakes locations process. Including land stations locations would imply adapting the velocity model to include continental lithosphere variability. This processing step was not included in this work.

A total of 794 seismic events were analysed, 746 of which in more than 3 stations. A total of 11901 phase picking, 4739 P-wave and 7612 S-wave first arrivals. For most stations the number of S-picking was larger than P-picking. In fact, some of the recorded events consisted exclusively by, or we could only recognize, S-wave arrivals (see appendix I for stations detections details). Apart from local earthquakes, teleseismic and regional were identified. These events were excluded from this work because we were only concerned with the local seismicity. In Figure III.14 is an example of a local earthquake recorded both in NEAREST and Land networks.

Preliminary earthquake location and local magnitude estimation was performed using the HYPOCENTER application from SEISAN 9.1 package (Havskov and Ottemöller, 2011). This application is a modified version of an early homonymous application (Lienert et al., 1986, Lienert, 1991, Lienert and Havskov, 1995). The HYPOCENTER uses as input the first arrival phases (P and S) and a layered velocity model to determine earthquake location. When absolute time in a station is not well constrained it can use relative arrival time differences (S-P). Detailed description of the location method is presented in Lienert et al. (1986). The interpreter must predefine several input values in a parameter file, STATION0.HYP. This file will also contain fundamental location parameters: station details and velocity model.

The velocity model used for preliminary locations was defined in the NEAREST 2008 Cruise Report R/V Urania. We excluded the velocity model used by IPMA (see Figure III.15) for locations based on the permanent network because it is defined exclusively for the continental lithospheric domains whereas Gulf of

Cadiz lithospheric domains are more complex (see elsewhere in this work). It was based on the velocity models inferred from wide-angle reflection (See SIS16 in Figure III.14) and refraction seismic profiles in Gutscher et al. (2002) and combining results from multichannel seismic reflection profile (IAM-03 in Figure III.14) with wide-angle land station records and gravity modelling in Gonzalez et al. (1996). We defined this model as MOD0 (see details in Figure III.15). The model is described for P-wave velocities only, the S-wave travel times are computed based on a Vp/Vs ratio of 1.75. The first 2 layers on MOD0 represent upper and lower sediments. The crust is subdivided in two layers (upper and lower crust) and the Moho is at 16km in depth. We exclude water velocity from the model MOD0 because NEAREST Network stations are coupled to the sea floor, so ray paths will not cross the water column.

For local magnitude (ML) estimation it was used Carrilho and Vales (2009) formulation for Portugal and adjacent areas:

$$M_L = logA + 1.287\, log\Delta + 0.00061\, \Delta - 2.147$$

A is the amplitude measured in a Wood- Anderson synthetic display (in nm) and Δ is the hypocentral distance (in km).

P and S phase consistence was tested using Wadati diagram. In this diagram, S-P times plot against absolute P-time should define a straight line. Phase outliers can easily be identified because will misfit this linear tendency (Figure III.16). Outliers can result both from error on the first arrival picking or misinterpretation of phases. So, misfit phase pickings were re-checked and re-tested in Wadati diagram. If required phase weight was adapted.

The focal depth for each event was established using a systematic search approach with application RMSDEP (Figure III.16) from SEISAN 9.1 (Havskov and Ottemöller, 2011). The RMSDEP routine uses, for a starting depth solution (if no initial location is provided), a value included in STATION0.HYP. To ensure that the final solution is not controlled by the user defined initial depths, we tested different input values. Finally, we assumed that the best solution was the one that best fits the data, retrieving the lowest RMS.

In Figure III.17, we present a preliminary earthquake location for the events acquired by NEAREST network using the method just described. The average *rms* of the time residuals for all 746 events analysed was 0.8s. From those, 590 events are located in the restricted area of the NEAREST network as defined by external envelope of the stations locations. The remaining events are distributed outside this area. The seismicity is concentrated between 30 and 60 km in depth and local magnitude estimation ranges from 0.9 to 4.8.

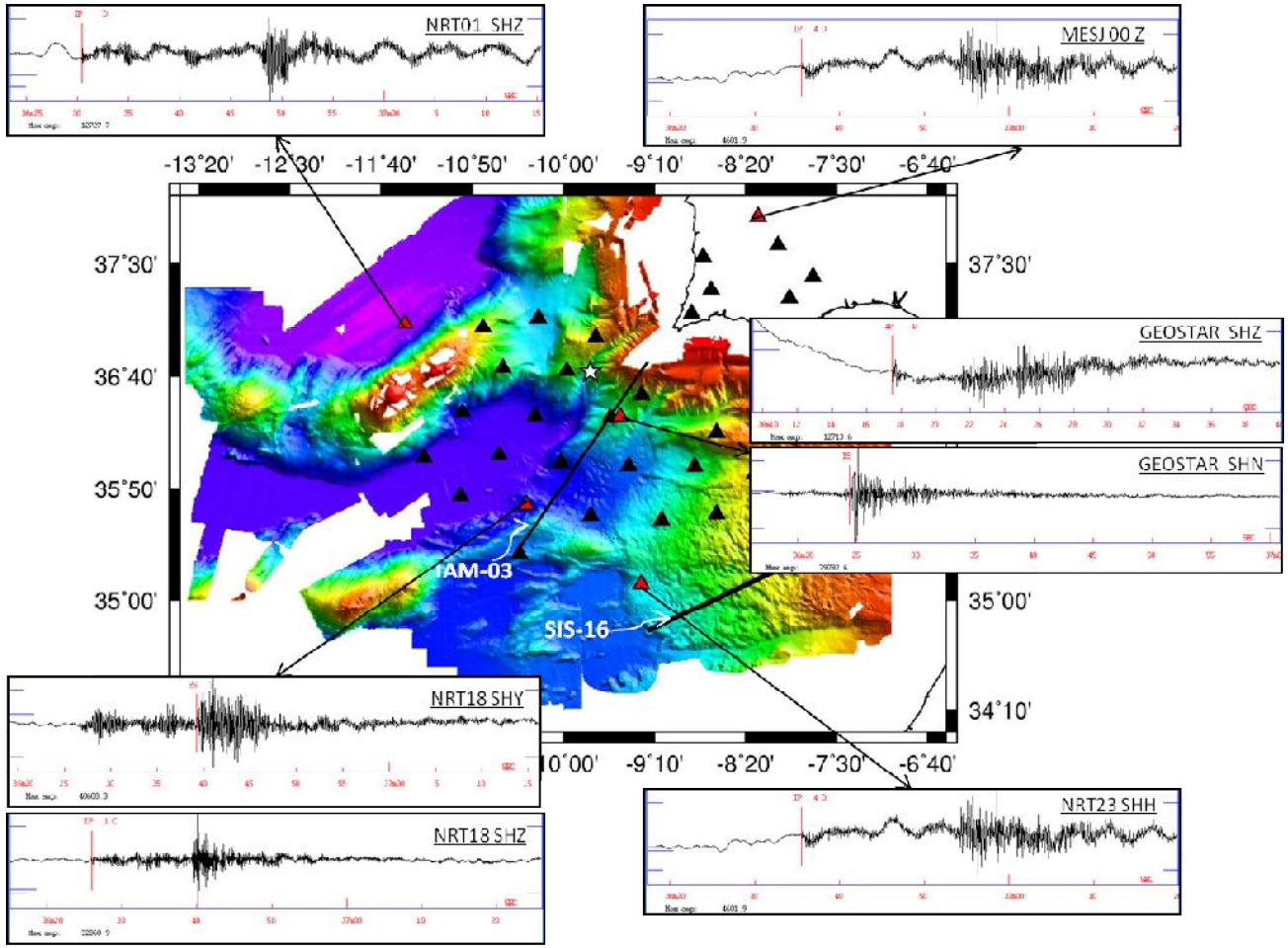

Figure III.14- Local earthquake with a local magnitude of 3.1 and examples of recording signals at some of the stations in NEAREST and Land networks (black triangles are seismic stations in NEAREST and land networks, red triangles are the selected stations and white star is the earthquake preliminary location, bathymetry compilation from Zitellini et al., 2009).

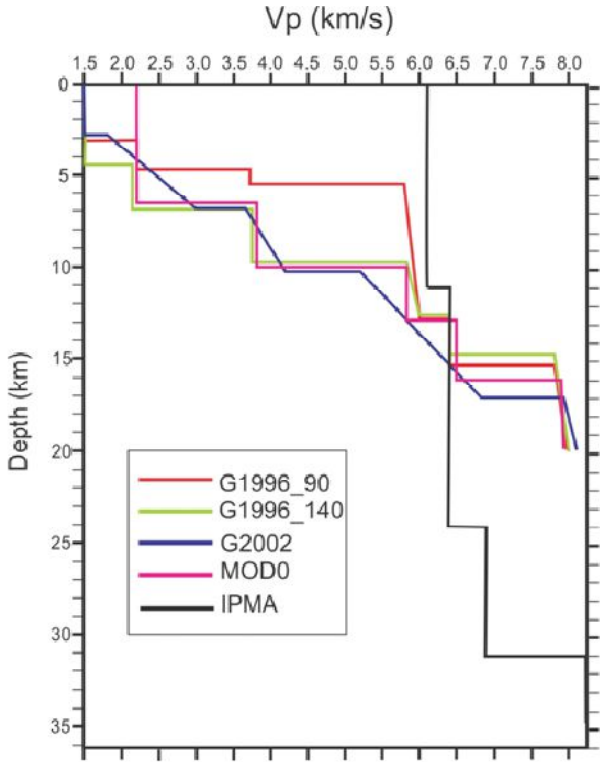

mod0		
Vp (km/s)	Depth (km)	Layer
2.20	0.00	Upper sediments
3.80	6.50	Lower sediments
5.80	10.00	Upper crust
6.50	13.00	Lower crust
7.90	16.00	Upper Mantle
8.10	20.00	
8.15	27.50	
8.20	35.00	
8.25	42.50	
8.30	50.00	
8.35	60.00	
8.40	70.00	
8.45	75.00	
8.50	90.00	

Figure III.15- Velocity models selected from previous published work and final proposed model (G1996_90 and G1996_140 are from Gonzalez et al. (1996), G2002 is from Gutscher et al. (2002) and MOD0 is the derived model).

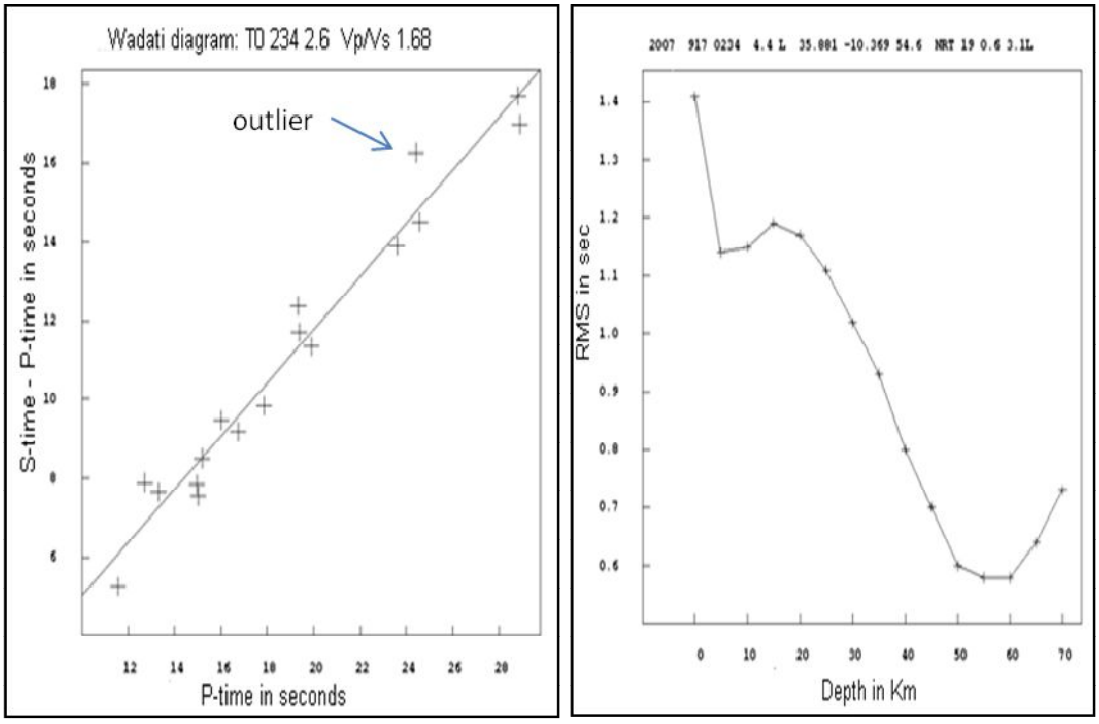

Figure III.16- In Wadati Diagram (left), we identify an outlier reading because misfits the linear tendency in a plot of S-time – P-time against P-time. In RMSDEP (right) graphic, we can define the best depth location for each event by selecting the solution with the lowest rms.

Within the NEAREST network area, earthquakes are clearly distributed in three clusters:

1. In the S. Vicente Canyon, where most of the seismicity is concentrated in a NE-SW alignment;
2. In the Gorringe Bank, where earthquakes have an asymmetric distribution, clustering in the SW part of this submarine mountain (Gettysburg high);
3. In the Horseshoe Abyssal Plain, where seismicity defines an NW-SE elongate alignment.

In the adjacent region, the seismicity is more diffuse with only a few events located in the area of the Gulf of Cadiz Accretionary Wedge and to the North of this structure. A detailed description and discussion of the seismicity in the deployment area will be presented in section III.4 after improving earthquake location. We will also compare the results with the locations provided by Land permanent network.

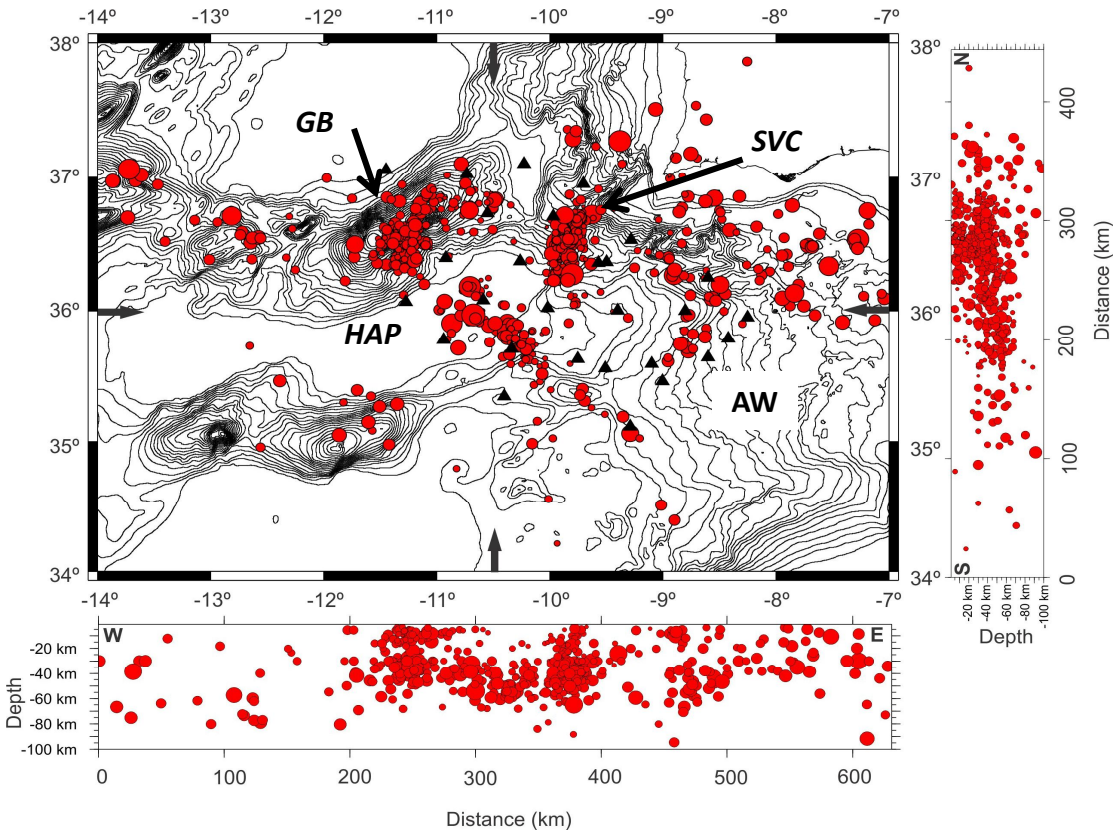

Figure III.17- Earthquakes preliminary location using NEAREST report velocity model: 746 events located by the NEAREST OBS network with M_L between 0.9 to 4.8 and an average rms of 0.8. (The black arrows mark the location of W-E and N-S profiles, *bathymetry from GEBCO*. Abbreviations: GB-Gorringe Bank, SVC- São Vicente Canyon, HAP-Horseshoe Abyssal Plain and AW- Accretionary Wedge).

Stations statistics were also scrutinized (see Appendix I for details). In Figure III.18, we plotted a preliminary events location versus events detected in each station. The stations with higher number of records are OBS 08, 17, 05 and 06. Except for OBS06, the remaining 3 equipments worked without x component during the operation. Both OBS 06 and 08 operated during the entire campaign. All stations are positioned near the identified clusters, OBS06 near the São Vicente Cluster, where most events are located; OBS05 as well as OBS08 are near the Gorringe Bank and the OBS17 in the Horseshoe Abyssal Plain cluster.

The stations with the worst statistics are OBS15, OBS16 and OBS21. The OBS 15 operated just for 7 month and stopped because the disk was full. Both OBS16 and 21 stopped for the same reason but recorded during 11 months. Three reasons can explain the poor events recovery as follows. Firstly, these stations are located in limit of deployment area and far from areas with higher seismic activity. Secondly, the three OBS were deployed on top of the Gulf of Cadiz accretionary wedge (seismic chaotic units in Figure III.19). This structure is characterized by high internal deformation and anisotropy which favour seismic energy dissipation during seismic waves propagation, resulting in poor recovery of the first arrivals. The S-waves signal could also be disturbed by the presence of fluids. Thirdly, OBS16 and OBS15 are located in the area of Mediterranean Outflow Water circulation that may introduce increasing background noise and disturb station-seafloor coupling.

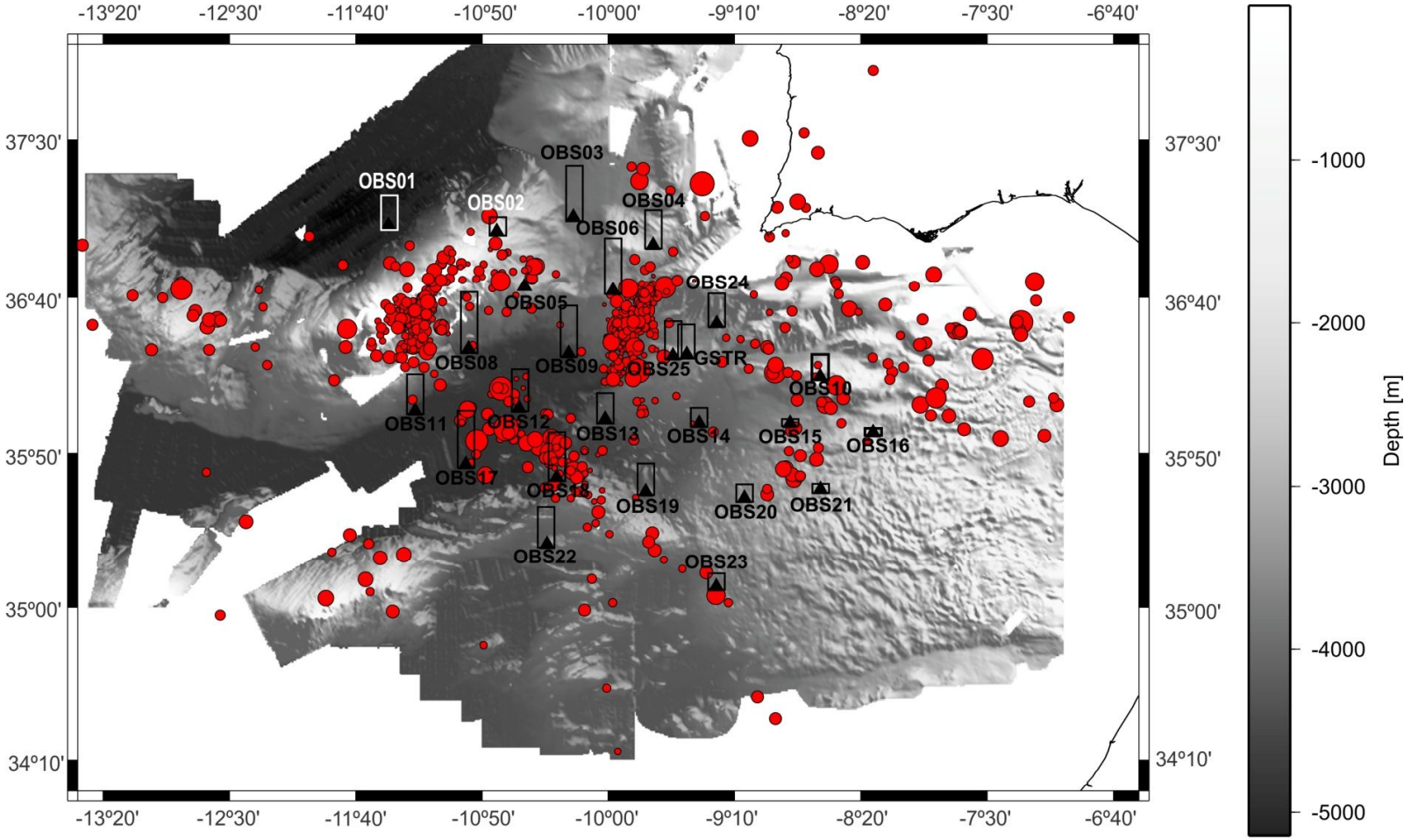

Figure III.18- Events location versus events detected in each station. Red circles are epicenters and the rectangular bar at each station express the number events detected, the highest bar is equivalent to 555 events (OBS08) and lowest represents 60 earthquakes (OBS15). The stations with the worst statistics are OBS15, OBS16 and OBS21. Several reasons explain this statistic: stations operation details, stations proximity to predominant seismically active zones, station-seafloor coupling conditions controlled by the presence of the Gulf of Cadiz accretionary wedge and/or Mediterranean Outflow Water circulation (bathymetry compilation from Zitellini et al., 2009).

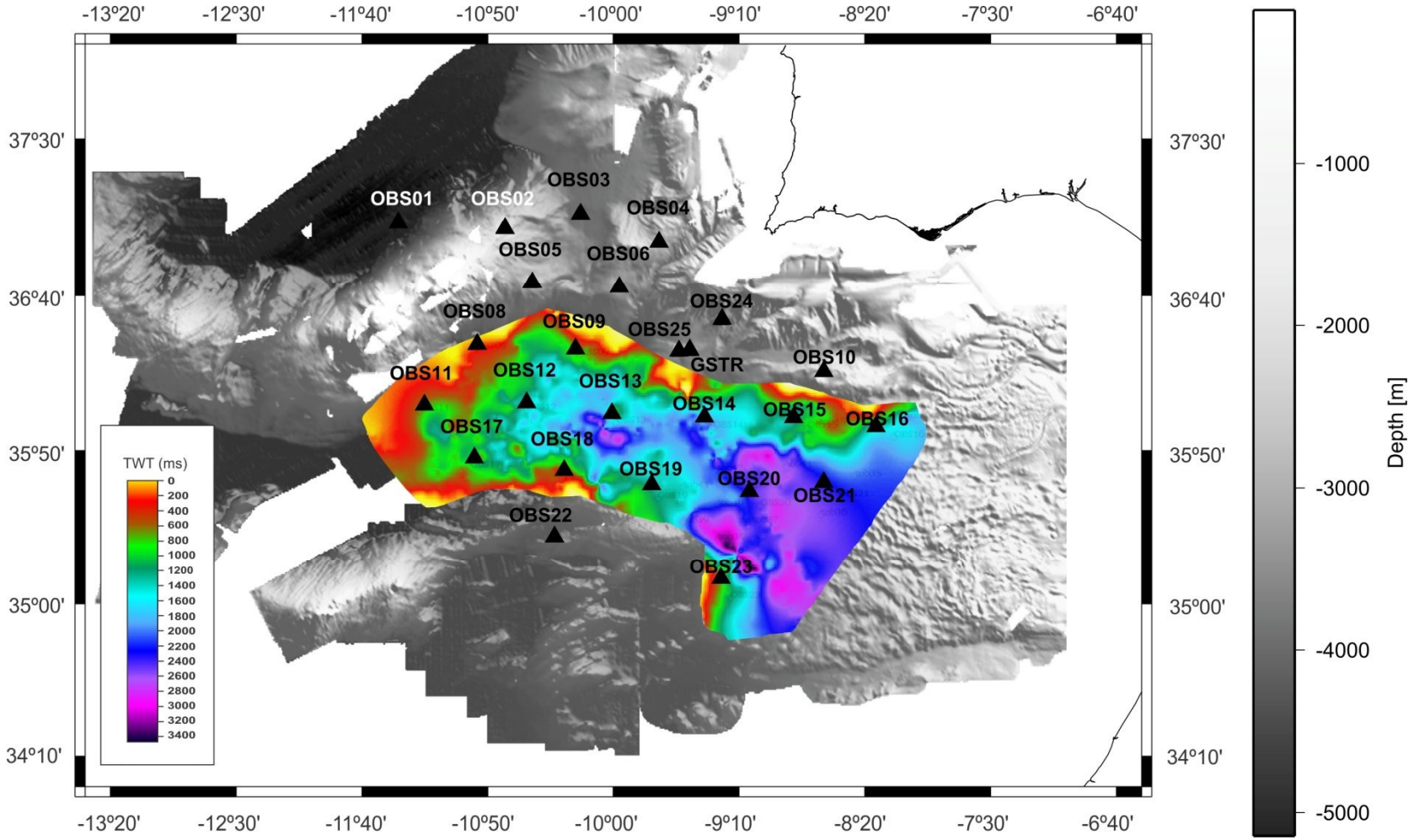

Figure III.19- Stations distribution versus the thickness of seismic chaotic units. One of the reasons that may lead for poor seismic records in some of the OBS is the presence of the Gulf of Cadiz accretionary wedge at the stations base. This structure is characterized by high internal deformation and anisotropy which favour seismic energy dissipation during seismic waves propagation, resulting in poor recovery of the first arrivals. The s-waves signal could also disturbed by the presence of fluids (bathymetry compilation from Zitellini et al., 2009).

III.2.Improving earthquake location

III.2.1.Joint Hypocenter Determination (JHD)

From the 746 located events based on the Nearest OBS experiment we selected a subset of 443 events restricted to the deployment area, i.e. within the external envelope of the station locations in the SW Portuguese margin that were identified in more than 6 stations. The initial average time residual for this selection was 0.76s. To improve earthquake location we began by applying a Joint Hypocenter Determination (JHD) method using HYPOCENTER from SEISAN 9.1 package (Havskov and Ottemöller, 2011) and PRN2RES (application created by Luis Matias to include independent P–wave corrections). This method retrieves stations corrections to account for 3D propagation effects and geological variability below each station (details on the method in chapter II). We used MOD0 velocity model to compute earthquake location but tested different Vp/Vs ratios.

After applying the JHD method we reduced the average time residual to 0.415s and find the best Vp/Vs between 1.77-1.78 (Figure III.20). The Vp/Vs is higher than the one used in preliminary location. We also ran the Wadati application to find the average Vp/Vs ratio for the all events selection and results point out to a smaller value-1.72. To compare results from both methods we applied a modified version of Wadati routine, the Wadati_sp (created by Luis Matias) adapted to extract S-wave and P-wave first arrivals time (Ts and Tp, respectively). The results and a linear tendency analysis are plotted in Figure III.20.

From Figure III.20, we observe Vp/Vs retrieved from JHD fits the slope of a linear tendency crossing the axis origin in a Ts-Tp plot while Wadati computed Vp/Vs ratio defines the slope of a general linear tendency. Final results discrepancies outcomes from different approaches to find Vp/Vs. JHD method finds the best fitting fixed Vp/Vs to all events locations while Wadati value results from the average of individual events computations (excluding any Vp/Vs value superior to 1.93 and lower than 1.54).

However, in marine deployment, which is the case of NEAREST network, the presence of top high porosity and water content marine sediments decrease S-velocity, increasing Vp/Vs ratio (e.g. Crawford and Singh, 2008). Also, we know, from refraction and multichannel reflection profiles, that half of the seismic network is located above large scale chaotic sequences (Horseshoe Gravitational Unit and the Gulf of Cadiz Imbricated Wedge, Table III.4 and Figure III.19) which can also decrease seismic velocities. Additionally, we have evidences for fluid circulation within the Gulf of Cadiz Imbricated Wedge testified by mud volcanoes activity (e.g. Pinheiro et al, 2003, Hensen et al., 2015, among other). This process will also decrease particularly S-wave velocity. So, we would expect to have higher Vp/Vs ratios. This is evidenced

with JHD approach because it results from fitting individual Vp/Vs calculations to a Ts –Tp plot but attenuated when computing average Vp/Vs (excluding higher Vp/vs ratios), which is the case of the Wadati application.

Table III.4-Sediment cover below NEAREST network stations (based on multichannel seismic reflections profiles interpretation).

Station	TWT sediment cover isopach (ms)	TWT Chaotic sequence isopach (ms)	Station	TWT sediment cover isopach (ms)	TWT Chaotic sequence isopach (ms)
OBS01	1490		OBS14	3256	1852
OBS02	1713		OBS15	2358	974
OBS03	2331		OBS16	3042	1709
OBS04	1752		OBS17	2252	866
OBS05	1865		OBS18	763	181
OBS06	1675		OBS19	3664	1207
OBS08	1862	221	OBS20	3517	2472
OBS09	2913.	776	OBS21	3189	2334
OBS10	2314		OBS22	1150	
OBS11	2309	661	OBS23	3466	1186
OBS12	2587	1454	OBS24	1296	
OBS13	2631	1592	OBS25	2186	
			GEOSTAR	2518	

In Figure III.21, we plotted P-wave stations delays derived from JHD method. This corrections result from the difference between calculated arrival time, based on the P-velocity model and the picked first arrival. It should reflect local velocity deviations (or geological variability) from the general velocity model-MOD0. However, if we compare stations corrections with values of sediment thickness in Table III.4 no clear dependence is established, except that highest positive delays (or slower local velocities) are correlated with high sediment thickness.

MOD0	Vp/Vs	1.70	1.71	1.72	1.73	1.74	1.75	1.76	1.77	1.78	1.79
	RMS	0.523	0.499	0.479	0.459	0.442	0.429	0.420	0.415	0.415	0.419

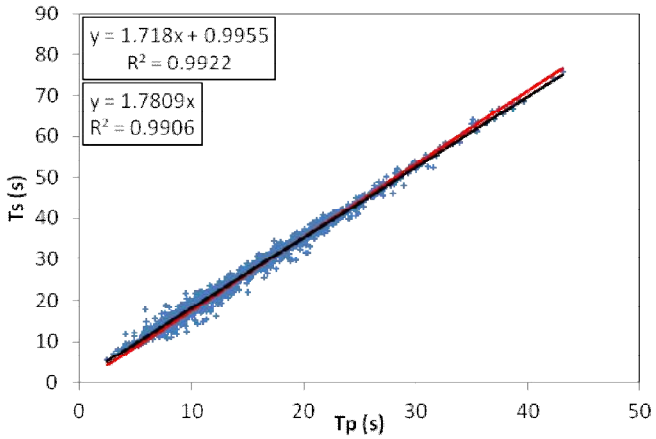

Figure III.20- On top table with RMS versus Vp/Vs. At the bottom S-arrival against P-arrival times and linear tendency approximation (data extracted using Wadati_sp routine, black tendency line is a general fit while red linear tendency is forced to cross axis origin. Both defining equations for general fit, on top, and crossing origin axis, on bottom, are also presented).

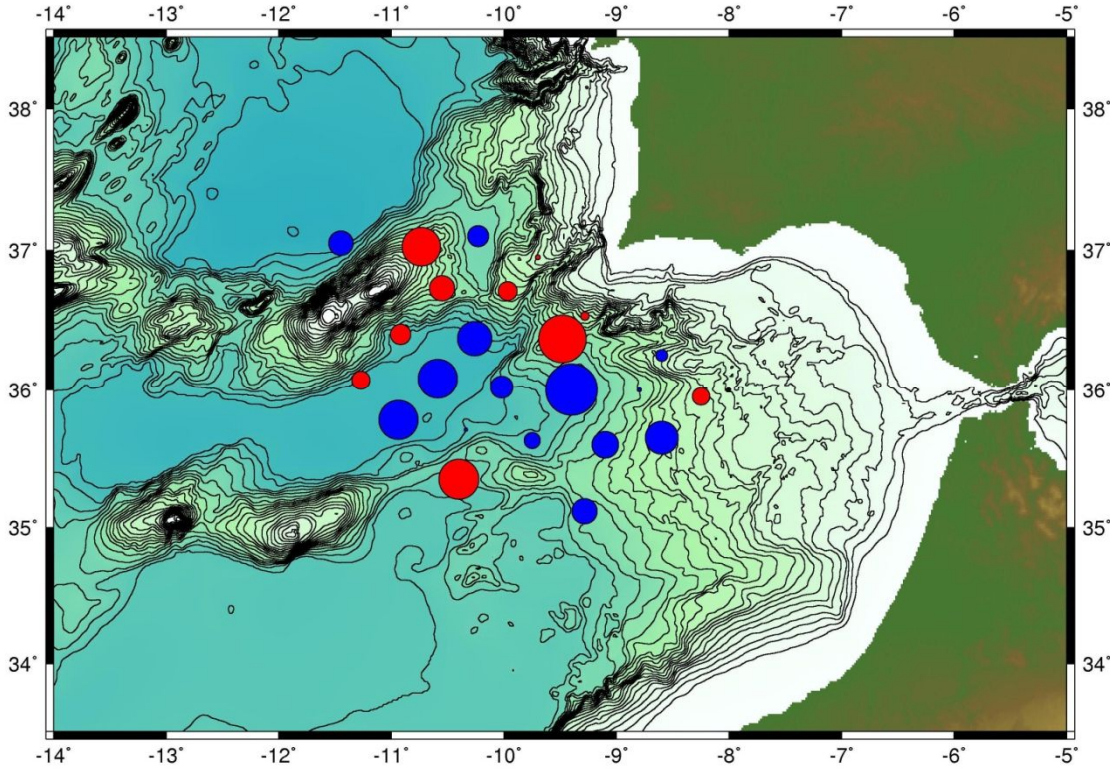

Figure III.21- P-wave stations delays derived from JHD method (blue is positive delay, meaning that arrival times in these stations reveal local slower P-velocities when compared with velocity model -MOD0; red is negative delay, reflecting local faster P-velocities). There is no clear dependence between stations corrections and sediment thickness in table III.4, except that highest positive delays (or slower local velocities) are correlated with high sediment thickness *(bathymetry from GEBCO*).

Based on the arguments discussed before, we conclude that introducing independent S-wave stations delays in the JHD method should be more adequate to our case study. We used HYP2 (routine modified Luis Matias to

include S independent delays) and PRN2RES2 applications to improve locations, also testing different Vp/Vs. The HYP2 routine defines S-delays as additional corrections to be added to the ones computed from P-delays and Vp/Vs.

With JHD method (including independent P and S stations corrections) we reduced the average RMS for earthquake location to 0.320s. The best fitting Vp/vs is 1.72 (see Figure III.22), equal to the one computed with Wadati routine. Once more we plotted Ts against Tp extracted with Wadati_sp application (Figure III.22). Equivalent slopes values result from general and forced to axis origin linear fits, both similar but smaller than the Vp/Vs derived from JHD and Wadati methods.

MOD0	Vp/Vs	1.71	1.72	1.73
	RMS	0.323	0.320	0.321

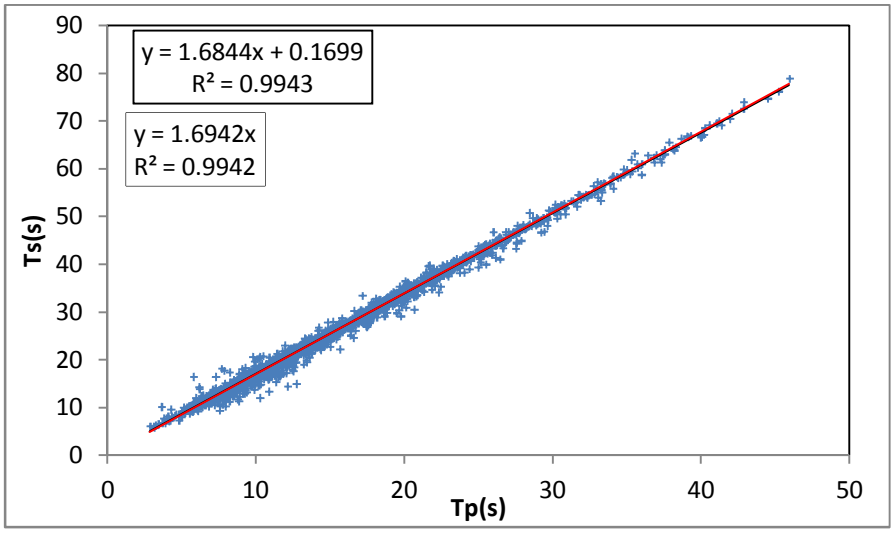

Figure III.22- On top table with RMS versus Vp/Vs. At the bottom S-arrival times against P-arrival times and linear tendency approximation (data extracted using Wadati_sp routine, black tendency line is a general fit while red linear tendency is forced to cross axis origin. Both defining equations for general fit, on top, and crossing origin axis, on bottom, are also presented).

P-stations delays computed by JHD are plotted in Figure III.23. Once more, there is no clear dependency between sediments thickness below stations and the observed P-delays. Moreover, with this method GSTAR station results the highest negative delay. In Figure III.24, we plotted S-wave additional corrections to those computed based on P-delays and Vp/Vs ratio. As we expected, all values are positive, reflecting local slower S-velocities when compared with the velocity model-MOD0. This velocity reduction is related to subsurface geology-top sedimentary layers with high porosity -water content and large seismic chaotic sequences (Horseshoe Gravitational Unit and the Gulf of Cadiz Accretionary Wedge) with localized fluid circulation, which will decrease S-wave velocity.

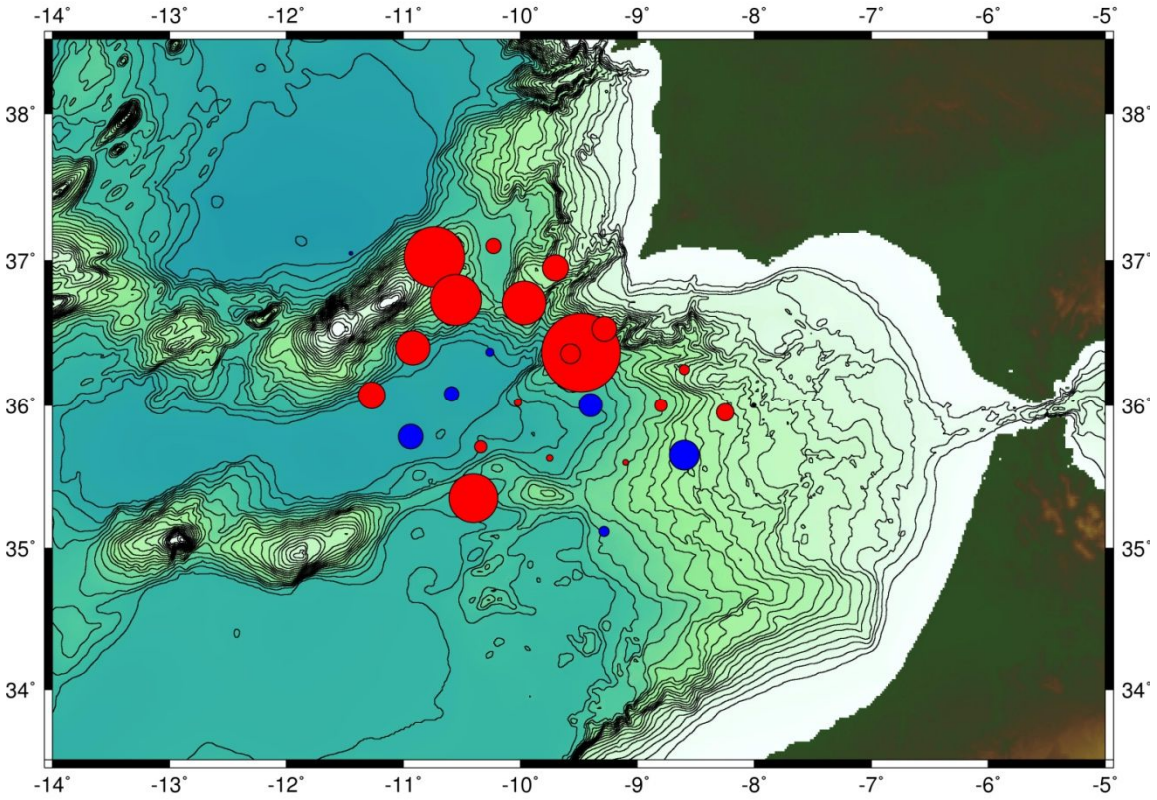
-14˚ -13˚ -12˚ -11˚ -10˚ -9˚ -8˚ -7˚ -6˚ -5˚
38˚
37˚
36˚
35˚
34˚

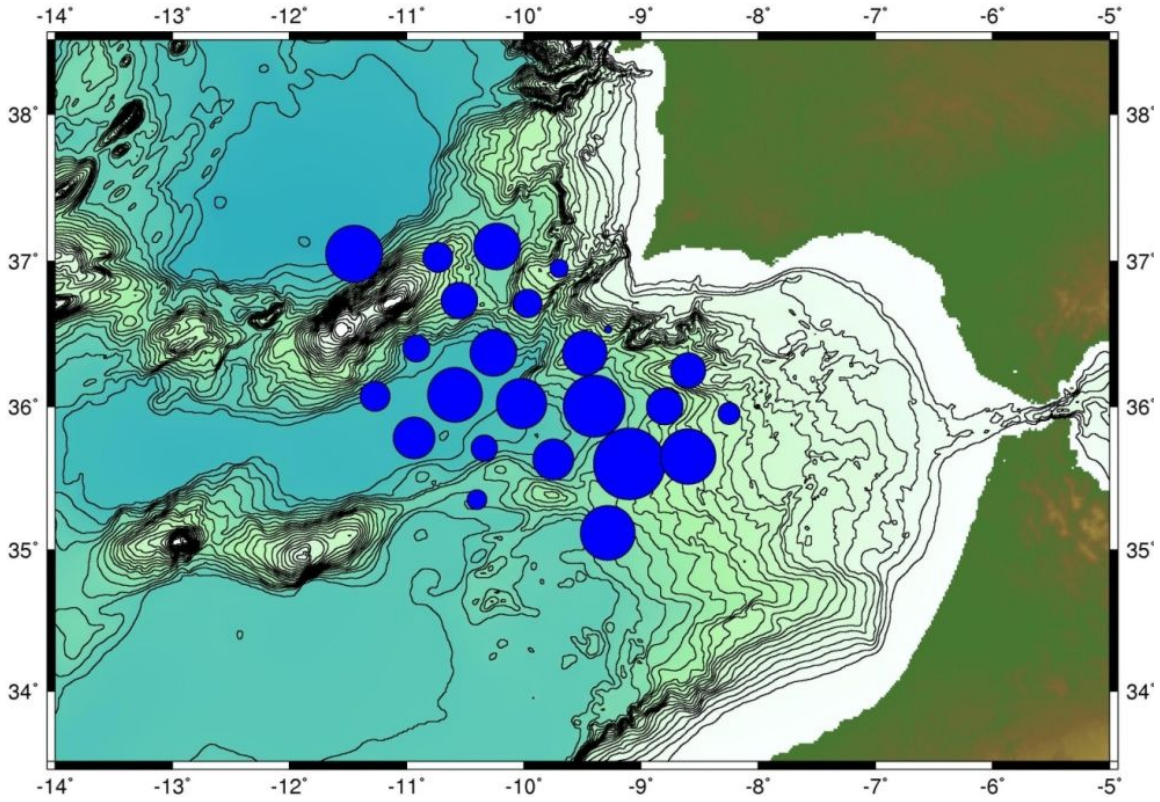
-14˚ -13˚ -12˚ -11˚ -10˚ -9˚ -8˚ -7˚ -6˚ -5˚
38˚
37˚
36˚
35˚
34˚

Figure III.23- P-wave stations delays derived from JHD method (blue is positive delay, meaning that arrival times in these stations reveal local slower P-velocities when compared with velocity model -MOD0; red is negative delay, reflecting local faster P-velocities, *bathymetry from GEBCO*). There is no clear dependency between sediments thickness below stations and the observed P-delays. GSTAR station has unexpectedly the highest negative delay.

Figure III.24- S-wave stations delays derived from JHD method (blue is positive delay, meaning that arrival times in these stations reveal local slower S-velocities when compared with velocity model -MOD0, bathymetry from GEBCO). All values are positive, reflecting local slower S-velocities when compared with the velocity model-MOD0. This velocity reduction is related to subsurface geology- top sedimentary layers with high porosity -water content and large seismic chaotic sequences (Horseshoe Gravitational unit and the Gulf of Cadiz accretionary wedge) with localized fluid circulation, which will decrease S-wave velocity).

At this stage we were able to reduce average time residuals from 0.425s (JHD with P-stations corrections) to 0.320s using JHD method with independent P and S stations delays. In Figure III.25, earthquakes locations resulting from this method are plotted. It is clear that most events are located between 20 and 50 km of depth. On a W-E profile we indentify a clear increase of the depth of the events from the SW Gorringe Bank (where the lower depth limit is around 40km) towards the Horseshoe Abyssal Plain (around 50-55 km), marking a step like structure defining the seismogenic layer limit in the Gulf of Cadiz region. Along a N-S profile, we observe that the events depth limit is located at 50-55km.

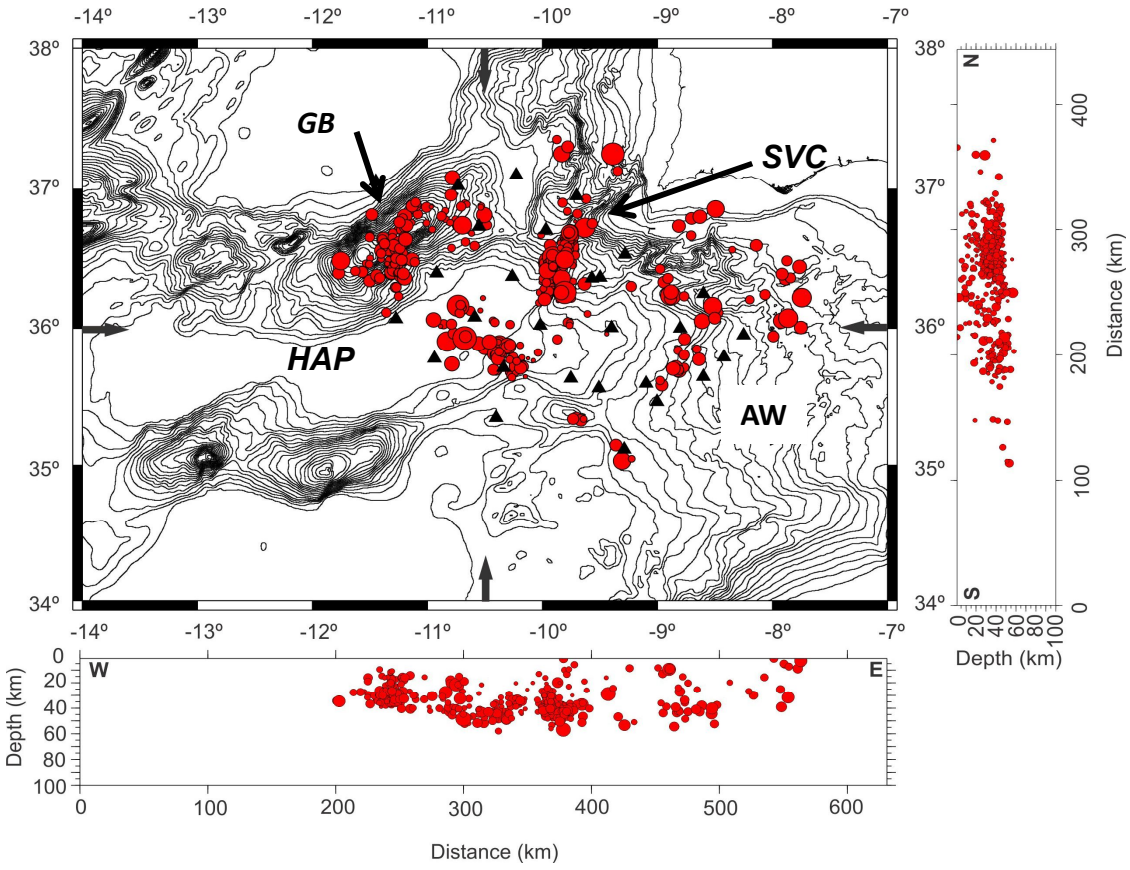

Figure III.25- Earthquake location resulting by JHD method with independent P and S –delays (the black arrows mark the location of W-E and N-S profiles, *bathymetry from GEBCO*). Most events are located at depths between 20 and 50 km. In a W-E profile, we indentify a increase in the events' depth from the SW Gorringe bank (where the lower depth limit is around 40km) to the Horseshoe Abyssal Plain (HAP-around 50-55 km), marking a step like structure defining seismogenic layer limit in the Gulf of Cadiz region. Along N-S profile, we observe that the events depth limit is located at 50-55km (Abbreviations: GB-Gorringe Bank, SVC- São Vicente Canyon, HAP-Horseshoe Abyssal Plain and AW- Accretionary Wedge)

One of the main constraints in hypocenter determination is the adequacy of the velocity model used by location routines. To introduce this issue we repeated the location procedure using different 1D velocities models extracted from Sallarès et al. (2011) and Sallarès et al. (2013) NEAREST refraction and wide-angle reflection seismic profile P2 and P1, respectively, located within the area of NEAREST Network (Figure III.26).

Sallarès et al. (2011) divides profile P2 in three domains: oceanic, transitional and continental. Our 1D velocity models were extracted exclusively from the first sector, assuming that most of the NEAREST OBS stations are located on the oceanic crust domain. This domain is characterized by (Sallarès et al., 2011): top sediments (comprising Gulf of Cadiz Imbricated Wedge and a thin layer of cover sediments) with lower velocities, ranging from 1.8km/s at top and 3.0 km/s at the base. Underlying these units are higher velocity sediments, vary from 2.8 km/s and 4.0 km/s. Crustal velocities below sediments cover vary from 4.6–4.8 km/s at the top to 6.9–7.1 km/s at the base. Upper mantle velocities are low, between 7.6 and .8 km/s, pointing out for some degree of serpentinization (Sallarès et al., 2011).

A total of 3 continuous p-wave velocities models were extracted (see Figure III.27A and C) and subsequently converted to average interval velocities profiles to be used in HYPOCENTER. Velocity intervals were defined in agreement with description presented in Sallarès et al. (2011) meaning that distinct velocity layers and *sub-layers* were respected, to a limit of the available data, roughly 20 km depth. All velocity models were then extrapolated to approximately 80 km depth.

Mod_P1 was provided by Sara Martinez (pers. communication) and extracted in an area coincident to Horseshoe cluster (see Figure III.26 for location). Sallarès et al. (2013) description of the P1 profile for the area of the Horseshoe Abyssal Plain (where extracted Mod_P1 is located) refers to: a sequence of Mesozoic and Cenozoic sediments overlaying directly on serpentinized mantle. The transition is marked by strong velocity gradient, increasing from 4km/s to 7.2km/s, in 3km (see Figure III.27B-C).

We recalculated earthquakes locations applying the JHD method with independent P and S stations delays, testing different velocity models and Vp/Vs ratios (between 1.68 and 1.79). After 7 iterations steps, the best fitting model was mod_70 extracted from P2 refraction profile with Vp/Vs of 1.71 and RMS of 0.317 (see Table III.5). Both mod100 and mod120 had reached similar

final RMS. The model extracted from NEAREST P1 profile shown the higher Vs/Vs ≈1.78 and the largest RMS≈0.358.

P and S waves' stations delays, resulting from JHD method with velocity mod70, are plotted in Figure III.28 and Figure III.29. For P-wave stations corrections no clear relation with subsurface geology is established and once more GSTAR had the largest negative delay. However, S-wave stations delays still all positive reflecting the effect of the shallower sedimentary layer.

Final earthquake locations in the deployment area, using JHD method with mod70, are plotted in Figure III.30. As in the previous locations, we can identify three seismicity clusters: Gorringe Bank cluster, Horseshoe Abyssal Plain cluster and São Vicente Canyon cluster. Both in N-S and W-E profiles, we observe that most hypocenters are located between 20 and 50 km deep. Shallower events are located outside these clusters, mostly to the North of the Accretionary Wedge. Within the clusters area, earthquakes depth increases from West to East, from the Gorringe cluster to Horseshoe and São Vicente clusters.

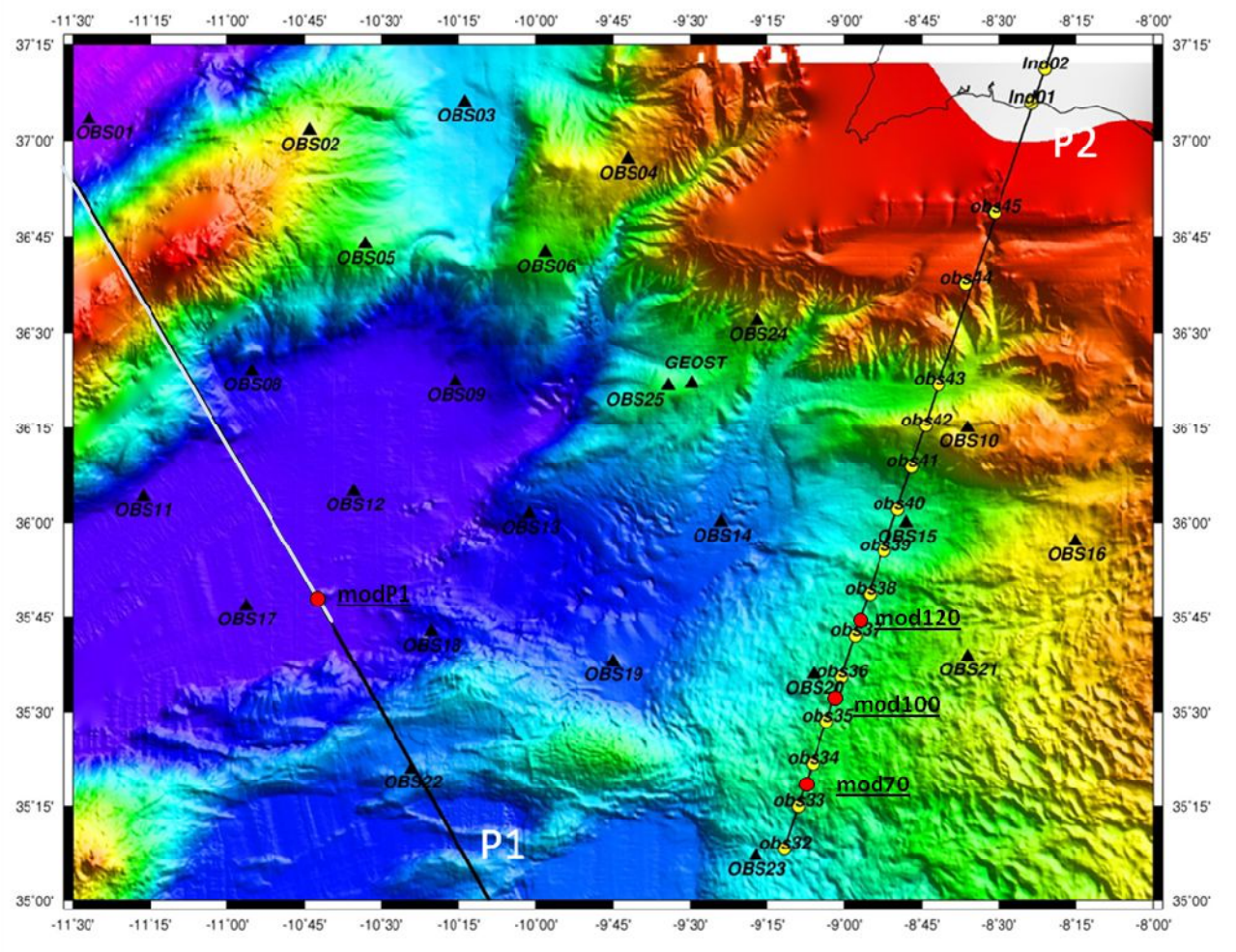

Figure III.26- Location of NEAREST refraction and wide-angle reflection seismic profile P2 and P1 from which it was extracted p-velocity profiles tested with JHD method (red circles mark the location of extracted P-velocity models, white line is locates the fraction of P1 profiles in figure III.27, bathymetry compilation from Zitellini et al., 2009).

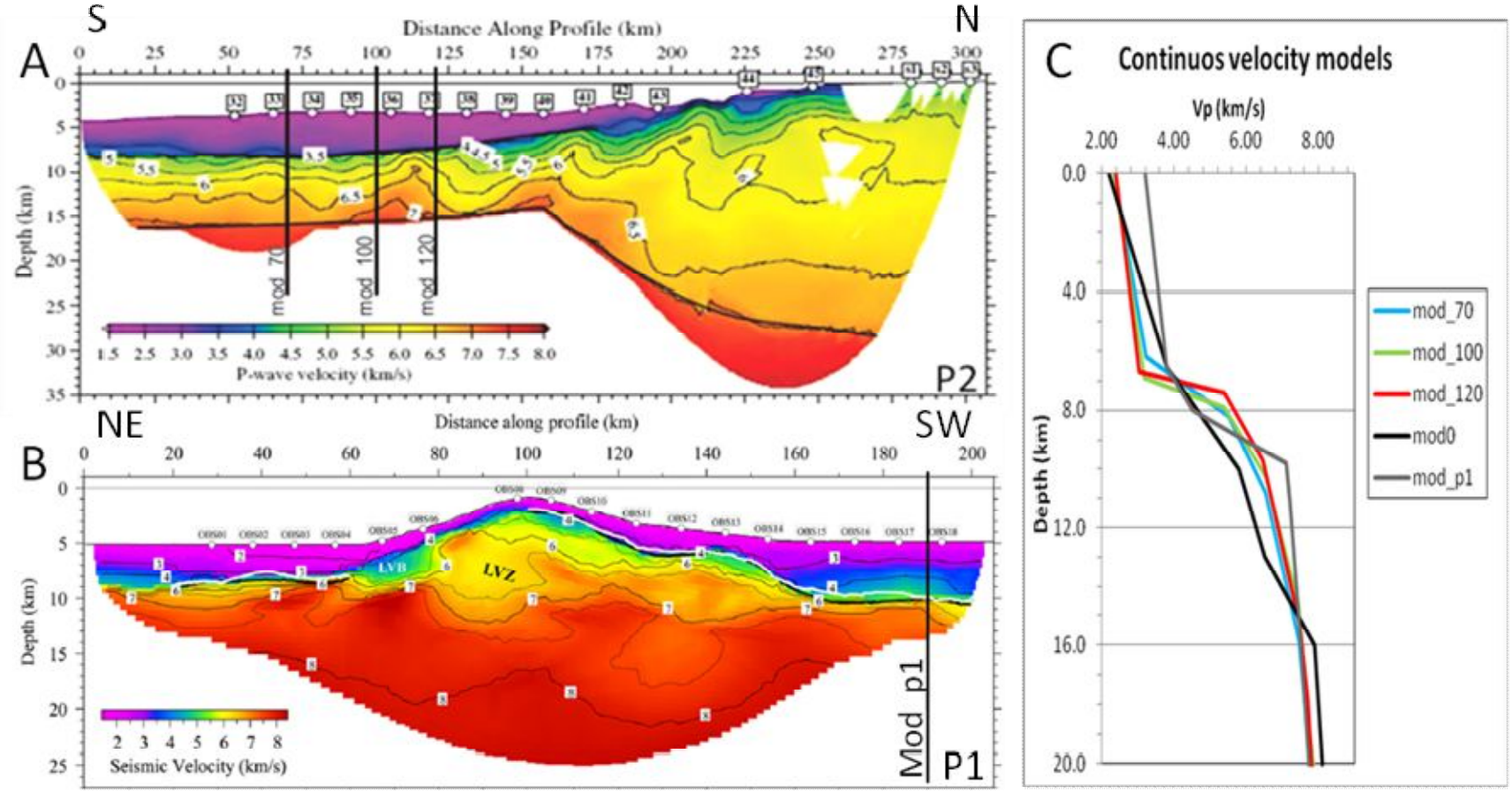

Figure III.27- P-velocity profile extracted from wide-angle reflection seismic profile P2 (Sallarès et al. 2011) and (Sallarès et al. 2013).

Table III.5-Best fitting Vp/Vs for the different velocity models tested. MOD70, extracted from P2-NEAREST refraction profile, outcomes as the best solution (details on velocity models in Figure III.27)

	HYP2 RES2	
Velocity model	Vp/Vs	RMS
MOD100	1.71	0.318
MOD120	1.71	0.318
MOD0	1.72	0.320
MOD70	1.71	0.317
MOD_P1	1.78	0.354

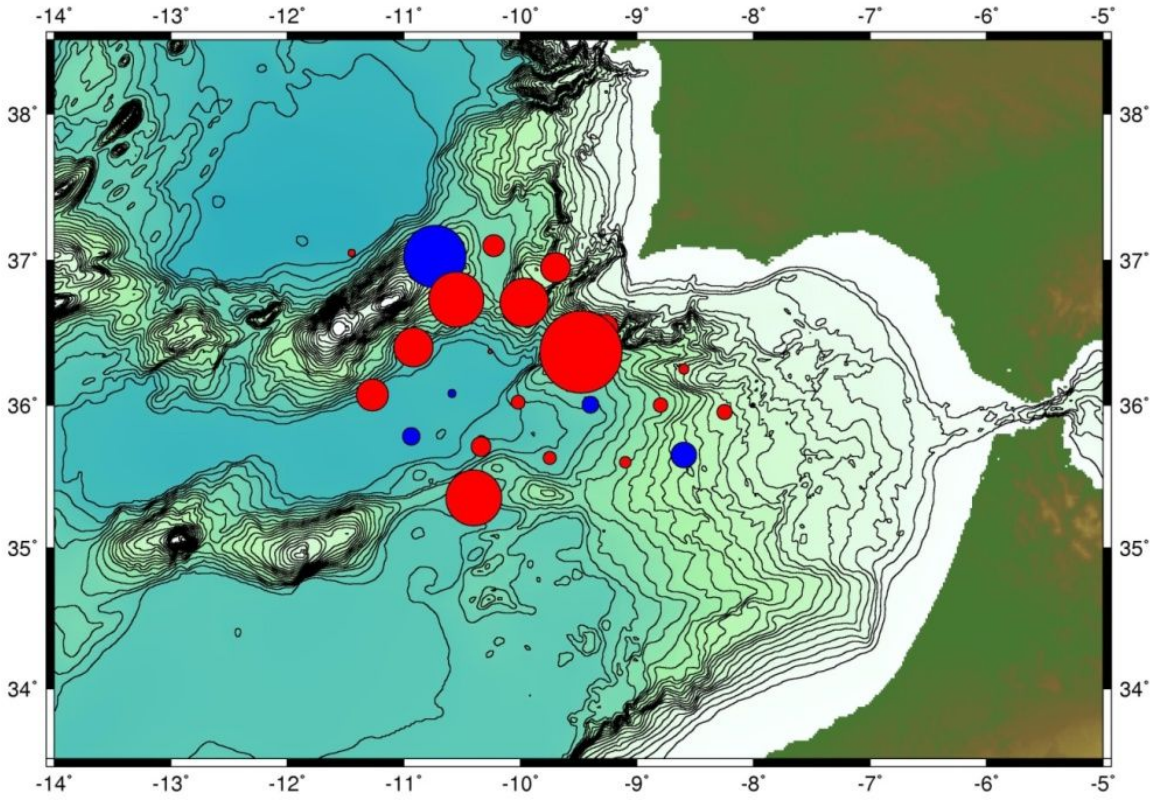

Figure III.28- P-wave stations delays derived from JHD method (blue is positive delay, meaning that arrival times in these stations reveal local slower P-velocities when compared with velocity model –MOD70; red is negative delay, reflecting local faster P-velocities). P-wave stations corrections show unclear relation with subsurface geology and GSTAR had an unexpected large negative delay *(bathymetry from GEBCO*).

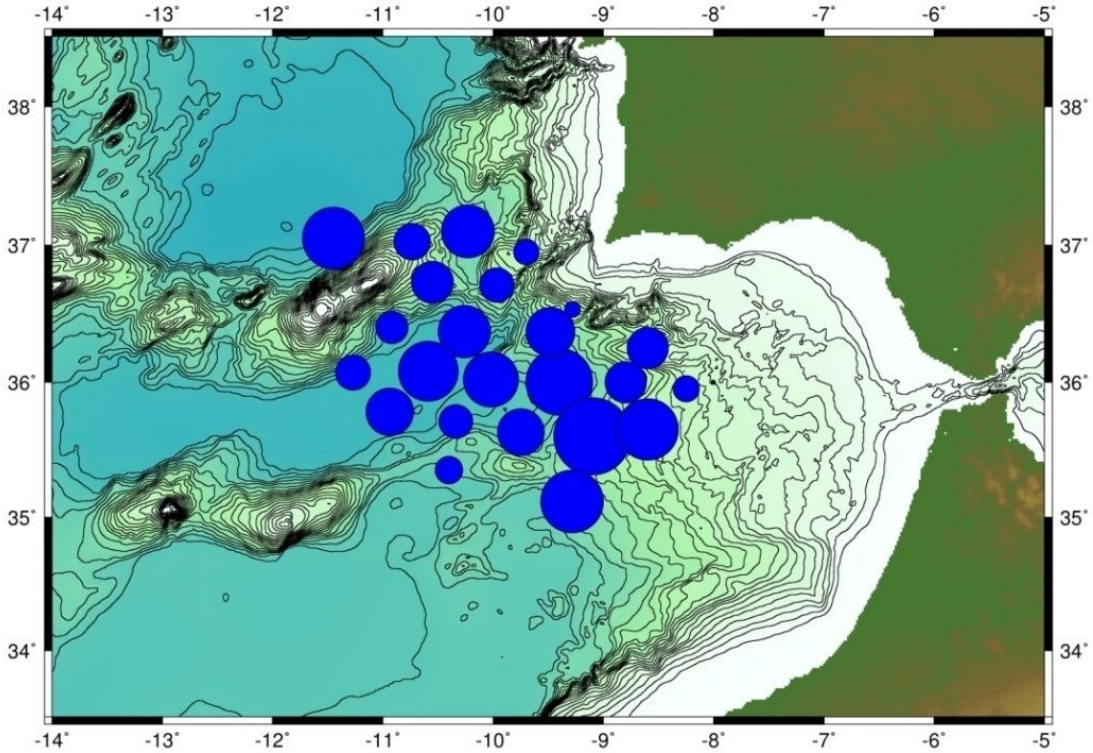

Figure III.29- S-wave stations independent delays derived from JHD method (blue is positive delay, meaning that arrival times in these stations reveal local slower S-velocities when compared with velocity model –MOD70, *bathymetry from GEBCO*). S-wave stations delays are all positive reflecting the effect of the shallower sedimentary layer.

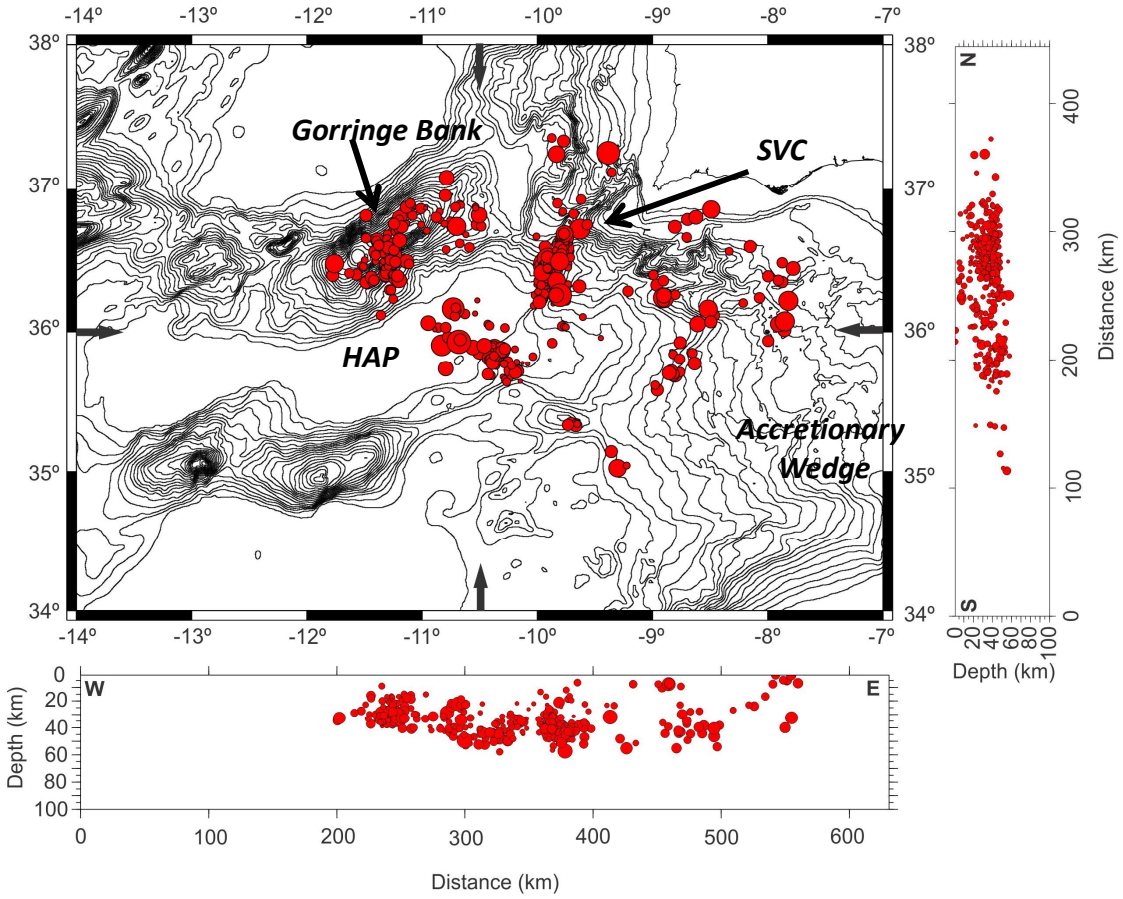

Figure III.30- Relocation of earthquakes acquired during the NEAREST OBS experiment, using JHD method with independent P and S stations delays (the black arrows mark the location of W-E and N-S profiles, *bathymetry from GEBCO*). The velocity model used in relocation process is MOD70 extracted from NEAREST refraction and wide-angle profile P2 (published in Salláres et al, 2011) with Vp/Vs of 1.71 and a final RMS of 0.317. Three clusters of seismicity are identified in the Gorringe Bank, the Horseshoe Abyssal Plain and the São Vicente Canyon cluster.

III.2.2.Determine 1D minimum velocity model

The arrival time of a seismic wave is a function of both hypocenter location and the propagation velocities along the ray path between the focus and the recording stations. This dependence is referred as the coupled hypocenter-velocity problem. For JHD methods the velocity model is fixed and the earthquake locations are improved by changes in the hypocenter parameters and stations corrections. In the previous section we showed that this approach helped to improve earthquakes locations. However, we were able to test only a limited range of 1D velocity models variability. In the area of the NEAREST OBS network deployment, the crustal structure is variable and so the simultaneous inversion for hypocenters and 1D velocity model seems more adequate.

We used the VELEST algorithm, for simultaneous inversion of hypocenter location, stations corrections and 1D velocity model for P and S waves (details on the method in Kissiling, 1988). As before, stations corrections will account for particularly subsurface geological variability below the recording stations and additional 1D model complexity can be introduced by consider Vp/Vs ratio variable layer by layer.

The VELEST method is a trial and error process, starting with a priori 1D velocity models (based on previous seismological studies, seismic reflection and refraction data), initial earthquakes locations and stations corrections. The initial model should itself have the lowest root mean square solution. Since in most cases the available geophysical data is insufficient, testing a wide range of initial velocity models will ensure that we will cover all possible solutions (Husen et al., 1999). In the context of the Gulf of Cadiz it is critical to try out several hypothetical models because is a region of high lithospheric variability ranging from old Jurassic oceanic, transitional to thinned continental (details in chapter I). As suggested in Kissling et al. (1994) for areas that comprise distinctly tectonic and composition domains we should at least test 3 different velocity models (with realistic and also extreme velocity variations). We should also try different velocity layering because VELEST inversion process only updates the velocity value within layer, maintaining the layer thickness.

Finally, the best velocity model will yield the smallest misfit (RMS) but must also show coherency between of lithospheric structure (particularly subsurface geological variability), Vp/Vs ratios and station delays results.

III.2.2.1.Event selection for the inversion process

One of the main considerations for accurate minimum 1D-velocity determination is the initial data quality (Husen et al. 1999). The initial dataset should include well located events with observations azimuthal gap lower than 180°and at least 10 P wave picks (Husen et al. 1999). As input, it is also suggested to use a minimum sample of 500 well located events. For the case study we have only have 443 events in the deployment area. From those, only a few match the desired parameters. So, we will consider less restrictive conditions as previously made by Dias (2005) and Carrilho et al. (2004).

From JHD method tests we defined that mod70 (extracted from P2 NEAREST refraction profile) was the best model with lowest root means square misfit (0.317s) on locations and a Vp/Vs =1.71. We used this model (including stations corrections) to select the events used as input for the minimum 1D velocity model determination. Before choosing the events we ran the *pharms* routine (created by Luis Matias) to identify phase *mispickings* or uncorrected weights. Next, we removed all redundant first phase pickings with weight 4 (less accurate and excluded from JHD location methods). The VELEST program only assumes one picking per phase, so if the first picking has weight 4 and the second is 0, it will consider the first. The final selection (details on the data in Figure III.31 to Figure III.33) was based on the following criteria:

1. minimum phase observations set to 10 (Figure III.31);
2. an azimuthal gap inferior to 210° (average GAP was 112°, Figure III.32);
3. Minimum of 3 p-wave first arrival observation (phase readings are dominated by S-wave pickings -Figure III.33. So, it is more important to constrain a minimum P-wave picking for events selection).

The final selection included 269 events with a RMS based on HYP2 and PRN2RES2 of 0.281s. The 269 events are distributed in three clusters: 109 are located in the area of São Vicente Cluster, 83 in the Gorringe cluster and 52 events in the Horseshoe cluster (Figure III.34). Most hypocentres are located between depths of 20-50 km.

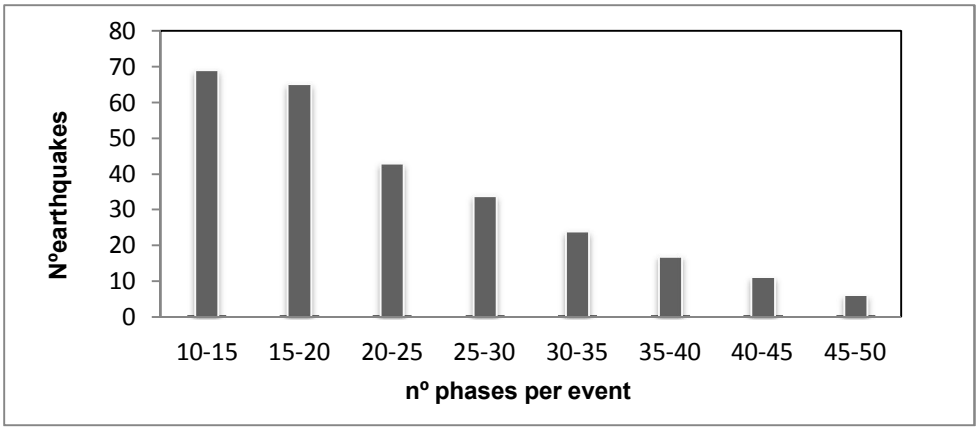

Figure III.31- Number of phases reading per event in the selected dataset for inversion. We established that the minimum phase observations as 10.

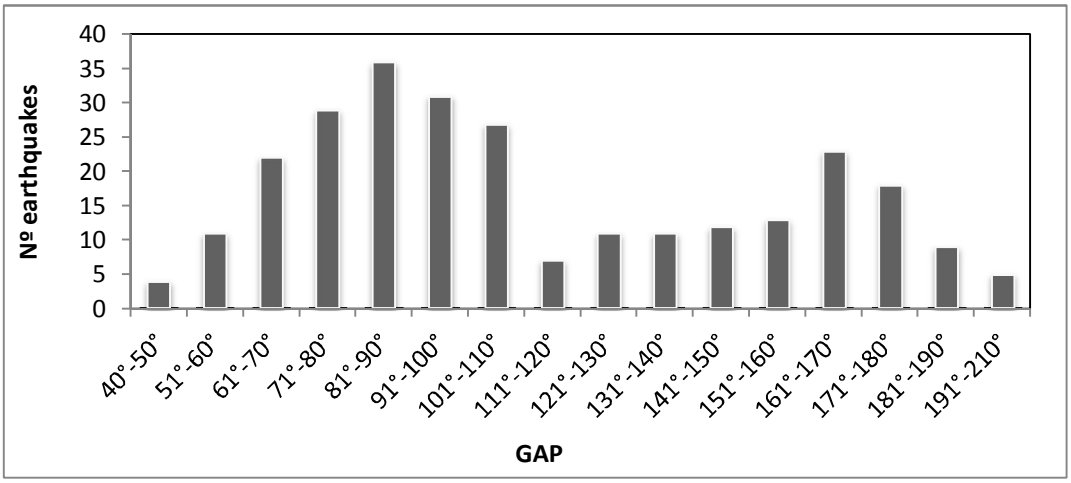

Figure III.32- Azimuthal gap distribution. The selected dataset has an azimuthal gap inferior to 210° (with an average GAP of 112°).

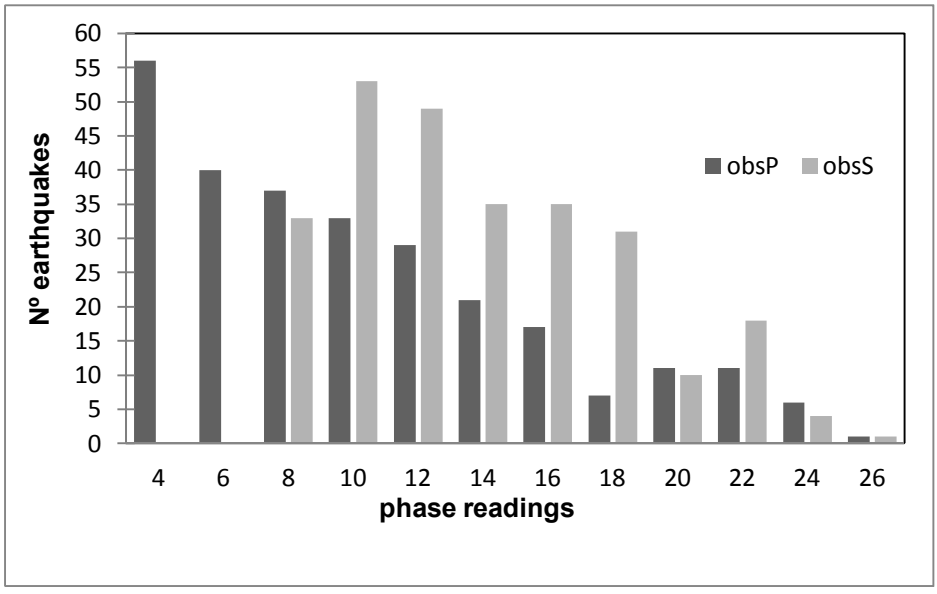

Figure III.33- Phase readings distribution. The dataset has a minimum of 3 observed p-wave first arrival. Since we have more S-wave pickings, we choose to constrain a minimum P-wave picking for events selection.

III.2.2.2.Reference station

The stations corrections in VELEST program are relative, calculated based on a reference station. Crosson (1976) points out that stations corrections are just additive adjustments to arrival times and will only be distinguished from other parameters corrections if they are relative. In this way, stations corrections will reflect model departure from lateral homogeneous velocity structure. So, the selection of the reference station is critical in hypocenter determination because stations corrections are the only way to adjust local tri-dimensional geological structure to the estimated 1D velocity model.

The reference station was selected based on the criteria suggested by Kissling et al. (1994):

1. Considering the continuity of the seismic record (at least 50% of the total possible readings);
2. central location within the seismic network;
3. the variability of the subsurface geology.

We selected station 9 (Figure III.34 to Figure III.35 as the reference station because: i) it is located in the middle of the seismic network; ii) it recorded most of the selected events; iii) it lies on top of the seismic chaotic sequence with a thickness is ≈770 ms (TWT) that is similar to the average thickness in NEAREST network area, around 700 ms (TWT); IV) it has one of the smallest station correction estimated by the JHD method.

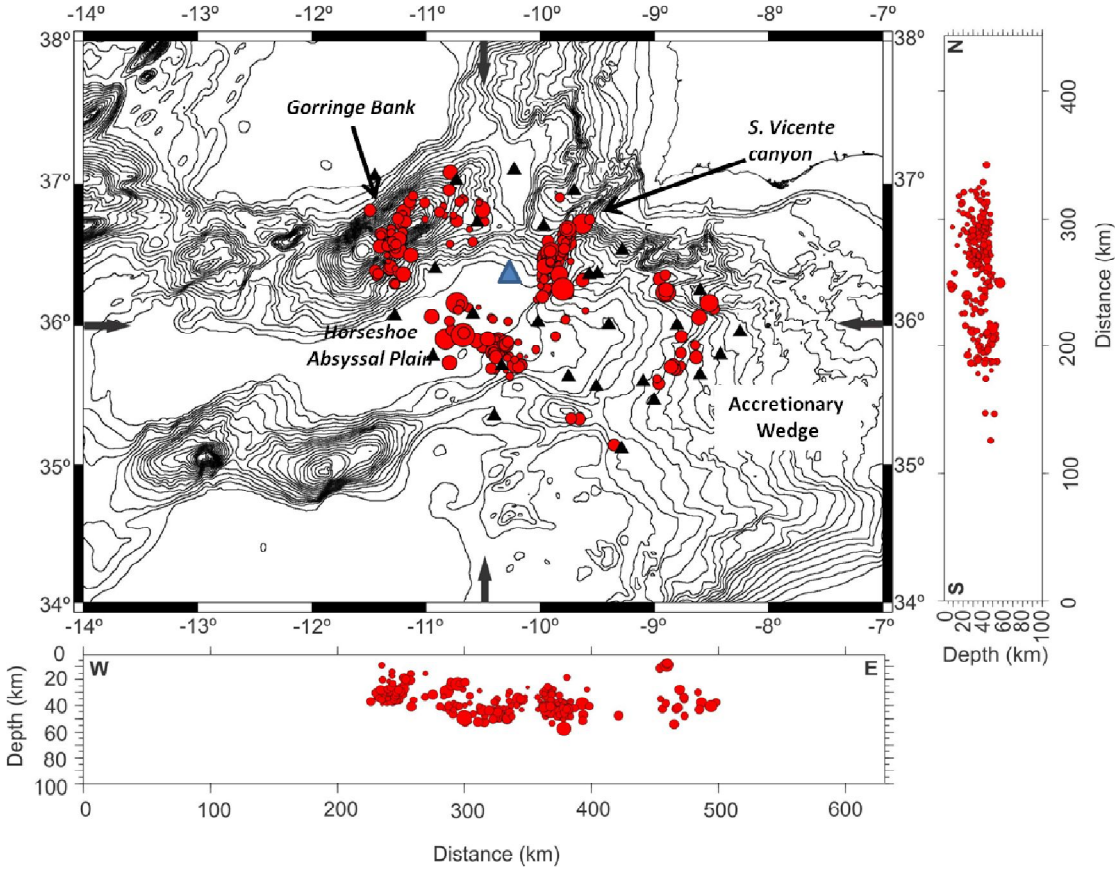

Figure III.34- Hypocenter distributions resulting from JHD approximation method for the 269 events selected for VELEST relocations: 109 events are located in the São Vicente canyon, 83 events in Gorringe Bank and 52 events in the Horseshoe Abyssal Plain. Most events are located between 30 and 50 km deep (the black arrows mark the location of W-E and N-S profiles, black triangles mark NEAREST stations and blue triangle NEAREST reference station-9 see section III.3.2.2, *bathymetry from GEBCO*).

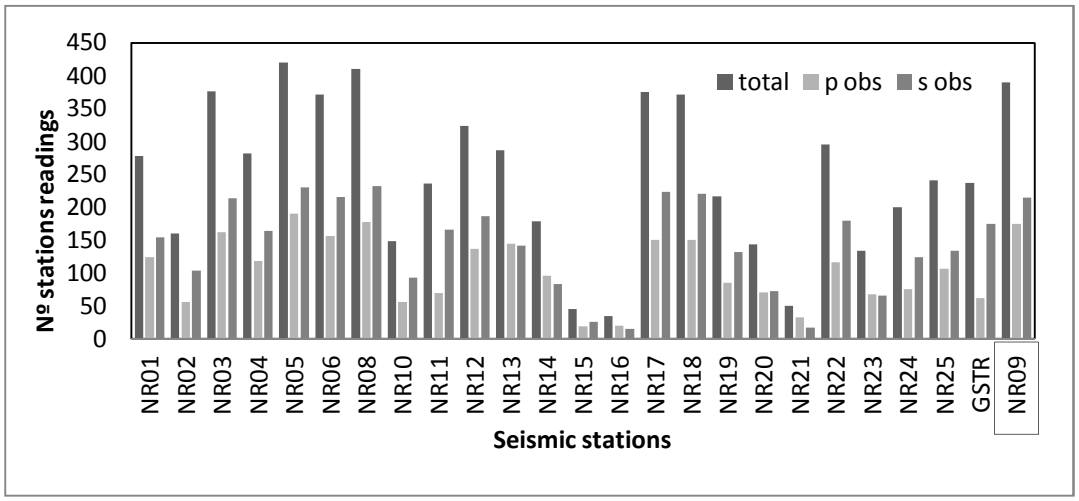

Figure III.35- Distribution of phase readings by seismic stations. Station 9 was selected as reference station because it recorded most of seismicity within the NEAREST OBS deployment area. Additionally, because it is located in the centre of the NEAREST seismic network and subsurface geology below this stations it is similar to geological variability expressed in velocity model, i.e. station correction deduced from JHD method is minimum.

III.2.2.3.Processing parameters and sequence

As suggested in Kissling (1995), defining the minimum 1-D velocity model requires multiple runs with VELEST to select and test control parameters appropriated to the data set. The final solution will be highly dependent on the values attributed to these parameters. A set of VELEST output files help in this procedure, providing detailed information about many intermediate calculation steps, even within one single iteration step (Kissling, 1995). From these intermediate results we can adjust the control parameters to obtain the best combination to proceed to the final runs of VELEST.

The VELEST program works with an input file (velest.cmn in Figure III.36) where the main parameters controlling the inversion process are defined. These parameters are described in detail in Kissling (1995); we will only refer here some critical input values.

The **nsp** factor (Figure III.36) controls the use of P and S phase pickings to estimate both hypocenter and velocity model. For nsp=1, only the P-wave readings are considered. This approach will help to constrain the velocity model but will be less effective in establishing hypocentre location. The use of S-readings will result in a more accurate hypocentre location, especially regarding focal depth (Husen et al., 1999). It can be included with fixed Vp/Vs (nsp=3) or

using independent S-readings and stations delays determinations (variable Vp/Vs, nsp=2). With the last option the earthquakes location was considerably improved.

We started by checking the best processing order based on these three options. The following sequence delivered the best solution. Initially, we started by inverting with P-phase readings only (nsp=1) to define the velocity model layering and minimize RMS values. We used the outputs as input to the next step where we included S-readings and tested the best fitting Vp/Vs ratio only in order to define the input models for next step with variable Vp/Vs ratio. In the last stage we integrated S-readings (nsp =2) with the best results from the previous tests as input. We tested fixed Vp/Vs option but the results delivered a much higher RMS than using variable Vp/Vs ratios. Husen et al. (1999) used the same procedure and also conclude that it resulted in the best RMS values. Additionally, in marine sediments the Vp/Vs ratio decreases significantly in the upper subsurface layers with the transition between unconsolidated and consolidated sediments (Crawford and Singh, 2008) unfavouring fixed Vp/Vs models. In the context of the study area other arguments favour the variable ratio approach:

- The presence of large scale seismic chaotic sequences (Horseshoe Gravitational Unit and Gulf of Cadiz Imbricated Wedge) which at least in shallow levels should decrease S-wave velocity. Additionally, there are evidences for widespread fluid circulation testified by mud volcanoes activity (e.g. Pinheiro et al, 2003, Hensen et al., 2015), that should also contribute to low S-wave velocities and high Vp/Vs ratios.
- The evidence for serpentinized upper mantle identified in P2 refraction profile (Sallarès et al., 2011). Serpentinization process decreases Vs velocity, increasing Vp/Vs ratio (Christensen, 2004).

```
******* CONTROL-FILE FOR PROGRAM  V E L E S T  *******
***
*** ( all lines starting with  *  are ignored! )
*** ( where no filename is specified,
***   leave the line BLANK. Do NOT delete!)
***
*** next line contains a title (printed on output):

***       starting model 1 based on
***  olat        olon   icoordsystem       zshift   itrial ztrial     ised
     36.356       10.290     0            0.000       0     0.00      0
***
*** neqs   nshot   rotate
     275       0      0.0
***
*** isingle   iresolcalc
       0           0
***
*** dmax    itopo     zmin      veladj    zadj   lowveloclay
     9999      0       5.00       0.20    5.00        1
***
*** nsp     swtfac   vpvs        nmod
     2       1.00    1.720         1
***
***    othet   xythet     zthet     vthet   stathet
       0.01    0.01       0.01      1.000   0.01
***
*** nsinv    nshcor    nshfix      iuseelev     iusestacorr
       1         0         0            1             1
***
*** iturbo     icnvout    istaout    ismpout
       1           1          2          0
***
*** irayout    idrvout    ialeout    idspout    irflout    irfroutiresout
       0           0          0          0          0          0      0
***
*** delmin    ittmax    invertratio
     0.010        9           2
***
```

Figure III.36 -Example of the control file for VELEST application.

Besides using P and S phase readings information, VELEST also allows differentiated relative weight between the phases (**swtfac**). This is an important factor because a clear S-wave reading is generally more difficult to identify than P-wave first arrival. A misinterpreted S-phase will increase uncertainties particularly in hypocentre location. In this study, we attributed the same weight for both phases because we already classified the S and P pickings with relative weight in preliminary locations. This weighting will be incorporated in VELEST process.

Stations corrections inversion is introduced by **nsinv** parameter and will primarily solve discrepancies between one-dimensional minimum velocity model and tri-dimensional subsurface geological variability below receiver stations. However, Dias (2005) pointed out that introducing these corrections in the early stage could inhibit initial velocity model to adjust to a more accurate velocity structure of the study area. We tested both hypotheses and observed that without introducing stations corrections in the early stages the models will converge faster to common velocity values particularly in the intermediate velocity layers.

The VELEST application limits station locations to the first layer of the velocity model, if there is a high discrepancy between stations elevation the inversion process can become unstable (Hussen et al., 1999). Since we are working with Ocean Bottom Seismometers with 3031m of maximum depth difference (OBS01 and OBS16 at 5100 m and 2069m depth, respectively), including stations elevations (**iuseelev** parameter) will decrease this layer thickness and

avoid processing instability. To avoid water and air quakes the minimum earthquake depth was set to 5km (***zmin***).

For damping factors in hypocenter location (**othet, xythet and zthet**) velocity (**vthet**) and stations (**stathet**) corrections we used the same values during the processing sequence with 0.01 for hypocenter location and stations corrections, 1.0 for velocity model, as suggested Kissling et al. (1994). For the velocity model, additional independent layer damping control can be included in the input velocity model file (input.mod). So, we increased damping factor for the top layers preventing unrealistic increase of velocity. Also in order to control hypocenter depth and velocity adjustments during the inversion process we can vary **Zadj** and **Vadj** values, respectively. In the initial running we set the **Vadj** to 0.5 and updated to 0.20 in the final steps. The **Zadj** was set to 5.0 during all processing sequence.

During the velocity inversion process the VELEST algorithm allows for low velocity layers (**lowveloclay**). However, this should be limited to the cases where this is clearly indicated by the data (reflection or refraction seismic profiles) because it will introduce instabilities (Kissling et al., 1994). We excluded low velocity layers in all tests.

The **ittmax** and **invertratio** parameters set the sequence for forward and inversion steps. During the processing sequence the **invertratio** was set to 2 (except for location steps which excluded inversion process) meaning that every second iteration will be an inversion. The iteration number was variable depending on the RMS evolution during a specific step.

The final processing sequence was the following,

I. *Invert for Vp initial model without introducing stations corrections*:

I.1. Invert for Vp initial model: improve location (9it) → invert for velocities (9it 2inv) → improve location (9it)

I.2. Defining best layering: merge similar velocity layers

I.3. Invert for both Vp: improve location (9it) → invert for velocities (9it 2inv) → improve location (9it)

II. *Invert for minimum velocity model introducing stations corrections:*

II.1. Invert for Vp: improve location (5it) → invert for velocities (9it 2inv) → invert for stations corrections (9it 2inv) → invert both velocities and stations not allowing low-velocities layers (5it 2inv)

II.2. Invert for both for minimum Vp and Vs (testing different Vp/Vs as input): improve location (5it) → invert for velocities (9it 2inv) → invert for stations corrections (9it 2inv) → invert both velocities and stations not allowing low-velocities layers (5it 2inv)

In every processing step, the previous output was used as input.

III.2.2.4.Results:

Invert for minimum Vp model based on P-phase readings (step I in processing sequence)

Initial 1D P-velocity models (step I.1 in processing sequence)

We started by testing velocity models extracted from available geophysical data: MOD0, n70 (mod70) and also some slower (s02 and s03), faster (f03, f04, f05) and intermediate velocity (t01, t02) models (Figure III.37 to Figure III.40). No initial stations corrections were included as suggested in Kissling (1995). With these models we will explore velocity values variations within the different layers and evaluate hypocenter distribution for the selected events. From Figure III.37 to Figure III.40, we present initial velocity models 1D profiles, events distribution by depth intervals in histograms and initial RMS.

It is worthwhile notice that all initial models have similar velocities in lowermost layers. So, we would expect that all velocity models converge rapidly in these layers. In Figure III.37 to Figure III.40, we detect that, for all velocity models (except for s02), hypocenters density is higher between 30 and 50 km, these layers should be the ones where velocity convergence is more successful. For velocity models f0, f04, f05, t01, n70 and mod0, we also identified a considerable number of earthquakes in the shallower layer. However, velocity inversion for topmost and bottom layers was conditioned by the hypocenters distributions. These boundary layers generally have lower resolution than the central layers where most hypocenters are located and velocity constraints resulted from combined information of direct and refracted ray paths. The RMS result after relocation (without stations corrections) is higher for intermediate velocity model t02-0.721s and lower for the fast model f05- 0.370s.

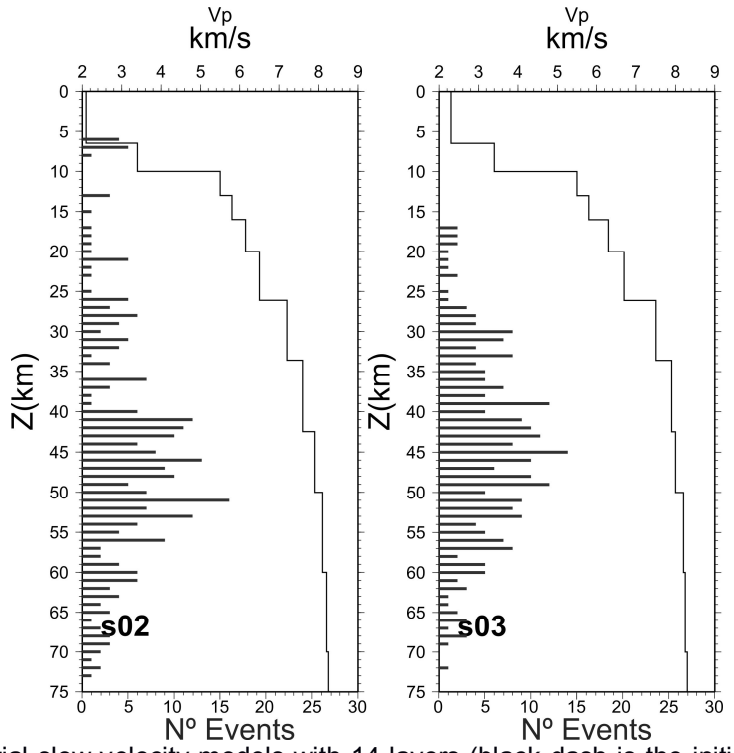

Figure III.37- Initial slow velocity models with 14 layers (black dash is the initial model with no initial stations corrections and blue bars are the earthquakes depth distribution). The initial RMS for earthquake relocation with models s02 and s03 are 0.464s and 0.469s, respectively.

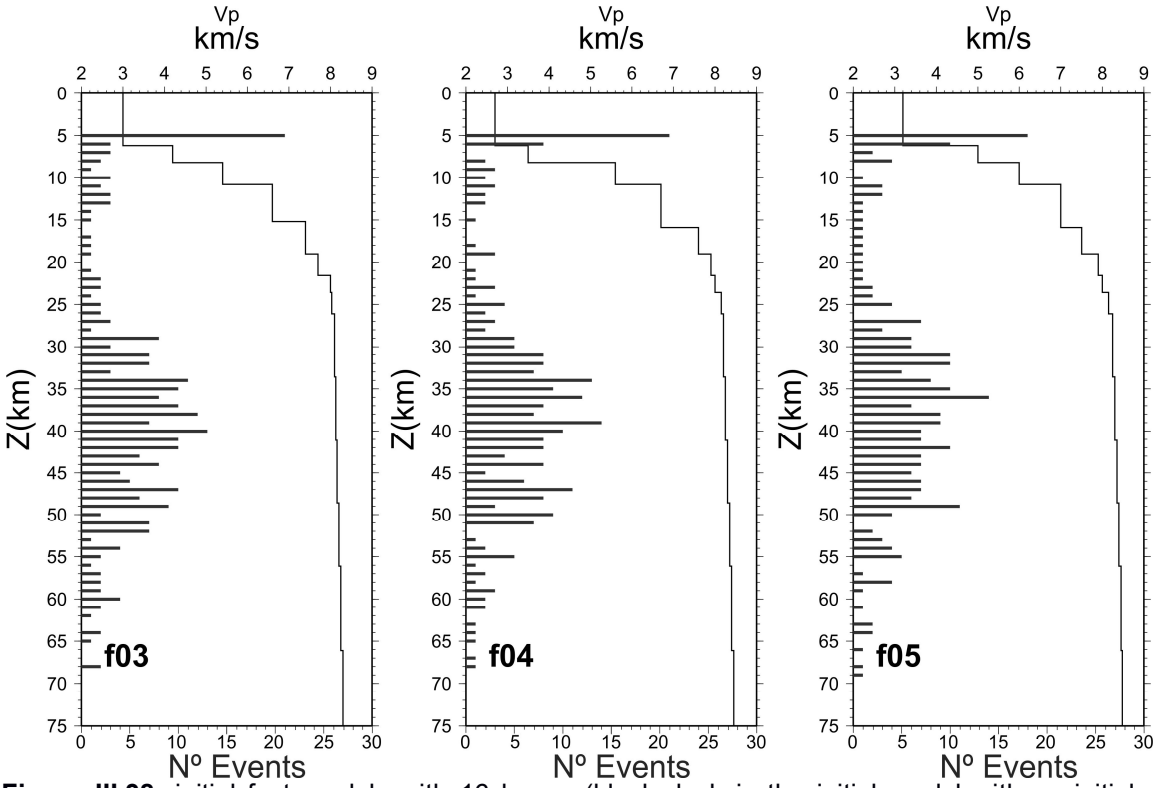

Figure III.38- initial fast models with 16 layers (black dash is the initial model with no initial stations corrections and blue bars are the earthquakes depth distribution). The initial RMS for earthquake relocation with models f03, f04 and f05 are 0.376s, 0.420 and 0.369s, respectively.

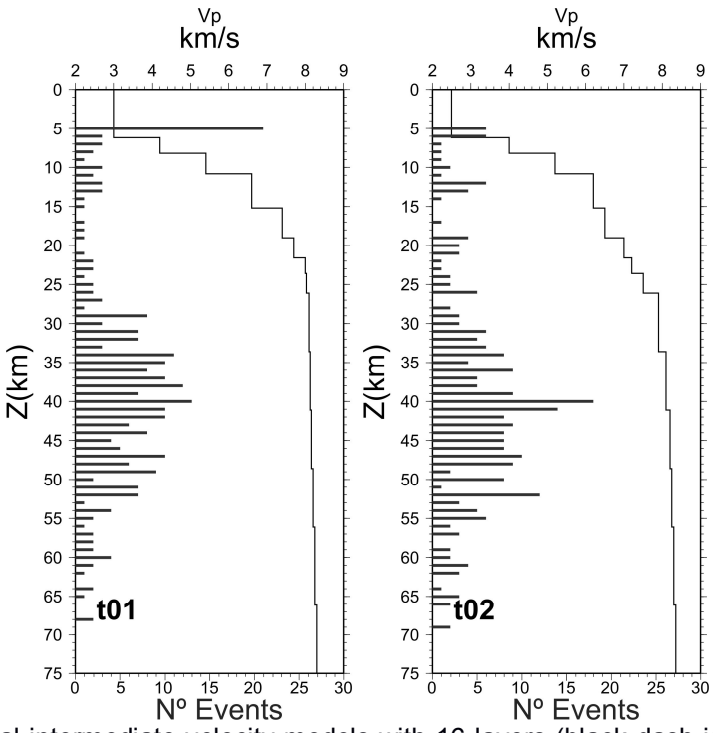

Figure III.39- Initial intermediate velocity models with 16 layers (black dash is the initial model with no initial stations corrections and blue bars are the earthquakes depth distribution). The initial RMS for earthquake relocation with models t01 and t02 are 0.416 and 0.7207, respectively.

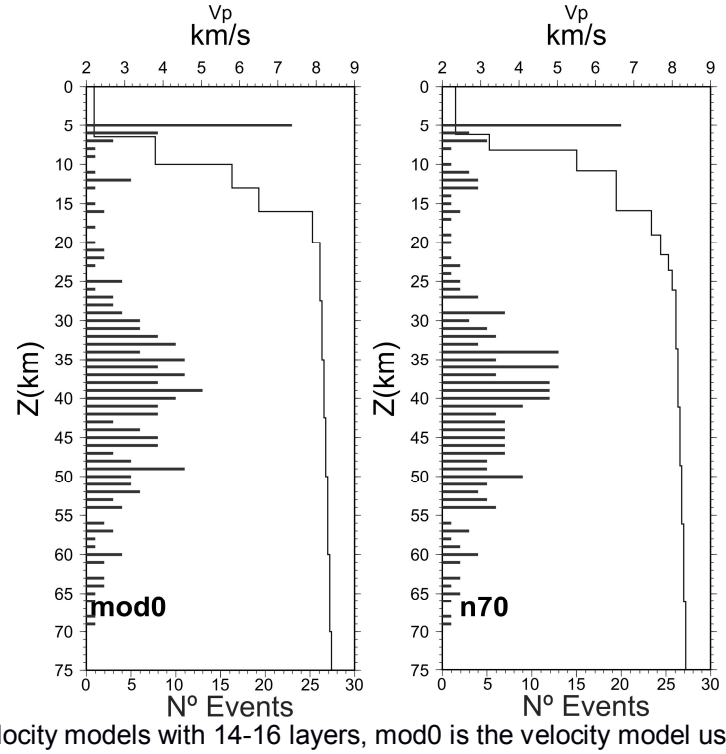

Figure III.40- Velocity models with 14-16 layers, mod0 is the velocity model used for preliminary locations published in NEAREST 2008 Cruise Report r/v Urania, n70 is a velocity profile extracted from Sallarès et al. (2011) NEAREST refraction and wide-angle reflection seismic profile P2 (black dash is the initial model with no initial stations corrections and blue bars are the earthquakes depth distribution). The initial RMS for earthquake relocation with models mod0 and n70 are 0.416s and 0.450s, respectively.

Since P wave readings were used in a seismic catalogue with 269 earthquakes, with a velocity layering with 14-16 levels and stations corrections were

excluded, 1090-1092 unknowns (4x 269 hypocentral parameters and 14 to 16 velocity parameters) were to be determined with the inversion problem. Because 2622 P-phase pickings were produced the inverse problem is *overdetermined* by a factor of 2.40.

Before starting the inversion procedure we relocated the events sequence in two steps:

1. With HYP2 application and station0.hyp updated with testing velocity;
2. With joint hypocenter determination using VELEST application (step 1 in processing sequence).

These steps minimize the impact of input locations in the inversion process. After relocation process the RMS values range from 0.3918s (mod0) to 0.3459 (moderated fast model f03 –Figure III.41). In the next running we inverted only for velocity model every second step (with a Vadj=0.5) and the RMS decreased below 0.35s. With the final location step the RMS improvement was minimum and the resulting values fluctuated between 0.3364s and 0.3258s.

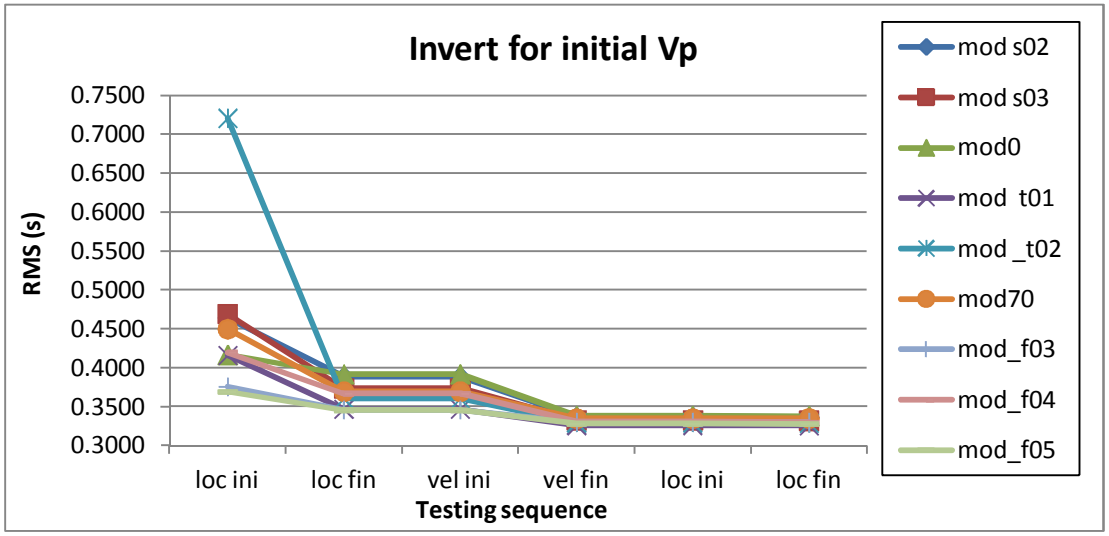

Figure III.41-RMS evolution along processing steps (in processing sequence, loc ini and loc fin define the initial relocation step, vel ini and vel fin is P- velocity inversion step and final relocation run RMS is defined by the last loc ini and loc fin). After initial relocation RMS decreases drastically, regardless the initial velocity model. It is clearer for intermediate velocity mod_t02. After the first inversion of the P-velocity model, all resulting location have similar misfits.

In Figure III.42 to Figure III.45, initial and final velocity models (with final hypocenters depth distribution) are displayed. The first velocity layer increases in all models (even with layer damping) and the final value is dependent on the input. For slower models (s02 and s03) reaches 3.1 to 3.2 km/s, in intermediate models (MOD0, n70, t02) 3.2-3.5 km/s and in fast models (f03, f04,f05) and model t01 results in values between 3.5 km/s and 3.7 km/s. After inversion most hypocenters are still located between 30 and 55 km in depth. However, the number of hypocenters in shallow levels decreased, with more impact for

models t01, n70 and mod0. This general decrease of shallower events is a consequence of the increase of P-seismic velocity at the topmost layer. Higher velocities will increase events depths.

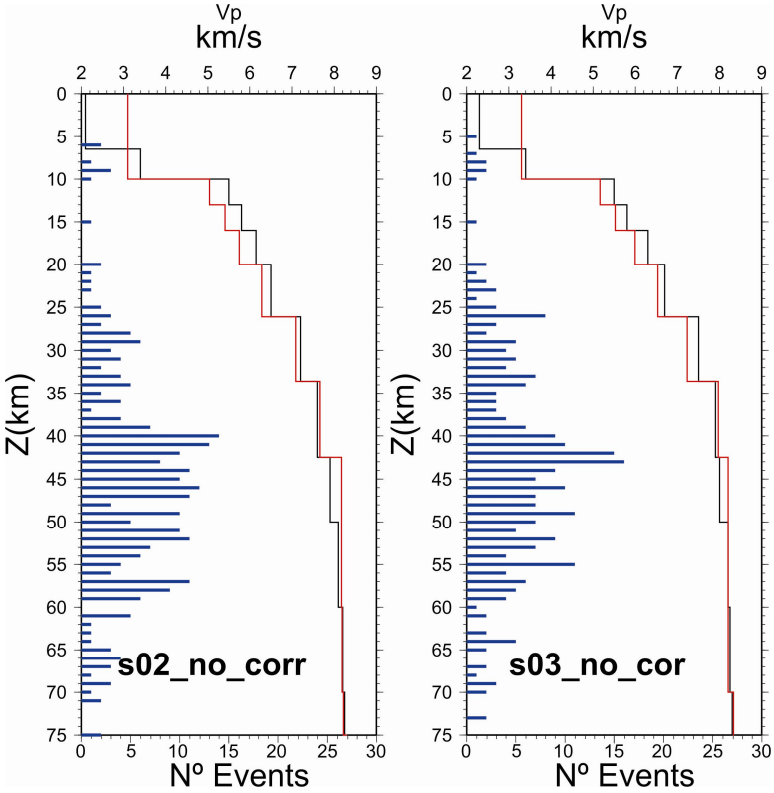

Figure III.42- Slow models with 14 layers, black dash is the initial model with no initial stations corrections, red dash is the model after inversion and blue bars are the earthquakes depth distribution after inversion. The final earthquake location RMS are 0.336 and 0.3321, for model s02 and s03, respectively. In general seismic velocity increases while both superficial (<15km) and deeper (>60km) earthquakes decrease.

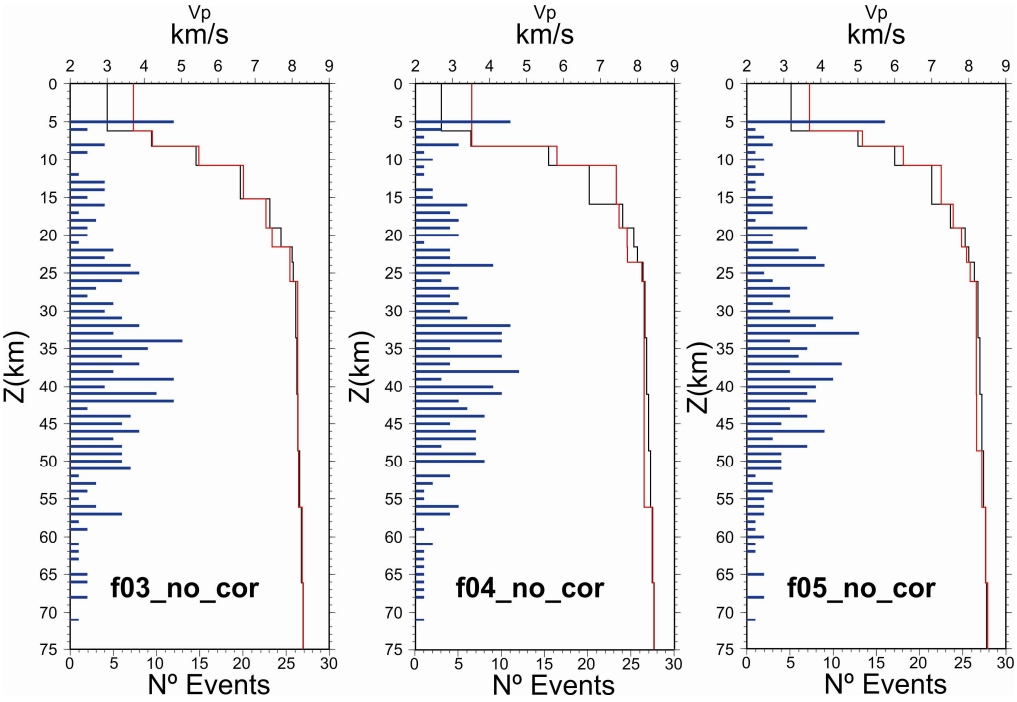

Figure III.43-Fast models with 16 layers, black dash is the initial model with no initial stations corrections, red dash is the model after inversion and blue bars are the earthquakes depth distribution after inversion. The final earthquake location RMS are 0.330, 0.330 and 0.328, for model f03, f04 and f05, respectively. Final velocities are faster than in the initial models. There is a decrease in events density both on the top and bottom layers. In the intermediate layers seismicity is distributed roughly uniformly.

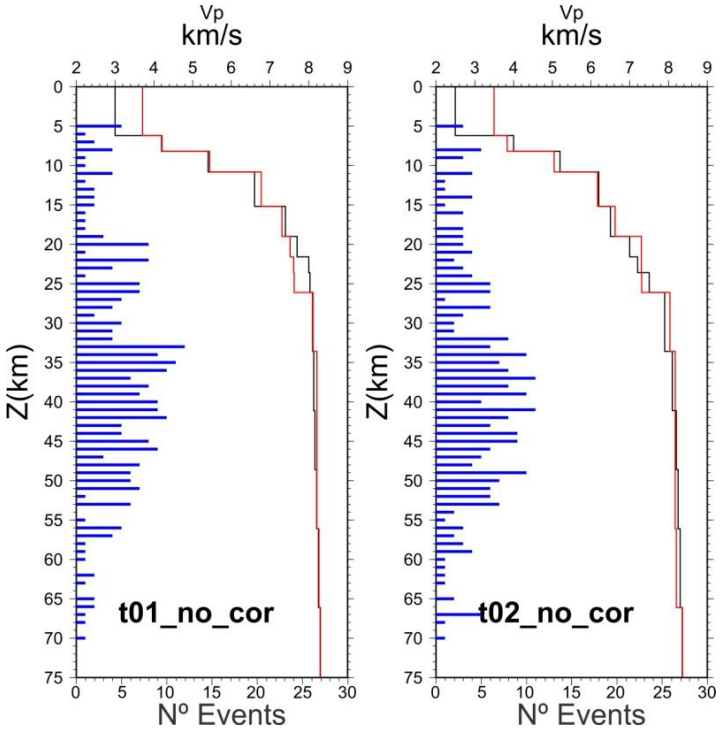

Figure III.44- Intermediate velocity models with 16 layers, black dash is the initial model with no initial stations corrections, red dash is the model after inversion and blue bars are the earthquakes depth distribution after inversion. The final earthquake locations RMS are 0.326 and 0.329, for model t01 and t02, respectively. In these models there is a remarkable decrease of earthquakes in the topmost layer. This result is a reflects the increase of the seismic velocity on the topmost layer: from 3 and 2.5 km/s to 3.7 and 3.5 km/s, for modt01 and modt02, respectively.

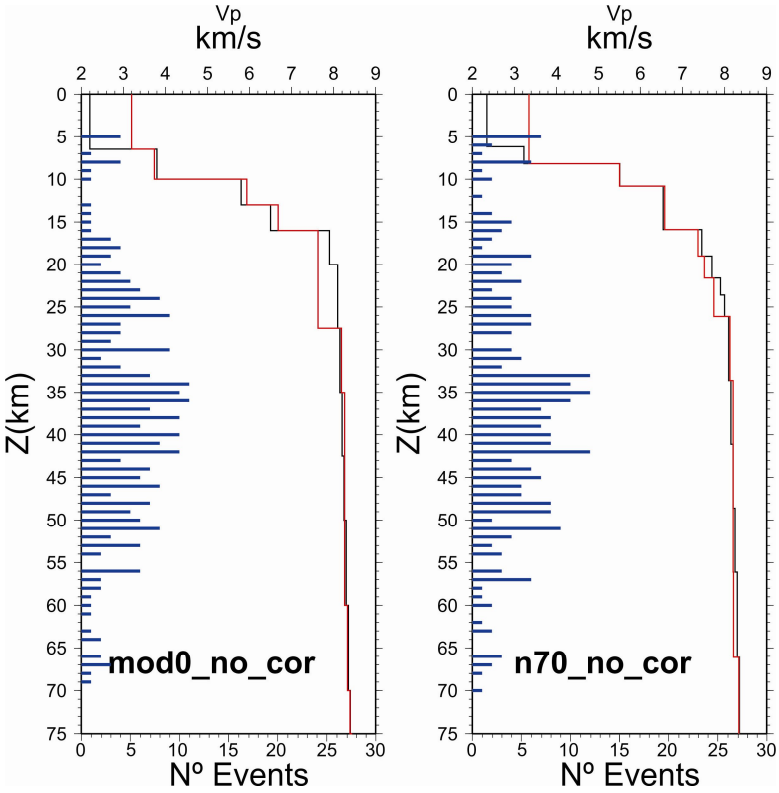

Figure III.45- Velocity models with 14-16 layers, mod0 is the velocity model used for preliminary locations published in NEAREST 2008 Cruise Report r/v Urania, n70 is a velocity profile extracted from Sallarès et al. (2011) NEAREST refraction and wide-angle reflection seismic profile P2 (black dash is the initial model with no initial stations corrections, red dash is the model after inversion and blue bars are the earthquakes depth distribution after inversion). In final earthquakes locations RMS are 0.338 and 0.335 for model mod0 and n70, respectively. There is a decrease on the number of events located on the topmost layer, concomitant with an increase on the P-seismic velocity. Events are redistributed to the intermediate levels (15 and 30 km in depth) as seismic velocity decreases slightly.

From the velocity models summary shown in Figure III.46, we recognize a convergence on the absolute velocities for the layers with higher concentration of hypocenters, common to all input model, mostly to 30 to 55km depth. This tendency increases for input models with similar velocities, extending to an interval 15-70 km depth. For velocity models f03, f04, f05, mod0 and n70, upper mantle velocities are defined in the 19km boundary, ranging from 7.46 to 7.80 km/s. For top layers, mostly crossed by subvertical ray paths, no convergence is observed. Also, we would expect based on seismic reflection and refraction data in this area, that there is high variability in subsurface geology below the recording stations. This variation should be, at least partially, solved with stations corrections.

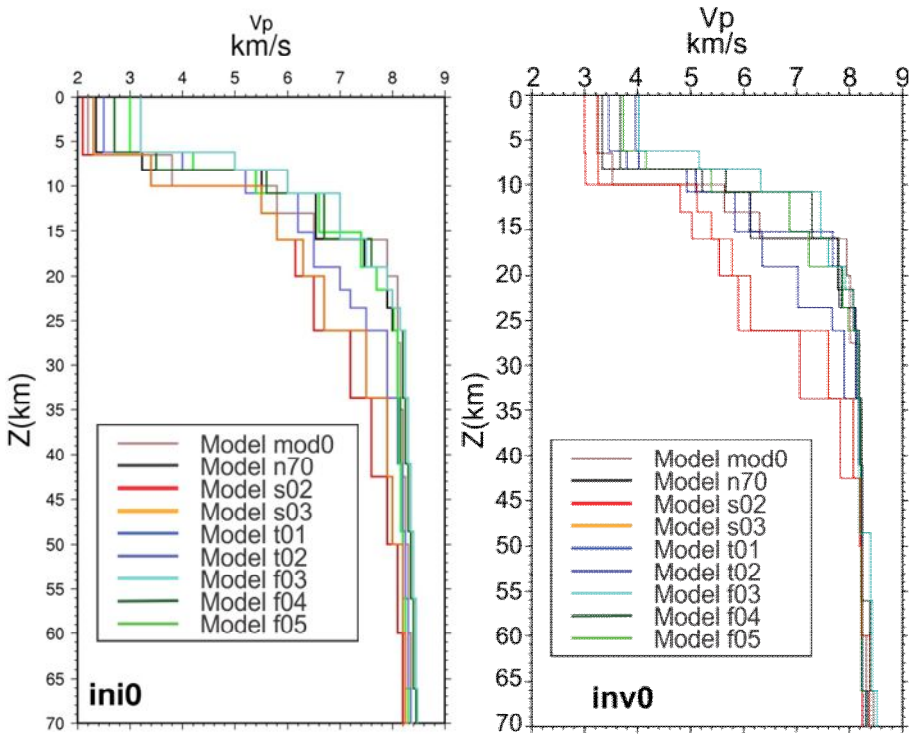

Figure III.46- Initial models with 14 -16 layers and resulting inversion models derived from p-wave readings. In topmost layers, p-wave velocities increase transversally to all models. In these layers, mostly crossed by subvertical ray paths, no convergence is observed is. Absolute velocities converge in the layers with higher hypocenters density, mostly to 30 to 55km depth (except for models s01 and s02).

Models with 24 layers (step I.1 in processing sequence)

To test velocity models geometry we converted previous input models to more complex structures with 24 layers (Figure III.48 to Figure III.51). For the upper layers (until 20km in depth) we included velocity increment every 1 to 2km, in the intermediate layers (from 20-40km) a 2 to 3 km thickness and for lower layers with 5 to 10 km thickness.

Since we are using the same sample with 269 events and a velocity layering with 24 levels, we will have 1100 unknowns to be determined with the inversion problem. We have 2622 P-phase pickings so the inverse problem is *overdetermined* by a factor of 2.38.

The processing sequence was the same applied in the previous test (Figure III.47). After initial relocation RMS values range between 0.3939 for the extreme slow s02_m24 and 0.3451 for the fast model f05_m24. After the velocity inversion step, the highest RMS value is 0.3836 and the lowest 0.3253. In the final step, we relocate the events with inverted velocity models. The RMS decreased for most models, ranging from 0.3617 (model f04_m24) to 0.3249 (model t01_m24). However, during the inversion process models f03_m24, f04_m24 and f05_m24 became instable and RMS solution increased.

In Figure III.48 to Figure III.51, we identify a few important modifications on the initial velocity model. For all models, significant changes summed up to decreasing models variability in terms of geometry, merging velocity layers (particularly when velocity increment was smaller).

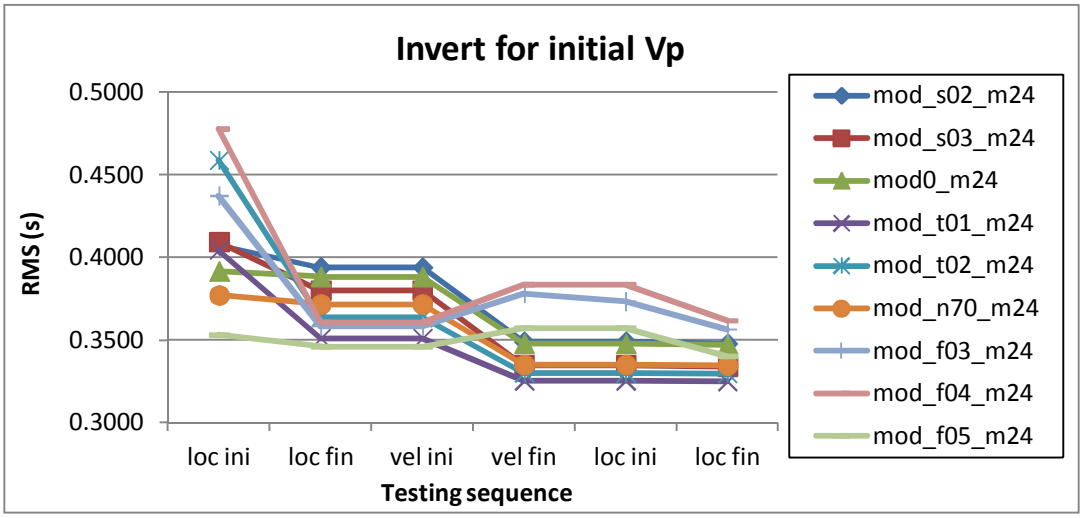

Figure III.47- RMS evolution along processing steps (in processing sequence, loc ini and loc fin define the initial relocation step, vel ini and vel fin is P- velocity inversion step and final relocation run RMS is defined by the last loc ini and loc fin). After initial relocation RMS values range between 0.394 and 0.345. With velocity inversion, the highest RMS value is 0.3836 and the lowest 0.3253. In the final relocation RMS decreased for most models, ranging from 0.3617 to 0.3249. However, during the inversion process the faster models became instable and RMS solution increased significantly.

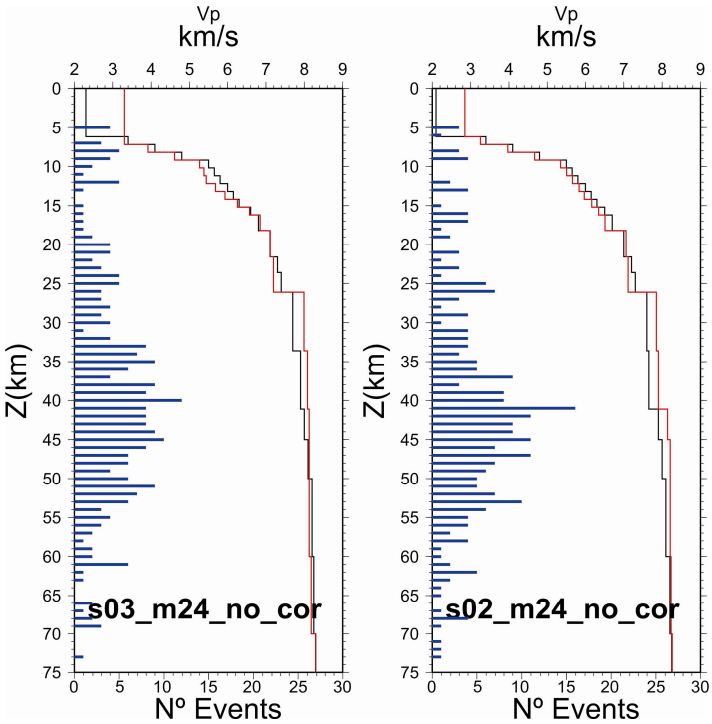

Figure III.48-Slow models with 24 layers, black dash is the initial model with no initial stations corrections, red dash is the model after inversion and blue bars are the earthquakes depth distribution after inversion. The final earthquakes locations RMS are 0.348 and 0.334 for model s02_m24 and s03_m24, respectively. Velocity at the topmost layers increased notably whereas the intermediate and bottommost layers remained roughly invariable.

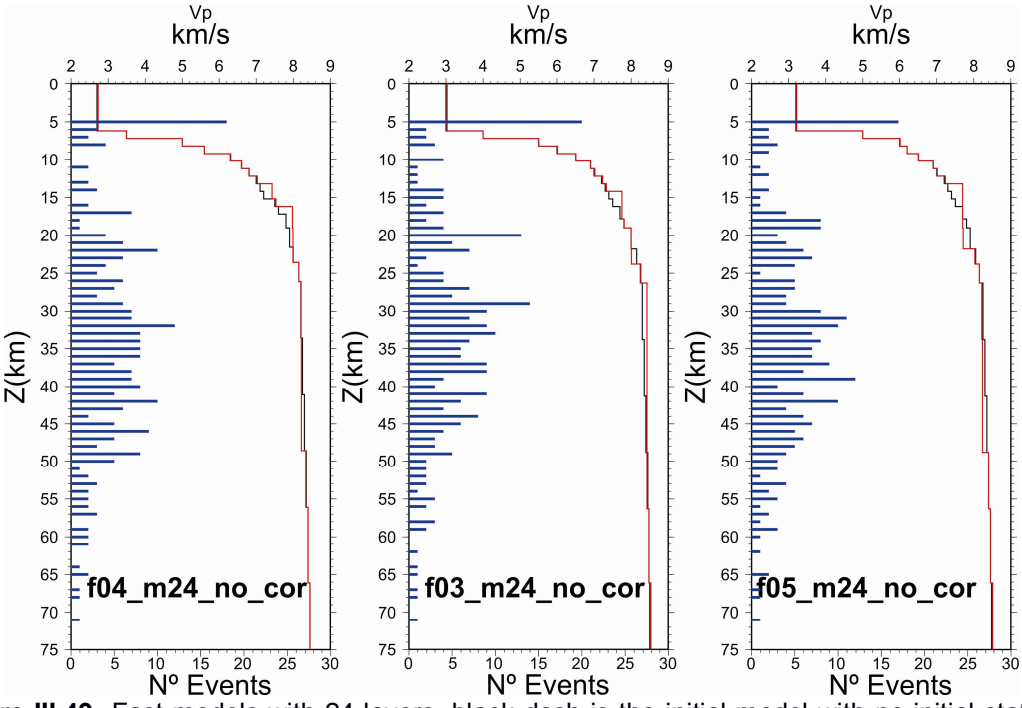

Figure III.49- Fast models with 24 layers, black dash is the initial model with no initial stations corrections, red dash is the model after inversion and blue bars are the earthquakes depth distribution after inversion. The final earthquakes locations RMS are 0.356, 0.362 and 0.340 for model f03_m24, f04_m24 and f05_m24, respectively. Faster models became unstable during the inversion of the velocity model so we failed to improve our results.

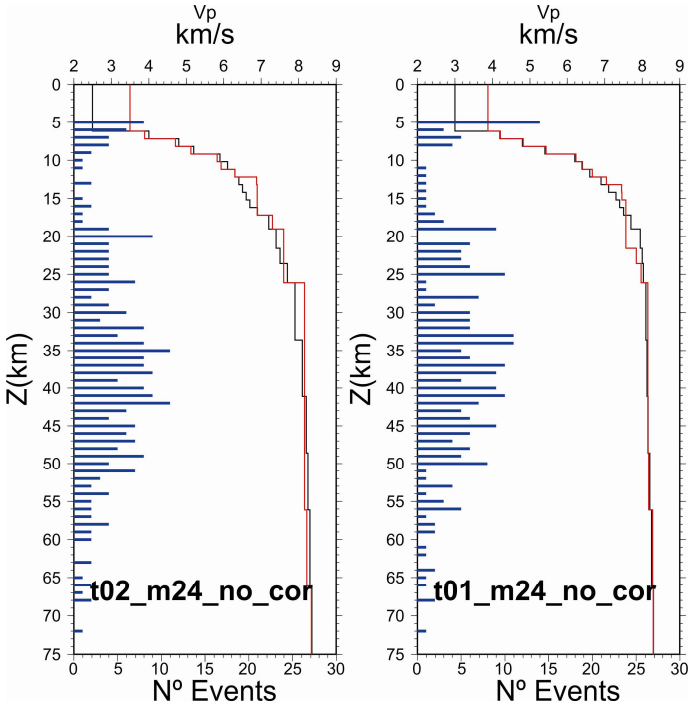

Figure III.50 -Intermediate velocity models with 16 layers, black dash is the initial model with no initial stations corrections, red dash is the model after inversion and blue bars are the earthquakes depth distribution after inversion. The final earthquakes locations RMS are 0.325 and 0.330 for model t01_m24 and t02_m24, respectively. As in slower models, topmost layers velocity increased considerably and the remaining layers velocities were roughly invariant.

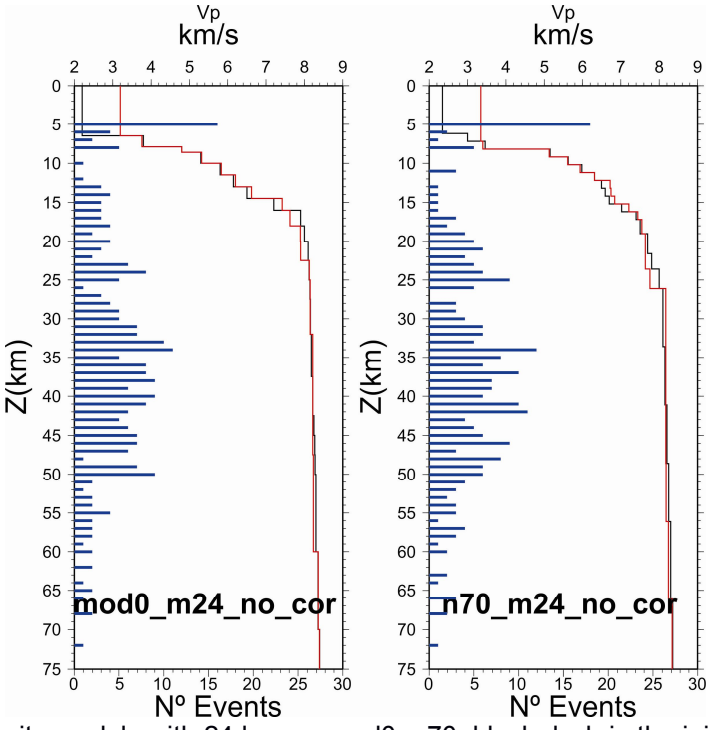

Figure III.51- Velocity models with 24 layers, mod0, n70, black dash is the initial model with no initial stations corrections, red dash is the model after inversion and blue bars are the earthquakes depth distribution after inversion. The final earthquakes locations RMS are 0.348 and 0.335 for model mod0_m24 and n70_m24, respectively. The topmost layers velocities increase while the other layers velocities remained nearly invariant during the inversion steps.

In Figure III.52, we observe that convergence in velocity models was more successful for depth larger than 25 km. However, from these initial tests, we realize that the geometry of the velocity models should be less complex. So, in the next steps, we tested models derived from the previous ones but merging layers with similar velocity values.

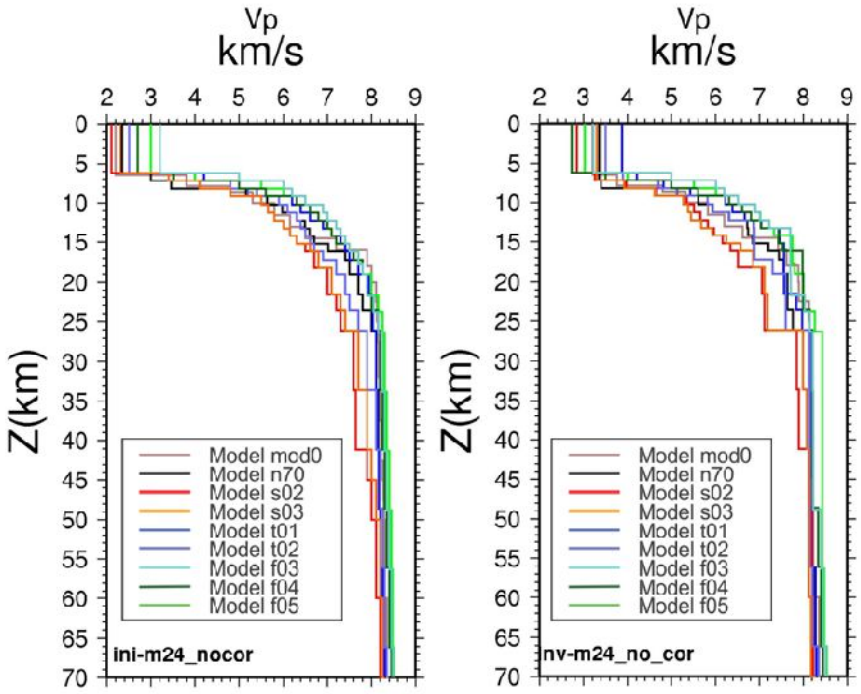

Figure III.52-Initial 24 layers models and resulting inversion models derived from p-wave readings. Convergence of the velocity models was more successful for depth larger than 25 km. From these initial tests, we realize that the geometry of the velocity models should be less complex.

Models with 11-14 layers (step I.2 and I.3 in processing sequence)

We converted model mod0 in 11 layers, models s03, t02 in 12 layers, models f03, f04, t01, s02 and n70 in 13 layers and finally f05 in to 14 layers. These models result from merging layers with similar velocity in P-velocity models resulted from step I.1.

We used the same earthquake selection (269 events), but we reduced the number of layers in the velocity model to11-14. In these processing steps, we have 1087-1090 unknowns to be determined with the inversion problem. We still use only 2622 P-phase pickings so the inverse problem is *overdetermined* by a factor of 2.4

The processing sequence was the same used in previous inversions and the result is shown in Figure III.53. During the inversion step some velocity models became unstable: f04_m13, s02_m13 and s03_m12 (fig.III.53). Even though, the majority of the starting models reached a smaller RMS values than in the previous processing sequence. The lowest RMS is reached with model t01_m13 (0.3220) and the highest with s02_m13 (0.3376).

The hypocentral depths reach similar distribution for models f04_m13, f05_14, mod0_11, n70_m13 (Figure III.55 and Figure III.57) where most events are located between 30 and 50km and there is a gap on seismic activity around 10 km. In intermediate velocity models (t01_m13 and t02_m12), this gap is around 15km (Figure III.56). For slower models (Figure III.54) hypocenter distribution is

concentrated in deeper layers (40-60km). The velocity models s02_m13 and s03_m12 remained unchanged except for topmost layers. The most significant modifications are observed in models t02_m12 and mod0, in the layers between 10 and 25 km in depth.

After the inversion process, the best improvement on velocity convergence is reached between 10 and 25 km in depth for all models (expect for slow models s02 and s03–Figure III.58). For deeper layers, velocity values remain roughly the same. Slowest models converge to common velocities around 43km (≈8.2 km/s). Topmost boundaries remain inconsistent across all models.

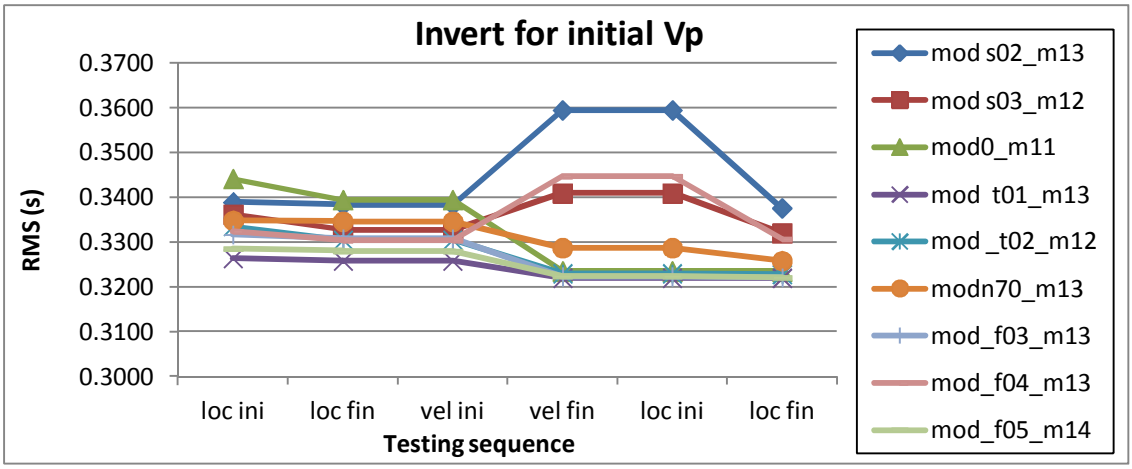

Figure III.53- RMS evolution along processing steps (in processing sequence, loc ini and loc fin define the initial relocation step, vel ini and vel fin is P- velocity inversion step and final relocation run RMS is defined by the last loc ini and loc fin). During the inversion step some velocity models became unstable: During the inversion step some velocity models became unstable: f04_m13, s02_m13 and s03_m12.

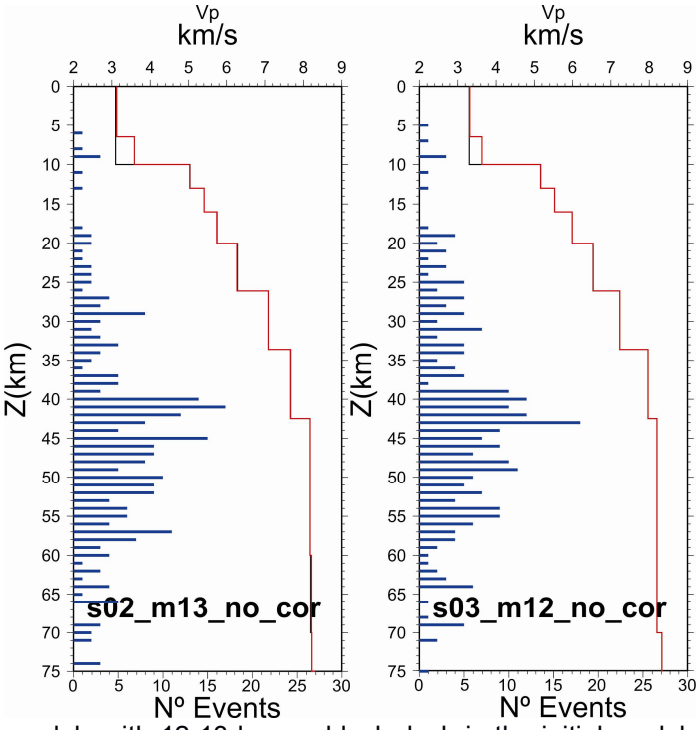

Figure III.54-Slow models with 12-13 layers, black dash is the initial model with initial stations corrections, red dash is the model after inversion and blue bars are the earthquakes depth distribution after inversion. The final earthquakes locations RMS are 0.338 and 0.332 for model s02_m13 and s03_m12, respectively. Slow models became unstable during the inversion as result no considerable change was added to the initial models.

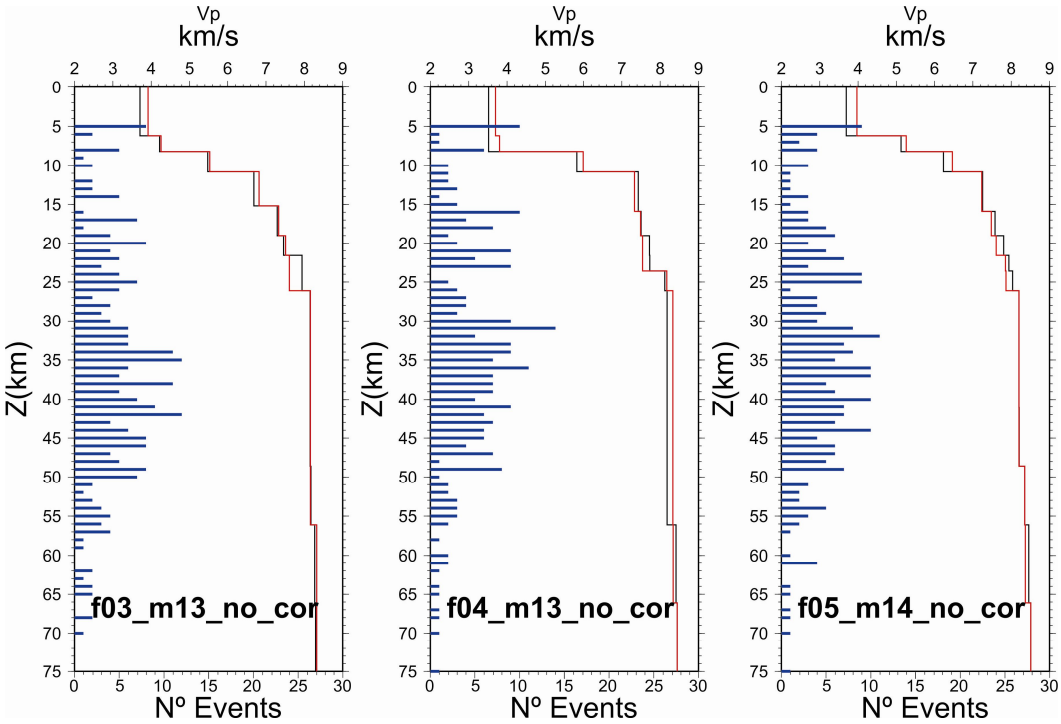

Figure III.55- Fast models with 13-14 layers, black dash is the initial model with initial stations corrections, red dash is the model after inversion and blue bars are the earthquakes depth distribution after inversion. The final earthquakes locations RMS are 0.322, 0.331 and 0.322 for model f03_m13, f04_m13 and f05_m14, respectively. The velocity models changes were minor, more centred in the intermediate levels between 10 and 25km. The topmost layer remains unstable with velocity increasing to unrealistic values.

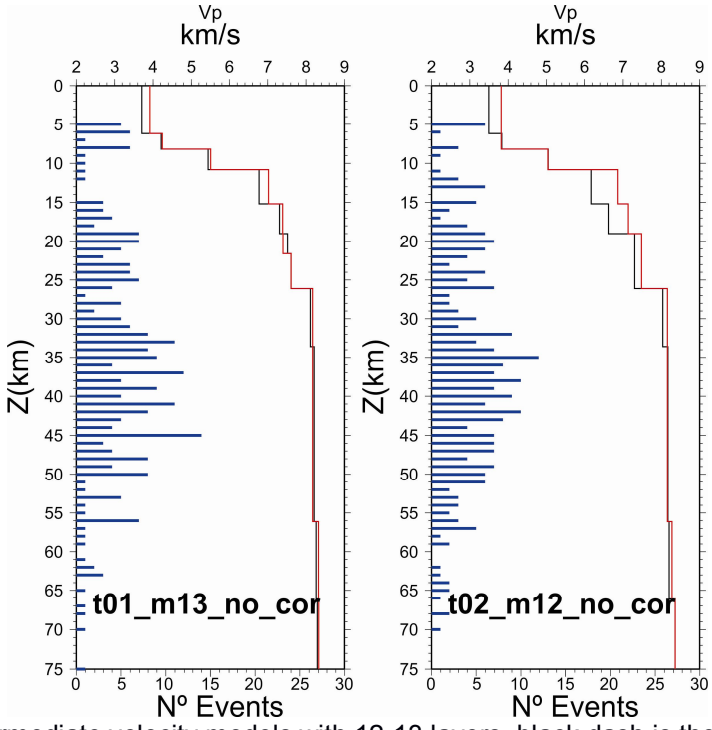

Figure III.56- Intermediate velocity models with 12-13 layers, black dash is the initial model with initial stations corrections, red dash is the model after inversion and blue bars are the earthquakes depth distribution after inversion. The final earthquakes locations RMS are 0.322 and 0.323 for model t01_m13 and t02_m12, respectively. Velocity in the topmost layers increased to unrealistic values. Intermediate layers, where most seismicity is located, remained roughly stable. A gap on the seismicity distribution is identified around 13-14 km in depth for model t01_m13.

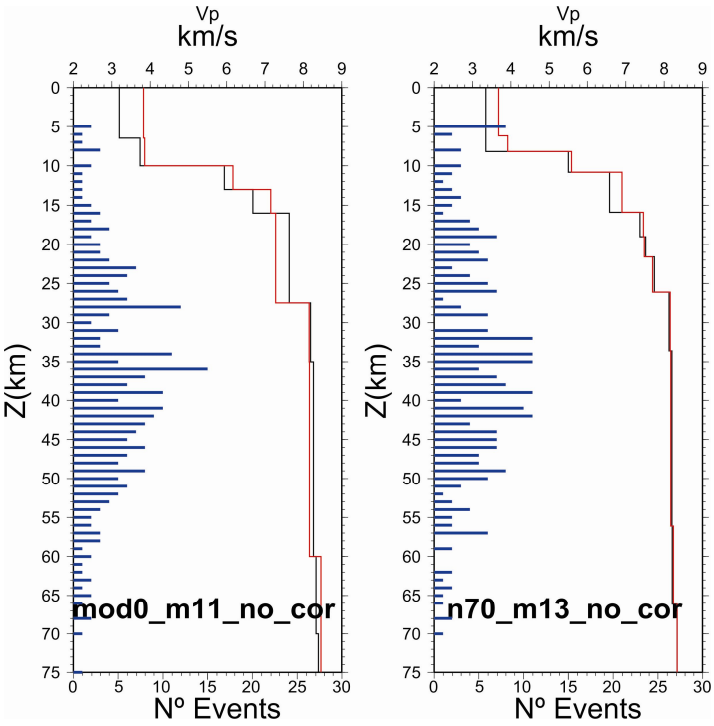

Figure III.57- Velocity models with 11-13 layers, mod0 and n70, black dash is the initial model with no initial stations corrections, red dash is the model after inversion and blue bars are the earthquakes depth distribution after inversion. The final earthquakes locations RMS are 0.323 and 0.326 for model mod0_m11 and n70_m13, respectively. Layers where most seismicity is located remained stable. In the topmost layers velocity values increased.

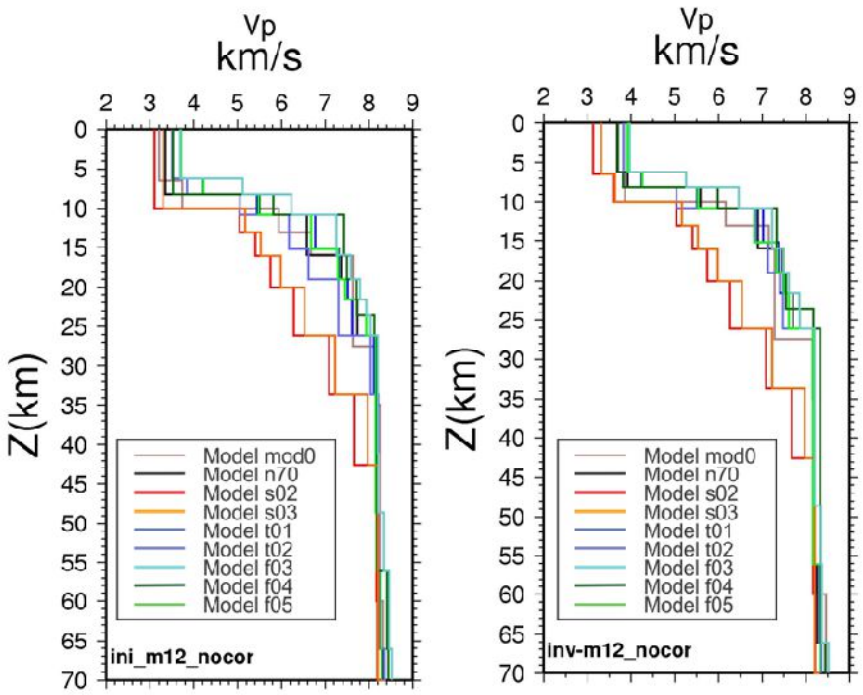

Figure III.58- Initial 12 layers models and resulting inversion models derived from p-wave readings. Models converge between 10 and 70km in depth (except for the slower models for which convergence is reached just at ≈40km in depth).

Models with 17-22 layers (step I.2 and I.3 in processing sequence)

Continuing to test geometric variability we converted the 24 layer models to 18-20 levels by merging similar velocities. We applied the same processing sequence. As before during velocity inversion step models mod0_m19, n70_m21, f03_m20 and f04_m20 became unstable (Figure III.59). Also, for mod0_m19, n70_m21 and all fast models, RMS results are worse than previous inversions with 24 layers. For the intermediate velocity models (t01_m19 and t02_m17), the final results were better than solutions for 24 layers but similar to the ones resulting from less complex models (with 12-13 layers). In fact, only slower models reached better RMS results with more complex models, for remaining models, 11-14 layers structures are the best solutions. From Figure III.60 to Figure III.63, we recognize that besides increasing upper layer velocity, models velocities remained almost unchanged.

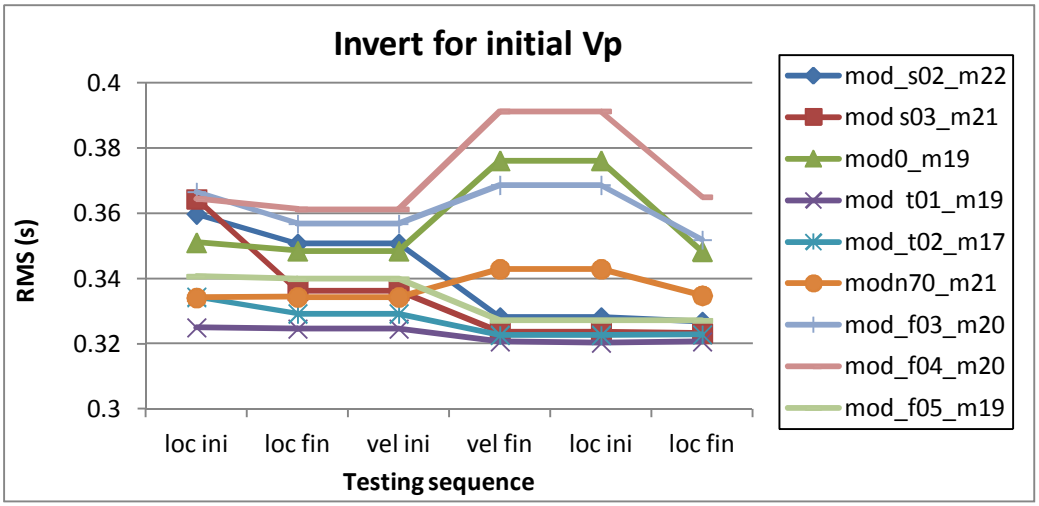

Figure III.59- RMS evolution along processing steps (in processing sequence, loc ini and loc fin define the initial relocation step, vel ini and vel fin is P- velocity inversion step and final relocation run RMS is defined by the last loc ini and loc fin). For mod0_m19, n70_m21 and all fast models, RMS results are worse than previous inversions with equivalent 24 layers models. For the intermediate velocity models (t01_m19 and t02_m17), the final results were better than solutions for24 layers but similar to the ones resulting from less complex models (with 12-13 layers). Inversion step became unstable for mod0_m19, n70_m21, f03_m20 and f04_m20.

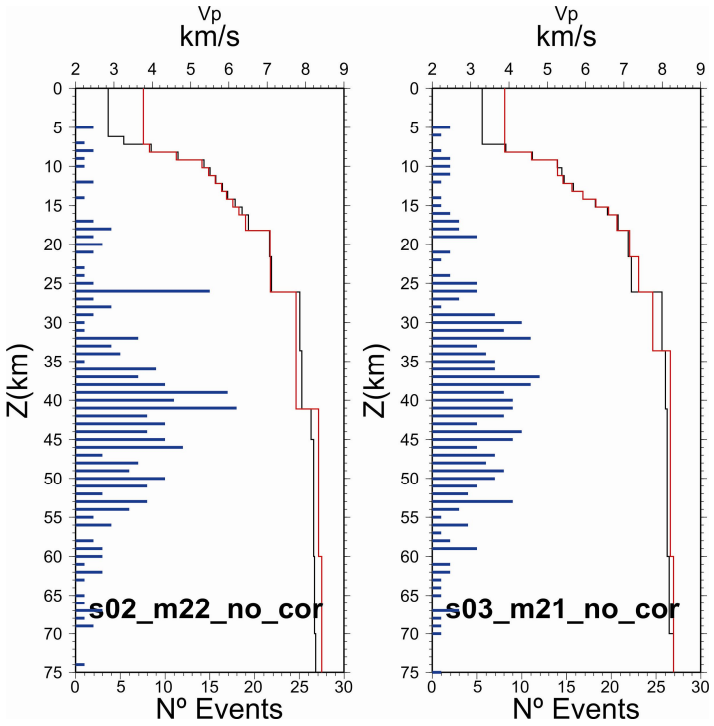

Figure III.60- Slow models with 21-22 layers, black dash is the initial model with no initial stations corrections, red dash is the model after inversion and blue bars are the earthquakes depth distribution after inversion. The final earthquakes locations RMS are 0.327 and 0.323 for model s02_m22 and s03_m21, respectively. Few changes are observed in the slow models, except for the topmost layer.

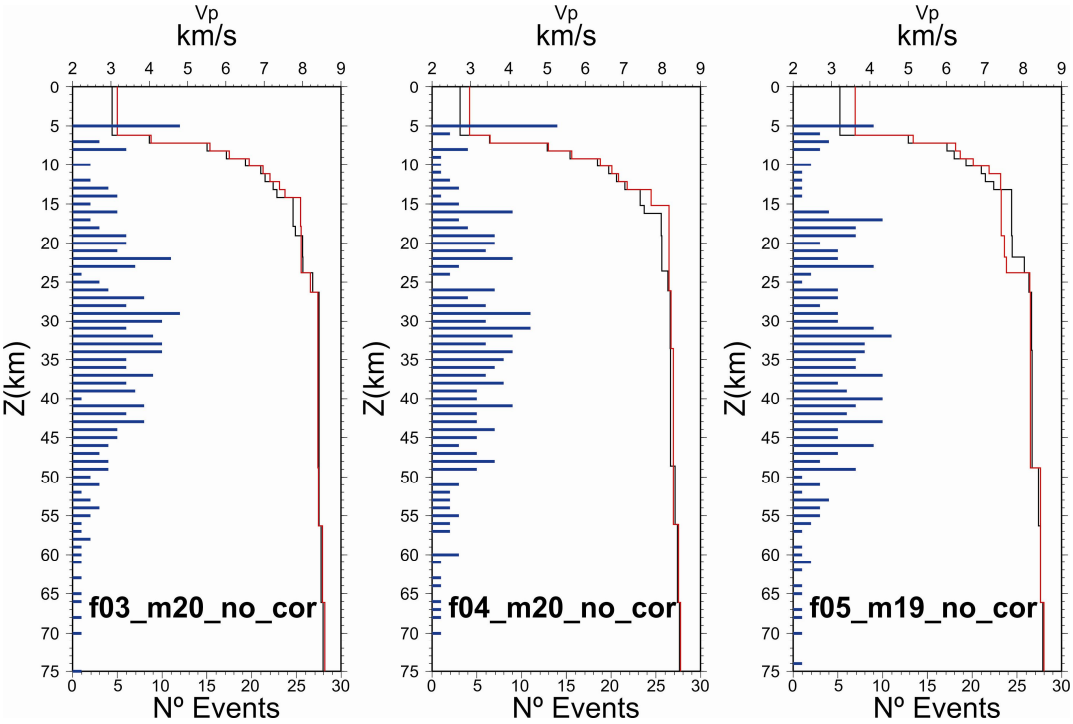

Figure III.61- Fast models with 19-20 layers (f03, f04 and f05), black dash is the initial model with no initial stations corrections, red dash is the model after inversion and blue bars are the earthquakes depth distribution after inversion. The final earthquakes locations RMS are 0.352 0.365 and 0.327 for model f03_m20, f04_m20 and f05_m19, respectively. After inversion, seismic velocities remains roughly the same as input models.

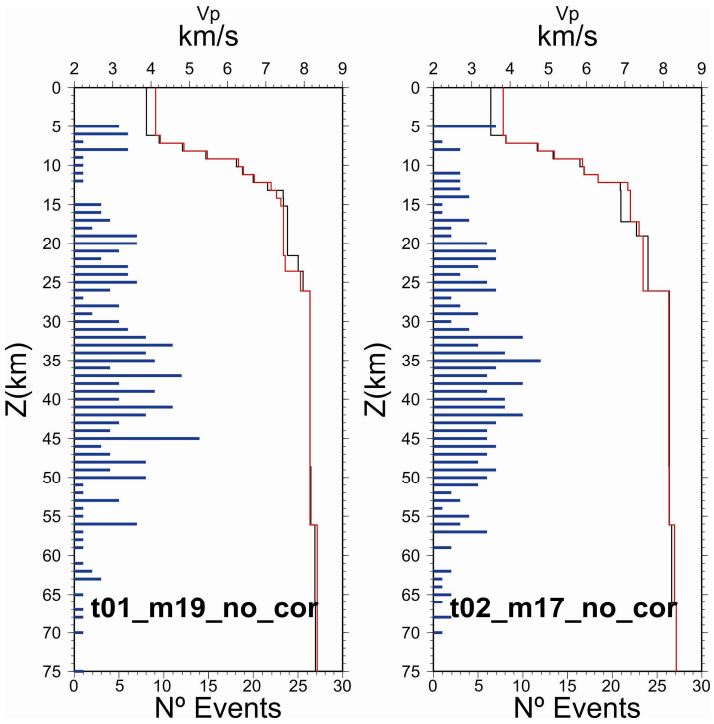

Figure III.62- Intermediate velocity models with 17-19 layers, black dash is the initial model with initial stations corrections, red dash is the model after inversion and blue bars are the earthquakes depth distribution after inversion. The final earthquakes locations RMS are 0.321 and 0.323 for model t01_m19 and t02_m17, respectively. Except for the topmost layer, seismic velocities remain unchanged.

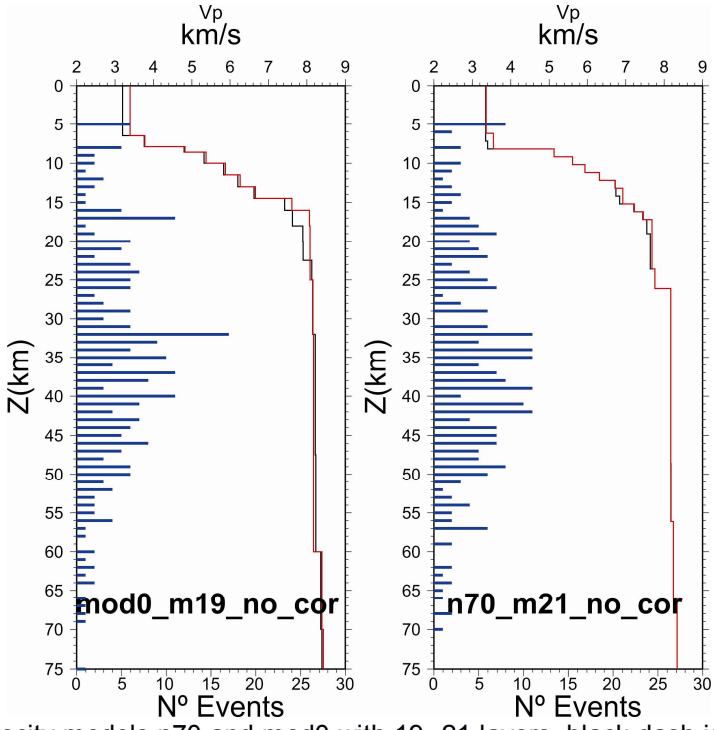

Figure III.63 - Velocity models n70 and mod0 with 19 -21 layers, black dash is the initial model with no initial stations corrections, red dash is the model after inversion and blue bars are the earthquakes depth distribution after inversion. The final earthquakes locations RMS are 0.348 and 0.335 for model mod0_m19 and n70_m21, respectively. Few exchanges were observed between initial and the inversion models.

All models (except for s02 and s03) start to converge the velocity values at ≈20km depth reaching upper mantle velocities. Slower model s03, converge at ≈33km and s02 at ≈40km depth (Figure III.64). However, results with complex models are worse than simplified geometries. With 17 to 22 layers convergence to a minimum P- velocity model is considerably less effective than the solutions with 11 to 14 layers (previous inversion sequence). In fact, if we compare initial and final models in Figure III.64, we recognize that velocities diverge from a common solution.

After this extensive testing of layers geometry, we decided to exclude complex geometries from the remaining processing sequences. In the next step, we will add the inversion for stations corrections using the simplified models from previous section (models with 11 to14 layers).

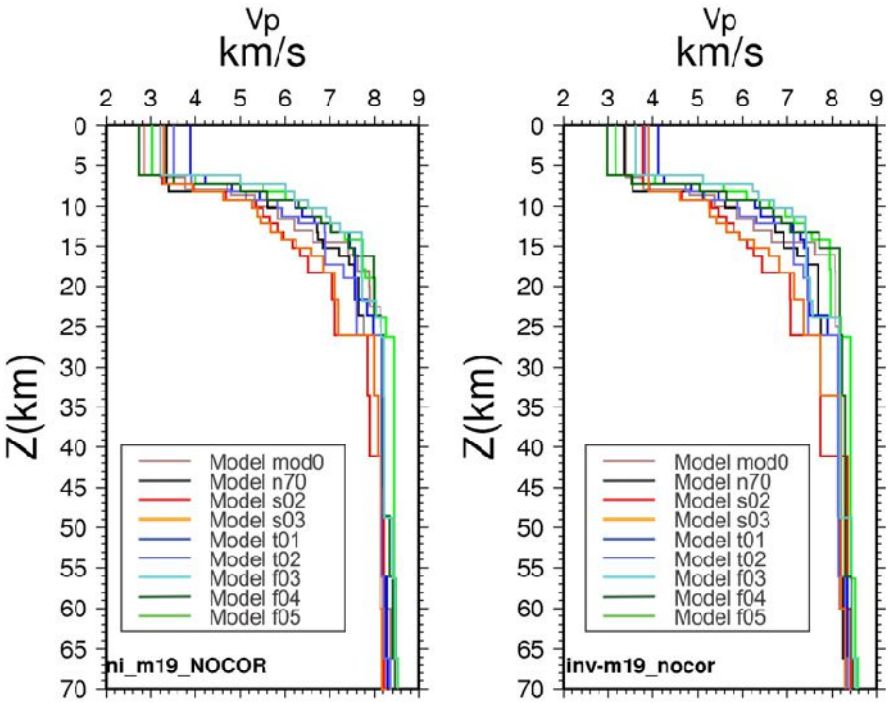

Figure III.64 - Initial 19 layers models and resulting inversion models derived from p-wave readings. Convergency for complex models is worse than simplified geometries. With 17 to 22 layers convergence to a minimum P- velocity model is considerably less effective than the solutions with 11 to 14 layers (previous inversion sequence).

Invert for minimum P velocity with stations corrections (step II.1 in processing sequence)

We used as input the output of *models with 11-14 layers* section. We forced the topmost layer to a more realistic velocity - 3 km/s. Since we included station corrections we increased the number of unknowns in the inversion process using selected 269 events with 11-14 velocity layers and 25 stations, defining 1112-1115 unknowns. We still use only 2622 P-phase pickings so the inverse problem is *overdetermined* by a factor of 2.35.

In the first step, we improve earthquake locations with JHD method using VELEST. For next iterations, we inverted for velocity model in a ratio of 2 out of 9. Improvement on RMS was minimal (Figure III.65). By introducing stations inversion, we decreased RMS solution to values between 0.1242s (t01_m13a) and 0.1184s (s02_m13a). Finally, we adjusted all parameters by simultaneously inverting for best locations, velocity models and stations delays. Final models reached similar RMS values ranging from 0.1109s (f04_m13a) and 0.1089s (t02_m12a and f03_m13a). The best model combines velocity structure with geological constrains and low RMS is n70_m13a. The results of the inversion procedure are detailed in Figure III.66 to Figure III.69. A synthesis is presented in Figure III.70.

In Figure III.66 to Figure III.69, the hypocenter distribution shows few shallow earthquakes, particularly for models: s02_m13a, s03_m12a, n70_m13a and mod0_m11a. Earthquakes density decreases near 18-20km in all models and

between 35 -38km (except to slow models), resulting in a roughly bimodal distribution in depth. In slow models hypocenters are distributed between 30 and 55 km.

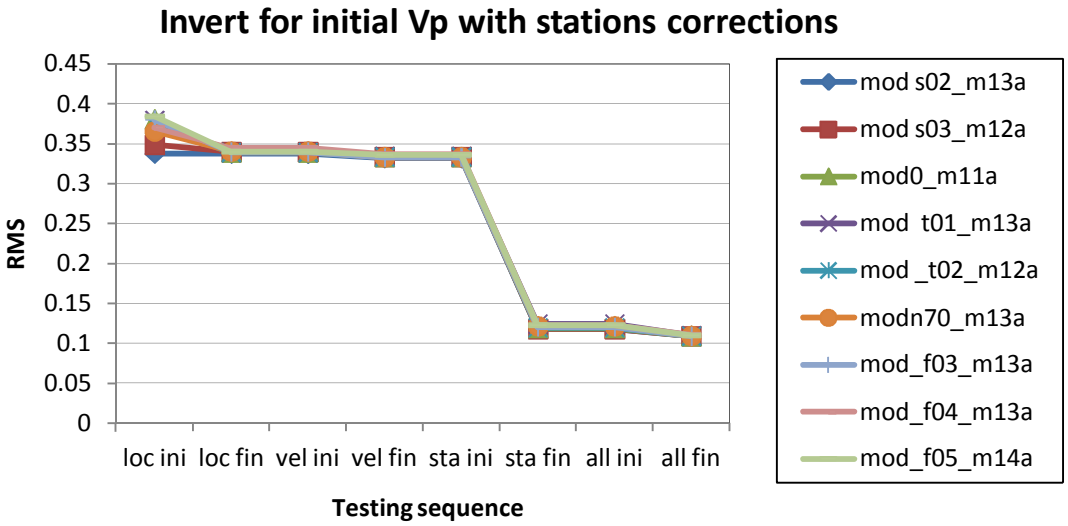

Figure III.65 -RMS evolution along processing steps (in processing sequence, loc ini and loc fin define the initial relocation step, vel ini and vel fin is P- velocity inversion step, stations inversion is introduced in steps sta ini to sta fin and final simultaneous stations corrections, hypocenters and velocity inversion is defined by all ini and all fin). Introduce station correction decreases models misfits drastically.

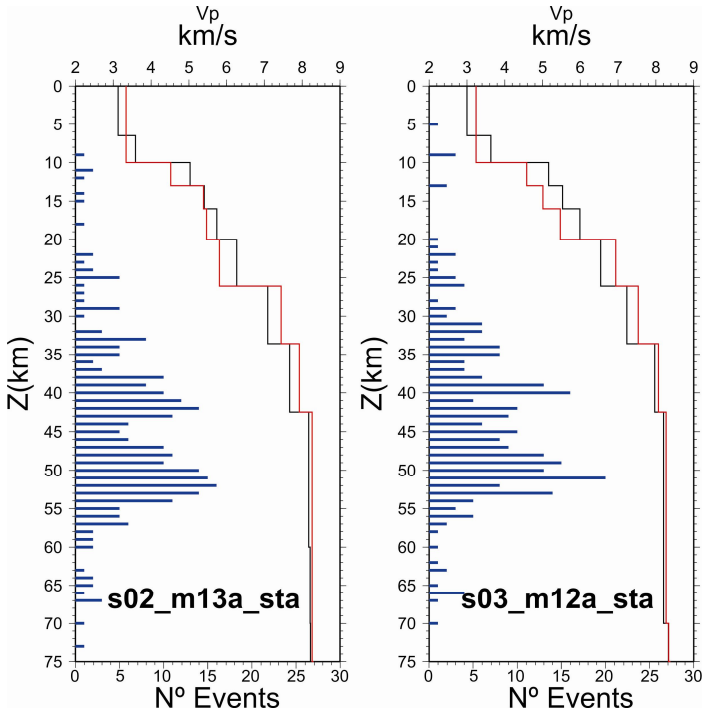

Figure III.66- Slow models with 12-13 layers, black dash is the initial model with initial stations corrections, red dash is the model after inversion and blue bars are the earthquakes depth distribution after inversion. The final earthquakes locations RMS are 0.109 for both model s02_m13a and s03_m12a. In these models, velocities decrease where there is low seismic activity and increased or remained stable for layers with higher seismic activity. Note that although topmost velocity was fixed to 3 km/s it increased slightly to 3.2 km/s.

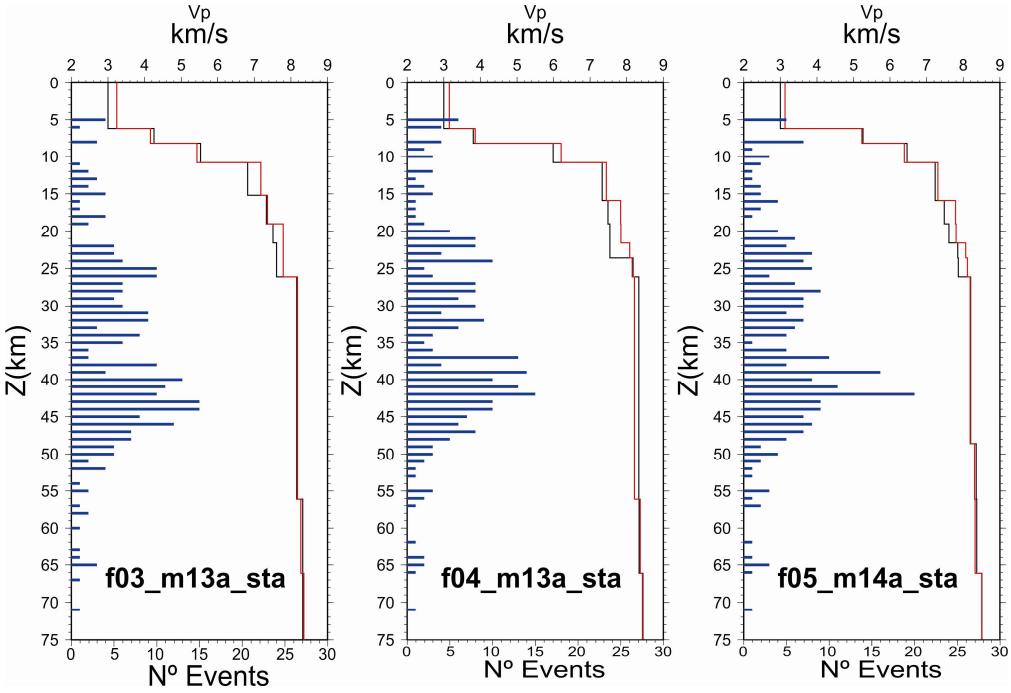

Figure III.67- Fast models with 13-14 layers, black dash is the initial model with initial stations corrections, red dash is the model after inversion and blue bars are the earthquakes depth distribution after inversion. The final earthquakes locations RMS are 0.109, 0.111 and 0.110 for model f03_m13a, f04_m13a and f05_m14, respectively. Events locations show a roughly trimodal distribution in depth defined by the intervals between 5 to 20 km, 20 to 35km and 35 to 55 km. These intervals were unclear in the same models without adding station corrections (Figure III.55). Few changes are observed in the velocity models. Again there is a small increase in the velocity of the topmost layer.

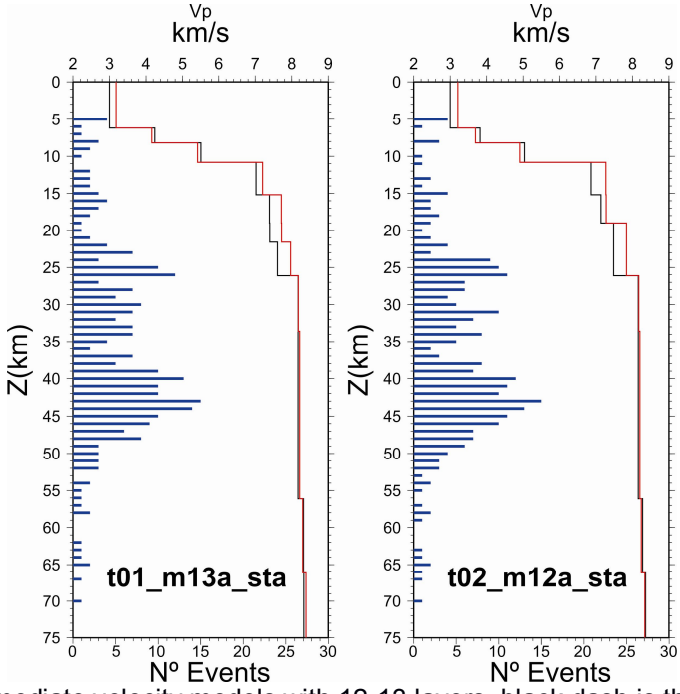

Figure III.68- Intermediate velocity models with 12-13 layers, black dash is the initial model with initial stations corrections, red dash is the model after inversion and blue bars are the earthquakes depth distribution after inversion. The final earthquakes locations RMS are 0.110 and 0.109 for model t01_m13a and t02_m12a, respectively. There is a small increase on the velocities of the topmost layer as well as between 10 and 25 km in depth. In the interval between 6 and 10 km in depth, seismic velocity decreased slightly. Hypocentres show an approximately bimodal distribution**.**

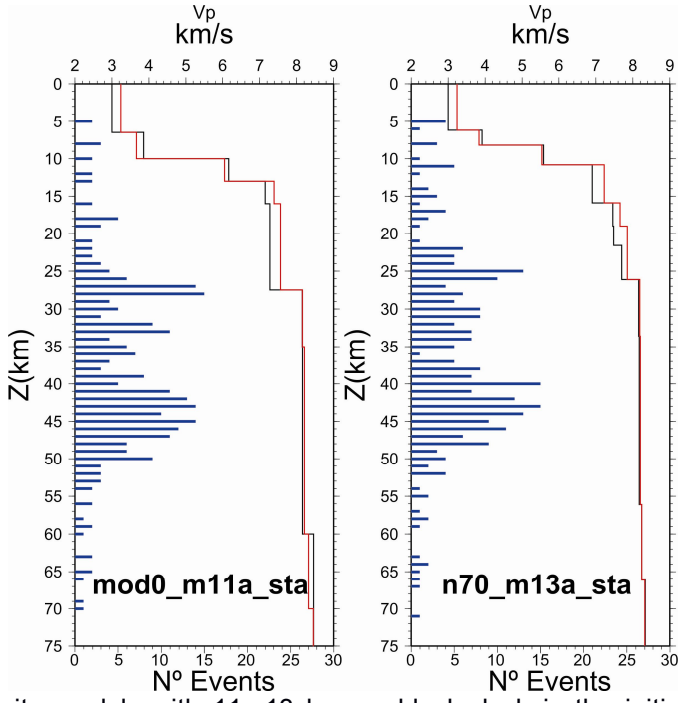

Figure III.69- Velocity models with 11 -13 layers, black dash is the initial model with initial stations corrections, red dash is the model after inversion and blue bars are the earthquakes depth distribution after inversion. The final earthquake location RMS is 0.109 for both model mod0_m11a and n70_m13a, respectively. The velocity of the topmost layer as well as between ≈13 and 25km increased in both models. Hypocentres are distributed mostly between 20 and 50 km in depth. Although less clear, we can still see a bimodal distribution of the hypocentres.

From Figure III.70, we recognize that the final slow models (s02 and s02) diverge from a common velocity solution (convergence is only reached below 43 km in depth). For the remaining models, absolute velocities are nearly coincident for the depth interval between ≈26 to 70 km. Similar velocities were also reached in layers between 10 and 26 km.

By adding stations delays and forcing the initial velocity for ≈ 3.0 km/s in all models the variability of topmost layer decreased. After inversion, the obtained velocity for the topmost layer is ≈3.2 km/s in all models. Crustal velocities range from 4.91 to 6.39 km/s between 8 and 10 km in depth, increasing to 6.9-7.2 km/s between 10 and 15 km. Upper mantle velocities are reached at ≈16 km boundary, with values from 7.4-7.8 km/s.

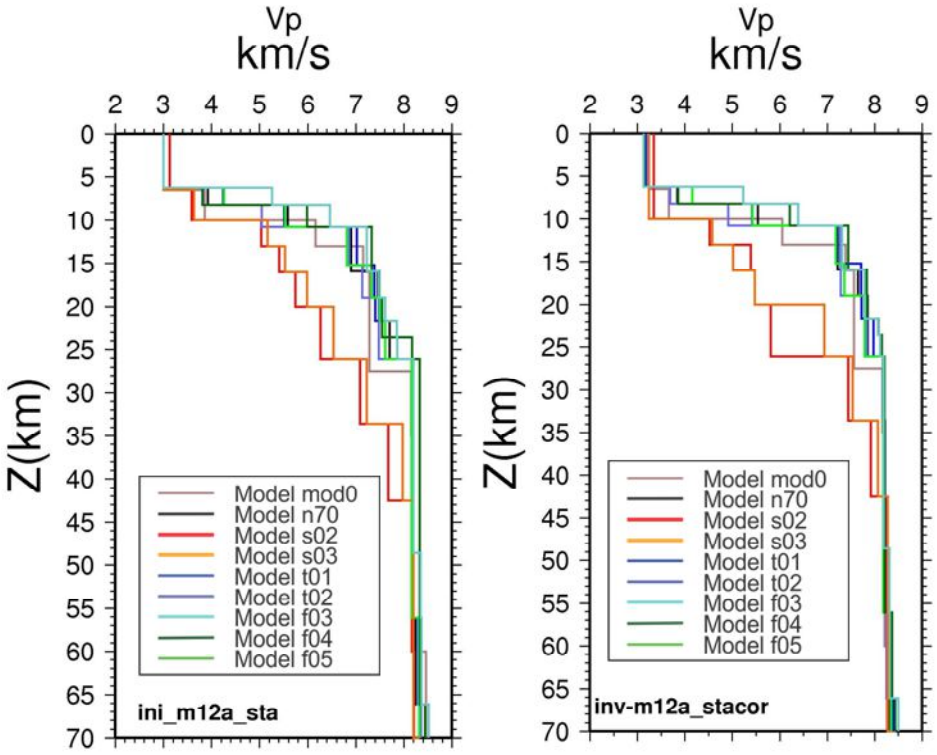

Figure III.70- Initial 11-14 layers models and resulting inversion models derived from p-wave readings. The final slow models (s02 and s03) diverge from a common velocity solution (convergence is only reached below 43 km in depth). For the remaining models, absolute velocities are nearly coincident for the depth interval between ≈26 to 70 km. Similar velocities were also reached in layers between 10 and 26 km.

The best model, that combines velocity structure and variability with geological constrains and low RMS is n70_m13a (n70 in Figure III.68 and details in Table III.8). Top sediment layers velocities range from 3.2 to 3.8 km/s. Crustal velocities start at 8.2 km with 5.5 km/s, set as an average of the remaining models. Bottom crustal velocity is 7.2 km/s and extends to 15.9 km. Upper mantle velocities are slower than a typical mantle value of ≈8.0 km/s, starting at 15.9 km with 7.65 km/s, increasing to 7.85 km/s at 19km and reaching 8.19 km/s at 26.1 km.

Relative stations corrections are described in Table III.6. All corrections are referenced to station NR09. Station NR21 correction has the highest positive delay. This station is located on top of the Gulf of Cadiz Imbricated Wedge Unit. GEOSTAR has the highest negative delay.

Table III.6-Details on final 1D P-velocity minimum model and stations corrections. Note that stations delays are relative based on a reference station (NR09). There is yet an unclear relation between sations corrections and subsurface geology. Nevertheless, station NR20, with the highest positive delay, is on top of the Gulf of Cadiz Accretionary Wedge.

Model n70_m13a					
Vp (km/s)	depth (km)	Stations	P-stations delays	Stations	P-stations delays
3.240	0.0	NR01	-0.02	NR15	-0.15
3.840	6.2	NR02	-0.86	NR16	-0.19
5.540	8.2	NR03	-0.33	NR17	0.46
7.220	10.8	NR04	-0.28	NR18	-0.15
7.650	15.9	NR05	-0.71	NR19	-0.05
7.850	19.0	NR06	-0.68	NR20	0.05
8.190	26.1	NR08	-0.49	NR21	0.65
8.200	33.6	NR09	0.00	NR22	-0.65
8.240	56.1	NR10	0.1	NR23	0.27
8.320	66.1	NR11	-0.26	NR24	-0.25
8.400	76.1	NR12	0.18	NR25	-0.24
8.450	81.1	NR13	-0.12	GSTR	-1.24
		NR14	0.35		

Invert for minimum Vp and Vs models with variable Vp/Vs (step II.2 in processing sequence)

The use of S-wave picking increases hypocenters accuracy, particularly regarding focal depth. As discussed previously, due to high subsurface geological variability a variable Vp/Vs ratio is more adequate than the use of fixed Vp/Vs ratios. So, we started by constructing different input S-velocity models based on fixed Vp/Vs ratio ranging from 1.68 to 1.76 (Husen et al. 1999), with increments of 0.01. In each case previous minimum 1D P-velocity model with corresponding corrections was taken as reference P-wave velocity model. Increased damp was applied to P-velocity model for topmost, crustal-mantle transition (layers at 15.90 and 19.0 km) and bottom layers to prevent unrealistic velocities.

Since we used P-wave and S-wave picking, we have a total of 6209 observations. With 269 events, 25 receiver stations and a 13 layers velocity models, a number of 1162 unknowns (4x269, 25x2 and 13x2) is to be determined with the inversion problem. So, the inverse problem is *overdetermined* by a factor of 5.34.

The first step in the processing sequence was to relocate the events using the new input velocity model. Introducing the velocity model with fixed Vp/ Vs and only P-stations corrections was clearly unadjusted to S-wave readings as RMS increased to values between 0.9946 and 0.6959. The relocation process resulted in insignificant reduction of RMS (Figure III.71). For the following step

we inverted only for stations corrections, introducing independent S-wave delays. The RMS solutions decreased to values ranging from 0.2393 to 0.2219. In the next running we inverted only for velocity models (with Vadj=0.2), resulting in RMS values between 0.2259 and 0.2206. In the last run we inverted both for stations corrections and velocity models. Small differences separate the final RMS solutions with values ranging from 0.2207 (initial Vp/Vs≈1.68) to 0.2189 (initial Vp/Vs≈1.73). A sum up on RMS evolution along the processing sequence is presented in Figure III.71. The initial and final models are plotted in Figure III.72 to Figure III.73 (initial models with fixed Vp/Vs ranging from 1.68 and 1.74).

From Figure III.73, we notice, except for the topmost boundary (with fixed Vp), small adjustments in the P-velocity in layers where we have low hypocenters density (even for levels with a damping factor of 10). In these layers, we also find higher divergence in S-wave velocities. For the remaining levels (≈20km to ≈55km) both P-wave and S-wave velocities converge to common values.

For Vp/Vs ratios, we observe higher values in the topmost layers. This result is in conformity with the expected properties for shallow marine sediments. Crawford and Singh (2007) describe Vp/Vs ratio variations from values >8 (unconsolidated sediments) to 2 (consolidated sediments) in the topmost 2km beneath the seafloor. Below ≈10 km in depth, Vp/Vs ratio becomes more consistent for all velocity models, and convergence is achieved for depth between ≈20 and 55 km.

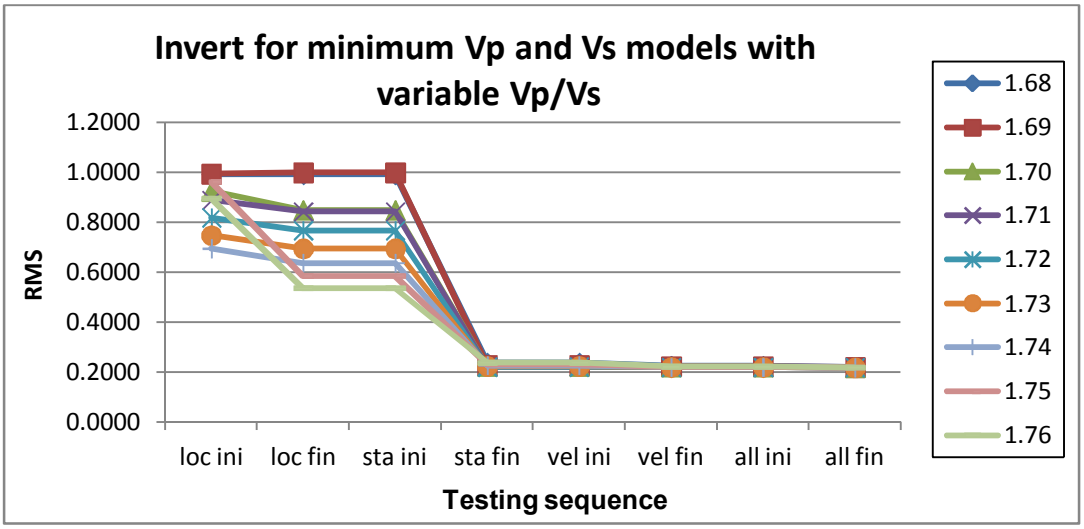

Figure III.71- RMS evolution along processing steps (in processing sequence, loc ini and loc fin define the initial relocation step, stations inversion is introduced in steps sta ini to sta fin, vel ini and vel fin is P- velocity inversion step, and final simultaneous stations corrections, hypocenters and velocity inversion is defined by all ini and all fin). Introducing the velocity model with fixed Vp/ Vs and only P-stations corrections was clearly unadjusted to S-wave readings as RMS increased to values between 0.9946 and 0.6959. Adding stations corrections to both s and p waves decreased drastically the models misfit.

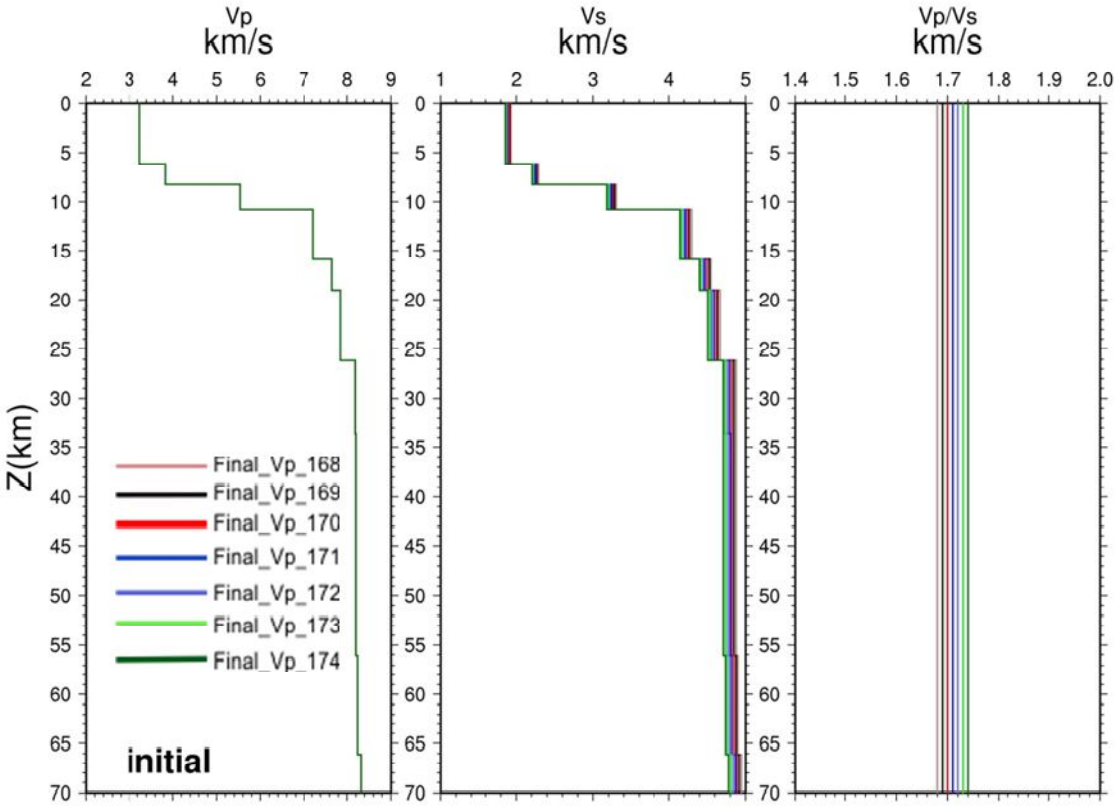

Figure III.72- Initial P-velocity model and S-velocities derived with fixed Vp/Vs ranging from 1.68 to 1.74.

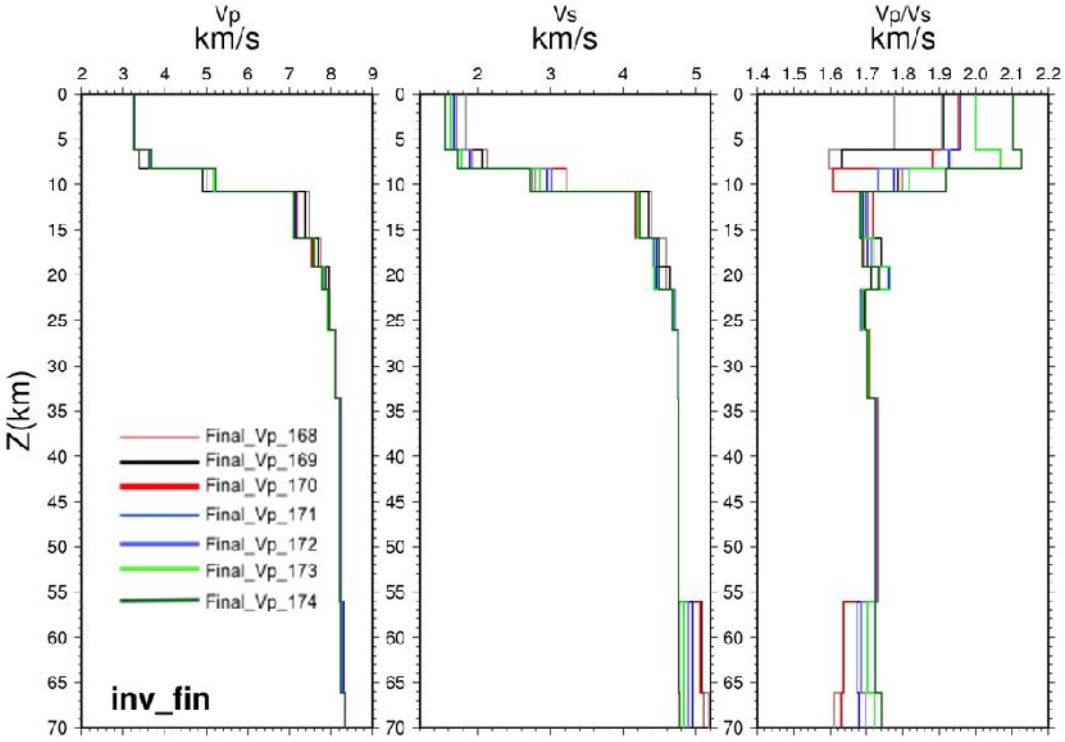

Figure III.73- Inverted P-velocity models and S-velocities derived from original fixed Vp/Vs ranging from 1.68 to 1.74. The final earthquake location RMS range from 0.2188 for initial Vp/Vs of 1.73 and 0.2207 with initial Vp/Vs of 1.68. The P-velocity had small adjustments in layers with the lowest hypocenters density (even for levels with a damping factor of 10). In these layers, we also find higher variability in S-wave velocities. For the remaining levels (≈20km to ≈55km) both P-wave and S-wave velocities converge to common values. Note that Vp/Vs ratios are higher at the topmost layers as we would expected based on for shallow marine sediments proprieties (detail on the text).

In Figure III.74, we plotted the velocity model with the best RMS solution (initial Vp/Vs≈1.73). With the new velocity models, including independent S-wave velocity, hypocenters are relocated in two distinct intervals: few shallower earthquakes ranging from 7 to 10 km in depth and most of the events are located between 15 and 50 km (particularly between 30 and 45 km). These two intervals are separated by a seismicity gap from 10 to 15 km. Ray statistics output for the last iteration step show that the number of hypocenters, the number and the length of refracted waves are higher for the layers between 21.6 and 56.1 km (see Table III.7). So, for these layers both focal depth and velocity will have the best resolution.

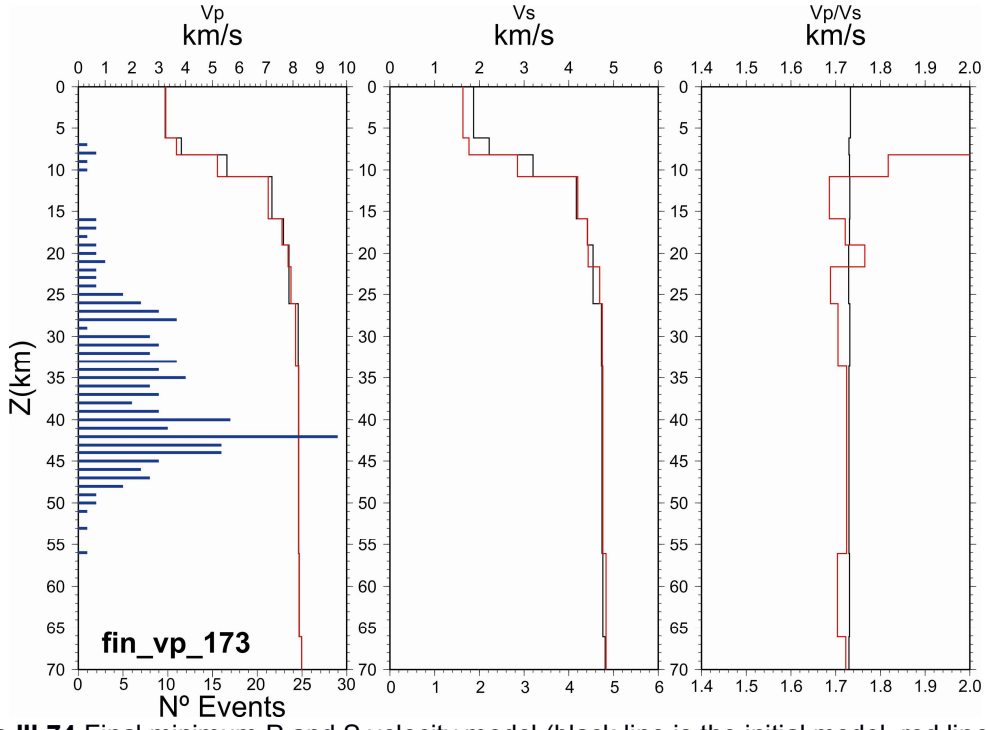

Figure III.74-Final minimum P and S velocity model (black line is the initial model, red line is the model after inversion and blue bars are hypocenters redistribution). Hypocenters have a bimodal distribution with few shallow earthquakes (between 7 to 10 km) and most of the events located between 15 and 50 km (particularly between 30 and 45 km).

Table III.7-Ray-statistics for the last iteration with P and S- minimum velocity models. According to this table, the number and the length of refracted waves are higher for the layers between 21.6 and 56.1 km. Accordingly, these will be the layers with the highest accurateness both for hypocentres and seismic velocities determinations.

nlay	top	bottom	P-velocity	velocity	NHYP	NREF	%len	NHIT	xy-km	z-km	Vp/Vs
1	0	6.2	3.26	1.63	0	0	0	6209	0.8	2.3	2.00
2	6.2	8.2	3.66	1.77	2	0	0	6267	0.8	2	2.07
3	8.2	10.8	5.18	2.85	3	0	0	6316	1.8	2.6	1.82
4	10.8	15.9	7.08	4.2	0	33	4.1	6283	7.8	5.1	1.69
5	15.9	19	7.59	4.41	6	7	0.9	6320	6.2	3.1	1.72
6	19	21.6	7.82	4.43	6	29	4.4	6317	5.9	2.6	1.77
7	21.6	26.1	7.92	4.69	15	144	29.3	6242	15	4.3	1.69
8	26.1	33.6	8.1	4.75	60	193	47.5	5786	30.4	6.4	1.71
9	33.6	56.1	8.21	4.76	177	58	13.9	4290	29.2	8.1	1.72
10	56.1	66.1	8.23	4.83	0	0	0	0	0	0	1.70
11	66.1	76.1	8.32	4.83	0	0	0	0	0	0	1.72
12	76.1	81.1	8.4	4.86	0	0	0	0	0	0	1.73
13	81.1	81.1	8.45	4.88	0	0	0	0	0	0	1.73

NHYP : nr of hypocenters in this layer
NREF : nr of headwaves in this layer
%len : % of "refracted km" in this layer with respect to all refracted kilometers
NHIT : nr of rays passed thru this layer
xy-km: average horizontal ray length [km] in layer
z-km : average vertical ray length [km] in layer

Testing final P and S- minimum velocity models stability

Following Husen et al. (1999), we tested the stability of the P and S minimum velocity models and earthquake locations by perturbing hypocenter locations before relocating them with JHD and coupled inversion methods using VELEST routine. If the coupled hypocenter-velocity solution is robust, we expected to have a minimum shift between resulting and original hypocenters locations and also small changes in the velocity model.

Accordingly, we started by relocate events with the initial velocity model-f05 (without stations), introducing a random shift in hypocenters locations (Figure III.75). The shifts for latitude were between -9.21km and 17.71km, for longitude between -12.03 km and 10.05 km and for depth between -30.07km and 39.76km. After relocating with P and S- minimum velocity models with JHD method, hypocenters were returned back to original position with small mean shifts in latitude and longitude, -0.08 km and -0.07km, respectively. For focal depth final mean shift was higher -0.63km; however, the original mean shift was also considerably higher. We repeated the same procedure with the initial velocity model s02 (again without stations corrections). Maximum and minimum initial shifts were -6.65-16.65 km, -10.05-6.0 km and -33.38 -8.72 km for latitude, longitude and depth, respectively (see Figure III.76). Once more, relocation with JHD method could locate the events back to the original position with small shifts (Figure III.76).

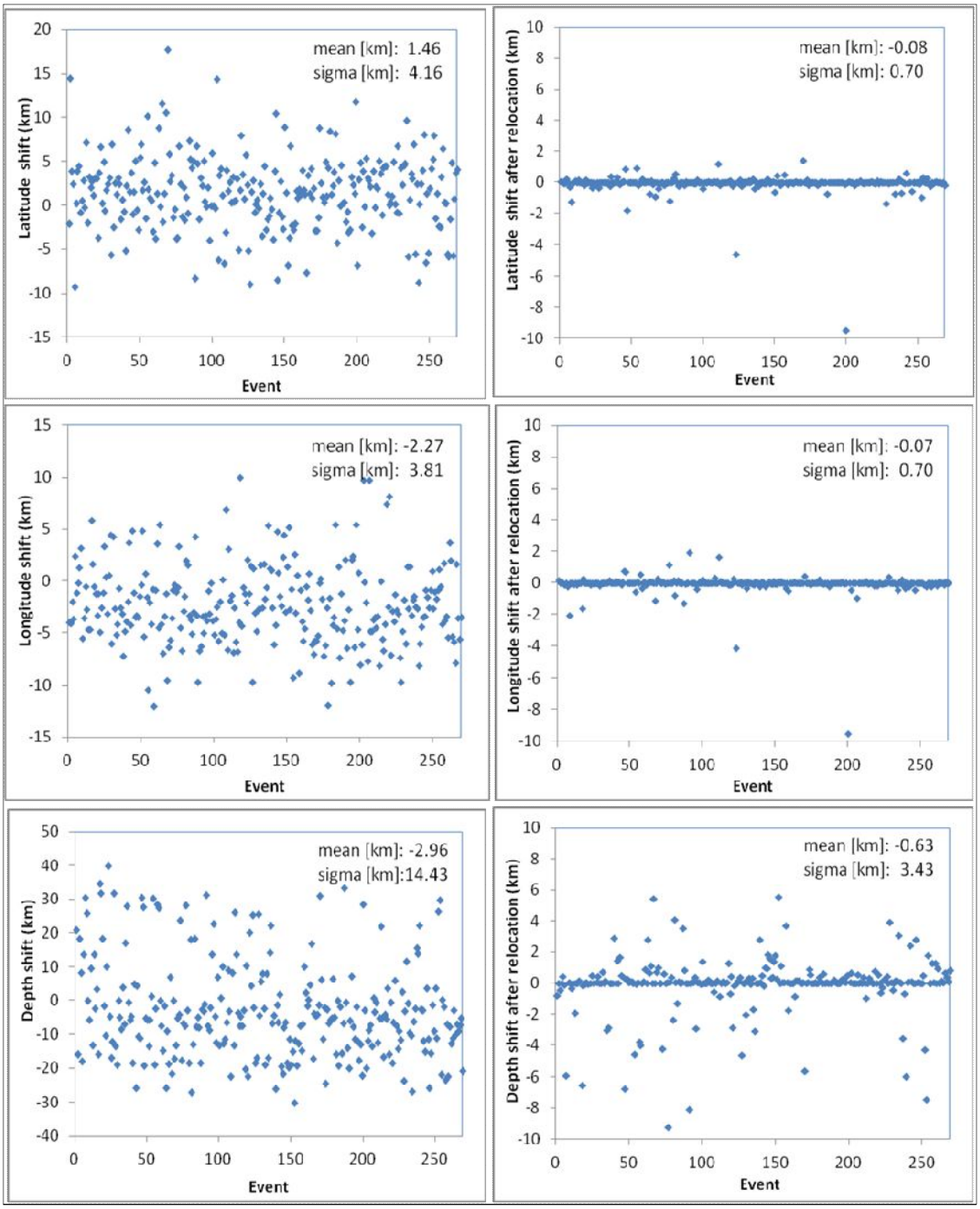

Figure III.75- Stability tests for hypocenters location resulting from VELEST. Earthquakes were shift from original position using initial velocity model F05 (without stations corrections- left figures) and relocated back using P and S- minimum velocity models (Right figures represent the shift in original earthquakes location after relocation. Note that vertical scale is not the same in the left and right graphics). After relocation, hypocenters are roughly at the same position. The highest misfit is found in depth.

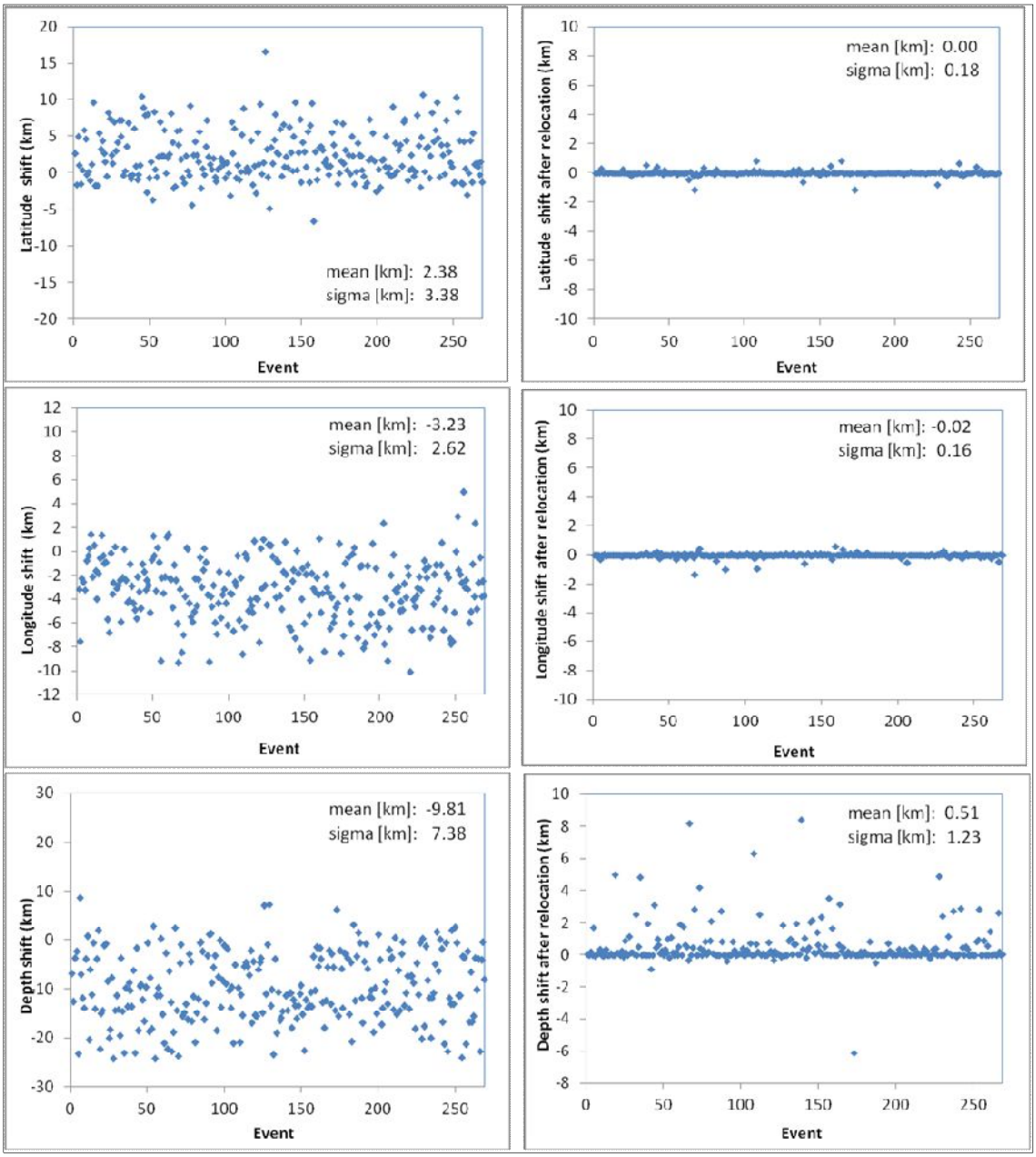

Figure III.76- Stability tests for hypocenters location resulting from VELEST. Earthquakes were shift from original position using initial velocity model s02 (without stations corrections- left figures) and relocated back using P and S- minimum velocity models (Right figures represent the shift in original earthquakes location after relocation Note that vertical scale is not the same in the left and right graphics). After relocation, hypocenters are roughly at the same position. The highest shift is found in depth relocation.

Finally, we relocated the events with a systematic shift of 10 km in depth. Fixed and damped velocity models are tested. In principle, if we have found a stable solution for coupled hypocenter-velocity problem than relocation will be achieved by moving the hypocenters back to the original solution or by small adjusts in the velocity models or by a combination of both processes (Husen et al., 1999). In Figure III.77 the results for inversion with fixed velocity models using VELEST application are shown. Events are again relocated back to the original hypocenter position with small residual shifts. With damped velocity

models (damp =5) epicenter locations return to the original position (Figure III.78) However, depth is retrieved with a ≈ 1km shift. We find that there is a weak dependence between epicenter parameters and focal depth determination. Also a small adjustment was applied to the velocity model (Figure III.79). The results presented attest the stability of the final minimum P and S-velocity models.

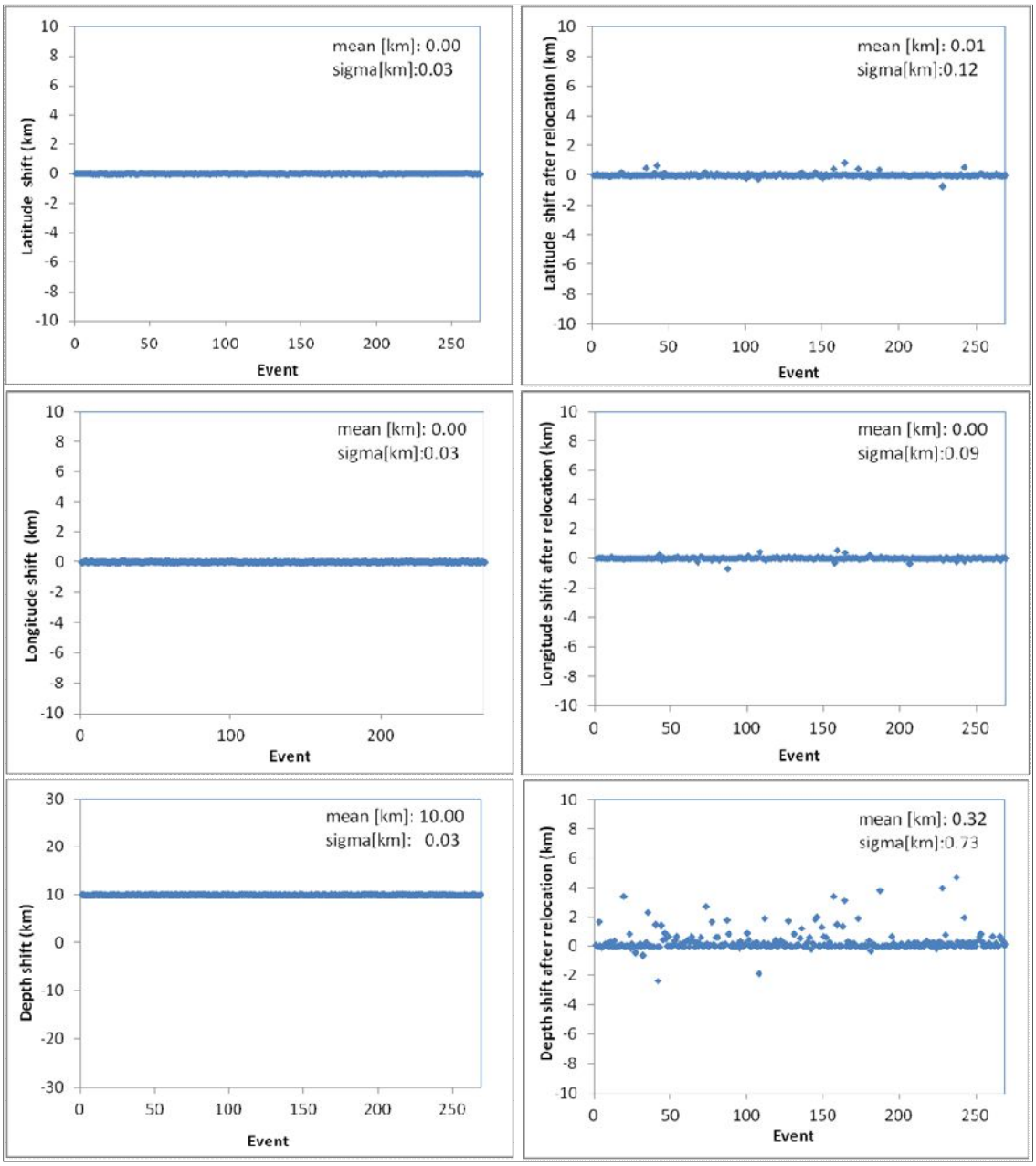

Figure III.77- Stability tests for P and S- minimum velocity models. Earthquakes were systematic shift in depth ≈10 km and relocated back using fixed P and S- minimum velocity models (left figures are the initial shift and right figures are the final shift. Note that vertical scale is not the same in the left and right graphics). We still observe some depth shift in relocated events. However, there is roughly any shift in latitude and longitude. We find that there is a weak dependence between epicentre parameters and focal depth determination.

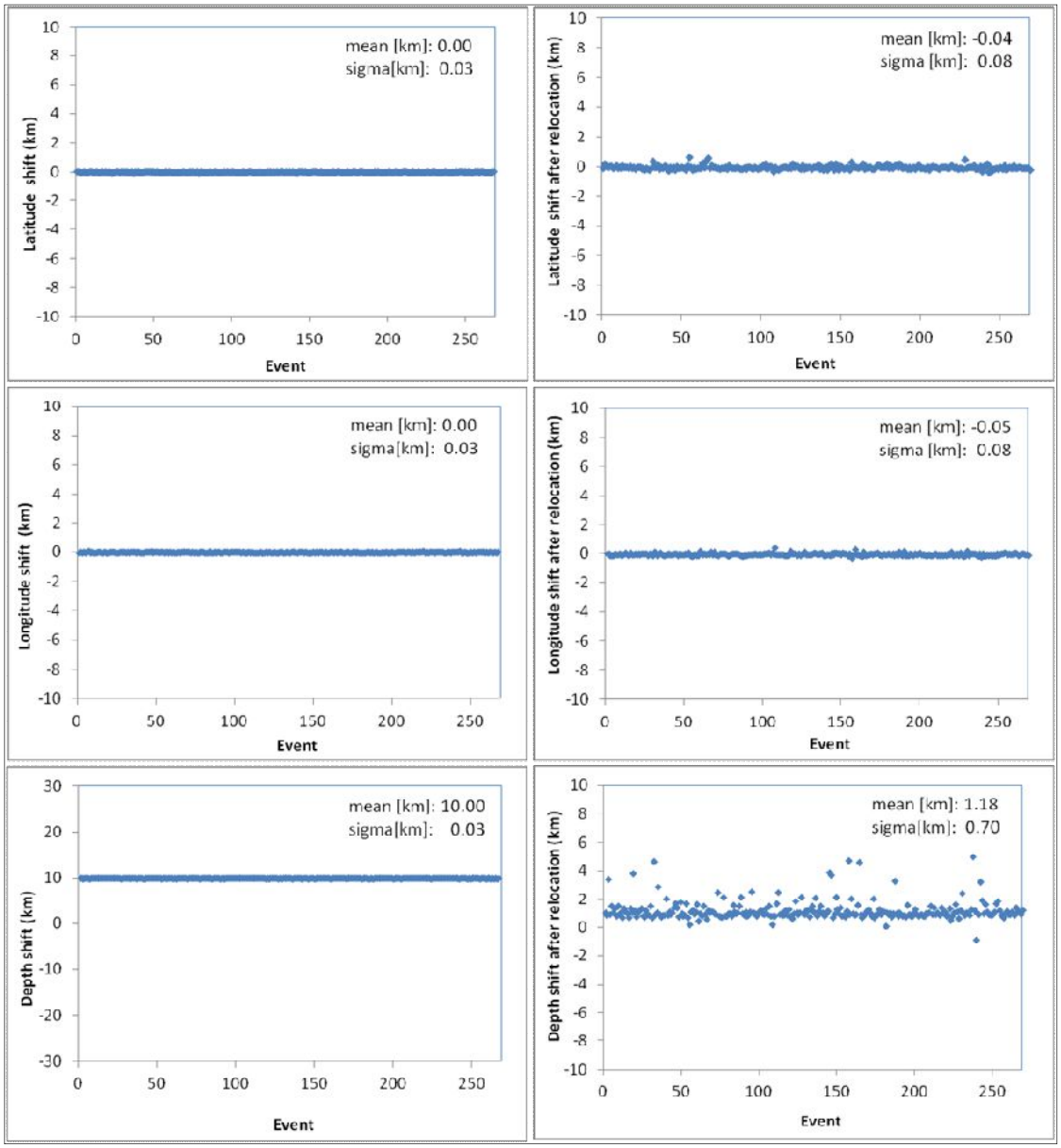

Figure III.78- Stability tests for P and S- minimum velocity models. Earthquakes were systematic shift in depth ≈10 km and relocated back using damped P and S- minimum velocity models (left figures are the initial shift and right figures are the final shift. Note that vertical scale is not the same in the left and right graphics). The events relocated again back to the original hypocenter position show small residual shifts in depth.

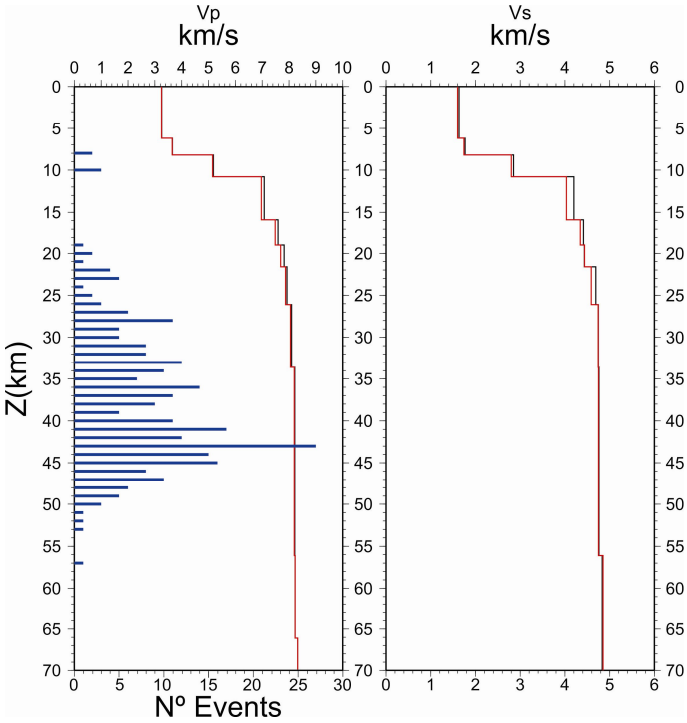

Figure III.79– Adjust in the P and S minimum velocity model after stability tests. Earthquakes were systematic shift in depth ≈10 km and relocated back simultaneous inversion with damped P and S- minimum velocity models. After relocation the hypocenters have roughly the same distribution in depth. Small adjustments in the seismic velocities occurred where earthquakes are absent or in smaller number.

III.2.2.5.P and S-minimum velocity models and stations corrections: discussion

The resulting minimum velocity models (Table III.9) reflect the best fit 1D model that justifies P and S observations for the investigated 269 events. However, since the NEAREST OBS deployment area is described as a region of some lithospheric variability (ranging from old Jurassic oceanic, transitional to thinned continental and exhumed serpentinized mantle- Sallarès et al., 2011, Gonzalez et al., 1996 and Sallarès et al., 2013) these velocity models are hardly related to a specific lithospheric structure. On the other hand, stations delays should account, at least, for this subsurface geological variability because it will be conditioned by their respective position in the deployment area (with respect to the selected reference station). Since the station correction for the reference station (obs09) is zero, we must assume that the derived 1D velocity model is a representation of the average lithosphere structure surrounding that particular station. Both P and S stations delays are in agreement with subsurface geology. Positive corrections are coincident with higher sediment thickness (in blue Figure III.80 and Figure III.81) and negative delays with lower (see Table III.8 and Figure III.19)

Table III.8- P and S stations delays based on VELEST final inversion. Note that reference station correction is set to zero only for P-delays, S-delay is free floating. Both P and S stations delays are in agreement with subsurface geology. Positive corrections are coincident with higher sediment thickness and negative delays with lower.

station	P-delays	S-delays	TWT (s) sediments	station	P-delays	S-delays	TWT (s) sediment
NR01	-0.29	1.2	1491	NR16	-0.07	0.19	3042
NR02	-1.03	-1.09	1713	NR17	0.5	2.18	2252
NR03	-0.49	0.54	2332	NR18	-0.04	0.67	763
NR04	-0.44	-0.39	1752	NR19	0.08	1.38	3664
NR05	-0.85	-0.53	1866	NR20	0.16	2.63	3518
NR06	-0.78	-0.61	1675	NR21	0.87	3.28	3189
NR08	-0.61	-0.3	1863	NR22	-0.57	-0.45	1151
NR10	0.11	1.09	2315	NR23	0.39	2.51	3467
NR11	-0.33	0.23	2309	NR24	-0.33	-0.57	1296
NR12	0.24	2.15	2587	NR25	-0.28	0.1	2187
NR13	-0.03	1.54	2632	GSTR	-1.29	-1.03	2518
NR14	0.41	2.65	3257	NR09	0	1.49	2914
NR15	-0.04	0.95	2358				

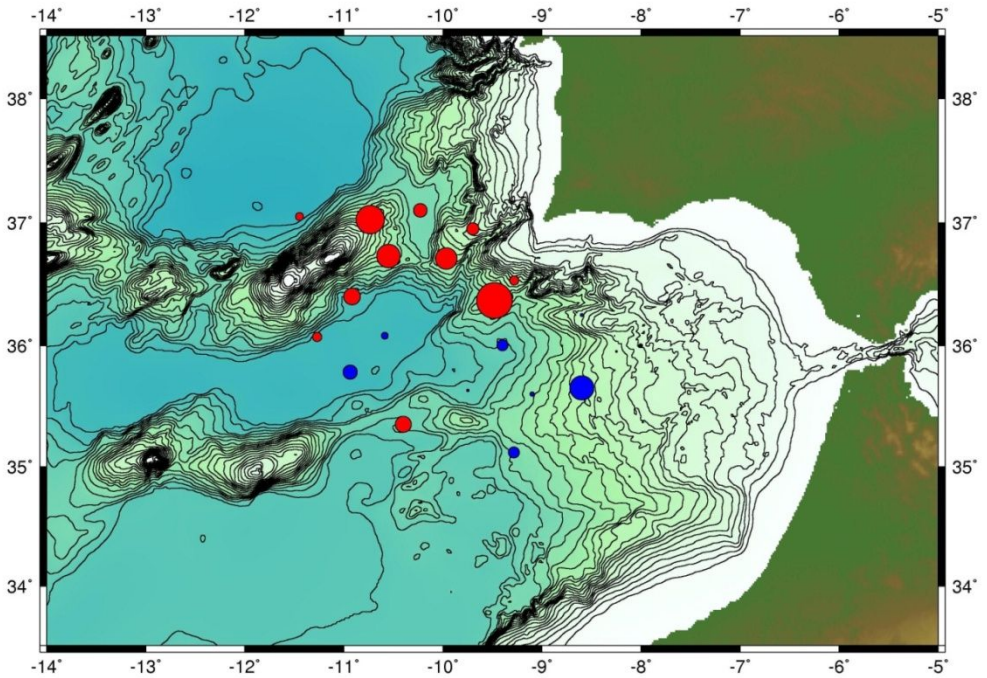

Figure III.80- P-wave stations delays derived from VELEST final run (blue is positive delay, meaning that arrival times in these stations reveal local slower P-velocities when compared with velocity model; red is negative delay, reflecting local faster P-velocities, *bathymetry from GEBCO*). Positive delays are coincident with higher sediments thickness.

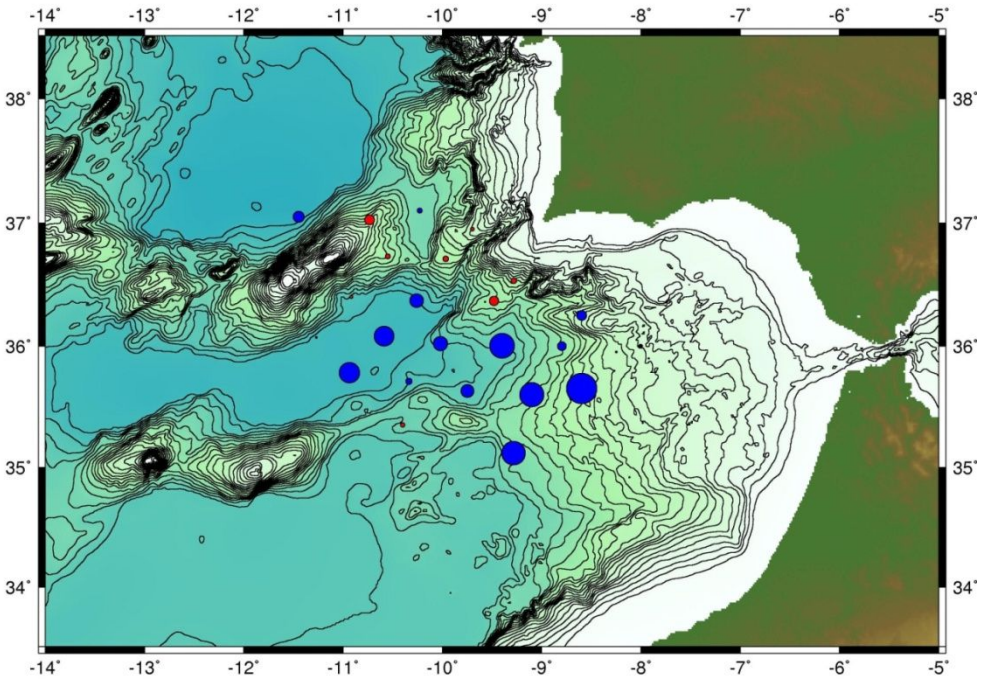

Figure III.81- S-wave stations delays derived from VELEST final run (blue is positive delay, meaning that arrival times in these stations reveal local slower S-velocities when compared with velocity model; red is negative delay, reflecting local faster S-velocities (*bathymetry from GEBCO*). Note that stations on top of high sediment thickness have positive delays.

Table III.9- Final Velocity model layering interpretation. The velocities models are hardly related to a specific lithospheric structure but should instead represent a balance of the upper lithospheric variability in the Gulf of Cadiz.

Final P and S- minimum velocity models				
depth (km)	Vp (km/s)	Vs (km/s)	Vp/Vs	layer
0.0	3.260	1.63	2.00	
6.2	3.660	1.77	2.07	upper sediments
8.2	5.180	2.85	1.82	upper crust
10.8	7.080	4.2	1.69	lower crust
15.9	7.590	4.41	1.72	upper mantle
19.0	7.820	4.43	1.77	upper mantle
21.6	7.920	4.69	1.69	upper mantle
26.1	8.100	4.75	1.71	upper mantle
33.6	8.210	4.76	1.73	upper mantle
56.1	8.230	4.83	1.71	upper mantle
66.1	8.320	4.83	1.72	upper mantle
76.1	8.400	4.86	1.73	upper mantle
81.1	8.450	4.88	1.73	upper mantle

If we compare P-minimum velocity model with the refraction and wide-angle reflection data in the Gulf of Cadiz area, we observe that for the upper sediments layers the velocities are higher. In Sallarès et al. (2011) velocity solutions range from 1.8 to 3.0km/s and 2.8 to 4.0 km/s for the upper and lower

layers, respectively. In our velocity model, in the upper layer Vp is 3.26 km/s and in the lower layer Vp is 3.66 km/s. We recall that for earthquakes location we replace layers resulting from gradient velocities (refraction data) with interval velocities layers. This will explain partially the differences here reported for velocities values. Also, we knew that during the derivation of the final models, the velocities in these layers were poorly constrained because very few hypocenters occur there. This would explain why even when overdamping this layer velocity to 3.00 km/s in the final Vp inversion step (step II.1 in processing sequence) this velocity increased. The resulting high Vp/Vs ratios are, however, in conformity with what is expected for top marine sediments (Crawford and Singh, 2007).

Crustal velocities range from 5.18 km/s to 7.08 km/s in the P-minimum model which is only slightly higher than the results from NEAREST refraction profile P2 (Sallarés et al., 2011) ranging from 4.6–4.8 km/s at the top to 6.9–7.1 km/s at the base. The transition between lower crust and upper mantle is ≈16km in depth. The Moho depth is in conformity with the results published in Sallarès et al. (2011). The slow upper mantle velocities are in agreement with Purdy (1975), Gonzalez et al. (1996), Sallarés et al. (2011) and Salláres et al. (2013). In both Sallarés et al. (2011) and Salláres et al. (2013) these velocities values are attributed to mantle serpentinization with characteristic low mantle velocities and high Vp/Vs ratios. For the final velocity model these two criteria are observed only in the layer between 19.0 -21.6km.

Final locations with P and S-minimum velocity models

All events in the deployment area were relocated using the initial JHD method, with the adapted HYPOCENTER and PRN2RES2 application (to include independent P and S delays). The final velocity model and stations delays that resulted from VELEST application were re-converted to the STATION0.HYP file using velest_steps routine (developed by Luis Matias). The JHD method was run in one iteration step to improve stations corrections. In the final solution, the RMS was reduced from 0.317s to 0.275s. From all events, 385 have an error inferior to 10 km both in horizontal and vertical locations. The statistics on RMS variation for events location is presented on Figure III.82. There is an increase of events with the lowest RMS (0.1-0.2).

For earthquakes locations, the differences are not considerable high. In latitude and longitude most events change only 0.01º to 0.02° and in depth only 2 km (Figure III.83). If we compare earthquakes depth location between the initial velocity model locations with the resulting models from VELEST, we observe that there is a decrease on the events located in the top most layers (0 -30km) and an increase in the hypocentres located between 30 and 45 km in depth (Figure III.84).

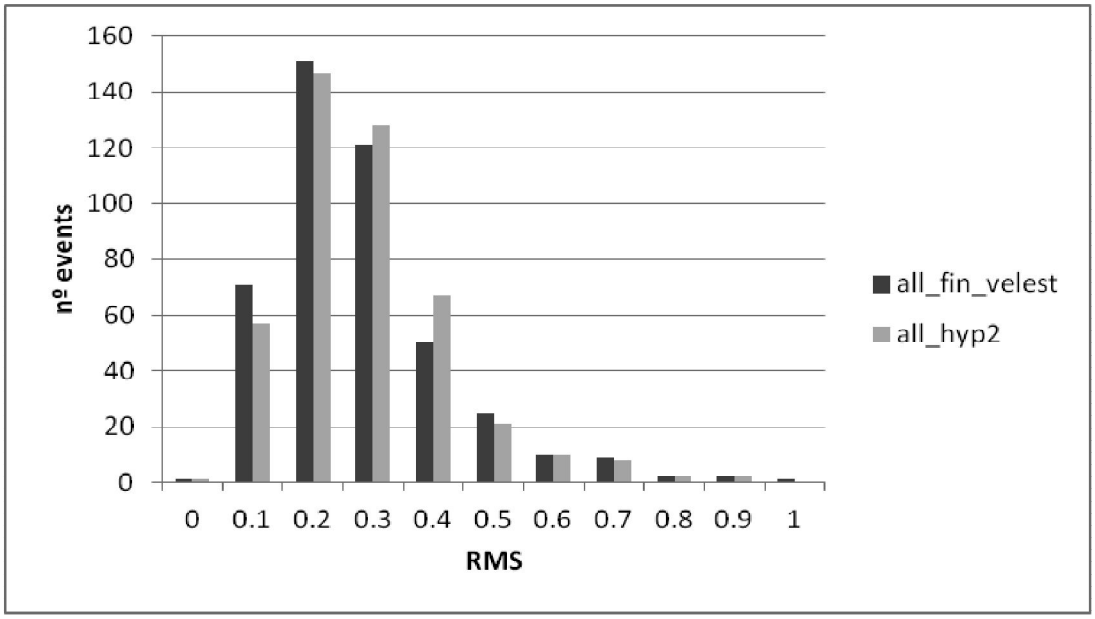

Figure III.82- Rms distribution for all events in the deployment area based on JHD method with mod70 velocity model (extracted from P2 NEAREST refraction profile) versus with P and S-minimum velocity models. There is an increase in the locations with the lowest misfit.

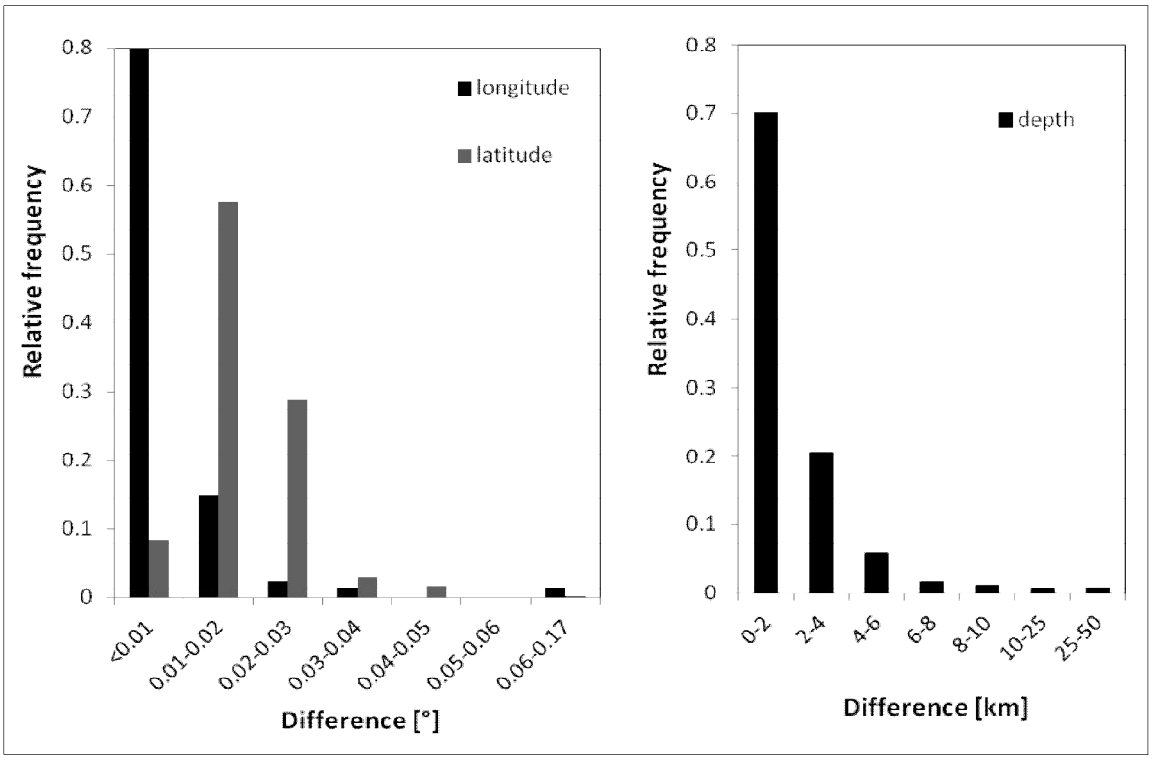

Figure III.83- Difference between initial locations based on JHD method with the initial velocity model versus with VELEST final velocity model.

From Figure III.84 we observe a bimodal distribution of the earthquake distribution were the transition coincident with Moho depth. In the W-E profile (Figure III.85), we also identify an area with few events which is limit to the uppermost 10 km in the Gorringe Bank area and deep to the E, were this interval becomes limit between 15-20 km in depth. In a N-S profile, this transition is observed at 15-20km.

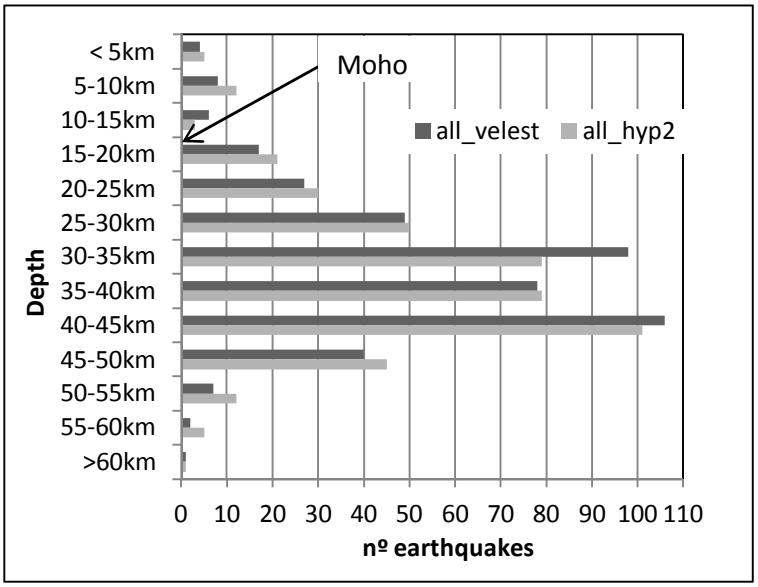

Figure III.84- Depth distribution of deployment area events based on JHD method with the initial velocity model (all_hyp2) versus with VELEST final velocity model (all_velest). Note that hypocenters define a bimodal distribution in depth. The transition between the two domains is coincident with Moho depth.

In the final earthquakes location we distinguish 3 clusters of seismicity in the São Vicente Canyon, in the Gorringe Bank and in the Horseshoe Abyssal Plain. On a W-E profile we observe that hypocentres depth increase from the Gorringe Bank cluster towards the Accretionary Wedge area. In S-N profile, we recognize that most events are located above 50-55 km depth which is considered to be the lower limit of seismogenic layer in the area.

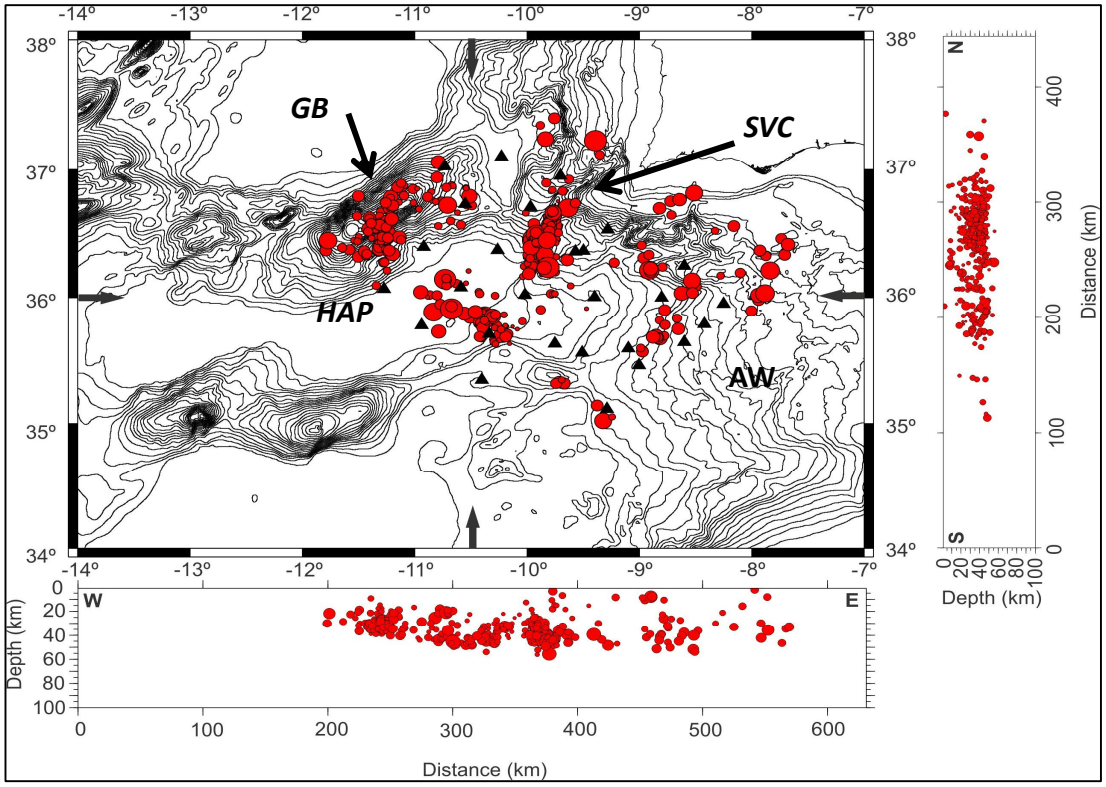

Figure III.85-All events locations based VELEST minimum 1D P and S velocity models (the black arrows mark the location of W-E and N-S profiles, *bathymetry from GEBCO*), distributed in three main clusters: the São Vicente canyon (SVC), Gorringe Bank (GB) and Horseshoe Abyssal Plain (HAP). Hypocenters' depths increase from Gorringe Bank to the Horseshoe Abyssal Plain. Shallower earthquakes are located both in the Gorringe Bank and in the São Vicente clusters (AW-Accretionary Wedge).

Compare with locations by land network

During NEAREST OBS experiment 291 events were recorded by land permanent network in area of the NEAREST OBS stations (data provided by Fernando Carrilho from IPMA, former IM, in *NEAREST 2008 Cruise Preliminary Report*), from which 179 events were located by both networks. If we compare the epicentre distributions, we observe that most of the land network locations are displaced landwards, reflecting the permanent network stations distribution (Figure III.86). In latitude and longitude most events locations shift between 0.1º to 0.2° whilst in depth this shift varies approximately 20 to 30 km (see Figure III.87).

Concerning depth distributions, we remark that land network locations are systematically shallower than NEARST OBS solutions, with maximum differences reaching 60 km (Figure III.86 and Figure III.87). Depth alignments around 15km and 30km that were clearly seen on land network locations are undetected with the NEAREST locations. These alignments are artificial constrains on depth locations. This disparity reflects the insufficiency of the land station distributions, velocity model and standard procedures to reach more

accurate earthquakes locations in the Gulf of Cadiz area, particularly for low to intermediate magnitude events.

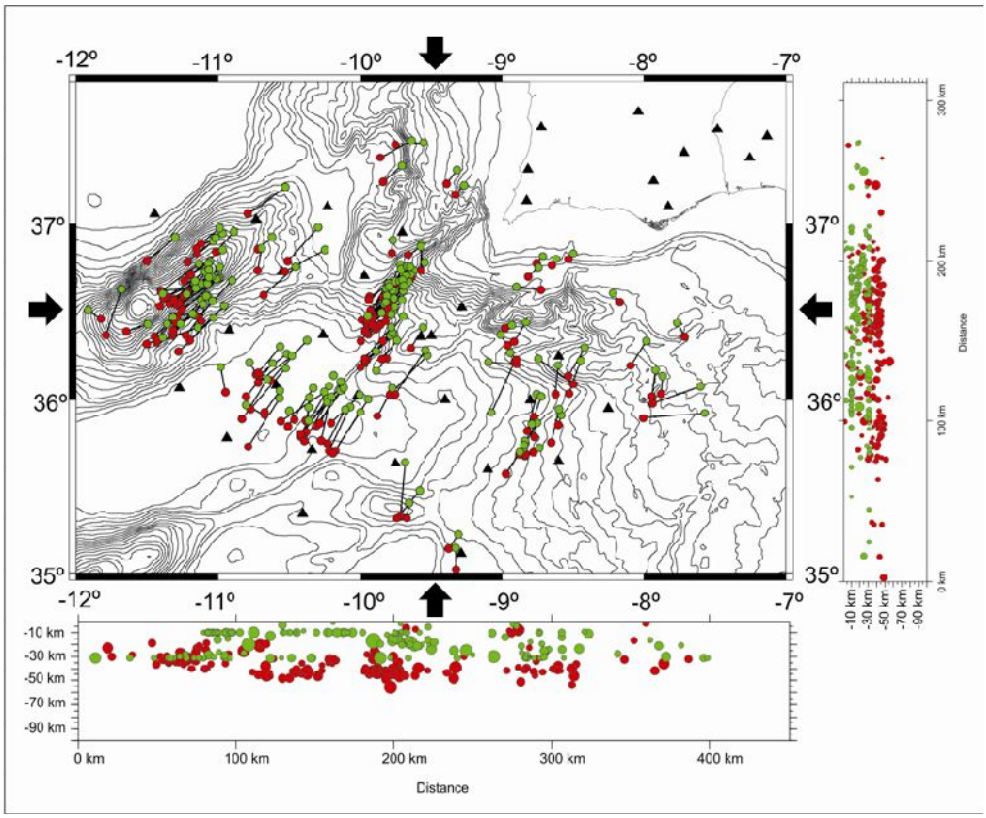

Figure III.86- Difference between locations derived from Land network (green circles) and from NEAREST OBS Network (red circles, the black arrows mark the location of W-E and N-S profiles, *bathymetry from GEBCO*). Epicenters located with the land network are displaced towards NE (landwards) and hypocenters are shallower.

Finally in Figure III.88, we compared local magnitude estimations in NEAREST and land permanent networks for the common set of events. Note that the formulation used to calculate local magnitude with NEAREST records is the same used by routine IPMA network estimations (defined in Carrilho and Vales, 2009). Except for two events, all NEAREST' estimated magnitudes are equal or higher than the results obtains based exclusively on the land permanent networks. For 45% of the estimated magnitudes have differences between 0.2 and 0.4. These discrepancies result from:

1. Differences in the stations-event distance between NEAREST and land networks. As discussed before, the land permanent network is concentrated on the mainland to NE of Gulf of Cadiz main seismic activity. For higher source-stations distances, anelastic attenuation increases inducing seismic waves to lose energy, diminishing the amplitude of the wave. Local magnitude estimations are based on the highest amplitude of the wave. To contradict anelastic attenuation, magnitude formulations include a distance correction term. Note that if amplitude estimations are roughly the same for both networks and land

network locations are systematically biased towards land then distance corrections are also lower for land network estimation. As a result magnitude would also be underestimated. Accordingly, it could explain the magnitude discrepancies between the NEAREST and permanent network estimation;

Other contribution may result from differences in routine procedures for wave amplitude measurement. IPMA routine procedures use regularly automatic and averaged amplitude measure based on the 3 seismometer components (with a correction term for vertical component). While, in NEAREST procedures, amplitude was determined manually, always in the horizontal component with the highest energy. These differences outcome on higher magnitude estimation in NEAREST results.

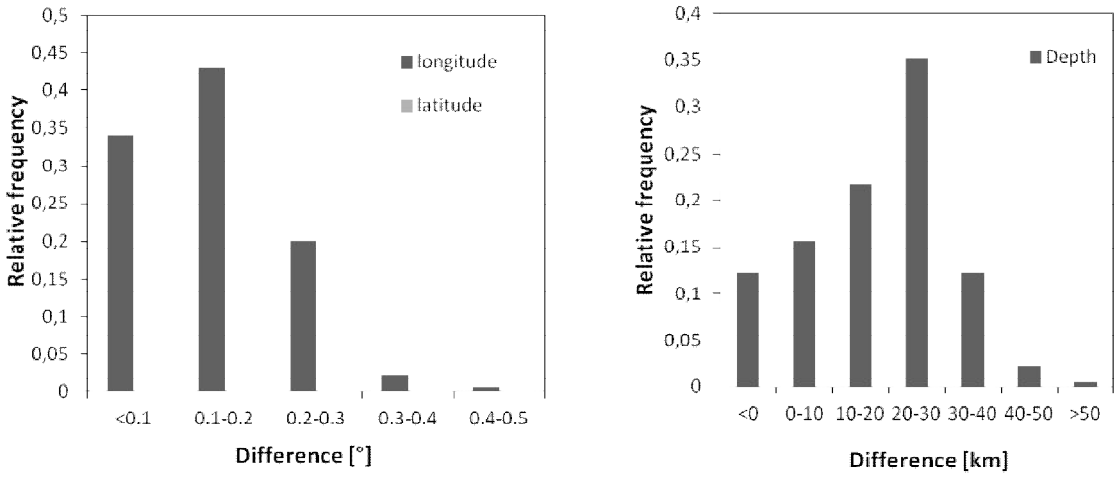

Figure III.87- Difference between locations based on NEAREST OBS network and previous locations based on land stations. In latitude and longitude most events locations shift between 0. 1 to 0.2° whilst in depth this shift varies approximately 20 to 30 km.

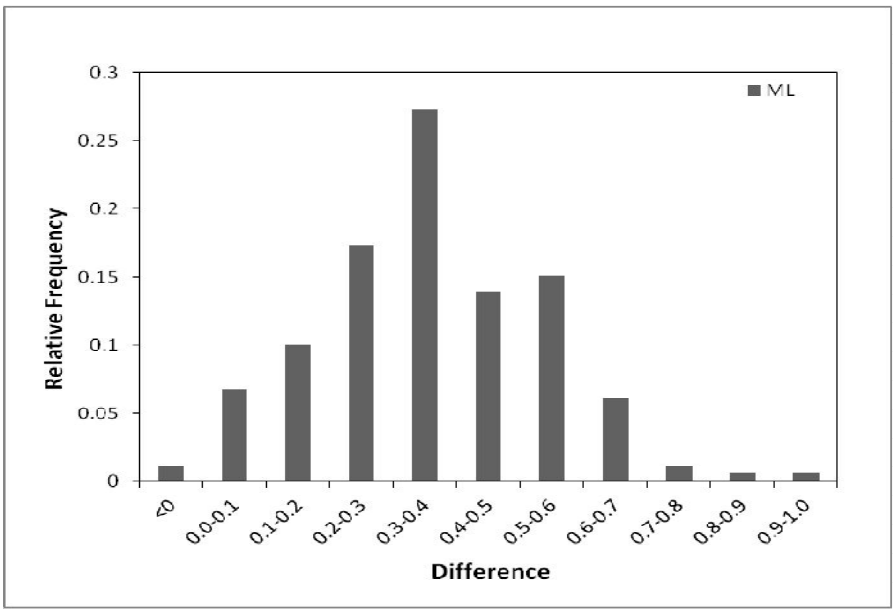

Figure III.88- Difference between local magnitude estimations based on NEAREST OBS network and previous estimations based on land stations, for a set of common events. Except for two events, all NEAREST' estimated local magnitudes are equal or higher than the ones calculated based on permanent land network.

III.2.3.Double-difference re-location

III.2.3.1.Introduction

The double-difference methods are useful if applied for a seismicity cluster with events closely related where two events are separated by a distance smaller than the velocity model resolution and events-station distance. In these conditions, it is assumed that geological transitions along ray-path between source region and a common station are the same, so any relative travel time differences between the two events result only from spatial offset at the hypocentres (see section II.4.2 for details on location methods). The double-difference technique uses any combination of common phase pickings from any earthquake catalogues that refers to the differential travel time (catalogue data) and/or high precision waveform cross-correlation (cross-correlation data).

We used the hypoDD program package (Felix Waldhauser, 2001) based on double-difference algorithm published in Waldhauser and Ellsworth (2000). Our tests are preliminary because it includes only catalogue differences. Cross-correlation data was tested but few matching sequences were identified. In detail, we identified 26 sequences (17 were doubles) in the São Vicente cluster, 12 sequences (10 doubles) in the Gorringe cluster and in the Horseshoe cluster 7 sequences (5 doubles). Consequently, these data were only included to calculate composite focal mechanisms (see section III.5 for processing steps and results). More improvement is necessary to include it in hypoDD re-location.

III.2.3.2.Processing sequence

Since this method is restricted to closely related earthquakes, we worked each cluster separately. However, hypoDD works with a series of input data transversal to all clusters. We started by extracting stations information and the velocity model from STATION0.HYP file (SEISAN) with a modified version of *nsta2dd* application (the original is provided in hypoDD package). Since, hypoDD only accepts a Vp velocity model (S-velocity is deduced by Vp/Vs ratio) we re-located the events with mod0 (for model details see section III.2.2) and the final Vp model was deduced with VELEST (Table III.6) with Vp/Vs =1.73. No stations corrections were added. In double-difference methods geological variability at stations is neglected because equally affects ray-paths between closely located events and common stations.

The seismicity re-location with hypoDD involves a two-steps process. First, we need to convert common catalogue files to an optimized combination of earthquakes pairs and common stations. We must ensure: i) strong linkage between events pairs-common station; ii) establish a net of well connected events; iii) minimize redundancy in the dataset. We start by convert phase picking files from Nordic to hypoDD format with *nor2pha* application (by Luis Matias). The output files are converted by *ph2dt* application (provided by hypoDD original package) into selected pairs of travel times and then store in a dt.ct file.

The *ph2dt* application works with an input file (*ph2dt.inp- an example in* Appendix II) with user defined criteria (see hypoDD manual for details). We want to define a network of links between the events within our cluster. Because we have few events, we use less constricted values in our variables. We used large distances to define the maximum distance in km connecting event pair – stations (MAXDIST- see hypoDD manual for variables details) and between hypocenters (MAXSEP), so that we could include the highest number of events. Since, we are re-locating each cluster independently we avoid pairing completely unrelated events. Also, as suggested in hypoDD manual for small catalogues, we set the minimum of observations (MINOBS) per pair to be 1 station and maximum (MAXOBS) to the number of station in the network. We set this MINLINK (minimum number of phase pairs to define a strong neighboring) to be 3, lower than the default (8) so that we could maximize the number of included events.

The second step is to determine double-difference hypocentres locations using hypoDD application. Several variables were defined in an input file-*hypoDD.inp* (an example in Appendix II) that can change for a different set of iterations. Our aim is to define a strong network of linked events within the same cluster. Because we are considering for each case a single cluster (OBSCT=0) than the network connectivity is controlled by the maximum hypocentral separation allowed between linked events controlled by WDCT (maximum events

separation for catalogue data). This variable is the same as MAXSEP for *ph2dt.inp*. As suggested by the author Waldhauser (2011) we set a larger distance for MAXSEP and constricted our data in WDCT. At first iteration steps we decided to maintain the values less constrictive. We defined WDCT to be -9, meaning that no event outlier is excluded in the initial 8 iterations. In the next iterations, we define WDCT as 20km. We used only catalogue data, with P and S waves' readings and we defined the least square solution to find the best fitting hypocentral locations (see more detail on the method in chapter II.4.2 Appendix II in the input data).

The hypoDD application runs retrieves several output files:

1. hypoDD.loc and hypoDD.reloc with initial and final location (including initial and final errors);
2. hypoDD.sta with stations residuals. It only includes final stations information, excluded stations are absent;
3. hypoDD.log with the details on critical parameters that reflects the performance of each iteration steps.

These files help stabilising new input values for future tests.

III.2.3.3.Results

In the next subsection we compare plots of the hypoDD.loc and .reloc in map and sections. Then we convert hypoDD.reloc into a Nordic file using *hdd2nor* application and compare VELEST with hypoDD results. These steps are repeated for each cluster.

In general, the RMS for final re-locations were considerably improved from initial solutions both with MOD0 and VELEST final Vp model (see details on Table III.10). In fact, final locations have similar average errors independently from the initial velocity. We present only the detailed results from hypoDD tests starting with VELEST final Vp model because these tests were compatible with a larger number of events. Accordingly, we only compare the latter locations, for each cluster, with VELEST results.

In Figure III.89 to Figure III.91 we show the results of hypoDD re-locations in map view and in two perpendicular profiles for each cluster. Because this application only allows a 1D-Velocity model and no stations corrections, our starting locations have high misfit (see also Table III.10). Accordingly, vertical misfit is considerable higher than horizontal because depth determination is more susceptible to subsurface geological variability that is minimized by stations corrections.

In the final results, the average misfit decreases significantly for the events located within the seismicity clusters. For the double-difference location methods improvement depends on events links. Since the events within the

centre of the cluster have more links their respective hypocentre determinations are more accurate. Accordingly, isolated events that exceed the maximum events separation for catalogue data are excluded from final location (set as >20km). In the Horseshoe and São Vicente clusters few events were excluded (4 in 244). In the Gorringe cluster 14 in 142 events were excluded (Figure III.89-Figure III.91 and Table III.10).

Table III.10- Comparing general statistics for hypoDD re-locations with different velocity models.

Vp		MOD0					
Details		Initial RMS	nºevents	Stations	Final RMS	nºevents	Stations
Cluster	SVC	0.5146	166	25	0.1704	166	25
	Hsh	0.5911	70	24	0.214	69	23
	GOR	0.5423	138	24	0.2054	130	24
Vp		Velest final Vp model					
Details		Initial RMS	nºevents	Stations	Final RMS	nºevents	Stations
Cluster	SVC	0.3509	173	25	0.1715	170	25
	Hsh	0.4249	71	24	0.2166	70	23
	GOR	0.3501	142	23	0.2102	129	23

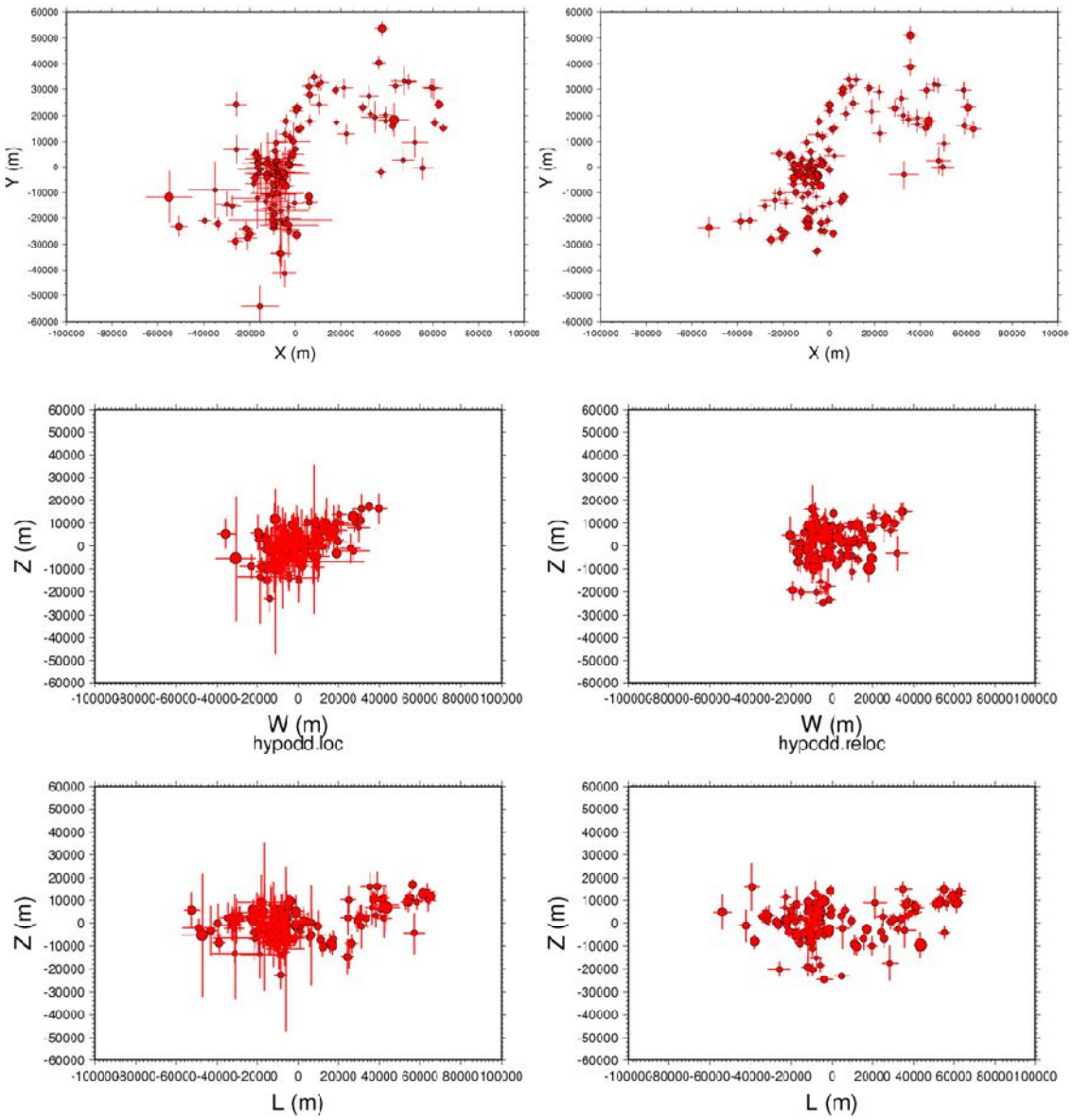

Figure III.89-Gorringe Cluster re-location with hypoDD: To the left are the original locations and on right are the relocated events (on top is map view, middle is transversal and bottom is along strike, full lines are error bars). Misfit of the events location largely decreases after re-location with hypoDD. Improvement is more successful for events located in the centre of the cluster. Isolated events were excluded from final locations.

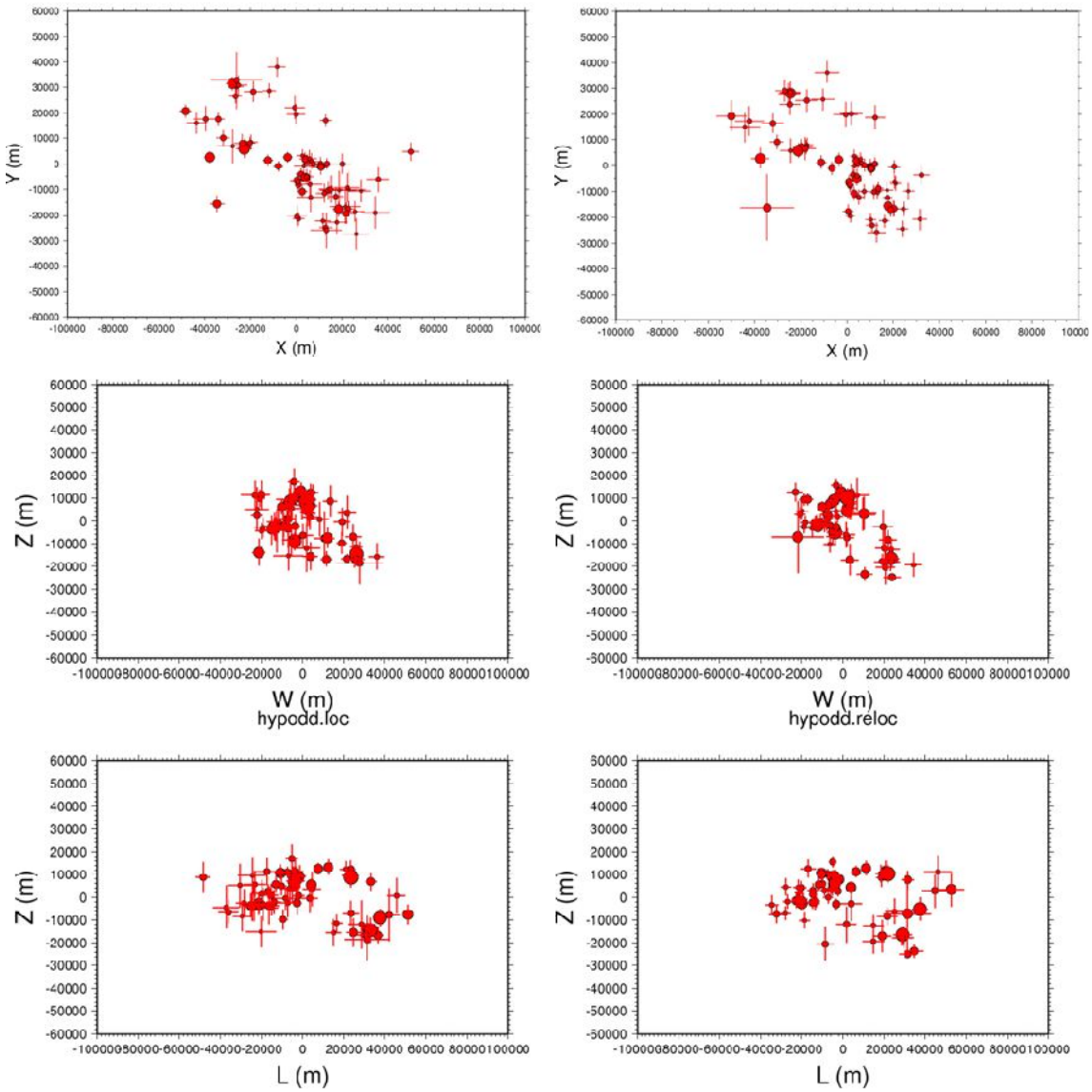

Figure III.90- Horseshoe Cluster re-location with hypoDD: To the left are the original locations and on right are the relocated events (on top is map view, middle is transversal and bottom is along cluster strike, full lines are error bars). Re-location with hypoDD reduced locations misfit. Decrease is less successful for events located in the clusters limits. That is particularly clear in the map view.

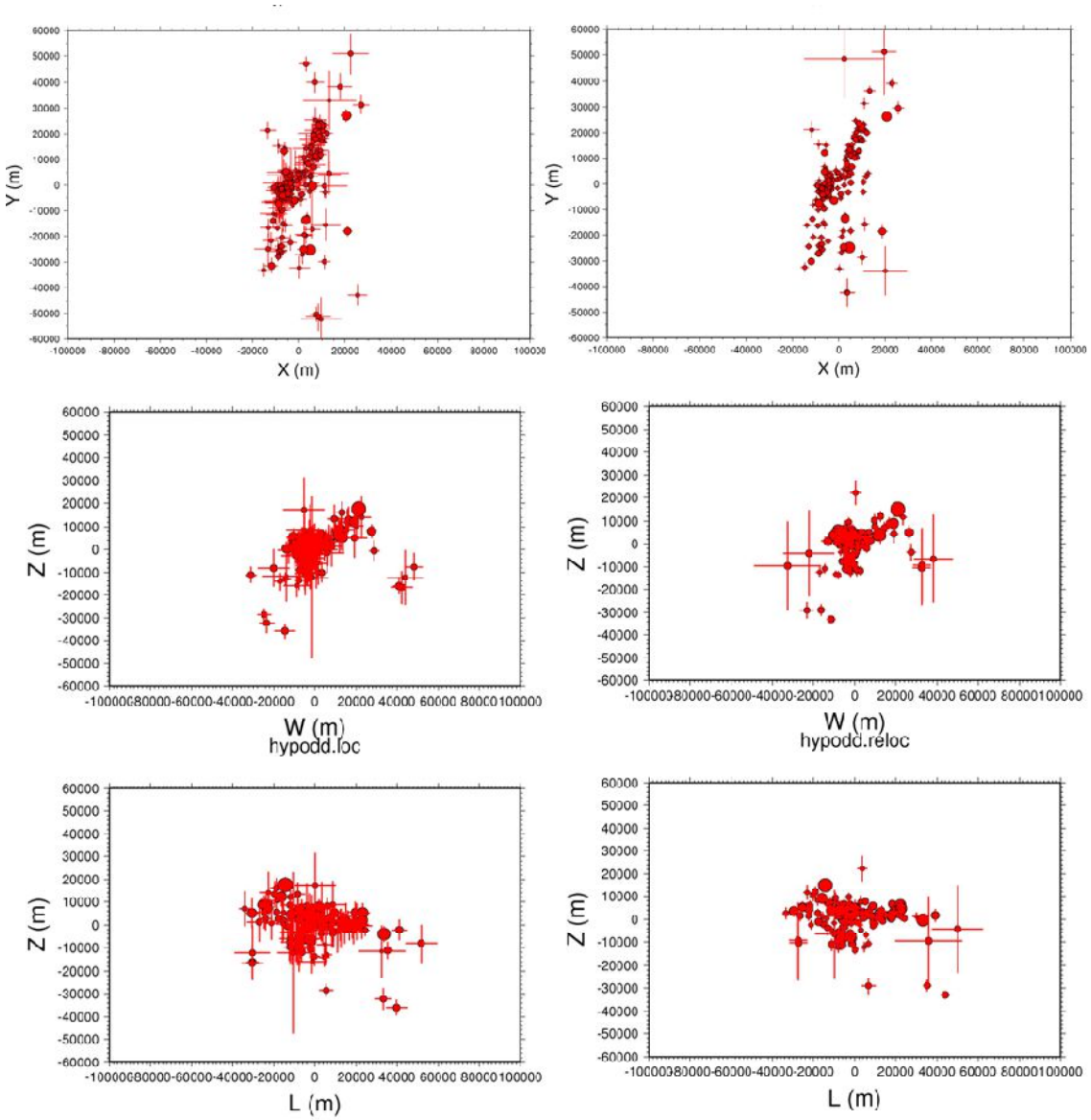

Figure III.91- São Vicente Cluster re-location with hypoDD: To the left are the original locations and on right are the relocated events (on top is map view, middle is transversal and bottom is along strike, full lines are error bars). In this cluster is also clear how misfit reduction is more effective for events with more links, located in the cluster´s centre.

We now compare events locations with hypoDD and VELEST in Figure III.92 to Figure III.100. In map view both methods show similar locations. However, in depth profiles we observe considerable differences. For both Gorringe and Horseshoe clusters seismicity becomes shallower with hypoDD method. In general most hypocenters are located at depth >20km yet hypoDD re-locations result in a larger number of events shallower than 20km (see Figures III.93-94 and III.96-97). In the São Vicente cluster, the depth distribution is roughly the same but hypocenters re-locations with hypoDD collapse, revealing or clarifying some possible alignments (see Figures III.99-100).

With hypoDD method, we would expect to have hypocenters re-located into a less diffuse distribution. However, this is only clearly achieved for the São Vicente Cluster that is originally more discrete or less diffuse if compared with

the remaining clusters. We recognize that with the introduction of waveform cross-correlation data and redefining some initial variables will improve our results.

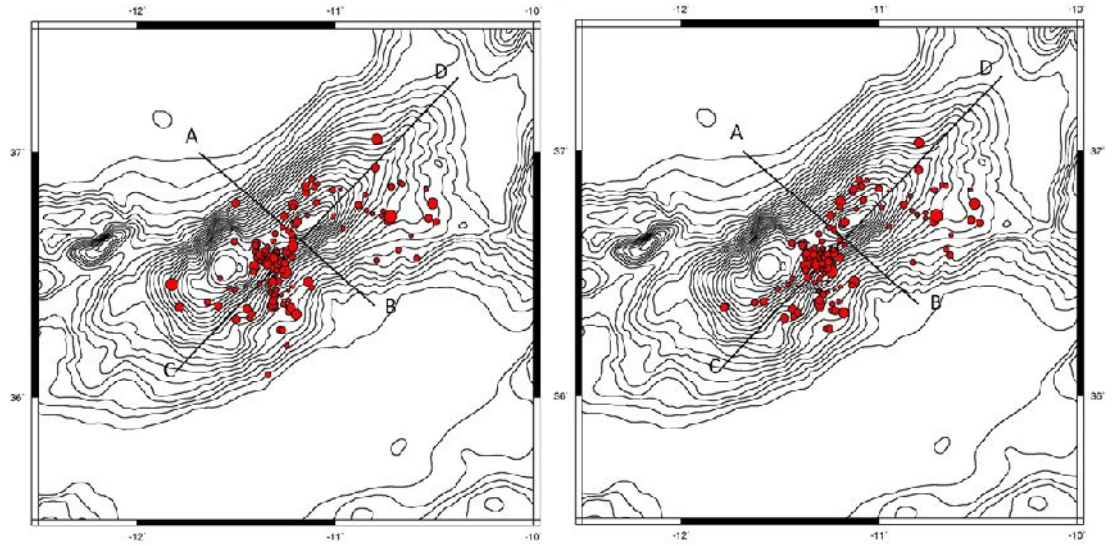

Figure III.92- Gorringe Bank cluster final locations (to the left VELEST locations and to the right hypoDD locations, *bathymetry from GEBCO*). In map view show similar locations with both methods

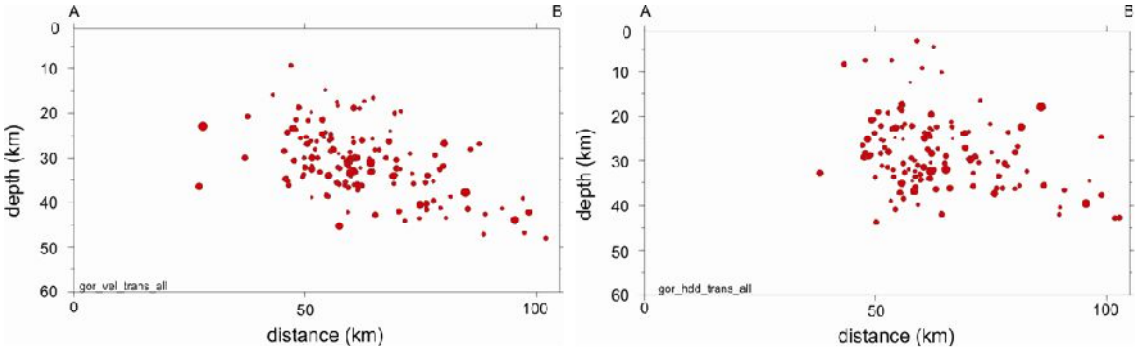

Figure III.93- Final locations in profiles transversal to Gorringe Bank striking direction (to the left VELEST locations and to the right hypoDD locations). In depth, hypocentres seems to be re-located to towards SE and into shallower depths with hypoDD.

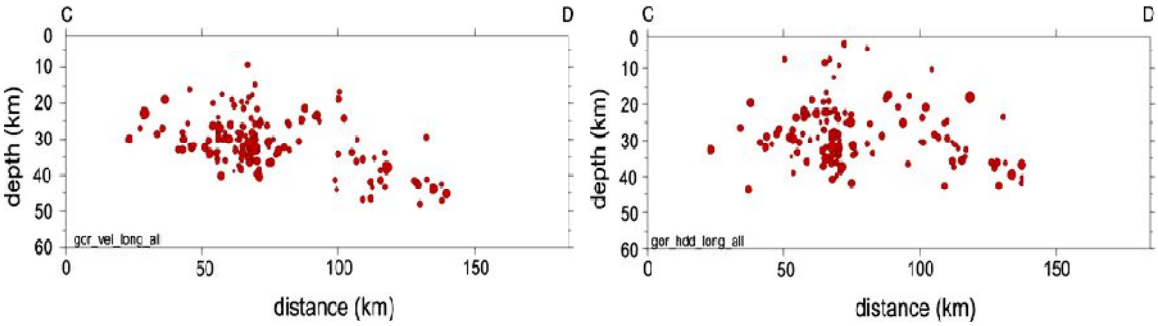

Figure III.94- Final locations in profiles along Gorringe Bank striking direction (to the left VELEST locations and to the right hypoDD locations). HypoDD retrieves shallower hypocentres. It seems that hypoDD locations are also more diffuse**.**

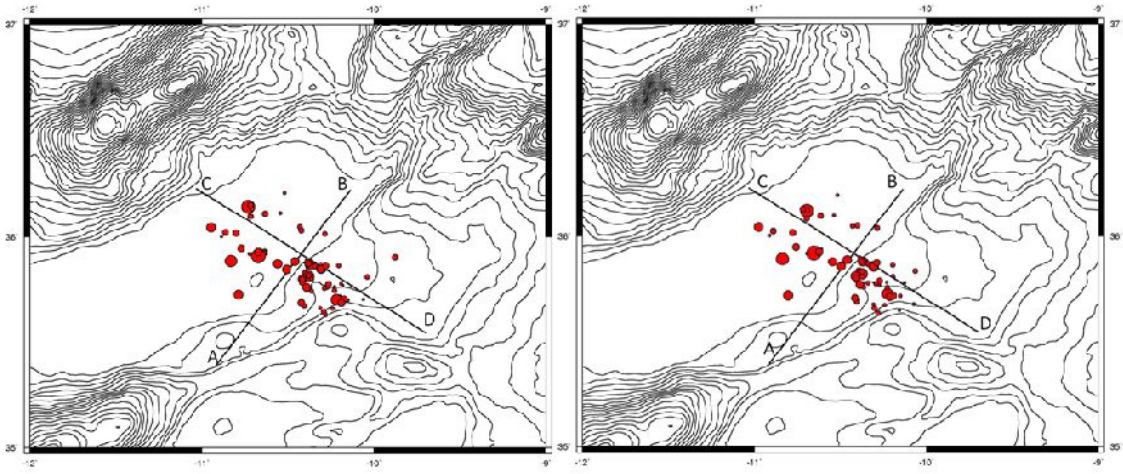

Figure III.95 - Horseshoe Abyssal Plain cluster final locations (to the left VELEST locations and to the right hypoDD locations, *bathymetry from GEBCO*). Few changes between the two methods are observed in map view.

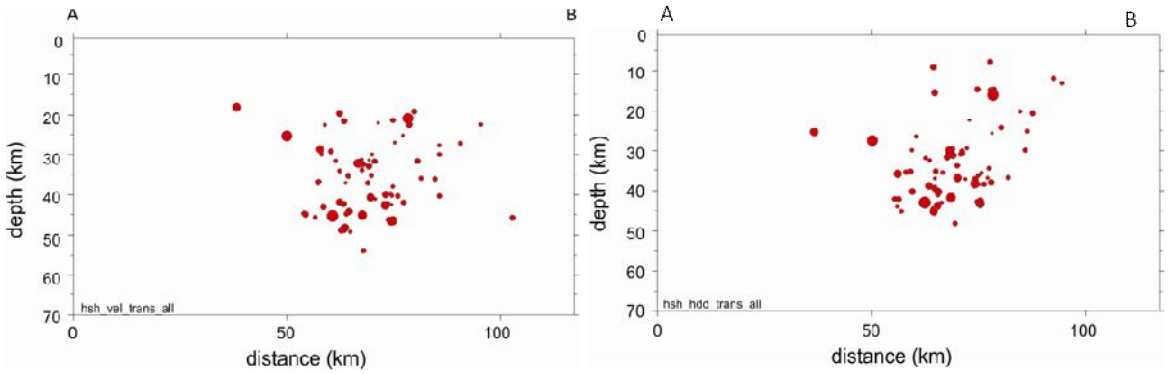

Figure III.96- Final locations in profiles transversal to Horseshoe cluster striking direction (to the left VELEST locations and to the right hypoDD locations). Earthquakes locations are shallower with hypoDD re-locations.

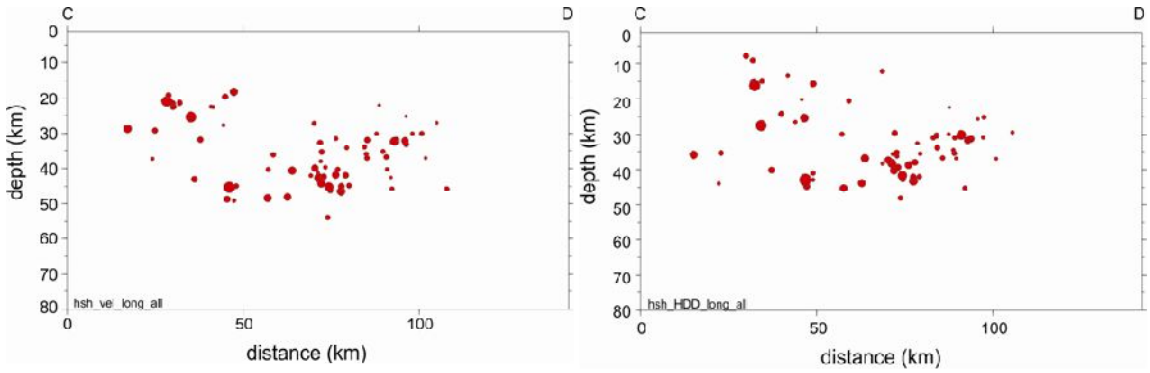

Figure III.97- Final locations in profiles along Horseshoe cluster striking direction (to the left VELEST locations and to the right hypoDD locations). Along the horseshoe cluster, events also are re-located to shallower depth and define a more diffuse cluster with hypoDD method.

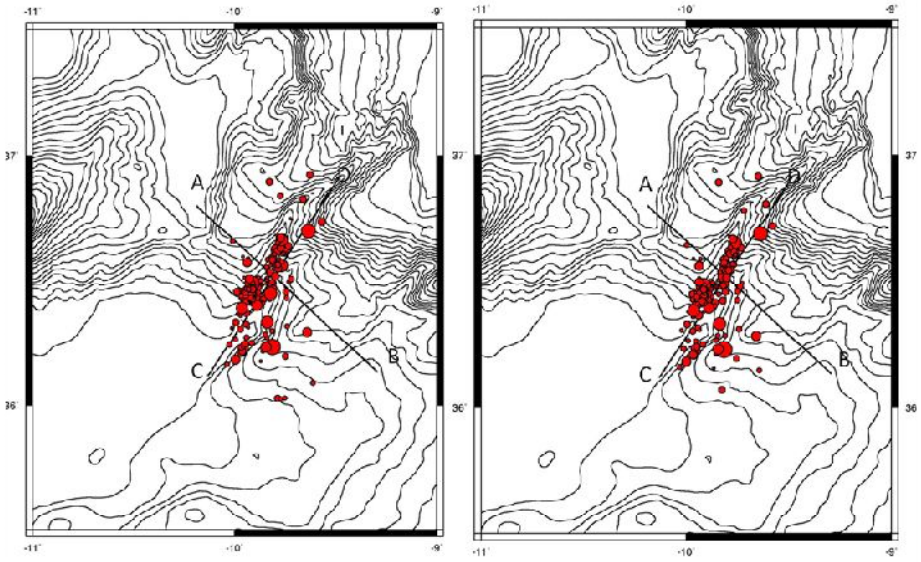

Figure III.98-São Vicente cluster final locations (to the left, VELEST locations and to the right, hypoDD locations, *bathymetry from GEBCO*). There are no considerable changes between the methods locations in map view.

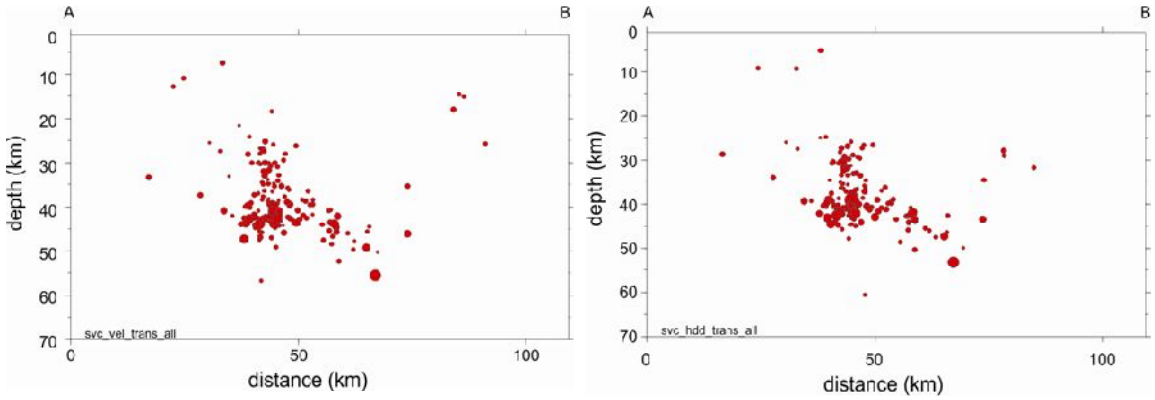

Figure III.99- Final locations in profiles transversal to São Vicente cluster striking direction (to the left VELEST locations and to the right hypoDD locations). HypoDD re-locations are more effective in this cluster. Here, we observe that with hypoDD, earthquakes are re-positioning defining more discrete alignments.

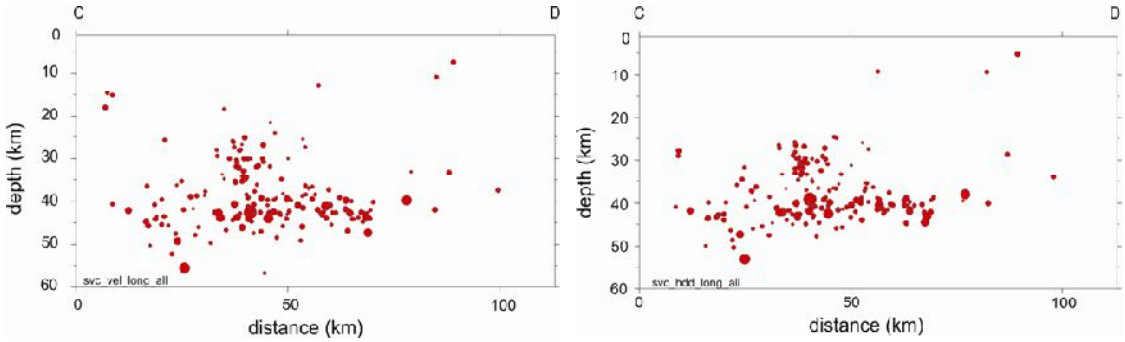

Figure III.100- Final locations in profiles along São Vicente cluster striking direction (to the left VELEST locations and to the right hypoDD locations). It is again clear that in this cluster hypoDD re-locations show a less diffuse distribution.

III.3.Focal mechanism solutions

III.3.1.Introduction

The SEISAN 9.1 package (Havskov and Ottemöller, 2011) includes several programs to determine the fault plane solutions (details on the methods in chapter II). In this work we used FPFIT (Reasenberg and Oppenheimer, 1985) and FOCMEC (Snoke et al., 1984). Both programs use first motions polarities and a grid search to define the source model. FOCMEC can also include amplitude ratios of P and S waves, which will help select or confirm the best solution. In our case we used only P-wave first motion polarities to determine focal mechanism solutions for the local seismicity.

The FOCMEC performs a grid search to find how many polarities fit each possible solution. All solutions are plotted within a limit of possible wrong polarities (Figure III.101). The preferred solution is then selected by the user. The maximum allowed polarities misfits are defined iteratively. In this work we display only the best solutions with minimum misfits (defined by -1). FOCMEC allows the user to select the degree of increment for the grid search, accordingly, we limited our value to 5 degrees for the majority of the solutions and only for less constrained solutions we used 8 degree search.

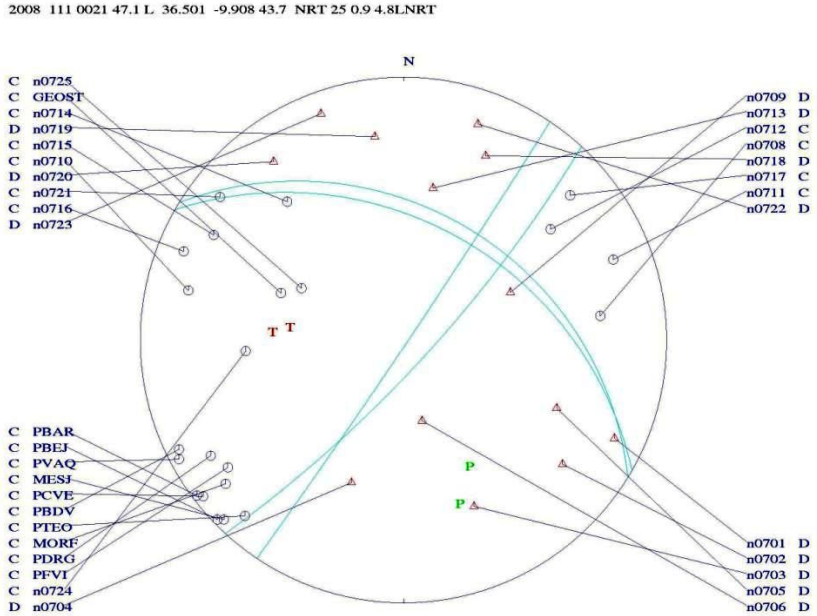

Figure III.101- Example of possible fault plane solutions plotted from FOCMEC program.

The FPFIT performs a two stage grid search to find the best fitting fault plane solutions. In the initial inversion a 20° increment was used to define the limits of strike, dip and rake minimum misfit. In the next stage a refined grid search with 5° variations around the best solutions found in the first stage was used. One advantage of using FPFIT is that the best fitting solutions are estimated based

on error statistics while, in contrast, with FOCMEC the best solution is selected visually by the user.

III.3.2.Processing sequence

We started by selecting events with at least 10 P-polarities readings as the minimum limit considered for fault source estimation. To constrain focal mechanism solutions, we also included P-wave polarities readings in the land stations.

To define the focal mechanism solutions several steps were taken:

1. We started by relocate the events with the minimum P and S velocity model;
2. In the next step, we ran FOCMEC application to define a preliminary source solution;
3. The final source solution is estimated using FPFIT program;
4. Both solutions are automatically saved to events individual file. We had a quality classification and flag the final solution (to prevent from overwrite stored solution by attending new estimations). The quality is defined based on the suggestion on FPFIT manual (Reasenberg and Oppenheimer, 1985) and is described in Table III.11. An additional class was added for focal plane solutions unconstrained with FOCMEC;
5. The data computed by FOCMEC (focmec.dat-with events polarities, focmec.out-with fault plane solutions) and from FPFIT (fpfit.fps-with final FPFIT solution) are converted to GMT format with faz_mecan.bat script and plotted using plo_mecan.bat GMT script (both from Luis Matias);
6. Since the seismicity is distributed in 3 main clusters, we selected the final solutions for each area based on quality criteria and computed composite focal mechanism, using both FOCMEC and FPFIT;
7. We also used sequence analysis to identify similar events in each cluster and afterwards compute composite focal mechanisms (see III.4.2.1 for processing details).

Table III.11-Quality classes based on FPFIT manual suggestion.

	FPFIT	Quality Factor
Fit error	Error in strike, dip, rake	
<0.025	<20	A
0.025 to 0.1	20 to 40	B
> 0.10	>40	C
Unconstrained with FOCMEC		D

III.3.2.1.Sequence analysis and composite focal mechanism solutions

In order to identify the possible sequences we must cross-correlate waveforms from the same component. Hence, we started by extracting from original waveforms files separated waveforms for each component and station using *wavnstap* code. The code uses the first arrival stored in events individual files to select the portion of the waveform that should be extracted. This information is set up in an input file along with other controlling parameters: station name, component, phase to be selected and the start – end time of extraction (e.g. 5s before and 10s after phase picking). The outputs for each selected station component are the waveforms and three text files: e.g. NRT01Z.log; NRT01Z.out and NRT01Z.lis. Both .log and .out describes operation steps while .lis is a list of the extracted waveforms.

The cross-correlation is performed by the application *multcorr* using an input file to define several controlling parameters, like the following example:

multicorr.inp

```
# Total of samples to use. 50% will be tapered.
512
# index of the center of window and offset (positive to the left)
500    50
# Low and High frequencies of filter
2.    10.
# lag to be computed (y/n)?
y
# c_tol
10.
```

Where the total of samples is defined in a power of 2 because it was used Fast Fourier Transforms to compute correlations. The time window is set based on a sample rate of 100 Hz. Accordingly, index of offset set to 50 indicated that the window starts 0.5s before the phase picking and the time window is centred at 5s. Before cross-correlation both waveforms are filtered by a band-pass Butterworth filter. The c_col allows negative correlation for values below 1.

The outputs are two files:

i. stationX.mat file (where X defines the component Z, Y, X) with the information of the correlation, the time –lag between waveforms and also the signal-noise ratio average between a master and a slave event;

ii. stationX.lis with the waveforms to be compared.

The sequence determination uses the matrix-sup application that combines all correlation matrixes computed above and outputs a list of sequences. It uses a parameter file that establishes the correlation limits to define a sequence, matrix-sup.inp, an example as follow:

matrix-sup.inp

 # c_min minimum value for a sequence to be declared

0.7

 # sn_min minimum s/n for a correlation to be accepted

1.5

 # sn_max saturation s/n. All values above will be truncated

10.

 # p_pow power to be applied to s/n to obtain the weigth (0 no weight)

0.7

Where c_min is minimum correlation, sn_minimum is signal to noise minimum, sn_max is signal to noise maximum and p_power is power value to determine s/n weigth. The outputs are files with lists of the events associated with each sequence. After determining all sequences, we evaluated the initial locations for each sequence and excluded the ones with events distantly related. We used the VELEST velocity model for the initial location. In the next step we improved sequence location by adapting station correction to each dataset. Finally, we computed composite focal mechanism solution for each sequence.

III.3.3.Results

The final focal mechanism solutions based on FPFIT estimations are displayed in Figure III.102. We could estimate 124 fault plane solutions, 68 % of those with A or B quality (a total of 82 events plotted in Figure III.103). The details on the solutions are on Appendix III and related individual plots are in Appendix IV.

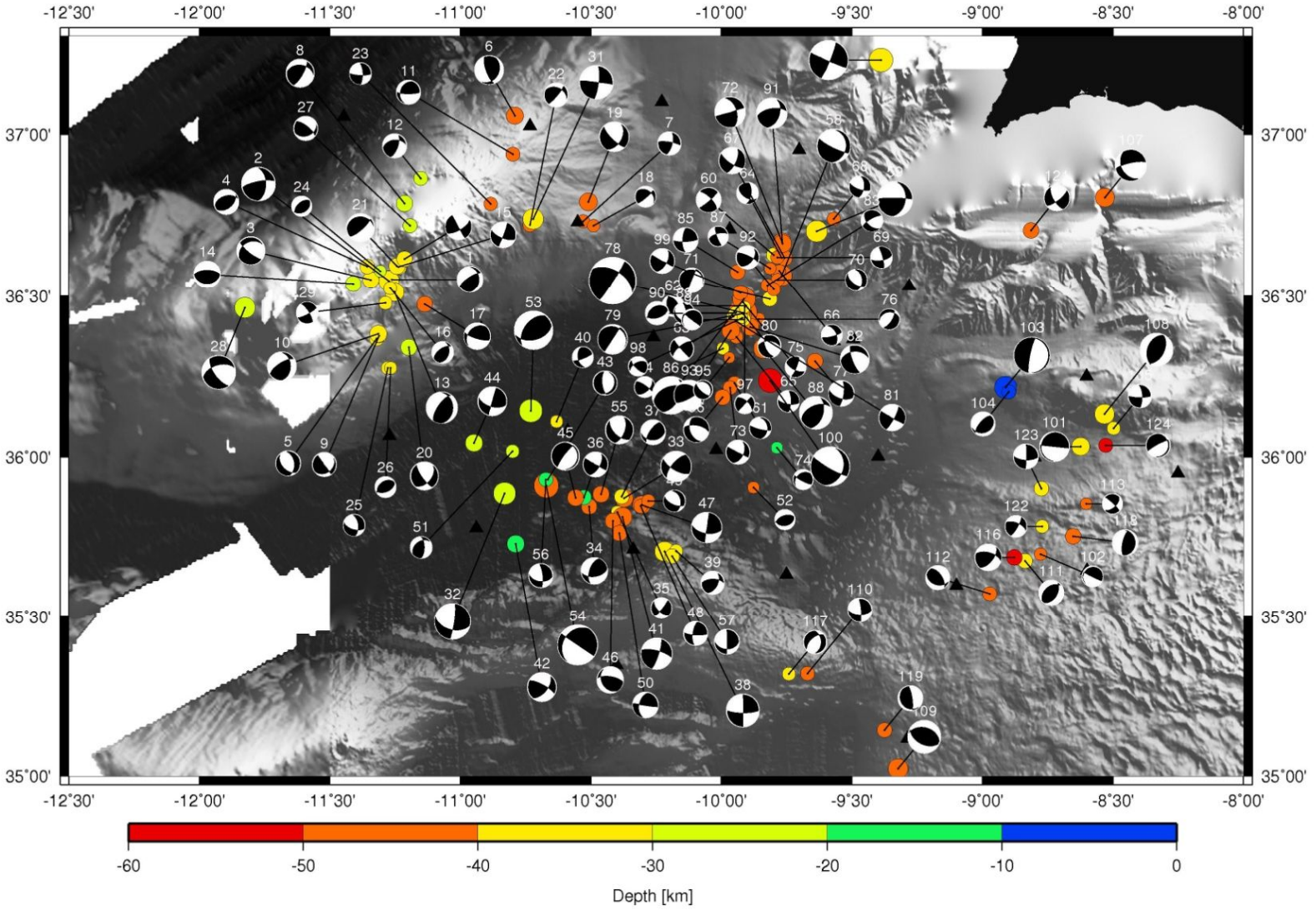
-12°30'
-12°00'
-11°30'
-11°00'
-10°30'
-10°00'
-9°30'
-9°00'
-8°30'
-8°00'
37°00'
36°30'
36°00'
35°30'
35°00'
-60
-50
-40
-30
-20
-10
0
Depth [km]

Figure III.102- Final Focal mechanism solutions (all quality classes are plotted, numbers are the reference to solutions details in Appendix III - IV, bathymetry compilation from Zitellini et al., 2009).

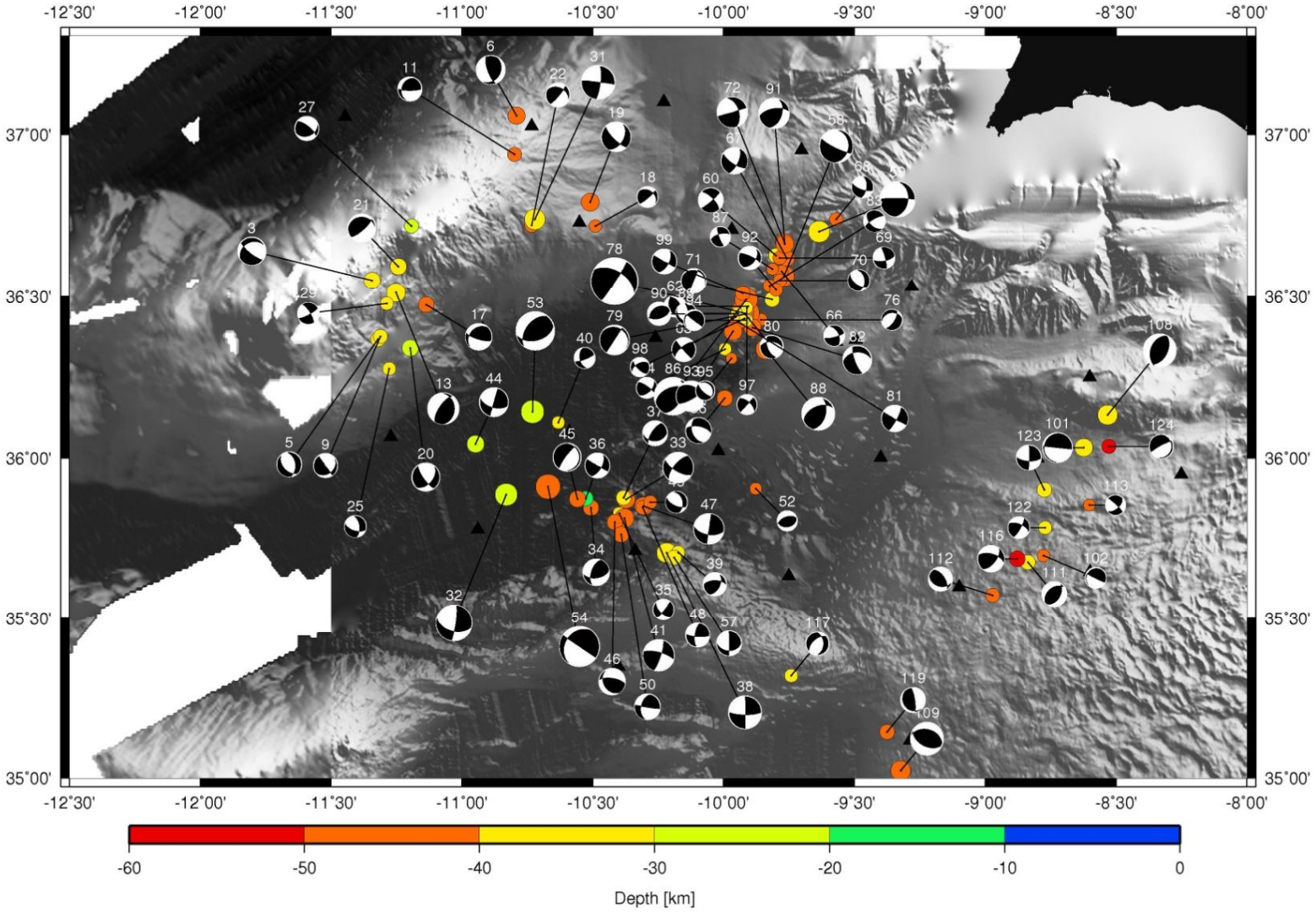
-12°30'
-12°00'
-11°30'
-11°00'
-10°30'
-10°00'
-9°30'
-9°00'
-8°30'
-8°00'
37°00'
36°30'
36°00'
35°30'
35°00'
-60
-50
-40
-30
-20
-10
0
Depth [km]

Figure III.103- Final focal mechanism solutions with quality A and B (numbers are the references to solutions details in APPENDIX III, bathymetry compilation from Zitellini et al., 2009).

In Geissler et al. (2010), 31 focal mechanisms computed with FOCMEC routine (and additionally the MECSEI algorithm), also using the P- wave first arrives polarities in OBS and Portuguese land stations were reported. These solutions were constrained using at least 8 polarities. With the final results of NEAREST OBS experiment, we added 58 new solutions, with A and B quality, to the previous catalogue. Because we consider events with at least 10 polarities, two events from Geissler et al. (2010) catalogue are not included in our work (events 5th and 21st of March 2008, with 9 polarities, in southern cluster at figure 3 of the referenced work). Also, 3 events solutions were classified with C quality (the 22nd of May 2008 at the southern cluster and outside the clusters area, both the 6th and the 7th of November 2007, ibid.).

From the A and B quality solutions, 39 % are located in São Vicente, 25% at Horseshoe and 17% at Gorringe clusters. The remaining events (17%) are located outside these clusters, mostly in the SW continental margin and below the Gulf of Cadiz Accretionary Wedge. These results reflect the following limitations of both NEAREST and Land networks coverage:

- The Gorringe cluster is displaced from land network distribution and at the edge of the NEAREST network;
- Outside the clusters, the events are located mostly out of the NEAREST network boundary or in the vicinity of poor recording stations (inhibited by the presence of the accretionary wedge - see III.3.2 for details)
- The Horseshoe cluster is well constrained by NEAREST network;
- The São Vicente Cluster, the area with higher seismic activity in the NEAREST deployment area, is covered both by NEAREST and land stations networks.

The diversity of the fault plane solutions identified, ranging from reverse dip-slip to strike-slip and even normal dip-slip, reflects the complexity of the source mechanisms to this low to intermediate magnitude seismicity (see Figure III.103). These results are also valid if we inspect each cluster individually (see Figure III.104 to Figure III.109).

In the Gorringe cluster, 31 focal mechanisms were computed, 15 of those with A and B quality (see Figure III.104). These new solutions considerably update the previous catalogues for this area where only a few focal mechanism solutions were known (e.g. Grimison and Chen, 1986; Burfon et al., 2004 and Stich et al, 2010).

The prevailing focal mechanisms are oblique (combinig strike-slip with a reverse slip) and reverse dip-slip. In fact, if we combine all polarities observations to define a composite focal mechanism, we obtain the oblique solution shown in Figure III.105. However, this solution is poorly constrained and has several incompatible polarities. We inspected the focal mechanism distribution in depth

based on two perpendicular profiles (Figure III.104), both cross-sections show an unclear relation between depth and a particular type of fault solutions. It is worthwhile noting the existence of normal dip-slip focal mechanisms at ≈ 30km in depth. In addition, from the two events sequences determined based on waveform cross-correlation resulted two composite focal mechanisms (see Table III.12 for details and Figure III.116 for solutions and polarities distributions), i) one with normal dip-slip solution also located at ≈40 km in depth (see SEQ08 in Table III.12 and Figure III.106 and Figure III.107), ii) whereas the sequence SEQ01 has a pure-strike slip solution (see Table III.12 and Figure III.106-Figure III.107) and is located in the transition between two different domains that will be discussed in the chapter IV. In opposition to sequence SEQ08 where several polarities are incompatible with the focal mechanism solution, SEQ01 composite solution is well constrained with only two unmatched polarities.

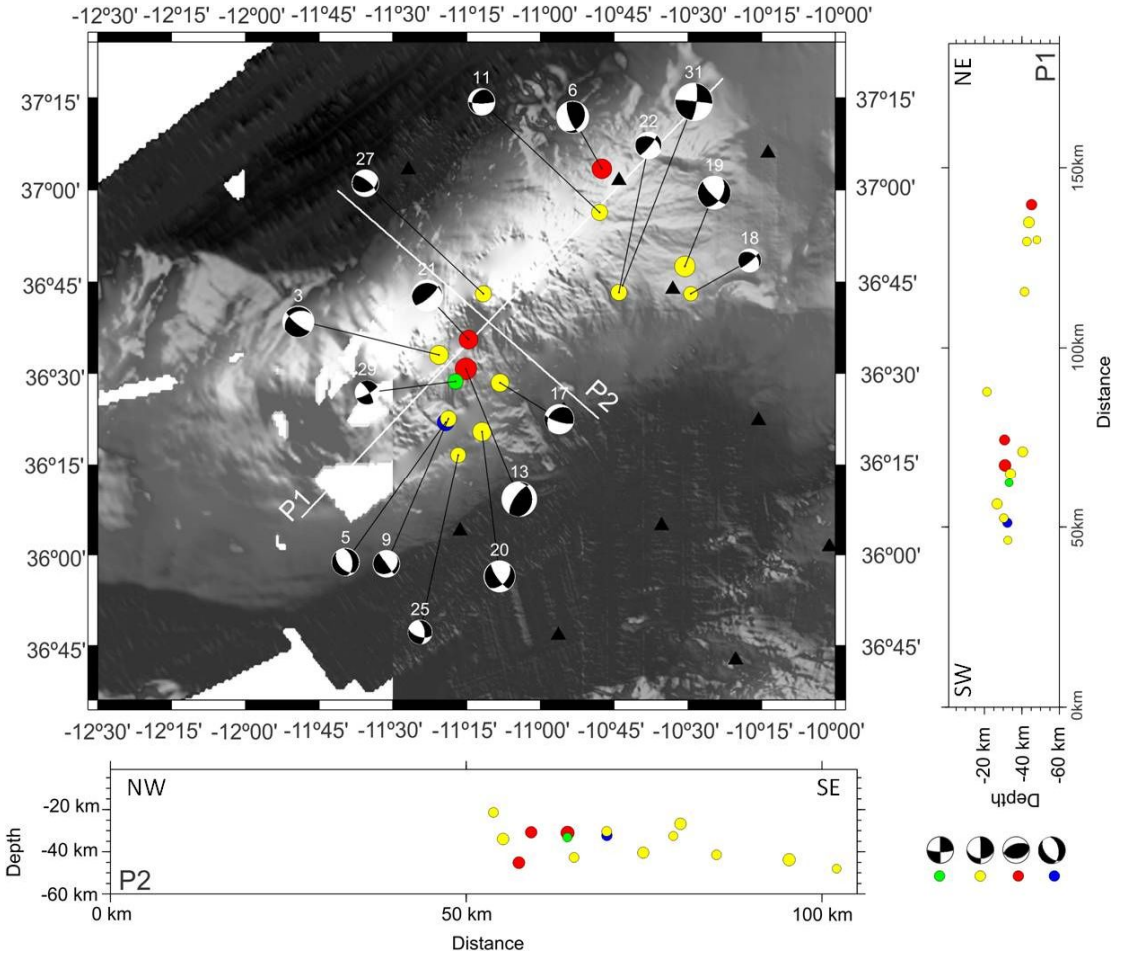

Figure III.104-Focal mechanism solutions with quality A and B in the Gorringe cluster area (green circles are pure strike-slip, red are reverse, blue are normal and yellow oblique solutions, bathymetry compilation from Zitellini et al., 2009). Note that both cross-sections show an unclear relation between depth and a particular type of fault solutions.

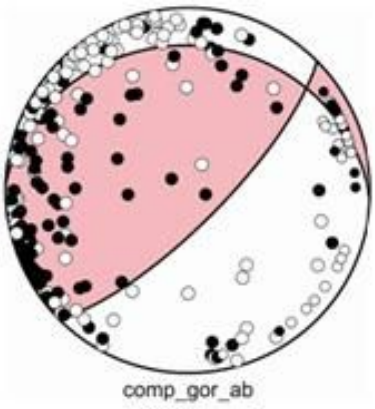

Figure III.105- Composite focal mechanism based on AB quality solution. It is clear that this solution is poorly constrained and has several incompatible polarities.

Table III.12- Details on the sequences resulted from cross-correlation analysis with events closely located.

Sequence	Nºevents	Nº polarities	INI_RMS	FIN_RMS
1	2	21	0.213	0.067
8	3	42	0.353	0.200

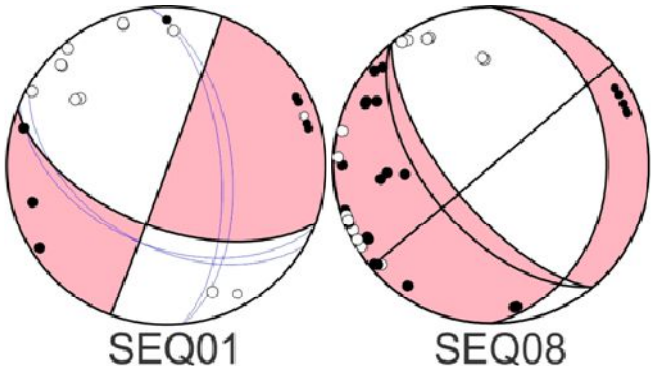

Figure III.106- Composite Fault plane solutions for sequences 01 and 08 (details on the sequences in table III.12). The focal mechanisms for SEQ01 defines a pure-strike slip solution and is well constrained with few incompatible polarities. Detail discussion on the events location and relation with geological structures will be presented in chapter IV. SEQ08 shows a roughly normal dip-slip solution. However, there are some incompatible polarities.

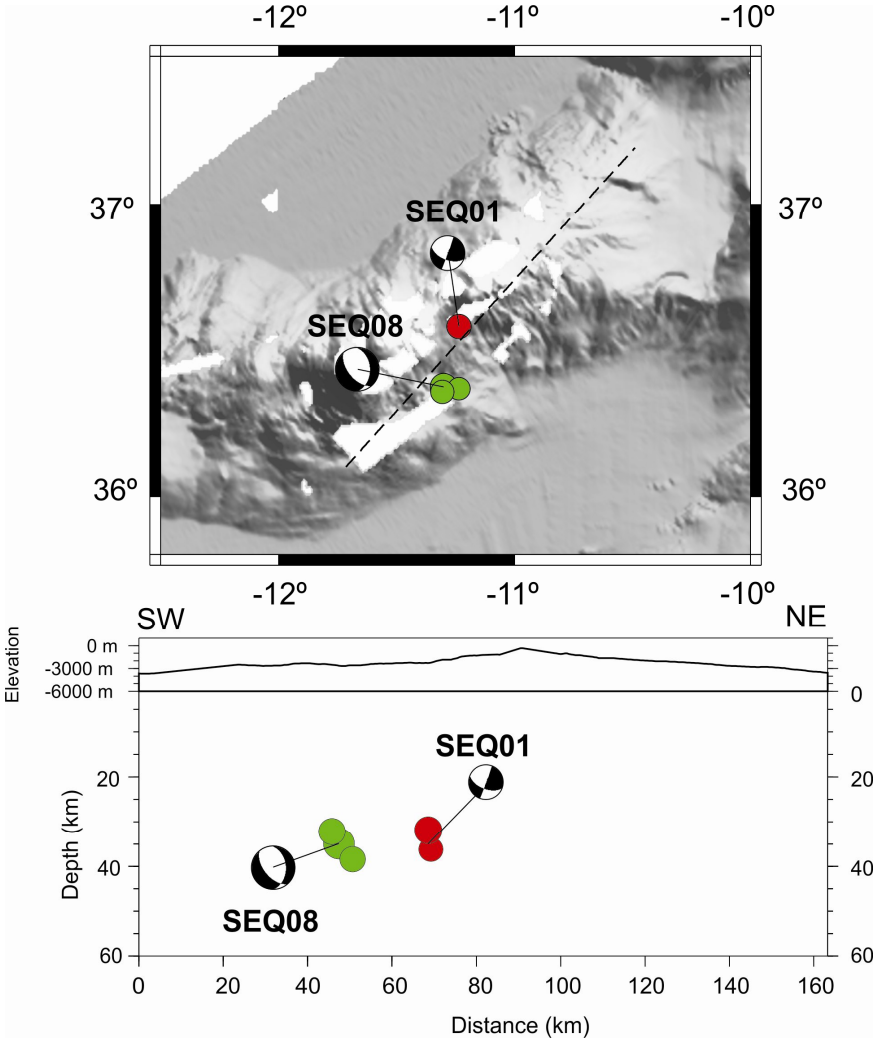

Figure III.107- Composite focal mechanisms for sequences depicted in Table III.12. On top is a map view with epicenters locations and on the bottom is a profile showing hypocenters locations (profile location is in map view-dashed line, circles with different colours separate events from distinct sequences, bathymetry compilation from Zitellini et al., 2009). Note that SEQ01 focal mechanism is located in the transition between Gettysberg and Ormonde seamounts. Detailed discussion on the SEQ01 location and relation with geological structures will be presented in chapter IV. SEQ08 defines a roughly normal dip-slip solution and is located at ≈35km in depth.

In the Horseshoe cluster 26 fault plane solutions were found with 10 events common to Geissler et al. (2010). From these, all events show similar solutions except for the 23rd February and the 5th May 2008 event (Figure III.108) for which the computed fault mechanism solution is considerably different from Geissler et al. (2010, in figure 3) possibly resulting from the use of different methods and/or data. In the first case, we added new polarities the fault plane solution (see Figure III.108). For the 5th May 2008 event, even though the same number of polarities was used we recovered different solutions. Discrepancies result from polarities re-distribution in the focal sphere with event location based on a different velocity model. This should be particularly critical for FPFIT solution since FOCMEC results match Geissler et al. (2010) solution. A moment tensor solution was also computed in Stich et al. (2010, figure 4). In this case, differences result from both method and data. The moment tensor solution was

computed based on signals recorded at seismic broadband stations from land networks in Portugal, Spain and Morocco.

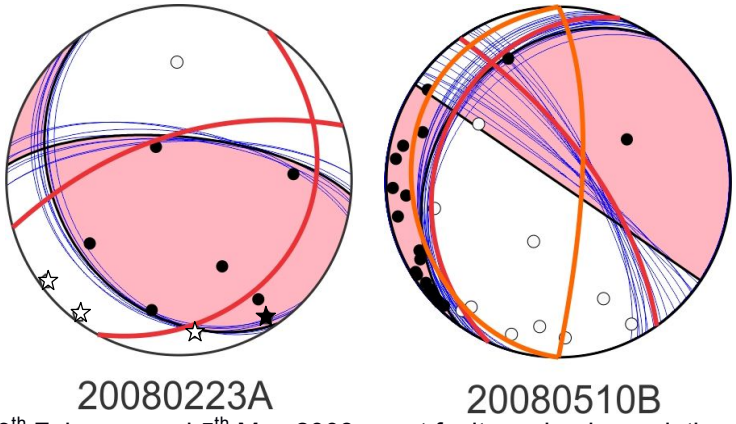

Figure III.108- 23th February and 5th May 2008 event fault mechanism solutions. Note that black line is FPFIT, blue line is FOCMEC, red line is MECSEI90 from Geissler et al., 2010 and orange line is the moment tensor in Stich et al., 2010. Discrepancies between focal mechanism solutions in our work and the ones in previous studies result mostly from using different methodologies and a datasets (in our work we added new polarities).

In general, the focal mechanisms in the Horseshoe cluster show mostly strike-slip solutions, particularly to the East (see profile P2 and map view in Figure III.109). To the west, focal mechanism show a more mixed pattern with solutions ranging between reverse to strike –slip kinematics, with a variety of combined oblique solutions. Normal dip-slip mechanisms at depth >40km were also obtained (Figure III.109). Similar solutions were already revealed by Stich et al. (2005, 2010) and Geissler et al. (2010). However, a plausible source mechanism was not proposed.

Composite focal mechanism for A and B quality events show solutions similar to general results: pure strike–slip and reverse mechanism with a slight strike-slip component, respectively (see Figure III.110). Yet, again, several polarities are incompatible with computed focal mechanisms. More reliable composite solutions resulted from sequence analysis. In table III.13 we sum up the details on the sequences resulted from cross-correlation analysis with events closely located.

The focal mechanism for sequence SEQ03 combines 3 events with 63 polarities. It shows a reverse solution with a minor strike-slip solution (see Figure III.111 to Figure III.112). This mechanism is similar to the 7th of May 2008 M_L 3.9 earthquake recorded in the NEAREST network (see event 53 in Figure III.109) and 28th February 1969 earthquake with Ms 7.9 (see Figure I.13). However, both events are located ≈ 20km deep while this sequence is at ≈ 40 km in depth and further to East.

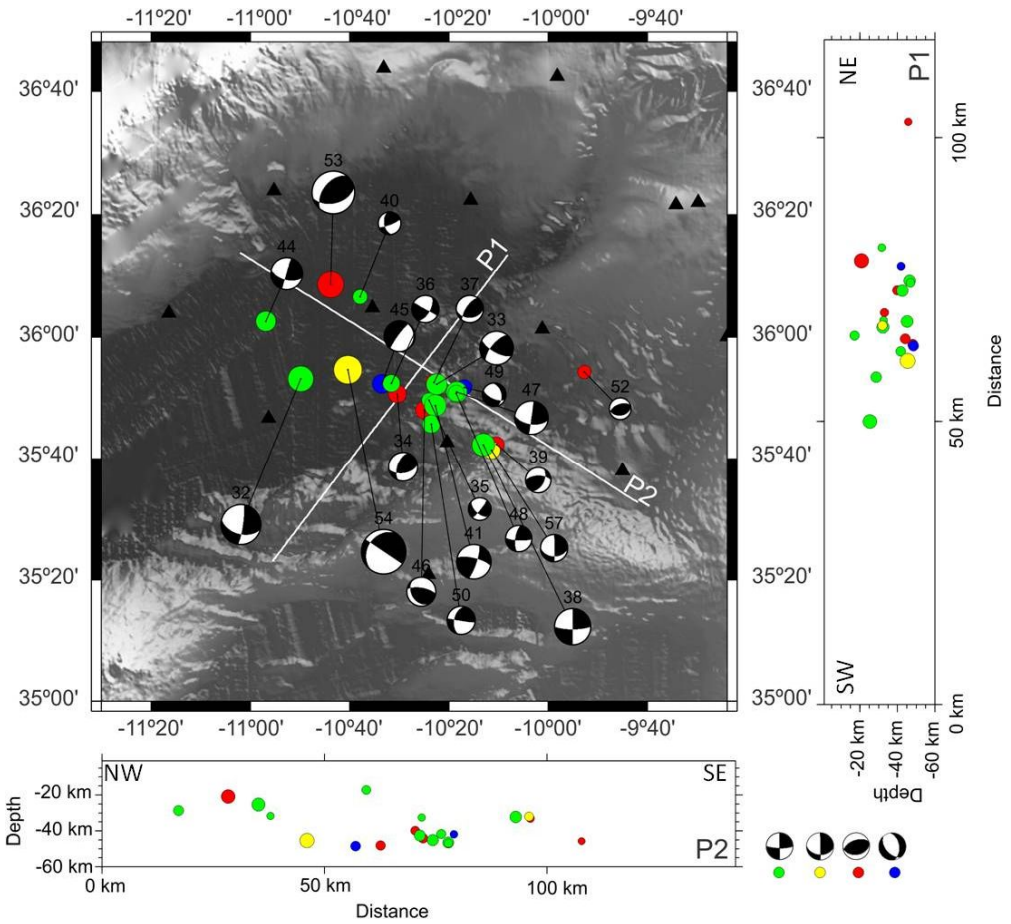

Figure III.109- Focal mechanism solutions with quality A and B in the Horseshoe cluster area (green circles are pure strike-slip, red are reverse, blue are normal and yellow oblique solutions, bathymetry compilation from Zitellini et al., 2009). To the SE, focal mechanism solutions are roughly pure strike-slip while to NW events show a more complex pattern. Note that few normal dip-slip solutions are located at ≈5okm in depth. The meaning of these location will be debated in the next chapter.

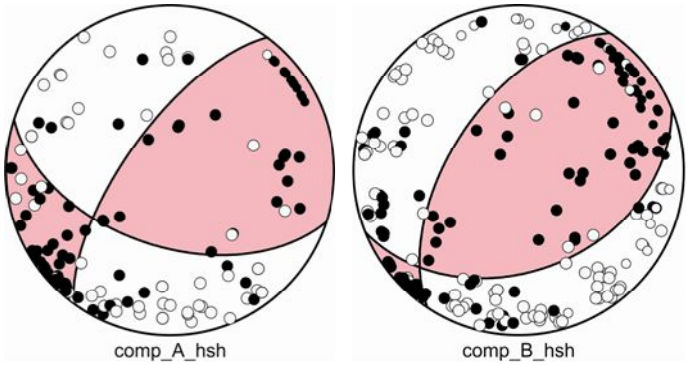

Figure III.110-Composite focal mechanisms based on A (left) and B (right) quality solutions. Composite focal mechanism show solutions similar to general results: pure strike–slip and reverse mechanism with a slight strike-slip component. Yet, again, several polarities are incompatible with computed focal mechanisms**.**

The sequences SEQ05 and SEQ06 are doubles with 26 and 38 polarities, respectively (see Table III.13, Figure III.111 and Figure III.112). Sequence SEQ06 shows a pure strike-slip mechanism while SEQ05 resulted in a strike-slip with a slight normal dip-slip component. How an extensional fault mechanism is generated at ≈40km in depth is unclear, as expressed early.

Table III.13- Details on the sequences resulted from cross-correlation analysis with events closely located.

Sequence	Nºevents	Nº polarities	INI_RMS	FIN_RMS
3	3	63	0.27	0.141
5	2	26	0.291	0.16
6	2	38	0.227	0.073

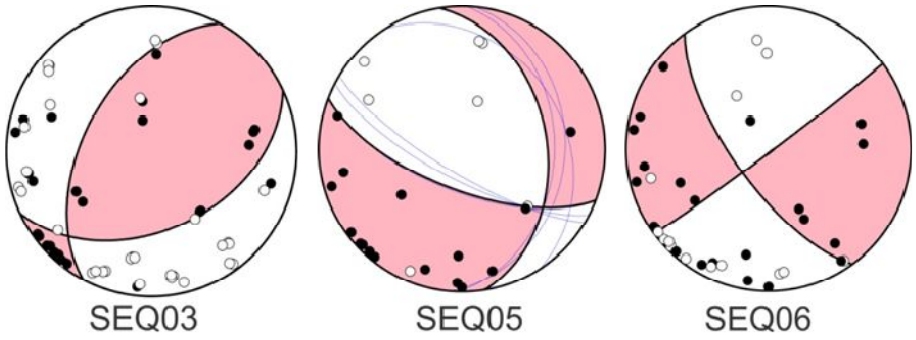

Figure III.111- Composite Fault plane solutions for sequences SEQ03, SEQ05 and SEQ06 (details on the sequences in table III.13). SEQ03 and SEQ05 are well constrained with few incompatible solutions while SEQ06 shows several mismatches.

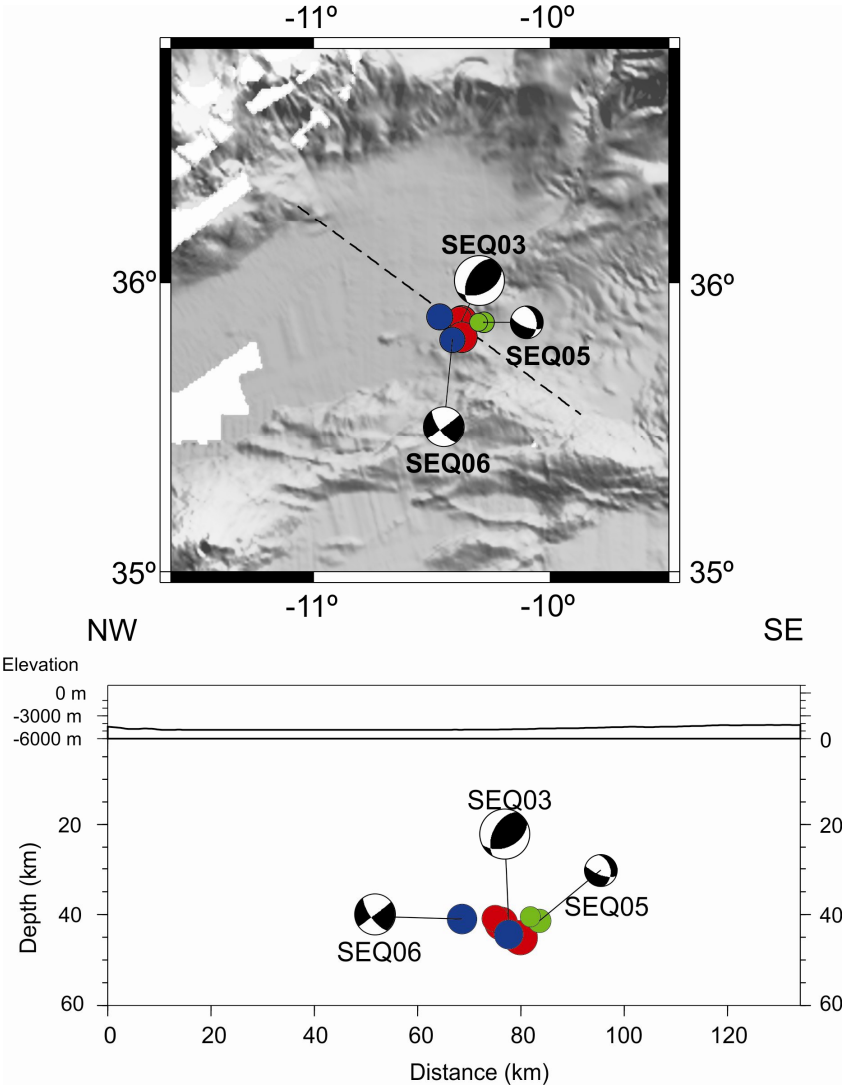

Figure III.112- Composite focal mechanisms for sequences depicted in Table III.13. On top is a map view with epicenters locations and on the bottom is a profile showing hypocenters locations (profile location is in map view-dashed line, circles with different colors separate events from distinct sequences, bathymetry compilation from Zitellini et al., 2009). It is worthwhile notice that the focal mechanism for SEQ03 is similar to the 7th of May 2008 M_L 3.9 earthquake recorded in the NEAREST network and 28th February 1969 earthquake with Ms 7.9. Yet, both events are located at ≈20km in depth while SEQ03 is located at ≈40km and further to theEast. SEQ05 shows a peculiar location since is a normal-dip slip mechanism at 40km in depth. SEQ06 defines pure-strike slip solution that is similar with several individual solutions retrieved from NEAREST network for earthquakes located in the area.

We identified 33 focal mechanism solutions in the São Vicente Cluster adding 17 new events to the previous dataset. Once more, we recognized some discrepancies with previous works. Two examples are shown in Figure III.113. In both cases our solutions are different from Geissler et al. (2010) mostly because we added new polarities to preliminary solutions. In the 20071125A event, we also re-interpreted some first arrivals with opposite polarities.

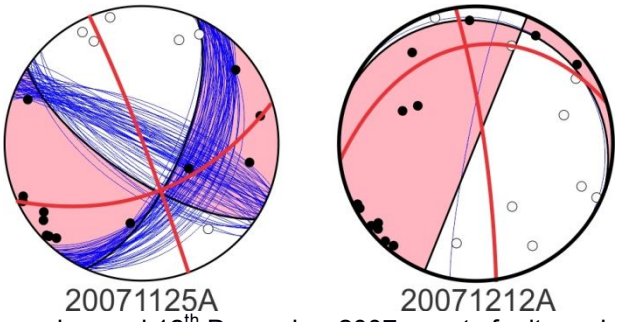

Figure III.113- 25th November and 12th December 2007 events fault mechanism solutions. Back line is FPFIT, blue line is FOCMEC and red line is MECSEI90 from Geissler et al. (2010). In both cases our solutions are different from Geissler et al. (2010) mostly because we added new polarities to preliminary solutions.

The São Vicente cluster is where most events occurred during the NEAREST experiment. Dominant focal mechanisms are strike-slip and reverse dip-slip. However there are several earthquakes with oblique solutions, mostly combining pure –strike slip with reverse dip-slip component. An example is the 11th January 2008 earthquake with M_L=4.8, the highest magnitude recorded during NEAREST experiment (see event 78 in Figure III.114 and details at Appendix IV.c). This focal mechanism is similar to the one defined to the 17th December 2009 earthquake, with local magnitude 6.0. Both events are located in the same area and at the depth range ≈35-40km. It is noteworthy that once more we have extensional events located at depth ≈20-40km (see Figure III.114).

Composite focal mechanism based on A and B quality events have similar solutions nearly pure-strike-slip kinematics (see Figure III.115). Contrasting is the diversity of fault plane solutions derived from identified sequences (see Table III.14 for details and Figure III.116-Figure III.117):

- Both sequences SEQ02 and SEQ10 have reverse dip-slip solutions with slightly horizontal component;

- Sequence SEQ05 and SEQ08 have similar focal mechanisms (strike-slip) and depth but separated by ≈50km;
- Sequence SEQ15 show roughly strike-slip solutions but striking in different direction than SEQ05 and SEQ08;
- The sequence SEQ09 have reverse dip-slip kinematics with a very low angle plane at ≈20 km or contrastingly a sub-vertical plane;

Sequence SEQ11 is located at ≈40km in depth and shows normal dip-slip kinematics.

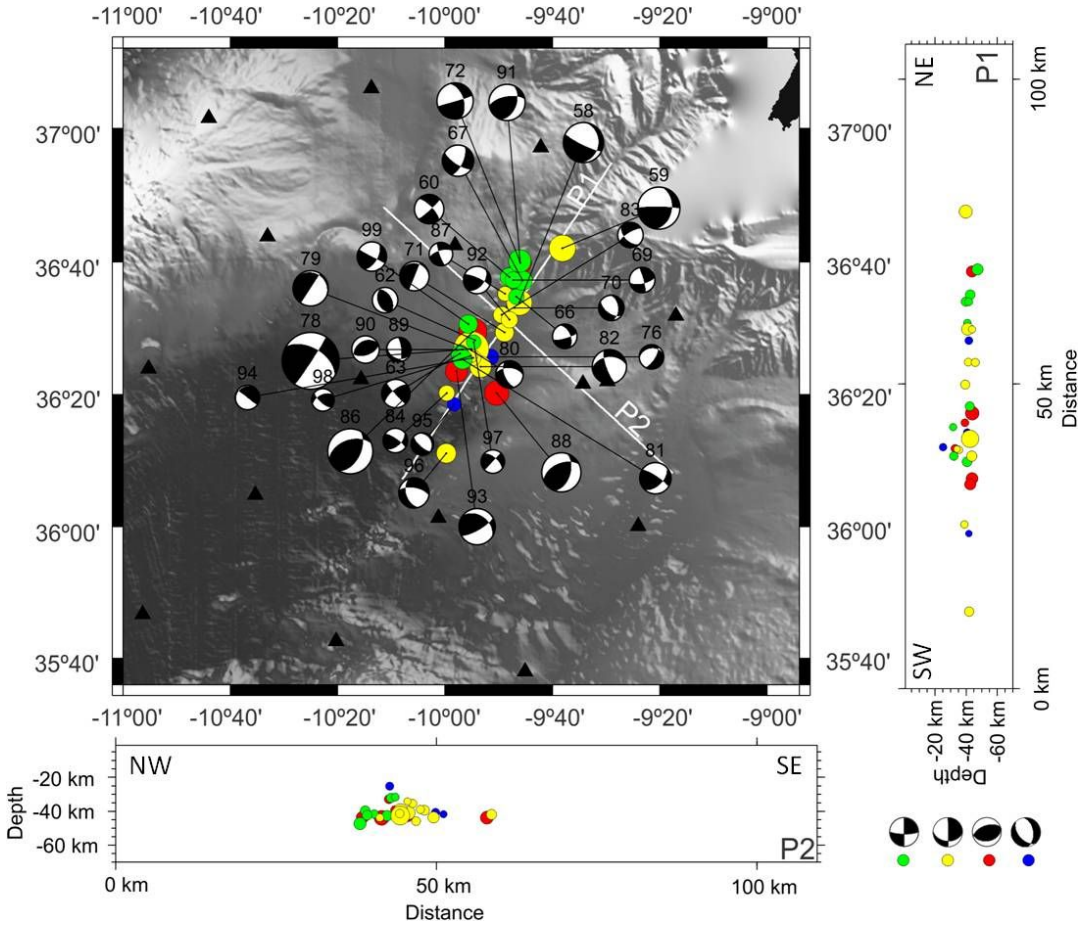

Figure III.114- Focal mechanism solutions with quality A and B in the São Vicente cluster area (green circles are pure strike-slip, red are reverse, blue are normal and yellow oblique solutions, bathymetry compilation from Zitellini et al., 2009). Dominant focal mechanisms are strike-slip and reverse dip-slip. However there are several earthquakes with oblique solutions, mostly combining pure –strike slip with reverse dip-slip component. An example is the 11th January 2008 earthquake with M_L=4.8, the highest magnitude recorded during NEAREST experiment (event number 78). This focal mechanism is similar to the one defined to the 17th December 2009 earthquake, with local magnitude 6.0.

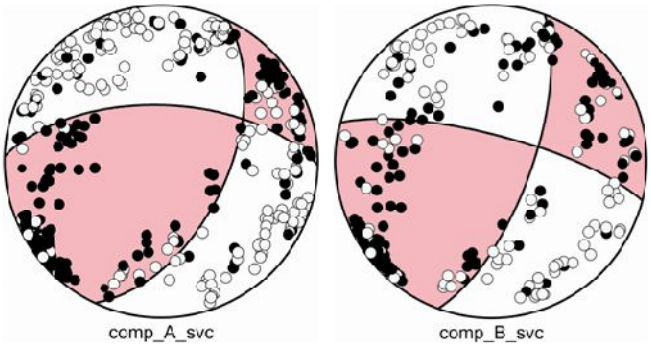

Figure III.115- Composite focal mechanisms based on A (left) and B (right) quality solutions. Composite focal mechanism based on A and B quality events have similar solutions nearly pure-strike-slip kinematics. However, several polarities are incompatible.

Table III.14- Details on the sequences resulted from cross-correlation analysis with events closely located.

Sequence	Nºevents	Nº polarities	INI_RMS	FIN_RMS
2	3	33	0.205	0.112
4	2	18	0.218	0.058
5	2	24	0.178	0.082
8	3	24	0.143	0.053
10	2	32	0.175	0.107
11	4	17	0.279	0.189
15	2	18	0.272	0.051

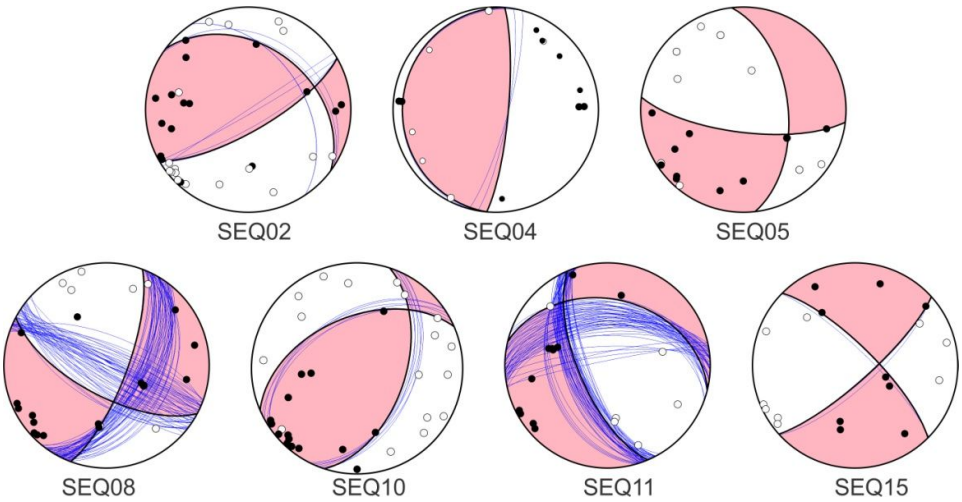

Figure III.116- Composite Fault plane solutions for sequences determined using cross-correlation (details on the sequences in table III.14). In the São Vicente cluster is where most events occurred during the NEAREST experiment. Note that because the events are closely correlated we could identify 7 sequences with reasonable focal mechanism solutions with few incompatible polarities.

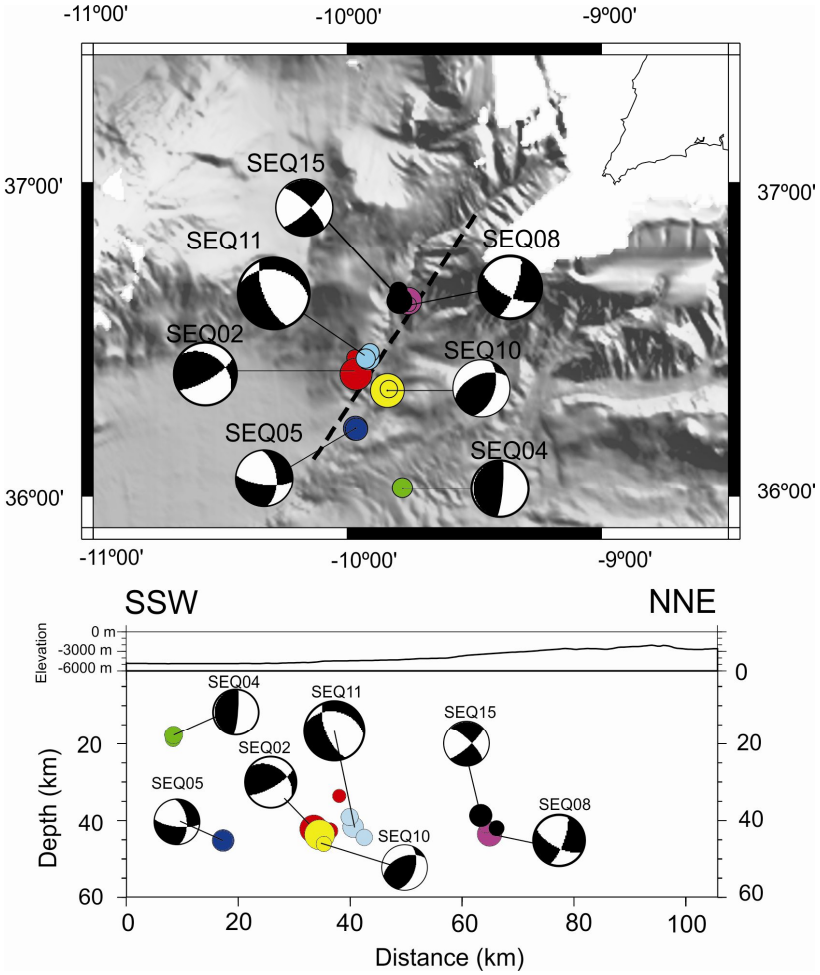

Figure III.117- Composite focal mechanisms for sequences depicted in Table III.14. On top is a map view with epicenters locations and on the bottom is a profile showing hypocenters (profile location is in map view-dashed line, circles with different colours separate events from distinct sequences, bathymetry compilation from Zitellini et al., 2009). There is no clear correlation between a type of focal mechanism with a particular area in the map view or in depth.

Finally, we present the fault plane solutions in the area of the Gulf of Cadiz Accretionary Wedge. It is important to note that this area is in the eastern limit of the NEAREST OBS network (see Figure III.118) thus the events locations and source mechanism are less accurate. Nevertheless, we computed 13 focal mechanism solutions, mostly reverse dip-slip and pure-strike-slip. Normal dip-slip focal mechanisms located at depth > 40km were also obtained.

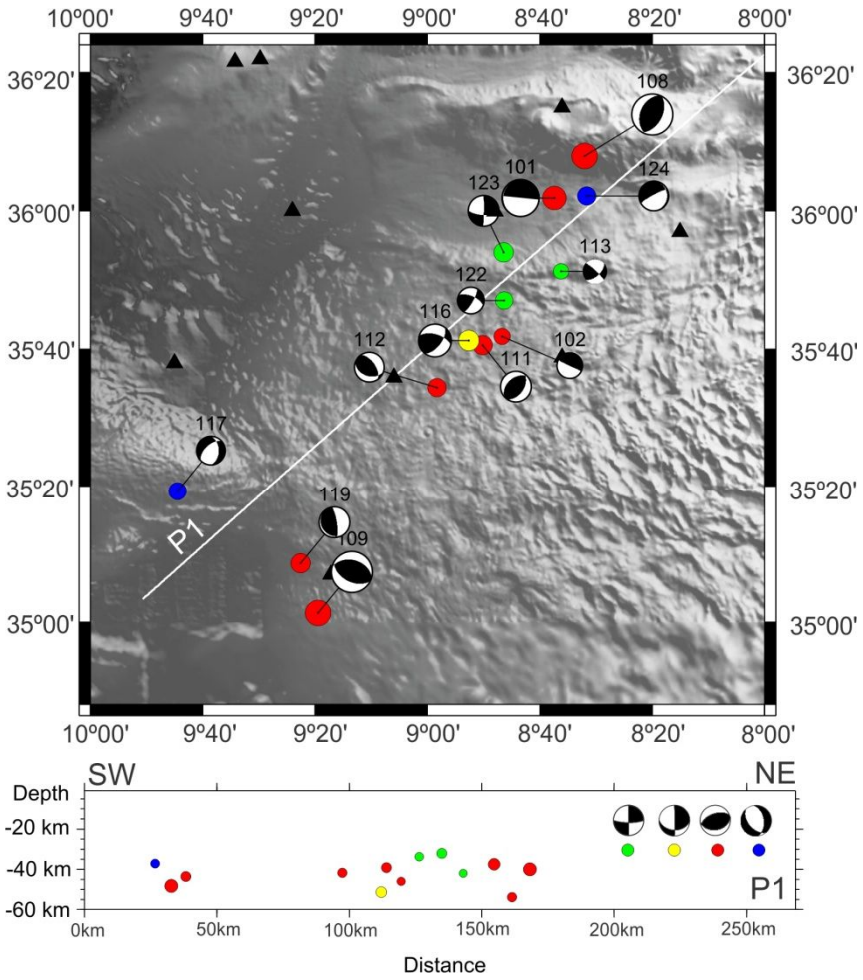

Figure III.118- Focal mechanism solutions with quality A and B in the Accretionary Wedge and Portimão bank area (green circles are pure strike-slip, red are reverse, blue are normal and yellow oblique solutions, bathymetry compilation from Zitellini et al., 2009). Several reverse dip-slip solutions are obtained sub-parallel to the accretionary wedge striking direction. Again it is worth notice a normal dip-slip focal mechanism solution at 40 km in depth.

The final results are in agreement with the preliminary solutions published by Geissler et al. (2010) based on the best events reported from the NEAREST experiment. Additionally, these results are also in conformity with previous studies for this area (Grimison and Chen, 1986; Buforn et al., 2004; Stich et al., 2010). Normal dip-slip solutions were also identified in the upper mantle, as it was already reported by Stich et al (2010) and Geissler et al. (2010).

Both individual focal mechanisms and composite solutions within the three seismicity clusters indicate that seismicity results from the combination of different deformation processes. The compressive SHmax resulting from most of the solutions is in agreement with the transpressive plate kinematics reported by several authors between Iberia and northwest Africa; however, the normal fault solutions located in the mantle require an alternative explanation.

III.4.Tensor analysis

III.4.1.Introduction

We used the **F**ocal **M**echanism **S**tress **I**nversion (FMSI) package to define the stress tensor of the studied area based on focal mechanism data. This program uses a grid search inversion technique to find the best fitting regional stress tensor, a method described in Gephart and Forsyth (1984). The process implies a simultaneous adjusts of individual fault plane solutions and the principal stress directions. The best stress model imposes the smallest rotation on fault plane solutions to consistently combine stress orientations with fault slip direction and sense (more details on the method in chapter II).

III.4.2.Processing sequence

The FMSI package was changed by Luis Matias to simplify processing sequence. So, the following steps were taken:

1. Since seismicity is distributed in three areas, we subdivided the FMSI analysis accordingly. The input data results from the conversion from GMT plotting *.mec* format to FMSI format *.inp* using dataset application. The data weight could be attributed from estimated magnitude;
2. A preliminary evaluation of the P and T data were established with a modified version of the PTplot application. This program uses also GMT plotting files format to plot a lower hemisphere equal area stereographic projection of the P and T axis derived from focal mechanism solution. This projection helps to identify the variability of the initial data;
3. The inversion for the stress tensor was reached using a modified version of the *fmsilm* application. This version uses an input file *fmsi.in* with the parameters for the inversion. In this input file the user defines the initial maximum and minimum stress axis directions (σ_1 and σ_3). The *fmsilm* application performs a three steps grid search of the best fitting stress model. In the first inversion, a coarse GRID search is defined with 10 degree spacing around a predefined σ_1 (maximum stress) and σ_3 (minimum stress) directions, an angular variation and principal stress relative magnitude ($R= (\sigma_2- \sigma_1)/ (\sigma_3- \sigma_1)$). The subsequent inversion steps uses grid searching of 5 and 2 degrees. The initial stress directions were defined by previous inversion solutions. In the input model one of the following methods for inversion process has to be defined: exact, approximate or pole rotation methods. We used the exact method which finds the minimum rotation about any axis of general orientation which is need to match the observed fault plane/slip directions with one consistent with a given stress model (Gephart and Forsyth, 1984). The output files are a .out file with the tested stress directions and misfit residual and a

.fmsi file with the best fitting stress model residuals, σ_1 and σ_3 directions and the relative stress magnitude estimation (R).

4. To evaluate the best stress tensor model we used Plo-s1.bat script which plots a stereonet with the contour residuals and the points used to constrain this contours lines.
5. Additionally, we checked fault plane solutions consistency with the best stress tensor using *fmsietab*. This application delivers an output file with the misfit rotations of each fault observation (for principal and auxiliary planes) and a given stress model computed based on the exact method. Planes with resulting low shear stress are marked with *. Another consistency criterion is unambiguity of the preferred fault plane selection. The difference between the rotation misfit of both planes (principal and auxiliary) should be > 10° so that we can clearly define the principal fault plane solution. The preferred fault plane should also have a misfit lower than 20°. This is automatically inspected with *bestslip* application (developed by Luis Matias).
6. Finally, we rechecked fault planes fit with the regional stress model in a Mohr's diagram. This allows the visual inspection of the consistence of a combination of fault planes with reasonable criteria of failure. Slip is most likely on planes with high shear stress and low normal stress (Gephart and Forsyth, 1984).
7. If the combination of fault plane solution and regional stress tensor resulted in a large misfit we repeated the processing steps with a new set of focal mechanism selection. This procedure was repeated until we meet a reasonable misfit.

III.4.3.Results

We started by testing the inversion process with a compilation of the best focal mechanism solution of each cluster and using local magnitude as weighting parameter. In all cases, for the same events selection, the average rotation misfit was higher with weighted data. As an example, in the Gorringe cluster the same dataset had a tensor solution with an average degree misfit of 8.26 and 7.95, with and without magnitude weighting, respectively. This can result from the heterogeneity of focal mechanism solutions in this micro-seismicity setting as discussed elsewhere in this work. Accordingly, we excluded weighting from subsequence tests. The main results are presented next.

Gorringe Bank cluster

The FMSI inversion is a trial and error process that can be improved by testing different datasets. In the first step, we included all the best focal mechanism solution (see Figure III.119) and subsequently improved the dataset by excluding events that were inconsistent with the best tensor solution. We

started with 16 events and an average error of 7.95° and concluded with 14 events and 4.40°. The details on the dataset are summed up in table III.15 (dataset all_AB).

We plotted P-T axis for all_AB dataset and resulting σ_1 in a stereographic equal area lower hemisphere projection (Figure III.120). The resulting σ_1 is in agreement with SHmax striking direction, roughly NW-SE, previously published data for the area (Grimison and Chen, 1986, Ribeiro et al, 1996, Stich et al, 2003, Carrilho et al, 2004). Finally, we recheck fault planes fitness with the regional stress model in a Mohr diagram (Figure III.121). Because slip on a fault is privileged in high shear and low normal stress conditions in some events slip is unfavored with this stress model because shear stress (τ) is low and normal stress (σ_n) is too high (e.g. 1, 4 and 5).

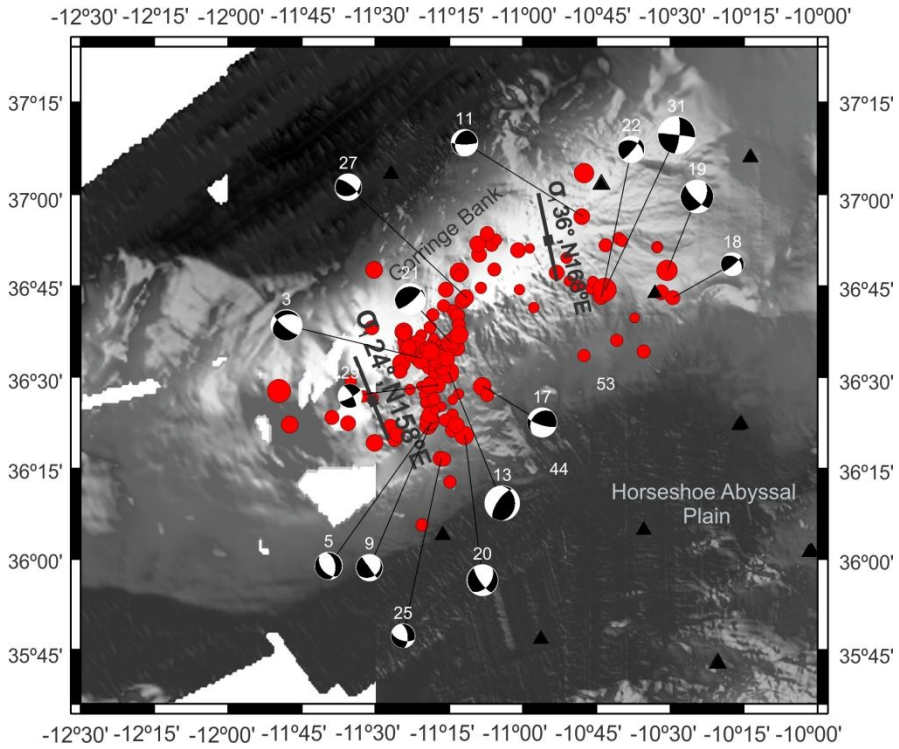

Figure III.119- Epicenters distribution in the Gorringe cluster (bathymetry compilation from Zitellini et al., 2009). Also is shown the focal mechanisms selected for tensor inversion. Initial, we used all events in the same dataset. Yet, because in the Gorringe bank seismicity is distributed asymmetrically, we subdivided our catalogue into to a NE and SW sub-clusters.

Table III.15-Statistics and resulting tensor based on selected datasets.

dataset	statistics		tensor						
	Nº events	RMS misfit (°)	σ1, dip (°)	σ1, az(°)	σ2, dip (°)	σ2, az(°)	σ3, dip (°)	σ3, az(°)	R
all_AB	14	4.403	58	120	29	329	13	231	0.4
NE	6	1.545	36	168	45	306	23	60	0.8
SW	7	2.302	24	158	65	358	8	251	0.4

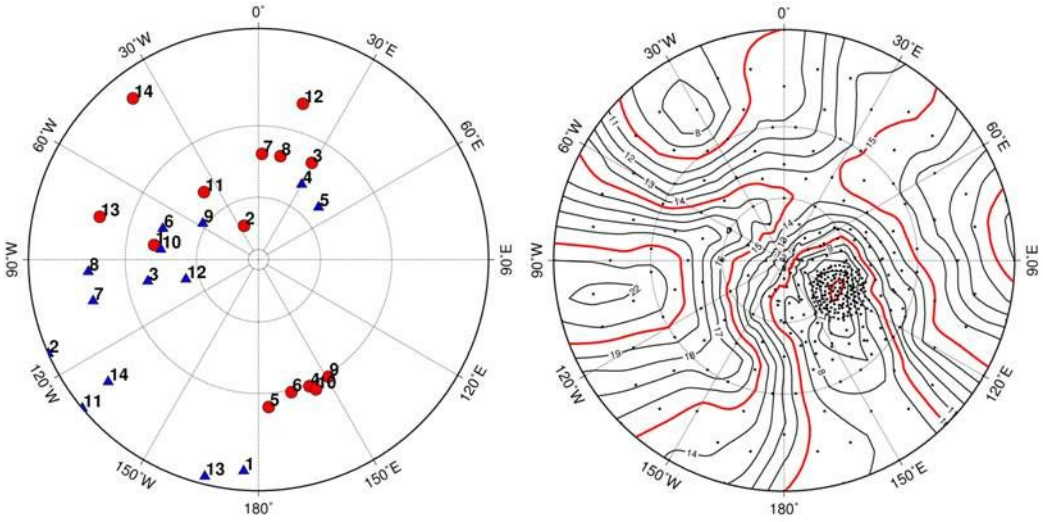

Figure III.120- - PT axis (left- red defines pressure and blue is tension) and stereographic misfit plot of the grid-search for σ_1 (right) for AB dataset (lower hemisphere equal area stereographic projection).

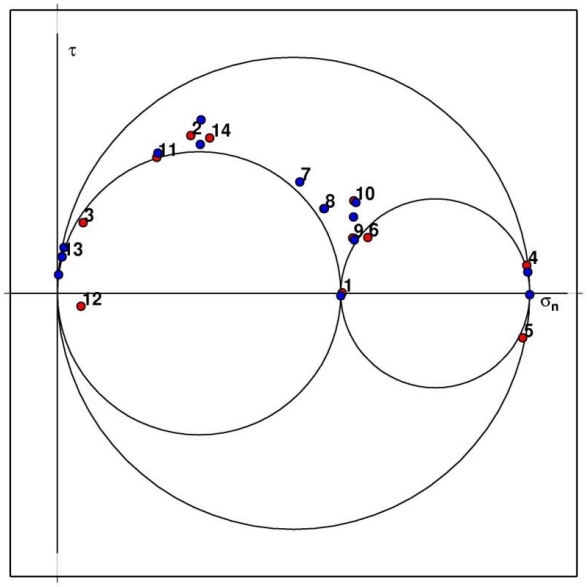

Figure III.121- The MOHR diagram for AB dataset with the best fitting fault plane solutions (blue are the rotated fault planes and red are the original). Note that for events 1, 4 or 5 slip is unfavored with this stress model because shear stress (τ) is low and normal stress (σ_n) is too high.

To improve fault plane solutions-stress tensor model consistency we subdivided the original AB focal mechanisms dataset in two sub-groups because the seismicity distribution along the Gorringe cluster is asymmetric (see Figure III.119):

1. One in the NE sector that initially integrated 12 events with an average minimum rotation misfit of 5.325 °. The final dataset, after excluding fault plane with low shear stress, included only 6 events and the minimum average misfit was 1.545 ° (sum up on the dataset and tensor directions in Table III.15, P-T axis and σ_1 stereographic projections in Figure III.122);

2. One in the SW sector, initially with 10 events and a RMS 6.595. After excluding 3 events, we reduced the average minimum degree misfit to 2.302 (sum up on the dataset and tensor directions in Table III.15, P-T axis and σ_1 stereographic projections in Figure III.124).

For both sub-clusters, the σ_1 azimuth is similar, 158° and 168°, for NE and SW datasets respectively. The dip angle is higher to the NE ≈36° and lower to the SE ≈24°. Both dip angle are considerably lower than the global solution (AB dataset) for which dip angle was 58°.

The tensor solution for the NE sub-cluster shows R=0.8, considerably different from the results for both global and SW datasets (R=0.4 for both, Table III.15). In the Mohr diagram (Figure III.123), the high R value results in the following relative proportions between the principal stress directions: dimension $\sigma_1 >> \sigma_2$ and σ_3. The NE sub-cluster is clearly in a compressional regime. Also note that at least two events are in an unfavorable slip condition (4 and 1). Accordingly, these events are the ones where P-axes diverge more clearly from σ_1 azimuth solution (see Figure III.122).

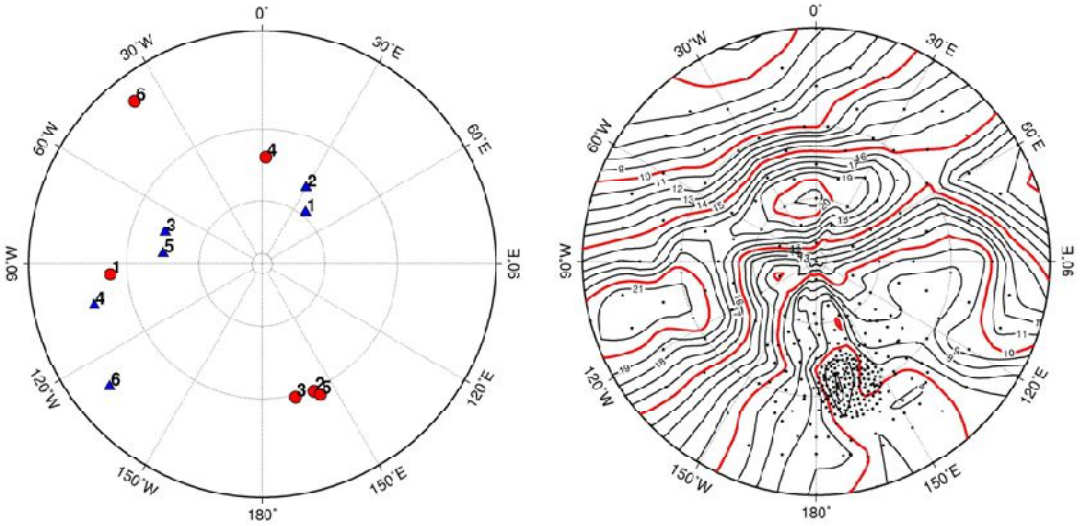

Figure III.122- P (red) T (blue) axes (to the left) and σ_1 (to the right) for NE dataset lower hemisphere equal area stereographic projection. The contour lines defines isolines of tensor model's misfits. Note that in this case the contour lines with lowest misfit are coincident with a group of P-axis in PT axis projection (left- events 2, 3 and 5).

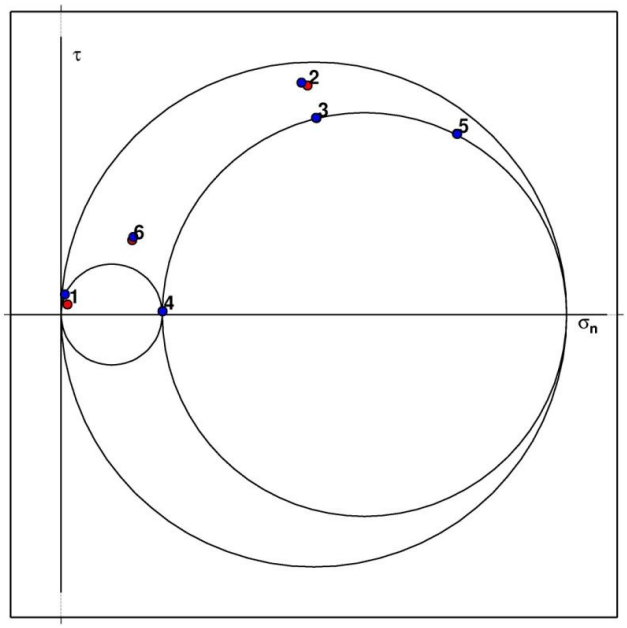

Figure III.123- The MOHR diagram for the northeastern dataset with the best fitting fault plane solutions (blue are the rotated fault planes and red are the original). Events 4 and 5 show unfavorable slip conditions.

In the SW sub-cluster, all events seem to be consistent with the resulting tensor model. In the Mohr diagram (Figure III.125) all events fit slip conditions. The relative proportion between the principal stress axes are in agreement with global stress dataset, R=0.4. These results indicate that:

1. The asymmetric distribution of the focal mechanism solution in the Gorringe cluster, with more events in the SW, biased the global dataset result.
2. The NE and SW-sub-clusters are distinct and may result from different seismogenic mechanisms.

Accordingly, the best fitting tensor are the solutions resulting from sub-cluster analyses.

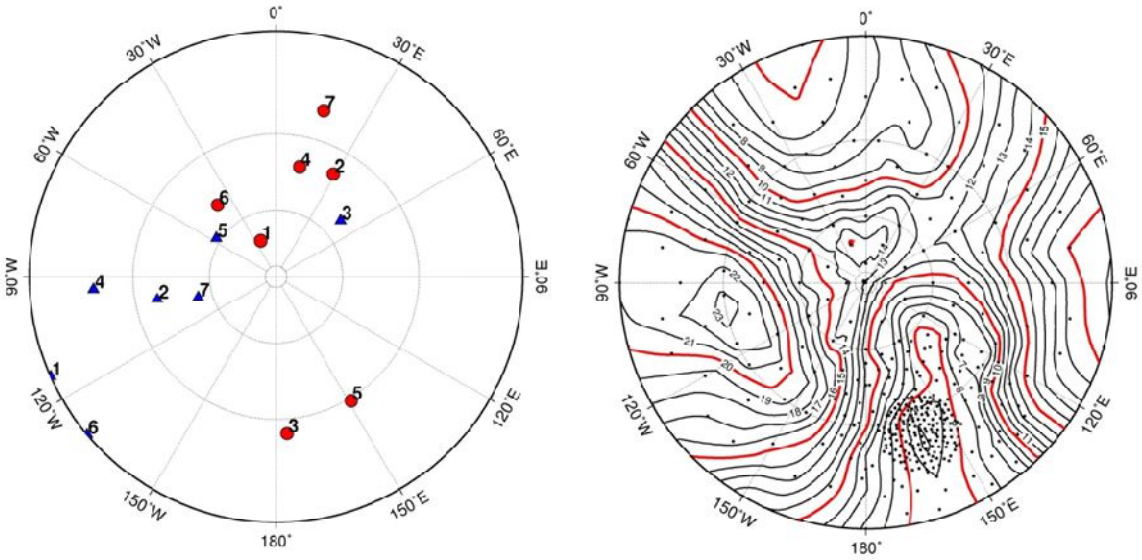

Figure III.124 - PT axis (left) and σ_1 (right) for SW dataset lower hemisphere equal area stereographic projection with contour lines of the misfit distribution.

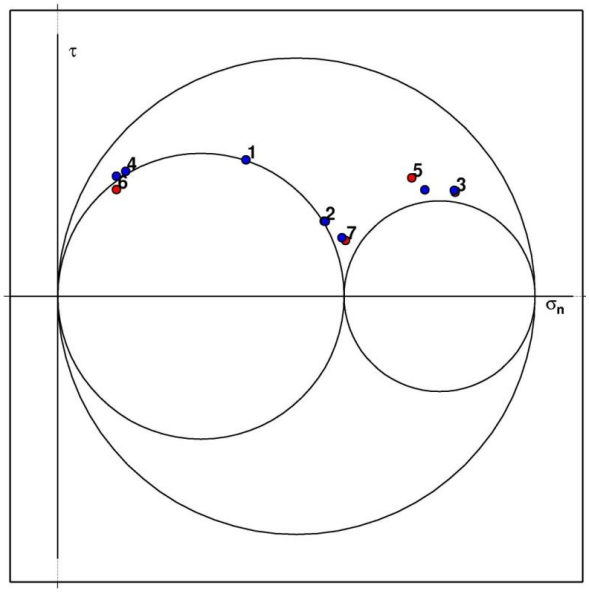

Figure III.125- The MOHR diagram for the southwestern dataset with the best fitting fault plane solutions (blue are the rotated fault planes and red are the original). All events seem to be consistent with the resulting tensor model.

Horseshoe cluster

We started the Horseshoe cluster analysis with 21 best focal mechanism solutions (see Figure III.126). The first inversion test resulted in an average minimum rotation misfit of 5.963 degrees, with 3 very low shear slip events. In the next step, we removed inconsistent data and ended up with all_AB dataset in Table III.16 (and Figure III.127 for P-T axes and sigma 1 details). In the Mohr diagram only one event (see event 9 in Figure III.128) is inconsistent with the tensor model.

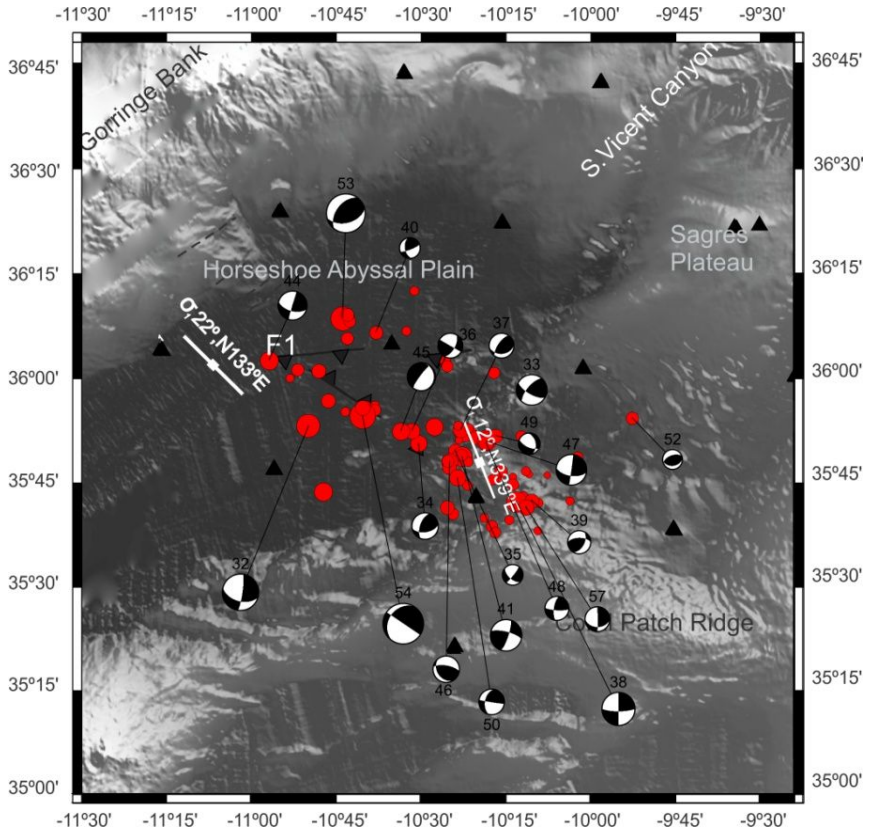

Figure III.126-Seismicity in the Horseshoe cluster, showing the focal mechanisms solutions selected for tensor inversion (bathymetry compilation from Zitellini et al., 2009). We tested two datasets, one including all the events and another with western and eastern sub-clusters. This subdivision is coherent with focal mechanism pattern. To the East, most fault-plane solutions are roughly strike-slip solutions while to the West; we observe a more complex pattern.

Table III.16- Statistics and resulting tensor based on selected datasets.

dataset	statistics		tensor						
	Nº events	RMS misfit (°)	σ1, dip (°)	σ1, az(°)	σ2, dip (°)	σ2, az(°)	σ3, dip (°)	σ3, az(°)	R
all_AB	19	3.946	11	338	63	226	24	73	0.5
E	12	3.271	12	339	65	221	21	74	0.5
W	5	1.116	22	133	61	269	19	35	0.7

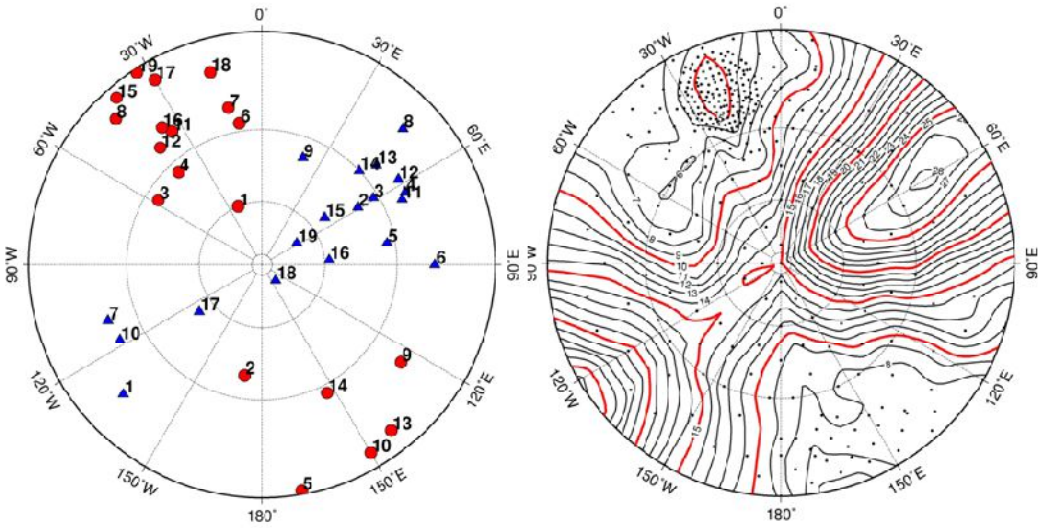

Figure III.127- PT axis (left) and to the right is the stereographic misfit plot of the grid-search for σ_1 for AB dataset.

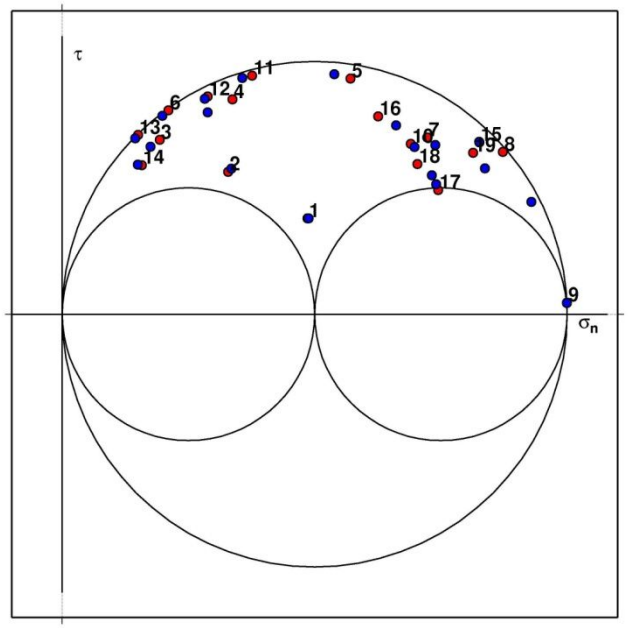

Figure III.128- The MOHR diagram for the AB dataset with the best fitting fault plane solutions (blue are the rotated fault planes and red are the original). Note that only event 9 is inconsistent with the resolved tensor model.

The resulting maximum compression is similar to Geissler et al. (2010) preliminary results for the same area (σ_1 with orientation 12 °, N351°E, see reference work). We consider that differences result from adding new events to initial dataset in Geissler et al (2010). Yet, divergence is larger for dip of the minimum stress axis that is≈2°and R solution ≈0.7 (idem) contrasting with our results, ≈63° and 0.5, respectively. It is worthwhile to consider that the average misfit is lower in the preliminary results ≈2.2° but only 13 events were included in the inversion process.

To improve our result we tested 2 sub-clusters; one to the East where most focal mechanism solutions are clearly strike –slip and to the W with a more

complex pattern (see Figure III.126). We started with 14 events in the E sub-cluster and a RMS of 6.43. The final dataset had 12 events and an average misfit of 3.271°. In the W sub-cluster, we selected 5 events and the final error was 1.116°. The eastern sub-cluster results (see Figure III.129 and Figure III.130) are similar to the total dataset but the error is lower. The stress tensor for western dataset is completely different from the remaining results but the error is considerably lower and stress directions are consistent with the Gorringe cluster, further to the west (see Figure III.131 and Figure III.132).

By subdividing the dataset into two sub-clusters, we decreased both the stress model misfit and improved the slip conditions fit to the fault plane solutions.

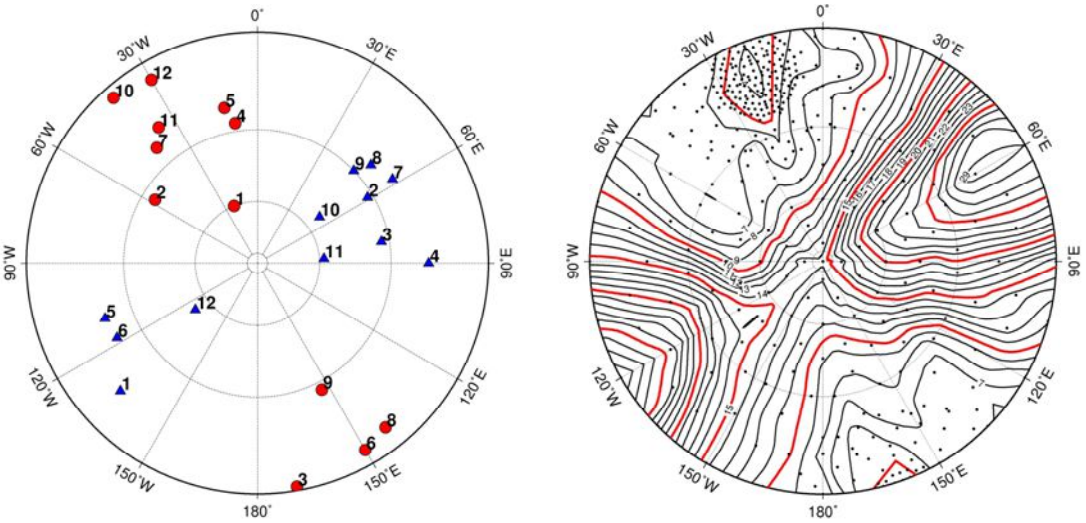

Figure III.129- PT axis (left) and σ_1 (right) for E dataset lower hemisphere equal area stereographic projection. Isolines define the result of gird search misfits for tested σ_1 solutions.

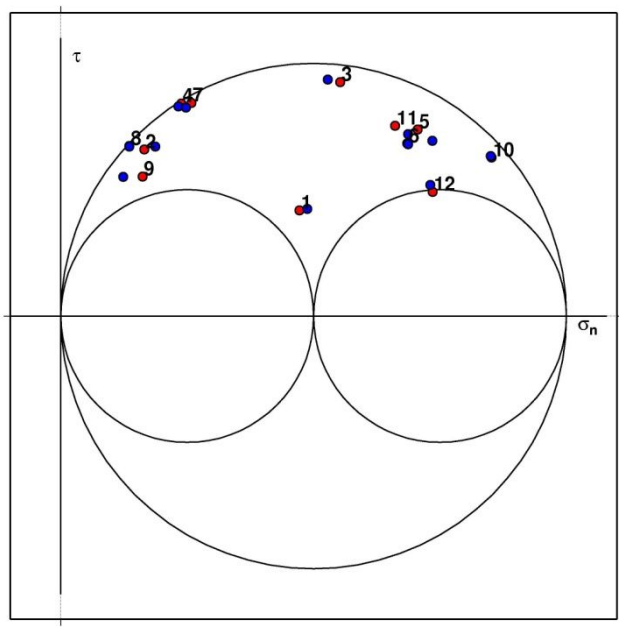

Figure III.130- The MOHR diagram for the east dataset with best fitting fault plane solutions (blue are the rotated fault planes and red are the original). All selected focal mechanisms are consistent with the tensor resulting from this sub-dataset.

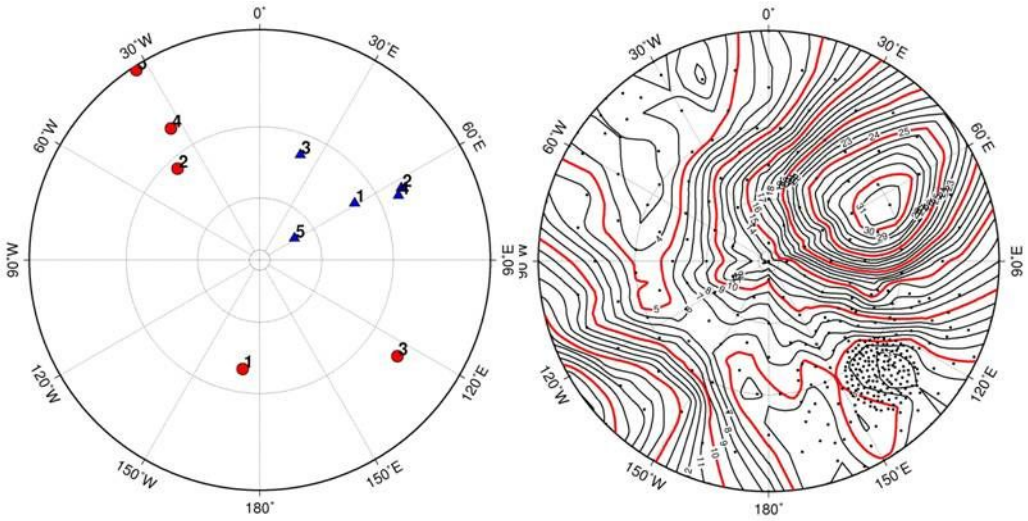

Figure III.131- PT axis (left) and σ_1 (right) for W dataset lower hemisphere equal area stereographic projection. Isolines define the result of gird search misfits for tested σ_1 solutions.

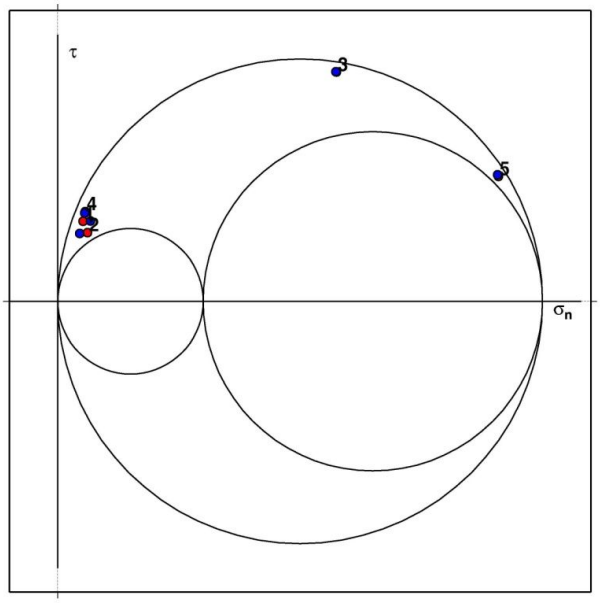

Figure III.132- The MOHR diagram for western dataset with the best fitting fault plane solutions (blue are the rotated fault planes and red are the original). All events are consistent with the stress tensor**.**

São Vicente cluster

The São Vicente cluster recorded the largest number of events (Figure III.133). The initial dataset included 32 events and the first inversion test resulted in an average misfit of 7.937°. The final dataset included 20 events and the average misfit was 3.836°. The P-T axes distribution in a stereographic projection (Figure III.134) is heterogeneous with strike direction ranging from 90°-180° and 300°-360°.

The best fitting σ_1 strike is approximately NW- SE (Figure III.134) diverging from Geissler et al., (2010) preliminary results (roughly WNW-ESE) but in agreement with previous works (e.g. Carrilho et al., 2004). The main difference between this work and Geissler et al. (2010) is the dataset as in this work we present a complete catalogue for NEAREST experiment. The additional data resulted in a different stress tensor model for São Vicente cluster. Also we could reduce the model misfit from 4.6° in the Geissler et al, (2010) to 3.8°. The Mohr diagram shows that for most events are located in favorable slip conditions (except event 9 or 20, see Figure III.135) for the derived stress tensor model.

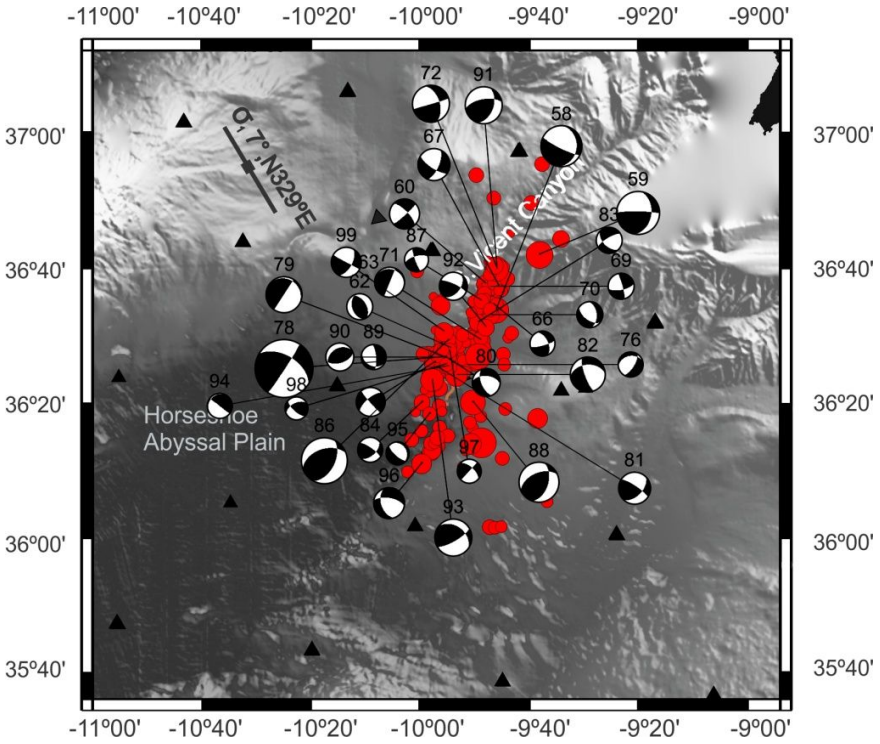

Figure III.133- Seismicity in the São Vicente Cluster (bathymetry compilation from Zitellini et al., 2009). We started by using all fault plane solutions in a single dataset. Afterwards, we subdivided the dataset into two sub-clusters.

Table III.17- Statistics and resulting tensor based on selected datasets.

dataset	statistics		tensor						
	Nº events	RMS misfit (°)	σ1, dip (°)	σ1, az(°)	σ2, dip (°)	σ2, az(°)	σ3, dip (°)	σ3, az(°)	R
all_AB	20	3.836	7	329	83	166	2	59	0.30
S	10	2.136	50	157	14	50	37	310	0.3
N	10	3.368	6	309	30	43	59	209	0.4

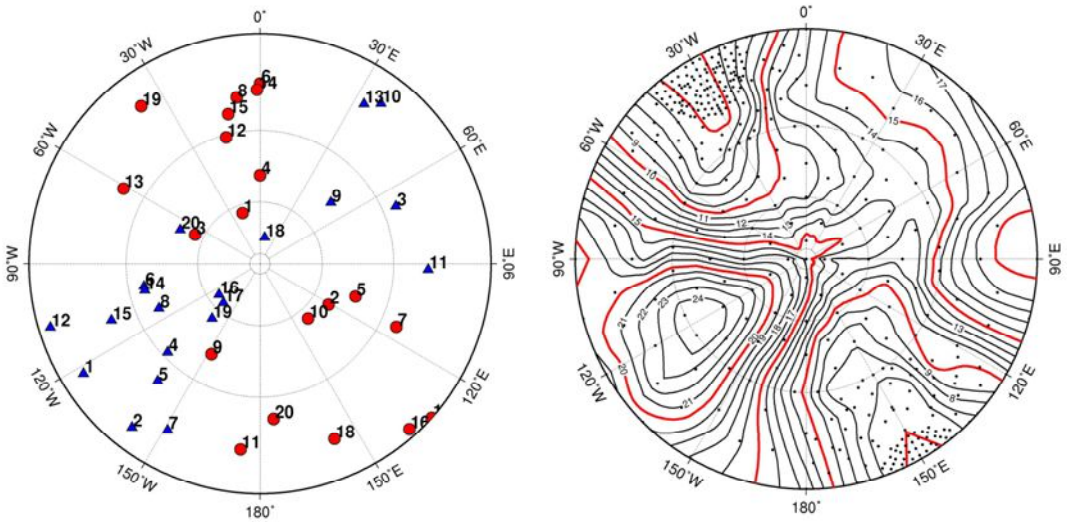

Figure III.134 - PT axis (left) and σ_1 (right) for AB dataset lower hemisphere equal area stereographic projection. Isolines define the result of gird search misfits for tested σ_1 solutions.

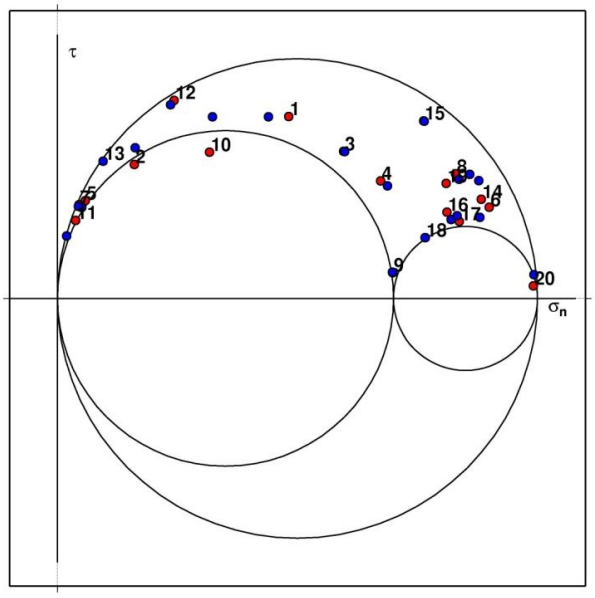

Figure III.135- The MOHR diagram for AB dataset with the best fitting fault plane solutions (blue are the rotated fault planes and red are the original). The Mohr diagram shows that most events are located in favorable slip conditions (except event 9 or 20).

Close inspection at the distribution of the seismic events in this cluster shows the existence of a roughly linear alignment of hypocentres along the São Vicente Canyon. Conversely, we observe that to the North events distribution is more discrete and to the South more diffuse. Accordingly, we divided the initial dataset in two sub-clusters, one to the North and the other to the South. The result shows that in the South dataset, the best fitting σ1 is roughly NNW-SSE and dipping 50° south. Yet, in the P-T axes stereographic projection (see Figure III.136) most plots are less steep, only 3 out of 10 events are in the dipping range between 30° and 60°. In the Mohr diagram we recognize that only 4 events have reasonable slip conditions (see events 7, 8, 1 and 10 in Figure III.137).

The North dataset shows a best fitting σ1 ≈NW-SE coherent with most P-T axes plot in the stereographic projection (see Figure III.138). The best fitting tensor has an average minimum degree misfit of 3.4°. In the Mohr diagram shows at least three events (1, 5 and 7 in Figure III.139) have unfavorable slip conditions with low shear stress and high normal stress at the principal fault plane solutions. Nevertheless, the stress direction is consistent with previous works.

In opposition to both Gorringe and Horseshoe clusters, in the São Vicente cluster the best fitting stress tensor results from the AB-dataset. Although, the events subdivision resulted in lower RMS misfit the faults slip conditions less favorable.

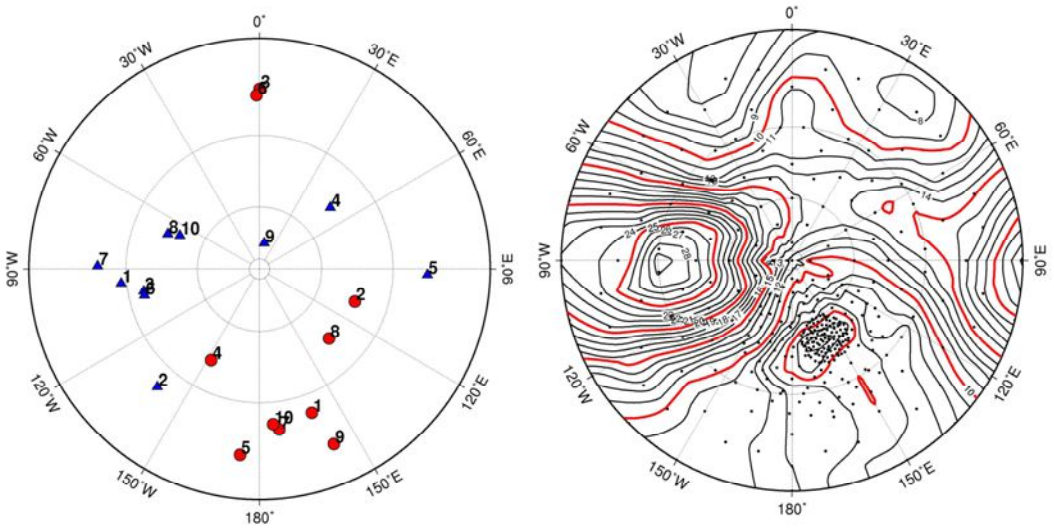

Figure III.136- PT axis (left) and σ_1 (right) for S dataset lower hemisphere equal area stereographic projection. Isolines define the result of gird search misfits for tested σ_1 solutions.

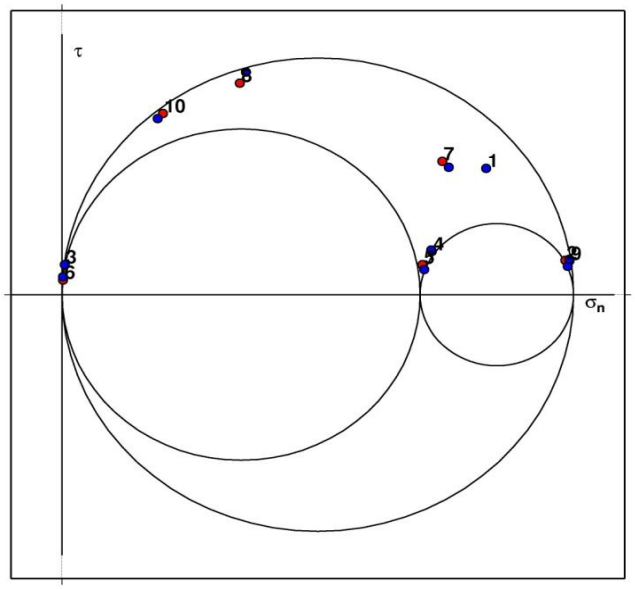

Figure III.137- The MOHR diagram for southern dataset with the best fitting fault plane solutions (blue are the rotated fault planes and red are the original). With this stress tensor, several events show unfavorable slip conditions (events 2, 3, 4, 5, 6 and 9).

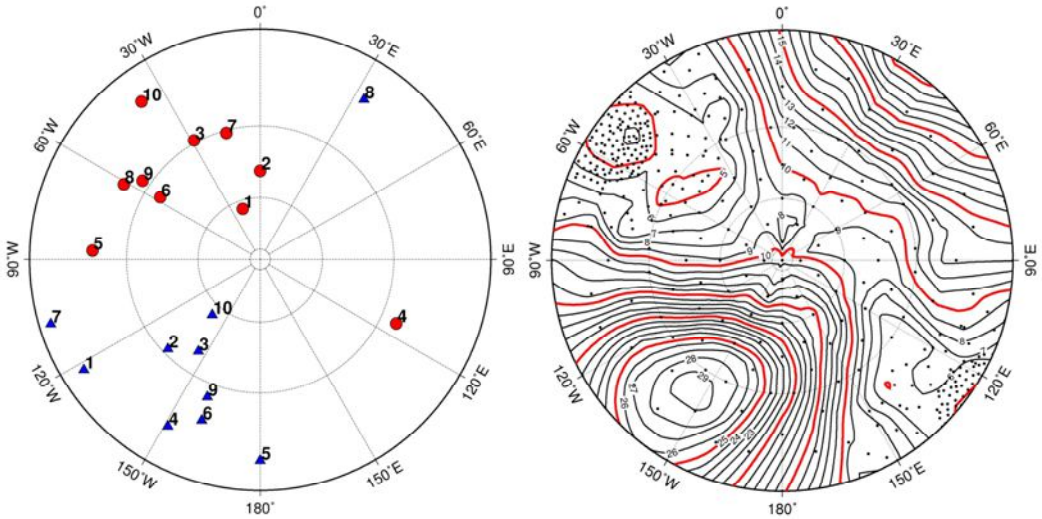

Figure III.138 - PT axis (left) and σ_1 (right) for N dataset lower hemisphere equal area stereographic projection. Isolines define the result of gird search misfits for tested σ_1 solutions.

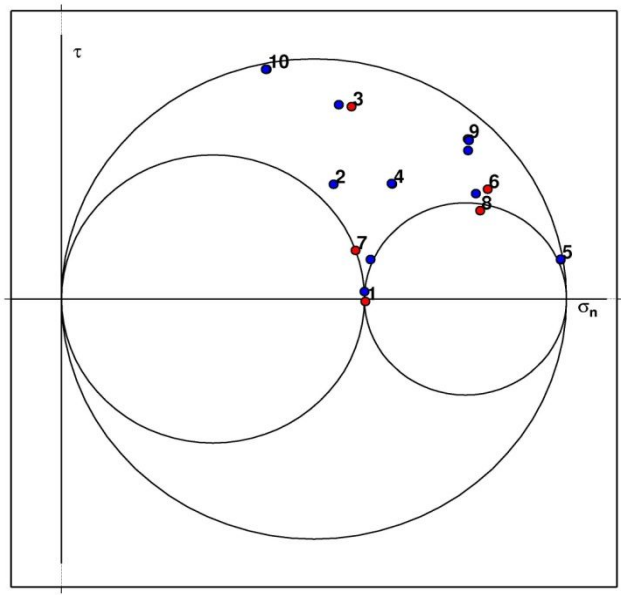

Figure III.139- The MOHR diagram for the northern dataset with the best fitting fault plane solutions (blue are the rotated fault planes and red are the original). Note that events 1 and 5 are inconsistent with the stress tensor model for this sub-dataset.

III.5.Summary and Discussion

The meaning of the persistent small to intermediate magnitude seismicity recognized in the Gulf of Cadiz is still particularly not understood. To address this problem the EC project NEAREST conducted a passive seismic experiment in the Gulf of Cadiz with the deployment of temporary OBS network. The examination of the continuous data stream presented here allowed the detection of a number of local events that were not identified by the land networks of Portugal, Spain or Morocco.

Preliminary earthquakes locations resulted in 590 events with local magnitude between 0.9-4.8, located in the deployment area with an average misfit ≈0.7s.

One of the main objectives was to obtain an accurate hypocentres location. Solving earthquakes locations depends on several factors including survey network geometry, seismic phase identification and arriving time readings accuracies as well as the knowledge on the structure and nature of the seismogenic lithosphere. Other limitation outcomes from applying one dimensional velocity model to determine hypocenter location in a tri-dimensional variable space. This problem is particularly relevant when there is a high lateral unpredictability in the lithospheric structure as in the case of our study area.

We improved hypocentres determination by selecting a restrict dataset (443 events), within the deployment area and applying three different location methods: Joint Hypocenter Determination (JHD), simultaneous inversion for hypocenter-velocity model and double-difference techniques. In JHD method, lithospheric variability and subsurface geology were introduced by testing different velocity models based on local geophysical data and adding independent P and S stations corrections. The average misfit of the initial locations decreased from 0.76s to 0.32s.

We used the VELEST, for simultaneous inversion of hypocenter location, stations corrections and 1D velocity model for P and S waves. As before, stations corrections will account for particularly subsurface geological variability. However, additional lithospheric variations could be introduced by adopting variable seismic velocities and Vp/Vs ratio for each layer within the limitation the 1D velocity model. We decreased final locations average misfit from 0.316 to 0.275 for the events within the deployment area.

Finally, we tested the double-difference location method with hypoDD. This method is adequate if applied for events closely related because in these conditions it is assumed that the travel time difference between two events recorded in the same station results exclusively from the distance between the hypocentres. Accordingly, hypoDD uses a P-velocity model; S-velocities are derived based on fixed Vp/Vs and no stations corrections. Preliminary results indicate that a decrease in depth distribution in compare with previous locations derived from JHD and VELEST. However, we need to improve the accuracy of our results by testing different parameters and including wave cross-correlations.

The analysis of the complete data set reveals 3 main clusters of earthquakes: in the Gorringe Bank, Horseshoe Abyssal Plain and São Vicente Canyon. The later coincide with the location of the 3 larger instrumental earthquakes in the area: i) both the 28th February 1969 (Mw≈7.8) and the 12th February 2007 (Mw=6.0) and ii) the 17th December 2009 (M_W=5.5), respectively. Most of the small magnitude earthquakes are located in the mantle (depth between 30 and 50 km), like the hypocenters of these three earthquakes derived from waveform inversion. With respect to land stations solutions it appears that the same earthquakes are relocated mainly to SW and deeper.

Seismicity depths reaching a maximum of 50 km for events with Mb > 5.0, in the Gulf of Cadiz, was already referred in Grimison and Chen (1986). In the same work, this depth is described as coincident with ≈600°C±100°C isotherm in an old oceanic lithosphere. Later on, Buforn et al., 2004 also suggested, based on a seismic catalogue comprising events with magnitudes ≥ 3.5, that seismicity in the area is mostly located above 50 km in depth. Our results are in agreement with these preview studies. However, earthquakes locations are improved with NEAREST network as result we can clearly identify a bimodal distribution of seismicity in depth, with a dominant interval between 30-50 km. This was not clear from previous works retrieved restrictedly from land permanent seismic networks locations. In NEAREST preliminary data published in Geissler et al. (2010), it was observed a striking absence of seismicity between 20 and 40 km in depth. In our study this interval is reduced to roughly between 10 and 20 km. In the Horseshoe Abyssal Plain there is an absence of events above 15 Km in depth and in the Gorringe Bank above 10 km. However, the São Vicente Canyon cluster has some events above 10 km but most seismicity is concentrate between 20 and 50 km.

Our focal mechanism solutions indicate a mixed pattern, mostly strike-slip and reverse dip-slip with a very few normal mechanisms, showing us that processes related with the local seismicity must be complex probably involving the interaction between different active geological structures and reflecting local rheological contrasts. These hypotheses will be further explored in the next chapter. The retrieved pattern was already envisaged in Geissler et al. (2010) and is coherent with Carrilho et al. (2004) results retrieved from events with $1.9>M_L> 3.7$ recorded at land seismic stations (IPMA).

NEAREST network dataset includes mostly micro-seismicity (only 6 out of 82 focal mechanism solutions with M_L >3.5). It is not clear that micro-seismicity and intermediate to high magnitude earthquakes have comparable or similar source mechanism. Conversely, NEAREST solutions are in agreement also with earlier studies of Grimison and Chen (1986), Borges et al. (2001), Buforn et al. (2004) or Stich et al. (2010) based on events with magnitudes >3.5. A rather puzzling result is the presence of normal dip-slip mechanisms at 30 or 50 km in depth. The same observation was already described both in Geissler et al. (2010) and Stich et al. (2010).

The stress tensor analysis show a maximum compression roughly parallel to NW-SE in the Western Horseshoe sub-cluster, the São Vicente cluster and the SW Gorringe to nearly NNW-SSE in the NE Gorringe and in the Eastern Horseshoe sub-clusters.

IV. Micro-seismicity in the Gulf of Cadiz. Is there a link between micro-seismicity, high magnitude earthquakes and active faults?

Sónia Silva, Pedro Terrinha, Luis Matias, João Duarte, Cristina Roque, Cesar Ranero, Wolfram Geissler, Nevio Zitellini

This chapter is presented in paper format as *accepted, with moderate revisions,* in Tectonophysics. Here, we compare the recorded seismicity with the locations of the major active faults and lithospheric transitions, pursuing evidences for minor and major earthquakes source mechanisms in Gulf of Cadiz area.

IV.1. Abstract

The seismicity in the Gulf of Cadiz is characterized by permanent low to intermediate magnitude earthquakes, occasionally disturbed by high magnitude events such as the M~8.7 1755 Great Lisbon earthquake or the M=7.9 event of 28th February 1969. Micro-seismicity was recorded during one year by a temporary network of 25 ocean bottom seismometers (OBSs) in an area of high seismic activity, encompassing the potential source areas of the mentioned large magnitude earthquakes. We combined micro-seismicity analysis with processing and interpretation of deep crustal seismic reflection profiles and available refraction data to investigate the possible tectonic control of the seismicity in the Gulf of Cadiz area. Three relationships with seismicity are explored: i) active tectonic structures, ii) lithospheric transitions and inherited Mesozoic architectures and iii) fault weakening mechanisms. Our results show that micro-seismicity is located mostly in the upper mantle. It seems to be associated with the tectonic inversion of extensional rift basins and to the transition between different lithospheric/rheological domains. Even though crustal tectonics is well imaged in the seismic profiles and in the bathymetry it shows low to inexistent seismic activity. This may be explained by the fact that thin-skinned (crustal) thrusts root on sub-horizontal décollements associated with aseismic serpentinization levels and co-seismically slip only during large magnitude events, remaining locked or slip aseismically for most of the inter-seismic cycle. We thus speculate that high magnitude earthquakes also nucleate in the lithospheric mantle and then propagate into the crust across the serpentinized layer.

Keywords**:** Nubia-Iberia plate boundary; micro-seismicity; serpentinization; neotectonics; aseismic slip; high-magnitude earthquakes

IV.2. Introduction

The Gulf of Cadiz is located in the eastern termination of the Azores-Gibraltar plate boundary between Africa and Eurasia, west of the Gibraltar arc (Fig. IV.1A). Here the plate boundary is known to be diffuse, whereas the deformation is partitioned along several discrete structures (e.g. Terrinha et al., 2009; Fig. IV.1B). The seismicity is characterized by scattered events of low to intermediate magnitude (Fig. IV.1C and Table IV.1), occasionally with high magnitude earthquakes. An example is the 1st of November 1755 Great Lisbon earthquake that had an estimated magnitude of 8.7 (Johnston, 1996) that produced a ocean-wide tsunami with waves up to 6 meter high in Lisbon and 10-15 meters at Cape São Vicente, in the Southern Portuguese coast (Baptista and Miranda, 2009). In the instrumental record, the most significant event was the 28th February of 1969 with a Ms ≈ 7.9 (Fukao, 1973, Fig. IV.1C and Table IV.1), which generated a small tsunami recorded in several tide-gauges reaching a maximum amplitude of 0.6 m in Casablanca (Baptista et al., 2009 and references therein).

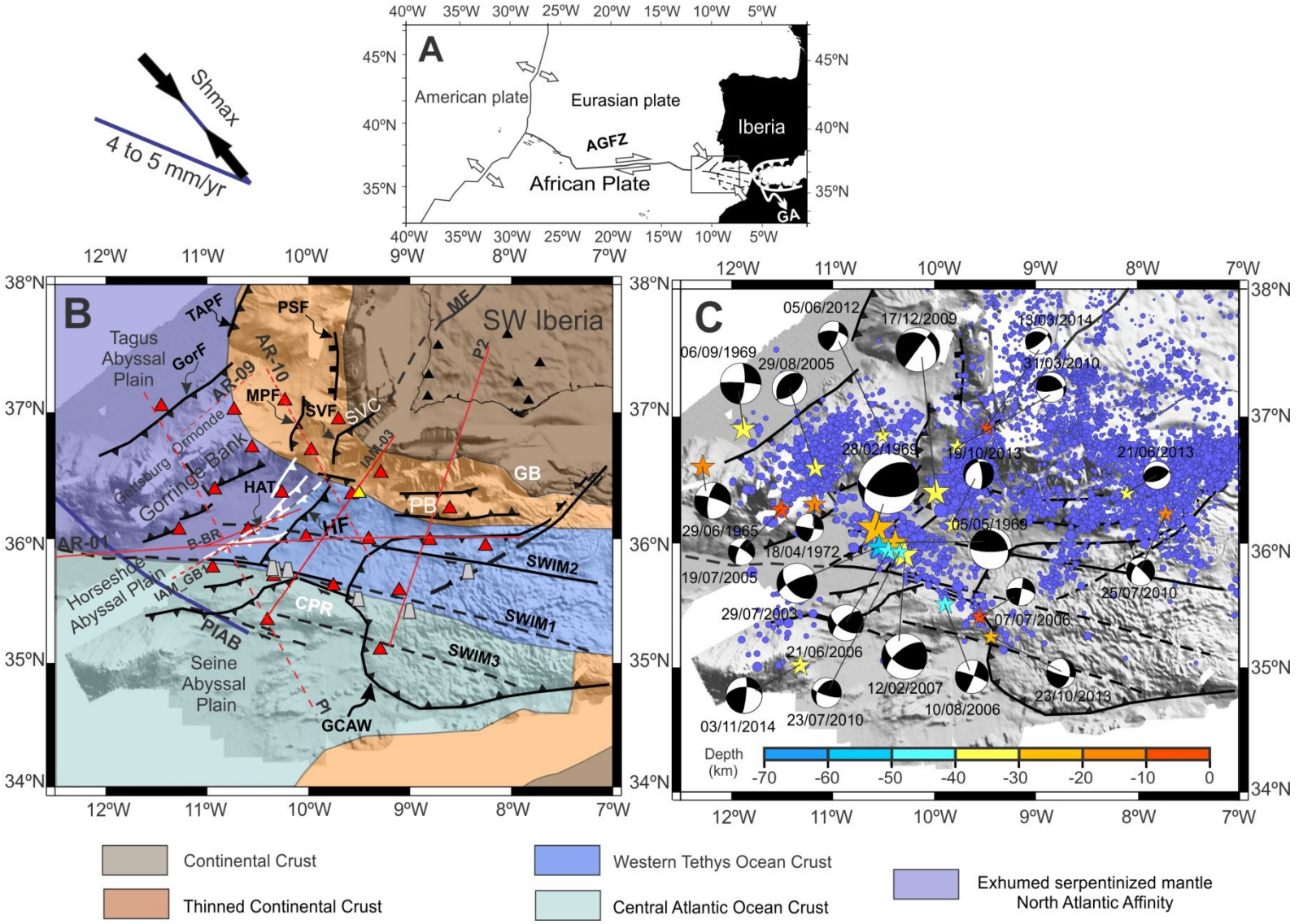
Shmax
4 to 5 mm/yr
A
American plate
Eurasian plate
Iberia
AGFZ
African Plate
GA
B
SW Iberia
Tagus Abyssal Plain
Horseshoe Abyssal Plain
Seine Abyssal Plain
Gorringe Bank
Ormonde
Gettysburg
TAPF
GorF
PSF
MPF
SVF
SVC
MF
P2
AR-01
AR-09
AR-10
IAM-03
IAM_GB
B-BR
HAT
HF
PB
GB
CPR
PIAB
PI
SWIM1
SWIM2
SWIM3
GCAW
C
05/06/2012
17/12/2009
13/03/2014
06/09/1969
29/08/2005
31/03/2010
28/02/1969
19/10/2013
21/06/2013
29/06/1965
05/05/1969
18/04/1972
19/07/2005
25/07/2010
29/07/2003
07/07/2006
21/06/2006
12/02/2007
23/10/2013
10/08/2006
03/11/2014
23/07/2010
Depth (km)
-70 -60 -50 -40 -30 -20 -10 0
Continental Crust
Thinned Continental Crust
Western Tethys Ocean Crust
Central Atlantic Ocean Crust
Exhumed serpentinized mantle North Atlantic Affinity

Figure IV.1 Gulf of Cadiz setting. A- Location of the studied area in a general geodynamic setting (AGFZ-Azores Gibraltar Fracture Zone; GA-Gibraltar arc). In the upper left, inset of the average horizontal maximum compression (black arrows, from Ribeiro et al. 1996, Borges et al., 2001, Stich et al., 2006 and Heidbach et al, 2008) and the present day average horizontal motion between Iberia and Nubia (blue line, from Argus et al., 1989, DeMets et al., 1994, Nocquet and Calais, 2004, Calais et al., 2003, Fernandes et al., 2003, Stich et al., 2006 and Serpelloni et al., 2007) B- The Gulf of Cadiz geodynamic setting. The main crustal domains are modified from Rovere et al., (2004), Gonzalez et al. (1996), Sallarès et al. (2011) and Martínez-Loriente et al. (2014). Inferred Late Jurassic–Early Cretaceous plate boundary between Iberia and Africa (PIAB in blue) is defined based on Rovere et al. (2004). Thin red lines show the location of refraction-wide-angle seismic profiles B-BR in Purdy (1975); P1 in from Sallarès et al. (2011) and P2 in Martínez-Loriente et al. (2014) as well as multichannel seismic reflection profiles IAM-03 in Gonzalez et al. (1996), AR-01 in Rovere et al. (2004), AR-10 in Zitellini et al. (2001) and IAM-GB1 in our work (dashed line are profiles shown in this work). The tectonic map is adapted from Duarte et al. (2013) while the mud volcanoes distribution (gray trapezes) were collect from Hensen et al. (2015). Solid black lines define active faults, white solid lines mark blind faults and black dashed lines depict probable faults. The NEAREST seismic network is represented by red triangles that define OBSs locations and a yellow triangle marks the GEOSTAR position (details on the sensors in chapter IV.3.1). The location of the land stations integrated in focal mechanisms computation is depicted at mainland (black triangles). The bathymetry is from Zitellini et al. (2009). Abbreviations: CPR-Coral Patch Ridge; GB-Guadalquivir Bank; GCAW-Gulf of Cadiz Accretionary Wedge, GorF-Gorringe Fault; HAT-Horseshoe Abyssal Plain Thrust (after Martínez-Loriente et al., 2014); HF- Horseshoe Fault; MF-Messejana Fault; MPF-Marques de Pombal Fault; PSF-Pereira de Sousa Fault, PB-Portimão Bank; SVC-São Vicente Canyon; SVF-São Vicente Fault; TAPF- Tagus Abyssal Plain Fault. C- Instrumental seismicity from 2000-2015 (recorded by the Instituto Português do Mar e da Atmosfera seismic network) and the highest magnitude instrumental events coincident with NEAREST deployment area (from Buforn et al.,1988, Stich et al., 2010 and Custódio et al., 2016) on top of the main tectonic structures in the Gulf of Cadiz.

In the last decades, research projects concerning the investigation of the seismogenic and tsunamigenic sources in the area favored the densification of bathymetry and near-vertical reflection, wide-angle reflection and refraction seismic coverage. This effort resulted in a remarkable increase of our understanding of the Gulf of Cadiz tectonic structures and associated activity. Notwithstanding, there is still a poor correlation between the seismicity and the identified active faults as illustrated in Figs. IV.1B-C. An example is the uncertainty about the source of the 28th February 1969 earthquake. The focal mechanism solution (FMs) shows reverse kinematics, but some authors favour an east-west striking fault plane (e.g Buforn et al., 1988) whereas others choose a N55^{0}E striking fault plane (e.g Fukao, 1973), parallel to the striking of the Gorringe Bank (Figs. IV.1B-C). Moreover, following the empirical laws for fault models in the Gulf of Cadiz lithosphere proposed by Matias et al. (2013), it would be expected that a M_W=7.8 event would produce a rupture area of ≈3,410 km^2, with a length of 64 km and a width of 53 km. However, there is no agreement to which is the tectonic structure that caused the 1969 event (see Fig. IV.1B-C).

More recently, the moment tensor inversion of the 12th February 2007 Mw=6.0 event showed a thrust kinematics with a small strike-slip component (USGS source). The preferred fault plane orientations are discussed in Stich et al. (2007) and Custódio et al. (2012) but they reached contradictory results. Stich et al. (2007) suggested an ENE-WSW solution, sub-parallel to the Horseshoe

Fault (Fig. IV.1B-C). However, the selected plane is located 20 km to east of the Horseshoe fault and dipping in the opposite direction to the fault, down to a depth of 40 km. On the other hand, Custódio et al. (2012) proposed a WNW-ESE solution, sub-parallel to the SWIM strike-slip faults (see Fig. IV. 1B for location) dipping 46º to the SW. Both Matias et al. (2013) fault model formulation and Stich et al, (2007) calculations report a rupture area of ≈54 km^2 with a length of ≈ 8.2 km and a width of 6.5 km. Even though this event had its source near known major active tectonic structures, none of these structures seems to be compatible with the proposed fault plane solutions.

One of the main restrictions in finding a cause-effect relationship between seismicity and associated tectonic faults results from the limited geographic and asymmetric distribution of the permanent seismic land networks used for earthquakes' location around the Gulf of Cadiz. These leads to high azimuthal gaps resulting in lower accuracy in hypocentre determination. A key goal of the NEAREST project (Integrated observation from NEAR shore sourcES of Tsunamis: towards an early warning system) was to improve the location of the seismogenic and tsunamigenic sources in the Gulf of Cadiz. In order to guaranty a better accuracy of the recorded seismicity, 24 ocean-bottom seismometers (LOBSTER- Long term Ocean Bottom Seismometer for Tsunami and Earthquake Research) and a multi-parametric station – GEOSTAR were deployed in this area to record seismic events for nearly one year (Carrara et al., 2008).

In the present work we will address the following questions: I) How micro-seismicity is distributed in the Gulf of Cadiz area; II) What are the relations between the rheology, tectonic and micro-seismicity distribution? III) Is there any spatial relationship between high and low magnitude seismicity? IV) Can micro-seismicity studies provide us with a new insight on the seismogenic and tsunamigenic faults in the study area?

Our study is based on the processing and analysis of the seismic data recorded with the NEAREST stations and by the permanent land stations network (from Instituto Português do Mar e da Atmosfera - IPMA and Instituto Dom Luiz - IDL) combined with processing of original multichannel seismic (MCS) reflection profiles and the re-interpretation/integration of published MCS and refraction profiles existing in the study area.

Table IV.1-Details on the major FMs of the instrumental record in the NEAREST deployment area (see in Fig. IV. 1C, abbreviations: Long-longitude, Lat-latitude and Mag-Magnitude)

Date (DDMMYYYY)	Long (deg)	Lat (deg)	Dep(km)	Strike	Dip	Rake	Mag.	Reference
29-06-1965	-12.300	36.600	15.0	192	69	-11	4.8 (Ms)	Buforn et al., 1988
28-02-1969	-10.600	36.100	22.0	231	47	54	8.0 (Ms)	Buforn et al., 1988
05-05-1969	-10.400	36.000	29.0	324	24	142	5.5 (Ms)	Buforn et al., 1988
06-09-1969	-11.900	36.900	35.0	273	85	165	5.4 (Ms)	Buforn et al., 1988
18-04-1972	-11.200	36.300	15.0	8	65	-2	4.7 (Ms)	Buforn et al., 1988
29-07-2003	-10.560	35.960	60.0	139	51	157	5.3 (Mw)	Stich et al., 2005
19-07-2005	-11.530	36.260	10.0	204	68	-16	4.5 (Mw)	Stich et al., 2010
29-08-2005	-11.190	36.590	40.0	52	57	99	4.6 (Mw)	Stich et al., 2010
21-06-2006	-10.470	35.930	50.0	122	57	152	4.7 (Mw)	Stich et al., 2010
07-07-2006	-9.570	35.400	8.0	279	68	178	3.8 (Mw)	Stich et al., 2010
10-08-2006	-9.910	35.500	50.0	21	83	8	4.4 (Mw)	Stich et al., 2010
27-02-2007	-10.310	35.900	40.0	122	55	147	6.0 (Mw)	Stich et al., 2010
17-12-2009	-10.000	36.400	36.0	217	89	-58	5.8 (Mw)	Pro et al., 2012
31-03-2010	-9.769	36.769	39.0	80	69	65	4.0 (Mw)	Custódio et al., 2016
23-07-2010	-10.340	35.934	45.0	107	76	129	4.0 (Mw)	Custódio et al., 2016
25-07-2010	-7.717	36.235	14.0	313	80	-138	3.8 (Mw)	Custódio et al., 2016
26-03-2011	-8.429	37.304	24.0	101	79	167	3.5 (Mw)	Custódio et al., 2016
01-10-2011	-7.185	42.526	13.0	175	57	-2	3.3 (Mw)	Custódio et al., 2016
03-05-2012	-7.786	37.242	16.0	179	83	-1	3.3 (Mw)	Custódio et al., 2016
05-06-2012	-10.510	36.860	38.0	20	70	30	4.0 (Mw)	Custódio et al., 2016
24-09-2012	-8.390	37.628	9.0	36	72	81	3.3 (Mw)	Custódio et al., 2016
21-06-2013	-8.100	36.400	31.0	67	58	78	3.7 (Mw)	Custódio et al., 2016
19-10-2013	-9.818	36.151	35.0	353	73	-115	4.1 (Mw)	Custódio et al., 2016
23-10-2013	-9.439	35.251	30.0	106	82	-129	3.9 (Mw)	Custódio et al., 2016
20-01-2014	-7.582	37.497	22.0	249	72	-157	3.0 (Mw)	Custódio et al., 2016
13-03-2014	-9.478	36.916	9.0	50	73	63	3.5 (Mw)	Custódio et al., 2016
03-11-2014	-11.320	35.021	38.0	269	52	169	4.8 (Mw)	Custódio et al., 2016

IV.3. Geodynamic Setting

The Gulf of Cadiz straddles across the present day Nubia-Eurasia plate boundary in the Central Atlantic Ocean, off the southwest Iberia and the northwest Morocco coasts. This plate boundary is defined by a wide zone of deformation comprising the WNW-ESE striking SWIM dextral strike-slip faults irregularly connected by major NE-SW thrust faults (Zitellini et al., 2009; Duarte et al., 2013, Hensen et al., 2015). According to recent seismic refraction and reflection data, the central part of the Gulf of Cadiz is floored by oceanic lithosphere (Sallarès et al., 2011; Martínez-Loriente et al., 2014, see Fig. IV.1B). This fragment of oceanic lithosphere corresponds to a narrow oceanic basin of the western Alpine-Tethys (Sallarès et al., 2011), a transtensional corridor that

connected the Tethyan and the Boreal seas (Terrinha et al., 2002; Duarte et al., 2011) probably from middle-late Jurassic.

The early continental tectonic extension in the Gulf of Cadiz region was largely controlled by late Variscan inherited NE-SW faults bounding distinct rifting basins and future abyssal plains in the Southwest Iberia (Pereira and Alves, 2013; see their Fig. IV. 2 and references therein). The southernmost of these faults is the 500 km Messejana Fault zone that hosts a ~200My dolerite dyke of the Central Atlantic Magmatic Province (Youbi et al., 2003) (Fig. IV. 1B). The São Vicente canyon, one of the major morphologic features of southwest Iberia is partially controlled by the NE-SW striking São Vicente Fault.

In the Horseshoe Abyssal plain, the transition between the North Atlantic from Western Tethys Jurassic basins is delineated by the Horseshoe Abyssal plain fault (HAT - Martínez-Loriente et al., 2014, Fig. IV. 1B). The HAT separates a band of exhumed serpentinized continental mantle, extending to the Gorringe Bank and Tagus Abyssal Plain, from the Western Tethyan Basin, formed during the early opening of the North Atlantic that initiated in the late Jurassic (Sallarès et al., 2013). This interpretation is in agreement with the early Purdy (1975) refraction data results that showed upper mantle velocities of 7.2–7.4 km/s and with the tectonic interpretation of MCS images by Rovere et al. (2004). Between rifting episodes, the Gulf of Cadiz area was marked by several inversion episodes, well described in the onshore Algarve basin, in the lower Jurassic, middle Jurassic to upper Jurassic transition and upper Jurassic to early Cretaceous (Terrinha et al., 2002). According to Terrinha et al. (2002), thermal subsiding episodes, local inversion of the oblique transtensional tectonics and ridge push are pointed-out as possible combined geodynamic mechanisms to explain these transient phases.

From late Cretaceous-Paleogene the convergence between Africa and Iberia was accommodated by the inversion of the extensional Mesozoic fabric (Roque, 2007, Duarte et al, 2009; Terrinha et al., 2009). During this period an accretionary wedge (or thrust belt) was formed that extended from Gibraltar across the Horseshoe Abyssal Plain (Terrinha et al, 2009).

From SE Iberia to the western Alps, the N-S convergence was accommodated in a subduction zone that consumed most of the Alpine-Tethys oceanic domain. In the Oligocene, the convergence of between Africa and Eurasia slowed down triggering the initiation of a southeast-directed subduction rollback (Rosenbaum et al., 2004 and references therein). Lonergan and White (1997) and Gutscher et al. (2002, 2006, 2012) showed how this subduction-arc-system evolved into an east-dipping subduction zone below the Gibraltar Arc down to ~700km in depth based on seismic tomography. Deep seismic reflection profiles showed the presence of an accretionary wedge (GCAW-Fig. IV. 1B) consisting of a pile of SW-verging thrust faults rooting in a NE-dipping décollement under the Gibraltar Arc. These are two of the most solid evidences for the existence of this

subduction zone, even though its present day activity is still disputed (e.g., Zitellini et al., 2009; Duarte et al., 2013).

A new tectonic map based on re-interpretation of the main active faults resulted in the idea that an incipient subduction zone may be forming and propagating along the Western Iberia, marked by a set of compressive structures (the Gorringe, Horseshoe and Marques de Pombal thrust faults, Duarte et al., 2013). The tectonic reactivation of this passive margin would be the result of the propagation of stresses from the fading Gibraltar subduction zone and stresses related to the large-scale convergence between Africa and Eurasia (Duarte et al., 2013; Terrinha et al., 2009).

According to Zitellini et al (2009), the SWIM Faults, a 600 km long, 80 km wide band of WNW-ESE dextral strike-slip faults (Fig. IV. 1B) is the precursor of a new transcurrent plate boundary connecting the Gloria Fault to the Rif-Tell Fault Zone. However, Cunha et al. (2012) investigated the neotectonics of the Gulf Cadiz using a thin-shell modeling approach for the region and conclude that models dominated by continuous 600km SWIM faults would absorb all the seismic strain and would not reproduce the deformation along the NE-SW thrust system (e.g Horseshoe and Gorringe Faults). Notwithstanding, the SWIM faults (continuous or discontinuous) appear to connect the two main compressive fronts in the region, the Gibraltar arc and the SW Iberia thrust system, acting as a major lithospheric transfer zone (Duarte et al., 2013). Neres et al. (2016) using the same numerical approach favored the existence of an independent Alboran plate overriding the Gibraltar subducted slab.

Present day kinematic models for the Eurasia (Iberia) – Africa (Nubia) plate boundary estimate a convergence rate of 4-5 mm/yr, with an approximate WNW-ESE to NW-SE horizontal motion (Fig. IV.1, Argus et al., 1989, DeMets et al., 1994, Nocquet and Calais, 2004, Calais et al., 2003, Fernandes et al., 2003, Stich et al., 2006 and Serpelloni et al., 2007) compatible with the SWIM faults dextral strike-slip kinematics. The average maximum horizontal compression (SH_{max}) is oriented NW-SE as defined by borehole, focal mechanisms and moment tensor analysis (Fig. IV.1, Ribeiro et al. 1996, Borges et al., 2001, Stich et al., 2006 and Heidbach et al, 2008). Preliminary tensor analysis based on 36 events recorded in NEAREST OBS network (Geissler et al., 2010) retrieved a roughly NNW-SSE, maximum horizontal compression in the Horseshoe Abyssal plain and nearly NW-SE in the São Vicente canyon, consistent with previous solutions for moderate to large earthquakes.

IV.4. Data and Methods

IV.4.1. Microseismicity data acquisition and processing

The NEAREST network consisted in 24 broadband OBSs (Ocean Bottom Seismometers) from the German DEPAS pool (Deutscher Geräte-Pool für

amphibische Seismologie / German instrument pool for amphibian seismology) and a multiparametric station GEOSTAR from INGV (Istituto Nazionale di Geofisica e Vulcanologia). Both the OBSs and the GEOSTAR were equipped with Güralp CMG-40T broadband seismometers and High-tech HTI-04-OBS PCA/ULF and OAS DC- 50 Hz hydrophones, respectively (see Fig. IV. 1B for locations). The instruments were deployed in August 2007 and acquired data continuously for 11 months, with a sampling rate of 100Hz recording teleseismic, regional and local events. All stations were operational during at least 8 months. The clocks were synchronized with GPS time before deployment and after recovering. The internal clock drifts in the operational stations were corrected by using a linear interpolation method.

The events were extracted from a continuous waveform data set using both an automatic REF-TEK trigger algorithm, short-time-average through long-time-average (STA/LTA), and by visual inspection of daily spectrograms from the vertical seismometer component. After extracting the events, we performed a preliminary quality check based on the consistency of the P and S waves arrivals recognized in the different stations. 767 events out of the identified 1357 events were considered to be of high to medium quality and could therefore be located. From the overall extracted events, 364 were also detected with the Portuguese land stations network (from the Instituto Português do Mar e da Atmosfera-IPMA and the Instituto Dom Luiz-IDL). However, 58 of these events were only recorded in land permanent stations but not in the NEAREST stations. These earthquakes were located outside or at the limit of the deployment area and near the Portuguese South coast (mostly in the Guadalquivir Bank region; See Fig. IV. 1B).

The data analysis was carried out using the SEISAN 9.0.1 Seismic Analysis package (Havskov and Ottemöller, 2011). All the events were picked and weighted manually for P and S waves' first arrivals, generally in the three components seismometer and in the unfiltered signal. The hydrophone was used only as alternative for P wave picking and polarity confirmations.

For preliminary earthquake location and magnitude estimation was used the HYP2, a modified version of HYPOCENTER of Lienert (1994) to include independent S delays. We started by adopting the same velocity model used in Geissler et al. (2010) but in addition we tested other models constrained by wide-angle seismic reflection and refraction data from Sallàres et al. (2011, 2013) and Martínez-Loriente et al. (2014). For each event, depth was checked using a systematic RMS (root mean square) misfit -depth search approach (Havskov and Ottemöller, 2011). The selected solution was the one with the lowest misfit.

For local magnitude (ML) estimation it was used Carrilho and Vales (2009) formulation for Portugal and adjacent areas:

$$M_L = log\, A + 1.287\, log\, \Delta + 0.00061\Delta - 2.147$$

Where A is the amplitude measured in a Wood- Anderson synthetic display (in nm) and Δ is the hypocentral distance. This is the same formulation applied in and in routine geophysical observation at the IPMA Seismological Operational Centre.

To improve events locations, we used the VELEST algorithm to simultaneous invert hypocenters locations; stations corrections and the velocity model (see details on the method in Kissiling, 1995). To determine an accurate minimum 1D-velocity, it is recommended to use well-located events with observational azimuthal gaps lower than 180° and at least 10 P wave picks (Husen et al.,. 1999). As input, it is also suggested to use a minimum sample of 500 well located events. For the present case study, we have only 443 events in the deployment area. From those, few match the desired parameters. So, we considered less restrictive conditions as previously assumed by e.g. Carrilho et al. (2004) or Ruiz et al. (2011). The final selection included 269 events with an RMS misfit of 0.281s, with a total number of P- and S- phase observations greater than 10, an azimuthal gap lower than 210º (the averaged GAP was 112º) and a minimum of 3 P-wave first arrival observations (phase readings are dominated by S-wave pickings due to dominant poor to fair S/N in locations with a thick sedimentary cover). One of the main constraints in using a 1D velocity model to determine earthquakes location in the Gulf of Cadiz is the diversity of crustal and upper mantle domains. Adding station delays to the velocity model helps to correct for subsurface geological variations below the recording stations. Finally, we re-located all events using the initial HYP2 application and the velocity model resulted from VELEST application. Note that HYP2 application allows the use of both independent Vp, Vs models (variable Vp/Vs) and P, S stations delays.

The FMs were derived from P wave first motion polarity both from the NEAREST network stations (BB OBS and GEOSTAR) and from the land stations (see Fig. IV. 1B). FMs were computed using the double-couple fault-plane solution program - FPFIT (Reasenberg and Oppenheimer, 1985). The minimum criterion for trying a solution was 10 polarities readings and a quality classification was determined based on polarity misfits and on the standard deviation parameters computed with FPFIT for each solution (quality parameters in table III. 11, in the previous subchapter III.4.2 and a display of all focal mechanism solutions is presented in detail in the appendix III and IV.A-D).

We used the Focal Mechanism Stress Inversion (FMSI, Gephart and Forsyth, 1984) package to derive the best stress tensor that explains the FMs determined in studied area. We restricted our data to the FMs recovered from NEAREST OBS experiment and analyzed in this work. Fault plane solutions published in previous works were based on land network records only, which

are intrinsically poorly constrained, particularly if low to intermediate magnitude seismicity was used. Conversely, better constrained higher magnitude events may express a regional stress tensor rather than a local complex interaction of rupture mechanisms that may be associated with the micro-seismicity.

The FMSI retrieves the orientation of the σ_1, σ_2, σ_3 and a stress magnitude parameter, $R= (\sigma_2-\sigma_1)/(\sigma_3-\sigma_1)$. These results were used to compute SH_{max} and the dominant stress regime in each area. We followed the World Stress Map Project guidelines for formal stress inversions of focal mechanisms. Accordingly, we used the formulation in Lund and Townend (2007) for SH-determination and in Zoback (1992) for dominant stress regime determinations.

IV.4.2. Multichannel seismic reflection and refraction profiles

The multichannel seismic reflection (MCS) and refraction profiles studied in this work were selected specifically to support geological and rheological understanding of the results retrieved from passive seismic experiment. Accordingly, all the selected MCS profiles, except for IAM-GB1, are depth sections which allowed a correlation between the tectonic fabric and seismicity distribution. The chosen profiles and references are presented in Fig. IV. 1B.

The Seismic profile IAM-GB1 was selected for depth conversion because it strikes perpendicularly to the southern cluster of hypocenters in Geissler et al. (2010) and to the boundary between the Central Atlantic Ocean Northern limit (Martínez et al., 2014). Therefore, we could expect to have a clear image of the crustal structure and its relation to the micro-seismicity (Fig. IV.10). Details on the acquisition parameters and processing sequence are presented in the next section.

IV.4.2.1. Acquisition parameters and processing sequence of multichannel seismic

IAM-GB1 profile (see Fig. IV. 1B for location) was acquired during the Iberian Atlantic Margins (IAM) project funded by the European Community project JOU2-CT92-0177 (Banda et al., 1995). The energy source was a SWAG air-gun array with a total energy volume of 7524 cu. in. The source depth was 10 m and the shot interval 75 m. The receivers were contained in a streamer with 192 groups with an interval of 25 m, with five auxiliary channels. The streamer was at a depth of 18 m. The sample rate was 4 ms and the record length 25 s. A high-cut filter at 92 Hz with a slope of 72 dB/oct and a constant gain of 24dB were applied during acquisition. No low-cut filter was applied. The primary navigation system was a Differential Global Positioning System (DGPS).

Seismic reflection profile IAM-GB1 was re-processed in order to obtain a clearer image of the basement structure across the SWIM faults and the Central Atlantic-Tethys Oceanic boundaries proposed by Martínez-Loriente et al. (2014). The IAM-GB1 seismic profile re-processing was performed using the

software Globe Claritas from GNS Science, a package for 2D and 3D land and marine seismic data. The processing sequence was trace mute, in-line geometry; trace editing, brute stack, velocity analysis, 2-window statistical deconvolution, stacking, time and space variant bandpass filtering, time and space velocity variant finite differences time migration and post-migration depth conversion, using a geologically meaningful velocity model. The velocity model used in the depth conversion was defined by picking several major horizons in the time migration. Subsequently, velocities were assigned to the different layers bounded by horizons. Velocities were extracted from refraction and wide-angle reflection seismic profile - P1 (Martínez-Loriente et al., 2014) acquired also under the scope of the NEAREST project (see Fig. IV. 1B for locations). We used interval velocities from 1800 m/s at the uppermost sediments to 4700 m/s at their base. Three layers were defined for the crustal basement velocities with velocities of 5800 m/s and, 6300 m/s and the lowermost layer with 7200 m/s.

IV.5. Results

IV.5.1. Seismological analysis

IV.5.1.1. Velocity model and stations corrections

The velocity model shown in Fig. IV. 2 is the best fit 1D velocity model that complies with P and S observations for the 269 investigated events (out of 443 events). The derivation of this velocity model included the computation of P and S stations corrections. The positive and negative corrections coincide with higher and lower sediment thickness, respectively, indicating a good correspondence between the model and sub-surface geology (see subchapter III.3.2.5).

However, since the NEAREST OBS deployment area is described as a region comprising different lithospheric domains as old Jurassic oceanic, thinned continental lithosphere and exhumed serpentinized mantle (Sallarès et al., 2011, Gonzalez et al., 1996, Sallarès et al., 2013 and Martínez-Loriente, 2014) our velocity model can be viewed as a mean representative value of the lithospheric structure of the study area.

If we compare P-minimum velocity model (Fig. IV.2A) with the refraction and wide-angle reflection data in the Gulf of Cadiz area, we observe that for the sediments layers the velocities are higher. Both in Sallarès et al. (2011) and Martínez –Loriente (2014) velocity solutions range from 1.8 to to 4.0 km/s for the upper and lower layers, respectively. In our velocity model, in the upper layer Vp is 3.3 km/s and in the lower layer Vp is 3.6 km/s. We recall that for earthquakes location we replace layers resulting from gradient velocities (refraction data) with interval velocities layers. This will explain partially the differences here reported for velocities values. Also, we knew that during the

derivation of the final models, the velocities in these layers were poorly constrained because few hypocenters occurred at these depths.

Crustal velocities range from 5.18 km/s to 7.08 km/s are slightly higher than the results from NEAREST refraction profile P2 (Sallarès et al., 2011) ranging from 4.6–4.8 km/s at the top to 6.9–7.1 km/s at the base. The transition between lower crust and upper mantle is ≈16km in depth. The Moho depth is in conformity with the results published in Sallarès et al. (2011). The uppermost part of the lithospheric mantle (16 to 22 km) yielded Vp in the range of 7.6 to 7.8 km/s and high Vp/Vs ratios (Fig. IV.2B) is compatible with hydrated mantle (Christensen, 2004). In Fig. IV. 2C, we established a general compositional model based on the computed Vp and comparison with previous seismic refraction results in the area.

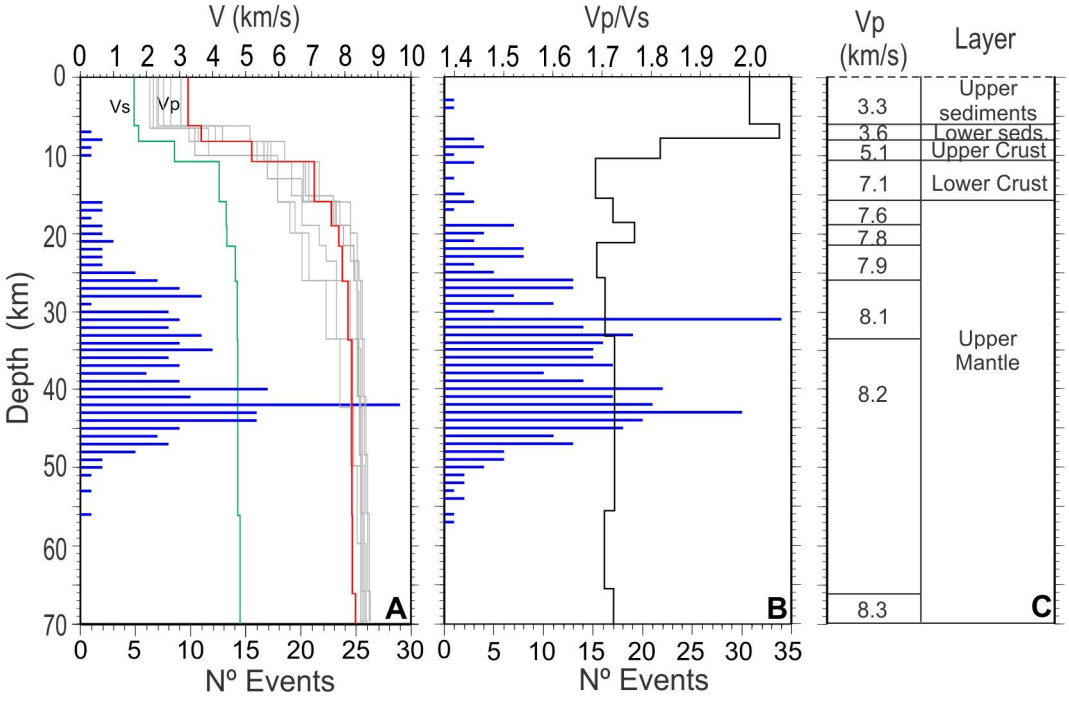

Figure IV.2 Final velocity model and depth distribution of the hypocenters recorded during the NEAREST experiment. A-Final P and S velocity model resulting from simultaneous inversion of hypocenter location, stations corrections and velocity model using VELEST algorithm. (Blue bars represent the 269 selected events distribution in depth after inversion ,see text for explanation), green line is Vs, red is Vp and grey lines define initial Vp models; B- Depth re-location of all 443 events based on the obtained velocity model (and stations corrections, black line defines Vp/Vs variation in depth) C- A compositional model of the upper lithosphere is proposed (abbreviation-seds-sediments). Note that the depth scale refers to the sea level.

IV.5.1.2.Seismicity in the Gulf of Cadiz

The NEAREST Network experiment allowed for better constrained earthquake locations in the Gulf of Cadiz area. Previous earthquake's detection and location were made using land station networks only, with restricted and asymmetric geographical distributions. This resulted in a limited control of the offshore seismic activity. Geissler et al. (2010) previous study, using a selection

of 36 events of the NEAREST network, showed the importance of using OBS networks to obtain more accurate hypocenter locations in this area.

The present work reports the final results from the NEAREST OBS experiment that include 443 events identified in more than 6 stations within the deployment area. The root mean square travel time residuals is 0.275s. The mean errors for longitude, latitude and depth are 2.6 km, 3.7 km and 6.8 km, respectively. A key finding is that 84% of the seismicity occurs at depths between 25 and 50 km, within unaltered lithospheric mantle (Figs. IV. 2 -3).

The seismicity recorded in the NEAREST network included local magnitudes ranging from 1.1 to 4.8. The highest magnitude earthquake (with M_L= 4.8) occurred in the São Vicente Canyon at 00:21 a.m. on the 11st of January, 2008.

Visual inspection of the hypocenters distribution in Fig. IV. 3 shows three well defined clusters: i) a northern cluster, in the area of the São Vicente Canyon, ii) a western cluster, in the Gorringe Bank, and iii) a southern cluster, at the SW termination of the Horseshoe Fault. In addition to these clusters, scattered seismicity was recorded in the areas of the Guadalquivir Bank, Portimão Bank, Coral Patch Ridge and Gulf of Cadiz Accretionary Wedge (see Fig. IV. 3). Some regional and teleseismic events were also recorded but they are not analyzed in this work (for more details see Monna *et al.*, 2013).

We observe that the São Vicente and Gorringe clusters are elongated along NNE-SSW to NE-SW directions, respectively, sub-parallel to active thrust faults. In the case of the São Vicente cluster, seismicity extends from the footwall of the Horseshoe Fault to the NE along the São Vicente Fault. The Gorringe cluster strikes parallel to the main NE-striking thrust fault that marks the NW limit of this submarine relief. Unlike the other clusters, the Horseshoe cluster has a WNW-ESE to NW-SE strike, slightly clockwise rotated with respect to the SWIM faults. The Guadalquivir Bank was previously described as an area of dense seismic activity (e.g. Buforn *et al*, 2004, Custódio et al., 2015), but few earthquakes were identified in this work, probably because it was outside the NEAREST network. It is worthwhile to note that some well-constrained events were recorded in the Portimão Bank and in the northwestern part of the accretionary wedge, which are located at the limit of the deployment area.

The analysis of the NEAREST OBS data resulted in the determination of 124 focal mechanisms, 82 of which were considered well defined with magnitudes ranging between 1.9 and 4.8 (see focal mechanism solution in Fig. IV. 4 and details on Appendix III and IV.A-D), i.e. we added 58 new solutions to previous catalogues and synthesis (Geissler et al., 2010, Stich et al., 2010, Domingues et al., 2013, Custódio et al., 2016). Because we considered events with at least 10 polarities, two events from Geissler et al. (2010) catalogue are not included in our (events 5th and 21st of March 2008, with 9 polarities, in the southern cluster in Fig. IV. 3 of the referenced work). In addition, three other solutions in

Geissler at al. (2010) were revised and evaluated as poorly constrained and thus were excluded from our catalogue (the 22nd of May 2008 in the southern cluster and outside the clusters area and both the 6th and the 7th of November 2007, ibid).

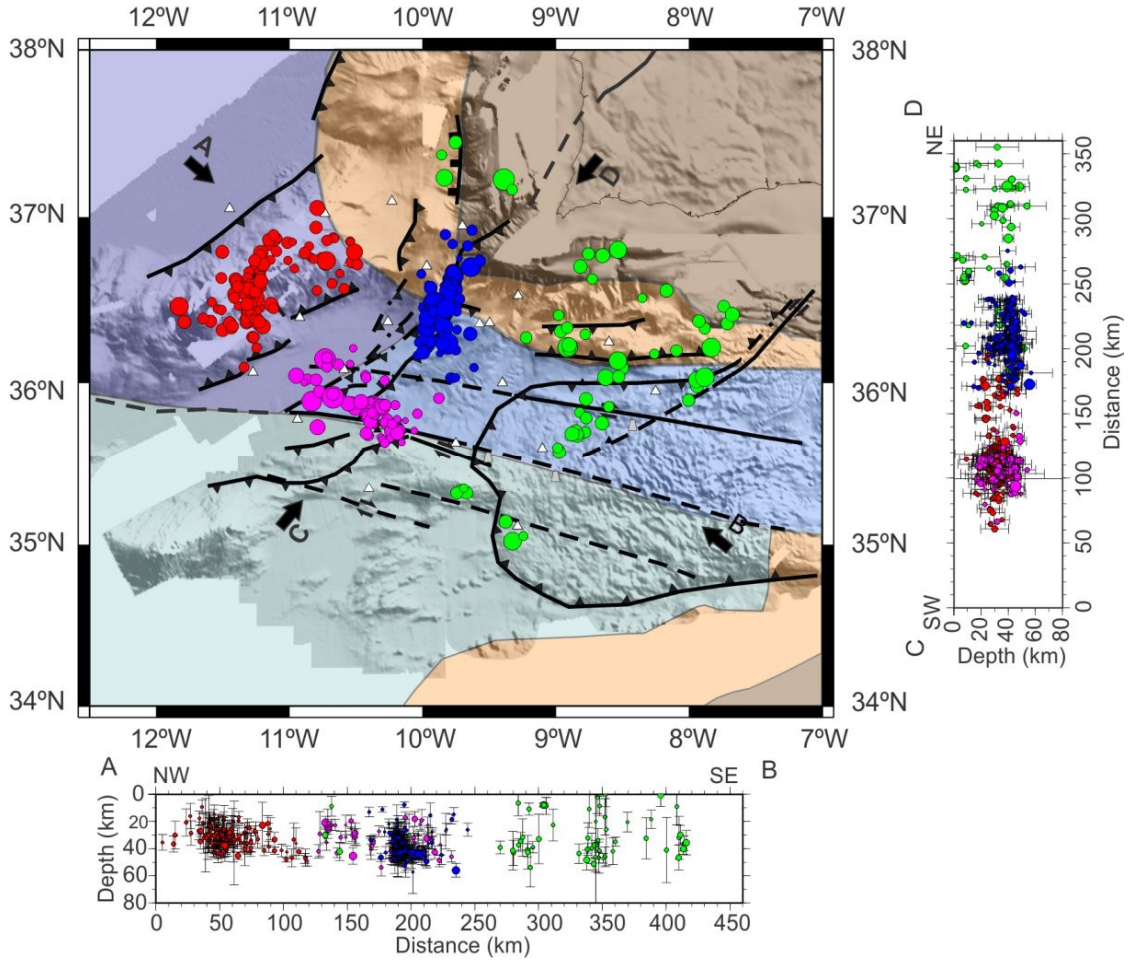

Figure IV.3-Seismicity results from NEAREST deployment experiment. We identified three clusters: Blue events were defined as the São Vicente cluster, red circles mark the Gorringe cluster and purple events define the Horseshoe cluster. The remaining circles in green mark the events located outside the clusters. AB- plot of all events in a NW-SE cross-section along the SH-max (Ribeiro et al. 1996, Borges et al., 2001, Stich et al., 2006 and Heidbach et al, 2008), black bars show vertical errors) and; CD- plot along a perpendicular cross-section. The background colors in the map define the same lithospheric domains as in Fig. IV. 1B. Faults as in Fig.IV.1B-C, for references see text.

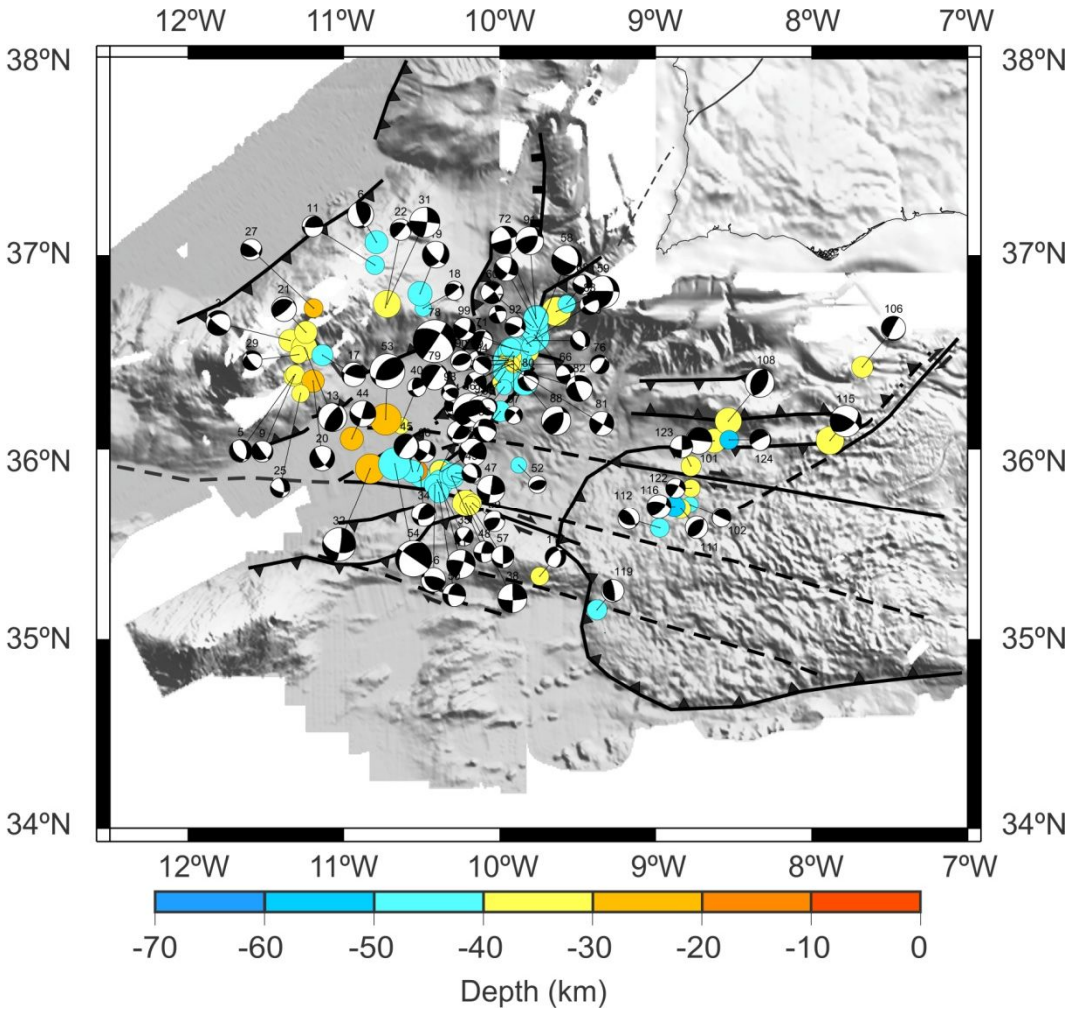

Figure IV.4 FMs obtained from the NEAREST network experiment (details on FMs are provided in Appendix III and IV.A-D). The results here presented add 58 new focal mechanisms to the previous catalogue in Geissler et al. (2010). Note that apart from the diversity of FMs, the predominant fault solutions are reverse dip-slip and strike-slip solutions with a few normal dip-slip.

In the Gorringe cluster, 31 FMs were computed (Fig. IV. 4, details on the events in Appendix III.A and IV_A). These new solutions are a substantial addition to the previous catalogues, where few FMs were known, particularly within the magnitude range of the NEAREST experiment (see Fig. IV. 1C, information from e.g. Grimison and Chen, 1986; Buforn et al., 2004, Stich et al, 2010 and Custódio et al., 2016). In the Horseshoe cluster, 26 fault plane solutions were obtained (Fig. IV. 4, details on the events in Appendix III.B and IV_B) with 10 events common to Geissler et al. (2010). We identified 33 FMs in the São Vicente Cluster (Fig. IV. 4, details on the events in Appendix III.C and IV_C) adding 17 new events to the previous dataset. We obtained some discrepancies in relation to the Geissler et al. (2010) events, mostly resulting from adding new polarities to their preliminary solutions.

Outside the clusters areas, particularly in the area of the Gulf of Cadiz Accretionary Wedge (GCAW) we computed few FMs (see Fig. IV.4 and details on the events in Appendix III.D and IV_D). In the GCAW we obtained some

nearly reverse dip-slip FMs (events 109, 111 and 112). Near the SWIM 2 fault, it was computed two pure strike-slip FMs (events 122 and 123). At the lower limit of the Portimão bank, we also computed a reverse dip-slip FMs (event 108). All these events are located between ≈30 and 40 km in depth. Since these FMs are located outside or in the limit of the NEAREST network, we will not discuss the source mechanism of these events.

In general, the predominant fault-plane solutions are reverse dip-slip and strike-slip solutions. These results are in agreement with the preliminary solutions published in Geissler et al. (2010) based on the best events reported from the NEAREST experiment. They are also consistent with previous studies carried out in this area for moderate to large earthquakes (e.g. Grimison and Chen, 1986; Buforn et al., 2004; Stich et al., 2010, Custodio et al., 2016). Notwithstanding, some normal dip-slip solutions were identified in the upper mantle, as already reported in Stich et al. (2010) and Geissler et al. (2010). The diversity of the FMs reflects the complexity of the source mechanisms of this low to intermediate magnitude seismicity. We cannot find a dominant fault mechanism or common fault plane for any of the clusters investigated.

During the NEAREST experiment 291 events were recorded and located by the permanent land network in the area of the OBS deployment (data provided by IPMA). From these, only 179 events were recorded and located by both networks. If we compare the epicenter distribution obtained from the two networks, we observe that most of the locations using the land stations are offset landwards (Fig. IV. 5). Most of the events are displaced between 0.1 and 0.3 degrees in latitude and longitude and 20 to 30 km in depth. In what regards the depth distribution, the locations based on the land network are systematically shallower than the NEAREST OBS solutions, with differences reaching up to 60 km (Fig. IV. 5). Sub-horizontal alignments around depths of 15 km and 30 km that were detected using the land network were not imaged by the NEAREST network. These alignments are probably artifacts produced by manually fixing earthquake's depths (which is typically done for poorly constrained events).

Finally, if we compare magnitudes estimations most events (98%) recorded by the land network are systematically underestimated (note that we used the same formulation for magnitude estimation as IPMA). Differences in magnitude vary between -0,1 and 1,0; however, in 83% of the events the underestimation by the land network is between 0,2-0,6, only. All these differences highlight the limitations of the land stations distribution and of the velocity models. Moreover, it outlines the necessity of using better stations distribution for the location of earthquakes in the Gulf of Cadiz region, in particular in what concerns low to intermediate magnitude events. A new strategy for the location of these events by the land networks should be developed in the light of the results obtained in this study.

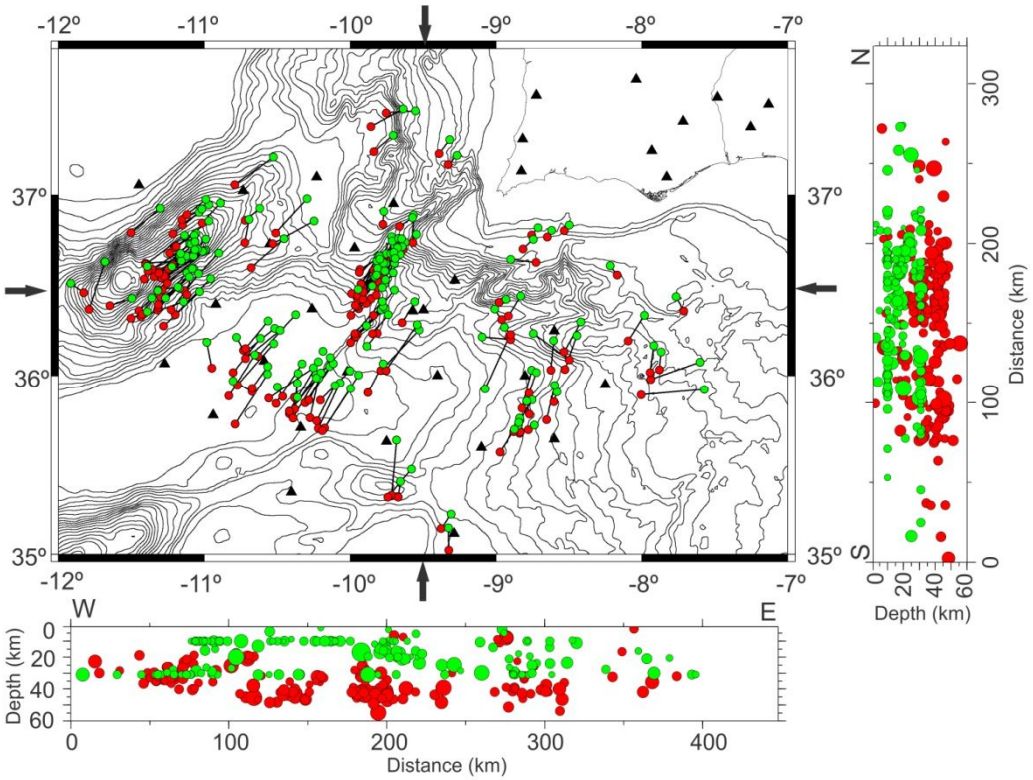

Figure IV.5- Differences in the location of seismic events recorded by the NEAREST network (red circles) and the permanent land network (green circles). It is possible to observe that the hypocentres located by the land stations are biased towards land and shallow depths. The black arrows mark the directions of the profiles also shown in the figure (N-S on the right and W-E on the bottom); the black triangles are the seismic stations location.

In the next sections, we will describe in detail the seismicity in the three clusters. We describe our results based on our observations in map view and in cross-sections. In both displays, we present the crustal-upper mantle transitions in the area. Note that these limits are speculated based on the available discontinuous geophysical data (refraction and wide angle reflection profiles, see references in Fig. IV.1B). In particular, we should point out that the layer with serpentinized mantle is drawn based on previous evidences for low upper mantle velocities down to ≈20km (down to 14 km in refraction profile B-BR from Purdy, 1975 and ≈20 km in MCS reflection profile IAM-03 from Gonzalez et al., 1996 as well as in NEAREST refraction profiles P2 and P1 from Sallarès et al., 2011 and Martínez-Loriente et al., 2014, see profiles location in Fig. IV. 1B). Furthermore, the serpentinization layer should be discontinuous; the geometry shown in the cross-sections is a simplification. Finally, we will also look in detail to the fault plane solutions in each cluster, the best fitting stress tensor, resulting maximum horizontal stress and general stress regime characterization (a resume in Table IV.2).

Table IV.2- Best fitting stress tensor details (grey highlighted rows show the preferred stress tensors for each cluster). Maximum horizontal stress compression and stress regime for selected stress tensors (az- Azimuth; pl-plunge and R= $(\sigma_2-\sigma_1)/(\sigma_3-\sigma_1)$)

Dataset	Tensor						R	RMS misfit (°)	SHmax (°)	Stress regime
	σ_1		σ_2		σ_3					
	pl (°)	az(°)	pl (°)	az(°)	pl (°)	az(°)				
Gorringe cluster										
All (14 EQs)	58	120	29	329	13	231	0.4	4.403	318	NF
NE (6 EQs)	36	168	45	306	23	60	0.8	1.545	344	SS
SW (7 EQs)	24	158	65	358	8	251	0.4	2.302	340	SS
São vicente cluster										
All (20 EQs)	7	329	83	166	2	59	0.3	3.836	329	SS
S (10 EQs)	50	157	14	50	37	310	0.3	2.136	302	NF
N (10 EQs)	6	309	30	43	59	209	0.4	3.368	306	TF
Horseshoe cluster										
All (19 EQs)	11	338	63	226	24	73	0.5	3.946	340	SS
W (5 EQs)	22	133	61	269	19	35	0.7	1.116	311	SS
E (12 EQs)	12	339	65	221	21	74	0.5	3.271	341	SS

IV.5.1.3.The Gorringe cluster

The Gorringe seismicity cluster is defined as a broad alignment of epicentres striking NE-SW along the Gorringe Bank (Fig. IV. 6A). Here the seismicity is asymmetric with a higher number of events concentrated to the southwest (see map and profiles PRF01-03 in Fig. IV. 6). In profile PRF02, we observe that the events distribution is diffuse (Fig. IV. 6C) while to the NE it becomes progressively more discrete, defining roughly a SE dipping alignment with a flat-ramp geometry (see profile PRF01 Fig. IV. 6B). The longitudinal profile PRF03 (Fig. IV. 6D) also shows a variation in the clustering pattern of the events. In this case, they are slightly more disperse to the SW. Below the Ormonde seamount, there is an alignment that plunges to the NE, towards the thinned continental domain (Fig. IV. 6D). The transition between the two sub-clusters is marked by a possible steep boundary (see profile PRF03 in Fig. IV. 6D).

In the Gorringe cluster, the dominant FMs are strike –slip and reverse dip-slip with a few normal fault events. In map view, it seems that pure-strike slip mechanisms are mostly located in the SW and NE limit of the Gorringe cluster, while reverse (and oblique) slip are found in the central part of the cluster, sub-parallel to the Gorringe fault.

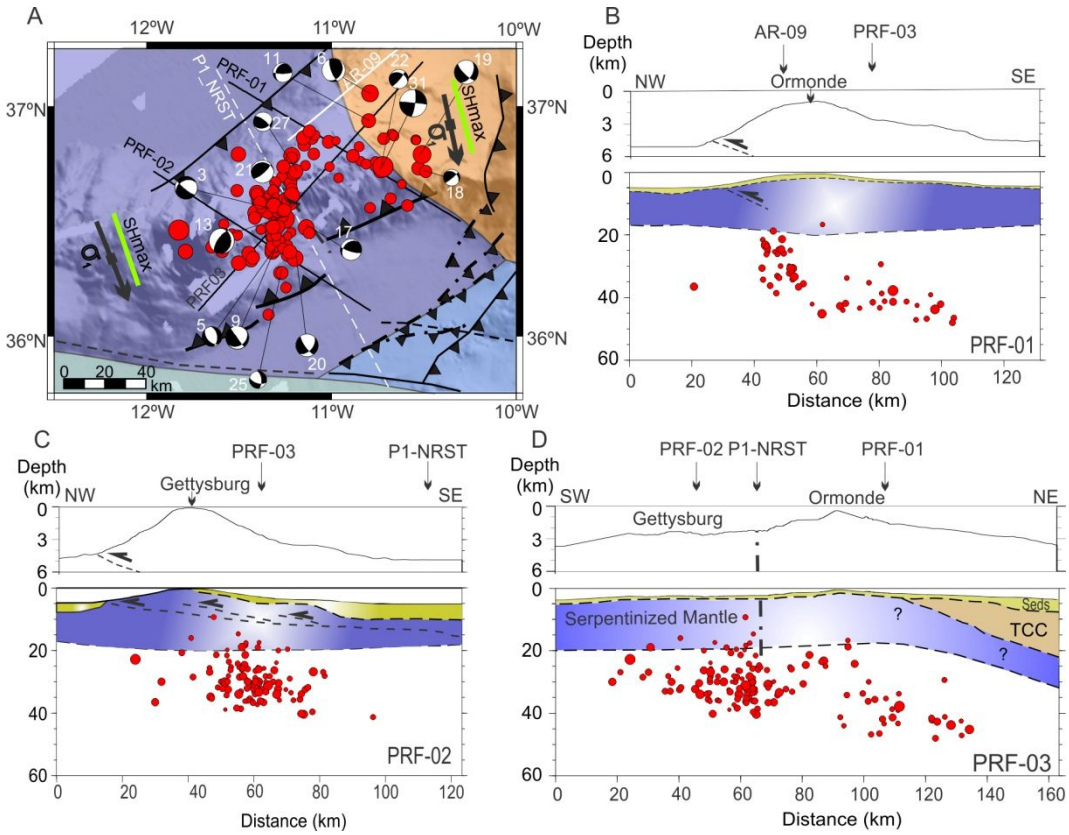

Figure IV.6- The Gorringe cluster. A. Map view with the epicenter distribution and FMs. We recognized that events roughly define a NE-SW alignment. Epicenter locations are asymmetric with more events to the SW. In NE and SW sub-clusters, SHmax is roughly NNW-SSE and sub-parallel to σ_1 trend (The background colors define the lithospheric limits in Fig. IV. 1B, details on the tensor and SHmax in Table IV.2). B-D- Cross-sections and bathymetric profiles across the seismicity cluster (bathymetric profiles with a vertical exaggeration of ≈ 2.5× and all the profiles are a projection of the earthquakes located within a 40 km wide band). B-C: NW-SE cross-sections are plotted in the profiles PRF-01 and PRF-02. In profile PRF-01, the seismicity is more diffuse while to NNE, in the profile PRF-02, it becomes more discrete and defines a flat-ramp geometry (faults geometry in the cross-sections based Martínez –Loriente et al., 2013). D. Profile PRF-03 shows a SW-NE cross-section drawn along the cluster elongation (TCC-Thinned Continental Crust). In this profile, we identify a sub-vertical limit at 60 km from the origin (dash-dot).

We computed the best fitting stress tensor (see Table IV.2), for the determined FMs, using the FMSI package (Gephart and Forsyth, 1984**).** Initially, we included all the best focal mechanism solution and subsequently improved the dataset by excluding events that were inconsistent with the best tensor solution. We started with 16 FMs and an average rotational misfit of 7.95° and concluded with 14 FMs and an average rotational misfit of 4.40°.In the next step, we subdivided the original focal mechanisms dataset in two sub-groups. This approach is coherent with our observations that seismicity distribution along the Gorringe cluster is asymmetric. We defined our final stress tensors for the NE and SW sub-clusters based on 6 and 7 events with improved average rotational misfits of 1.55º and 2.30º, respectively. The σ_1 orientation is ≈ NNW-SSE, similar for both SW and NE sub-clusters, differing by approximately 10º in strike and dip. In the NE sub-cluster, the lowest compressive direction (σ_3) dips towards ESE, to the thinned continental domain while in the SW sub-cluster, it

dips gently towards WSW. Finally, the SHmax azimuths are nearly NNW-SSE in both sub-clusters. According to Zoback (1992) formulation, the Gorringe cluster has a dominant strike-slip regime (see Table IV.2 and Fig. IV. 6A).

IV.5.1.4. The São Vicente Cluster

The São Vicente seismicity cluster is parallel to the São Vicente Canyon and the São Vicente Fault, which terminates near the NE limit of the Horseshoe Fault (see Figs. 1B and 7A). The profiles across the cluster long axis show that the hypocentres define sub-vertical to SE-dipping trends (see profiles PRF 01 and 02 in Figs. 7B-C). Hypocenters in the profile PRF01 suggest the existence of a sub-vertical discontinuity, while to the SW, in profile PRF02, the seismicity distribution displays both vertical and SE-dipping discontinuities. The lower limit of the seismogenic layer is at around a depth of 50 km, increasing towards the oceanic domain where it reaches depths close to 60 km (PRF03-Fig. IV.7D). The depth distribution of the micro-seismicity is in agreement with Grevemeyer et al., (2016).

The prevailing FMs are pure strike-slip and oblique slip, combining strike-slip with a small reverse dip-slip component. A few normal faults are also observed.

The best fitting σ_1 orientation is approximately NW-SE, sub-horizontal, oblique to the cluster elongation (Table IV.2, Fig. IV. 7). We started with an initial dataset of 32 events and an average misfit of 7.937°. The final dataset included 20 events and the average misfit was 3.836°. It deviates from Geissler et al., (2010) preliminary results (which is nearly WNW-ESE). The main difference between this work and Geissler et al. (2010) is the dataset, as here we present a complete catalogue for the NEAREST experiment. The additional data resulted in a different stress tensor model for São Vicente cluster. However, the additional data in this work also yields a lower average rotational misfit, of 3.8°, while in Geissler et al. (2010) was 4.6°.

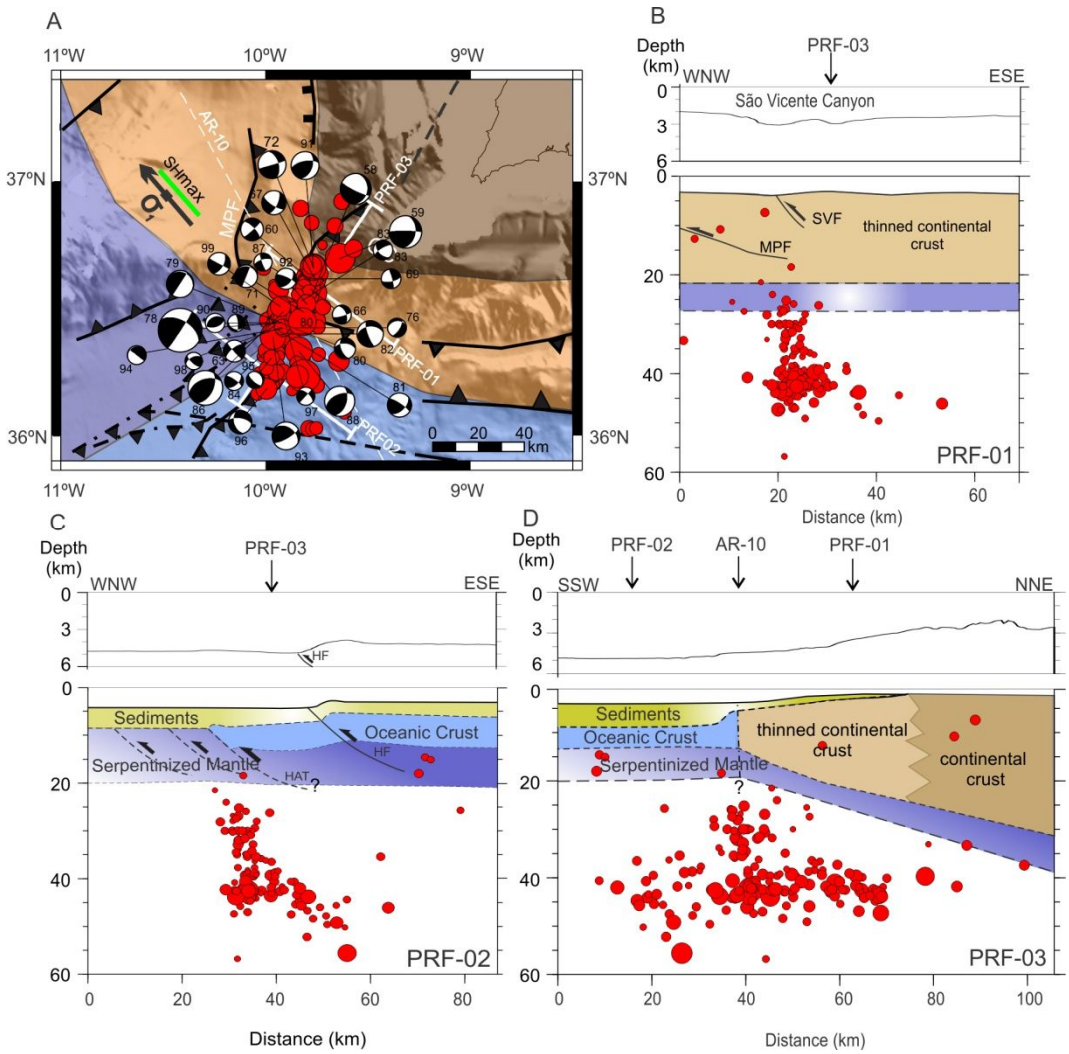

Figure IV.7- Seismicity at the São Vicente cluster. A. Map view with epicenter distribution and FMs. SHmax is roughly NW-SE and sub-parallel to σ_1 striking direction and roughly perpendicular to epicenters NE-SW trend(The background colors define the lithospheric limits in Fig. IV. 1B, details on the tensor and SHmax in Table IV.2)B-D- Cross-sections and bathymetric profiles across the seismicity cluster (bathymetric profiles with a vertical exaggeration of ≈ 2.0× and all the profiles are a projection of the earthquakes located within a 40 km wide band). B-C. WNW–ESE cross-sections are shown in profiles PRF01-02. D. SSW-NNE cross-section is presented in profile PRF03. We observe that in profile PRF-01 the hypocenters are mostly aligned in a sub-vertical plane while in profiles PRF-02 and PRF03 we can identify ESE and NE dipping planes, respectively. The profile PRF-03 is longitudinal to the cluster elongation. In this profile, we recognize that the bottom boundary of the hypocentres is located around 50 km depth, with rare deeper events (Fault abbreviations and background colors described in Fig. IV. 1B).

IV.5.1.5.The Horseshoe Cluster

The Horseshoe seismicity cluster displays a broad NW-SE trend in epicenter distribution (Fig. IV. 8A). The profiles orthogonal to this trend show that dispersion is higher to the West (PRF-01, Fig. IV.8B) than in the East (PRF-02, Fig. IV.8C). In the longitudinal profile PRF-03, we observe SE-dipping and sub-vertical alignments of events (Fig. IV. 8D), limited between 20 and 50km depth, approximately. This seismicity is distributed across three types of basement, two oceanic and one consisting of hydrated mantle. Adding to this, it should be

noted that this profile cross cuts four main discontinuities, three of which are first order faults deforming the seafloor the HF, the SWIM 1 and SWIM 2. Hypocenters laying to the south of SWIM 1 Fault follow a roughly vertical trend, whilst hypocenters to the north of SWIM 1 Fault show a SE dipping trend.

The focal mechanisms solutions are mostly pure strike-slip and few reverse dip-slip events, with some normal faulting also. Note that in contrast with the NE-SW trend of seismicity, most strike-slip solutions show a fault plane striking WNW-ESE to W-E, sub-parallel to the SWIM faults (Fig. IV. 8A). These observations are clearer in the vicinity of SWIM 1 fault to the East of the Horseshoe fault. To the West, FMs are more variable.

In relation to the stress tensor inversion modeling, we started the Horseshoe cluster analysis with 21 the best focal mechanism solutions. The first inversion test resulted in an average minimum rotation misfit of 5.96°. We removed inconsistent data and end up with 19 events and a misfit of 3.95° (see Table IV.2). The resulting maximum compression is similar to Geissler et al. (2010) preliminary results for the same area (σ_1 with orientation 12 °, N351°E, see reference work). Yet, divergence is larger for the extensional axis dip that is≈2°and R solution ≈0.7 (idem) contrasting with our results, ≈63° and 0.5, respectively. We consider that differences result from adding new events to initial dataset in Geissler et al (2010).

To improve our result we tested 2 sub-clusters that we consider coherent with our observations of FMs distributions. One sub-cluster to the East of the HF where most FMs are clearly strike –slip and another to the W of this fault, where FMs have a more complex pattern (Fig. IV. 8A).

We started with 14 events in the E sub-cluster and a RMS of 6.43. The final dataset had 12 events and an average misfit of 3.271. The maximum compression is similar to the results previously reported in Geissler et al. (2010), roughly NNW-SSE and coincident with the SHmax direction.

In the W sub-cluster, we selected 5 events and the final error was 1.116°. The stress tensor for western dataset is diverges from the remaining results, with σ_1 trend approximately NW-SE sub-parallel to SHmax orientation. This trend is also sub-parallel to the SHmax direction in the São Vicente cluster.

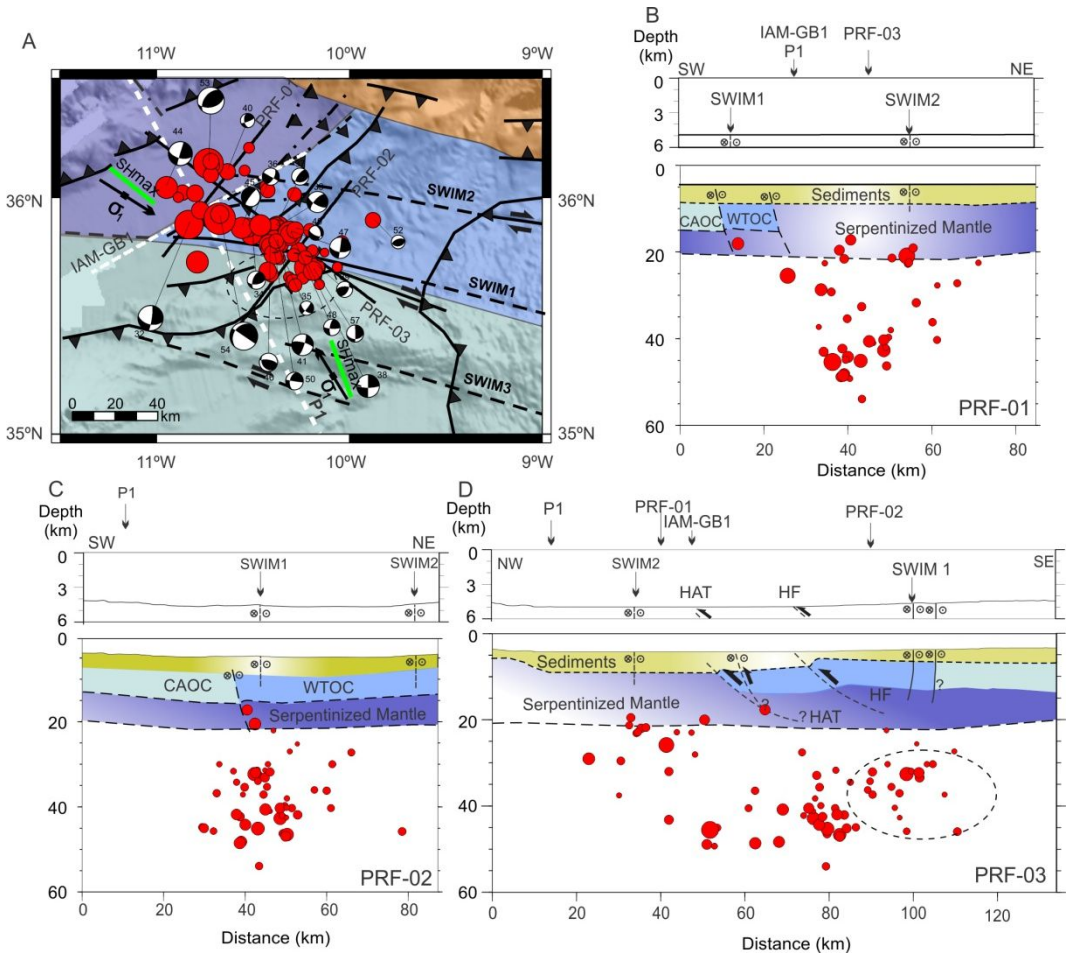

Figure IV.8 - Horseshoe cluster seismicity. A. Map view with epicenter distribution and FMs. The events are distributed following a broad NW-SE trend. In E and W sub-clusters, SHmax is roughly NNW-SSE and NW-SE, respectively. These directions are sub-parallel to σ_1 trends (The background colors define the lithospheric limits in Fig. IV. 1B, details on the tensor and SHmax in Table IV.2). B-D. Cross-sections and bathymetric profiles across the seismicity cluster (bathymetric profiles with a vertical exaggeration of ≈ 2.5× and all the profiles are a projection of the earthquakes located within a 40 km wide band). B-C. SW-NE cross-sections are shown in profiles PRF01 – 02 (CAOC- Central Atlantic Oceanic Crust and WTOC- Western Tethys Oceanic Crust). In profile PRF-01, the seismicity is more diffuse while to East in profile PRF-02 it becomes more discrete and defines a roughly sub-vertical alignment coincident with SWIM1 fault. D. Profile PRF-03 shows a NW-SE cross-section along the cluster maximum elongation. The hypocenters define roughly SE dipping planes; however they seem to root deeper or are offset from the known faults in the area (note that the events in the dashed line ellipse are located to the south of the SWIM1 fault). Fault abbreviations and background colors described in Fig. IV. 1B.

IV.5.2. Horseshoe Abyssal Plain tectonic structure

Several studies have already used depth converted profiles in the same areas where we identified the Gorringe and São Vicente seismicity clusters to investigate the crustal structure (e.g. Sartori et al., 1994, Zitellini et al., 1999 and Jimenez –Munt et al.,2010 and Sallarès et al., 2013). However, this was never attempted in the area of the Horseshoe cluster. This cluster straddles across various types of oceanic basement as derived from palinspastic reconstructions and seismic refraction models (Fig. IV. 1B). The processing, depth conversion and interpretation of the MCS profile IAM GB1 (Fig. IV. 1B, 9 and details on

processing in Appendix V), transversal to the Horseshoe cluster, allows a new view on the top of the basement morphology and tectonics. In the present section, we will present and discuss this seismic profile.

The IAM-GB1 seismic profile (Fig. IV.9 and Appendix VI) strikes SW-NE and crosses the Eastern Horseshoe Abyssal Plain, intersecting the Horseshoe cluster at an oblique angle (see Fig. IV. 8A). The structure and acoustic signature of the basement changes along the seismic profile. In the southwestern end of the profile up to the CDP 4700 a block-like structured basement is observed, similar to the oceanic crust structure reported by Rovere et al. (2004) in the profile AR01. On the contrary, to the Northeast, the basement morphology is smoother (not suggesting an oceanic crust affinity) and cut by several reverse blind faults. Some of these faults possibly correspond to the reactivation of extensional structures and affect the overlying seismic units (Fig. IV. 9).

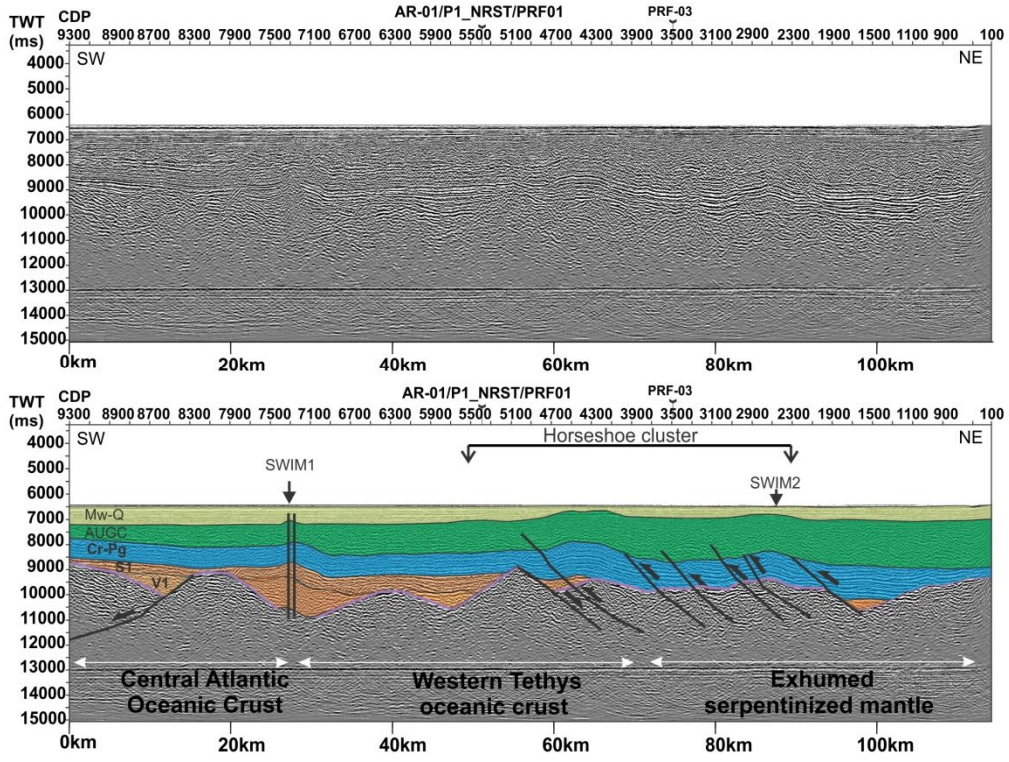

Figure IV.9 – IAM-GB1 MCS profile with/without interpretation and the projection of the horseshoe cluster area. See text for details and Fig. IV. 1B and Fig. IV. 8 for the location of the profile. Seismic unit S1-V1 are interpreted as volcaniclastic sequences associated with rift episodes, from the Jurassic to the Lower Cretaceous; Seismic unit Cr-Pg (Cretaceous - Paleogene) are post-rift deep sediments; AUGC is the Allocthonous Unit of the Gulf of Cadiz; Seismic unit Mw-Q are Miocene-Quaternary hemi-pelagic sediments and turbidite. Both SWIM1 and 2 fault are observed. SWIM1 fault is more discrete while SWIM2 fault is associated with a wide zone of deformation.

Above the basement we identified the following seismic units whose calibration was based on Hayward et al. (1999) and Roque (2007):

Seismic unit S1-V1 is a basal discontinuous unit mainly filling basement depressions. It comprises two seismic sub-units V1 and S1. The first has a transparent and low amplitude acoustic signature. Sub-unit S1 is discontinuous with internal divergent reflections and with increasing thickness towards SW-dipping reflectors in the basement. Seismic unit S1-V1 could be related to volcaniclastic sequences associated with rift episodes that in this region lasted from the Jurassic to the Lower Cretaceous;

Seismic unit Cr-Pg (Cretaceous -Paleogene) is characterized by continuous, high amplitude and subparallel internal reflections. Locally, between shot points 100 and 1500 these reflections onlap the basement. Between shot points 1500 and 4500, seismic unit Cr-Pg covers unconformably the basement. We interpret the basal unconformity as the surface marking the end of the oceanic rifting episodes. This unit probably consists of deep-sea sediments deposited in a post-rift thermally subsiding basin.

The Allocthonous Unit of the Gulf of Cadiz (AUGC) is characterized by internal chaotic reflections. From southwest to the northeast, it becomes more chaotic and the internal deformation increases, showing thrust faults dipping to northeast. Also the thickness of the AUGC increases towards NE. The AUGC was previously described as a succession of gravitational bodies (i.e. olistostromes, Torelli et al., 1997, Iribarren et al., 2007) corresponding to massive and a rapid succession of from large submarine landslides. Both Roque (2007) and Terrinha et al. (2009) based on the internal deformation, interpreted this seismic unit as an accretionary wedge. The building up of Gorringe and Coral Patch seamounts in the Miocene could also have acted as local sources of gravitational deposits that were integrated in the AUGC (Roque, 2007 and Iribarren et al., 2007). As the compression increased with the Westwards migration of the Betic-Rif arc, the AUGC sequence became more deformed and thick (from NE to SW). This sequence is interpreted as being of Oligocene-Miocene age.

Seismic unit Mw-Q (Miocene-Quaternary) shows continuous parallel internal reflections with high amplitude and larger thickness in the Southwest sector. The lower boundary truncates the underlying sequence. The Mw-Q seismic unit is probably related to the deposition of hemi-pelagic sediments and turbidites from Miocene through present.

The Pliocene-Quaternary deformation imaged in the IAM-GB1 is mostly localized in Northeast sector and is materialized by a NE-dipping thrust system with exception of the zone of intersection with the SWIM1 strike-slip fault in the Horseshoe Abyssal Plain. Some of the faults show evidences for early extensional kinematics affecting up to the seismic unit Cr-Pg. The basement compressive tectonics affect the top of the AUGC. To the Southwest, the SWIM 1 fault zone, which has been shown to mediate seafloor to basement fluid circulation (Hensen et al., 2015) is depicted down to the basement. The cross

cut relationship between these faults and the recent sediments cannot be assessed using IAM-GB1 due to its low vertical resolution. However, it has been reported by various authors, such as Zitellini et al. (2009).

The asymmetry in the distribution of the tectonic deformation is coincident with morphologic transitions in the basement. The compressive tectonic deformation concentrates on i) the limit between crustal oceanic affinity and what is presumed to be exhumed continental mantle (Figs. 9 and 12) and ii) the location of the Horseshoe seismic cluster. The discrepancy between oceanic and exhumed serpentinized mantle boundaries of this work and Martínez-Loriente et al. (2014) are minor and may result from the limited resolution of the available data.

IV.6. Discussion

IV.6.1. Seismicity clusters and tectonic structures

In this study we identified three seismicity clusters showing that the micro-seismic activity is the Gulf of Cadiz is not randomly distributed. The existence of these clusters was already revealed in Geissler et al., (2010) and Custódio et al., (2016). However, our data allowed a more comprehensive evaluation (i.e. larger dataset and lesser errors) of the seismicity distribution showing that seismic activity is generated mainly in the lithospheric mantle.

The São Vicente and Gorringe clusters are elongated parallel to the strike of the main thrust faults in the region, which coincide with the strike of the main Mesozoic rifting-related extensional faults in the SW Iberia mainland, i.e. NNE-SSW to NE-SW (Terrinha et al., 2002). The São Vicente cluster is sub-parallel to the strike of the São Vicente fault and Marquês de Pombal thrust fault, which results from tectonic inversion of a rift fault (Terrinha et al*.,* 2003). The NE-SW trending frontal thrust of the Gorringe Bank is parallel, not only to the continental crust rifting faults, but also to the oceanic crust extensional fabric described by Hayward et al. (1999) and Zitellini et al. (2009), which is well exposed also in the Coral Patch Ridge (see Fig. IV.1B for location). The constant strike of the Mesozoic rifting faults from the Gorringe seamount to the Gibraltar arc argues for a NW-SE extensional direction during Early Jurassic to end of Early Cretaceous times, which is compatible with various kinematic reconstructions (e.g. Dewey et al., 1989, Schettino and Turco, 2011).

This strongly suggests that in the Gorringe and São Vicente clusters the mantle is responding to the shortening induced by the present day stress field by reactivating extensional rift tectonic fabrics in zones of fault intersection, i.e. ~NE-SW thrusts with ~W-E strike-slip faults. Present day NNE-SSW to NE-SW striking faults correspond to reactivation of Mesozoic rift faults, while ~W-E striking faults (the SWIM faults) may arise from the reactivation of oceanic transfer / rift faults and ocean-continent transition structures associated with the

Tethyan and Atlantic Ocean seafloor expansion. We hypothesize that these fault planes in the crust are expressed in the mantle by SE- dipping and vertical alignments of hypocenters, respectively (see figs 6-7).

Beneath the Gorringe Bank most micro-seismicity is located between 20 and 40 km in depth, below or within the limit of the serpentinized upper mantle (see Fig. IV. 10). According to Sallarès et al. (2013), velocity is lower than upper mantle values (8.0–8.2km/s) up to ≈20 km in depth (see Fig. IV.3 at the referenced work). In contrast, some of the intermediate to high magnitude earthquakes are located near this limit (see also Fig. IV. 10). This may indicate different seismic propagation mechanisms for micro and larger earthquakes as discussed elsewhere in this work.

Note that both higher magnitude and micro-seismicity focal mechanisms show reverse dip-slip solutions compatible with a NW-SE strike of Shmax. The southeastwards plunge of the σ_1 can be interpreted as a deflection from the regional sub-horizontal near the Gorringe mantle thrust. The seismicity cannot be related to either the HAT fault or the Gorringe Fault as described by Martinez-Loriente et al., 2014, 2016 and Sallarès et al, 2013 (see Fig. IV.10). The micro-seismicity should be related to a deeper thrust fault zone located west of the HAT (see Fig. IV. 10).

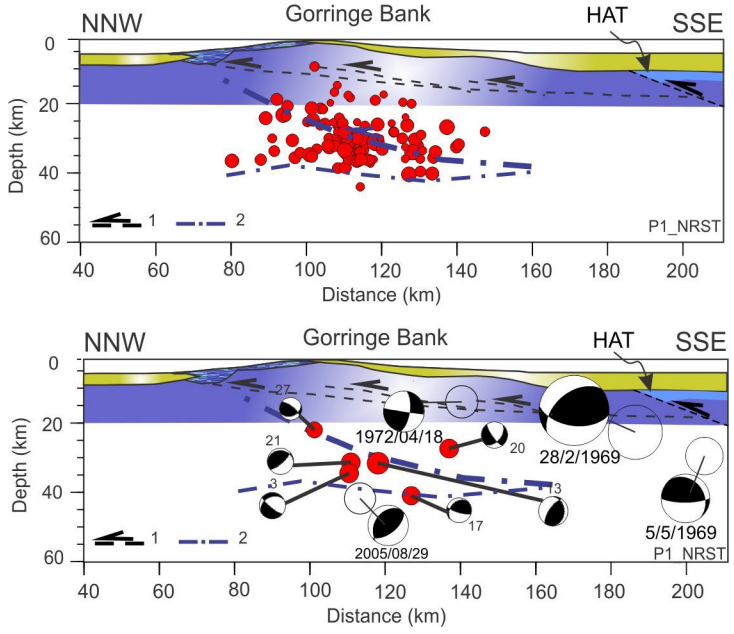

Figure IV.10- - Projection of the seismicity across the Gorringe bank along a schematic representation of the NRST (NEAREST)-P1 refraction profile (adapted from Sallarès et al., 2013, location in Fig. IV. 6, colors define the same lithospheric limits as in Fig. IV. 1B). M>5 events (open circles) are from Buforn et al.1988 and Stich et al., 2010. Note that the focal mechanisms preserve the map view geometry. Few events are coincident with the Gorringe Fault. Notwithstanding, the seismicity seems to be related with a replication of this fault in depth at upper mantle levels.(1- Gorringe fault from Sallarès et al., 2013 and HAT from Martínez-Loriente et al., 2014); 2- possible deeper thrust faults, No vertical exaggeration.)

We also speculate that strike-slip focal mechanism in the SW and NE limit of the seismicity cluster may be related to E-W to WNW-ESE transfer fault zones and OCT (see Fig. IV. 6A).

The São Vicente cluster is elongated parallel to the Marques de Pombal and the São Vicente faults, cutting across the ocean-thinned continental crust boundary (see Figs. IV. 7A-D) with prevailing seismicity located between 20 and 40 km depth, i.e. in the mantle. The OCT coincides with a sub-vertical alignment of hypocenters (see Figs. 7A-D), which suggests that a fault zone extending from the crust into the mantle is accommodating brittle displacement in the mantle. This is in agreement with the OCT being reactivated as fault zone as suggested by Martínez-Loriente et al., (2014). Note that according to our results, the micro-seismicity in this area cannot be explained by the MPF-BTF system as initially postulated in Zitellini et al., (2001, see Fig. IV.11).

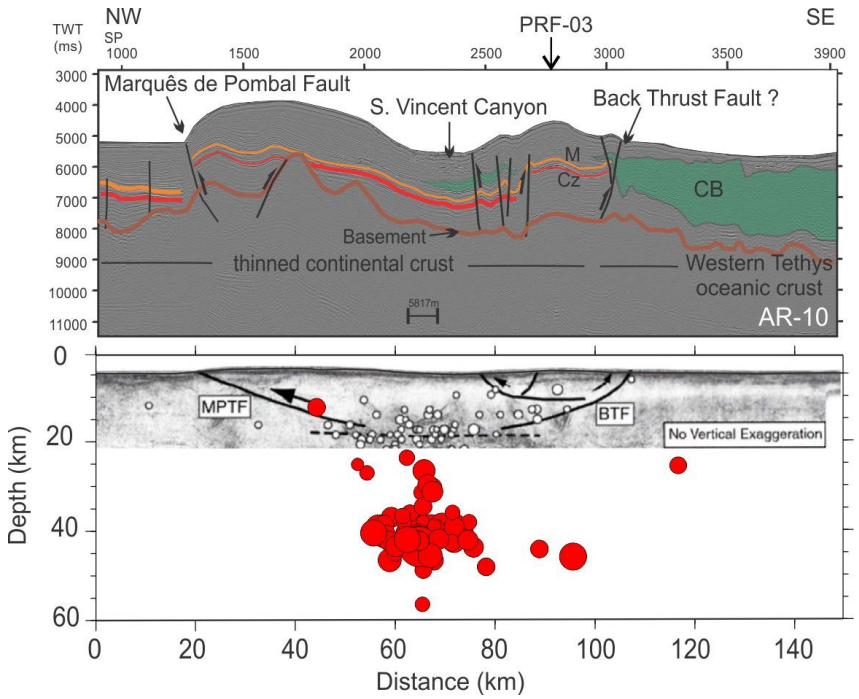

Figure IV.11 Projection of the seismicity in São Vicente Cluster along the AR-10 MCS profile (with a projection of the earthquakes located within 20 km of both sides of the profile). On top is the interpretation of the AR-10 seismic profile (M- Miocene Unconformity; Cz- Discontinuity between the lower Cretaceous and Paleocene; CB-Chaotic body, PRF-03 as is in Fig. IV. 5D). On the bottom Marquês de Pombal and Back-Thrust Faults (MPF-BTF) are a simplified representation of Zitellini et al. (2001) depth converted AR-10 interpretation. According to NEAREST experiment, most micro-seismicity is located off the MPF-BTF system.

During the NEAREST experiment, the earthquake with the highest magnitude (M_L=4.8) was located in this cluster. The focal mechanism solution of this event (code 78 in Figures 4, 7A and Appendix III.C and IV_C) is strike-slip with a small reverse dip-slip component. One of the fault planes is roughly NE-SW, subvertical, while the other is a WNW-ESE, a shallower dipping fault dipping towards NE (see Fig. IV.4). This FM nearly coincides with the FM solution for the December 17th, 2009 Mw=5.8 earthquake, located in the same area and at a depth between 36 and 43 km (see Figs. 1C and 4 as well as Appendix III.B

and IV_B). Neither of these events is related to Marques de Pombal or SWIM-like Faults. We suggest that these events may be related either to a transfer zone marking the limit between the North Atlantic and the Tethys oceanic domains (considering the vertical fault plane) or to a shallow dipping tectonic fabric inherited from the Mesozoic Tethys extension Note that these structures are also compatible with the depth location of micro-seismicity and that both fabrics (vertical and sub-horizontal) were identified in profiles 1-3 in Figs. 7B-D.

The epicenters of the Horseshoe seismicity cluster are distributed across the Horseshoe Abyssal Thrust, the Horseshoe thrust, the SWIM-1 and SWIM-2 strike-slip faults and also across three different basement types, Central Atlantic, Western Tethys crusts and exhumed serpentinized mantle domain (see Fig. IV. 8A-D, Fig. IV.9). This cluster is sub-parallel to the average Shmax direction and focal mechanisms are strike-slip (mostly) and thrust. Inspection of the hypocenters profiles and IAM GB1 seismic profile suggests that the events of this cluster result from the reactivation of all mentioned discontinuities, except for the Horseshoe Fault because this thrust is too shallow, with a maximum depth of approximately 20 km (see Fig. IV.9 in Martínez-Loriente et al., 2016). These results argue in favor of assigning strike-slip events to the SWIM faults, which was until present considered an aseismic fault (Figs. 8A, 8D and 12). The thrust events can be related to blind thrusts in the mantle lying between the HF and the Gorringe thrust (see Fig. IV. 1B).

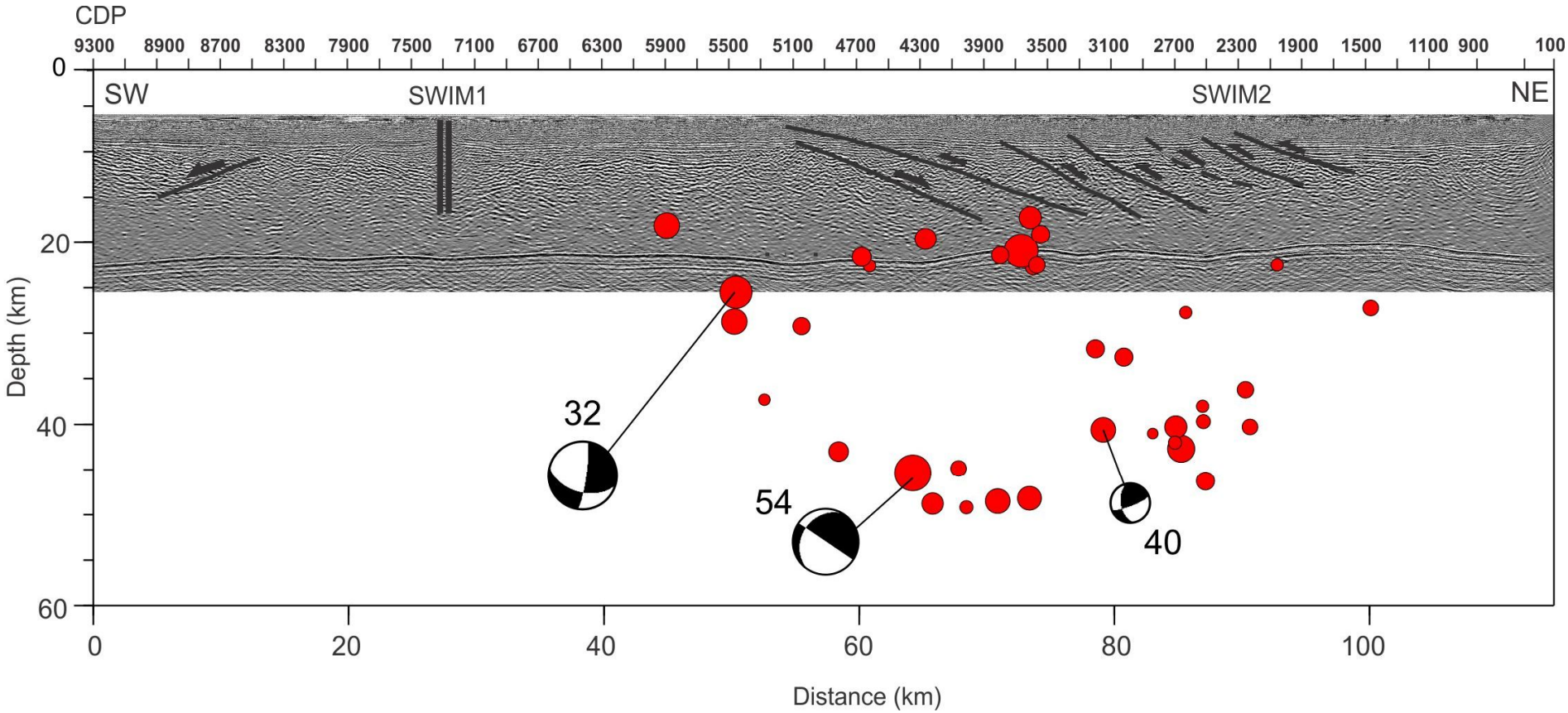

Figure IV.12 - Depth converted IAM-GB1 MCS profile with hypocenters distribution and FMs projected in the same cross-section (the focal mechanisms preserve the map view). For the two-way travel time profile see Fig. IV. 10. Seismic events are selected from 20km of each side of the cross-section. For structural interpretation see Fig. IV. 9.

From this work it results that all three seismicity clusters are located in fault interference zones. The intersection of faults was shown to be an area of stress-strain concentration using analogue and numerical models that were used to investigate fault interference in the study area (see Rosas et al., 2012). The map of lithospheric domains by Martínez-Loriente et al. (2014) suggests that some of the fault interference zones of the study area are associated with the boundaries of different lithospheric domains. Although crustal faults are active and coincident with these boundaries zones, they are too shallow to generate the seismicity recorded in NEAREST experiment, mostly located between 30 km and 50 km in depth. Instead, this seismic activity could be related to the replication at depth of this shallower fabric into the upper mantle controlled by the 3D localization of these tectonic-rheological boundaries (Figs. 3, 6-9).

IV.6.2. Aseismic-seismic slip

In what concerns fault slip and fault seismicity in the study area, four points must be highlighted, *firstly*, there are major thrusts and strike-slip faults imaged in the sediments and basement with accumulated slip that can exceed 1.5km in the Pliocene-Quaternary; *secondly*, seismicity clusters do not coincide with thrust prolongation in depth, *thirdly*, there is barely any seismicity in the crust, i.e. it occurs predominately in the mantle regardless of the different lithospheric domains (Fig. IV. 13); *fourthly*, there is both historical and instrumental evidences for events M~8 or larger.

For example, the western part of the Horseshoe seismicity cluster is located off to the west of the footwall of the Horseshoe fault at a depth of ≈30 km, which is not compatible with the prolongation in depth of this fault that detaches at 15-20 km of depth. Nonetheless, the Horseshoe Fault accumulated ~1.0 km of slip during the Pliocene-Quaternary (Gràcia et al., 2003, Zitellini et al., 2004, Terrinha et al., 2009 and Martínez-Loriente et al., 2016).

Considering that displacement is either accommodated by stick-slip and/or by creep, understanding the transition between these two mechanisms can be important to find the possible link between active faults, high magnitude earthquakes and micro-seismicity in the study area.

Serpentinization may be a controlling mechanism of seismic to aseismic slip partitioning, as described in different tectonic settings by Guillot et al. (2015). Reinen et al. (1994) experiments with serpentinite materials at shallow depth indicate that only fault creep can occur at typical rates of plate motion. According to these authors, serpentinized areas do not favor seismicity but will promote local weakening allowing seismic slip to propagate into a serpentinized region.

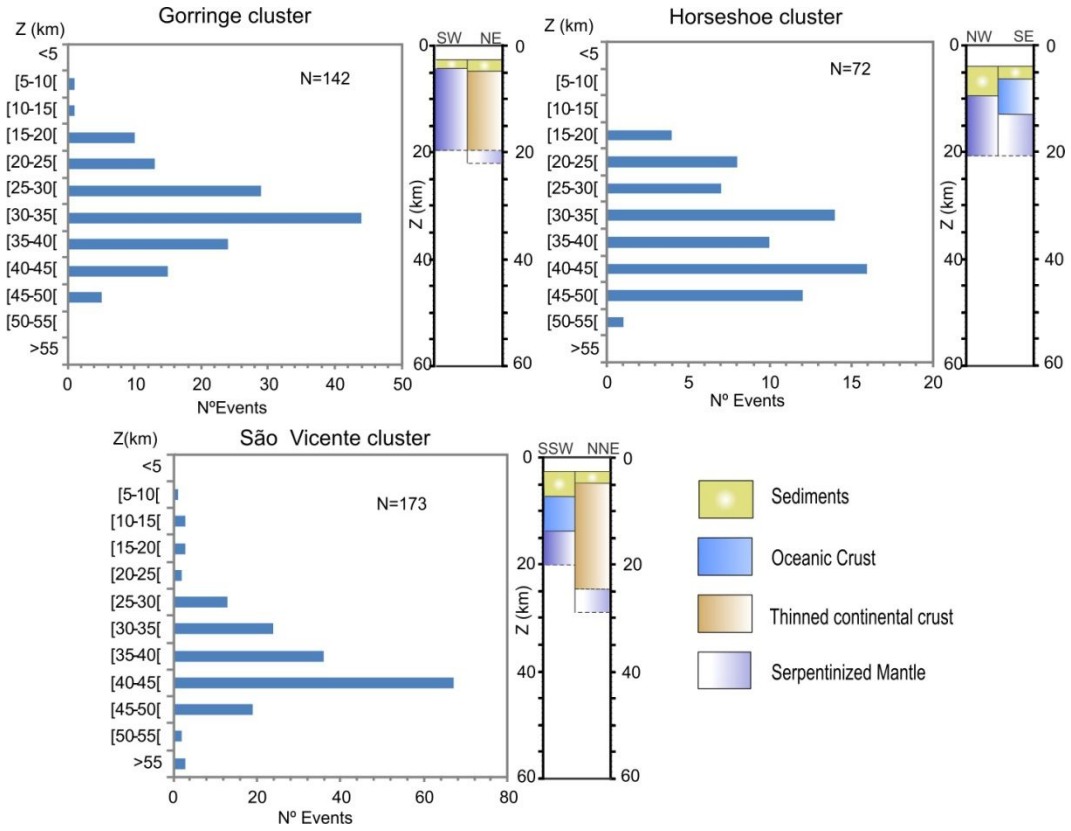

Figure IV.13- Earthquakes distribution in depth for the three identified clusters. The absence (or low) of seismicity in the crust is clearly illustrated here. This is transversal to the all clusters and lithospheric domains (the depth scale refers to the sea level). Note that seismicity is located mostly below the serpentinization limit

Knowing that the Horseshoe Abyssal Plain sediments are floored by a serpentized layer at least down to 20 km in depth (Sallarès et al., 2013 and Martínez-Loriente et al., 2014) we should consider the rheology of serpentine when interpreting the seismicity clusters. Serpentinization can have two origins, i) a primary one during mantle exhumation at the formation of the oceanic crust and ii) a secondary one associated to fracturing and deep sea water circulation (Rosas et al., 2012 and Hensen et al.,2015).

Another side effect of aseismic deformation is the increase of pore fluid pressure due to local tectonic compaction on the surrounding rocks. Pore fluid pressure buildup promotes frictional slip at comparatively lower shear strains producing cracking and porosity in the fault zone promoting fluid circulation. A new group of mud volcanoes reported by Hensen et al. (2015) in the Horseshoe - SWIM faults interference zone occurs above the Horseshoe seismicity cluster. Fluid signatures show a mixed pattern between minor clay dehydration, carbonates recrystallization and oceanic crust alteration that is explained by upward fluids migration suggesting that strike-slip faults provide pathways for deep-seated fluids.

Co-seismic dehydration of serpentinite can be a key mechanism in fault weakening during a high-velocity frictional slip occurring during large magnitude events (Lin et al., 2013). Frictional heating of serpentine-rich fault zones during these events can thus lead to the release of large amounts of water vapor, resulting in increase of pore pressure, decrease of the effective stresses, i.e. weakening of fault zones and fluid migration into neighbor faults promoting extra slip. The transition from creep to stick-slip behaviors in fault zones due to dynamic weakening mechanism is used to explain unexpected high rupture patterns in subduction zones such as the 1999, Mw 7.6 Chi-Chi earthquake (Noda and Lapusta, 2013). The same authors refer this as a plausible rupture mechanism also in other geodynamic settings such as major strike-slip fault like San Andreas Fault.

Micro-seismicity can be used as a proxy for the deep limit of the seismogenic zone. A gap of micro-seismicity can also indicate ductile recovery after a large magnitude event. According to Jiang and Lapusta (2016) this is an explanation for the absence of micro-seismicity at in the area of the 1857 Mw 7.9 Fort Tejon earthquake on the San Andreas/San Jacinto faults system and seismically quiescent megathrusts such as the Cascadia subduction zone.

During 1755-like events the rupture area can extend down to 90 km in depth (Matias et al., 2013), below the seismogenic zone for a Jurassic oceanic lithosphere. We hypothesize that the micro-seismicity gap on the HF (between the Horseshoe and São Vicente clusters) can eventually be the result of ductile recovery that followed this event.

Based on the above it is suggested that:

- The existence of the serpentinized layer results in a decoupling between the crustal and upper mantle tectonics. Accordingly, the serpentinization level should accounts for the absence or scarcity of seismicity above 15km.

- High magnitude events will propagate from upper mantle into crustal levels across the serpentinized layer inducing superficial rupture. In contrast, present-day micro-seismicity is mainly restricted to the upper mantle (Figure IV.13).

- The large magnitude events (M>8) can propagate the slip both up and downwards, i.e. into and across the serpentinized layer as well as into and across brittle-ductile boundary and disturbing the lithosphere-asthenosphere boundary (Figure IV.14).

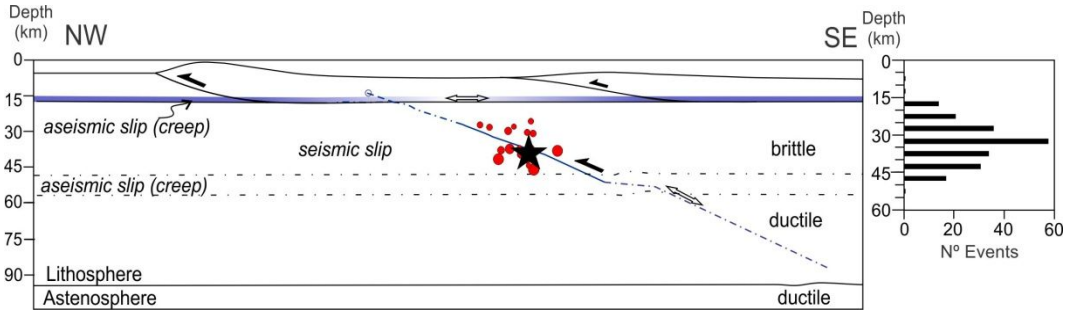

Figure IV.14-- Schematic cross-section illustrating the relation between the stable creep domains, with low to intermediate magnitude seismicity (red circles) distribution, tectonic slip distribution (white arrows) and fault kinematics (black arrows). Micro-seismicity is constrained between two aseismic slip layers, between 15 and 50 km in depth (see the histogram with the depth distribution of the events from the Gorringe and the horseshoe clusters). A top is limited by the serpentinization layer and at the bottom by the brittle-ductile transition zone. During a large magnitude earthquake (black star) the rupture area propagates both upwards and downwards, i.e. slip propagates into the upper crust faults showing surface rupture or not (blind faults). For a 1755-like event extend below the limit of the seismogenic zone down to 90 km in depth.

IV.7. Conclusion

The main conclusions of this work are:

We identified three seismicity clusters located in the areas of the Gorringe Bank, São Vicente Canyon and along the Horseshoe Abyssal plain showing that seismicity is not uniformly distributed in the Gulf of Cadiz area also as suggested by NEAREST preliminary results (Geissler et al., 2010) and clustering analysis in Custódio et al, (2016);

The three seismicity clusters characterized in this work show that the present day micro-seismic activity is generated in the lithospheric mantle and concentrates at fault's intersections, suggesting that the crustal fabric may be replicated in the lithospheric mantle;

The inferred fault interference zones in the upper mantle are associated with boundaries of lithospheric domains localizing stress and seismic strain;

Active crustal faults with bathymetric expression, such as the Horseshoe and Marquês de Pombal faults are either locked or move through slow aseismic slip. Frictional slip may only result from high magnitude earthquakes;

Serpentinization controls seismicity distribution by inducing tectonic decoupling and inhibiting micro-seismicity to occur above the serpentinized layer. Only during high-magnitude events it is expected seismic rupture to propagate upwards across the serpentinized layer up to the surface.

Slip propagation from a non-serpentinized mantle into serpentinized mantle is a possible mechanism to produce larger slip areas, due to the release of pore fluid pressure accumulated during previous aseismic events. This mechanism can account for larger than expected slip for a high magnitude earthquake, like

it is assumed for the 1755 event from numerical modelling of tsunami and inundation (Johnston, 1996, Gradin et al., 2007, Baptista et al.1998, 2011).

V. Discussion and conclusion

The results of the present study allow for the discussion of the following topics:

Our study started with the following main objectives:

- origin and characterization of the micro-seismicity in the study area;
- slip distribution in the active faults,
- what mechanisms control seismicity distribution;
- strain partitioning mechanisms;
- the plate boundary position in the area.

In this final chapter we will sum up and discuss our findings in the scope of the proposed objectives and point out possible future work.

V.1.The micro-seismicity in the study area

The micro-seismicity distribution in the Gulf of Cadiz was studied based on the data recorded in 11 months temporary deployment of 25 ocean-bottom seismic network. The initial dataset included 746 events recorded in ≥ 3 stations. From those, 590 events are located in the restricted area of the NEAREST network as defined by external envelope of the stations locations. Events locations were improved and tested using different methodologies. The final location results from the simultaneous inversion of a 1D velocity model including stations corrections to incorporate sub-surface geological variability (details in chapter III).

The micro-seismicity concentrates in the upper mantle (between 30 and 50 km in depth) in the 3 following clusters, the Gorringe Bank, the São Vicente Canyon and in the vicinity of SWIM 1 and Horseshoe Fault, the Horseshoe cluster. The remaining seismicity was mostly located below the Gulf of Cadiz Accretionary, the Portimão bank, and Guadalquivir bank. It is worthwhile noting that the depth distribution of the hypocentres is common to all clusters regardless the lithospheric domain.

The three clusters are also the loci of intermediate and large magnitude earthquakes. The Horseshoe cluster hosted the Mw=7.8, 28th of February 1969 (the highest magnitude instrumental event in the area) and the Mw ≈ 6.0, 12th of February 2007 earthquakes. While, the São Vicente cluster is the location of the 17th December earthquake with Mw=5.5. The Gorringe cluster is coincident with Mw≈4.5 events, in 19th of July and 29th of August 2005. Note that all clusters are also located in the vicinity of major active faults.

Focal mechanism solutions are found with a double-couple fault-plane solution program based on the polarities of P-wave first arrival. The results showed 82

well constrained solutions. Most events indicate a reverse (21%) and strike-slip solutions (32%). In the São Vicente cluster, the dominant fault plane solutions were strike- or oblique slip. In the Gorringe cluster, we had mostly reverse and oblique slip. While the Horseshoe cluster and the area of the accretionary wedge showed mostly reverse and strike-slip solutions.

The stress tensor inversion showed a NW-SE maximum compression in the Western Horseshoe sub-cluster, the São Vicente cluster and the SW Gorringe sub-cluster and nearly NNW-SSE in the Eastern Horseshoe and the NE Gorringe sub-clusters. These results, in general, diverge from Geissler et al., 2010 preliminary results. In the São Vicente cluster (Northern cluster in the reference work) is referred a maximum compression nearly WNW-ESE, while in the Horseshoe cluster (southern cluster in the reference paper) is roughly NNE-SSW. Some discrepancies with Geissler et al. (2010) probably arise from the fact that the present study added 33 new focal mechanism solutions to the catalogue.

The maximum horizontal compression (SHmax) and dominant stress regime based on the stress tensor details for each cluster was calculated following the World Stress Map Project guidelines.

In the São Vicente cluster, SHmax is roughly NW-SE, at ≈50º angle with the NNE-SSW cluster striking direction. The dominant stress regime is strike-slip, in agreement with prevailing focal mechanisms solutions.

In the Horseshoe cluster, SHmax is roughly NNW-SSE in the E and NW-SE in the W. In the E, SHmax defines a ~50º angle with the main SWIM strike-slip fault, the expected maximum compression direction on a strike-slip fault. Conversely, in the W, SHmax direction is perpendicular to the Horseshoe thrust fault, consistent with the thrust kinematics and sub-parallel to the cluster alignment. Nevertheless, both sub-clusters have a strike-slip dominant stress regime compatible with the E FMs solutions but unclearly explained in the Western domain.

The Gorringe cluster SHmax is roughly NNW-SSE oriented, defining a high angle (70º-75º) with the Gorringe fault strike, compatible with thrust kinematics. However the dominant stress regime is strike–slip, as the prevailing FMs are mostly oblique, combining strike-slip with reverse-slip.

All the above SHmax orientations are in reasonable agreement with SHmax determination derived from neotectonic numerical modeling in the area of Neres et al. (2016) that used GPS plate kinematics, potential fields and seismic strain. This agreement from independent approaches is interpreted as a validation of the methodology used in the present work

V.2.Lithospheric domains and the limits of the seismogenic zone

It is argued in this work that micro-seismicity provides valuable information about the limits of seismogenic zone based on the following.

One of the main results of this work is the comprehensive understanding of depth limit of low to intermediate magnitude earthquakes in the study area. Using 1 D velocity model to define EQs hypocentres in areas with high lithospheric variability such as the Gulf of Cadiz was overcome with stations corrections in our location models. Different locations methods and velocity models to control the depth variability were tested.

According to our results all EQ events are located in the upper mantle with maximum depths of 50-55 km. This observation is common to all clusters regardless of the lithospheric transitions and composition.

The lower limit for cold Jurassic oceanic lithosphere seismogenic zone or brittle-ductile transition is roughly between 50 and 55 km, coinciding with the ≈600ºC geotherm, for simple temperature dependent models (e.g. Mackenzie et al, 2005), which is also the transition between velocity weakening - velocity strengthening behaviors of dry olivine (Boettcher et al., 2007). More comprehensive models of the oceanic lithosphere (combining temperature-pressure-dependent thermal properties, hydrothermal circulation and oceanic crust contributions) set this limit to 700ºC-800ºC (Grose et al., 2013), also at 50-55 km depth.

It is known that in continental lithosphere seismicity is also restricted to temperatures below 600ºC (e.g. Sloan et al, 2010). However, the upper mantle is generally above 600ºC (e.g Mckenzie et al., 2005), thus usually seismicity occurs in the crust within continental lithosphere.

At continental margins, seismic activity can display a combination of the seismogenic behaviour of both continental and oceanic settings (Craig et al., 2011), such as for eastern and north-eastern African margins where seismicity extends below the expected depth for the typical continental lithosphere but not below the seismogenic limit at the adjacent old oceanic lithosphere. The authors argue that this is due to a compositional transition between the two types of lithosphere.

The existence of seismicity in the continental upper mantle in the Gulf of Cadiz was reported by several previous studies based on teleseismic records (e.g Stich et al., 2010) and in local temporary deployments (Geissler et la., 2010, Grevemeyer et., 2016 in attachment)

Let us assume a simple model where seismicity in the continental lithosphere is limited by the 600ºC isotherm. To explore this thermal limit in the Gulf of Cadiz, we created simplified geothermal gradient models, as follows. We combined heat flow measurements with stratified geological models of the lithosphere (deduced from geophysical and core data, Hayes et al., 1972, Ryan et al., 1973 Gonzalez et al. (1996), Rovere et al., (2004), Sallarès et al. (2011) and Martínez-Loriente et al. (2014)). The conductive geotherm in a horizontally stratified subsurface is calculated by solving the steady state heat flow equation

$$\frac{\partial^2 T(z)}{\partial z^2} = \frac{-A(z)}{k(z)}$$

Where T is temperature, z is depth, A is heat production and k is the thermal conductivity. Heat flow variation in depth can be deduced based on the following approximation, assuming that heat flow (q_z) has a linear relation with depth and heat radioactivity:

$$q_z = q_0 - A(z) \times dz$$

where, q_0 is the surface heat flow.

In the next step, we estimate the steady –state temperature in depth z as follow (Anderson, 1989):

$$T_z = T_0 + \frac{0.5 \times (q_0 + q_z)}{k(z)} \times dz$$

The heat flow data was extracted from Grevemeyer et al. (2009, 2017) and Jimenez –Munt et al. (2010). We used the thermal proprieties in Fernandez et al, (1998), Watts and Burov (2003), Vilá et al. (2010) and Grevemeyer et al., (2017).

We defined the following different layered models to compare with the local setting of the three clusters:

- a three layer model to simulate the exhumed serpentinized mantle domain (details in the Table V.1): sediments, hydrated mantle and unaltered mantle;
- four layered model to describe the oceanic lithosphere domain (details in the Table V.2)
- five layered model to define the thinned continental lithospheric domains: sediments, upper crust, lower crust, hydrated mantle and unaltered mantle (details in the Table V.3).

We consider that all layers have isotropic and homogeneous thermal properties and heat production.

The exhumed serpentinized mantle domain:

In the exhumed mantle models we explored two initial surface heat flow (SHF) values 60.7 and 65 mW/m^2 and two sediments thickness, 0.5 and 4 km. These values reflect the heat flow data observed in the vicinity of Gorringe bank and in Horseshoe Abyssal plain (HAP) area (within the exhumed mantle domain, Grevemeyer et al., 2017 and Jimenez-Munt et al., 2010). Also both MCS reflection and refraction seismic profiles (e.g. Jimenez-Munt et al., 2010 and Martinez-Loriente et al., 2013) show that the sediments thickness in the GB is ≈ 0.5 km while in the HAP is nearly 4km (see Figure V.1A). We limited the

serpentinization level to 20 km in depth as observed P1-NEAREST refraction profile (Martinez et al., 2013).

Our models are plotted in the Figure V.1B. Initial higher SHF values and thicker sediment cover lead to hotter models (red lines). Note that having a thin sediment cover with higher SHF (full red line in Figure V.1B) and thick sediment cover with lower SHF (dashed blue line in Figure V.1B) leads to similar thermal models. Our models plot the 600ºC geotherm between 46-53 km in depth (45-52 km below sea floor) in the Gorringe Bank (see Figure V.1A and full line models in Figure V.1B) and between 45-50km in the HAP (see Figure V.1A and dashed line models in Figure V.1B).

The highest SHF values are observed in the vicinity of the Gorringe Bank and decreases towards the East, in HAP (e.g. Jimenez-Munt et al., 2010). We may consider that the model with the thinner sediment cover and highest SHF (full red line in Figure V.1B) is more adequate to define the SW Gorringe sub-cluster setting while the 4 km thick sediment cover with lower SHF value fits the W HAP sub-cluster.

Our results show that seismicity in the SW Gorringe sub-cluster (to the left in Figure V.1A) is located above the 600ºC limit. This is observed even if we consider a hotter model, with SHF≈65 mW/m^2 (red full line in Figure V.1B). However, in the HAP cluster, 3 events are located below this thermal limit if we consider SHF of 65 mW/m^2.

Another interesting result is that 8 events in the SW Gorringe sub-cluster and 3 events in the W HAP sub-clusters are located in the serpentinized mantle. Accordingly, it may indicate that seismicity may be also generated in the partially serpentinized layer or alternatively, that serpentinization may be heterogeneously distributed both in Gorringe bank and HAP.

However, these results should be taken with caution as the the average depth errors are 5.7km and 7.7km in the SW Gorringe sub-cluster and W HAP sub-cluster, respectively, and, as we can observe in Figure V.1C, the Vp and Vs velocity models used to located the NEAREST dataset do not reflect the compositional models of these two sub-clusters.

Table V.1-Exhumed serpentinized mantle thermal models. We consider surface heat flows of 60.7 and 65 mW/m^2 (details the text).

Layer	**Sediments**	**Hydrated mantle**	**Mantle**
Thickness (km)	0.5-4	11-17.5	14.5
Thermal Conductivity (W/K.m)	2.5	3	3.4
Radiogenic heat production (W/m^3)	9.00E-07	1.50E-06	2.00E-07

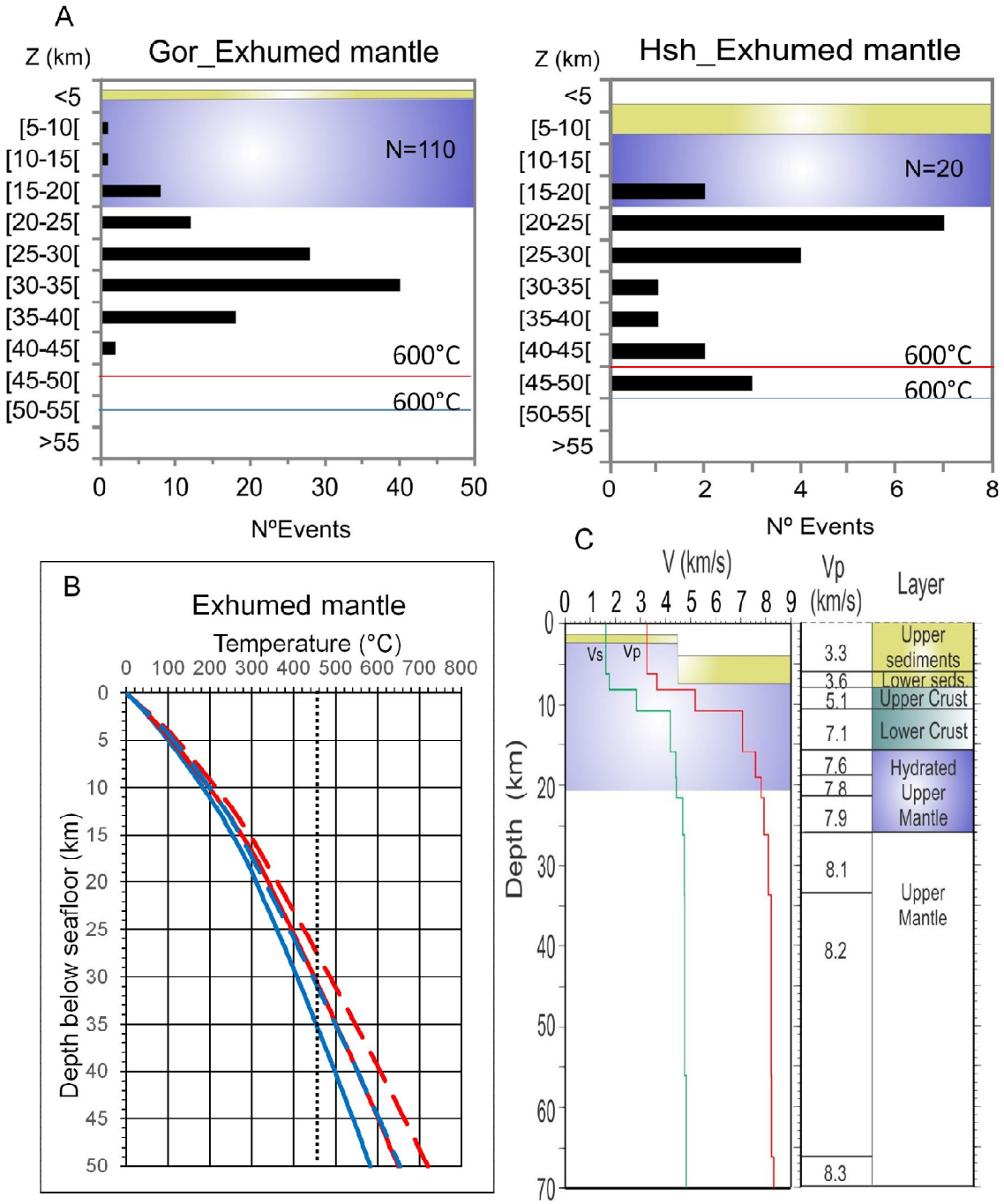

Figure V.1-The limits of seismogenic zone in the exhumed serpentinized mantle domains. A- The depth distribution of the hypocenters plotted on top of the geological layering, to the left in the SW Gorringe sub-cluster and to the right in the NW HAP sub-cluster (yellow and purple layers define the sediment and serpentinized mantle levels). Red and blue lines define the location of the 600ºC isotherm (derived from models in Figure V.1B). B – Thermal models based on the parameters depicted in the Table V.1 (Full lines define the models with thin sediment layer while dashed lines refers to 4km thick sediment layer. Blue and red lines refer to SHF of 60.7 and 65 $mW/m^{2,}$ respectively; dashed black line defines the 460ºC, antigorite breakdown initiation temperature.). C- Composite velocity models versus compositional layer in the sub-clusters area. To the left are the Vp and Vs velocity models on top of the compositional models in the Gorringe bank (left) and in the Horseshoe Abyssal plain (right). To the right is the compositional model of the upper lithosphere is proposed based on the Vp model derived in chapter III.3.2.

The oceanic lithosphere domain

We tested two models simulating the lithospheric layering in the southern limit of the SVC and in the western HAP sub-cluster. The main differences are the sediment and crustal thickness (see Table V.2 and Figure V.2A-C). Both models had a SHF of 57mW/m^2, in agreement with the values in Grevemeyer et al. (2009) and Jimenez-Munt et al. (2010). The velocity model resulted from hypocenter-velocity inversion method (Figure V.2C).

Our results are plotted in the Figure V.2 B. The 600°C isotherm is located between 47 and 50 km in depth. Thinner sediment and thicker crustal layers result in a relatively hotter model. One hypocenter in the Horseshoe sub-cluster and 5 in the southern limit of SVC were located below this limit (Figure V.2A). Like in the previous models some events are located in the hydrated mantle domain. The average depth error is 5.3km in the western HAP sub-cluster and 6km in the southern SVC.

We consider that our results indicated that the selected thermal models describe the lithospheric structure in the two sub-clusters.

Table V.2- Oceanic lithospheric domain thermal models. We consider a surface heat flow of 57mW/m^2 (details the text).

Layer	**Sediments**	**Oceanic Crust**	**Hydrated mantle**	**Mantle**
Thickness (km)	2-4	8-6	9	30
Thermal Conductivity (W/K.m)	2	3.0	3	3.4
Radiogenic heat production (W/m3)	9.00E-07	3.50E-07	1.50E-06	2.00E-07

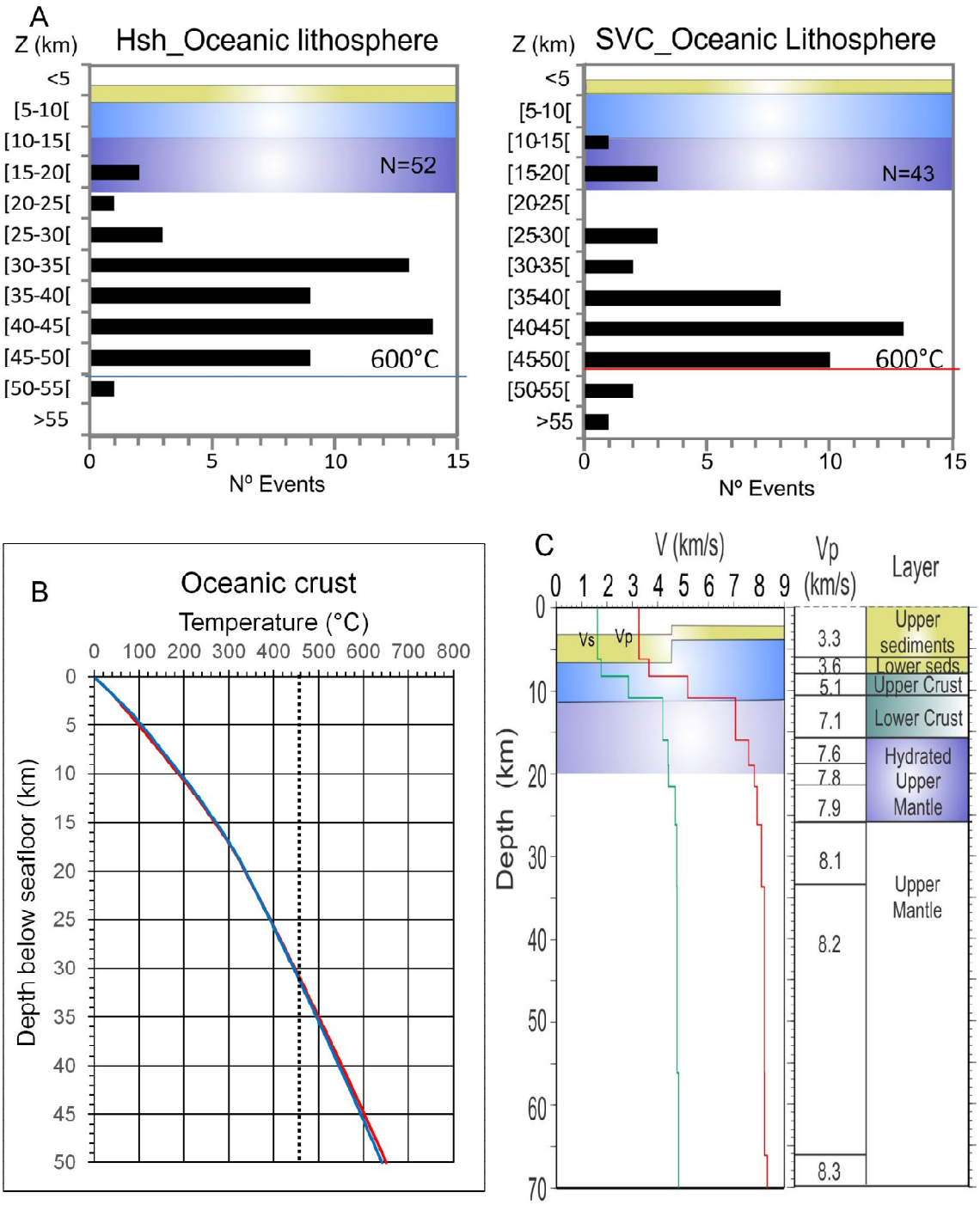

Figure V.2 - The limits of seismogenic zone in the oceanic lithosphere domains. A- The depth distribution of the hypocenters plotted on top of the geological layering, to the left in the SE HAP sub-cluster and to the right in the southern area of the SVC cluster (yellow, blue and purple layers define the sediment, oceanic crust and serpentinized mantle levels). Red and blue lines define the location of the 600ºC isotherm (derived from models in Figure V.2B). B – Thermal models based on the parameters depicted in the Table V.2 (blue and red lines refers to 2km and 4km sediment layer, respectively; dashed black line defines the 460ºC, antigorite breakdown initiation temperature .). C- Composite velocity models versus compositional layer in the sub-clusters area. To the left are the Vp and Vs velocity models on top of the compositional models in the SE HAP sub-cluster (left) and in the southern area of the SVC cluster (right). To the right is the compositional model of the upper lithosphere is proposed based on the Vp model derived in chapter III.3.2.

The thinned continental lithosphere domain

We initially tested two different models to describe the thermal model in the NE limit of the Gorringe and the N limit of the São Vicente clusters, located in the thinned continental lithospheric domain (see Figure V.4 based on Rovere et al., 2004, Gonzalez et al., 1996, Sallarès et al., 2011 and Martinez-Loriente et al., 2013). The thermal proprieties and layering are presented in the Table V.3. We considered a surface heat flow of 59mW/m2 based on values described for the Marques de Pombal Fault area, after topography correction, in Grevemeyer et al., (2009). According to the authors, the MPF tectonic activity has low influence on the surface heat flow value.

In the Gorringe cluster area, the model was 11km thick for both the continental crust (upper and lower crust) and the serpentinized mantle. In the São Vicente cluster area, we considered 17km and 7km thick for the crust and hydrated mantle, respectively (Table V.3. and Figure V.3A).These values were taken from analysis of Sallarés et al 2011 and Rovere et al. 2004.

Our models show that the 600°C limit is located at 39 km and 45km in the São Vicente and Gorringe sub-clusters, respectively (Figure V.3A-B). Based on these results, 5 earthquakes, in the Gorringe Sub-cluster, are located below this limit although within the depth error limit (5.2km). In the northern São Vicente area 65 events lie below the 600ºC isothermal, 15 of which below the error limit (5.6 km)

The results indicate that assumed thermal models reasonably fit the Gorringe bank compositional layering. However, it may fail to reproduce the lithospheric structuring in the northern São Vicente sub-cluster. We point out the following hypotheses:

a) Incorrect layered model?

The selected number of layers agrees with the information provided by geophysical data (wide-angle seismic reflection and refraction profiles in Gonzalez et al., 1996 and Sallarès et al., 2011). However, there is some uncertainty in the thickness of selected layers particularly in the crustal levels. Our tests showed that any increase in the crustal thickness moved the 600ºC isotherm into shallow levels, increasing the number of events below this rheological limit. Decreasing the crustal thickness would not agree with constraints imposed by the available geophysical data.

b) Inadequate velocity model?

We should also discuss if our general velocity model is adequate to define the compositional model in the northern São Vicente sub-cluster. In Figure V.3C, we see that the general model is in roughly faster than the thinned continental layering in both NE Gorringe and Northern SVC. Some of these differences should be absorbed by stations corrections included in the location method.

c)The thermal proprieties are inaccurate?

The heat production and thermal conductivity in the models are mostly extracted from the Vilà et al., (2010). Since both areas are at a continental margin, we considered that the crust was more mafic with lower heat production. So, we slightly increase the heat production to 9.80E-07W/m3 and 3.70E-07W/m3 in the upper and lower crust, respectively. Accordingly, the 600ºC isotherm moved down to 49km in depth (blue full line in B and see details in the Table V.3). As a result few hypocentres were located below this depth limit (Figure V.3A).

In general thermal models are in good agreement depth distribution of the hypocentres. For all, selected areas seismicity is mostly located above the 600ºC limit. This is the typical temperature limit at the oceanic domain.

At the continental domain seismicity is mostly located at the crust. Our results show that hypocentres, in continental domain are mostly located at the upper mantle, but above the 600ºC isotherm.

These results also attest the adequacy of the earthquakes location method applied in our study.

Table V.3- Thinned continental lithosphere thermal models. We consider a surface heat flow of 59mW/m^2 (details the text).

Layer	**Sediments**	**Upper Crust**	**Lower Crust**	**Hydrated mantle**	**Mantle**
Thickness (km)	1	10-15	1-2	7-11	25-27
Thermal Conductivity (W/K.m)	2.0	3.0	2.1	3.0	3.3
Radiogenic heat production (W/m3)	9.00E-07	3.50E-07-9.80E-07	1.50E-07-3.70E-07	1.50E-06	2.00E-07

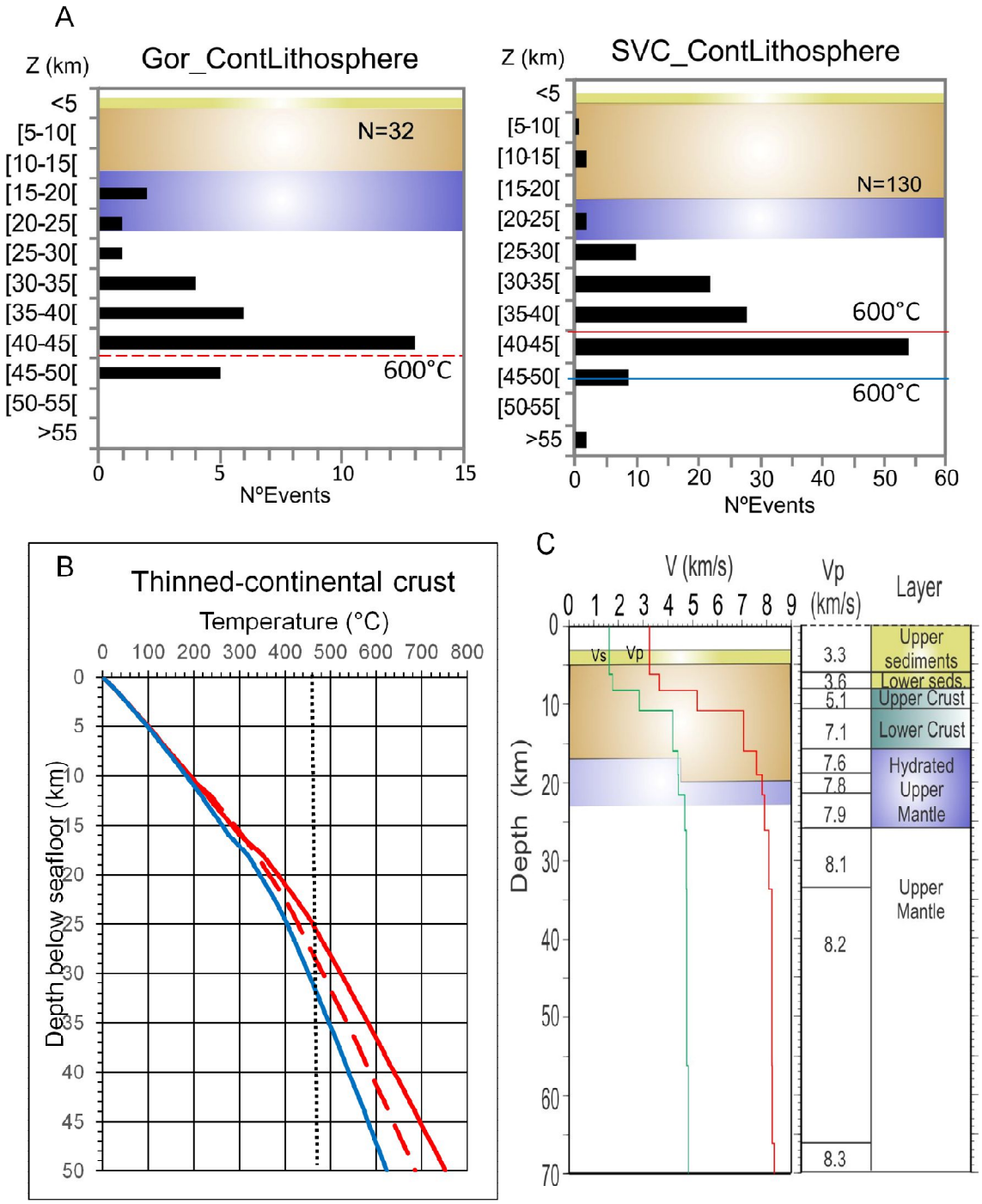
A
Gor_ContLithosphere
Z (km)
<5
[5-10[
[10-15[
[15-20[
[20-25[
[25-30[
[30-35[
[35-40[
[40-45[
[45-50[
[50-55[
>55
N=32
600°C
0
5
10
15
N°Events
SVC_ContLithosphere
Z (km)
<5
[5-10[
[10-15[
[15-20[
[20-25[
[25-30[
[30-35[
[35-40[
[40-45[
[45-50[
[50-55[
>55
N=130
600°C
600°C
0
10
20
30
40
50
60
N°Events
B
Thinned-continental crust
Temperature (°C)
0 100 200 300 400 500 600 700 800
Depth below seafloor (km)
0
5
10
15
20
25
30
35
40
45
50
C
V (km/s)
0 1 2 3 4 5 6 7 8 9
Vp (km/s)
Layer
Depth (km)
0
10
20
30
40
50
60
70
Vs
Vp
3.3
3.6
5.1
7.1
7.6
7.8
7.9
8.1
8.2
8.3
Upper sediments
Lower seds
Upper Crust
Lower Crust
Hydrated Upper Mantle
Upper Mantle

Figure V.3- The limits of seismogenic zone in the thinned continental lithosphere domains. A- The depth distribution of the hypocenters plotted on top of the compositional layering, to the left in the NE Gorringe sub-cluster and to the right in the northern area of São Vicente cluster (yellow, brown and purples layers define the sediment, *thinned* continental crust and serpentinized mantle levels). Red and blue lines define the location of the 600ºC isotherm (derived from models in Figure V.3B). B – Thermal models based on the parameters depicted in the Table V.3 (dashed red line define a *Gorringe–like* layering while full red and blue lines refer to a *SVC-like* layering with lower and higher crustal heat production, respectively; dashed black line defines the 460ºC, antigorite breakdown initiation temperature.). C- Composite velocity models versus compositional layer in the sub-clusters area. To the left are the Vp and Vs velocity models on top of the compositional models in the Gorringe bank (left) and in the São Vicente (right) sub-clusters. To the right is the compositional model of the upper lithosphere is proposed based on the Vp model derived in chapter III.3.2

V.3.Seismicity and the active faults in the Gulf of Cadiz

Seismicity in the Gulf of Cadiz area is located at intermediate depth (mostly 30-50km) below the limits of observation for MCS seismic and refraction profiles. However, keeping in mind these limitations, we can still compare geological patterns and crustal transitions observed at shallow depth with the hypocenters trends and fault-plane solutions derived from our seismological data.

Both the Gorringe and the São Vicente clusters define alignments sub-parallel to the striking direction of major active ~NE-SW striking thrust faults and associated seamounts.

In the Gorringe cluster, seismicity is aligned sub-parallel to the Gorringe Fault that limits to NW, the Gorringe Bank. According to Jiménez-Munt et al. (2010), this fault is a major NW verging, sub-crustal thrust fault with a ramp and flat geometry related with at least 20 km shortening in the 5-10 Ma interval (upper-middle Miocene). Sallarès et al. (2013) also identified a low angle SE-dipping, high serpentinization zone resulting as an additional evidence for the presence of a major thrust fault.

The prevailling FMs in the area are strike-slip and reverse dip-slip both for $M_L \geq 3$ recorded in the NEAREST experiment and higher magnitude earthquakes compiled from permenent land networks (see Figure V.4). However, none of these are related to the Gorringe Fault as inferred from MCS seismic profiles since this is too shallow in the crust. Seismicity should be related to a deeper structure. However, it is puzzling that only two events with $M_L \geq 3$ have reverse dip-slip solutions, the remaining earthquakes show nearly pure strike-slip solutions, with fault plane solutions striking ≈N-S to NNE-SSW and ≈ E-W to NW-SE. This is also in agreement with the dominant stress regime in Neres et al, (2016) or estimations based on the only on NEAREST dataset (even though it refers to low to intermediate magnitude events).

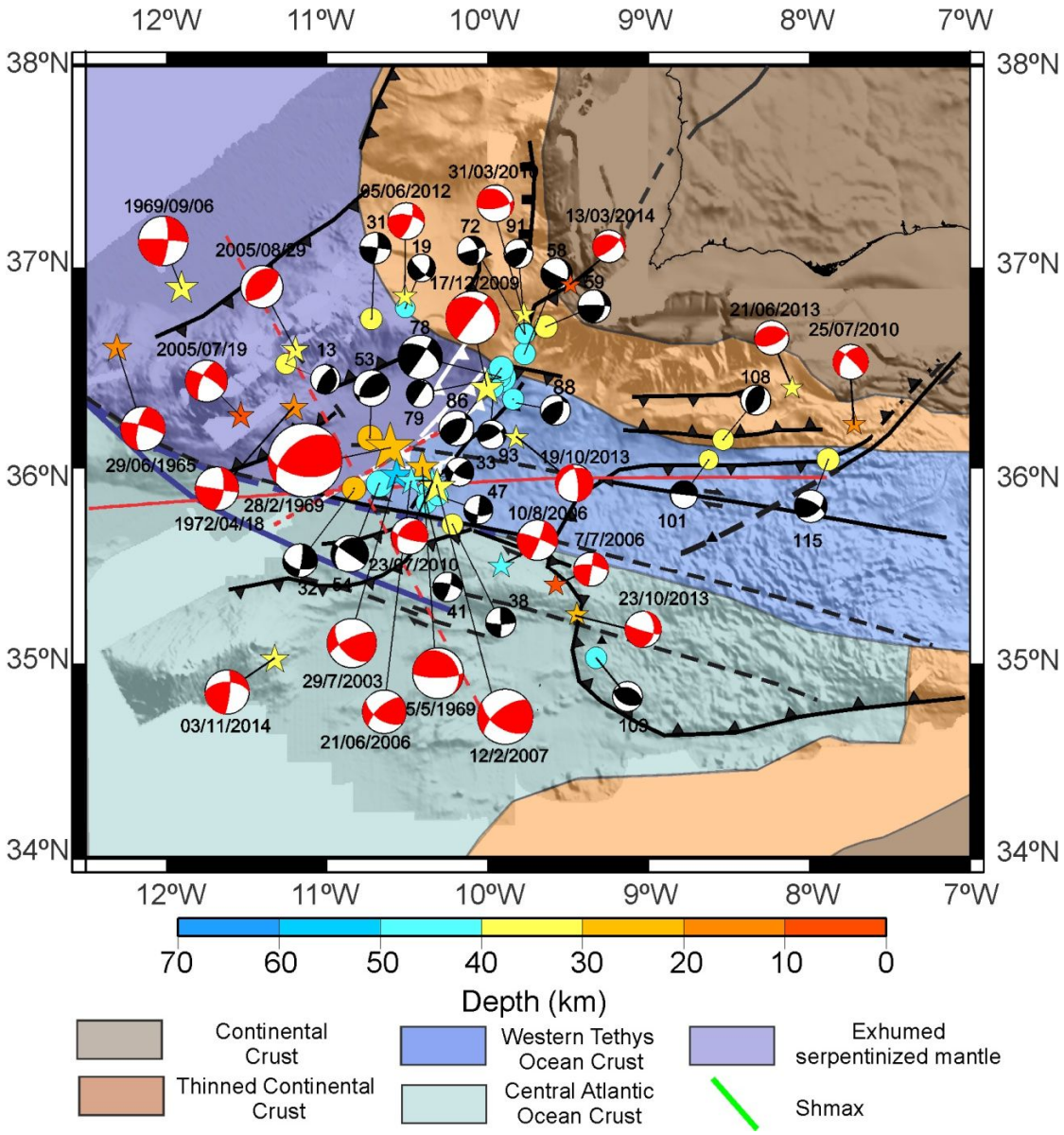

Figure V.4-Focal mechanism solutions of earthquakes with $M_L \geq 3.0$ recorded in the NEAREST OBS network (max M_L=4.8, with black compression quadrants) and the fault plane solution for the highest magnitude earthquakes recorded in the land network (red compression, full black lines define active faults, dashed lines are inferred or possible active faults, white lines are blind faults and blue line is the PIAB- Paleo Iberia-Africa plate Boundary, from Rovere et al., 2004).

The Gorringe seamount comprehends the intersection of the NW-SE trending OCT, the NE-SW striking Gorringe thrust and the western prolongation of the ~W-E striking strike-slip SWIM faults. It appears that all these tectonic faults and discontinuities are being reactivated generating micro-seismicity in the shallow lithospheric mantle (figure V.1).

The São Vicente cluster of epicentres is at the intersection of NNE-SSW to NE-SW striking thrust faults (S. Vicente canyon fault and Marquês de Pombal thrust) and one WNW-ESE striking SWIM strike-slip fault that is coincident with the Ocean-Continent Transition.

The MP thrust fault soling out at approximately 20 km of depth was described as a good candidate to the 1755 earthquake source, combined either with a Back-Thrust Fault (BTF- Zitellini et al., 2001) system or with Horseshoe Fault (Ribeiro et al, 2006). However, these faults are too shallow to account for the recorded micro-seismicity.

Recent earthquakes with magnitude >4, (e.g. 17th December 2009 event with Mw≈5.5) and also the highest magnitude event recorded in NEAREST network with M_L=4.8 are located in this cluster. Both resulted from similar FMs, oblique solution combining strike-slip with reverse dip-slip component (Figure V.4). One of the fault planes is roughly NE-SW, sub-vertical, while the other is a WNW-ESE, a shallower dipping fault dipping towards NE. Neither of these events is also related to Marques de Pombal or SWIM-like Faults.

Alternatively, the first fault plane is sub-parallel to the SVF, that strikes ≈NE-SW steeply dipping to the SE. In Pereira and Alves (2013) is described as the possible offshore extension of the Messejana-Plasencia Fault Zone (MPFZ) more than 400 km long hosting a dolerite dyke with tens of meters of thickness, indicating a deep origin of this fault. The other fault plane is may be related to a shallow dipping tectonic fabric inherited from the Mesozoic Tethys extension.

Hence it is proposed that the NE-SW striking steep faults (S. Vicente fault system) and the SWIM strike-slip faults and sub-parallel OCT accommodate earthquake slip and strain partitioning in the S. Vicente seismicity cluster.

In the Horseshoe cluster seismicity is distributed along a NW-SE alignment, sub-parallel to the transition between exhumed serpentinized mantle or of Western Tethys domains and the Central Atlantic oceanic crust. It is also on the tail of the Gorringe thrust and extends to the East across the intersection of the Horseshoe thrust and SWIM faults (Figure V.4). This cluster contains the source area of 28th February 1969 earthquake with Ms≈8.0, located at 22-33km in depth, the largest instrumental event reported in the Gulf of Cadiz region. Again, the NEAREST dataset also reported an event located with ML≈3.9, in the same area, at the same depth with similar FMs (event 53, Figure V.4). The events are located on top or at the footwall of the HAT but vertically displaced from this structure. To the East is the source area of the 12 February 2007 had Mw ≈ 6.0, with a hypocenter at 40 km beneath the seafloor and a moment tensor indicating thrust faulting with a small component of strike slip (Figure V.4).

In this cluster, the prevailing FMs are: a) nearly pure reverse dip-slip solution to the west of the HAT; b) pure strike-slip solutions to the East of the Horseshoe fault or in the vicinity of the SWIM faults system; c) oblique slip (combining strike-slip with reverse dip-slip) on top of the Horseshoe Fault and the interference zone with the SWIM fault system. Accordingly, we speculate that the fault zones imaged at crustal levels may be the expression of similar structures in the mantle, here replicated by distribution of the focal mechanism solutions.

From the NEAREST experiment results that all three seismicity clusters are located in fault interference zones. The map of lithospheric domains by Martinez-Loriente et al. (2014) suggests that the fault interference zones of the area are also associated with the boundaries of different lithospheric domains. Although crustal faults are active and coincident with these interference zones they are too shallow to generate the seismicity recorded in NEAREST experiment. Instead, this seismic activity can be related to the replication of this shallow tectonic fabric into the upper mantle controlled also by the location of these lithospheric transitions.

Outside the NEAREST network area, the earthquakes identification and location become less accurate. However, we could recover some events and define a few focal mechanism solutions. In Figure V.5, we show the events locations in map view and projected along the P2 NEAREST refraction profile, respectively.

Few events are located in the upper crust at the continental domain. Outside this area, seismicity is restricted to the upper mantle below 20 km in depth. As in the Gorringe cluster, it seems that in the South Portuguese continental margin the hypocenters distribution dip to the N, following the continental-ocean boundary zone slope (see Figure V.5). The relation between the bending stresses associated with flexural isostasy in the OCT and seismicity distribution in the Gulf of Cadiz was already explored in Neves and Neves (2009). However, the authors suggest that flexure bending stress is not sufficient to produce brittle failure and earthquakes in the crust and upper mantle. An additional weakening mechanism is necessary to reduce the brittle strength in the ocean–continent transition. They suggest inherited mechanical weaknesses as a possible additional mechanism.

Focal mechanisms show mostly strike-slip and reverse-slip solutions, compatible with SWIM and thrust faults kinematics. However, the reverse-slip solutions are located at mantle depths, displaced by 30 km from the accretionary wedge limit. Accordingly, these focal mechanisms are speculatively associated with a deeper thrust fault that is compatible with the east-dipping subduction zone under the Gibraltar arc described in Gutscher et al. 2002 and Duarte et al., 2013.

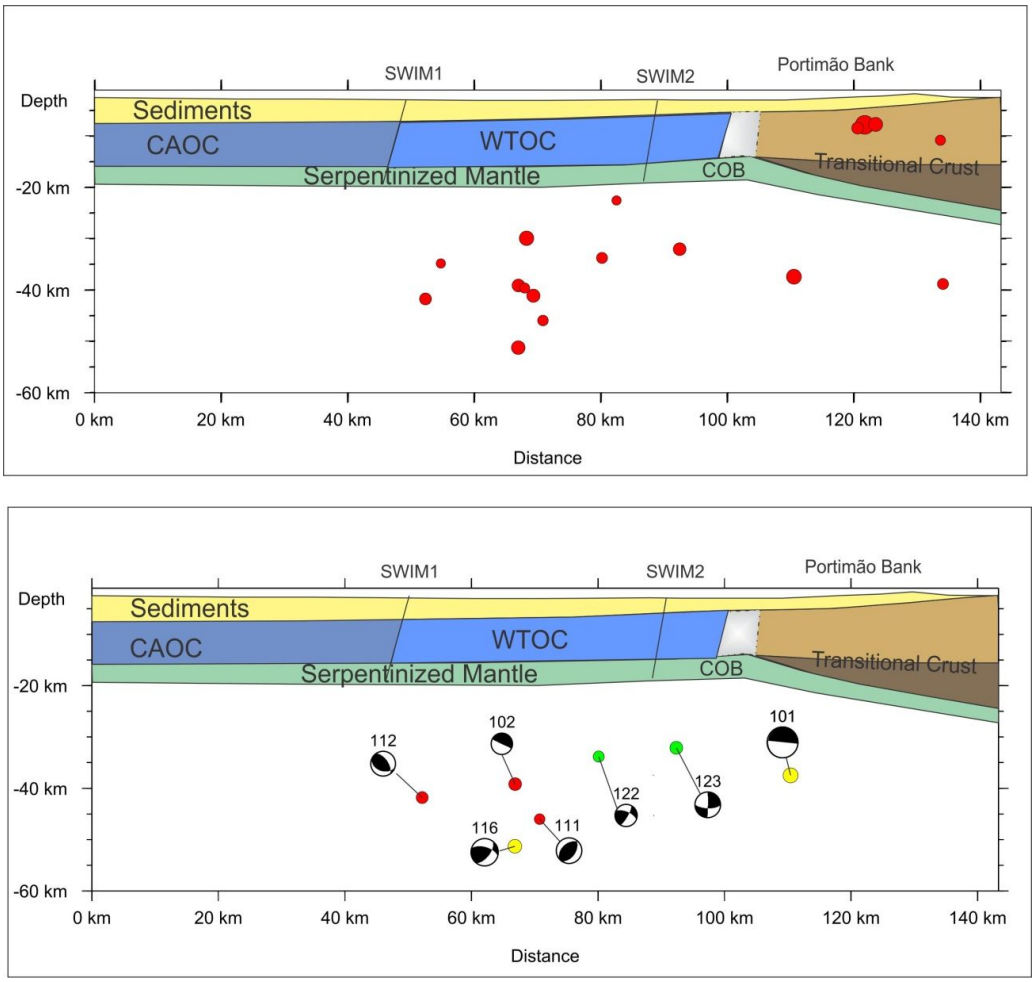

Figure V.5- Schematic representation of the P2 NEAREST refraction profile (adapted from Salláres et al. (2011) and Martinez-Loriente et al. (2013) with a projection of the earthquakes located within 10 km of both sides of the profile. Abbreviations: CAOC- Central Atlantic Oceanic Crust and WTOC- Western Tethys Oceanic Crust**.**

V.4.Strain partitioning, aseismic and seismic slip:

Strain partitioning in the Gulf of Cadiz is described in previous works. Terrinha et al. (2009) based on swath bathymetry and MCS seismics suggested that the present day NW-wards movement of Nubia with respect to Iberia is accommodated by strain partitioning in dextral wrenching on WNW–ESE trending steep faults and thrusting on the NE–SW trending fault.

Our study shows that micro-seismicity results from fault plane solutions with prevailing strike-slip and reverse dip-slip kinematics. This is common to the three clusters. Hence, it may indicate that seismic strain is partitioned in two fault systems with the similar striking directions to the crustal structures. Yet, seismicity is located at intermediate depths in the upper lithospheric mantle suggesting a tectonic pattern and strain partitioning mechanism similar to the one described for the shallow crust replicated in the uppermost mantle.

If micro-seismicity is, detached from the crustal thrusts, how does slip accumulate/propagate in crustal thrusts? Are high magnitude earthquakes also generated in mantle faults? In Figure V.4, we plotted the focal mechanism and

moment tensors with M≥3 recorded in the NEAREST network (in black) and in the permanent land networks (in red). Most events are located >20km in depth and the shallower events are mostly strike-slip solutions. For M≥5, the fault plane solutions show oblique motion, combining reverse dip-slip with strike-slip. According to geological interpretation in the chapter IV, none of these events could be related to the crustal faults.

Previous works have described the crustal faults systems to be active. For example, the Horseshoe Fault accumulated ~1.0 km of slip during the Pliocene-Quaternary (Gràcia et al., 2003, Zitellini et al., 2004, Terrinha et al., 2009 and Martínez-Loriente et al., 2016). Note that displacement in active faults is either accommodated by stick-slip and/or by creep. The transition between these two mechanisms is largely dependent on the characteristic of the fault zone, such as frictional proprieties (e,g Sholz, 1998).

Serpentinization may be a controlling mechanism of seismic to aseismic slip partitioning, as described in different tectonic settings by Guillot et al. (2015). Reinen et al. (1994) experiments with serpentinite materials at shallow depth indicate that only fault creep can occur at typical rates of plate motion. According to these authors, serpentinized areas do not favor seismicity but will promote local weakening allowing seismic slip to propagate into a serpentinized region.

Knowing that to the W of the HAT, the Horseshoe Abyssal Plain sediments are floored by a serpentinized layer at least down to 20 km in depth (Sallarès et al., 2013 and Martínez-Loriente et al., 2014) we should consider the rheology of serpentine when interpreting the seismicity clusters. Serpentinization can have two origins, i) a primary one during mantle exhumation at the formation of the oceanic crust and ii) a secondary one associated to fracturing and deep sea water circulation (Rosas et al., 2012 and Hensen et al.,2015 Silva et al., in press, in chapter IV).

Another side effect of aseismic deformation is the increase of pore fluid pressure due to local tectonic compaction on the surrounding rocks. Pore fluid pressure build up promotes frictional slip at comparatively lower shear strains producing cracking and porosity in the fault zone promoting fluid circulation. A new group of mud volcanoes reported by Hensen et al. (2015) in the Horseshoe - SWIM faults interference zone occurs above the Horseshoe seismicity cluster. Fluid signatures show a mixed pattern between minor clay dehydration, carbonates recrystallization and oceanic crust alteration that is explained by upward fluids migration suggesting that strike-slip faults provide pathways for deep-seated fluids.

Co-seismic dehydration of serpentinite can be a key mechanism in fault weakening during a high-velocity frictional slip occurring during large magnitude events (Lin et al., 2013). Frictional heating of serpentine-rich fault zones during

these events can thus lead to the release of large amounts of water vapor, resulting in increase of pore pressure, decrease of the effective stresses, i.e. weakening of fault zones and fluid migration into neighbor faults promoting extra slip. The transition from creep to stick-slip behaviors in fault zones due to dynamic weakening mechanism is used to explain unexpected high rupture patterns in subduction zones such as the 1999, Mw 7.6 Chi-Chi earthquake (Noda and Lapusta, 2013). The same authors refer this as a plausible rupture mechanism also in other geodynamic settings such as major strike-slip fault like San Andreas Fault.

Micro-seismicity can be used as a proxy for the deep limit of the seismogenic zone. A gap of micro-seismicity can also indicate ductile recovery after a large magnitude event. According to Jiang and Lapusta (2016) this is an explanation for the absence of micro-seismicity in the area of the 1857 Mw 7.9 Fort Tejon earthquake on the San Andreas/San Jacinto faults system and seismically quiescent megathrusts such as the Cascadia subduction zone.

During 1755-like events the rupture area can extend down to 90 km in depth (Matias et al., 2013), below the seismogenic zone for a Jurassic oceanic lithosphere. We hypothesize that the micro-seismicity gap on the HF (between the Horseshoe and São Vicente clusters) can eventually be the result of ductile recovery that followed this event.

Based on the above it is suggested that:

- The existence of the serpentinized layer results in a decoupling between the crustal and upper mantle tectonics. Accordingly, the serpentinization level should account for the absence or scarcity of seismicity above 15km.

- High magnitude events will propagate from upper mantle into crustal levels across the serpentinized layer inducing superficial rupture. In contrast, present-day micro-seismicity is mainly restricted to the upper mantle.

- Slip of large magnitude events (M>8) can propagate both up and downwards, i.e. into and across the serpentinized layer, as well as into and across brittle-ductile boundary, disturbing the lithosphere-asthenosphere boundary (see Fig. IV.14).

V.5.The plate boundary in the study area

Although this study did not report the existence of a series of aligned linear seismicity cluster that could help defining a plate boundary we think it contributed to its understanding.

Seismicity occurs in clusters at large faults intersections. All these clusters indicate the seismic activity of various fault sets, including the SWIM faults, probably the best candidates for accommodating the wrench displacement of Nubia with respect to SW Iberia.

It also results from the present study that widespread serpentinization proposed by Sallarés et al. 2011 is probably a still active mechanism. The deformation of the NE-SW striking thrusts and large segments of the SWIM faults are locked or aseismic during the quiescence gap of large to mega earthquakes. Aseismic slip may be promoted by the serpentinization layer.

The NEAREST network recorded some seismic activity below the Gulf of Cadiz accretionary wedge. Some focal mechanism solutions show reverse dip-slip solutions compatible with east-dipping subduction zone described in Gutscher et al. 2002 and Duarte et al., 2013. Note that these events are located outside the deployment area of the NEAREST network and are poorly constrained.

The micro-seismicity distribution is also related to the inherited limits of Atlantic and Tethys basins. The São Vicente cluster may mark the limit between the Mesozoic North Atlantic and Western Tethys margins. The Central Atlantic and Tethys oceans paleo-plate boundary may be aligned with the Horseshoe abyssal plain cluster.

V.6.Conclusion

The main conclusions of this work are:

- We identified three seismicity clusters located in the areas of the Gorringe Bank, São Vicente Canyon and along the Horseshoe Abyssal plain showing that seismicity is not uniformly distributed in the Gulf of Cadiz area also as suggested by NEAREST preliminary results (Geissler et al., 2010) and clustering analysis in Custódio et al, (2016);
- The three seismicity clusters characterized in this work show that the present day micro-seismic activity is generated in the lithospheric mantle and concentrates at faults intersections mapped on the sea floor using swath bathymetry, suggesting that the crustal fabric may be replicated in the lithospheric mantle; these cluster also show that seismic strain concentrates on fault intersection loci; The inferred fault interference zones in the upper mantle are associated with boundaries of lithospheric domains localizing stress and seismic strain;
- Active crustal faults with bathymetric expression, such as the Horseshoe and Marquês de Pombal faults are either locked or move through slow aseismic slip. Frictional slip may only result from high magnitude earthquakes;
- Serpentinization controls seismicity distribution by inducing tectonic decoupling and inhibiting micro-seismicity to occur above the serpentinized layer. Only during high-magnitude events it is expected seismic rupture to propagate upwards across the serpentinized layer up to the surface.

- Slip propagation from a non-serpentinized mantle into serpentinized mantle is a possible mechanism to produce larger slip areas, due to the release of pore fluid pressure accumulated during previous aseismic events. This mechanism can account for larger than expected slip for a high magnitude earthquake, like it is assumed for the 1755 event from numerical modelling of tsunami and inundation (Johnston, 1996, Gradin et al., 2007, Baptista et al.1998, 2009).

V.7.Future work

Seismological studies:

- Re-locate the NEAREST dataset using the double difference method (HypoDD- Waldhouser and Ellsworth, 2000). We tested this method during our study but it needs to be improved. In seismicity distribution with associated clustering, this method may improve events locations.
- Apply the stress tensor inversion to intermediate to high magnitude earthquakes reported in the Gulf of Cadiz by land permanent network and compare with NEAREST results. The idea is to explore if the stress tensors are similar for the different scales of magnitude. This may indicate if the mechanism associated with earthquakes generation is the same.
- Explore in the NEAREST dataset the evidences of low frequency earthquakes that can be evidences for fluid fault interactions.
- OBS networks deployments off-shore SW-W Iberian margins. Temporary deployment result in more accurate measurement of off-shore seismic activity.

Numerical modelling:

- Test 3D numerical models for the extrapolated mantle fault zones;
- Create fault plane models incorporating patches of serpentinized mantle to explore the influence of this lithology on the slip propagation during high magnitude earthquakes. Also explore the control of low friction lithologies on slip during the seismic cycle (interseismic, coseimic and postseismic periods).

Geological/geophysical studies:

- Depth migration of key MCS reflection profiles to study depth extends of the active faults in the study area. In the last decades, as part of different European projects (see chapter II), several MCS reflection profiles were acquired in Gulf of Cadiz area. Some of these profiles have deep penetration, with seismic signal extending down 14s (TWT, e.g IAM MCS profiles).

- Acquire wide-angle seismic reflection and refraction profiles NE-SW across the Gorringe Bank and the HAP. These profiles would contribute to define the lithospheric limits in the study area.

VI.REFERENCES

Abe, K., 1979. Size of Great Earthquakes of 1837-1974 Inferred from Tsunami Data. Journal of Geophysical Research, 84 (NB4), 1561-1568.

Afilhado, A., Matias, L., Shiobara, H., Hirn, A., Mendes-Victor, L., Shimamura, H., 2008. From unthinned continent to ocean: the deep structure of the west Iberia passive continental margin at 381N. Tectonophysics, 458 (1–4), 9–50.

Afonso, J. C., Ranalli, G., 2004. Crustal and mantle strengths in continental lithosphere: Is the jelly sandwich model obsolete? Tectonophysics, 394, 221–232, *doi:*10.1016/j.tecto.2004.08.006.

Amiguet, E., Van De Moortèle, B. Cordier, P. Hilairet, N., Reynard, B., 2014. Deformation mechanisms and rheology of serpentines in experiments and in nature, J. Geophys. Res. Solid Earth, 119, 4640–4655, doi:10.1002/2013JB010791.

Argus, D.F., Gordon, R.G., DeMets, C., Stein, S., 1989. Closure of the Africa–Eurasia–North America plate motion circuit and tectonics of the Gloria fault. Journal of Geophysical Research 94 (B5), 5585–5602, http://doi.wiley.com/10.1029/JB094iB05p05585.

Banda E.; Torné, M., the Iberian Atlantic Margins Group, 1995. Iberian Atlantic Margins group investigates deep structure of ocean margins. Eos trans. AGU 76 (3), 25-29, doi:10.1029/EO076i003p00025.

Baptista, M.A., Miranda, J. M., 2009. Revision of the Portuguese catalogue of tsunamis. Natural Hazards and Earth System Sciences, Volume: 9, Issue: 1, 25-42, http://www.nat-hazards-earth-syst-sci.net/9/25/2009/.

Baptista, M. A., Miranda, J. M., Chierici, F., Zitellini. N .2003, New study of the 1755 earthquake source based on multi-channel seismic survey data and tsunami modeling. Natural Hazards and Earth System Science, Copernicus Publications on behalf of the European Geosciences Union,3 (5), pp.333-340.<hal-00299044>

Baptista M.A., Miranda J.M., Lopes Fernando C., Luis Joaquim F., 2007. The source of the 1722 Algarve earthquake: evidence from MCS and tsunami data. Journal of Seismology, 11, 4, 371-380. DOI: http://doi.org/10.1007/s10950-007-9058-y

Baptista, M.A., Miranda, P.M.A., Miranda, J.M., Victor, L.M., 1998. Constrains on the source of the 1755 Lisbon tsunami inferred from numerical modelling of historical data on the source of the 1755 Lisbon tsunami. Journal of Geodynamics 25 (1–2),159–174.

Bartolome, R., Gràcia, E., Stich, D., Martínez-Loriente, S., Klaeschen, D., Mancilla, F.L., Lolacono, Cl., Dañobeitia, J.J., Zitellini, N., 2012. Evidence for active strike-slip faulting along the Eurasia–Africa convergence zone:

implications for seismic hazards on the SW Iberian Margin. Geology, 10.1130/G33107.1.

Borges, J. F., Fitas, A. J. S., Bezzeghoud, M., Teves-Costa, P., 2001. Seismotectonics of Portugal and its Adjacent Atlantic area. Tectonophysics, 331, 373–387. doi:10.1016/S0040-1951(00)00291-2.

Bormann, P. (Ed.) (2012) New Manual of Seismological Observatory Practice (NMSOP-2), IASPEI, GFZ German Research Centre for Geosciences, Potsdam; http://nmsop.gfz-potsdam.de; DOI: 10.2312/GFZ.NMSOP-2; urn:nbn:de:kobv:b103-NMSOP-2

Boettcher, M.S., Hirth, G., Evans, B., .2007. Olivine friction at the base of oceanic seismogenic zones. Journal of Geophysical Research, 112 http://dx.doi.org/10.1029/2006JB004301

Brace, W. F., Byerlee, J. D. (1966). Stick-slip as a mechanism for earthquakes. Science, 153, 990- 992.

Buforn, E., Bezzeghoud, A., Udías, Pro, C., 2004. Seismic Sources on the Iberian-African Plate Boundary and their Tectonic Implications. Pure and Applied Geophysics 161, 623-646, http://dx.doi.org/10.1007/s00024-003-2466-1

Buforn, E., Udías, A. and Colombas, A., 1988. Seismicity, source mechanisms and tectonics of the Azores-Gibraltar plate boundary. Tectonophysics 152, 89–118, doi:10.1016/0040-1951(88)90031-5.

Calais, E., DeMets, C., Nocquet, J.M., 2003. Evidence for a post-3.16-Ma change in Nubia–Eurasia–North America plate motions? Earth and Planetary Science Letters 216, 81–92, doi:10.1016/S0012-821X(03)00482-5.

Carrara, G., Matias, L., Geissler, W., D'Oriano, F. (Eds.) 2008. NEAREST 2008 cruise report R/V Urania, 1st Aug 2008–4th Sept 2008 GOCE Contract 037110., 79 pp., Ist. di Sci. Mar., Bologna, Italy, http://nearest.bo.ismar.cnr.it/documentation.

Carrilho, F. (2005) Estudo da Sismicidade da Zona Sudoeste de Portugal Continental, *Mestrado em Ciências Geofísicas, Especialização em Geofísica Interna*, Faculdade de Ciências da Universidade de Lisboa, 158 pp.

Carrilho, F., Pena, J. A., Nunes, J. C (2010). Sismicidade, in "Estudo do risco sísmico e de tsunamis do Algarve". ANPC. ISBN: 978-989-8343-06-2.

Carrilho, F., Teves-Costa, P., Morais, I., Pagarete, J., Dias, R., 2004. GEOALGAR Project: First Results on Seismicity and Fault-plane Solutions. Pure and Applied Geophysics 161, 589-606, doi:10.1007/s00024-003-02464-3.

Carrilho, F., Vales, D., 2009. Calibration of magnitude ML for Portugal and adjacent areas, in 6° Symposio de Meteorologia e Geofisica da APMG, pp. 48–53, Associação Portuguesa de Meteorologia e Geofisica, Lisbon.

Christensen, N. I., 2004. Serpentinites, Peridotites, and Seismology., International Geology Review, 46:9, 795-816, http://dx.doi.org/10.2747/0020-6814.46.9.795.

Craig, T. J., Jackson, J. A., Priestley, K., McKenzie; D., 2011. Earthquake distribution patterns in Africa: their relationship to variations in lithospheric and geological structure, and their rheological implications. Geophysics Journal International; 185 (1): 403-434. doi: 10.1111/j.1365-246X.2011.04950.x

Crawford, W. C. and Singh, S. C. (2008) Sediment shear properties from seafloor compliance measurements: Faroes-Shetland basin case study. *Geophysical Prospecting*, **56**, 313–325 doi:10.1111/j.1365-2478.2007.00672.x.

Crosson, R. S. (1976) Crustal Structure Modeling of Earthquake Data .1. Simultaneous Least- Squares Estimation of Hypocenter and Velocity Parameters. Journal of Geophysical Research, 81, 3036-3046.

Cunha, T. A, Matias, L. M., Terrinha, P., Negredo, A. M., Rosas, F., Fernandes, R. M. S., Pinheiro, L. M., 2012. Neotectonics of the SW Iberia margin, Gulf of Cadiz and Alboran Sea: a reassessment including recent structural, seismic and geodetic data. Geophysical Journal International, 188 (3): 850-872, doi:10.1111/j.1365-246X.2011.05328.x.

Custódio, S., Cesca, S., Heimann, S., 2012. Fast Kinematic Waveform Inversion and Robustness Analysis: Application to the 2007 Mw 5.9 Horseshoe Abyssal Plain Earthquake Offshore Southwest Iberia. Bulletin of the Seismological Society of America, Vol. 102, No. 1, 361–376, http://dx.doi.org/10.1785/0120110125.

Custódio, S., Lima, V., Vales, D.,Cesca, S., Carrilho F., 2016. Imaging active faults in a region of distributed deformation from the joint clustering of focal mechanisms and hypocenters: Application to the Azores-Western Mediterranean region. Tectonophysics 676, 70-89, doi: 10.1016/j.tecto.2016.03.013.

Custódio, S., N. A. Dias, F. Carrilho, E. Góngora, I. Rio, C. Marreiros, I. Morais, P. Alves, L. Matias, 2015. Earthquakes in western Iberia: improving the understanding of lithospheric deformation in a slowly deforming region. Geophysical Journal International, 203(1):127–145, doi:10.1093/gji/ggv285.

DeMets, C., Gordon, R.G., Argus, D.F., Stein, S., 1994. Effect of recent revisions to the geomagnetic reversal time scale on estimates of current plate motions. Geophysical Research Letters (20), 2191–2194, doi:10.1029/94GL02118.

Dewey, J. F., Helman, M. L., Turco, E., Hutton, D. H.W., Knott, S.D., 1989. Kinematics of the Western Mediterranean. Alpine Tectonics, Vol.45, 265–283, Coward, M. P., Dietrich, D. and Park, R. G (eds)., Geological Society Special Publication, doi:10.1144/GSL.SP.1989.045.01.15.

Dias NA (2005) Estudo da sequência sísmica gerada pelo sismo do Faial de 9 de Julho de 1998: anisotropia crustal, inversão tomográfica e caracterização sismo-tectónica. Ph.D. Thesis, Universidade de Lisboa, Lisboa.

Domingues, A., Custódio, S., Cesca, S., 2013. Waveform inversion of small to moderate earthquakes located offshore southwest Iberia. Geophysics Journal International 192 (1), 248-259, doi:10.1093/gji/ggs010.

Duarte, J.C. (2011) Tectonics of the gulf of cadiz: the role of the gibraltar arc in the reactivation of the SW Iberia Margin, PhD thesis, University of Lisbon, 304pp

Duarte, J. C., Rosas, F. M., Terrinha, P., Schellart, W. P., Boutelier, D., Gutscher, M.-A., Ribeiro, A., 2013. Are subduction zones invading the Atlantic? Evidence from the southwest Iberia margin. Geology, 41, 8, 839-842 doi:10.1130/G34100.1.

Duarte, J.C., Rosas, F.M., Terrinha, P., Gutscher, M.-A., Malavieille, J., Silva, S., Matias, L., 2011. Thrust-wrench interference tectonics in the Gulf of Cadiz (Africa-Iberia plate boundary in the North-East Atlantic): Insights from analog models. Marine Geology, 289, 135–149, doi:10.1016/j.margeo.2011.09.014.

Duarte, J.C., Valadares, V., Terrinha, P., Rosas, F., Zitellini, N., Gràcia, E., 2009. Anatomy and tectonic significance of WNW-ESE and NE-SW lineaments at a transpressive plate boundary (Nubia-Iberia). Trabajos de Geología 29, 237-241.

Escartin, J., G. Hirth, Evans, B., 2001. Strength of slightly serpentinized peridotites: Implications for the tectonics of oceanic lithosphere, Geology, 29, 1023–1026.

Fernandes, R.M.S., Ambrosius, B.A.C., Noomen, R., Bastos, L., Wortel, M.J.R., Spakman, W., Govers, R., 2003. The relative motion between Africa and Eurasia as derived from ITRF2000 and GPS data. Geophysical Research Letters 30 (16), doi:10.1029/2003GL017089

Fernàndez, M., I. Marzán, A. Correia, and E. Ramalho, 1998. Heat flow, heat production, and lithospheric thermal regime in the Iberian Peninsula, Tectonophysics, 291, 29–53.

Frohlich, C. (1979) An efficient method for joint hypocenter determination for large groups of earthquakes, Comput. and Geosci. 5, 387-389.

Fukao, Y., 1973. Thrust faulting at a lithospheric plate boundary, The Portugal earthquake of 1969. Earth and Planetary Science Letters, 18, 205-216, doi:10.1016/0012-821X(73)90058-7

Grandin, R., Borges, J., Bezzeghoud, M., Caldeira, B., Carrilho; F., (2007) Simulations of strong ground motion in SW Iberia for the 1969 February 28 (M_S = 8.0) and the 1755 November 1 ($M\sim$ 8.5) earthquakes - II. Strong ground

motion simulations. *Geophys J Int*; 171 (2): 807-822. doi: 10.1111/j.1365-246X.2007.03571.x

Geissler, W. H., Matias, L., Stich, D., Carrilho, F., Jokat, W., Monna, S., IbenBrahim, A. Mancilla, F., Gutscher, M.□A., Sallarès, V., Zitellini, N., 2010. Focal mechanisms for sub–crustal earthquakes in the Gulf of Cadiz from a dense OBS deployment. Geophysical Research Letters 37, L18309, doi:10.1029/2010GL044289.

Gephart, J. W. 1990a. FMSI: a FORTRAN program for inverting fault/slickenslide and earthquake focal mechanism data to obtain the regional stress tensor, *Comp. Geosci*. Vol 16, 953–989.

Gephart, J. W. 1990b. Stress and the direction of slip on fault planes, *Tectonics* 9, no. 4, 845–858.

Gephart, J. W., Forsyth, D. W., 1984. An improved method for determining the regional stress tensor using earthquake focal mechanism data: application to the San Fernando earthquake sequence. Journal of Geophysical Research 89, B11, 9305–9320, doi:10.1029/JB080i011p09305.

Girardeau, J., Cornen, G., Beslier, M.O., Le Gall, B., Monnier, C., Agrinier, P., Dubuisson, G., Pinheiro, L., Ribeiro, A., Whitechurch, H. (1998), Extensional tectonics in the Gorringe Bank rocks, eastern Atlantic ocean: Evidence of an oceanic ultra-slow mantellic accreting centre, Terra Nova, 10, 330–336.

González, A., Córdoba, D., Vegas, R. and L. M. Matias (1998), Seismic crustal structure in the southwest of the Iberian Peninsula and the Gulf of Cadiz, *Tectonophysics*, 296, 317–331.

González, A., Torné, M., Córdoba, D., Vidal, N., Matias, L.M., Díaz, J.,1996. Crustal thinning in the Southwestern Iberia margin. Geophysical Research Letters 23, 2477-2480, doi:10.1029/96GL02299.

Gràcia, E., Dañobeitia, J.J., Vergés, J., PARSIFAL Team, 2003. Mapping active faults offshore Portugal (36ºN- 38ºN): Implications for seismic hazard assessment along the southwest Iberian margin. Geology, 31(1), 83-86, doi:10.1130/0091-7613(2003)031<0083:MAFOPN>2.0.CO;2.

Gràcia and SWIM SWIM cruise party, 2006. SWIM-2006 Cruise Report (unpublished)

Grevemeyer, I., Kaul, N., and Kopf, A., 2008. Heat flow anomalies in the Gulf of Cadiz and off Cape San Vicente, Portugal. Marine and Petroleum Geology, doi:10.1016/j.marpetgeo.2008.08.006.

Grevemeyer, I., Matias, L., Silva, S., 2016. Mantle earthquakes beneath the South Iberia continental margin and Gulf of Cadiz – constraints from an onshore-offshore seismological network. Journal of Geodynamics, 99, 39-50, http://dx.doi.org/10.1016/j.jog.2016.06.001.

Grevemeyer, I., D. Lange, H. Villinger, S. Custódio, and L. Matias (2017), Seismotectonics of the Horseshoe Abyssal Plain and Gorringe Bank, eastern Atlantic Ocean: Constraints from ocean bottom seismometer data, J. Geophys. Res. Solid Earth, 122, 63–78, doi:10.1002/2016JB013586.

Grimison, N. L., Chen, W. P., 1986. The Azores-Gibraltar plate boundary: focal mechanism, depths of earthquakes and their tectonic implications. Journal Geophysical Research 91 (B2), 2029–2047, doi:10.1029/JB091iB02p02029

Grose, G., Afonso, J.C., 2013. Comprehensive plate models for the thermal evolution of oceanic lithosphere. Geochemistry, Geophysics and Geosystems., 14 (2013), p. 9 http://dx.doi.org/10.1002/ggge.20232

Guillot, S., Schwartz, S., Reynard, B., Agard, P., Prigent, C., 2015. Tectonic significance of serpentinites. Tectonophysics 646, 1–19, http://dx.doi.org/10.1016/j.tecto.2015.01.020

Gutscher, M. A, Baptista, M., Miranda, J. M., 2006. The Gibraltar Arc seismogenic zone (part 2): Constraints on a shallow east dipping fault plane source for the 1755 Lisbon earthquake provided by tsunami modelling and seismic intensity. Tectonophysics 426, 153-166, doi:10.1016/j.tecto.2006.02.025

Gutscher, M.A., Dominguez, S., Westbrook, G.K., Le Roy, P., Rosas, F., Duarte, J.C., Terrinha, P., Miranda, J.M., Graindorge, D., Gailler, A., Sallares, V., Bartolome, R., 2012. The Gibraltar subduction: A decade of new geophysical data. Tectonophysics 574, 72–91, doi:10.1016/j.tecto.2012.08.038.

Gutscher, M.A., Malod, J., Rehault, J.-P., Contrucci, I., Klingelhoefer, F., Mendes-Victor, L., Spakman, W., 2002. Evidence for active subduction beneath Gibraltar. Geology 30 (12), 1071–1074, doi:10.1130/00917613(2002)030<1071:EFASBG>2.0.CO;2

Havskov, J., Ottemöller, L. Eds., 2011. SEISAN: The Earthquake Analysis Software for Windows, Solaris, Linux and Macosx, Version 9.1., 276 pp.

Hayes, D. E.; Pimm A. C., Beckmann, J. P.; Benson, W. E.; Berger, W. H.; Roth, P. H.; Supko, P. R.; Rad, U. 1972. Site 135. In: Hayes, D. E.; Pimm A. C., et al.; 1972. Site DSDP 135. Initial Reports of the Deep Sea Drilling Project, 14, p. 15-48.

Hayward, A., Watts, A. B., Westbrook G. K., Collier J. S., 1999. A seismic reflection and GLORIA study of compressional deformation in the Gorringe Bank region, Eastern North Atlantic. Geophysical Journal International 138, 831–850, doi:10.1046/j.1365-246x.1999.00912.x.

Heidbach, O., Tingay, M., Barth, A., Reinecker, J., Kurfeß, D., Müller, B., 2008.The World Stress Map database release 2008 doi:10.1594/GFZ.WSM.Rel2008.

Hensen, C., Scholz, F., Nuzzo, M., Valadares, V., Gràcia, E.; Terrinha, P.; Liebetrau, V., Kaul, N., Silva, S., Martínez-Loriente, S., Bartolome, R., Piñero, E., Magalhães, V. H., Schmidt, M., Weise, S. M., Cunha, M., Hilario, A., Perea, H., Rovelli, L., Lackschewitz, K., 2015. Strike-slip faults mediate the rise of crustal-derived fluids and mud volcanism in the deep sea. Geology, 43(4): 339-342, http://dx.doi.org/10.1130/G36359.1

Hiroyuki, N., Lapusta, N., 2013. Stable creeping fault segments can become destructive as a result of dynamic weakening. Nature, 493, 518–521, doi: 10.1038/nature11703

Husen, S., Kissling, E., Flueh, E., Asch, G., 1999. Accurate hypocentre determination in the seismogenic zone of the subducting Nazca Plate in northern Chile using a combined on-/offshore network. Geophysical Journal International 138, 687-701, doi:10.1046/j.1365-246x.1999.00893.x.

Iribarren, L., Vergés, J., Camurri, F., Fullea, J., Fernàndez, M. 2007. The structure of the Atlantic-Mediterranean transition zone from the Alboran Sea to the Horseshoe Abyssal Plain (Iberia–Africa plate boundary). Marine Geology 243, 97–119, doi:10.1016/j.margeo.2007.05.011.

Jiang, J., Lapusta, N., 2016. Deeper penetration of large earthquakes on seismically quiescent faults. Science 352 (6291), 1293-1297, doi:10.1126/science.aaf1496.

Jiménez-Munt, I., Fernàndez, M., Vergés, J., Afonso, J.C., Garcia-Castellanos, D., Fullea, J., 2010. Lithospheric structure of the Gorringe Bank: Insights into its origin and tectonic evolution. Tectonics 29. doi:10.1029/2009TC002458.

Johnston, A. C.,1996. Seismic moment assessment of earthquakes in stable continental regions – III, New Madrid 1811–1812, Charleston 1886, and Lisbon 1755. Geophysical Journal International 126, 314–344, doi:10.1111/j.1365-246X.1996.tb05294.x.

Kissling, E., 1995. Program VELEST user's guide - Short introduction. 26 pp.

Kissling, E., W. L. Ellsworth, D. Eberhart-Phillips, Kradolfer, U., 1994. Initial Reference Models in Local Earthquake Tomography. Journal Geophysical Research, **99**, 19635-19646.

Kohli, A. H., Goldsby, D. L., Hirth, G., Tullis, T., 2011. Flash weakening of serpentinite at near-seismic slip rates, J. Geophys. Res., 116, B03202, doi:10.1029/2010JB007833.

Moore D.E., Lockner, D.A., Tanaka, H., Iwata, K., 2004. The coefficient of friction of Chrysotile gouge at seismogenic depths, International Geology Review, 46 (5) pp. 385–398

Lee, W. H. *K.* and Stewart, S. W., (1981). Principles and applications of microearthquake networks, *Academic Press*, New York, 293 pp .

Lienert, B. R. E. (1991) Report on modifications made to Hypocenter. Institute of Solid Earth Physics, University of Bergen.

Lienert, B.R.E, Havskov, J., 1995. A computer program for locating earthquakes both locally and globally. Seismological Research Letters, 66, 26-36, doi:10.1785/gssrl.66.5.26.

Lienert, B.R.E., Frazer L. N. (1986) Hypocenter: An earthquake location method using centered, scaled, and adaptively least squares, Bulletin of the Seismological Society of America, Vol **76**, 771-783.

Lin A, Takano S, Hirono T, Kanagawa K, 2013. Coseismic dehydration of serpentinite: evidence from high-velocity friction experiments. Chemical Geology 344:50–62, doi:10.1016/j.chemgeo.2013.02.013.

Lo Iacono, C., Gracia, E., Zaniboni, F., Pagnoni, G., Tinti, S., Bartolome, R., Masson, D. G., Wynn, R. B., Lourenco, N., Pinto de Abreu, M., Danobeitia, J. J. and Zitellini, N. (2012) Large, deepwater slope failures: Implications for landslide-generated tsunamis Geology, 40 (10). pp. 931-934. doi:10.1130/G33446.1.

Lonergan, L., White, N., 1997. Origin of the Betic-Rif mountain belt. Tectonics16, 504–522, doi:10.1029/96TC03937.

López-Arroyo, A., Udías, A., (1972) Aftershock sequence and focal parameters of the February 28th, 1969 earthquake of the Azores–Gibraltar Fracture Zone. Bulletin of the Seismological Society of America 62 (3), 699–720.

Lund, B., Townend, J., 2007. Calculating horizontal stress orientations with full or partial knowledge of the tectonic stress tensor. Geophysical Journal International, 170, 1328-1335, doi:10.1111/j.1365-246X.2007.03468.x.

Maggi, A. Jackson, J.A., McKenzie, D., Priestley, K., 2000. Earthquake focal depths, effective elastic thickness, and the strength of the continental lithosphere, Geology, 28, pp. 459–498

Martínez-Loriente, S., E. Gràcia, R. Bartolome, V. Sallarès, C. Connors, H. Perea, C. Lo Iacono, D. Klaeschen, P. Terrinha, J. J. Dañobeitia, and N. Zitellini (2013) Active deformation in old oceanic lithosphere and significance for earthquake hazard: Seismic imaging of the Coral Patch Ridge area and neighboring abyssal plains (SW Iberian Margin), Geochemistry, Geophysics and Geosystems., 14, 2206–2231, doi:10.1002/ggge.20173.

Martínez-Loriente, S., Gràcia, E., Bartolome, R., Perea, H., Klaeschen, D., Dañobeitia, J. J., Zitellini, N., Wynn, R. B. and Masson, D. G. (2016), Morphostructure, tectono-sedimentary evolution and seismic potential of the Horseshoe Fault, SW Iberian Margin. Basin Res. doi:10.1111/bre.12225

Martínez-Loriente,S., Sallarès, V., Gràcia, E., Bartolome, R., Dañobeitia, JJ., Zitellini, N., 2014. Seismic and gravity constraints on the nature of the basement

in the Africa-Eurasia plate boundary: New insights for the geodynamic evolution of the SW Iberian Margin. Journal of Geophysical Research 119, 127-149, doi:10.1002/2013JB010476.

Martins I., Mendes Victor L.A., 2001. Contribuiçao para o estudo da sismicidade da regiao oeste da peninsula iberica, Universidade de Lisboa, Instituto Geofisico do Infante D. Luis, Publ. N. 25, 67 pp.

Matias, L. M., Cunha, T., Annunziato, A., Baptista, M. A., Carrilho, F., 2013. Tsunamigenic earthquakes in the Gulf of Cadiz: fault model and recurrence. Natural Hazards and Earth System Science 13(1), 1–13, doi:10.5194/nhess-13-1-2013.

McKenzie, D., Jackson, J., Priestley, K., 2005. Thermal structure of oceanic and continental lithosphere. Earth and Planetary Science Letters, 233, 337–349, doi:10.1016/j.epsl.2005.02.005.

Mitchum, R.M., Vail, P.R., Thompson, S., 1977.Seismic stratigraphy and global changes of sea-level,part 2: the depositional sequence as a basic unit for stratigraphic analysis. In: Payton, C.E. (ed.), Seismic Stratigraphy – Applications to Hydrocarbon Exploration. American Association of Petroleum Geologists Memoir 26, 53–62

Monna, S., Cimini, G. B., Montuori, C., Matias, L., Geissler, W. H., Favali, P., 2013. New insights from seismic tomography on the complex geodynamic evolution of two adjacent domains: Gulf of Cadiz and Alboran Sea, Journal of Geophysical Research, Solid Earth, 118, 1587–1601, doi:10.1029/2012JB009607.

Moores, E. M. and Twiss, R. J. (1995) Tectonics, *W. H. Freeman*, New York,415 pp

Munro, K. (2004) Automatic event detection and picking of P-wave arrivals, *CREWES Research Report,* Vol. 16

Neres, M., Carafa, M. M. C., Fernandes, R. M. S., Matias, L., Duarte, J. C., Barba S., Terrinha, P., 2016, Lithospheric deformation in the Africa-Iberia plate boundary: Improved neotectonic modeling testing a basal driven Alboran plate. Journal of Geophysical Research, Solid Earth, 121, doi:10.1002/2016JB013012.

Nocquet, J. M., Calais, E., 2004. Geodetic measurements of crustal deformation in the Western Mediterranean and Europe. Pure and Applied Geophysics, 161, 661–681. doi:10.1007/s00024-003-2468-z.

Noda, H., Lapusta, N. 2013.Stable creeping fault segments can become destructive as a result of dynamic weakening, Nature, http://dx.doi.org/10.1038/nature11703

Peng, Z. and J. Gomberg, An integrated perspective of the continuum between earthquakes and slow-slip phenomena: Nature Geosciences, v. 3, p. 599-607, doi:10.1038/ngeo940.

Pereira, R., Alves, T., 2013.. Crustal deformation and submarine canyon incision in a Meso-Cenozoic first-order transfer zone (SW Iberia, North Atlantic Ocean). Tectonophysics 601, 148–162, http://dx.doi.org/10.1016/j.tecto.2013.05.007.

Pinheiro, L., Ivanov, M.K, Sautkin, A, Akhmanov, G., Magalhaes, V., Volkonskaya, A., Monteiro,J.H., Somoza, L., Gardner,j.. Hamouni, N., Cunha, M.R., 2003. Mud volcanism in the Gulf ofCadiz: results from the TIR-10 cruise. Marine Geology 195, 131-151.

Pro, C., Buforn, E., Bezzeghoud, M., Udias., A., 2012. The earthquakes of 29 July 2003, 12 February 2007, and 17 December 2009 in the region of Cape Saint Vincent (SW Iberia) and their relation with the 1755 Lisbon earthquake. Tectonophysics 583, 16-27, http://dx.doi.org/10.1016/j.tecto.2012.10.010.

Pujol, J., (2000). Joint Event Location - the JHD technique and applications to data from local seismic networks. Advances in Seismic Event Location, C. H. Thurber and N. Rabinowitz, Eds., Kluwer, 163-204.

Purdy, G. M., 1975. The Eastern end of the Azores-Gibraltar plate boundary. Geophys. J. R. Astron. Soc., 43, 123–150, doi:10.1111/j.1365-246X.1975.tb06206.x.

Purdy GM, Detrick RS (1986) Crustal structure of the Mid-Atlantic Ridge at 23°N from seismic refraction studies. Journal of Geophysical Research 91(83):3739–3762.

Ramos, A., Fernández, O., Terrinha, P., Muñoz, J. A., 2016. Extension and inversion structures in the Tethys–Atlantic linkage zone, Algarve Basin, Portugal. International Journal of Earth Sciences 105, 1663–1679, doi:10.1007/s00531-015-1280-1,

Ranalli, G., Murphy, D.C., 1987. Rheological stratification of the lithosphere. Tectonophysics 132, 281–295.

Reasenberg, P. A., Oppenheimer, D. H., 1985. FPFIT, FPPLOT and FPPAGE: Fortran computers programs for calculating and displaying earthquake fault-plane solutions. United States Geological Survey Open File Report, 85-739.

Reinen, L. A., Tullis, T.E., Weeks, J.D., 1994. The frictional behavior of antigorite and lizardite serpentinite: experiments, constitutive models, and implications for natural faults. Pure and Applied Geophysics 143, 317-358, doi:10.1007/BF00874334.

Ribeiro, A., Cabral, J., Batista, R., Matias, L., 1996. Stress pattern in Portugal mainland and the adjacent Atlantic region, West Iberia. Tectonics, 15 (2), 641-659, doi:10.1029/95TC03683.

Ribeiro, A., Mendes-Victor, L., Cabral, J., Matias, L. and Terrinha, P. (2006). The 1755 Lisbon Earthquake and the beginning of closure of the Atlantic, European Review, Vol.14, nº2, 193-205.

Rice, J. R., Cocco, M. (2007), Seismic fault rheology and earthquake dynamics, in Tectonic Faults: Agents of Change on a Dynamic Earth, edited by M. R. Handy et al., chap. 5, pp. 99–137, MIT Press, Cambridge, Mass.

Richter, C. (1958) Elementary Seismology W.H. Freeman and Company, San Francisco

Romsdorf, M., 2010. Untersuchungen zur lokalen Seismizitätim Golf von Cadiz mit dem NEAREST OBS-Netzwerk, Msc thesis, Technische Universität Bergakademie Freiberg, Fakultät für Geowissenschaften, Institut für Geophysik, Lehrstuhl für Prospektionsgeophysik Diplomarbeit, 266 pp

Roque, C., 2007. Tectonostratigrafia do Cenózoico das margens continentais sul e nordeste portuguesas: um modelo de correlação sismostratigráfica, PhD thesis, University of Lisbon,310 pp.

Rosas, F.M., Duarte, J.C., Neves, M.C., Terrinha, P., Silva, S., Matias, L., Gr acia, E., Bartolome, R., 2012. Thrust-wrench interference between major active faults in the Gulf of Cadiz (Africa-Eurasia plate boundary, offshore SW Iberia): tectonic implications from coupled analogue and numerical modelling. Tectonophysics 548-549, 1-21, doi:10.1016/j.tecto.2012.04.013

Rosas, F.M., J. C. Duarte, P. Terrinha, V. Valadares, and L. Matias (2009) Morphotectonic characterization of major bathymetric lineaments in Gulf of Cadiz (Africa – Iberia plate boundary): insights from analogue modeling experiments, Marine Geology, 261 (1-4), 33-47, doi: 10.1016/j.margeo.2008.08.002.

Rosenbaum, G., Lister, G.S., 2004. Formation of arcuate orogenic belts in the western Mediterranean region. in Sussman, A.J., and Weil, A.B., eds., Orogenic curvature: Integrating paleomagnetic and structural analyses: Boulder, Colorado, Geological Society of America Special Paper 383, p. 41–56 http://dx.doi.org/10.1130/0-8137-2383-3(2004)383[41:FOAOBI]2.0.CO;2.

Rovere, M., Ranero, C.R, Sartori, S., Torelli, L., Zitellini, N., 2004. Seismic images and magnetic signature of the Late Jurassic to Early Cretaceous Africa-Eurasia plate boundary of SW Iberia. Geophysical Journal International 158, 554-568, doi:10.1111/j.1365-246X.2004.02339.x.

Ruiz, M., Galve, A., Monfret, T., Sapin, M., Charvis, P., Laigle, M., Evain, M., Hirn, A., Flueh, E., Gallart, J., Diaz, J., Lebrun, J.F., The Lesser Antilles Thales scientific party, 2011. Seismic activity offshore Martinique and Dominica islands

(Central Lesser Antilles subduction zone) from temporary onshore and offshore seismic networks. Tectonophysics 603, 68–78, doi:10.1016/j.tecto.2011.08.006.

Ryan, W. B. F., K. J. Hsü, M. B. Cita, P. Dumitrica, J. Lort, W. Maync, W. D. Nesteroff, G. Pautot, H. Stradner, and F. C. Wezel, 1973. Gorringe Bank—Site 120, Initial Rep. Deep Sea Drill. Proj.,13, 19–41, doi:10.2973/dsdp.proc.2913.2102.1973.

Sallarès, V., A. Gailler, M. A. Gutscher, D. Graindorge, R. Bartolome, E. Gràcia, J. Dıaz, J. J. Dañobeitia, Zitellini, N., 2011. Seismic evidence for the presence of Jurassic oceanic crust in the central Gulf of Cadiz (SW Iberia margin). Earth and Planetary Science Letters 311, 112–123, doi:10.1016/ j.epsl.2011.09.003.

Sallarès, V., S. Martínez-Loriente, M. Prada, E. Gràcia, C. R.Ranero, M. A. Gutscher, R. Bartolome, A. Gailler, J. J. Dañobeitia. Zitellini, N., 2013. Seismic evidence of exhumed mantle rock basement at the Gorringe Bank and the adjacent Horseshoe and Tagus abyssal plains (SW Iberia). Earth and Planetary Science Letters 365, 120–131, doi:10.1016/j.epsl.2013.01.021.

Sartori, R., Torelli, L., Zitellini, N., Peis, D., Lodolo, E., 1994. Eastern segment of the Azores□Gibraltar line (central□eastern Atlantic): An oceanic plate boundary with diffuse compressional deformation. Geology, 22, 555–558. doi:10.1130/0091-7613(1994)022<0555:ESOTAG>2.3.CO;2.

Schettino, A., Turco, E., 2011. Tectonic history of the western Tethys since the LateTriassic. Geological Society American Bulletin. 123, 89–105, http://dx.doi.org/10.1130/B30064.

Scholz, C.H., 1998. Earthquakes and friction laws. Nature 391 (6662), 37-42, doi:10.1038/34097.

Serpelloni, E., G. Vannucci, S. Pondrelli, A. Argnani, G. Casula, M. Anzidei, P. Baldi, Gasperini, P., 2007. Kinematics of the Western Africa-Eurasia plate boundary from focal mechanisms and GPS data. Geophysical Journal International, 169(3): 1180-1200. doi:10.1111/j.1365-246X.2007.03367.x

Sheriff, R.E. and Geldart, L.P., 1995. Exploration Seismology (2nd edition), *Cambridge University Press*, 592pp.

Sloan, R. A., Jackson, J. A., McKenzie, D., Priestley, K., 2011. Earthquake depth distributions in central Asia, and their relations with lithospheric thickness, shortening and extension, Geophysical Journal International, 185, 1–29, doi:10.1111/j.1365-246X.2010.04882.x.

Snoke, J .A., Munsey, J. W., Teague, A. G., and Bollinger, G. A., 1984. A program for focal mechanism determination by combined use of polarity and SV-P amplitude ratio data. Earthquake notes, 55.

Solares J., Arroyo A., 2004. The great historical 1755 earthquake, effects and damage in Spain. J. Seism. 8, 275-294. DOI: http://doi.org/10.1023/B:JOSE.0000021365.94606.03

Srivastava, S.P., Roest, W.R., Kovacs, L.C., Oakey, G., Lévesque, S., Verhoef, J., Macnab, R.,1990. Motion of Iberia since the Late Jurassic: results from detailed aeromagnetic measurements in the Newfoundland Basin. Tectonophysics 184, 229–260, doi:10.1016/0040-1951(90)90442-B.

Stein, S. and Michael E. Wysession (2003). An introduction to seismology, earthquakes, and earth structure. *Wiley-Blackwell*, ISBN 0-86542-078-5, 498pp

Stich, D., Mancilla, F. D. L., Pondrelli, S., Morales, J., 2007 . Source analysis of the February 12th 2007, Mw 6.0 Horseshoe earthquake: implications for the 1755 Lisbon earthquake. Geophysical Research Letters 34 (L12308), doi:10.1029/2007GL030012

Stich, D., Martín, R., Morales, J., 2010. Moment tensor inversion for Iberia–Maghreb earthquakes 2005–2008. Tectonophysics, 483, 390–398, doi:10.1016/j.tecto.2009.11.006.

Stich, D., Serpelloni, E., Mancilla, F., Morales, J., 2006. Kinematics of the Iberia–Maghreb plate contact from seismic moment tensors and GPS observations. Tectonophysics, 426 (3–4), 295–317, doi:10.1016/j.tecto.2006.08.004

Terrinha, P., Matias, L., Vicente, J., Duarte, J., Luís, J., Pinheiro, L., Lourenço, N., Diez, S., Rosas, F., Magalhães, V., Valadares, V., Zitellini, N., Roque, C., Víctor, L.M., 2009. Morphotectonics and strain partitioning at the Iberia–Africa plate boundary from multibeam and seismic reflection data. Marine Geology 267, 156–174, doi:10.1016/j.margeo.2009.09.012

Terrinha, P., Pinheiro, L., Henriet, J.-P., Matias, L., Ivanov, M., Monteiro,J., Akhmetzhanov, A., Volkonskaya, A., Cunha, T., Shaskin, P., Rovere, M., 2003. Tsunamigenic-seismogenic structures, neotectonics, sedimentary processes and slope instability on the southwest Portuguese Margin. Marine Geology, 195(1–4), 55 – 73, doi:10.1016/S0025-3227(02)00682-5

Terrinha, P., Ribeiro, C., Kullberg, J.C., Rocha, R., Ribeiro, A., 2002. Compression episodes during rifting and faunal isolation in the Algarve Basins. SW Iberia. Journal of Geology 110, 101-113, doi:10.1086/324206.

Thiebot, E. and Gutscher, M. 2006. The Gibraltar Arc seismogenic zone (part 1): Constraints on a shallow east dipping fault plane source for the 1755 Lisbon earthquake provided by seismic data, gravity and thermal modeling, Tectonophysics, Volume 426, Issues 1–2, Pages 135-152, ISSN 0040-1951, http://dx.doi.org/10.1016/j.tecto.2006.02.024.

Torelli, L., Sartori, R., Zitellini, N., 1997. The giant chaotic body in the Atlantic Ocean off Gibraltar: new results from a deep seismic reflection survey. Marine and Petroleum Geology 14 (2), 125–134, doi:10.1016/S0264-8172(96)00060-8.

Valadares, V. (2012) The morphotectonics offshore Southwest Iberia and the origin and the evolution of the South Portuguese submarine canyons, PhD thesis, University of Lisbon, 255 pp

Vila M, Fernandez M, Jiminez-Munt I (2010) Radiogenic heat production variability of some common lithological groups and its significance to lithospheric thermal modeling. Tectonophysics, 490, 152–64.

Vilanova, S. P., Fonseca, J. F. B. D, 2004. Seismic hazard impact of the Lower Tagus Valley Fault Zone (SW Iberia). Journal of Seismology, 8, 331-345.

Waldhauser, F. and W.L. Ellsworth, (2000) A double-difference earthquake location algorithm: Method and application to the northern Hayward fault, Bulletin of the Seismological Society of America, 90, 1353-1368 .

Waldhauser, F., (2001) HypoDD: A computer program to compute double-difference earthquake locations, *USGS Open File Rep.,* 01-113.

Watts B. A, Burov, E.B, 2003. Lithospheric strength and its relationship to the elastic and seismogenic layer thickness. Earth and Planetary Science Letters, 213 (2003), pp. 113–131

Yilmaz, O., (1993) Seismic Data Processing, Stephen M. Doherty editor, Society of Exploration Geophysicists, Tulsa Oklahoma, 526 pp.

Yilmaz, O., (2001) Seismic Data Analysis, Society of Exploration Geophysicists, Tulsa Oklahoma,

Youbi, N., Martins, L. T., Munhá, J. M., Ibouh, H., Madeira, J., Ait Chayeb, H., El Boukhari, A., 2003. The Late Triassic-Early Jurassic Volcanism of Morocco and Portugal in the Framework of the Central Atlantic Magmatic province: An Overview. In: Hames, W. E., Machone, J. G., Renne, P. R., Ruppel, C. (Eds.) The Central Atlantic Magmatic Province: Insights from Fragments of Pangea. American Geophysical Union Geophysical Monograph Series, 136, 179-207, doi:10.1029/136GM010.

Zitellini, N., Berton, E., Bortoluzzi, G., Calafato, N., Centorami, G., Chierici, F., Landuzzi, V., Ligi, M., Penitenti, D., Scipionii, E., Rovere, M., Casoni, L., Correggiari, A., Magagnoli, A., Marozzi, G., Vigliotti, L., Jornet, P., Rodriguez, P., Thompson, I., Zahinos, A., Bartolome, R., Gracia, E. Terrinha, P., Ribeiro, A., (2010). Project BIGSETS: report on seismic and magnetic investigations during cruise bs98 with R/V Urania. RAPPORTI ISMAR 1, 1–17

Zitellini, N., Gràcia, E., Matias, L., Terrinha, P., Abreu, M. A., DeAlteriis, G., Henriet, J. P., Dañobeitia, J. J., Masson, D. G., Mulder, T., Ramella, R., Somoza, L., Diez, S., 2009. The quest for the Africa-Eurasia plate boundary

west of the Strait of Gibraltar. Earth and Planetary Science Letters 280, 13-50, doi:10.1016/j.epsl.2008.12.005.

Zitellini, N., Ligi, M., Matias, L., Rovere, M. and Shipboard Scientific Parties, 2002. VOLTAIRE cruise report. www.doc.igm.bo.cnr.it

Zitellini, N., Mendes, L. A., Cordoba, D., Danobeitia, J., Nicolich, R., Pellis, G., Ribeiro, A., Sartori, R., Torelli, L., Bartolomé, R., Bortoluzzi, G., Calafato, A., Carrilho, F., Casoni, L., Chierici, F., Corela, C., Correggiari, A., Della Vedova, B., Gràcia, E., Jornet, P., Landuzzi, M., Ligi, M., Magagnoli, A., Marozzi, G., Matias, L., Penitenti, D., Rodriguez, P., Rovere, M., Terrinha, P., Vigliotti, L., Zahinos Ruiz, A., 2001. Source of 1755 Lisbon Earthquake and Tsunami Investigated. Eos, Transactions American Geophysical Union 82, 285, 290–291, doi:10.1029/EO082i026p00285-01.

Zitellini, N., Rovere, M., Terrinha, P., Chierici, F., Matias, L., Bigsets Team, 2004. Neogene through Quaternary tectonic reactivation of SW Iberian passive margin. Pure and Applied Geophysics 161 (3), 565–587, doi:10.1007/s00024-003-2463-4

Zoback, M.L., 1992. First- and second-order patterns of stress in the lithosphere: The World Stress Map project. Journal Geophysical Research, 97, 11,703-11,728, doi:10.1029/92JB00132.

VII.Appendixes

Appendix I – Stations detections details

Station	Nºevents	P-picking	S-picking	Total phase readings	S-picking/ P-picking	Nº recording months	Failing components
GSTAR	308	85	297	382	3.5	11	
NRT01	311	214	272	486	1.3	10	x
NRT02	167	68	153	221	2.3	9	z
NRT03	499	316	450	766	1.4	11	x
NRT04	347	207	322	529	1.6	9	
NRT05	513	322	457	779	1.4	10	x
NRT06	503	288	487	775	1.7	11	
NRT08	555	381	529	910	1.4	12	x
NRT09	462	292	413	705	1.4	8	x
NRT10	230	149	214	363	1.4	10	
NRT11	358	106	342	448	3.2	8	xz
NRT12	378	232	359	591	1.5	11	
NRT13	278	216	238	454	1.1	11	x
NRT14	170	143	137	280	1.0	11	
NRT15	60	33	54	87	1.6	7	y
NRT16	62	48	41	89	0.9	11	
NRT17	514	311	469	780	1.5	10	x
NRT18	441	275	424	699	1.5	11	
NRT19	281	149	266	415	1.8	11	
NRT20	160	126	122	248	1.0	11	
NRT21	81	69	45	114	0.7	11	
NRT22	366	204	336	540	1.6	11	x
NRT23	151	116	122	238	1.1	10	x
NRT24	301	157	292	449	1.9	9	
NRT25	342	232	321	553	1.4	9	
Total		4739	7162	Average	1.6	11	

Appendix II- ph2dt.inp and hypoDD.inp examples

Ph2dt.inp

```
* ph2dt.inp - input control file for program ph2dt
* Input station file:
station.dat
* Input phase file:
hsh.pha
*MINWGHT: min. pick weight allowed [0]
*MAXDIST: max. distance in km between event pair and stations [200]
*MAXSEP: max. hypocentral separation in km [10]
*MAXNGH: max. number of neighbors per event [10]
*MINLNK: min. number of links required to define a neighbor [8]
*MINOBS: min. number of links per pair saved [8]
*MAXOBS: max. number of links per pair saved [20]
*MINWGHT MAXDIST MAXSEP MAXNGH MINLNK MINOBS MAXOBS
   0.          9999.       999.    1000        3        1        1000
```

hypoDD.inp

```
* RELOC.INP: ****************** BOTH CT and CC DATA USED  ****************
*--- input file selection
* cross correlation diff times:
dt.cc
*
*catalog P diff times:
dt.ct
*
* event file:
event.dat
*
* station file:
station.dat
*
*--- output file selection
* original locations:
hypoDD.loc
* relocations:
hypoDD.reloc
* station information:
hypoDD.sta
* residual information:
hypoDD.res
* source paramater information:
*hypoDD.src

*--- data type selection:
* IDAT:  0 = synthetics; 1= cross corr; 2= catalog; 3= cross & cat
```

```
* IPHA: 1= P; 2= S; 3= P&S
* DIST:max dist [km] between cluster centroid and station
* IDAT   IPHA   DIST
   2         3       500.
*
*--- event clustering:
* OBSCC:    min # of obs/pair for crosstime data (0= no clustering)
* OBSCT:    min # of obs/pair for network data (0= no clustering)
* OBSCC  OBSCT
    0          0
*
*--- solution control:
* ISTART:       1 = from centroid;      2 = from catalog
* ISOLV:        1 = SVD, 2=lsqr
* NSET:         number of sets of iteration with specifications following
*  ISTART  ISOLV  NSET
   2           2         2
*
*--- data weighting and re-weighting:
* NITER:              last iteration to used the following weights
* WTCCP, WTCCS:         weight cross P, S
* WTCTP, WTCTS:         weight catalog P, S
* WRCC, WRCT:              residual threshold in sec for cross, catalog data, factors of
RMS
* WDCC, WDCT:          max dist [km] between cross, catalog linked pairs
* DAMP:               damping (for lsqr only)
*       ---  CROSS DATA ----- ----CATALOG DATA ----
* NITER WTCCP WTCCS WRCC WDCC WTCTP WTCTS WRCT WDCT DAMP
  8       -9.    -9    -9   -9   1.     1.     -9         -9          5
  8       -9.  -9    -9   -9   1.     1.    6          20         5
*
*--- 1D model:
* NLAY:         number of model layers
* RATIO:        vp/vs ratio
* TOP:          depths of top of layer (km)
* VEL:          layer velocities (km/s)
* NLAY RATIO
 12  1.78
* TOP:
    .00  6.00 8.00 10.00 15.00 19.00 26.00 33.00 56.00 66.00 76.00 81.00
* VEL:
   3.24  3.84  5.54  7.22  7.65  7.85  8.19  8.20  8.24  8.32  8.40  8.45
*
*--- event selection:
* CID:  cluster to be relocated (0 = all)
* ID:   cuspids of event to be relocated (8 per line)
* CID
    0
* ID
```

Appendix III- Focal Mechanism Details

Appendix III.A-Gorringe Cluster (NST-number of stations, RMS-root mean square and ML-local magnitude)

Event ID		Event Location									Parameters				Focal Mechanism			
Nº	Event	Year Date	HR MM Sec	Error	Latitude	Error	Longitude	Error	Depth	Error	NST	RMS	GAP	Ml	STRIKE	DIP	RAKE	Quality
1	20070919C	2007 919	0123 47.2	0.41	36.552	0.9	-11.263	1.7	33.1	3.1	16	0.2	163	2.6	1	28	38	C
2	20070920C	2007 920	2235 17.0	0.61	36.547	1.3	-11.274	2.3	33.0	3.8	22	0.3	165	3.4	0	52	18	C
3	20071005B	2007 10 5	0400 22.2	0.40	36.551	1.1	-11.344	1.9	33.9	4.5	14	0.1	194	2.8	129	77	-59	B
4	20071007C	2007 10 7	1122 8.1	0.43	36.592	1.1	-11.357	2.1	32.5	4.0	14	0.2	178	2.5	50	46	73	C
5	20071020B	20071020	0534 52.9	0.60	36.367	1.6	-11.321	2.9	32.3	5.6	17	0.2	179	2.5	139	48	-114	B
6	20071023B	20071023	0620 23.7	0.49	37.057	1.6	-10.791	1.7	45.2	2.7	17	0.2	174	2.9	31	28	138	B
7	20071101C	2007 11 1	1046 30.5	0.44	36.732	1.2	-10.53	1.4	42.1	2.8	15	0.2	62	2.3	14	67	13	C
8	20071104C	2007 11 4	1549 6.4	0.61	36.787	1.6	-11.214	2.4	23.3	7.9	13	0.2	141	2.8	30	74	56	C
9	20071203B	2007 12 3	1228 22.8	0.90	36.376	2.4	-11.312	4.4	30.4	8.3	14	0.3	177	2.4	53	28	-1	B
10	20071207C	2007 12 7	2038 4.3	0.65	36.382	1.6	-11.315	2.8	34.0	5.5	18	0.3	177	2.9	0	35	38	C
11	20080112B	2008 112	1911 37.3	0.46	36.939	1.9	-10.800	1.8	42.7	3.9	12	0.3	148	2.4	90	79	118	B
12	20080113C	2008 113	2237 45.1	0.56	36.864	2.1	-11.153	2.8	24.2	6.9	20	0.3	122	2.4	20	65	51	C
13	20080203B	2008 2 3	0452 36.1	0.89	36.513	2.1	-11.252	3.4	31.0	6.3	19	0.3	162	3.2	0	26	58	B
14	20080211C	2008 211	0111 19.6	0.40	36.538	1.3	-11.411	3.0	30.0	8.7	8	0.1	190	2.7	90	28	90	C
15	20080220C	2008 220	2206 59.8	0.55	36.591	1.9	-11.237	2.9	30.7	9.3	12	0.2	157	2.6	112	68	-177	C
16	20080224C	2008 224	1050 38.2	0.50	36.525	1.5	-11.269	2.9	36.3	7.0	10	0.2	165	2.2	17	38	58	C
17	20080227B	2008 227	0519 18.2	0.47	36.475	1.1	-11.137	1.7	40.4	3.6	15	0.2	142	2.7	107	75	118	B
18	20080319B	2008 319	0810 13.8	0.32	36.718	0.9	-10.491	1.1	48.0	1.8	19	0.1	61	2.1	50	82	57	A
19	20080319A	2008 319	1811 24.9	0.68	36.792	1.6	-10.511	1.5	43.8	3.0	24	0.3	74	3.0	30	48	-21	B
20	20080401B	2008 4 1	1305 13.1	0.46	36.341	1.0	-11.198	2.0	26.8	4.5	14	0.2	152	2.8	40	48	-21	B
21	20080421B	2008 421	1652 10.3	0.36	36.593	0.9	-11.244	1.5	30.8	4.6	16	0.1	158	2.8	49	75	78	B
22	20080422B	2008 422	0326 18.4	0.42	36.721	1.2	-10.734	1.7	41.4	2.7	16	0.2	95	2.4	40	80	56	B

23	20080424C	2008 424	1145 23.4	0.40	36.786	1.4	-10.884	1.8	41.9	3.7	12	0.2	116	2.2	92	78	-161	C
24	20080424a_C	2008 424	1813 22.5	0.80	36.578	2.5	-11.308	4.0	25.7	8.6	11	0.3	170	2.0	60	38	98	C
25	20080429B	2008 429	0552 8.7	0.54	36.277	1.5	-11.278	3.0	32.5	4.6	13	0.2	171	2.2	107	58	-141	B
26	20080502C	2008 5 2	1306 32.7	0.72	36.276	1.7	-11.268	3.5	31.8	5.1	11	0.3	169	2.1	68	51	98	C
27	20080505B	2008 5 5	0044 17.2	0.65	36.718	1.8	-11.193	3.0	21.4	5.9	9	0.2	161	2.4	68	35	35	B
28	20080610C	2008 610	0652 28.8	1.09	36.463	3.6	-11.826	6.1	22.8	17.0	20	0.5	254	3.4	145	68	-41	C
29	20080630C	2008 630	1901 8.4	1.27	36.478	5.0	-11.288	13.6	33.2	12.1	8	0.4	266	2.2	61	78	-165	C
30	20080713C	2008 713	2335 42.8	0.66	36.616	2.9	-11.214	5.6	33.4	5.4	10	0.4	266	2.7	60	68	-1	C
31	20080718B	2008 718	0712 41.5	1.13	36.739	4.5	-10.722	5.8	37.8	11.6	8	0.4	202	3.4	7	78	2	B

Appendix III.B-Horseshoe Cluster (NST-number of stations, RMS-root mean square and ML-local magnitude)

Event ID		Event Location									Parameters				Focal Mechanism			
Nº	Event	Date	HR MM Sec	Error	Latitude	Error	Longitude	Error	Depth	Error	NST	RMS	GAP	Ml	STRIKE	DIP	RAKE	Quality
32	20070906A	20070906	0644 31.1	0.53	35.886	1.6	-10.831	1.9	25.4	3.8	22	0.3	78	3.7	8	82	-41	A
33	20070917A	20070917	0234 5.6	0.67	35.871	1.6	-10.374	2.2	42.6	4.7	19	0.3	76	3.1	120	68	155	A
34	20070922B	20070922	0007 45.2	0.49	35.845	2.1	-10.507	1.9	48.2	3.5	14	0.2	89	2.7	81	53	138	B
35	20071028A	20071028	0050 27.4	0.84	35.828	2.1	-10.400	2.5	32.6	7.8	14	0.2	84	2.1	133	58	-172	A
36	20071107B	20071107	1425 31.6	0.64	35.874	1.4	-10.527	1.8	17.2	4.3	17	0.2	85	2.5	29	60	-1	B
37	20071117A	20071117	0754 52.5	0.63	35.877	1.8	-10.383	2.1	40.3	6.2	16	0.3	76	2.5	88	35	138	A
38	20071123B	20071123	0428 58.0	0.58	35.705	1.5	-10.218	1.5	32.3	2.9	19	0.2	76	3.3	90	78	-179	B
39	20071123a_B	20071123	1952 31.3	0.91	35.707	2.9	-10.174	2.8	33.1	6.9	14	0.4	106	2.3	27	51	40	B
40	20071125B	20071125	2346 39.2	0.63	36.110	1.5	-10.632	2.9	31.7	4.5	9	0.4	104	2.1	69	78	138	B
41	20071227B	20071227	2020 40.8	0.51	35.813	1.1	-10.379	1.4	45.1	2.8	20	0.2	84	3.2	18	78	18	B
42	20080106C	20080106	1201 42.2	0.84	35.729	2.5	-10.788	2.5	18.1	5.4	21	0.3	152	2.9	38	57	18	C
43	20080115C	20080115	0116 40.4	0.78	35.930	1.6	-10.666	2.1	48.8	4.6	22	0.3	76	2.4	20	22	-66	C
44	20080124A	20080124	0315 39.8	0.71	36.043	1.9	-10.948	2.7	28.7	7.5	18	0.3	97	2.9	105	58	178	A
45	20080215B	20080215	0737 5.1	0.51	35.873	1.4	-10.559	1.6	48.5	3.7	19	0.2	87	2.8	0	10	-126	B
46	20080223A	20080223	1637 34.9	0.59	35.801	1.6	-10.416	2.1	44.2	4.7	14	0.2	89	2.7	148	32	134	A
47	20080224A	20080224	2253 22.3	0.59	35.850	1.2	-10.307	1.3	46.5	2.9	22	0.2	72	3.1	99	58	-179	A
48	20080227A	20080227	0250 51.9	0.63	35.847	1.7	-10.309	2.8	46.9	4.1	15	0.3	73	2.4	93	78	158	A
49	20080310B	20080310	0040 44.1	0.61	35.863	1.6	-10.281	2.3	41.9	4.9	16	0.3	64	2.2	115	62	-121	B
50	20080327B	20080327	1526 51.4	0.63	35.762	1.9	-10.392	1.5	41.8	3.5	21	0.2	91	2.6	99	88	138	B
51	20080417C	20080417	0219 20.9	0.61	36.018	1.8	-10.801	2.4	21.6	10.8	10	0.3	72	2.2	0	63	58	C
52	20080426B	20080426	0827 51.8	0.38	35.905	1.2	-9.878	1.4	45.8	4.0	13	0.2	72	2.0	81	36	98	B
53	20080507B	20080507	1512 39.9	0.95	36.143	1.9	-10.731	3.0	20.9	4.7	21	0.3	123	3.9	76	48	118	B
54	20080510B	20080510	1633 10.7	1.05	35.911	2.4	-10.672	3.4	45.4	6.0	22	0.3	93	4.1	127	78	-179	B
55	20080522C	20080522	1812 30.6	0.68	35.884	1.6	-10.461	2.1	40.6	3.8	17	0.2	80	2.8	134	56	-141	C

56	20080528C	20080528	1027 59.9	0.55	35.930	1.3	-10.673	2.6	19.6	4.4	11	0.2	102	2.4	96	48	-162	C
57	20080616B	20080616	2003 42.0	1.20	35.691	3.0	-10.190	4.0	32.0	8.0	17	0.5	79	2.5	92	38	-177	B

Appendix III.C-São Vicente Cluster (NST-number of stations, RMS-root mean square and ML-local magnitude)

Event ID		Event Location									Parameters				Focal Mechanism			
Nº	Event	Year Date	HR MM Sec	Error	Latitude	Error	Longitude	Error	Depth	Error	NST	RMS	GAP	Ml	STRIKE	DIP	RAKE	Quality
58	20070909A	20070909	0316 41.4	0.91	36.564	2.5	-9.770	2.9	41.0	5.4	19	0.4	142	3.4	7	26	-21	A
59	20070914A	20070914	1740 26.3	0.55	36.701	1.5	-9.636	2.0	39.7	3.6	22	0.3	130	3.6	8	38	9	A
60	20071004A	20071004	1925 19.6	0.56	36.628	1.9	-9.800	2.1	39.7	4.7	18	0.3	97	2.5	48	83	-161	A
61	20071006C	20071006	1312 13.2	0.57	36.230	1.3	-9.951	1.8	44.1	3.8	18	0.2	55	2.2	103	80	-123	C
62	20071010B	20071010	1445 8.6	0.67	36.470	2.1	-9.906	2.8	39.2	7.1	17	0.3	120	2.2	160	42	98	B
63	20071021B	20071021	0738 48.8	0.45	36.436	1.3	-9.953	1.4	32.1	5.1	17	0.2	78	2.4	138	86	158	B
64	20071107C	20071107	2022 52.1	0.56	36.619	2.7	-9.770	3.3	46.9	5.3	10	0.3	174	2.2	122	53	38	C
65	20071112C	20071112	1815 44.7	0.75	36.373	1.5	-9.943	2.7	42.5	5.1	15	0.3	72	2.2	98	68	-161	C
66	20071113B	20071113	1105 8.8	0.59	36.579	1.9	-9.778	2.8	40.8	4.3	10	0.2	122	2.1	75	78	-141	B
67	20071125A	20071125	0023 13.0	0.49	36.619	1.8	-9.759	1.8	42.6	4.5	17	0.2	103	2.7	24	66	-21	A
68	20071204D	20071204	0353 10.0	0.35	36.739	1.4	-9.570	1.8	41.8	3.3	11	0.1	158	2.2	6	58	-24	D
69	20071204B	20071204	0704 21.7	0.42	36.621	1.2	-9.787	1.5	41.7	2.9	15	0.2	91	2.2	78	67	-172	B
70	20071204a_B	20071204	1931 15.0	0.35	36.551	1.3	-9.784	1.4	41.8	3.0	11	0.1	93	2.2	127	56	-121	B
71	20071212A	20071212	0513 28.4	0.66	36.490	2.1	-9.815	2.6	39.4	4.8	16	0.3	103	2.5	22	90	78	A
72	20071213A	20071213	0536 9.1	0.92	36.668	2.6	-9.768	2.8	47.3	4.7	21	0.3	98	3.1	73	89	-142	A
73	20071216C	20071216	1315 41.7	0.36	36.215	0.9	-9.967	1.0	44.7	2.3	20	0.1	44	2.4	116	88	-139	C
74	20071220C	20071220	1925 28.5	0.58	36.029	1.4	-9.788	1.7	18.0	3.7	13	0.2	81	2.0	118	78	118	C
75	20071221C	20071221	0011 53.6	0.35	36.480	0.9	-9.917	1.3	26.9	4.2	13	0.1	88	2.1	117	65	11	C
76	20071227B	20071227	0811 38.7	0.43	36.428	1.3	-9.858	2.3	40.7	3.7	10	0.1	88	2.1	32	68	-113	B
77	20080105C	20080105	2031 21.6	0.56	36.297	1.3	-9.642	1.4	46.1	3.0	24	0.2	46	2.6	108	58	-161	C
78	20080111A	20080111	0021 47.7	0.66	36.448	1.2	-9.918	1.2	42.5	3.0	25	0.2	62	4.8	33	87	38	A
79	20080111a_A	20080111	0135 27.7	0.55	36.445	1.0	-9.918	1.1	44.0	2.4	25	0.2	61	3.0	33	90	78	A
80	20080111b_A	20080111	0653 4.4	0.77	36.444	1.7	-9.917	2.0	41.9	4.2	21	0.4	61	2.3	158	61	-46	A
81	20080302A	20080302	2158 0.0	0.52	36.422	1.5	-9.946	1.5	40.6	4.3	20	0.3	58	2.7	29	78	-1	A

82	20080306B	20080306	1233 52.0	0.41	36.403	1.2	-9.890	1.4	43.6	3.1	19	0.2	81	2.9	160	77	-50	B
83	20080313B	20080313	0353 32.7	0.50	36.534	1.2	-9.824	1.5	41.4	3.4	17	0.2	77	2.2	136	51	-21	B
84	20080314A	20080314	0637 3.9	0.55	36.337	1.0	-9.994	1.1	38.9	3.2	22	0.2	50	2.1	46	54	18	A
85	20080321C	20080321	1118 57.2	0.66	36.575	1.5	-9.938	1.5	40.8	3.4	22	0.3	68	2.5	87	78	158	C
86	20080402A	20080402	0046 26.8	0.67	36.491	1.2	-9.914	1.4	43.9	3.2	24	0.2	65	3.8	26	52	58	A
87	20080406B	20080406	2344 12.4	0.38	36.586	1.2	-9.813	1.3	43.8	2.4	12	0.2	83	2.0	160	81	-25	B
88	20080412A	20080412	1436 33.4	0.54	36.337	1.0	-9.839	1.3	43.8	2.7	22	0.2	56	3.3	18	51	55	A
89	20080414A	20080414	0800 52.2	0.39	36.447	1.3	-9.944	1.5	25.2	4.6	14	0.2	81	2.1	120	28	-141	A
90	20080416B	20080416	2033 44.5	0.49	36.446	1.2	-9.947	1.4	32.9	3.8	16	0.2	60	2.3	73	56	98	B
91	20080425A	20080425	1336 15.6	1.02	36.664	2.1	-9.767	2.3	43.7	4.7	22	0.3	98	3.1	20	47	40	A
92	20080523A	20080523	1139 10.7	0.68	36.521	1.8	-9.800	2	45.9	4.5	18	0.4	78	2.3	37	48	18	A
93	20080529B	20080529	2327 41.5	0.75	36.392	1.6	-9.964	2.0	42.6	6.1	16	0.3	67	3.1	60	74	56	B
94	20080605B	20080605	1134 2.2	0.56	36.426	1.3	-9.913	1.9	35.4	5.0	11	0.2	67	2.1	128	88	101	B
95	20080613B	20080613	2242 18.5	0.63	36.309	1.5	-9.971	1.8	41.8	4.6	16	0.3	50	1.9	328	20	-75	B
96	20080622A	20080622	1637 23.0	1.04	36.185	2.1	-9.996	2.6	42.0	7.3	16	0.4	56	2.6	160	47	-41	A
97	20080626A	20080626	0706 38.7	1.16	36.465	3.6	-9.911	4.2	31.6	10.8	12	0.5	116	2.0	42	90	29	A
98	20080630A	20080630	1449 31.9	0.64	36.431	2.5	-9.920	2.8	34.2	7.2	8	0.3	87	1.9	133	68	138	A
99	20080704B	20080704	0311 33.7	0.82	36.510	2.6	-9.927	3.0	42.3	7.2	12	0.4	97	2.5	28	58	-1	B
100	20080717C	20080717	1922 9.3	0.68	36.237	1.7	-9.814	2.5	55.6	5.0	9	0.2	84	4.0	120	82	-121	C

Appendix III.D- Outside the clusters area (NST-number of stations, RMS-root mean square and ML-local magnitude)

Event ID		Event Location									Parameters				Focal Mechanism			
Nº	Events	Date	HR MM Sec	Error	Latitude	Error	Longitude	Error	Depth	Error	NST	RMS	GAP	Ml	STRIKE	DIP	RAKE	Quality
101	20070903B	2007 9 3	0307 18.4	0.75	36.032	2.5	-8.624	3.4	37.5	3.7	20	0.3	100	3.0	-84	90	-97	B
102	20071101B	2007 11 1	1541 43.1	0.57	35.697	2.2	-8.778	3.4	46.0	7.3	12	0.2	107	2.1	116	87	98	B
103	20071106C	2007 11 6	2309 53.8	0.69	36.216	2.0	-8.911	2.4	7.9	1.4	22	0.3	123	3.7	0	8	-101	C
104	20071107C	2007 11 7	1428 2.7	0.99	36.202	5.7	-8.899	2.9	8.5	6.3	10	0.4	119	2.4	72	26	118	C
105	20071109C	2007 11 9	0606 28.3	0.51	36.089	3.3	-8.498	4.1	36.1	5.7	13	0.4	152	2.3	90	81	-161	C
106	20071206B	2007 12 6	1822 58.6	1.14	36.414	8.1	-7.675	9.7	32.9	18.2	14	0.5	295	2.7	97	10	-21	B
107	20071210C	2007 1210	1725 47.4	0.75	36.805	3.4	-8.532	4.0	46.5	9.3	22	0.4	260	3.2	151	38	-21	C
108	20080101A	2008 1 1	1400 40.4	0.74	36.133	2.2	-8.533	3.3	40.0	4.1	23	0.3	154	3.3	28	50	94	A
109	20080111B	2008 111	0741 41.6	0.85	35.023	3.4	-9.324	3.0	48.3	7.4	22	0.3	247	3.3	117	50	98	B
110	20080112C	2008 112	2111 36.2	1.17	35.321	4.5	-9.67	3.8	46.4	10.7	12	0.4	150	2.4	90	58	-171	C
111	20080204B	2008 2 4	1544 2.2	0.49	35.676	1.8	-8.837	2.1	39.2	4.7	17	0.2	115	2.5	33	48	78	B
112	20080213A	2008 213	1730 36.1	1.05	35.573	4.2	-8.972	4.7	41.8	8.8	11	0.4	133	2.4	107	38	58	A
113	20080221B	2008 221	1010 58.5	0.86	35.854	4.0	-8.603	5.1	42.0	9.8	9	0.4	108	2.0	48	58	-171	B
114	20080221C	2008 221	2039 8.0	1.19	36.018	3.8	-7.942	6.1	42.1	6.7	21	0.4	287	3.0	91	38	38	C
115	20080306B	2008 3 6	1635 41.6	0.93	36.034	3.1	-7.881	5.1	35.6	9.1	24	0.3	289	3.5	50	48	30	B
116	20080313B	2008 313	0337 59.0	0.96	35.687	2.5	-8.878	2.8	51.3	4.4	25	0.3	110	2.7	38	59	38	B
117	20080320B	2008 320	1755 52.9	0.66	35.32	2.1	-9.742	1.7	37.2	4.7	23	0.4	155	2.3	0	45	-128	B
118	20080326C	2008 326	0759 54.6	0.59	35.753	1.7	-8.653	2.6	40.5	4.5	24	0.3	99	2.6	0	20	78	C
119	20080411A	2008 411	2251 40.5	0.86	35.144	4.1	-9.376	3.1	43.6	7.1	15	0.3	187	2.5	138	15	58	A
120	20080414C	2008 414	0333 6.9	0.93	37.227	3.4	-9.39	3.5	39.2	8.6	24	0.3	239	4.0	113	87	-174	C
121	20080418C	2008 418	0228 49.6	1.16	36.704	5.2	-8.815	5.9	42.6	12.3	20	0.5	229	2.6	150	67	-162	C
122	20080428B	2008 428	2351 44.4	0.81	35.784	2.5	-8.772	3.9	33.8	8.8	15	0.4	78	2.2	30	76	29	B
123	20080611A	2008 611	1440 31.0	1.22	35.901	2.8	-8.774	4.4	32.1	11.2	16	0.4	68	2.5	92	67	-177	A
124	20080719B	2008 719	1251 52.6	0.82	36.036	5.4	-8.528	8.4	53.8	14.3	8	0.3	297	2.4	10	12	-141	B

Appendix IV-Focal Mechanisms

Appendix IV.A-Gorringe Cluster

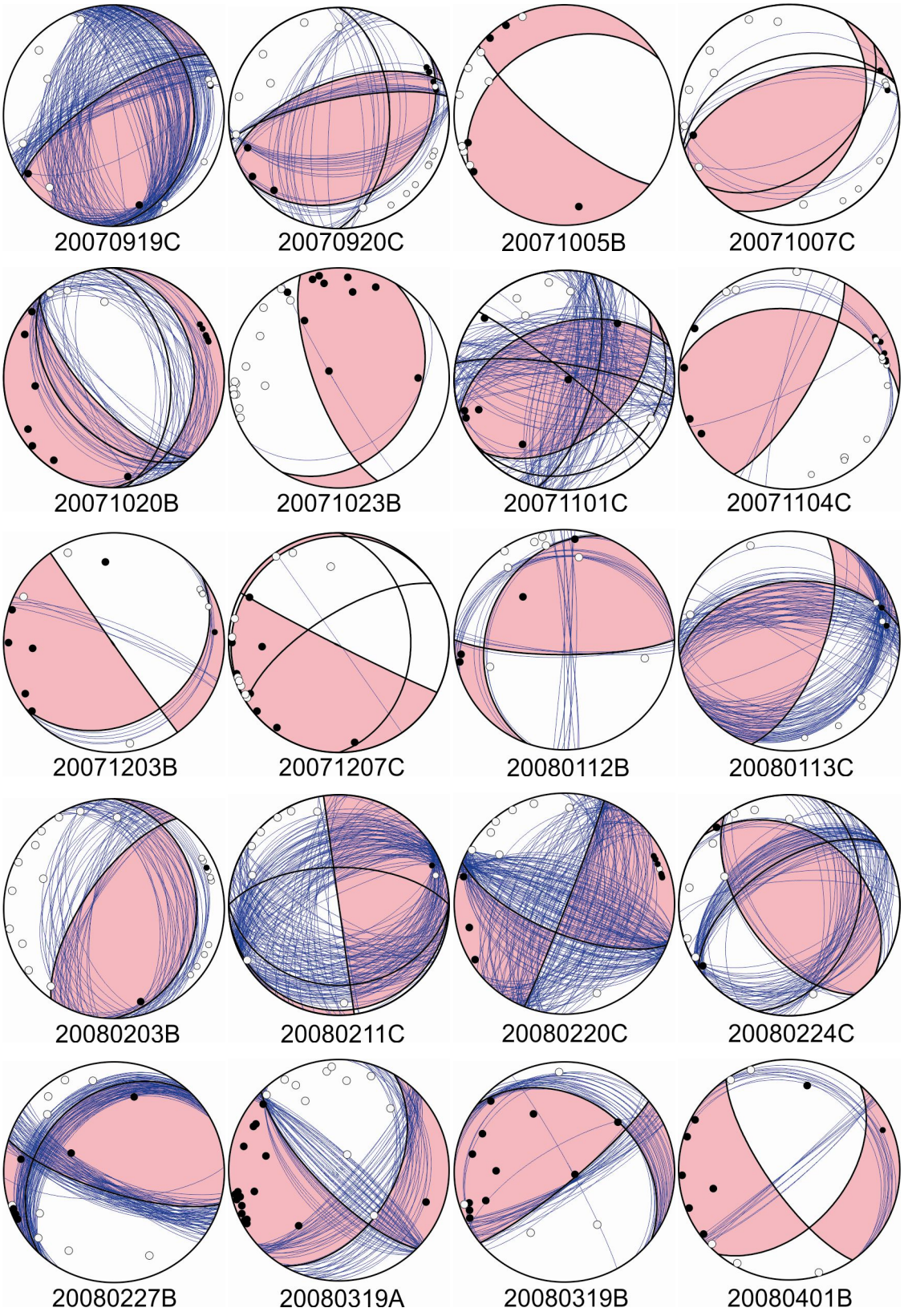

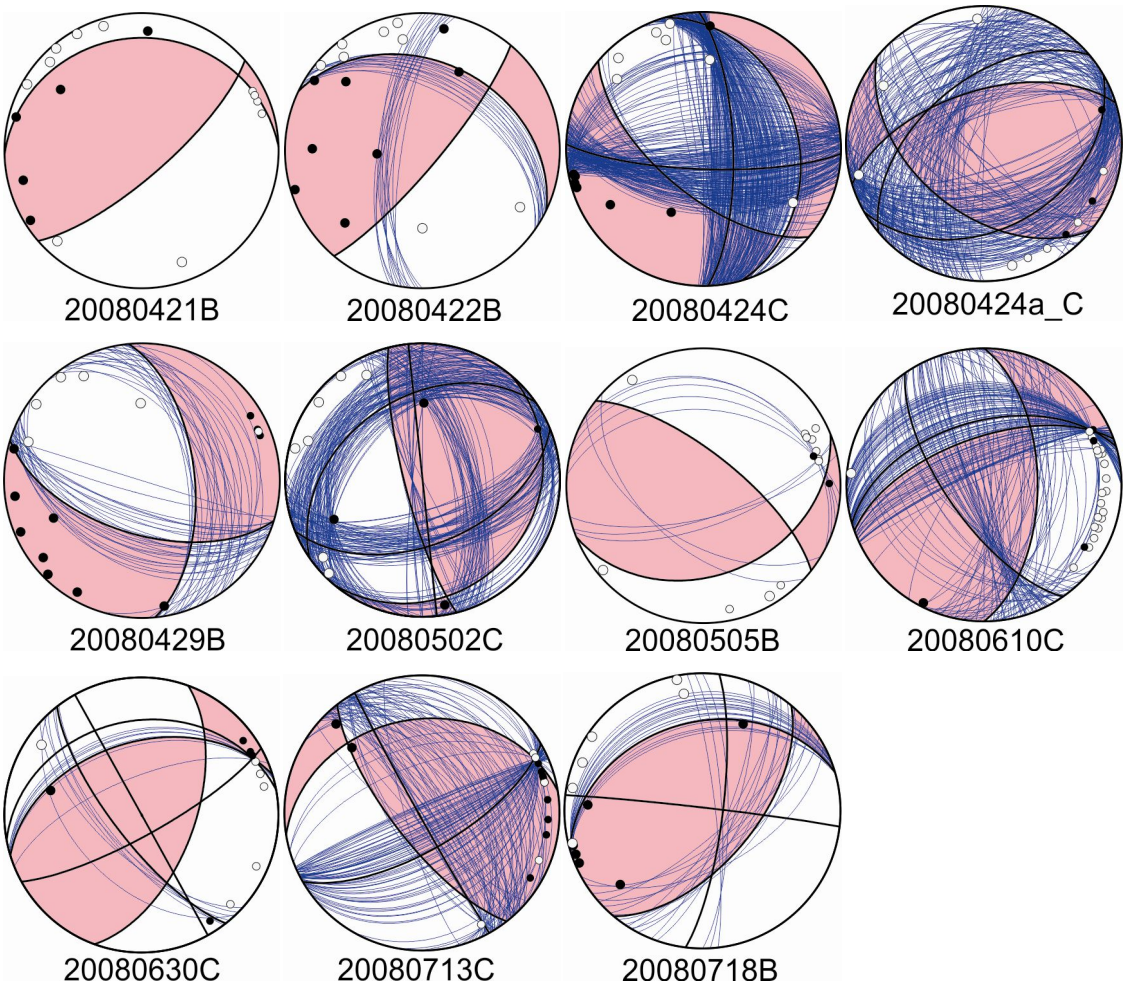

Composite AB

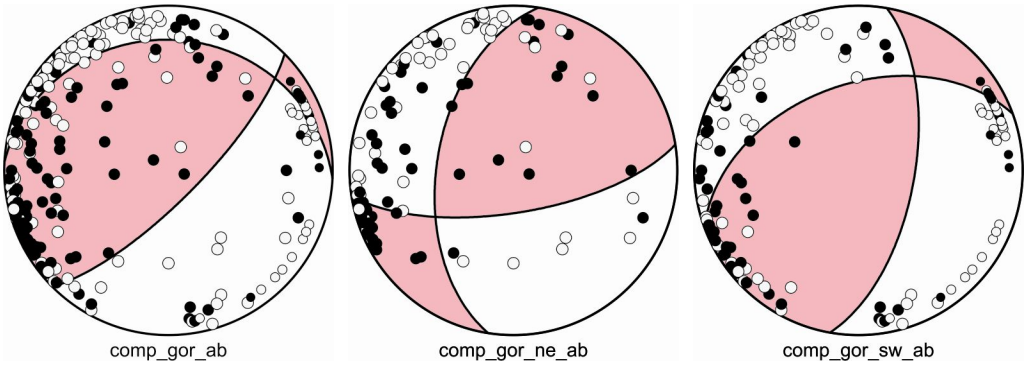

Appendix IV.B- Horseshoe Cluster

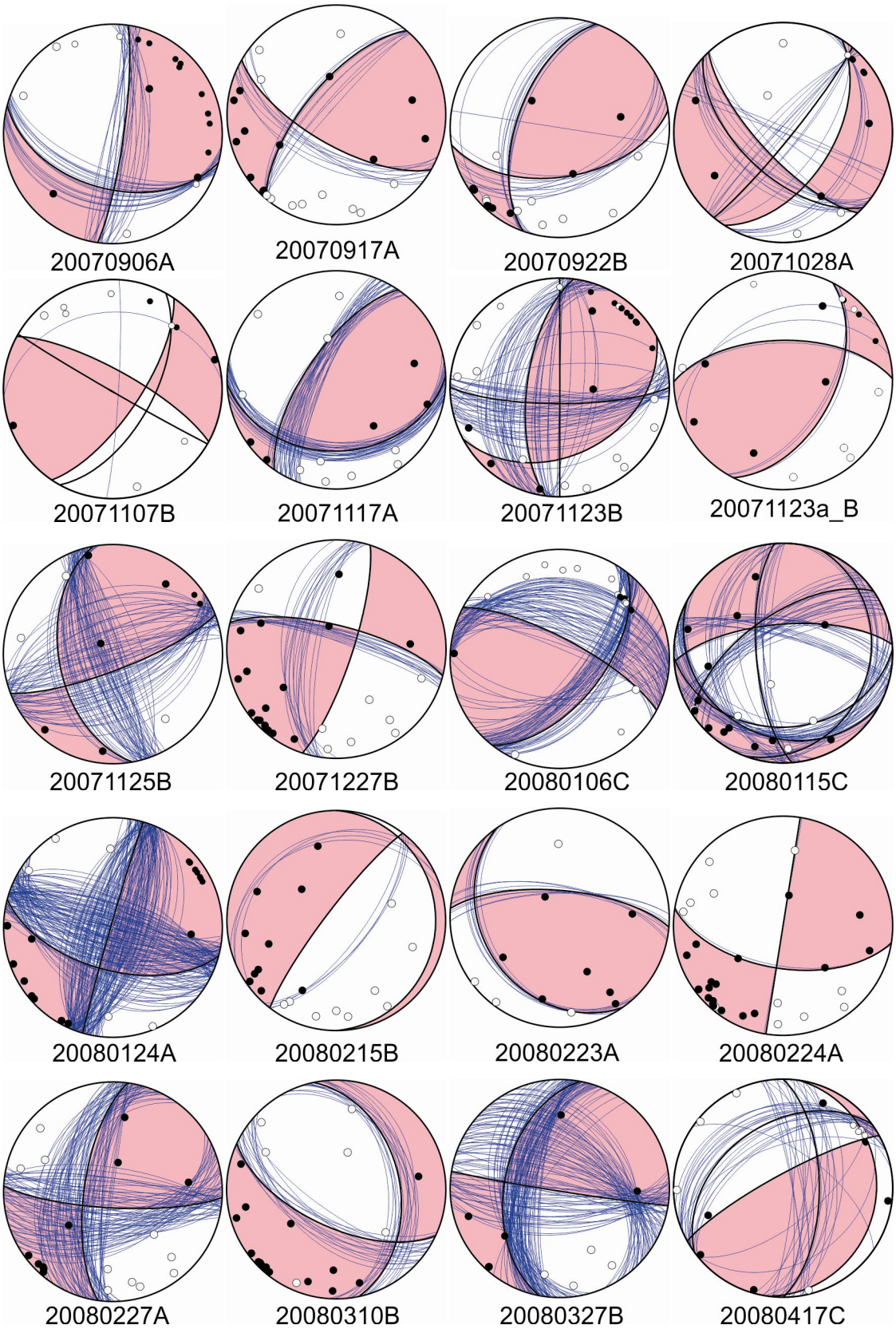

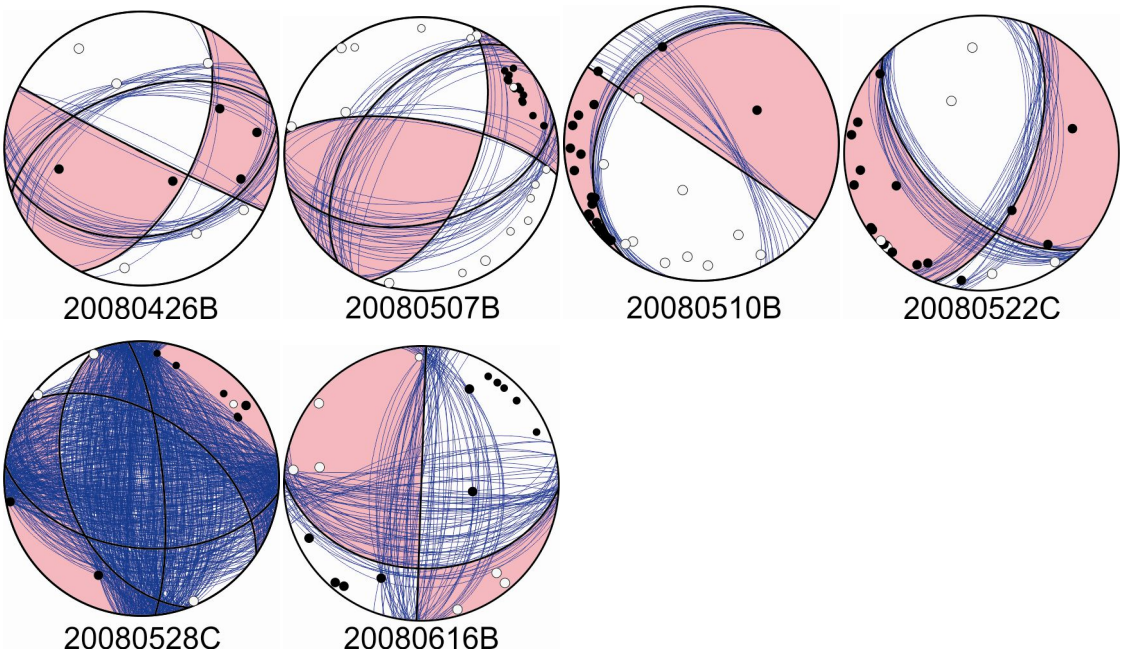

Composite A

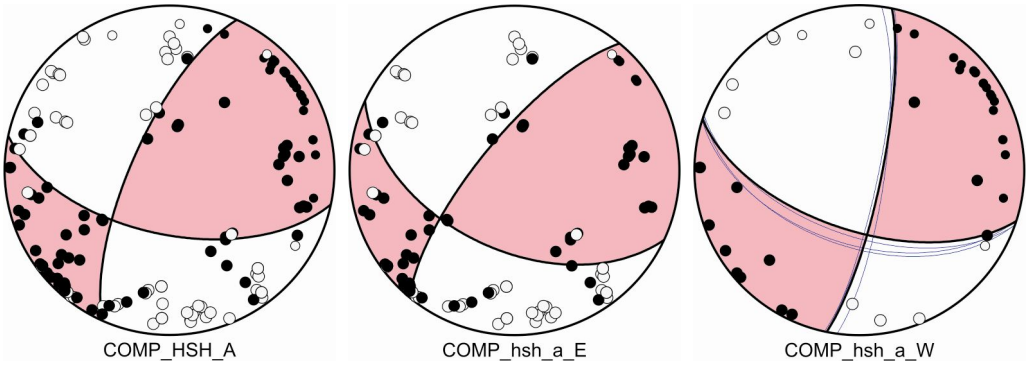

Composite B

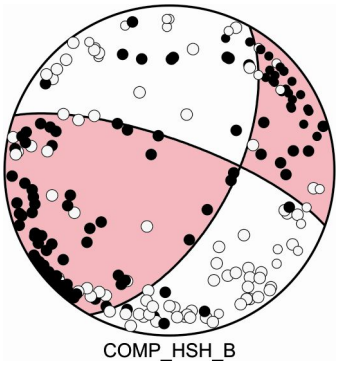

Composite AB

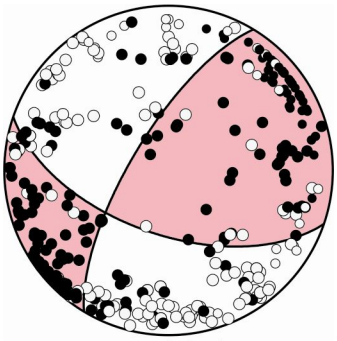

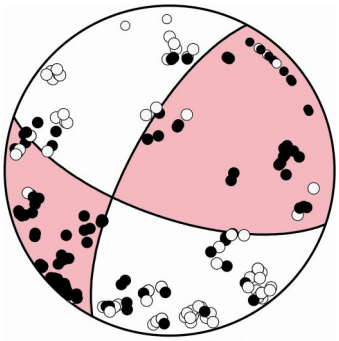

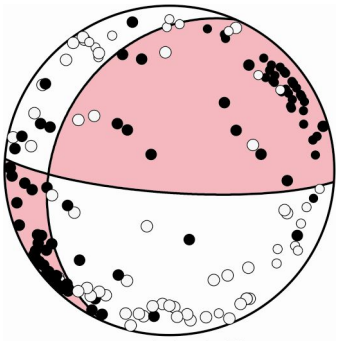

Composite C

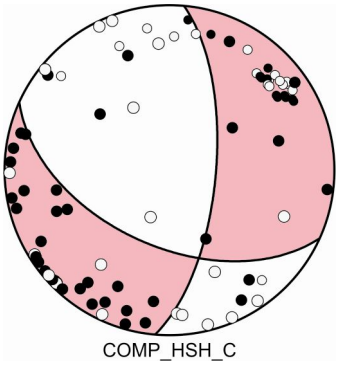

Appendix IV.C- São Vicente Cluster

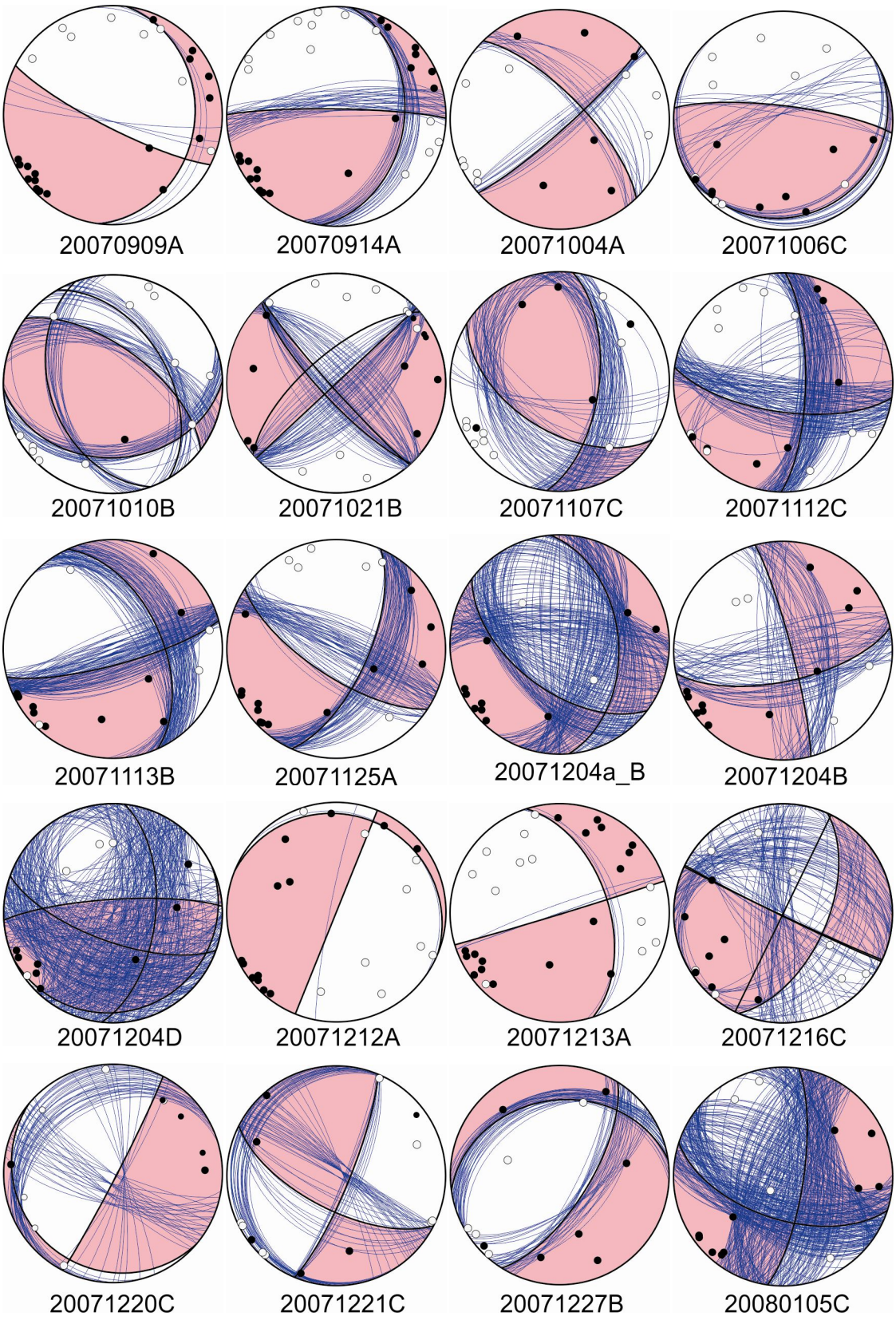

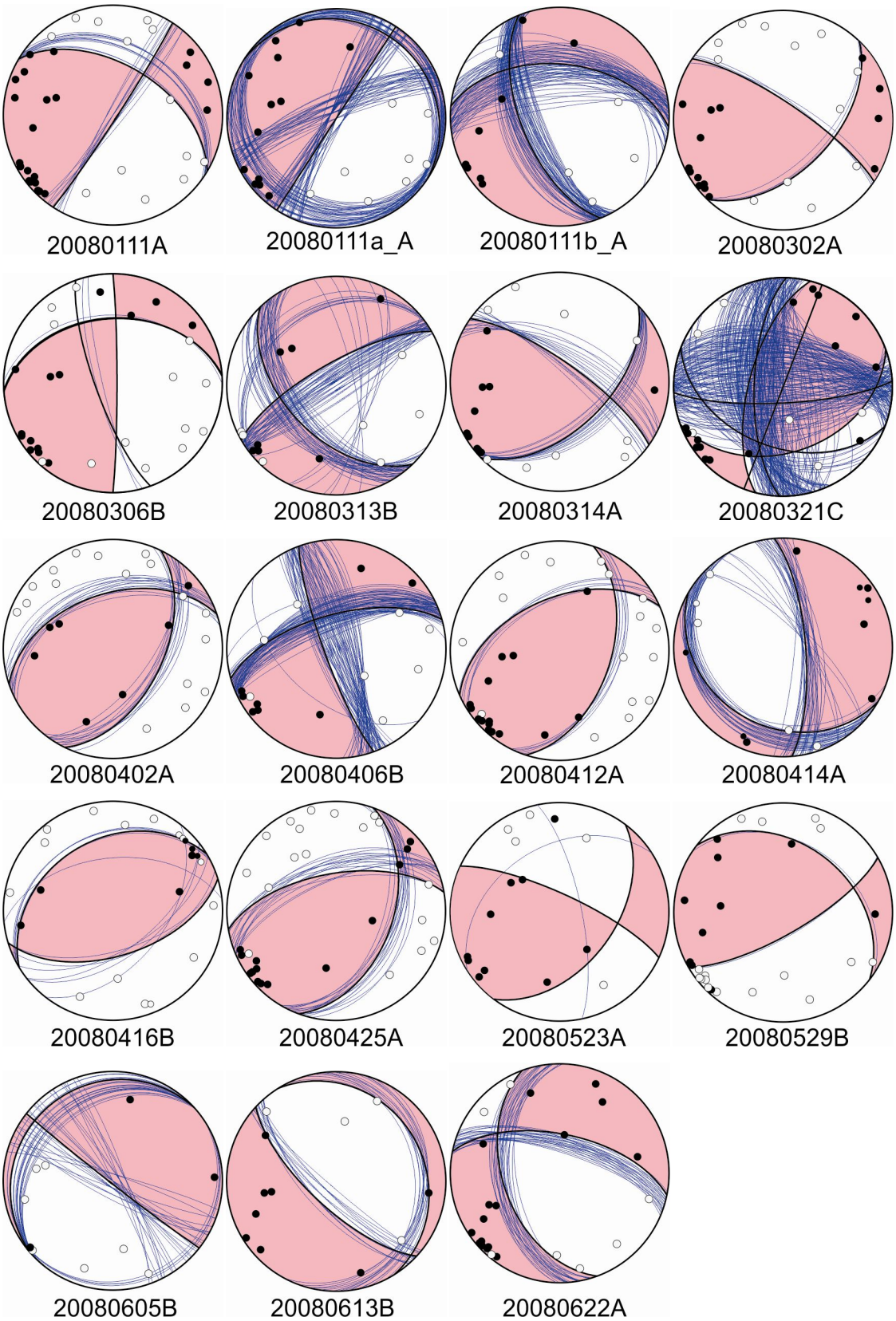
20080111A
20080111a_A
20080111b_A
20080302A
20080306B
20080313B
20080314A
20080321C
20080402A
20080406B
20080412A
20080414A
20080416B
20080425A
20080523A
20080529B
20080605B
20080613B
20080622A

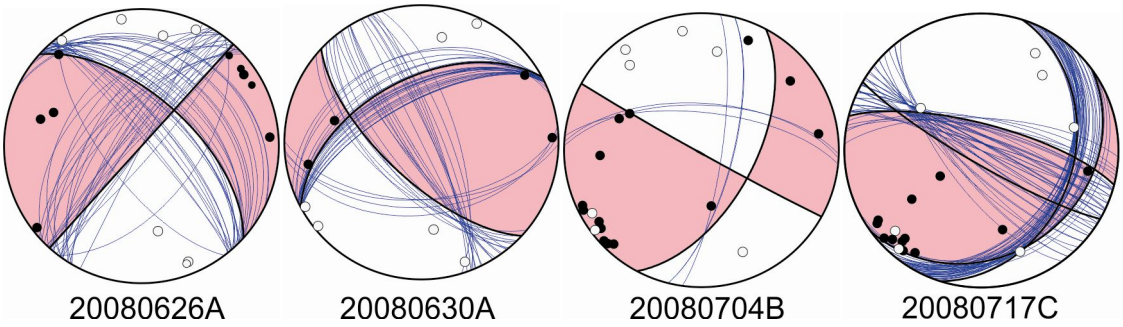

Composite A

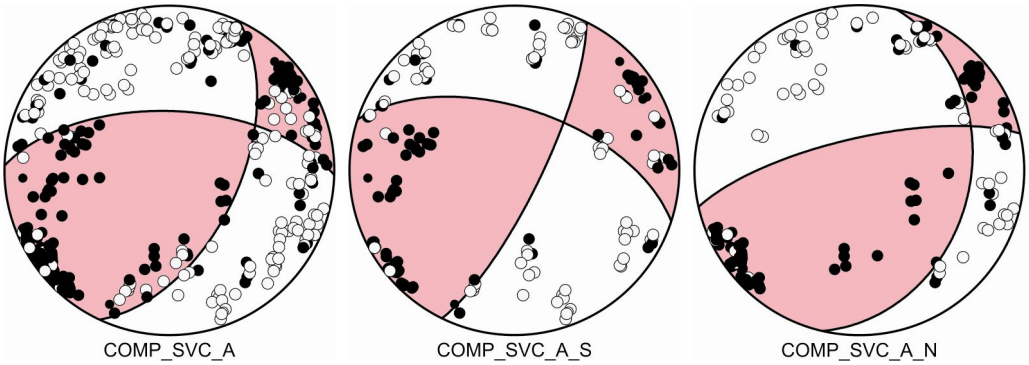

Composite B

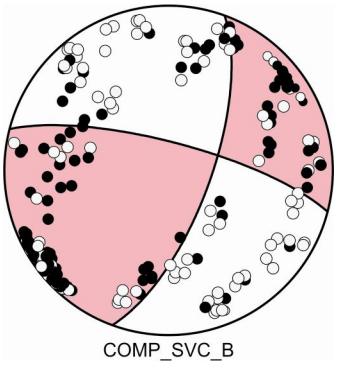

Composite AB

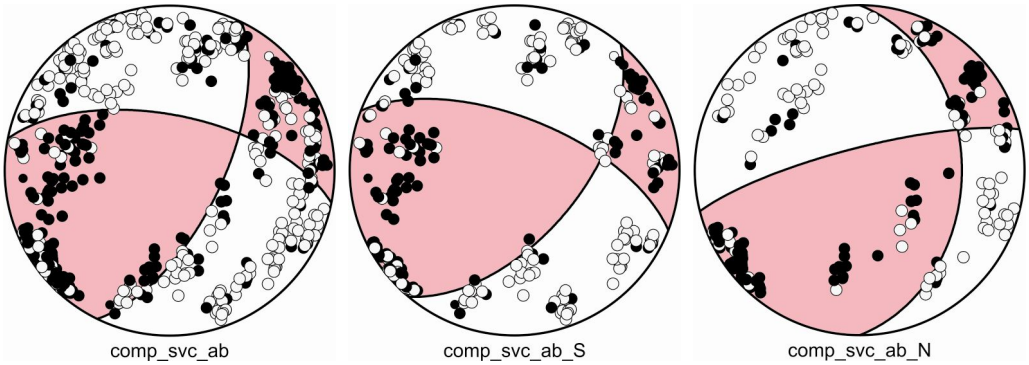

Composite C

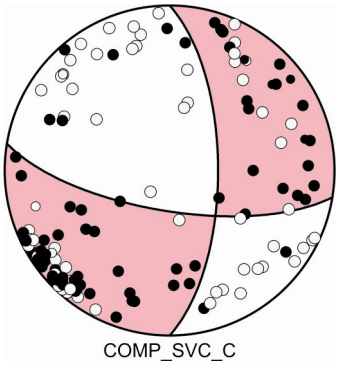

Appendix IV.D- Outside the clusters area

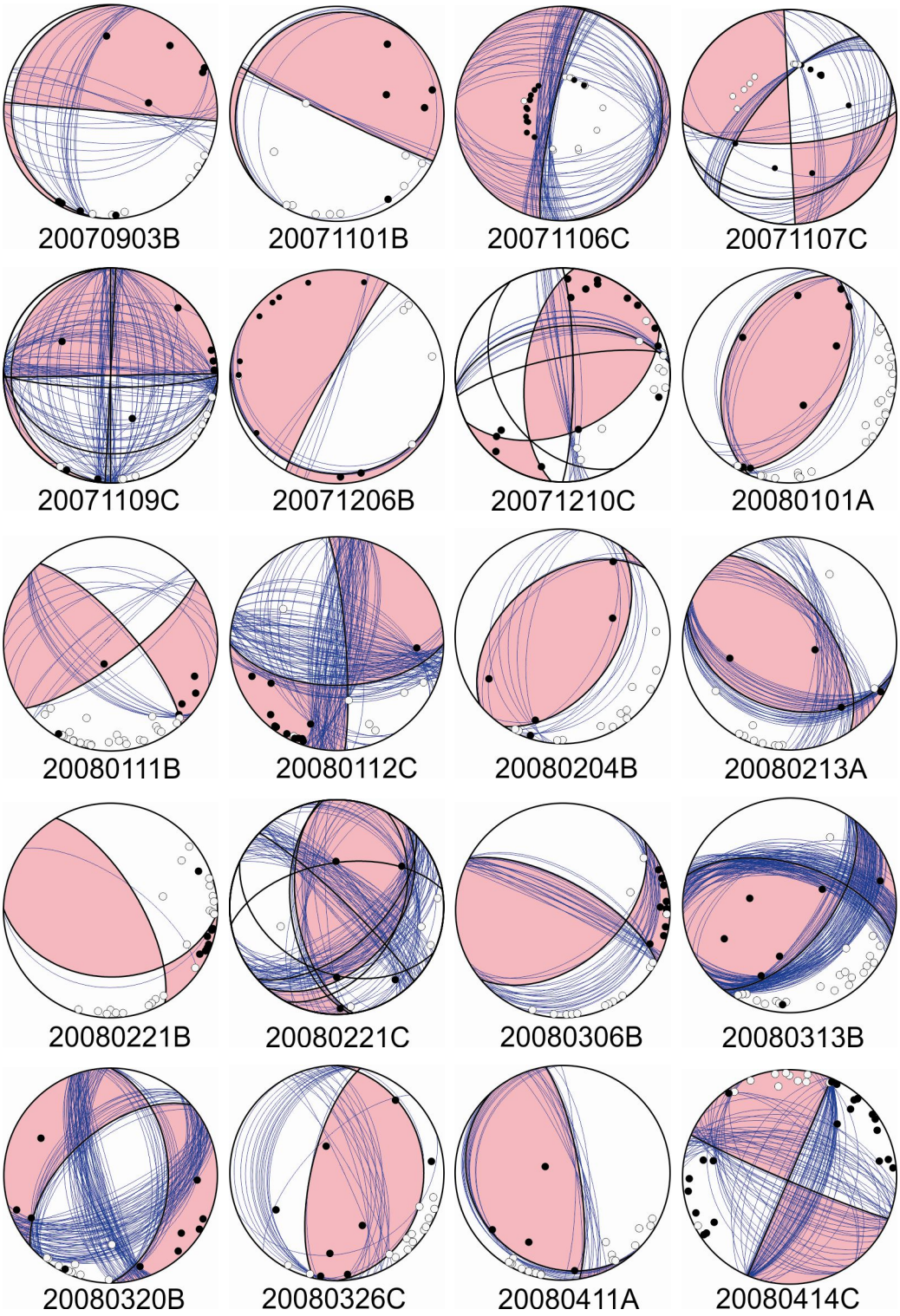

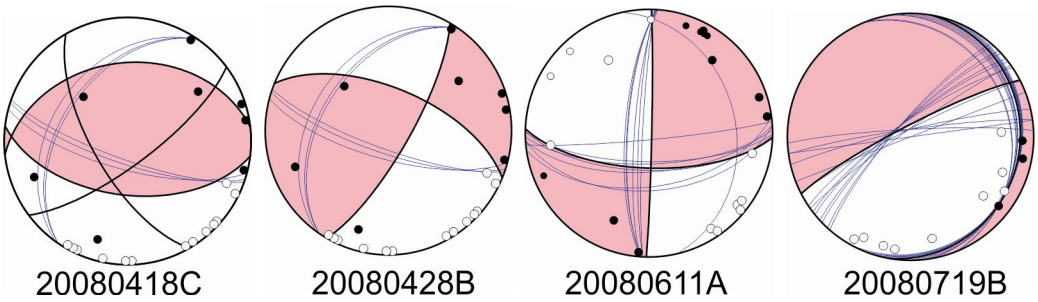

Composite Accretionary Wedge

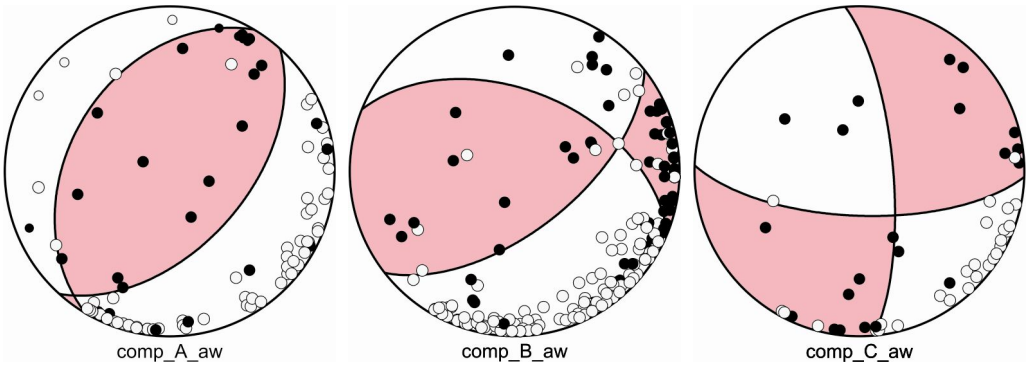

Appendix V – IAM-GB1 acquiring parameters and processing sequence

Acquisition parameters

The IAM-GB1 multichannel reflection seismic profile was acquired using a SWAG air-gun array with a total energy volume of 7524 cu. in. The source depth was of 10m and the shot interval of 75m. The receivers were distributed on a streamer with 192 groups with an interval of 25m, with five auxiliary channels. The cable was at a depth of 18m. The in line the near offset was 254m (Figure A. 1). The streamer length, between the centres of the first and last receivers groups, was 4775m. The sample rate was 4ms and the record length 25s. No low-cut filter was applied in the acquisition system only a high-cut filter at 92Hz with a slope of 72dB/oct and a gain constant of 24dB. The primary navigation system was DGPS.

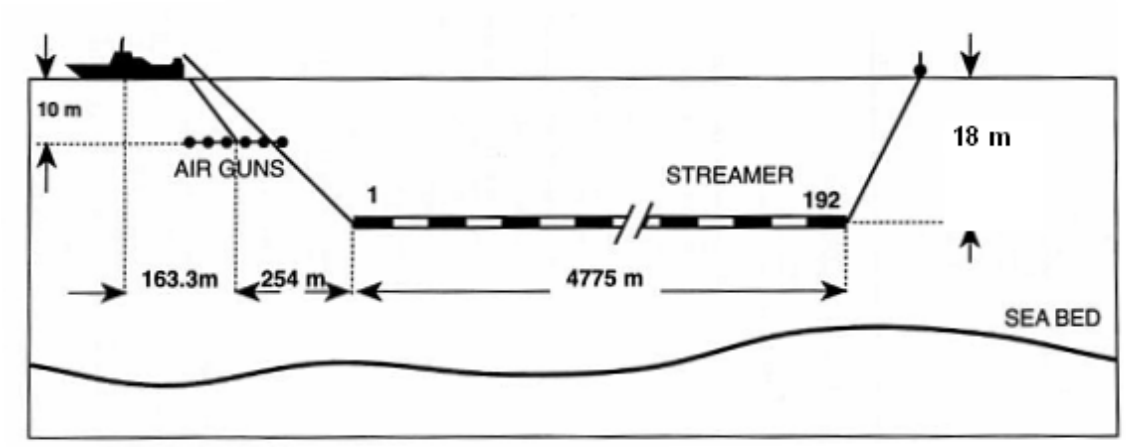

Figure A. 1-.Shooting configuration (adapted to IAM-GB1 configuration from IAM final scientific report): sample rate-4ms; record Length:25s; Shot-point interval 75m; number of channels 192; group interval 25m; cable depth 18m; near in-line offset:254m

Processing sequence

The IAM-GB1 re-processing work was performed using Globe Claritas from GNS Science a software package for 2D and 3D land and marine seismic data at Barcelona Centre for Subsurface imaging under supervision of the Research Professor César Ranero. The processing sequence was trace mute; defining in-line geometry; trace editing; velocity analysis; de-convolution; stacking; time migration and depth conversion. We used NEAREST P1 refraction velocities to convert time migrated profile in depth.

Defining in–line geometry

Since no navigation files were available, the geometry was established using acquisition parameters, assuming a regular geometry. On most 2D marine surveys it is considered that the cable followed directly behind the boat in a straight line (Figure A. 1). This assumption allows us to have a simple linkage

between the shot point number, the channel number, the offset and the CMP (common midpoint) number. The processing sequence is shown in Figure A. 2.

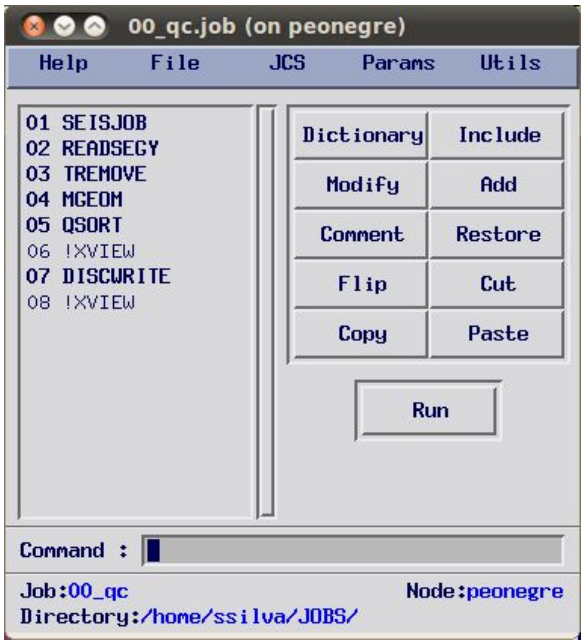

Figure A. 2-Processing flow to establish in-line geometry

In the Claritas' software, the processing steps are defined using work-flows (jobs), which include the user defined operations (modules). The first module of any job is SEISJOB where is included information on the processing line (e.g the line number).

The READSEGY is the module process to import SEGY data into Claritas environment. The TREMOVE module was used to remove dummy and auxiliary traces. In the current example it was used to exclude auxiliary traces in the beginning of the profile. The selected trace kind was Nonlive, removing all traces with TRTYPE not set to 1 (live seismic data).

The MGEOM process module of Claritas is designed to set a regular 2D marine geometry (Figure A. 3). It is appropriate to those cases when navigation is not available. The MGEOM reads the information in a geometry file (Figure A. 3) or directly from more advanced parameters items and defines a linear shot-CMP (common midpoint) relationship. We applied the MODE = "CDP (common depth point) & OFFSET", i.e. the existing shot-point and channel trace headers were used to calculate CDP & OFFSET. Note that although this parameter refers to CDP that is only correct if the reflectors are sub-horizontal.

We show the different parameters defining the geometry in Figure A. 4, note that the first shot point and CMP were set to 101 and 100, respectively. Finally we used the QSORT module to define marine CMP sort outputs (Figure A. 5). Shots were the input data and CMPs are output. The geometry for the line was

defined using the same geometry file in MGEOM. The output from QSORT is ordered within CMPs in increasing offset order (Figure A. 6).

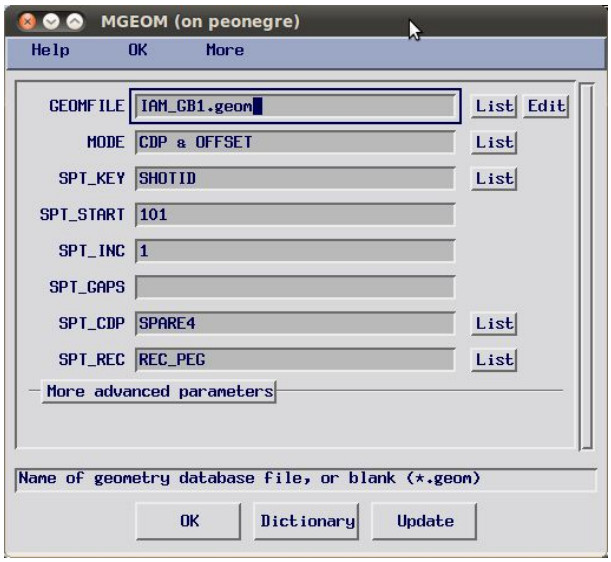

Figure A. 3- Parameters in the MGEOM module

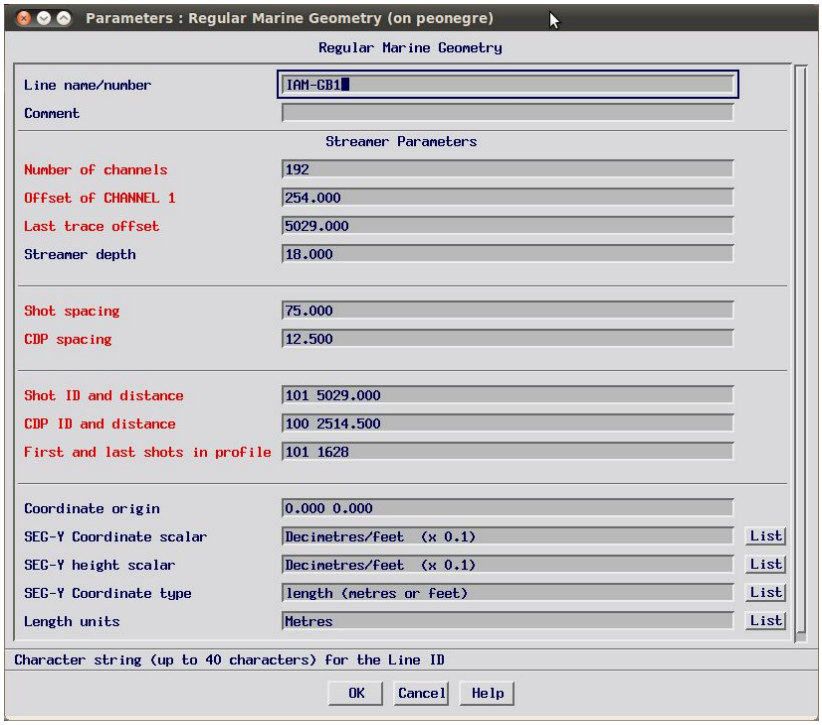

Figure A. 4- Parameters in the geometry file

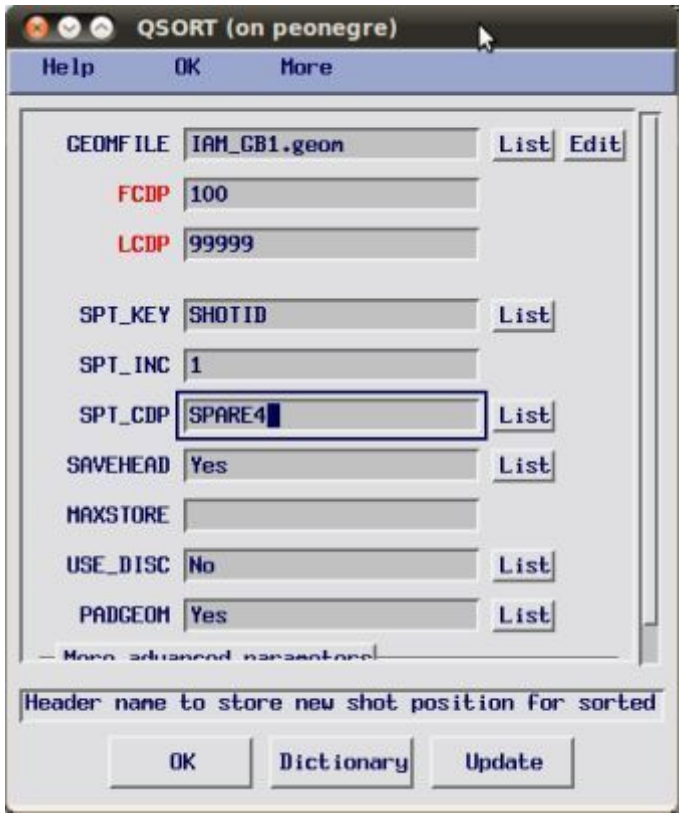

Figure A. 5- QSORT parameters

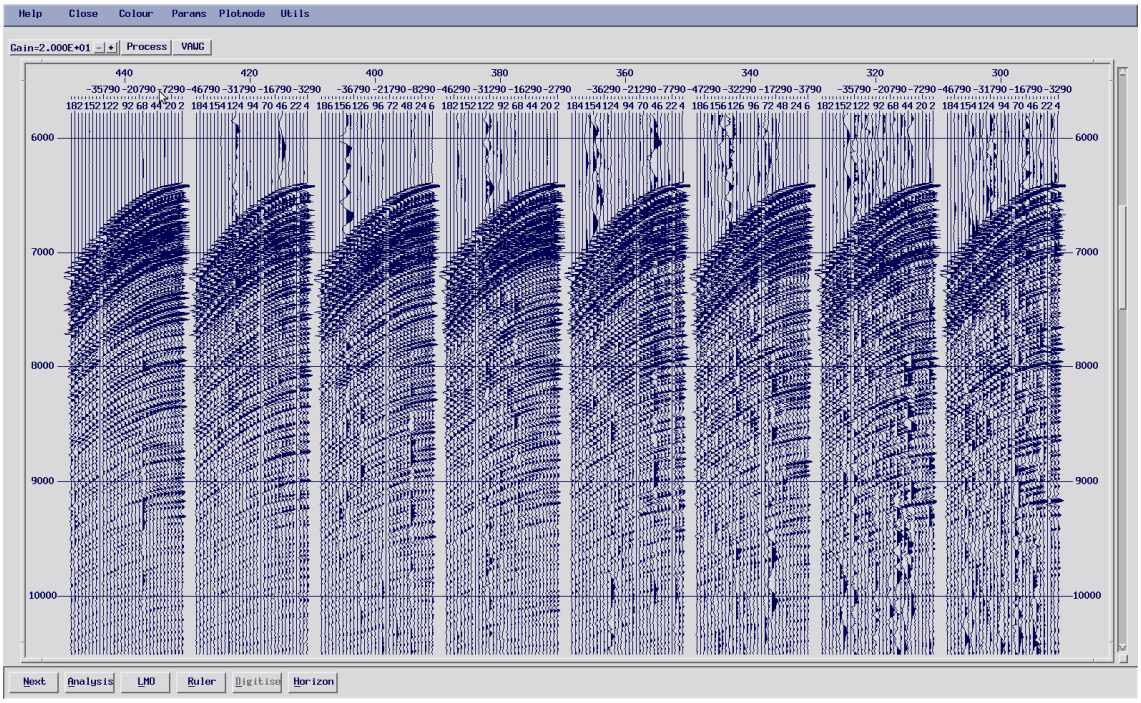

Figure A. 6- CMP gathers

Pre-stack Noise attenuation

Increasing the signal to noise ratio is a central step in the processing flow. In the beginning of the profile it was identified random noise derived from swell and

cable noise. In this context, different processing modules were tested to attenuate this noise. Finally, we selected FXDECONV module (Figure A. 7). This module transforms each trace into frequency domain, than a complex Wiener deconvolution is applied for each frequency in X direction and finally the traces are transformed back into the time domain.

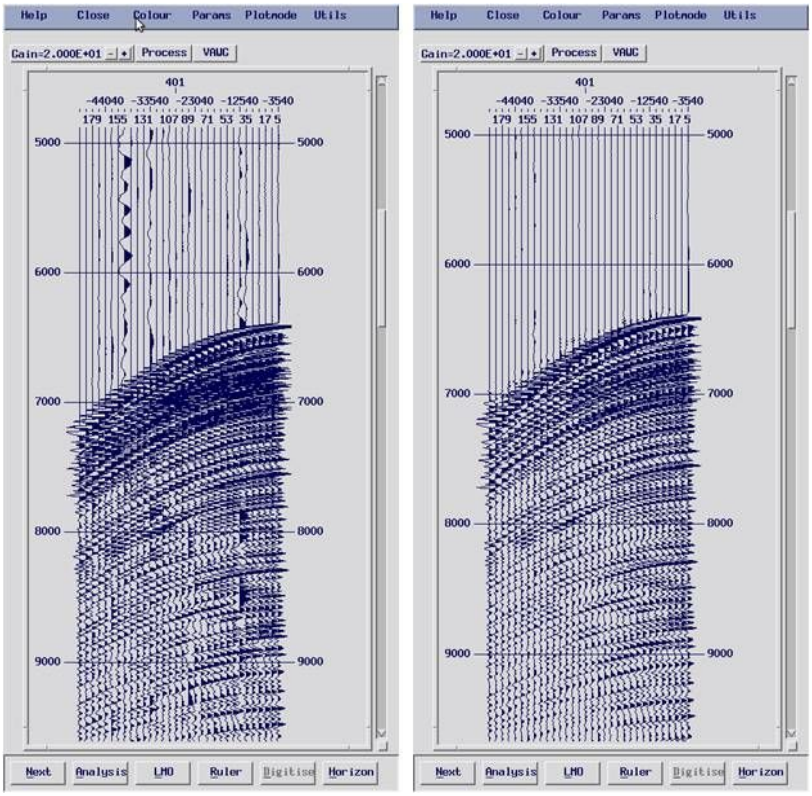

Figure A. 7- Compare CMP gather before (on the left) and after (on the right) FXDECONV random noise attenuation

Velocity analysis

The velocity analysis was performed in different steps and consumed most of the processing time. We started by creating an initial stack (including only CDPTRACES 1-10) using a normal move out correction based in a constant velocity of 1500 km/s and amplitude scaling. In the next step we identified and picked the main horizons in the IAM-GB1 line (Figure A. 8). Following we generated an interval velocity file based on the horizons picking and predefined velocity model based on the previous information on velocities for the area. This file was converted to root mean square (rms) velocities and a new stacking file was generated including all CDPTRACES.

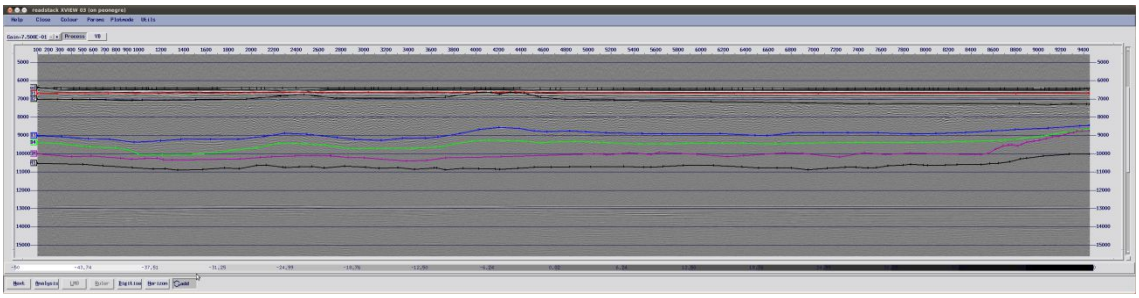

Figure A. 8- First stacking with horizons picking

In the final step we used constant velocity analysis tool in Claritas' software to improve velocity model using semblance analysis. With this tool we could observe simultaneously in different windows the stacking image, the CMP gather and the semblance analysis. In this way we could observe the improvements in normal move out corrections and the effects on stacking display. The final velocity model is presented in Figure A. 9.

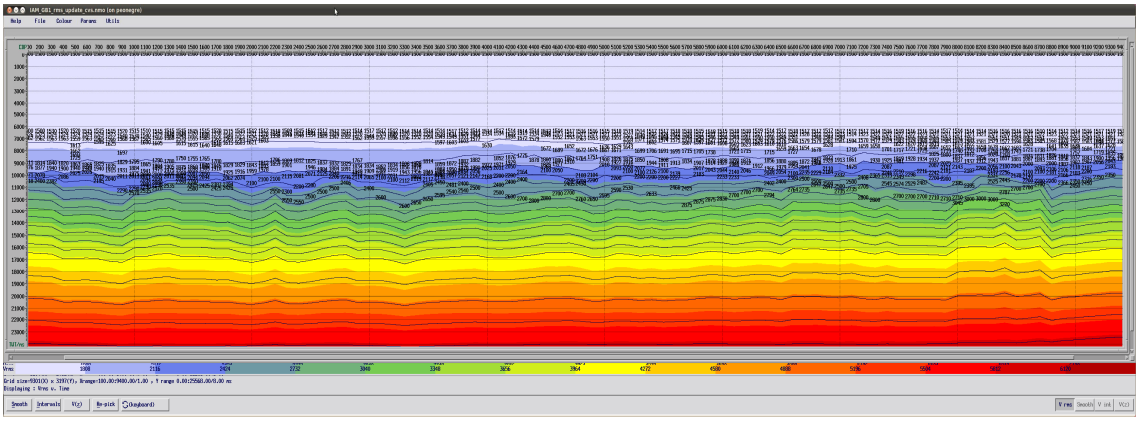

Figure A. 9-Final rms velocity model

Final stacking:

Before the final stack we applied to the CMP gather a time-varying and spatially-varying predictive deconvolution using DECONW module. The deconvolution is applied to the seismic trace over a set of time gates. The filters (one for each time gate) are designed within the design time gates, and are applied over the application time gates. These design windows were picked in CMP gathers with intervals of 400 CMPs. We tested a different set of filters (workflow in Figure A. 10). In Figure A. 11, we compare a fraction of the stacking line with and without deconvolution.

Before the final stack, we applied the NMO correction using the final rms velocity model and a space variant inner trace mute. The final stack is presented in Figure A. 12.

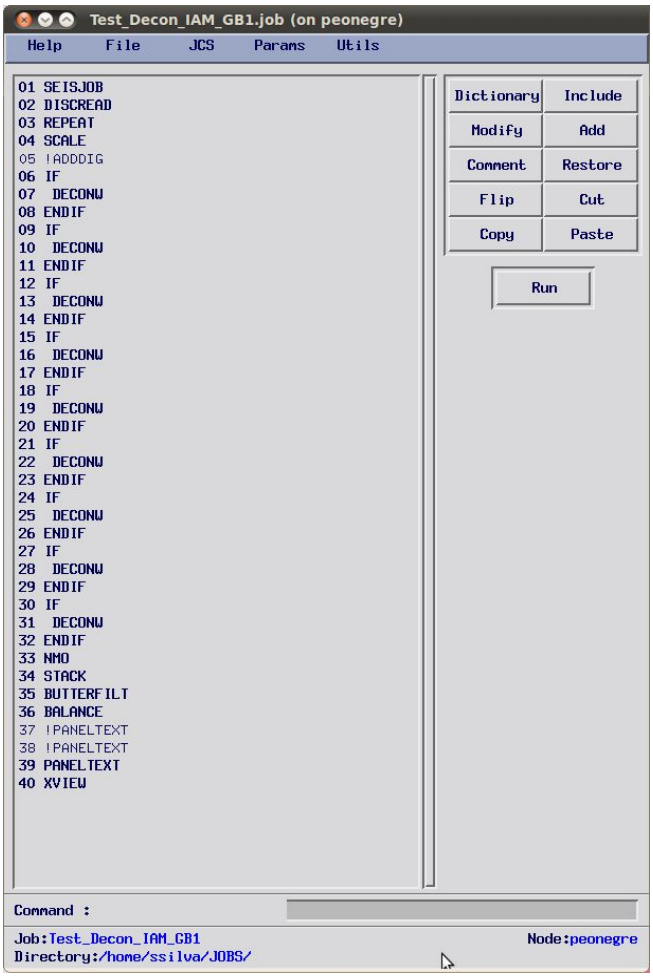

Figure A. 10- Workflow for testing different deconvolution filters

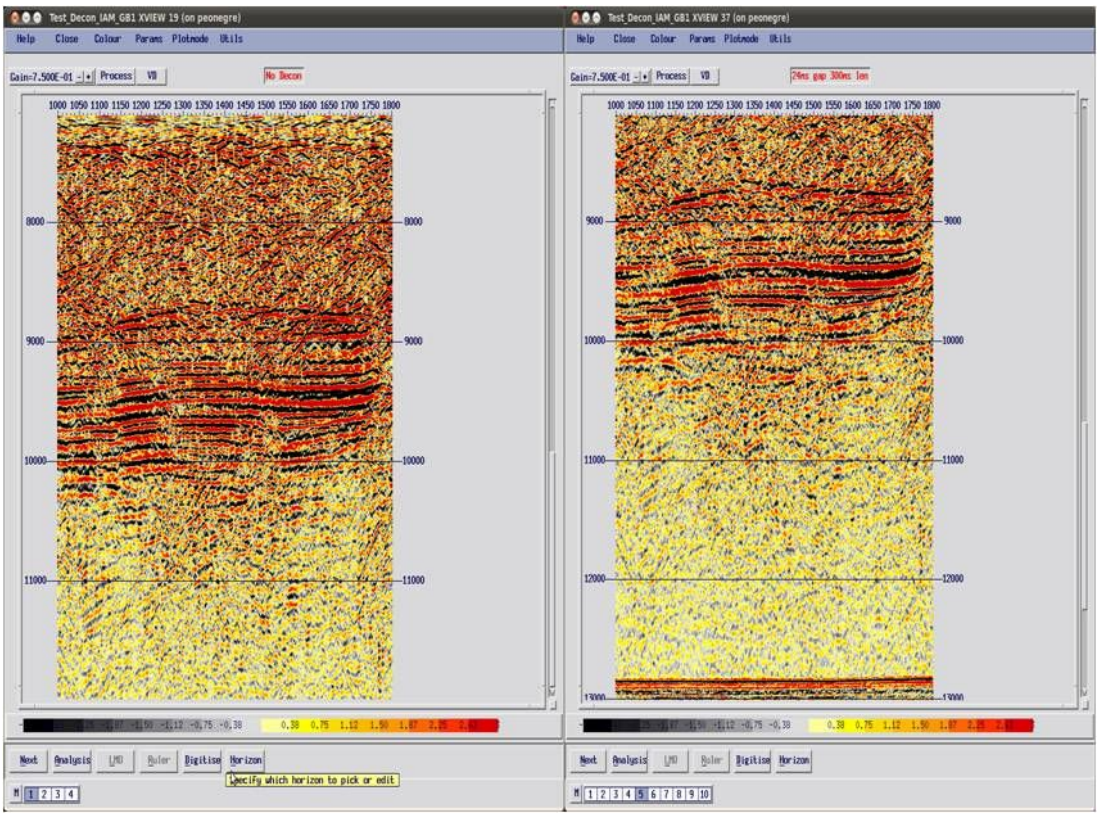

Figure A. 11-Seismic stacking section without and with deconvolution

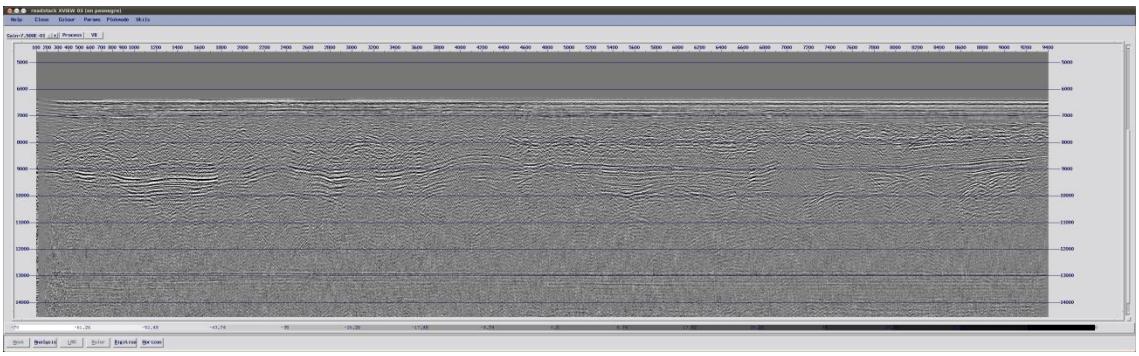

Figure A. 12- Final stack

Time Migration

To apply the pos-stack time migration, we converted stacking velocities to interval velocities. We started by re-picking seismic horizons in the final stack (Figure A. 13). In the next step, we introduced the horizons and the stacking velocity model in Claritas' isovels application to create an interval velocity model and then we smooth this model.

We used the FDMIG module to apply a finite difference time migration with the above interval velocity model. The results are presented in Figure A. 14.

Depth conversion:

The TDCONV1 module performs a depth conversion on stacked data using previously defined interval velocities. The velocities were extracted from NEAREST refraction profile P1 in the interval of intersection of this profile with the IAM-GB1 line (see Figure A. 15). We converted these data to interval velocities (based on the picked seismic horizons). The velocity model is presented in Figure A. 15 and we compare it with previous data extracted from a parallel refraction profile B-BR in Purdy et al. (1975). In detail, we observe that particularly for intermediate layers and in the IAM-GB1 SW or NE limits, the velocities used are higher. In the central part of the profile, between CMPs 500 and 8500, the velocities are more consistent with the work Purdy et al. (1975). The velocity model is also in conformity with the pre-stack velocities in intersection area of AR-01 with IAM-GB1 (fig.6 in Rovere et al., 2004 for details on the velocity model). The final depth converted IAM-GB1 profile is in Figure A. 16.

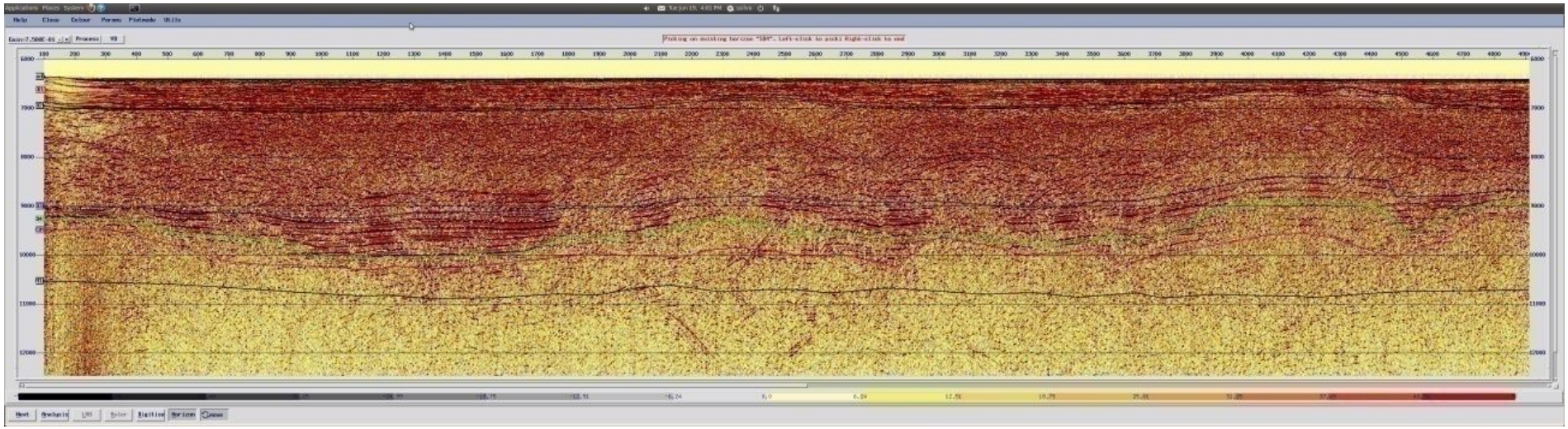

Figure A. 13-Final stack with horizons picking

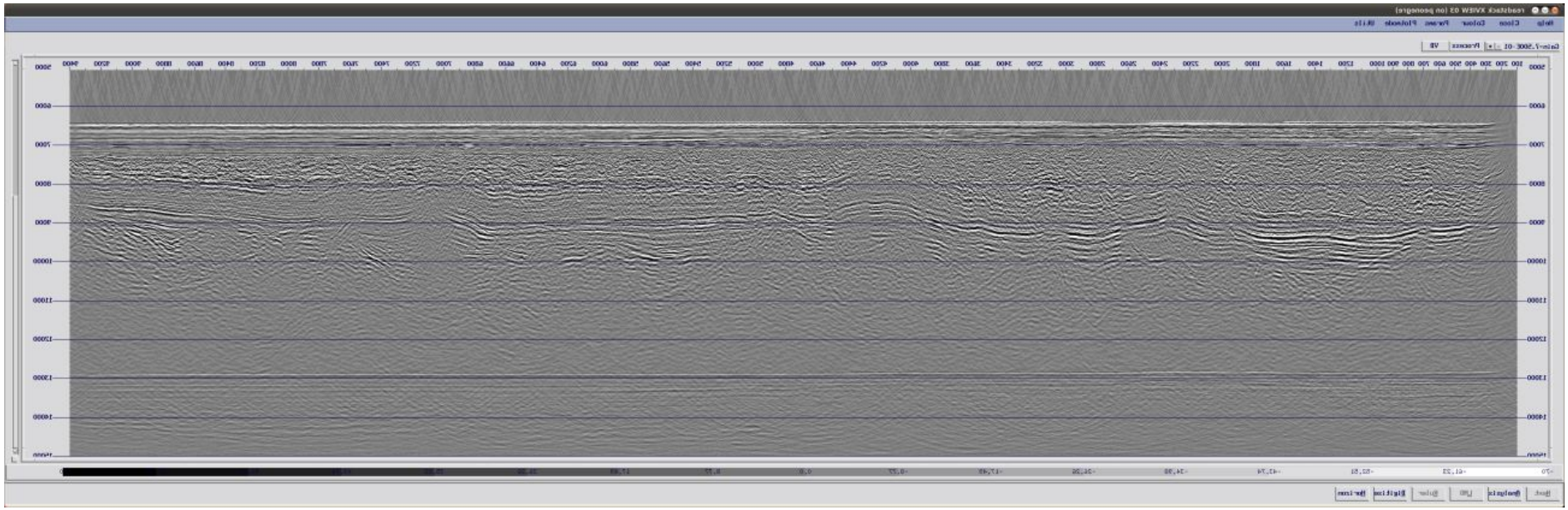

Figure A. 14- IAM-GB1 with time migration

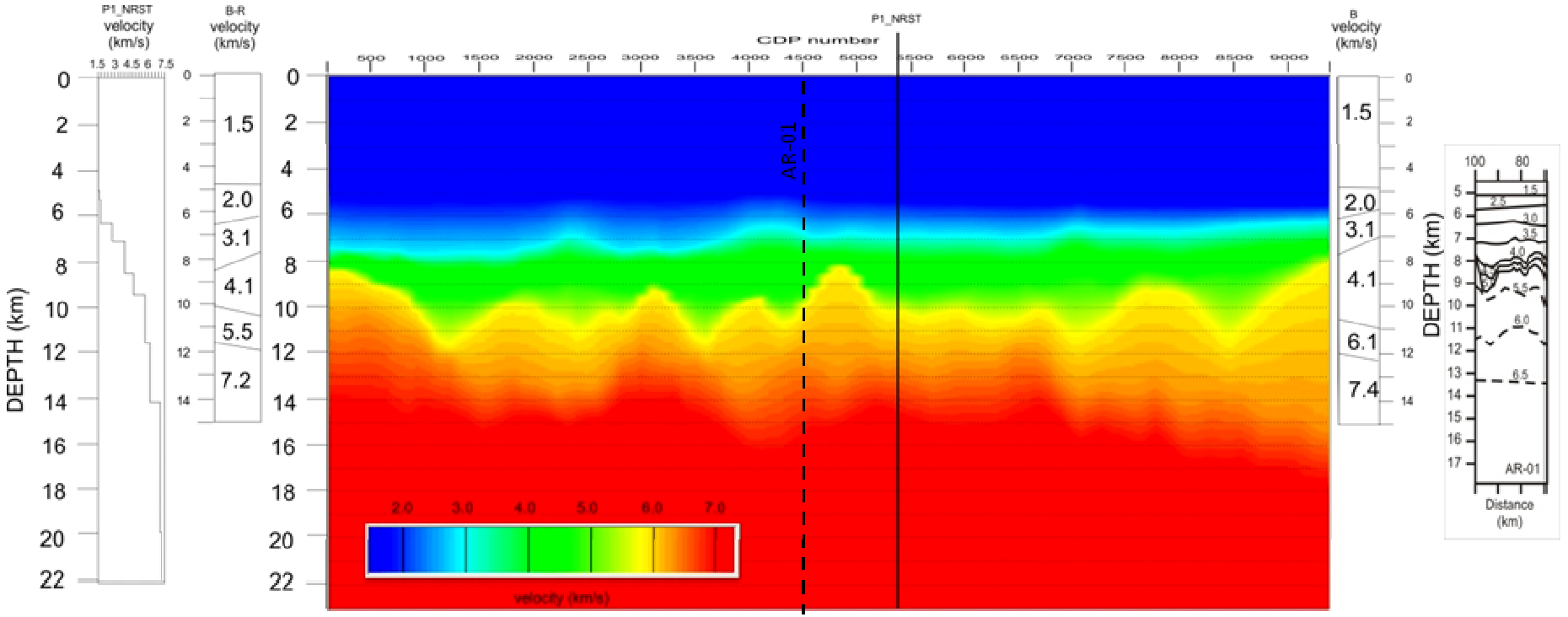

Figure A. 15- Final velocity model for depth conversion, the velocity profile extracted from P1 NEAREST refraction profile, the velocities from Prudy et al., 1975 and AR-01 pre-stack velocities in the intersection with IAM-GB1 seismic profile (profile B-BR, in figs. 3 and 8 of Prudy et al., 1975,; AR-01 pre-stack velocity model in Rovere et al., 2004, fig. 6)

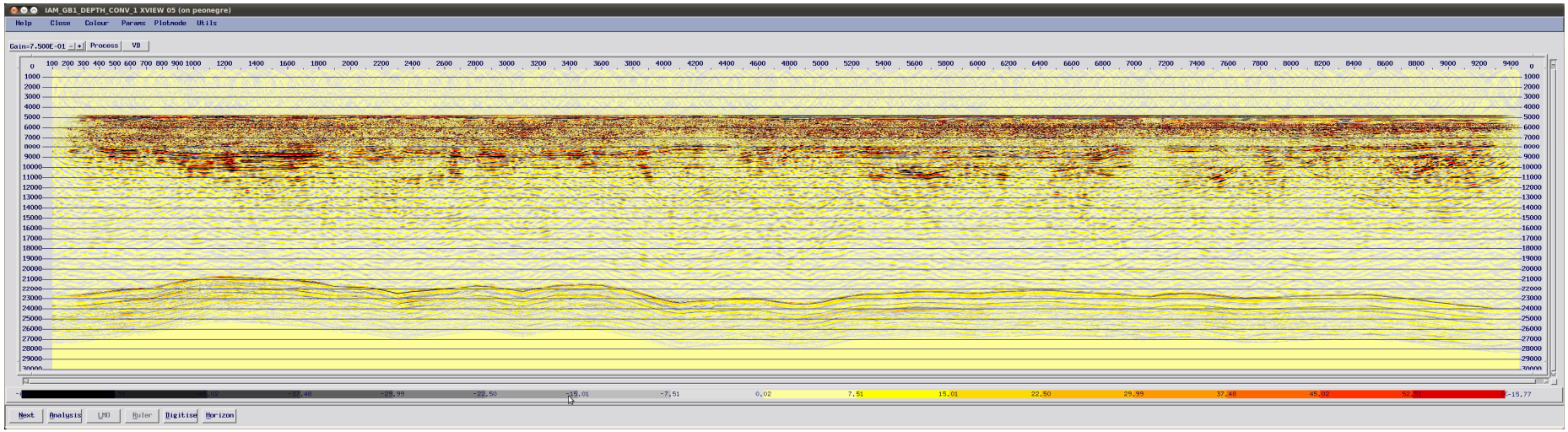

Figure A. 16-Depth converted IAM-GB1

Appendix VI – IAM-GB1 MCS reflection profile in TWT with and without interpretation

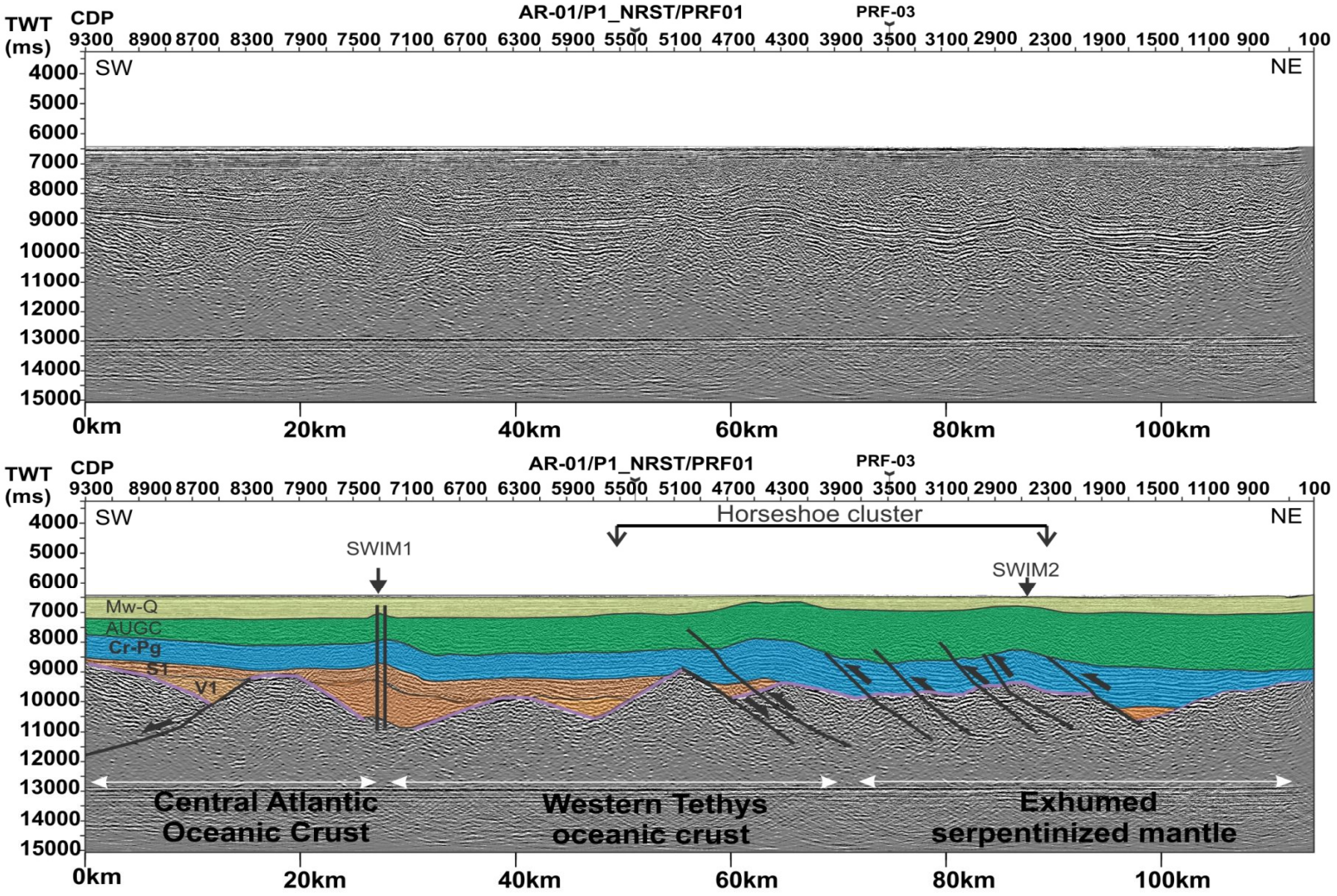

Appendix VII – list of publications in co-authorship

During the PhD thesis the author collaborated in the following publications (in attachment):

*Grevemeyer, I., Matias, L., **Silva, S.,** 2016. Mantle earthquakes beneath the South Iberia continental margin and Gulf of Cadiz – constraints from an onshore-offshore seismological network, Journal of Geodynamics, Volume 99, September 2016, Pages 39–50,* http://dx.doi.org/10.1016/j.jog.2016.06.001

In this work, the author participated in the OBS recovering campaign. In the publication, contributed with comments and collaborated in the general writing up of the manuscript, particularly, in the discussion of seismicity distribution in the Gulf of Cadiz.

*Hensen, C., Scholz, F., Nuzzo, M., Valadares, V., Gràcia, E.; Terrinha, P.; Liebetrau, V., Kaul, N., **Silva, S**., Martínez-Loriente, S., Bartolome, R., Piñero, E., Magalhães, V. H., Schmidt, M., Weise, S. M., Cunha, M., Hilario, A., Perea, H., Rovelli, L., Lackschewitz, K., 2015. Strike-slip faults mediate the rise of crustal-derived fluids and mud volcanism in the deep sea, Geology, 43(4): 339-342,* http://dx.doi.org/10.1130/G36359.1

In this publication, the author collaborated with the data and discussion concerning the seismicity distribution in the study area including planning of the site surveys.

*Rosas, F.M.,Duarte, J.C., Neves, M.C., Terrinha, P., **Silva, S.,** Matias, L., 2012. Thrust-wrench interference between major active faults in the Gulf of Cadiz (Africa-Eurasia plate boundary, offshore SW Iberia): tectonic implications from analogue and numerical modeling. Tectonophysics, 548-549, 1 – 2*

In this work, the author collaborated in the analogue experiments and discussion, particularly in the seismicity distribution and the influence of serpentinization in the fault interference zone.

*Duarte, J.C., F.M. Rosas, P. Terrinha, M-A Gutscher, J. Malavieille, **S. Silva**, L. Matias, 2011. Thrust - wrench interference tectonics in the Gulf of Cadiz (Africa - Iberia plate boundary): insights from (sand-box) analog models. Marine Geology 289, 135–149.*

In this publication, the author collaborated in the analogue experiments and discussion.

Journal of Geodynamics xxx (2016) xxx–xxx

Contents lists available at ScienceDirect

Journal of Geodynamics

journal homepage: http://www.elsevier.com/locate/jog

Mantle earthquakes beneath the South Iberia continental margin and Gulf of Cadiz – constraints from an onshore-offshore seismological network

Ingo Grevemeyer[a,*], Luis Matias[b], Sonia Silva[b]

[a] GEOMAR Helmholtz Centre of Ocean Research, Wischhofstrasse 1-3, 24148 Kiel, Germany
[b] Instituto Dom Luiz, Faculdade de Ciências, Universidade de, Lisboa, Portugal

ARTICLE INFO

Article history:
Received 22 December 2015
Received in revised form 3 May 2016
Accepted 8 June 2016
Available online xxx

Keywords:
Earthquakes
Passive margins
Active deformation
Seismic hazard
Iberia
Gulf of Cadiz

ABSTRACT

The Gulf of Cadiz and the passive continental margin of southern Iberia to the west of the Strait of Gibraltar locally accommodate the presently ongoing convergence between Africa and Eurasia by widespread, rather diffusive, seismic activity. Seismicity of the northern Gulf of Cadiz was derived from an amphibious seismological network, including 24 temporary marine offshore stations, besides the permanent networks in Portugal, Spain, and Morocco. During the 6 month of the offshore network operation, in total 86 local earthquakes were located at six or more offshore stations with the majority of earthquakes occurring to the southwest of Iberia and along the Algarve continental margin off southern Iberia. The distribution of events along the Algarve margin mimics features reported for the Atlantic passive continental margins of both South and North America. Focal mechanisms at the Portimão Bank support that seismically active areas are associated with compression. Similar stress patterns are reported for the east coast of South and North America. However, while earthquakes along the American east coast occur at crustal levels, earthquakes in the northern Gulf of Cadiz occur both in the lower crust and upper mantle, with the majority of events rupturing within the mantle, including a number of well-located earthquakes beneath crust forming the continent-ocean transition zone. The large number of earthquakes in the mantle might be caused by the unique geological setting, where deformation occurs in cool lithosphere of Mesozoic age. We suggest that seismicity along the Algarve margin is caused by re-activation of pre-existing margin-parallel faults rather than corresponding to newly formed structures related to a new developing plate boundary.

1. Introduction

The ocean-continent boundary of southern Iberia to the west of the Strait of Gibraltar is defined as a passive continental margin, along which the continent and seafloor are part of the same plate (Fig. 1). In the framework of plate tectonics (e.g., McKenzie and Parker, 1967; Morgan, 1968) the interior of plates is defined as being seismically inactive. However, even stable continental regions (SCR), including passive continental margins, show occasionally seismic activity. World-wide, Schulte and Mooney (2005) reported 1371 crustal earthquakes with magnitude larger than 4.5 hitting stable continental lithosphere, with roughly 50% of the seismicity occurring at Mesozoic passive margins. Earthquakes rupturing along passive margins occur both onshore and offshore and may reach magnitude 7 (Wolin et al., 2012). It is generally believed that these events are related to the reactivation of favourably oriented pre-existing fault planes in response to broad-scale uniform regional stress fields (Zoback, 1992; Wolin et al., 2012). This idea is supported by observation that passive margins are often reactivated in compression (Cloetingh et al., 2008).

Wolin et al. (2012) called the Eastern US passive continental margin off Virginia "a passive-aggressive" margin after on 23rd of August 2011 a magnitude M = 5.8 hit the town of Mineral. The entire eastern coast of North American has a long record of several magnitude 6–7 earthquakes, including the M = 7.2 1929 Grand Banks earthquake, causing a landslide and tsunami (Bent, 1995). In addition to far-field stresses, glacial isostatic rebound has been suggested to control earthquakes at passive margins. However, farther south along the margin of eastern Brazil earthquakes with magnitudes of larger than 5 occur every 20–25 years (Assumpcao

* Corresponding author.
E-mail address: igrevemeyer@geomar.de (I. Grevemeyer).

http://dx.doi.org/10.1016/j.jog.2016.06.001
0264-3707/

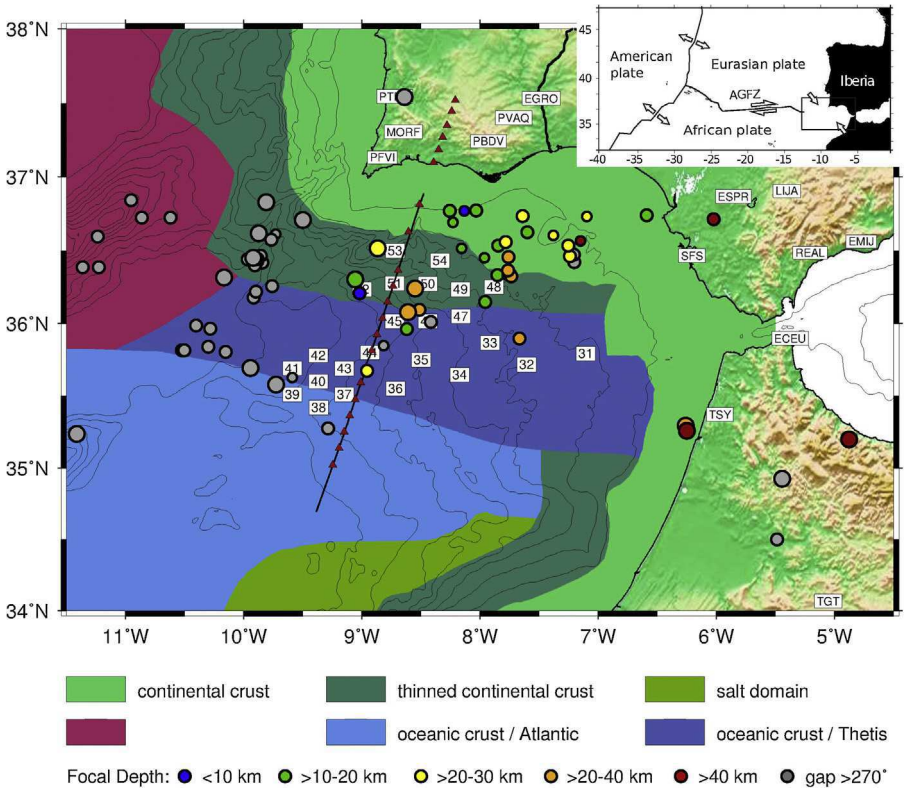

Fig. 1. Deployment of an amphibious onshore-offshore seismological network in the Gulf of Cadiz, Iberia and Morocco. Colour coded offshore domains are geological units as defined by Martinez-Loriente et al. (2014). Tectonic features are from Duarte et al. (2011). Numbered squares are TOPO-MED ocean-bottom-seismometers (OBS) and labelled squares are permanent seismic stations deployed in Portugal, Spain and Morocco. Coloured dots are earthquakes coded by depth and quality. Grey dots are earthquakes with a gap > 200°. Blue: depth z < 5 km; green: depth 5 < z < 15 km; yellow 15 < z < 30; orange 30 < z < 50 km; red z > 50 km. Thin black line and triangles mark the seismic line and seismic stations of Sallares et al. (2011), shown in Fig. 7. Plate motions (inset) are from DeMets et al. (2010).

et al., 2011), indicating that forces other than isostatic adjustments contribute to control seismicity along passive margins.

Passive continental margins occur generally several thousands of kilometres away from major plate boundary faults. The southern passive margin of Iberia, including the Algarve margin, however, is located near or at the Azores-Gibraltar seismic zone, marking the plate boundary between Eurasia/Iberia and Africa. To the east of 14°W the plate boundary is not well defined and seismicity is rather diffuse (Sartori et al., 1994; Buforn et al., 2004) and the WNW-ESE plate convergence of ~4 mm/yr (DeMets et al., 2010) is accommodated through widespread tectonically active deformation (Sartori et al., 1994; Hayward et al., 1999). Consequently, convergence may have caused Neogene to Quaternary reactivation of Mesozoic rifting structures (Zitellini et al., 2004), which in turn may control tectonic and seismic activity along the passive margin of southern Iberia and in the Gulf of Cadiz (e.g., Borges et al., 2001; Buforn et al., 2004; Stich et al., 2005).

Bathymetric and multi-channel seismic (MCS) data suggest that today's plate boundary might be defined by a set of WNW-ESE trending faults (called the South-West Iberia Margin or SWIM faults; Zitellini et al., 2009; Bartolome et al., 2012), running to the south of ~36°N. In this scenario the seismicity paralleling the Algarve margin might not be related to a newly developing plate boundary, but still might be associated with far-field stresses caused by convergence. In a scenario of active westward retreat of a narrow slab (e.g., Gutscher, 2004; Gutscher et al., 2012) hanging under the western Alboran Sea and the southern Betics (Gutscher et al., 2002; Garcia-Castellanos and Villaseñor, 2011) seismicity along the Algarve margin might be caused by a so called Subduction-Transform Edge Propagator, or STEP fault (Govers and Wortel, 2005).

Here, we report results from a large amphibious seismic network, including 24 offshore ocean-bottom-seismometers (OBS) installed in the Gulf of Cadiz to the north of 35°25′N and east of 9°30′W (Figs. 1 and 2). The network allows robust source estimates of offshore seismicity and hence may yield constraints on the active deformation of crust und upper mantle of the reactivated Mesozoic passive margin and seismicity in the Gulf of Cadiz. Our interpretations are nurtured by a new seismic refraction and wide-angle profile shot in the area (Sallares et al., 2011) that provides robust estimates on the nature of crust underlying the Gulf of Cadiz sedimentary prism and the southern Iberian continental margin. We will discuss micro-earthquake activity in the Gulf of Cadiz with respect to different tectonic settings, including other passive continental margins like the east coast of both North and South America. However, seismicity might be controlled by a newly developing plate boundary and we will hence discuss features with respect to a reorientation of the Eurasian-African plate boundary. Further, the seismicity pattern derived from the deployment will be discussed with respect to scenarios envisioning either active eastward dipping subduction (Gutscher et al., 2002) or active strike-slip faulting along the SWIM faults (e.g, Zitellini et al., 2009; Bartolome et al., 2012; Duarte et al., 2011).

2. Tectonic setting

In the Gulf of Cadiz to the west of the Gibraltar Arc, the plate boundary between Eurasia and Africa is rather poorly defined. Instead, WNW-ESE plate convergence of 4 mm/yr (DeMets et al., 2010) is accommodated over a wide and diffuse deformation zone (Sartori et al., 1994; Hayward et al., 1999), following a large scale strain partitioning scenario (Terrinha et al., 2009) and showing sig-

Please cite this article in press as: Grevemeyer, I., et al., Mantle earthquakes beneath the South Iberia continental margin and Gulf of Cadiz – constraints from an onshore-offshore seismological network. J. Geodyn. (2016), http://dx.doi.org/10.1016/j.jog.2016.06.001

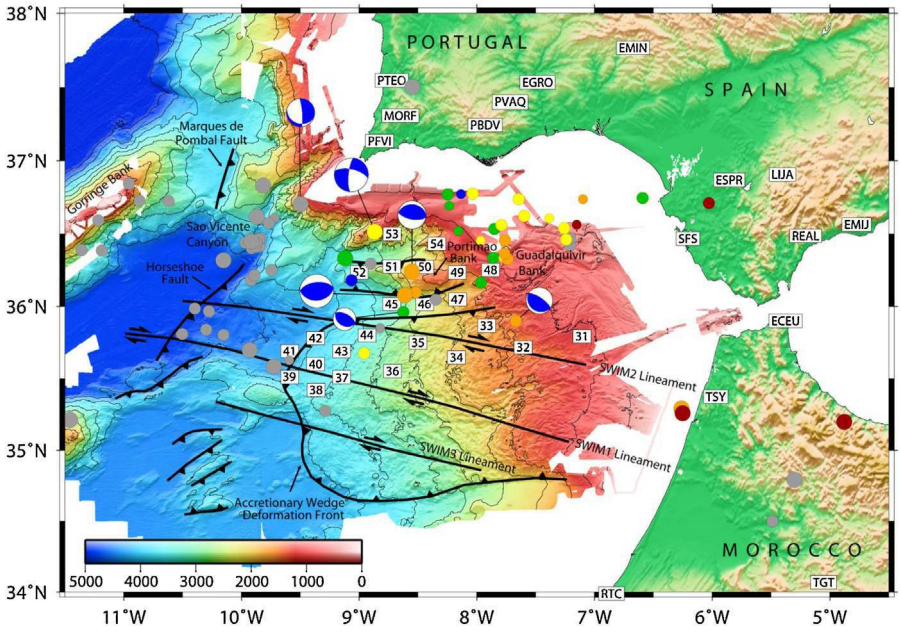

Fig. 2. Same as Fig. 1 but with bathymetry from the Gulf of Cadiz (Zitellini et al., 2009). Numbered squares are OBS and labelled squares are permanent seismic stations. Epicentres are coloured as in Fig. 1. In addition, focal mechanisms are shown.

nificant and widespread seismic activity (e.g., Stich et al., 2005; Buforn et al., 2004; Geissler et al., 2010). The region is also characterized by large earthquakes and tsunamis, such as the Great Lisbon earthquake of 1st of November 1755 with an estimated magnitude of Mw ~ 8.5–8.8 (Martinez-Solares et al., 1979; Johnston, 1996) and the 1969 Mw = 7.9 Horseshoe Abyssal Plain earthquake (Fukao, 1973).

Crustal domains in the central Gulf of Cadiz and at the Mesozoic continental margin of the Algarve, Southern Portugal/Iberia, can be defined by seismic refraction and wide-angle data (Sallares et al., 2011; Martinez-Loriente et al., 2014; Fig. 1), indicating 28–30 km thick continental crust near the coast line, a 60 km wide transition zone, where the crust thins to ~20 km, and a 7 km thick oceanic crust roughly 100–120 km off the coast (Fig. 1). The passive margin of southern Iberia and the Algarve formed during the Triassic breakup of Pangea (Heymann, 1989). However, oceanic crust flooring the Gulf of Cadiz postdates margin formation. Plate tectonic models (e.g., Schettino and Turco, 2011) suggests that between 185 Ma and ~145 Ma rifting between Africa and North America opened the Atlantic while farther east the Tethys ocean formed. Plate motion caused by the opening of the Atlantic was transferred to the Tethyan realm through a system of transform faults between Iberia and Morocco. Sallares et al. (2011) suggested that oceanic crustal formation occurred at the end of the opening of the Tethys at ~145 Ma, probably by oblique sinistral seafloor spreading which ceased when Newfoundland broke apart from Western Iberia at ~130 Ma.

Plate reconstructions suggest that convergence between Africa and Eurasia started between 120 to 83 Ma. From the Paleocene to Eocene, African and Eurasian convergence was mostly accommodated in the Alpine collision zone. Since about 35 Ma the western Mediterranean and the Gibraltar arc were affected by slab roll-back (Royden, 1993; Faccenna et al., 2001; Spakman and Wortel, 2004). Geodynamic modelling suggests that northward subduction occurred initially at the Balearic margin. At about 30 Ma, the trench and subduction rotated and westward slab roll-back occurred until Tortonian, suggesting that both subduction and slab roll back is stalled since 8 Ma (Chertova et al., 2014).

Today, the main morphotectonic feature of the Gulf of Cadiz is the up to 10 km thick sedimentary wedge (e.g., Thiebot and Gutscher, 2006). Its formation is still controversially discussed. The wedge itself is formed by large allochthonous masses with seismically chaotic reflections at the forefront of the Gibraltar Arc (e.g., Torelli et al., 1997; Maldonado et al., 1999; Gràcia et al., 2003; Rovere et al., 2004). The chaotic sedimentary melange shows signs of intense deformation and westward transport, attributed primarily to wrench faulting between Africa and Eurasia as well as gravity sliding (Torelli et al., 1997; Maldonado et al., 1999). However, the observed features can also be interpreted as accretionary complex of an eastward dipping subduction zone (e.g., Gutscher et al., 2002), supporting the tectonic framework introduced above. Miocene eastward subduction is supported by ample evidence, including arc-formation in the Alboran Sea (Duggen et al., 2003, 2004; Booth-Rea et al., 2007) and seismological imaging of a subducted slab and intermediate seismicity under the West Alboran Sea (Gutscher et al., 2002; Garcia-Castellanos and Villaseñor, 2011; Grevemeyer et al., 2015) and mantle flow (Díaz and Gallart, 2014). Gutscher et al. (2006) suggested that still active subduction may have caused the Great Lisbon earthquake of 1755. However, deformation pattern and geodynamic modelling may suggest that subduction is stalled since Tortonian (e.g., Iribarren et al., 2007; Chertova et al., 2014).

Simulations of seismic ground motions of the Great Lisbon earthquake favour a source to the west of Cape Sao Vicente (Grandin et al., 2007) in the Horseshoe abyssal plain or at the Gorringe Bank (Johnston, 1996). Baptista et al. (1998, 2011) analyzed all evidences on the 1755 tsunami and concluded that wave amplitudes and tsunami travel times estimated from historical records are best explained by a tectonic source in the SW of Iberia closer to the coast, excluding the Gorringe Bank and Gulf of Cadiz accretionary wedge as possible sources.

High-resolution bathymetric mapping of the Gulf of Cadiz and the adjacent Horseshoe abyssal plain indicated a set of almost linear and sub parallel dextral strike–slip faults, the South-West-Iberia-Margin or SWIM faults (Zitellini et al., 2009). The features form a narrow band of deformation over a length of 600 km and roughly coincide with a small circle centred on the pole of rotation of Africa with respect to Eurasia. Zitellini et al. (2009) suggested that the

Please cite this article in press as: Grevemeyer, I., et al., Mantle earthquakes beneath the South Iberia continental margin and Gulf of Cadiz – constraints from an onshore-offshore seismological network. J. Geodyn. (2016), http://dx.doi.org/10.1016/j.jog.2016.06.001

SWIM faults may connect to the Eurasian-African plate boundary farther west and east and hence may indicate a newly developing segment of the plate boundary between Africa and Eurasia. Seismic reflection imaging revealed that the SWIM lineaments cut down to at least 10 km (Bartolome et al., 2012). Terrinha et al. (2009) and Duarte et al. (2011) suggest that the lineaments represent the reactivation of Mesocoic faults that root in the underlying basement. Seismically neither the SWIM lineaments nor the proposed Gulf of Cadiz subduction thrust showed any prominent seismic activity detectable utilizing onshore seismic monitoring (e.g., Buforn et al., 2004; Stich et al., 2005).

3. Seismological data and methodology

3.1. Data

In the Gulf of Cadiz 24 ocean-bottom-seismometers (OBS) were deployed along the southern Iberian continental margin and on the Gulf of Cadiz accretionary wedge (Figs. 1 and 2). The deployment was part of the European Science Foundation (ESF) coordinated programme TOPO-Europe. Marine deployments of our exercise, called TOPO-MED, were supplemented by the permanent seismic networks operated in Portugal, Spain, and Morocco (Fig. 2).

The offshore network was operated between 20th of January 2010 and 21st of July 2010. The network consisted of 24 OBS, including 5 wide-band OBS operating a three-component Guralp CMG-40T (60 s) seismometer and a HighTech HTI-04-PCA/ULF hydrophone from the German DEPAS pool. In addition, 19 GEOMAR-OBS, equipped with a hydrophone and 3-compenent short-period seismometers with a natural frequency of 4.5 Hz, were operated. Seismic events were detected automatically in the continuous OBS record using a short-term-average versus a long-term-average (STA/LTA) triggering approach. We used a STA window of 0.5 s and a LTA window of 60 s. The trigger ratio was 4.0 and the de-trigger ratio was 2.5. The trigger parameters were applied to unfiltered vertical component data. We consider a trigger to be an earthquake when it was detected on six or more OBS stations. Visual inspection of the data suggested that we obtained generally less than ~5% false triggers and lose only those events that were recorded on a few stations and characterized by a poor signal noise ratio, while all major events were included. Surprisingly, only a reasonable small number of <100 events was detected and the detected events generally coincide with earthquakes reported in the national catalogue of Portugal. We believe that the up to 12 km thick sedimentary prism (Thiebot and Gutscher, 2006) caused a very high attenuation. Further, the area is inherently affected by strong noise caused by ship's traffic through the Strait of Gibraltar (Fig. 3), requiring earthquakes with magnitudes of larger ~2 to be detected within the offshore network. This interpretation is supported by the fact that the smallest magnitude of local earthquakes was roughly one order of magnitude larger than for an OBS network operated in the Alboran Sea to the east of Gibraltar (Grevemeyer et al., 2015). The OBS farthest to the east, sitting on the thickest portion of the prism, provided the smallest number of readings of local earthquakes, supporting the interpretation that thicker sediments provide higher attenuation. However, the OBS network detected all offshore events occurring within the network that were reported in either the catalogue of the Instituto Português do Mar e da Atmosfera (IPMA, Portugal) or the Spanish Instituto Geografico Nacional (IGN, Spain). In addition, four and six additional events were detected with respect to the IPMA and IGN catalogue, respectively.

All events were registered into a SEISAN database (Havskov and Ottemöller, 2000), using a 3 min long time window from the continuous OBS records and data from the Portuguese network, starting 20 s prior to trigger time. P-wave and S-wave arrival times were hand-picked. In total, we obtained 86 local earthquakes from the Gulf of Cadiz and adjacent domains. The reading weighting scheme ranges from factor 0, corresponding to the lowest uncertainty (±0.05 s), to factor 4 (>0.3 s) for doubtful readings that were not used. The total average P wave reading error is estimated at ±0.12 s. Latter, additional onset times from land stations in Spain and Morocco were added to the database (http://www.isc.ac.uk/iscbulletin/search/bulletin).

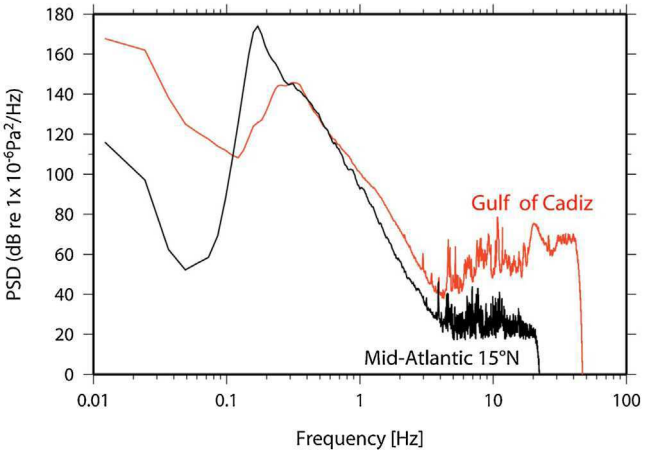

Fig. 3. Power Spectral Density (PSD) of OBS36 (red line) in the Gulf of Cadiz and an OBS deployed at the Mid-Atlantic Ridge (MAR) near 15° N (black line). Note the much higher noise level observed in the Gulf of Cadiz. It might be reasonable to suggest that strong noise from ship's traffic affected seismic recordings, resulting in a much lower detection of small earthquakes with respect to quieter settings. OBS from the MAR is from Grevemeyer et al. (2013). (For interpretation of the references to colour in this figure legend, the reader is referred to the web version of this article.)

3.2. Location procedure and velocity models

To constrain epicentres and focal depth we surveyed four different 1D velocity models and used two different algorithms. Earthquakes were located (1) with the program HYPOCENTER, which employs an iterative solution to the nonlinear localization problem (Lienert et al., 1986; Lienert and Havskov, 1995) and (2) using the non-linear probabilistic location procedure NonLinLoc of Lomax et al. (2000). Unfortunately, the number of events within the network was too small to derived robust station corrections. We therefore used for both location procedures station elevations to constrain differences in topography between onshore and offshore domains.

Locating earthquakes in the Gulf of Cadiz using a 1-D reference model is a difficult task since crustal thickness for onshore stations will be in the order of 30 km while OBS on the prism will sit on thin oceanic crust covered by 3–8 km of sediments. We therefore utilized different velocity models and location algorithms to provide an effective way to explore the uncertainties associated with each earthquake and the bias caused by different velocity models. For event location we used (i) the global AK135 model (Kennett et al., 1995), (ii) the model that Geissler et al. (2010) used to locate local earthquakes to the SW of Portugal (Fig. 4a, red line; called G-16); (iii) the velocity structure to the north of the Portimão Bank (Fig. 4a, blue line; called OBS-Portimão) derived from 2-D seismic refraction data (Sallares et al., 2011), representing extended continental crust, and (iv) the velocity structure of the distal imbricated wedge derived from 2-D seismic refraction data (Sallares et al., 2011), representing Jurassic oceanic crust covered by 5 km of sediment (Fig. 4a, green line; called OBS-prism).

In the individual location procedures, most earthquakes produced formal errors of ±0.5–2 km for the epicentre and ±2–5 km

Please cite this article in press as: Grevemeyer, I., et al., Mantle earthquakes beneath the South Iberia continental margin and Gulf of Cadiz – constraints from an onshore-offshore seismological network. J. Geodyn. (2016), http://dx.doi.org/10.1016/j.jog.2016.06.001

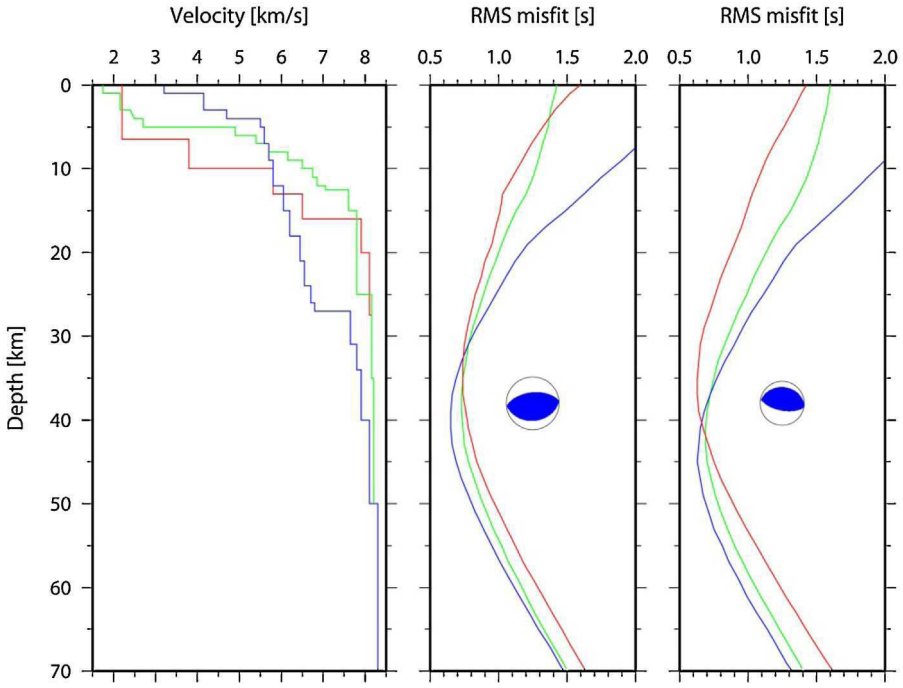

Fig. 4. (a) Seismic velocity-depth functions used to yield location and focal depth utilizing HYPOCENTER (Lienert et al., 1986; Lienert and Havskov, 1995). Red: model G-16 of Geissler et al. (2010), Green: model OBS-prism, and Blue: model OBS-Portimão (see text for discussion). (b) rms misfit of the Mw = 3.6 5th March 2010 thrust earthquake, Portimão Bank; (c) rms misfit of the Mw = 2.9 18th May 2010 thrust earthquake, Portimão Bank. (For interpretation of the references to colour in this figure legend and the text, the reader is referred to the web version of this article.)

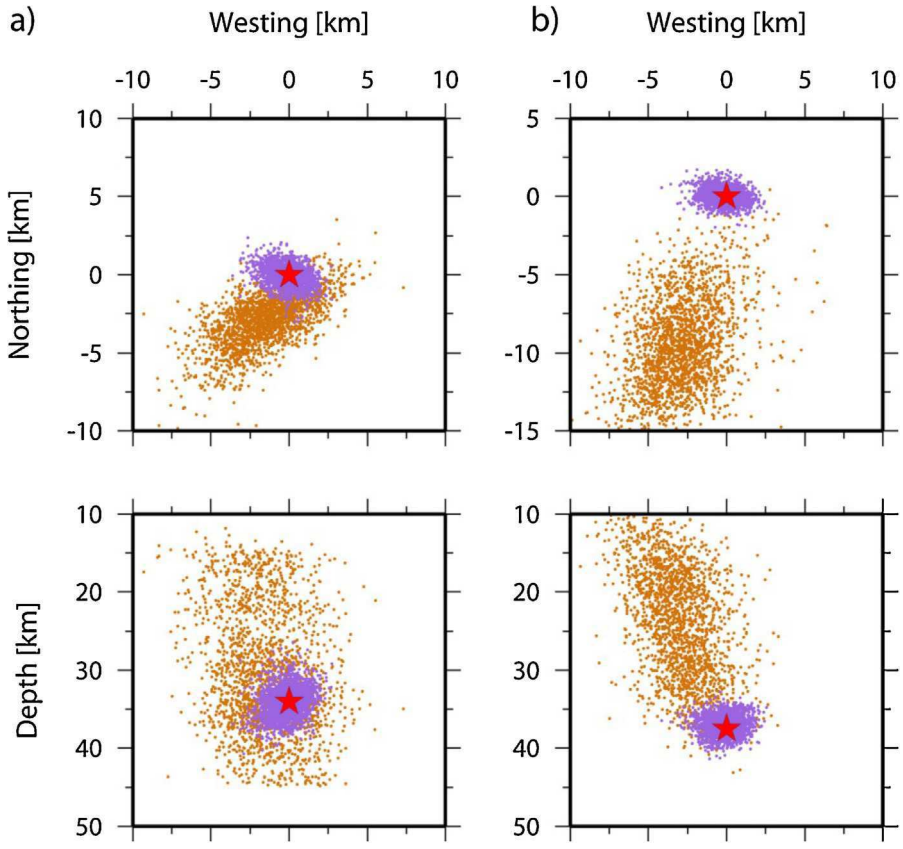

Fig. 5. Plot of the Probability-Density-Function (PDF) of two thrust earthquakes in the vicinity of the Portimão Bank located with the velocity model G-16 using NonLinLoc. (a) Mw = 3.6 mantle earthquake of 5th March 2010, (b) Mw = 2.9 mantle earthquake of 18th May 2010. Light blue: probability density function (PDF) using all stations; orange: PDF locating events without offshore OBS stations.

Please cite this article in press as: Grevemeyer, I., et al., Mantle earthquakes beneath the South Iberia continental margin and Gulf of Cadiz – constraints from an onshore-offshore seismological network. J. Geodyn. (2016), http://dx.doi.org/10.1016/j.jog.2016.06.001

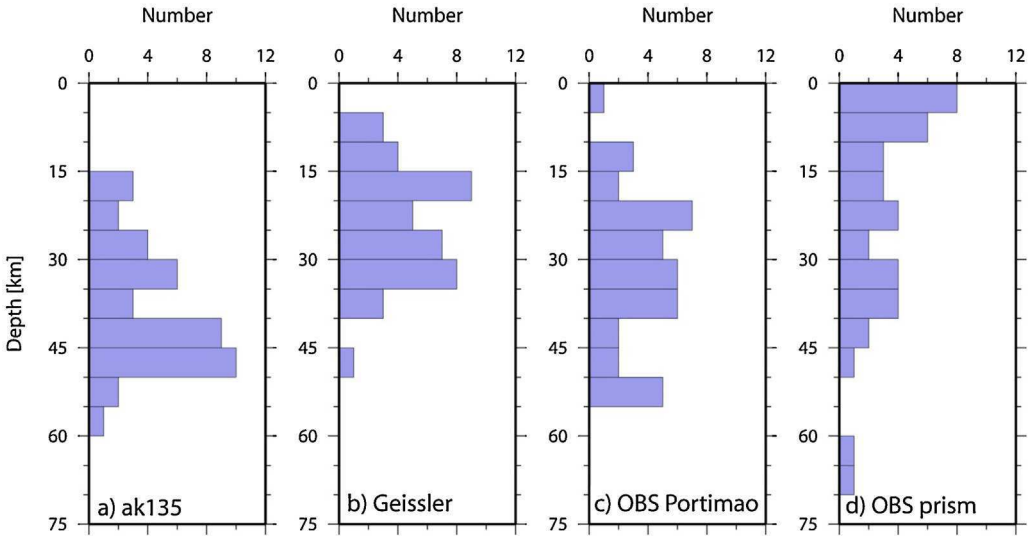

Fig. 6. Histograms of depth distribution of all located events as a function of the velocity depth model used for relocations: (a) Global model ak135 (Kennett et al., 1995), (b) Model G-16 of Geissler et al. (2010), (c) Model OBS-Portimão, representing seismic structure of the Algarve coast (Sallares et al., 2011), (d) OBS-prism, representing seismic structure of the central Gulf of Cadiz (Sallares et al., 2011).

Table 1
Focal mechanism derived from first motion polarities.

Date	Time	Latitude	Longitude	Depth (km)	Magnitude	strike/dip/rake
2010/01/26	05:8	35.961914	−8.624268	17.0	2.4	118/30/90
2010/02/27	08:13	6.514486	−8.865356	27.5	3.6	186/76/-27
2010/03/05	17:10	36.079102	−8.609619	34.0	3.6	85/34//90
2010/04/08	14:51	35.899251	−7.666626	39.9	2.8	124/18/90
2010/05/02	14:08	36.704102	−9.498291	17.4	3.0	355/81/-70
2010/05/18	10:52	36.239827	−8.550110	37.4	3.0	275/27/85

in focal depth. However, deeper earthquakes (>30 km) may have larger epicentral errors of ±2–4 km and ±3–8 km in focal depth (Fig. 4). Overall, seismic events with good azimuthal coverage provided very similar depth estimates, like two very well located thrust events at the Portimão Bank. The events occurred clearly within the upper mantle at 30–45 km (Figs. 4 and 5). Depending on the velocity structure used for event location, event depth may vary by ~10 km and epicentral locations may vary in the order of 2–20 km. However, in a map view, changes of epicentres were generally minor. With respect to depth, changes are much more significant. The AK135 model provided the most compact depth distribution of all velocity models (Fig. 6a) with basically all earthquakes occurring in the upper mantle. However, both crustal thickness and mantle velocity poorly match constraints from seismic data in the area. In fact AK135 includes a much thicker crust and faster mantle velocity than observed off SW Iberia (e.g., Sallares et al., 2011). The model G-16 of Geissler et al. (2010) approximates the onshore and offshore domains by using a crustal thickness of 16 km, which is thinner than the crust of Iberia but thicker than the Jurassic oceanic crust sampled offshore (Sallares et al., 2011). In general, depth distribution of earthquakes is rather compact, ranging from ~5 km to ~45 km (Fig. 6b). Thus, earthquakes occur both in the crust and upper mantle. The model OBS-Portimão has a crustal thickness of 28 km and a continental crust-type velocity structure. Depth distribution of earthquakes is similar to the model G-16, but showed a wider range in depth (Fig. 6c). The model OBS-prism has approximately 5 km of sediments covering 7 km of oceanic crust. The depth distribution is scattered over a much larger depth range (Fig. 6d). With respect to the average rms fit all four models provided in the NonLinLoc location procedure rather similar fits. Due to its compactness of depth distribution, we prefer the model G-16. The fact that all models provide evidence for earthquakes rupturing at 30–50 km depth clearly supports the fact that a large number of earthquakes occurred within the mantle of the continental domain as defined by Martinez-Loriente et al. (2014, Fig. 1).

The seismic velocity models constrained only the P-wave velocity structure. To constrain Vp/Vs ratios, we used Wadati diagrams (S-P time versus P time) and calculated an average Vp/Vs ratio (Havskov and Ottemöller, 2000). To constrain the Vp/Vs ratio we used 81 earthquakes with at least eight P-wave and S-wave pairs, a rms event location misfit of 0.3 or better, and a correlation coefficient of the fit of S-P time versus P time of >0.9. The resulting Vp/Vs ratio was 1.68.

To explore the benefit of having an amphibious network, we removed the OBS arrival times from the catalogue and re-located the events. For most offshore events the uncertainty increased and errors are doubled or even tripled. As an example Fig. 5 shows the two thrust events of 5 and 18 of May of 2010. Removing the offshore stations, epicentres are shifted 5–10 km to the southwest and the probability-density-function (PDF) is smeared in SW-NE direction, indicating uncertainties of ±5–8 km. In depth, the PDF for the first event is not well defined (non Gaussian distribution) and uncertainties are in the order of ±10–15 km. For the second event, the preferred depth estimate would be at 20 km rather than at 38 km. Like for the previous event, uncertainties are in the order ±10–15 km. Thus, offshore seismometers clearly improve the quality of event locations. Therefore, constraints from onshore networks alone might be profoundly biased. Supplementary Fig. S1 shows the mis-location between regional catalogues and our estimates as a function of offset from the margin.

Please cite this article in press as: Grevemeyer, I., et al., Mantle earthquakes beneath the South Iberia continental margin and Gulf of Cadiz – constraints from an onshore-offshore seismological network. J. Geodyn. (2016), http://dx.doi.org/10.1016/j.jog.2016.06.001

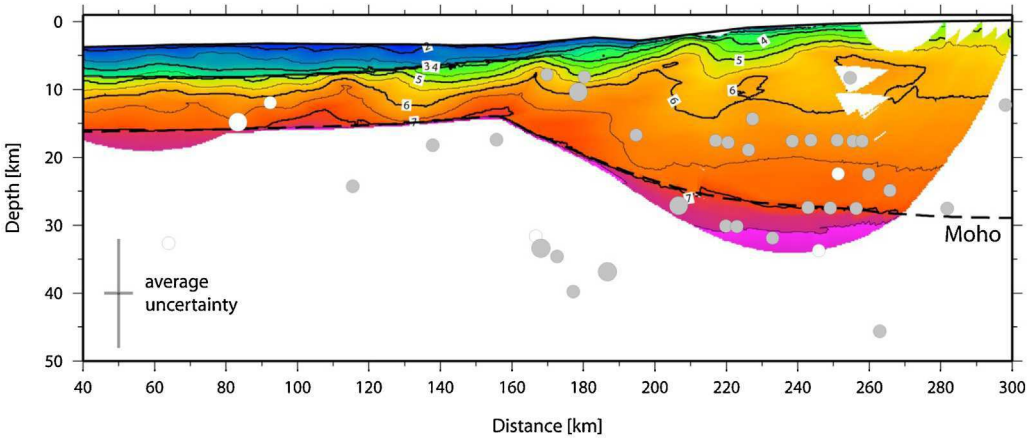

Fig. 7. Colour-coded seismic velocity model (Sallares et al., 2011) of the South Algarve margin and Gulf of Cadiz (see Fig. 1 for location). Grey dots are earthquake hypocentres projected onto the profile, white dots have a gap >200°. Earthquakes were located with LinLinLoc using the velocity model G-16.

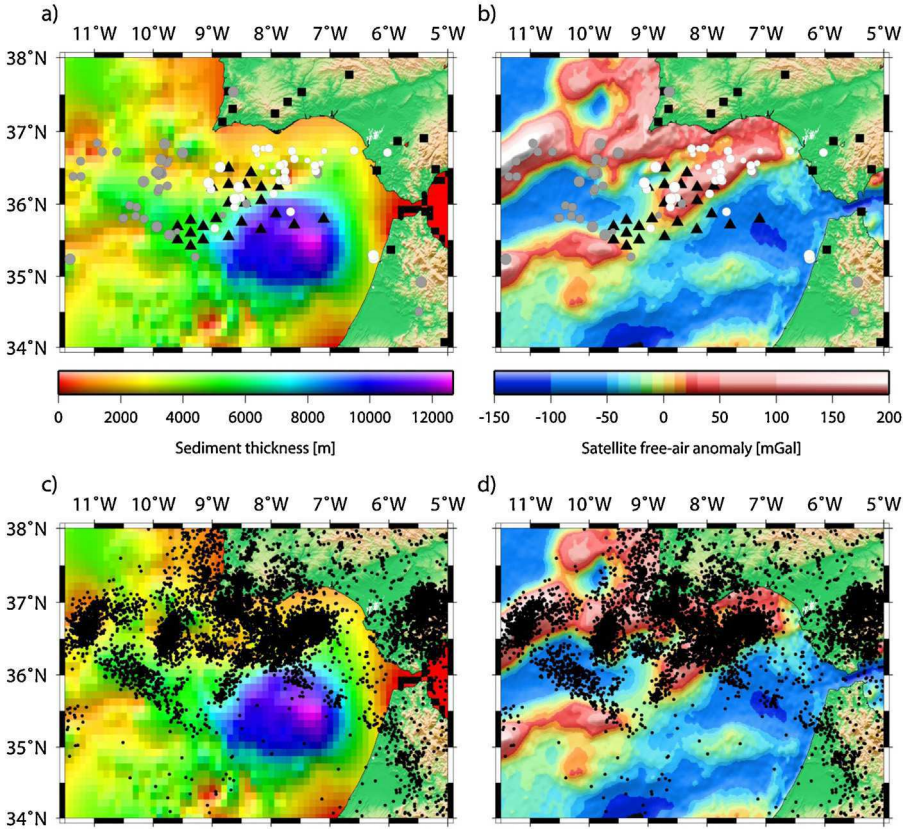

Fig. 8. Relationship between sediment thickness, gravity field anomaly and seismicity. (a, b) show seismicity recorded during our deployment; black dots have a gap <200°, grey dot have a gap >200°, (c, d) is seismicity (2000–2015) from the IPMA catalogue. (a, c) Sediment thickness (Thiebot and Gutscher, 2006) and (b, d) gravity field (Sandwell et al., 2014) over the Gulf of Cadiz.

3.3. Magnitudes

Moment magnitudes were estimated for the CMG-40T sensors and onshore stations in Portugal using the method of Ottemöller and Havskov (2003). The two largest earthquakes recorded within the offshore network were a Mw = 3.6 thrust faulting earthquake in the vicinity of the Portimão Bank near OBS45 and a Mw = 3.6 strike slip earthquake to the northwest of the Portimão Bank just west of OBS53. The largest earthquake that occurred during the deployment was a magnitude 4.3 event near the Moroccan coast about 180 km west of the city of Fez (~30 km to the south west of seismic stations TSY), hitting on 22 April 2010. Most events, however, had magnitudes of Mw = 2.2 to 2.9. The smallest earthquakes had magnitudes of ~1.8.

3.4. Focal mechanisms

In local marine earthquake studies, double-couple focal mechanisms are generally derived from first motion. Unfortunately, all recorded events were too small to allow regional moment tensor inversion using permanent networks. Thus, we derived fault plane solutions using HASH and FOCMEC algorithms (Hardebeck

Please cite this article in press as: Grevemeyer, I., et al., Mantle earthquakes beneath the South Iberia continental margin and Gulf of Cadiz – constraints from an onshore-offshore seismological network. J. Geodyn. (2016), http://dx.doi.org/10.1016/j.jog.2016.06.001

and Shearer, 2002; Snoke et al., 1984) and did not allow any polarity errors (Supplementary Fig. S2). Here, we report only 6 mechanisms where both approaches provided similar solutions (Table 1).

4. Results

4.1. Distribution of seismicity

Seismicity in the Gulf of Cadiz and to the southwest of Portugal is not evenly distributed in space but highly clustered. During the deployment about half of the observed seismicity occurred to the west of the network, including areas of major activity at the Gorringe Bank, at the Sao Vicente Canyon to the south of the Cape Sao Vicente, and across the Horseshoe fault.

The area of largest activity well covered by the network occurred along the continental margin of southern Iberia to the north of 36°N, including a number of Mw > 3 earthquakes at or in the vicinity of the Portimão Bank offshore the Algarve (Fig. 2). With a depth range of 15 to ~40 km, the majority of hypocentres occurred both within the lower crust and upper mantle. The two strongest and best located events occurred at >30 km depth (independent of velocity model) and hence within the uppermost mantle (Figs. 4 and 5). Fig. 7 shows earthquakes to the east of 9°30′W (located with model G-16) projected on to the seismic refraction and wide-angle profile of Sallares et al. (2011). Interestingly, all earthquakes occurred below the 5-km/s-contour line, suggesting that earthquakes occur within the basement and preferentially in the lower continental crust and uppermost mantle. Due to structural heterogeneities in the area and the fact that a 1-D reference model was used to locate the events, we carried out the same exercise using the other velocity models (Supplementary Fig. 3). Overall, the features are very similar, supporting that the majority of earthquakes ruptured either in the lower crust or upper mantle. However, as indicated by the histograms in Fig. 6, the portion of earthquakes at mantle depth increases using either a thicker crust or global model.

On 22 of April 2010 the largest recorded event occurred roughly 100 km to the east of the marine network at the Moroccan coast line near the seismic station TSY. The earthquake with a magnitude of m_b = 4.5 was recorded on nearly all stations of the network. The large spacing of seismic stations near the epicentre resulted in large uncertainties of focal depth. However, like the International Seismological Centre (ISC) (http://www.isc.ac.uk/iscbulletin/search/bulletin) we located the event within the mantle at >40 km.

An interesting feature is the almost lack of seismicity to the south of 36°N where sediment is thickest and the eastward dipping subduction thrust has been imaged (Gutscher et al., 2002). Thus, basically all earthquakes occurred to the north of the 5–12 km thick accretionary prism (Fig. 8a). Furthermore, in the same area major strike slip faults (Zitellini et al., 2009; Bartolome et al., 2012) have been deduced from bathymetric and seismic data (labelled SWIM1 and SWIM2 in Figs. 1 and 2). However, over the six month of network operation little evidence for seismogenic slip along the faults was observed. Just to the west of OBS39 and OBS41, some seismicity might be associated with the SWIM1 fault. Trade-offs between epicentral location and focal depth cause too large uncertainties to draw any robust conclusions regarding these particular events.

Most earthquakes along the margin might be related to the structure of the margin. Gràcia et al. (2003) highlighted a prominent SW-NE striking gravity anomaly – the Guadalquivir-Portimao lineament – terminating at the Portimão Bank. Most earthquakes at the margin seem to occur in the vicinity of this anomaly (Fig. 8b), suggesting that the structure of the margin controls the distribution of seismicity. Plotting data obtained from regional catalogues, like the IPMA or IGN seismic bulletins, provide basically the same pattern (Fig. 8c and d).

4.2. Stress pattern

Focal mechanisms were derived for six earthquakes. In the vicinity of the Portimão Bank thrusting dominates (Fig. 2). However, the same stress pattern may be compatible with two sets of conjugate faults, both accommodating general N-S trending shortening. To the northwest of the Portimão Bank two strike-slip events were deduced (Fig. 2). Overall, focal mechanisms and hence stress pattern mimic features observed in previous studies (e.g., Borges et al., 2001; Stich et al., 2005).

5. Discussion

5.1. Seismicity to the southwest of Portugal

The seismicity reported routinely by the Portuguese IPMA or the Spanish IGN shows clustered seismicity at Gorringe Bank and at the Sao Vicente Canyon, indicating different active fault systems (e.g., Geissler et al., 2010). All areas showed seismic activity during the 6 month of network operation. Unfortunately, events recorded at both the Gorringe Bank and at the Horseshoe Fault where well outside of the network and hence hypocentral parameters have too large uncertainties. Trade-offs between focal depth and epicentral distance prevent robust estimates of either focal depth or stress pattern. However, due to its proximity to seismic stations in Portugal and the marine network, seismicity at the Sao Vicente Canyon can be studied in much more detail. Over the deployment period we recorded more than 20 earthquakes that clustered near the southwestern terminus of the canyon, making it one of the seismically most active sites. Focal depth of 20–40 km indicates that seismicity is generally located within the mantle. Geissler et al. (2010) located earthquakes in the vicinity of the Sao Vicente fault at a greater depth of 40–55 km. Focal mechanism and stress tensor inversion of Geissler et al. (2010) yielded an obliquely oriented compressive regime. The single focal mechanisms obtained during our deployment supports the stress pattern observed previously.

5.2. Seismicity of the southern Iberia continental margin

The northern Gulf of Cadiz has been divided into an inner part (off the city of Cadiz), a middle part with the Guadalquivir Bank, and an outer part with the Portimão Bank (Gràcia et al., 2003). The outer part is characterized by a rough topography and is dominated by large submarine canyons that are deeply incised in platformal areas. To the south, both the Portimão Bank and Guadalquivir Bank show thrust faults (Gràcia et al., 2003). During the marine deployment, the middle and outer part of the Gulf of Cadiz were seismically very active. Three thrust faulting events occurred at the Portimão Bank and focal depth of the thrust events clearly support that they rupture within the mantle (Figs. 4, 5 and 7). Based on bathymetric and seismic data, it has been suggested that the Bank is bounded at both flanks by thrust faults (Gràcia et al., 2003; Terrinha et al., 2009). Sallares et al. (2011) found southward dipping seismic velocity anomalies that were interpreted as crustal scale normal faults formed during the formation of the passive margin in the Mesozoic. It might be reasonable to suggest that these faults cut into the mantle and are reactivated in response to the convergence between Africa and Eurasia as thrusts.

For the US east coast stress pattern indicated roughly margin parallel compression (Zoback, 1992), which is similar to stresses caused by modelled intraplate stresses due to plate-wide forces. Earthquakes along the eastern continental margin of the US are generally believed to reflect reactivation of ancient faults (Wolin et al., 2012). Along the Iberian margin, Zitellini et al. (2004) suggested that seismic activity occurs along reactivated Mesozoic rift

Please cite this article in press as: Grevemeyer, I., et al., Mantle earthquakes beneath the South Iberia continental margin and Gulf of Cadiz – constraints from an onshore-offshore seismological network. J. Geodyn. (2016), http://dx.doi.org/10.1016/j.jog.2016.06.001

structures. Thus, earthquakes along the south Iberian continental margin mimic stresses and features envisioned for the US east coast. The increased seismicity rate for the Iberian margin, however, may reflect its proximity to the African/Eurasian plate boundary.

The main difference, however, is the much larger focal depth of most earthquakes reported in our study. Typical earthquakes along passive continental margins, like the 23rd August 2011 Mineral, Virginia event (Wolin et al., 2012) or the 23rd April 2008 Sao Vicente, Brazil event (Assumpcao et al., 2011), occurred within the crust. In contrast, earthquakes along the southern Iberia margin occurred predominately within the mantle. We hypothesize that this feature is caused by the proximity to the plate boundary and by an elastic rheology of the continent-ocean transition zone (see discussion below).

Overall, our new depth estimates support previous results obtained from global catalogues and regional waveform modelling (Stich et al., 2005), showing seismicity both in the crust and upper mantle. However, events as deep as 60 km, that were previously reported (Stich et al., 2005), have not been observed during our deployment. The stress pattern derived from the amphibious network support features obtained previously (e.g., Borges et al., 2001; Stich et al., 2005), suggesting that the Southern Iberian margin is under horizontal compression. However, there is not a dominant faulting regime, hence reverse, strike-slip, and normal faulting mechanisms coexist in the Gulf of Cadiz and SW Iberia (e.g., Borges et al., 2001; Buforn et al., 2004; Stich et al., 2005; Geissler et al., 2010). Terrinha et al. (2009) suggested that such pattern might be related to convergence and strain partitioning by means of dextral wrenching on WNW-ESE trending steep faults and thrusting on the NE-SW trending fault in the Gulf of Cadiz and Horseshoe Abyssal Plain. Approaching the base of the continental slope, NNE-SSW to N-S westerly dipping thrusts accommodate shortening in an area where wrenching has not been observed.

5.3. Rheology of crust and mantle

In continental lithosphere it has been observed that during rifting the upper crust is deformed by faulting while the lower crust generally supports ductile deformation (e.g., Odedra et al., 2001; Moeller et al., 2013). The transition from brittle to ductile deformation depends on the temperature structure and the rock type. Earthquakes are generally restricted to domains of brittle deformation. The fact that earthquakes in the Gulf of Cadiz occur within the lower crust and the upper mantle supports elastic rheology for both domains. Thus, both the lower crust and upper mantle are strong. This interpretation is supported by very low crustal heat flow of <50 mW/m^2 (Grevemeyer et al., 2009), resulting in cooler geotherms than generally found in rift basins (e.g., McKenzie, 1978) and hence favouring elastic rheology.

Brittle deformation in the oceanic mantle is a common features and generally restricted to temperatures <600 °C (e.g., McKenzie et al., 2005; Craig et al., 2014). Thus, only near mid-ocean ridges is seismicity confined to crustal levels (e.g., Grevemeyer et al., 2013). Crustal deformation of mature oceanic lithosphere may cause brittle deformation to extend until depths of several tens of kilometres into the mantle (Lefeldt et al., 2009; Craig et al., 2014). In our study the majority of earthquakes rupturing within the mantle occurred landward of the domain of Jurassic oceanic crust, either in the 60-km-wide continent-ocean transition zone or in the continental domain near the coast line as defined by seismic data (Sallares et al., 2011; Martinez-Loriente et al., 2014; Fig. 1).

Earthquakes in the continental domain of the South Iberia margin are focused in the lower crust and uppermost mantle. Neves and Neves (2009) suggested that flexural loading caused by density contrasts between adjacent oceanic and continental crust may cause flexure and hence deformation. In their model compressive stresses and deformation concentrates below Moho. However, some of the best located earthquakes occur in the continent-ocean transitions zone (line-km 160–190 in Fig. 5) at ~40 km depth where the flexural model of Neves and Neves (2009) predicts tensile stresses. In contrast, observed focal mechanisms support thrusting and hence compression.

Seismicity and brittle deformation in both oceanic and continental mantle off southern Iberia seems to be a common feature and have been revealed using a wide range of techniques, including regional waveform modelling (Stich et al., 2005) and local monitoring of seismicity using our amphibious network. Elsewhere in continental lithosphere earthquakes occurring at mantle depth are known to be rare. It was therefore inferred that the continental mantle is rather weak and probably related to higher water content (Maggi et al., 2000). Mantle earthquakes, however, were detected beneath the East African Rift at 53–60 km (Lindenfeld and Rümpker, 2011), but might be associated to deep-seated magmatic processes. Recently, Alinaghi and Krüger (2014) confirmed the occurrence of some earthquakes in continental mantle below the Tien Shan, Central Asia, supporting a strong lower crust and upper mantle.

5.4. Seismic quiescence of the Gulf of Cadiz sedimentary prism and SWIM faults

A large number of ocean-bottom-seismometers was placed on the accretionary prism of the Gulf of Cadiz (Fig. 2; Gutscher et al., 2002; Thiebot and Gutscher, 2006). Seismically the area remained inactive, both during the time of our deployment and during the much longer time scale of seismicity recorded by national networks in Portugal and Spain (Fig. 8). Seven OBS (no. 37–43) where located on top of the main SWIM fault running through the centre of the Gulf (labelled SWIM1 in Figs. 1 and 2). These stations were deployed as a dense array with a station separation of <10 km. Nevertheless, they did not reveal any earthquakes within the network that cluster along the fault. However, some events farther west but outside of the network might be associated with the SWIM1 fault. One interpretation would be that both the subduction thrust and the SWIM faults are largely inactive. However, large strike-slip faults might be segmented, like the San Andreas Fault in California (e.g., Bennett et al., 2004). Consequently, the segment of the SWIM fault covered by the network might be either inactive, creeping or being lock, while farther west, where a number of earthquakes cluster in the vicinity of the fault, earthquakes may indicate fault activity.

The idea of active subduction in the Gulf of Cadiz is still under debate. Plate tectonic reconstructions of the Western Mediterranean suggests that the Oligocene/Miocene evolution was driven by subduction and slab roll-back (e.g., Faccenna et al., 2001). A remaining slab of eastward subduction has been imaged under the western Alboran Sea (e.g., Garcia-Castellanos and Villaseñor, 2011; Bezada et al., 2013) and geochemical studies of magmatic rocks from the Alboran Sea suggest that subduction related volcanism occurred until Miocene times (Duggen et al., 2003, 2004). The existence of a Miocene magmatic arc in the Alboran Sea has been supported by seismic reflection imaging (Booth-Rea et al., 2007). However, arc magmatism in the Alboran Sea stopped in the Miocene (Duggen et al., 2003, 2004) and the stratigraphic analysis of seismic data from the Gulf of Cadiz may support the interpretation that accretion has stopped several million years ago (Iribarren et al., 2007). This conclusion is sustained by simulating the tectonic reconstruction of the western Mediterranean using 3-D numerical modelling, indicating that subduction roll-back is stalled since Tortonian (~8 Ma) (Chertova et al., 2014). In terms of these results it seems reasonable to suggest that subduction has largely ceased and hence the former megathrust might be seismically inactive. However, a lack of seismicity itself cannot be used to argue that subduction ceased. For example, a number of subduction megath-

Please cite this article in press as: Grevemeyer, I., et al., Mantle earthquakes beneath the South Iberia continental margin and Gulf of Cadiz – constraints from an onshore-offshore seismological network. J. Geodyn. (2016), http://dx.doi.org/10.1016/j.jog.2016.06.001

rusts remain seismically inactive, like the Cascadia subduction zone offshore of Oregon and British Columbia. Tsunami deposit found in the trench of Cascadia and even thousands of kilometres away in Japan suggest that Cascadia suffers from a major magnitude M ~ 9 earthquake every 300–800 years (Satake et al., 1996, 2003). Thus, depending on convergence rate, such settings may support catastrophic earthquakes with large recurrence intervals of several hundreds to thousands of years. Consequently, the observed quiescence to the south of 36°N cannot be used to rule out a future megathrust earthquake.

Zitellini et al. (2009) presented the SWIM faults as being a developing plate boundary. The fact that the plate boundary is yet not fully developed has been indicated by current stress indicators, like GPS velocities and earthquake rates (Cunha et al., 2012). However, an alternative interpretation might be that the SWIM faults comprise several smaller fault segments rather than acting like a single 600 km long faults zone. The fact that some segments of the SWIM faults are actively slipping is supported by seismic reflection imaging (Bartolome et al., 2012) and probably by a number of not so well located earthquakes to the west of the network. In addition, Geissler et al. (2010) reported a single strike-slip mechanism in the vicinity of the SWIM1 fault. Thus, the observed seismicity pattern and the lack of seismicity along major parts of the fault could also be interpreted as being related to a segmented fault and the seismic cycle. Today, we know that earthquakes are the result of a stick–slip frictional instability (Brace and Byerlee, 1966), where "the earthquake is the 'slip' and the 'stick' is the interseismic period of elastic strain accumulation" (Scholtz, 1998). Within the cycle, the interseismic stain accumulation might be aseismic. Such features were observed along the most prominent fault in the Gulf of Almeria – the 100 km long northeast-southwest trending left-lateral strike-slip Carboneras Fault (Gràcia et al., 2006). The fault remained seismically inactive during a 5 months long seismic monitoring campaign (Grevemeyer et al., 2015). However, the Carboneras Fault is associated with a number of historic earthquakes, affecting the city of Almeria in southern Spain. Furthermore, geomorphic features found along the strike-slip fault clearly indicated active motion (Gràcia et al., 2006). In terms of the evidence found at the Carboneras Fault, we suggest that the SWIM faults mimic the Carboneras Fault. Thus, they might be either creeping or accumulating strain being released in future seismic activity.

5.5. A passive-aggressive margin or an active plate boundary?

The features discussed above clearly indicate that seismicity along the southern Iberia margin resembles activity found along the passive continental margins of the eastern US (Zoback, 1992; Wolin et al., 2012) and Brazil (Assumpcao et al., 2011); the main differences being that earthquakes tend to occur at crustal levels along the American passive margins, while most events in the Gulf of Cadiz rupture at mantle depth. Moreover, the rate of seismicity off Iberia is much higher.

An active plate boundary or STEP fault (Govers and Wortel, 2005) running from the Betics into the Gulf of Cadiz would favour a rather continuous band of seismicity. However, it is observed that seismicity and deformation is spread over a wider area rather than representing a discrete fault (e.g., Sartori et al., 1994; Hayward et al., 1999), supporting a rather diffusive plate boundary. Alternatively, Terrinha et al. (2009) advocated a regional (large scale) strain partitioning scenario, suggesting that the WNW-ESE convergence between both plates is simultaneously accommodated by (i) right-lateral strike-slip movement (along the SWIM fault system) and (ii) thrusting along NNE-SSW to N-S directed faults. Either, a rather diffusive plate boundary or strain partitioning may explain the much higher rate of seismicity off Iberia when compared to other passive margins. Besides, passive margins are generally several thousands of kilometres from any plate boundary and hence in the plate interior. In contrast, the south Iberian margin is situated about 100–200 km off Africa. Thus, normal passive margins suffer from far field stresses, while southern Iberia suffers from regional stresses caused by collision.

The fact that mantle earthquakes dominate in the Gulf of Cadiz might be caused by deformation associated with a rather unique setting. First, the Triassic to Jurassic age of the margin makes Iberia one of the oldest passive margins. Second, collision is generally not associated with active subduction. Third, in the center of the Gulf of Cadiz a fragment of Jurassic oceanic lithosphere (Fig. 1; Sallares et al., 2011; Martinez-Loriente et al., 2014) is sandwiched between African and Eurasian continental lithosphere. Thus, convergence between both continents will push thick Jurassic oceanic lithosphere against Triassic continental lithosphere. Shortening and deformation of such old and hence rigid lithosphere may cause intense deformation at mantle depth, explaining the large number of mantle earthquakes.

If the margin parallel seismicity would be related to an active STEP fault (Govers and Wortel, 2005) and westward slab retreat (e.g. Gutscher, 2004; Gutscher et al., 2012), we would expect a rather continuous band of seismicity outlining a major active fault. However, neither the Portuguese nor the Spanish national catalogues indicate such features, but show two unrelated clusters of activity at the Algarve margin and in the Betics (Fig. 8). An inactive STEP fault would be supported by stalled subduction and slab retreat (Chertova et al., 2014). Off the Algarve coast to the west of 7°W, earthquakes are co-located with a prominent gravity anomaly, supporting that seismicity is related to pre-existing features of the passive margin that are re-activated by the convergence between Africa and Eurasia (Zitellini et al., 2004). A new plate boundary fault may develop further south (Zitellini et al., 2009) along the SWIM faults. We therefore suggest classifying the margin of southern Iberia as a rather active and hence seismically aggressive-passive margin.

6. Conclusions

An amphibious micro-seismicity survey was conducted in the northern Gulf of Cadiz and Algarve passive margin, indicating that the majority of earthquakes was either located in the lower crust or the upper mantle. Roughly 50% of the detected events occurred either in the oceanic mantle of Jurassic lithosphere or beneath the continent-ocean transition zone and continental crust of the south Algarve-Iberia margin.

(i) Seismicity pattern supports a strong lower crust and upper continental mantle.
(ii) We consider the margin as a rather active or "aggressive" passive margin where pre-existing faults are re-activated by the African/Eurasian plate convergence. This conclusion is supported by the fact that seismicity found along the Algarve margin mimics the fault pattern along the passive margin of the Eastern US (Zoback, 1992; Wolin et al., 2012) and Eastern Brazil (Assumpcao et al., 2011).
(iii) Little evidence was found that the SWIM faults, as lithospheric scale W-E trending strike-slip faults, were seismically active during the offshore deployment.
(iv) We did not observe any earthquakes supporting an active eastward dipping subduction zone.

Acknowledgements

This study is part of the TOPO-EUROPE initiative of the EUROCORES Programme of the European Science Foundation (ESF). The

German efforts of TOPO-MED were funded by the German Science Foundation (DFG grant GR1964/12-1) and COST Action ES1301 "FLOWS". We thank the "German Instrument Pool for Amphibian Seismology (DEPAS)", hosted by the Alfred Wegener Institute Bremerhaven, providing five OBS operating CMG-40T sensors. We like to thanks Captain Michael Schneider and his crew of R/V Poseidon cruise POS393 and Captain Friedhelm von Star and the crew of R/V Maria S. Merian cruise MSM15/5 for excellent sea-going support. We are thankful to Anke Dannowski, Wiebke Leuchters, Helene Kraft, Arne Schwenk, Erick Labahn and students for technical assistance in operating ocean-bottom-seismometers. We greatly appreciate the detailed reviews of two anonymous referees that greatly improved the discussion of implications introduced by our new data. Figures were produced using the Generic Mapping Tools (GMT) software (Wessel and Smith, 1998). This work included data from the PM and WM seismic networks obtained from the GEOFON data centre.

Appendix A. Supplementary data

Supplementary data associated with this article can be found, in the online version, at http://dx.doi.org/10.1016/j.jog.2016.06.001.

References

Alinaghi, A., Krüger, F., 2014. Seismic array analysis and redetermination of depth of earthquakes in Tien-Shan: implications for strength of the crust and lithosphere. Geophys. J. Int. 198, 1111–1129, http://dx.doi.org/10.1093/gji/guu141.

Assumpcao, M., Dourado, J.C., Ribotta, L.C., Mohriak, W.U., Dias, F.L., Barosa, J.R., 2011. The Sa Vicente earthquakes of 2008 April and seismicity in the continental shelf off SE Brazil: further evidence for flexural stresses. Geophy. J. Int. 187, 1076–1088, http://dx.doi.org/10.1111/j.1365-246X.2011.05198.x.

Baptista, M.A., Miranda, P.M.A., Miranda, J.M., Victor, L.M., 1998. Constrains on the source of the 1755 Lisbon tsunami inferred from numerical modelling of historical data. J. Geodyn. 25, 159–174.

Baptista, M.A., Miranda, J.M., Omira, R., Antunes, C., 2011. Potential inundation of Lisbon downtown by a 1755-like tsunami. Nat. Hazards Earth Syst. Sci. 11, 3319–3326.

Bartolome, R., Gràcia, E., Stich, D., Martinez-Loriente, S., Klaeschen, D., Mancilla, F., Iacono, C., Danobeitia, J.J., Zitellini, N., 2012. Evidence for active strike-slip faulting along the Eurasia-Africa convergence zone: implications for seismic hazard in the southwest Iberia margin. Geology 40, 495–498, http://dx.doi.org/10.1130/G33107.1.

Bennett, R.A., Friedrich, A.M., Furlong, K.P., 2004. Codependent histories of the San Andreas and San Jacinto fault zones from inversion of fault displacement rates. Geology 32, 961–964, http://dx.doi.org/10.1130/G20806.1.

Bent, A.L., 1995. A complex double-couple source mechanism for the ms 7: 2 1929 grand banks earthquake. Bull. Seismol. Soc. Am. 85, 1003–1020.

Bezada, M.J., Humphreys, E.D., Toomey, D.R., Harnafi, M., Davila, J.M., 2013. Evidence for slab rollback in westernmost Mediterranean from improved upper mantle imaging. Earth Planet. Sci. Lett. 368, 51–60.

Booth-Rea, G., Ranero, C.R., Martinez-Martinez, J.M., Grevemeyer, I., 2007. Crustal types and tertiary tectonic evolution of the Alboran Sea, western Mediterranean. Geochem. Geophys. Geosyst. 8, http://dx.doi.org/10.1029/2007GC001639.

Borges, J.F., Fitas, A.J.S., Bezzeghoud, M., Teves-Costa, P., 2001. Seismotectonics of Portugal and its adjacent Atlantic area. Tectonophysics 337, 373–387.

Brace, W.F., Byerlee, J.D., 1966. Stick-slip as a mechanism for earthquakes. Science 153, 990.

Buforn, E., Bezzeghoud, M., Udías, A., Pro, C., 2004. Seismic sources on the Iberia-African plate boundary and their tectonic implications. Pure App. Geophys. 161, 623–646.

Chertova, M.V., Spakman, W., van den Berg, A.P., van Hinsbergen, D.J.J., 2014. Absolute plate motions and regional subduction evolution. Geochem. Geophys. Geosyst. 15, http://dx.doi.org/10.1002/2014GC005494.

Cloetingh, S., Beekman, F., Ziegler, P., van Wees, J., Sokoutis, D., 2008. Post-rift compressional reactivation potential of passive margins and extensional basins, in Nature and Origin of Compression in Passive Margins. Geol. Soc. Spec. Publ. 306, 27–70, http://dx.doi.org/10.1144/SP306.2.

Craig, T.J., Copley, A., Jackson, J., 2014. A reassessment of outer-rise seismicity and its implications for the mechanics of oceanic lithosphere. Geophys. J. Int. 197, 63–89, http://dx.doi.org/10.1093/gji/ggu013.

Cunha, T.A., Matias, L.M., Terrinha, P., Negredo, A., Rosas, F., Fernandes, R.M.S., Pinheiro, L.M., 2012. Neotectonics of the SW Iberia margin, Gulf of Cadiz and Alboran Sea: a reassessment including recent structural, seismic and geodetic data. Geophys. J. Int. 188, 850–872.

Díaz, J., Gallart, J., 2014. Seismic anisotropy from the Variscan core of Iberia to the Western African Craton: new constrains on upper mantle flow at regional scales. Earth Planet. Sci. Lett. 394, http://dx.doi.org/10.1016/j.epsl.2014.03.005.

DeMets, C., Gordon, R.G., Argus, D.F., 2010. Geologically current plate motions. Geophys. J. Int. 181, 1–80.

Duarte, J.C., Rosas, F.M., Terrinh, P., Gutscher, M.-A., Malavieille, J., Silva, S., Matias, L., 2011. Thrust–wrench interference tectonics in the Gulf of Cadiz (Africa–Iberia plate boundary in the north-east Atlantic): insights from analog models. Mar. Geol. 289, 135–149.

Duggen, S., Hoernle, K., van den Bogaard, P., Rüpke, L., Phipps Morgan, J., 2003. Deep roots of the Messinian salinity crisis. Nature 422, 359–363.

Duggen, S., Hoernle, K., van den Bogaard, P., Harris, C., 2004. The role of subduction in forming the western Mediterranean and causing the Messinian salinity crisis. Earth Planet. Sci. Lett. 218, 91–108.

Faccenna, C., Becker, T.W., Pio-Lucente, F., Jolivet, L., Rosseti, F., 2001. History of subduction and backarc extension in the Central Mediterranean. Geophys. J. Int. 145, 809–820.

Fukao, Y., 1973. Thrust faulting at a lithospheric plate boundary, the Portugal earthquake of 1969. Earth Planet. Sci. Lett. 18, 205–216.

Garcia-Castellanos, D., Villaseñor, A., 2011. Messinian salinity crisis regulated by competing tectonics and erosion at the Gibraltar arc. Nature 480, 359–363.

Geissler, W.H., et al., 2010. Focal mechanisms for sub-crustal earthquakes in the Gulf of Cadiz from a dense OBS deployment. Geophys. Res. Lett. 37, http://dx.doi.org/10.1029/2010GL044289, L18309.

Govers, R., Wortel, M.J.R., 2005. Lithosphere tearing at STEP faults: response to edges of subduction zones. Earth Planet. Sci. Lett. 236, 505–523.

Gràcia, E., Danobeitia, J.J., Verges, J., Bartolome, R., 2003. Crustal architecture and tectonic evolution of the Gulf of Cadiz (SW Iberian margin) at the convergence of the Eurasian and African plates. Tectonics 22, 1033, http://dx.doi.org/10.1029/2001TC901045.

Gràcia, E., Pallàs, R., Soto, J.I., Comas, M., Moreno, X., Masana, E., Santanach, P., Diez, S., García, M., Dañobeitia, J.J., 2006. Active faulting offshore SE Spain (Alboran Sea): implications for earthquake hazard assessment in the Southern Iberia Margin. Earth Planet. Sci. Lett. 241, 734–749.

Grandin, R., Borges, J.F., Bezzeghoud, M., Caldeira, B., Carrilho, F., 2007. Simulations of strong ground motion in SW iberia for the 1969 february 20 (Ms = 8: 0) and the 1755 november 1 (M ~ 8) 5) earthquakes—II. strong ground motion simulations. Geophys. J. Int. 171, 807–822.

Grevemeyer, I., Kaul, N., Kopf, A., 2009. Heat flow anomalies in the Gulf of Cadiz and off Cape San Vincente, Portugal. Mar. Petrol. Geol. 26, 795–804, http://dx.doi.org/10.1016/j.marpetgeo.2008.08.006.

Grevemeyer, I., Reston, T.J., Moeller, S., 2013. Microseismicity of the Mid-Atlantic Ridge at 7°S-8°15′S and at the Logatchev Massif oceanic core complex at 14°40′N-14°50′N. Geochem. Geophys. Geosyst. 14, 3532–3554, http://dx.doi.org/10.1002/ggge.20179.

Grevemeyer, I., Gràcia, E., Villaseñor, A., Leuchters, W., Watts, A.B., 2015. Seismicity and active tectonics in the Alboran Sea, Western Mediterranean: constraints from an offshore-onshore seismological network and swath bathymetry data. J. Geophys. Res. 120, http://dx.doi.org/10.1002/2015JB012073.

Gutscher, M.-A., Malod, J., Rehault, J.-P., Contrucci, I., Klingelhoefer, F., Mendes-Victor, L., Sparkman, W., 2002. Evidence for active subduction beneath Gibraltar. Geology 30, 1071–1074.

Gutscher, M.A., Baptista, M.A., Miranda, J.M., 2006. The Gibraltar Arc seismogenic zone: part 2. Constraints on a shallow east dipping fault plane source for the 1755 Lisbon earthquake provided by tsunami modeling and seismic intensity. Tectonophysics 426, 153–166.

Gutscher, M.A., et al., 2012. The Gibraltar subduction: a decade of new geophysical data. Tectonophysics 574–575, 72–91, http://dx.doi.org/10.1016/j.tecto.2012.08.038.

Gutscher, M.A., 2004. What caused the great Lisbon earthquake? Science 305, 1247–1248.

Hardebeck, J.L., Shearer, P.M., 2002. A new method for determining first-motion focal mechanisms. Bull. Seismol. Soc. Am. 92, 2264–2276, http://dx.doi.org/10.1785/0120010200.

Havskov, J., Ottemöller, L., 2000. SEISAN earthquake analysis software. Seismol. Res. Lett. 70, 532–534.

Heymann, M.A.W., 1989. Tectonic and depositional history of the Moroccan continental margin. In: Tankard, A.J., Balkwill, H.R. (Eds.), Extensional Tectonics and Stratigraphy of the Northern Atlantic Margins. Am. Assoc. Pet. Geol., Can. Geol. Found. AAPG Mem. 46, 323–340.

Hayward, N., Watts, A.B., Westbrook, G.K., Collier, J.S., 1999. A seismic reflection and GLORIA study of compressional deformation in the Gorringe Bank region, eastern north Atlantic. Geophy. J. Int. 138, 831–850.

Iribarren, L., Verges, J., Camurri, F., Fullea, J., Fernandez, M., 2007. The structure of the Atlantic-Mediterranean transition zone from the Alboran Sea to the Horseshoe Abyssal Plain (Iberia-Africa plate boundary). Mar. Geol. 243, 97–119.

Johnston, A., 1996. Seismic moment assessment of earthquakes in stable continental regions—III. New Madrid, 1811–1812, Charleston 1886 and Lisbon 1755. Geophys. J. Int. 126, 314–344.

Kennett, B.L.N., Engdahl, E.R., Buland, R., 1995. Constraints on seismic velocities in the Earth from traveltimes. Geophys. J. Int. 122, 108–124, http://dx.doi.org/10.1111/j.1365-246X.1995.tb03540.x.

Lefeldt, M., Grevemeyer, I., Gossler, J., Bialas, J., 2009. 2009., Intraplate seismicity and related mantle hydration at the Nicaraguan trench outer rise. Geophys. J. Int. 178, 742–752, http://dx.doi.org/10.1111/j.1365-246X.2009.04167.x.

Lienert, B.R., Havskov, J., 1995. Hypocenter 3.2 A computer program for locating earthquakes locally, regionally and globally. Seismol. Res. Lett. 66, 26–36.
Lienert, B.R., Berg, E., Frazer, L.N., 1986. Hypocenter: an earthquake location method using centered, scaled, and adaptively least squares. Bull. Seismol. Soc. Am. 76, 771–783.
Lindenfeld, M., Rümpker, G., 2011. Detection of mantle earthquakes beneath the East African Rift. Geophys. J. Int. 186, 1–5, http://dx.doi.org/10.1111/j.1365-246X.2011.05048.x.
Lomax, A., Virieux, A.J., Volant, P., Berge, C., 2000. In: Thurber, C.H., Rabinowitz, N. (Eds.), Probabilistic Earthquake Location in 3D and Layered Models: Introduction of a Metropolis-Gibbs Method and Comparison with Linear Locations, in Advances in Seismic Event Location. Kluwer Amsterdam, pp. 101–134.
Maggi, A., Jackson, J.A., McKenzie, D., Priestley, K., 2000. Earthquake focal depth, effective elastic thickness, and the strength of the continental lithosphere. Geology 28, 495–498.
Maldonado, A., Somoza, L., Pallarés, L., 1999. The Betic orogen and the Iberian-African boundary in the Gulf of Cadiz: geological evolution (Central North Atlantic). Mar. Geol. 155, 9–43.
Martinez-Loriente, S., et al., 2014. Seismic and gravity constraints on the nature of the basement in the Africa-Eurasia plate boundary: new insights for the geodynamic evolution of the SW Iberian margin. J. Geophys. Res. 119, 127–149, http://dx.doi.org/10.1002/2013JB010476.
Martinez-Solares, J.M., Lopez, A., Mezcua, J., 1979. Isoseismal map of the 1755 Lisbon earthquake obtained from Spanish data. Tectonophysics 53, 301–313.
McKenzie, D., Parker, R.L., 1967. The North Pacific: an example of tectonics on a sphere. Nature 216, 1276–1280, http://dx.doi.org/10.1038/2161276a0.
McKenzie, D., Jackson, J.A., Priestley, K., 2005. Thermal structure of oceanic and continental lithosphere. Earth Planet. Sci. Lett. 233, 337–349, http://dx.doi.org/10.1016/j.epsl2005.02.005.
McKenzie, D., 1978. Some remarks on the development of sedimentary basins. Earth Plant. Sci. Lett. 40, 25–32.
Moeller, S., Grevemeyer, I., Ranero, C.R., Berndt, C., Klaeschen, D., Sallares, V., Zitellini, N., de Franco, R., 2013. Early-stage rifting of the northern Tyrrhenian Sea Basin: results from a combined wide-angle and multichannel seismic study. Geochem. Geophys. Geosyst. 14, 3032–3052, http://dx.doi.org/10.1002/ggge.20180.
Morgan, W.J., 1968. Rises, trenches great faults, and crustal blocks. J. Geophys. Res. 73, 1959–1982, http://dx.doi.org/10.1029/JB073i006p01959.
Neves, M.C., Neves, R.G.M., 2009. Flexure and seismicity across the ocean-continent transition in the Gulf of Cadiz. J. Geodyn. 47, 119–129.
Odedra, A., Ohnaka, M., Mochizuki, H., Sammonds, P., 2001. Temperature and pore pressure effects on the shear of strength of granite in the Brittle-Plastic Transition Regime. Geophys. Res. Lett. 28, 3011–3014, http://dx.doi.org/10.1029/2001GL013321.
Ottemöller, L., Havskov, J., 2003. Moment magnitude determination for local and regional earthquakes based on source spectra. Bull. Seismol. Soc. Am. 93, 203–214.
Rovere, M., Ranero, C.R., Sartori, R., Torelli, L., Zitellini, N., 2004. Seismic images and magnetic signature of Late Jurassic to Early Cretaceous Africa-Eurasia plate boundary off SW Iberia. Geophys. J. Int. 158, 554–568.
Royden, L.H., 1993. Evolution of retreating subduction boundaries formed during continental collision. Tectonics 12, 629–638.
Sallares, V., et al., 2011. Seismic evidence for the presence of Jurassic oceanic crust in the central Gulf of Cadiz (SW Iberia margin). Earth Plant. Sci. Lett. 311, 112–123, http://dx.doi.org/10.1016/j.epsl.2011.09.003.
Sandwell, D.T., Müller, R.D., Smith, W.H.F., Garcia, E., Francis, R., 2014. New global marine gravity model from CryoSat-2 and Jason-1 reveals buried tectonic structure. Science 346, 65–67, http://dx.doi.org/10.1126/science.1258213.
Sartori, R., Torelli, I., Zitellini, N., Peis, D., Lodolo, E., 1994. Eastern segment of the Azores–Gibraltar line (central-eastern Atlantic): an oceanic plate boundary with diffuse compressional deformation. Geology 22, 555–558.
Satake, K., Shimazaki Tsuji, K., Ueda, K., 1996. Time and size of a giant earthquake in Cascadia inferred from Japanese tsunami record of January 1700. Nature 379, 246–249.
Satake, K., Wang, K., Atwater, B.F., 2003. Fault slip and seismic moment of the 1700 Cascadia earthquake inferred from Japanese tsunami description. J. Gephys. Res. 108, 2325, http://dx.doi.org/10.1019/2003JB002521.
Schettino, A., Turco, E., 2011. Tectonic history of the western Tethys since the Late Triassic. Geol. Soc. Am. Bull. 123, 89–105, http://dx.doi.org/10.1130/B30064.1.
Scholtz, C.H., 2016. Earthquakes and friction laws. Nature 391, 38–42.
Schulte, S.M., Mooney, W.D., 2005. An updated global earthquake catalogue for stable continental regions. Geophys. J. Int. 161, 707–721, http://dx.doi.org/10.1111/j.1365-246X.2005.02554.x.
Snoke, J.A., Munsey, J.W., Teague, A.G., Bollinger, G.A., 1984. A program for focal mechanism determination by combined use of polarity and SV-P amplitude ratio data. Earthquake Notes, 55.
Spakman, W., Wortel, R., 2004. A tomographic view on Western Mediterranean Geodynamics. In: Cavazza, W., Roure, F., Spakman, W., Stampfli, G.M., Ziegler, P. (Eds.), The TRANSMED Atlas, The Mediterranean Region from Crust to Mantle. Springer-Verlag, Heidelberg, pp. 31–52.
Stich, D., de Lis Mancilla, F., Morales, J., 2005. Crust-mantle coupling in the gulf of cadiz (SW-Iberia). Geophys. Res. Lett. 32, http://dx.doi.org/10.1029/2005GL023098.
Terrinha, P., et al., 2009. Morphotectonics and strain partitioning at the Iberia-Africa plate boundary from multibeam and seismic refl ection data. Mar. Geol. 267, 156–174, http://dx.doi.org/10.1016/j.margeo.2009.09.012.
Thiebot, E., Gutscher, M.A., 2006. The Gibraltar Arc seismogenic zone (part1): constraints on a shallow east dipping fault plane source for the 1755 Lisbon earthquake provided by seismic data, gravity and thermal modeling. Tectonophysics 427, 135–152.
Torelli, L., Sartori, R., Zitellini, N., 1997. The giant chaotic body in the Atlantic ocean of Gibraltar. New result from a deep seismic reflection survey. Mar. Petrol. Geol. 14, 125–138.
Wessel, P., Smith, W.H.F., 1998. New improved version of the generic mapping tool released, EOS trans. Am. Geophys. Union 79, 579.
Wolin, E., Stein, S., Pazzaglia, F., Meltzer, A., Kafka, A., Berti, C., 2012. Mineral, Virginia, earthquake illustrates seismicity of a passive-aggressive margin. Geophys. Res. Lett. 39, http://dx.doi.org/10.1029/2011GL050310, L02305.
Zitellini, N., Rovere, M., Terrinha, P., Chierici, F., Matias, L., 2004. Neogene through Quaternary tectonic reactivation of SW Iberian passive margin. Pure Appl. Geophys. 161, 565–587.
Zitellini, N., et al., 2009. The quest for the Africa-Eurasia plate boundary west of the Strait of Gibraltar. Earth Plant. Sci. Lett. 280, 13–50, http://dx.doi.org/10.1016/j.epsl.2088.12.005.
Zoback, M.L., 1992. Stress field constraints on intraplate seismicity in eastern North America. J Geophys Res, 97, http://dx.doi.org/10.1029/92JB00221, 11, 761–11, 782.

Please cite this article in press as: Grevemeyer, I., et al., Mantle earthquakes beneath the South Iberia continental margin and Gulf of Cadiz – constraints from an onshore-offshore seismological network. J. Geodyn. (2016), http://dx.doi.org/10.1016/j.jog.2016.06.001

Geology, published online on 27 February 2015 as doi:10.1130/G36359.1

Strike-slip faults mediate the rise of crustal-derived fluids and mud volcanism in the deep sea

Christian Hensen[1], Florian Scholz[1], Marianne Nuzzo[2,3], Vasco Valadares[3], Eulàlia Gràcia[4], Pedro Terrinha[3], Volker Liebetrau[1], Norbert Kaul[5], Sonia Silva[3], Sara Martínez-Loriente[4], Rafael Bartolome[4], Elena Piñero[1], Vitor H. Magalhães[3], Mark Schmidt[1], Stephan M. Weise[6], Marina Cunha[7], Ana Hilario[7], Hector Perea[4], Lorenzo Rovelli[8], Klas Lackschewitz[1]

[1]GEOMAR Helmholtz-Centre for Ocean Research Kiel, 24148 Kiel, Germany
[2]IGI Ltd., Hallsannery, EX39 5HE Bideford, UK
[3]Portuguese Institute for the Sea and the Atmosphere (IPMA), 1749-077 Lisbon, Portugal
[4]Barcelona Center for Subsurface Imaging, Institut de Ciències del Mar-CSIC, E-08003 Barcelona, Spain
[5]Department of Geosciences, University of Bremen, 28359 Bremen, Germany
[6]UFZ Helmholtz Centre for Environmental Research, 06120 Halle, Germany
[7]Department of Biology & Centre for Environmental and Marine Studies, University of Aveiro, 3810-193 Aveiro, Portugal
[8]The Scottish Association for Marine Science, PA37 1QA Oban, UK

ABSTRACT

We report on newly discovered mud volcanoes located at ~4500 m water depth ~90 km west of the deformation front of the accretionary wedge of the Gulf of Cadiz, and thus outside of their typical geotectonic environment. Seismic data suggest that fluid flow is mediated by a >400-km-long strike-slip fault marking the transcurrent plate boundary between Africa and Eurasia. Geochemical data (Cl, B, Sr, $^{87}Sr/^{86}Sr$, $\delta^{18}O$, δD) reveal that fluids originate in oceanic crust older than 140 Ma. On their rise to the surface, these fluids receive strong geochemical signals from recrystallization of Upper Jurassic carbonates and clay-mineral dehydration in younger terrigeneous units. At present, reports of mud volcanoes in similar deep-sea settings are rare, but given that the large area of transform-type plate boundaries has been barely investigated, such pathways of fluid discharge may provide an important, yet unappreciated link between the deeply buried oceanic crust and the deep ocean.

INTRODUCTION

Fluid seepage and mud volcanism are common at active and passive continental margins (Kopf, 2002); typical driving mechanisms are (1) rapid sedimentation in combination with compaction and tectonic stress, (2) intrusive processes like salt diapirism, (3) dewatering of hydrous minerals, and (4) formation of hydrocarbons. These factors are met in the Gulf of Cadiz, where several kilometer-thick Mesozoic to Holocene sediments accumulated in an accretionary wedge, hosting numerous mud volcanoes (MVs) preferentially at fault intersections (Fig. 1; Magalhães et al., 2012). Proximal to the coast, MV fluids are strongly influenced by clay-mineral dehydration and leaching of Upper Triassic evaporites (Haffert et al., 2013). With increasing distance from the coast, the fluid signature changes, and fluid interaction with the underlying oceanic crust was postulated based on results from the Porto MV (Scholz et al., 2009). The occurrence of MVs located at water depths >2500 m is closely tied to the presence of active strike-slip faults (Duarte et al., 2013; Fig. 1), which provide deeply rooted fluid pathways (Hensen et al., 2007). In 2012, R/V *Meteor* cruise M86/5 was conducted to test hypothesized fluid seepage along deep-rooted strike-slip faults also in distal segments outside the accretionary wedge. Our findings call for a reappraisal of oceanic transform-type faults as fluid conduits and support current hypotheses about ongoing fluid circulation in "aged" upper oceanic crust.

GENERAL OBSERVATIONS

Acoustic backscatter anomalies recorded during previous bathymetric surveys led to the discovery of three new MVs on cruise M86/5: Abzu, Tiamat, and Michael Ivanov (ATI MVs hereafter; Fig. 1A) at water depths of ~4500 m at the southern rim of the Horseshoe Valley, ~90 km west of the deformation front of the accretionary wedge (Fig. 1A; Duarte et al., 2013). These MVs are smaller than those found on the accretionary wedge and consist of isolated cones (Fig. 1B) aligned on the Lineament South (LS) trend (Bartolome et al., 2012; Terrinha et al., 2009). The position of the MVs along the LS fault coincides with a seismically active zone with earthquakes of magnitudes $M_w \leq 6$ nucleating in the upper mantle between 40 km and 60 km depth (Fig. 1A; Geissler et al., 2010). This suggests a fault intersection scenario similar to the situation on the accretionary wedge. Five gravity cores of up to 4.75 m length were obtained from active fluid emanation sites at ATI and Porto MVs (see Appendix DR1 in the GSA Data Repository[1]). Pore water was extracted in intervals ≤25 cm and analyzed for major and minor element composition using standard analytical procedures (Appendix DR2; e.g., Scholz et al., 2009). MV sediments typically consist of olive-gray mud breccias with claystone clasts of millimeter to centimeter size, and are highly enriched in H_2S and methane. Gas hydrates are found below the zone of anaerobic oxidation of methane (AOM). Dissolved methane escaping from the MV sediment forms plumes above the seafloor and feeds chemosymbiotic assemblages including several species of bivalves and tubeworms (Cunha et al., 2013).

[1]GSA Data Repository item 2015124, supporting information on locations, fluid geochemical data, analytical methods, Sr-isotope data of mud clasts, and heat flow measurements, is available online at www.geosociety.org/pubs/ft2015.htm, or on request from editing@geosociety.org or Documents Secretary, GSA, P.O. Box 9140, Boulder, CO 80301, USA.

FLUID SOURCES AND IMPLICATIONS

At ATI MVs, a shallow AOM zone prevails (40–200 cm sediment depth) due to advection of methane-rich fluids. Below the AOM zone, mixing with ambient bottom water is minor so that the chemical composition of rising deep fluids can be studied on samples from this depth, defined as "local endmembers" of a core (e.g., Scholz et al., 2009). Local endmembers from four cores sampled on cruise M86/5 at ATI MVs and one core from Porto MV were selected and compared to previously published (Hensen et al., 2007; Scholz et al., 2009) local endmembers from MVs on the accretionary wedge (Fig. 2; Appendix DR1; distal MVs: Carlos Ribeiro [CRMV], Bonjardim, Porto; proximal MVs: Mercator, Captain Arutyunov [CAMV]).

Fluid data reveal positive and negative correlations of $\delta^{18}O$ and Cl versus B (Fig. 2A) and $\delta^{18}O$ versus δD (Fig. 2B), respectively. Such trends are typical for clay-mineral dehydration, a major fluid source in the Gulf of Cadiz (Hensen et al., 2007). Clay dehydration causes freshening of fluids (depletion of conservative elements such as Cl), a characteristic signal of $\delta^{18}O$ above and δD below standard seawater composition (Vienna standard mean ocean water, VSMOW), as well as enrichments of boron and other fluid-mobile elements (Dählmann and de Lange, 2003).

Similarly, MV endmembers of Sr (Fig. 2C) and $^{87}Sr/^{86}Sr$ ratios (Fig. 2D) were plotted versus Cl. Data from non-ATI MVs in Figure 2C show a similar relationship as in Figures 2A and 2B,

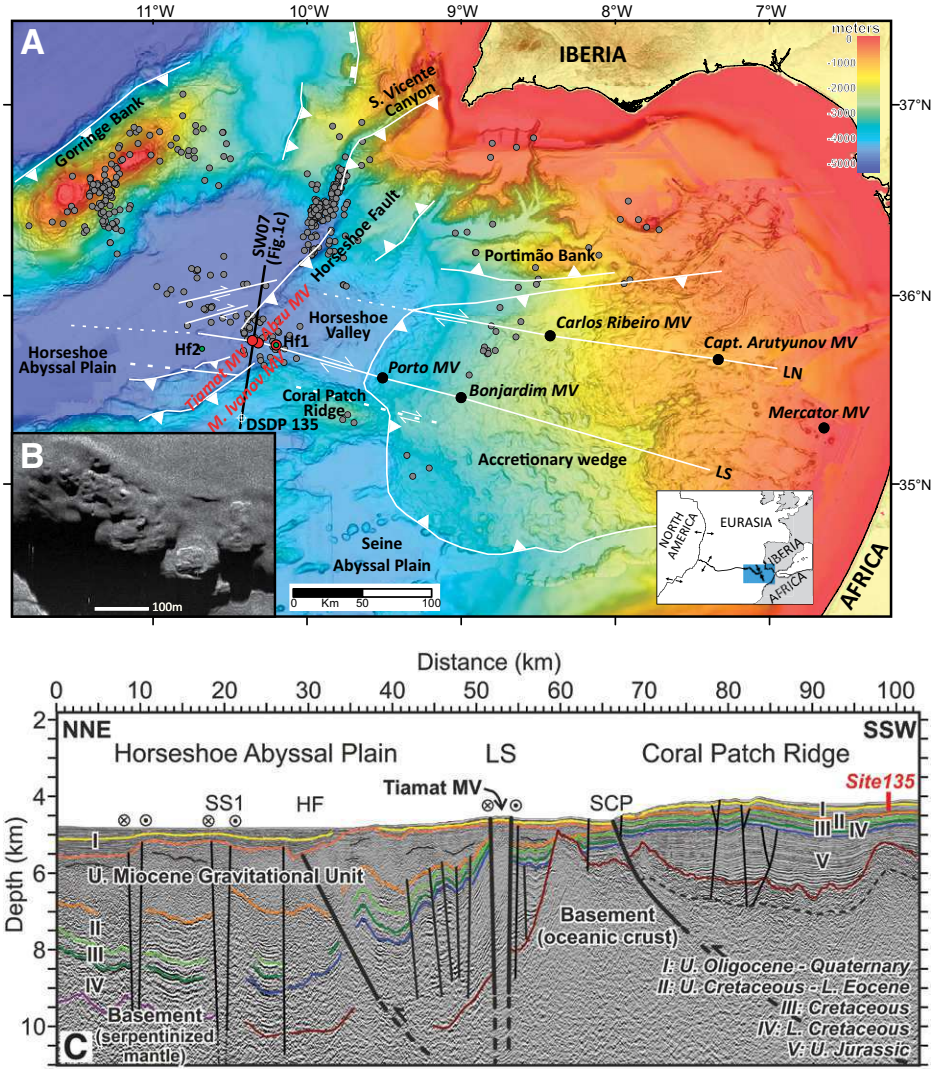

Figure 1. Study area, Gulf of Cadiz, and structural framework. A: Bathymetric map of the southwest Iberian margin from ~90 m digital grids (Zitellini et al., 2009); seismicity data (gray dots) from the NEAREST (Integrated Observation from Near Shore Sources of Tsunami) project temporary deployment; seismic profile SW07 (black line) running across the Lineament South (LS) and Deep Sea Drilling Project (DSDP) site 135; Hf1 and Hf2 (heat flow stations; Appendix DR4 [see footnote 1]). MV—mud volcano. Inset: Plate tectonic setting of the southwest Iberian margin (blue rectangle corresponds to the area depicted in A). B: Detail of a high-resolution sidescan sonar image of Michael Ivanov mud volcano. The entire structure consists of numerous single cones, being typically <100 m in diameter. C: Interpreted prestack depth-migrated seismic profile SW07 across the LS (at Tiamat MV), from the Coral Patch Ridge region to the Horseshoe Abyssal Plain. HF—Horseshoe fault; SS1—Strike-slip fault 1 (Martínez-Loriente et al., 2013); SCP—South Coral Patch Ridge fault; LN—Lineament North; U.—Upper; L.—Lower; vertical exaggeration: 5×.

and can be defined by mixing between a certain range of Sr-enriched clay endmembers and sea water (shaded area Fig. 2C). This suggests that Sr is also derived from clay dehydration. By contrast, ATI MV fluids are clearly offset from this trend. Explaining this offset by mixing of clay-mineral–derived water and seawater would require an unrealistically strong Sr source in clays. Moreover, Sr released from clays has a high (radiogenic) $^{87}Sr/^{86}Sr$ ratio (Scholz et al., 2009; Appendix DR3) so that a strong Sr input from clays at ATI MVs should cause a positive offset in the isotopic signature, which is not the case (Fig. 2D). Instead, the $^{87}Sr/^{86}Sr$ signal of fluids at all distal MVs indicate the decreasing influence of clay-mineral dewatering (Scholz et al., 2009) suggesting a low (less radiogenic) $^{87}Sr/^{86}Sr$ ratio of the source at ATI MVs. Two possible sources of Sr can induce such a low $^{87}Sr/^{86}Sr$ signal in this geological setting: deeply buried oceanic crust, and recrystallization of Mesozoic carbonates. Sr concentrations in hydrothermal vent fluids vary between 80 µM and 300 µM (Butterfield et al., 1994; Campbell et al., 1988; Mottl et al., 2000; Von Damm, 1990), which is below the level measured in most of the MV fluids. Therefore, oceanic crust is unlikely to be the dominant source of Sr at the ATI MVs. Pore waters of (pelagic) limestones can be enriched in Sr by >1 mM. The Sr enrichment is related to recrystallization (Gieskes and Lawrence, 1981) of Sr-rich, meta-stable aragonite to Sr-poor, stable calcite. The $^{87}Sr/^{86}Sr$ ratio of fluids affected by this process may be as low as 0.7068 ($^{87}Sr/^{86}Sr$ of Upper Jurassic seawater and carbonates; Banner, 2004). Seismostratigraphy calibrated with results of nearby Deep Sea Drilling Project (DSDP) Site 135 (Fig. 1) shows an exceptionally thick (2.5 km) sequence of Upper Jurassic sediments on top of the oceanic basement below the ATI MVs (Fig. 1C; Martínez-Loriente et al., 2013). Evidence from DSDP Site 105 (Hollister et al., 1972), the western Atlantic counterpart to Site 135, suggests that Upper Jurassic sediments in the study area are indeed pelagic limestones.

To further explore how potential sources may affect the MV fluid compositions, we examine a plot of Sr/B versus $^{87}Sr/^{86}Sr$ (Fig. 3). This combination of parameters allows for a clear discrimination between (1) clay (strongly radiogenic $^{87}Sr/^{86}Sr$), (2) carbonates ($^{87}Sr/^{86}Sr$ between present-day and the Late Jurassic Ocean; high Sr/B), and (3) oceanic crust (well-defined, strongly non-radiogenic $^{87}Sr/^{86}Sr$) as potential sources. The fluid composition of the proximal MVs is close to the suggested end-member of clay-mineral dewatering, while that of ATI MVs shows a strong imprint of recrystallization of Upper Jurassic carbonates (Fig. 3). The distal, non-ATI MVs plot within the binary mixing field of "clay" and "crust", suggesting a negligible influence of carbonate recrystallization there. This interpretation is in line with stratigraphic evidence for the subsurface extension of Upper Jurassic sediments (Fig. 4). Consequently, only ATI MVs receive the strong signal from carbonate recrystallization.

Unlike clay minerals, sedimentary carbonates do not store water in their lattice, and the process of recrystallization only enriches ambient pore waters in Sr. Therefore, an additional transport mechanism is required to carry the signal of carbonate recrystallization to the seafloor. Freshwater release from clay is presumably low in carbonate-rich sediments. In addition, clay-mineral dehydration occurs at temperatures between 60 °C and 150 °C (Hensen et al., 2007), which translates into sub-seafloor depths of ~1–3 km (geothermal gradient 45–50 K km^{-1}; Appendix DR4; Grevemeyer et al., 2009). Thus, there is only a limited overlap with the Upper Jurassic sediments (2–4.5 km sub-seafloor depth). As the Upper Jurassic unit corresponds to the deepest sedimentary deposits located right above the oceanic crust, only a scenario where crustal-derived fluids carry the geochemical signals upward (mixing of all three sources in Fig. 3) can explain observed

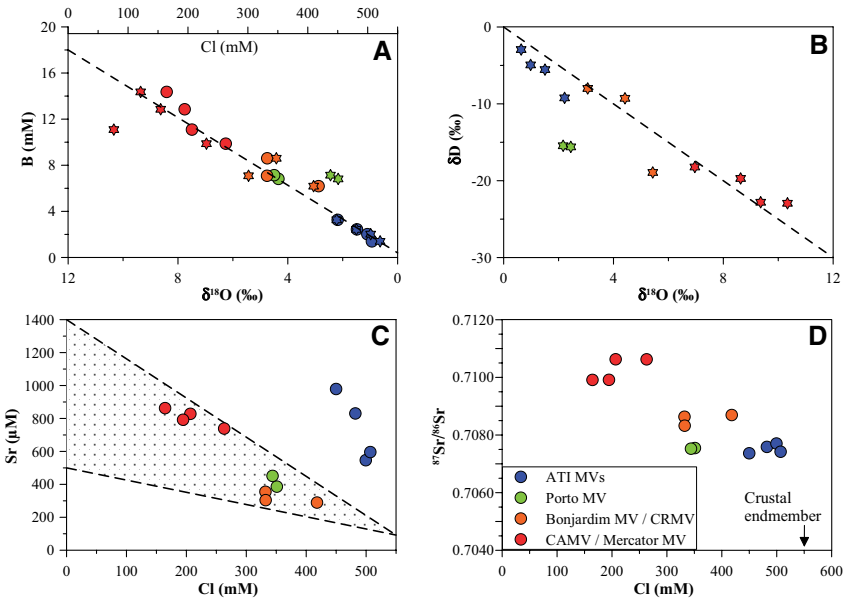

Figure 2. Endmember plots for various mud volcano (MV) fluids. A: $\delta^{18}O$ versus boron (stars) and Cl versus boron. B: $\delta^{18}O$ versus δD (stars). ATI MVs—Abzu, Tiamat, and Michael Ivanov MVs; CRMV—Carlos Ribeiro MV; CAMV—Captain Arutyunov MV. Dashed lines in A and B indicate trends with suggested endmember concentrations of clay-mineral–derived water (B = 18, Cl = 0, $\delta^{18}O$ = 12; δD = –30) and seawater (B = 0.4, Cl = 550, $\delta^{18}O$ = 0; δD = 0). C: Cl versus Sr. Shaded field between the dashed lines defines the mixing area between minimum and maximum Sr endmembers at Cl = 0 and seawater. D: Cl versus $^{87}Sr/^{86}Sr$. Note that Cl^- concentrations for samples from Mercator MV and Captain Arutyunov MV (CAMV) in A were corrected using the equation of Hensen et al. (2007), because fluids at those sites were affected by salt dissolution (see Appendix DR1 in the Data Repository [see footnote 1]).

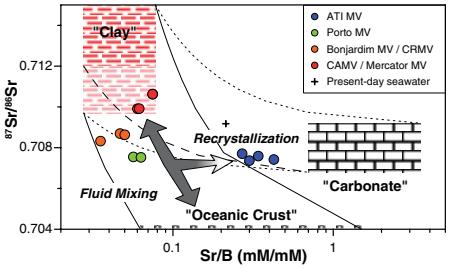

Figure 3. Endmembers of mud volcano (MV) fluids (symbols) and assumed fluid sources (boxes). Ranges were derived as follows. Clay-mineral dewatering: Lower and upper boundary of $^{87}Sr/^{86}Sr$ = 0.7094–0.7150 (derived from clay clasts; see Appendix DR3 [see footnote 1]; Scholz et al., 2009), Sr/B from linear extrapolation of data to Cl = 0 mM (Figs. 2A and 2C). Carbonates: $^{87}Sr/^{86}Sr$ = 0.7068–0.7092 (range from Late Jurassic to contemporaneous seawater), Sr = 300–1500 µM, B = 0.43 mM (seawater). Crustal derived fluids: $^{87}Sr/^{86}Sr$ = 0.7040, Sr/B min/max derived from Butterfield et al. (1994), Campbell et al. (1988), Mottl et al. (2000), Von Damm (1990). Lines indicate two-endmember mixing of reservoirs: solid (clay-crust), stippled (clay-carbonate). Hatched line for clay-carbonate mixing uses the average value of all clast samples ($^{87}Sr/^{86}Sr$ = 0.7120) and thus the most likely lower endmember value of clay clasts (indicated by faded red color below this value). ATI MVs—Abzu, Tiamat, and Michael Ivanov MVs; CRMV—Carlos Ribeiro MV; CAMV—Captain Arutyunov MV.

fluid compositions. Such a scenario is in compliance with the evidence for crustal alteration in MV fluids in the Gulf of Cadiz (Scholz et al., 2009). Our observations are summarized in a synthetic cross section (Fig. 4). Overall, fluids at Porto MV carry the strongest signal from oceanic crust alteration (Fig. 3), which is in agreement with the thinnest sediment cover at this site (Fig. 4). Compared to all other sites, there is also an obvious negative offset in $\delta^{18}O$ values at this location. Negative shifts in $\delta^{18}O$, i.e., opposite to the effect observed during clay dehydration, are typical for mineral hydration processes such as the alteration of volcanic ash or oceanic crust (Gieskes and Lawrence, 1981). This trend is hardly visible at ATI MVs, likely due to the strong imprint of carbonate recrystallization favoring the formation of ^{18}O-enriched fluids at elevated temperatures (Lawrence et al., 1975) and counteracting any negative crustal-derived $\delta^{18}O$ signal.

In spite of the clear geochemical evidence, the precise mechanism driving fluid flow remains elusive. The major strike-slip fault (LS) provides a deep-reaching, permeable conduit that serves as pathway for ascending fluids. Strike-slip faulting has been previously suggested as a mechanism for the release of overpressure, eventually leading to pulses of fluid flow (Mazzini et al., 2009; Sibson, 1987; Viola et al., 2005). Deep seismic activity in the vicinity of ATI MVs (Fig. 1) indeed supports this hypothesis. In addition, pore water convection, related to the existence of local basement highs (e.g., Coral Patch Ridge; Figs. 1 and 4), could provide an alternative scenario of crustal-derived flow. To date, examples for fluid convection are mainly reported from the eastern Pacific, where pore fluids circulate through interconnected seamounts in young oceanic crust (Fisher et al., 2003).

CONCLUSIONS

Our findings confirm that seismogenic strike-slip faults provide pathways for deep-seated fluids, sustaining mud volcanism even in abyssal regions, outside areas of rapid sediment accumulation. Moreover, strike-slip faults tap fluid sources in oceanic crust older than 140 Ma, contradicting previous assumptions that fluid circulation terminates at a crustal age of ca. 65 ± 10 Ma (Stein et al., 1995). Although the exact mechanism remains poorly constrained, our data provide evidence for fluid flow within old oceanic crust in an area of strong topographic contrasts and deep basement faults as suggested by Von Herzen (2004). Interestingly, MVs expel-

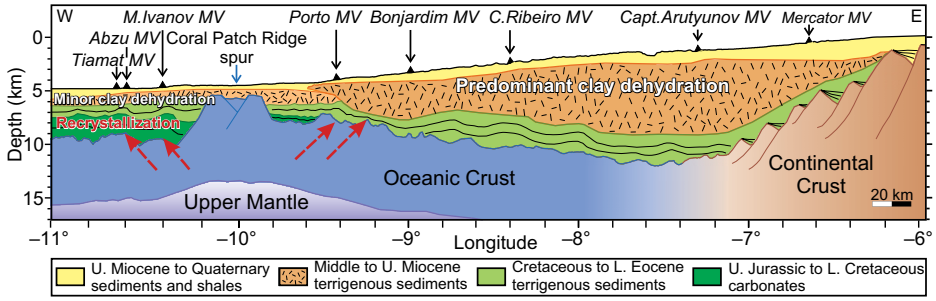

Figure 4. Regional synthetic (west to east) cross section from the continental shelf to the deep Horseshoe Basin north of Coral Patch Ridge (roughly following the Lineament South [LS]) illustrating major sources and processes affecting the fluid composition of distal mud volcanoes (MVs) in the Gulf of Cadiz. The largest potential for clay-mineral dehydration exists within the suitable temperature/depth range in the Middle to Upper Miocene terrigeneous units. MVs are projected along the profile. Note that Coral Patch Ridge is a prominent basement elevation appearing as buried spur and corresponds to a significant elevation of the seafloor, south of LS (Fig. 1). U.—Upper; L.—Lower. Vertical exaggeration: ~5×.

ling geochemically distinct fluids off the Barbados Accretionary Prism (Godon et al., 2004) are found in a tectonic setting comparable to that in the Gulf of Cadiz. Those are aligned along a major fracture zone and it was suggested that mud volcanism was initiated by changes in plate motion along this fracture (Sumner and Westbrook, 2001). Globally, transform-type plate boundaries are of similar length as divergent and convergent plate boundaries (Bird, 2003) and the latter are known for intense vent and seep activity. We suggest that transform-type plate boundaries and fracture zones may also provide important pathways for fluid exchange between the lithosphere and the deep ocean, and hence deserve more intense future exploration to evaluate their role in terms of heat and element exchange.

ACKNOWLEDGMENTS

We thank Captain Schwarze and his crew onboard R/V *Meteor* for excellent support at sea. We are indebted to our colleagues A. Bleyer, B. Domeyer, A. Kolevica, and R. Surberg for lab support. A great "thank you" to the AUV *Abyss* team at GEOMAR. A. Reitz and M. Haeckel are thanked for their support and helpful discussions. The manuscript benefitted from constructive reviews of M. Huuse, F. Meneghini, G. Viola, and an anonymous reviewer. Cruise M 86/5 was funded by the German Research Foundation (TransFlux grant) with additional support by SHAKE, SWIMGLO, MODELINK, and FLOWS (EU-COST, ES 1301) projects.

REFERENCES CITED

Banner, J.L., 2004, Radiogenic isotopes: systematics and applications to earth surface processes and chemical stratigraphy: Earth-Science Reviews, v. 65, p. 141–194, doi:10.1016/S0012-8252(03)00086-2.

Bartolome, R., Gràcia, E., Stich, D., Martínez-Loriente, S., Klaeschen, D., Mancilla, F., Lo Iacono, C., Dañobeitia, J.J., and Zitellini, N., 2012, Evidence for active strike-slip faulting along the Eurasia-Africa convergence zone: Implications for seismic hazard in the southwest Iberian margin: Geology, v. 40, p. 495–498, doi:10.1130/G33107.1.

Bird, P., 2003, An updated digital model of plate boundaries: Geochemistry Geophysics Geosystems, v. 4, p. 1027, doi:10.1029/2001GC000252.

Butterfield, D.A., McDuff, R.E., Mottl, M.J., Lilley, M.D., Lupton, J.E., and Massoth, G.J., 1994, Gradients in the composition of hydrothermal fluids from the Endeavour segment vent field: Phase separation and brine loss: Journal of Geophysical Research, v. 99, p. 9561–9583, doi:10.1029/93JB03132.

Campbell, A.C., et al., 1988, Chemistry of hot springs on the Mid-Atlantic Ridge: Nature, v. 335, p. 514–519, doi:10.1038/335514a0.

Cunha, M.R., Rodrigues, C.F., Génio, L., Hilário, A., Ravara, A., and Pfannkuche, O., 2013, Macrofaunal assemblages from mud volcanoes in the Gulf of Cadiz: abundance, biodiversity and diversity partitioning across spatial scales: Biogeosciences, v. 10, p. 2553–2568, doi:10.5194/bg-10-2553-2013.

Dählmann, A., and de Lange, G.J., 2003, Fluid-sediment interactions at Eastern Mediterranean mud volcanoes: a stable isotope study from ODP Leg 160: Earth and Planetary Science Letters, v. 212, p. 377–391, doi:10.1016/S0012-821X(03)00227-9.

Duarte, J.C., Rosas, F.M., Terrinha, P., Schellart, W.P., Boutelier, D., Gutscher, M.-A., and Ribeiro, A., 2013, Are subduction zones invading the Atlantic? Evidence from the southwest Iberia margin: Geology, v. 41, p. 839–842, doi:10.1130/G34100.1.

Fisher, A., et al., 2003, Hydrothermal recharge and discharge across 50 km guided by seamounts on a young ridge flank: Nature, v. 421, p. 618–621, doi:10.1038/nature01352.

Geissler, W.H., Matias, L., Stich, D., Carrilho, F., Jokat, W., Monna, S., IbenBrahim, A., Mancilla, F., Gutscher, M.A., Sallarès, V., and Zitellini, N., 2010, Focal mechanisms for sub-crustal earthquakes in the Gulf of Cadiz from a dense OBS deployment: Geophysical Research Letters, v. 37, L18309, doi:10.1029/2010GL044289.

Gieskes, J.M., and Lawrence, J.R., 1981, Alteration of volcanic matter in deep-sea sediments: evidence from the chemical composition of interstitial waters from deep-sea drilling cores: Geochimica et Cosmochimica Acta, v. 45, p. 1687–1703, doi:10.1016/0016-7037(81)90004-1.

Godon, A., Jendrzejewski, N., Castrec-Rouelle, M., Dia, A., Pineau, F., Boulegue, J., and Javoy, M., 2004, Origin and evolution of fluids from mud volcanoes in the Barbados accretionary complex: Geochimica et Cosmochimica Acta, v. 68, p. 2153–2165, doi:10.1016/j.gca.2003.08.021.

Grevemeyer, I., Kaul, N., and Kopf, A., 2009, Heat flow anomalies in the Gulf of Cadiz and off Cape San Vincente, Portugal: Marine and Petroleum Geology, v. 26, p. 795–804, doi:10.1016/j.marpetgeo.2008.08.006.

Haffert, L., Haeckel, M., Liebetrau, V., Berndt, C., Hensen, C., Nuzzo, M., Reitz, A., Scholz, F., Schönfeld, J., Perez-Garcia, C., and Weise, S.M., 2013, Fluid evolution and authigenic mineral paragenesis related to salt diapirism - The Mercator mud volcano in the Gulf of Cadiz: Geochimica et Cosmochimica Acta, v. 106, p. 261–286, doi:10.1016/j.gca.2012.12.016.

Hensen, C., Nuzzo, M., Hornibrook, E., Pinheiro, L.M., Bock, B., Magalhães, V.H., and Brückmann, W., 2007, Sources of mud volcano fluids in the Gulf of Cadiz - indications for hydrothermal imprint: Geochimica et Cosmochimica Acta, v. 71, p. 1232–1248, doi:10.1016/j.gca.2006.11.022.

Hollister, C.D., Ewing, J.I., Habib, D., Hathaway, J.C., Lancelot, Y., Luterbacher, H., Paulus, F.J., Poag, C.W., Wilcoxon, J.A., and Worstell, P., 1972, Site 105 - Lower continental rise hills: Deep Sea Drilling Program, Initial Reports Volume 11: Washington, D.C., Deep Sea Drilling Program, p. 219–312.

Kopf, A., 2002, Significance of mud volcanism: Reviews of Geophysics, v. 40, p. 1–52, doi:10.1029/2000RG000093.

Lawrence, J.R., Gieskes, J.M., and Broecker, W.S., 1975, Oxygen isotope and cation composition of DSDP pore waters and the alteration of Layer II basalts: Earth and Planetary Science Letters, v. 27, p. 1–10, doi:10.1016/0012-821X(75)90154-5.

Magalhães, V.H., et al., 2012, Formation processes of methane-derived authigenic carbonates from the Gulf of Cadiz: Sedimentary Geology, v. 243–244, p. 155–168, doi:10.1016/j.sedgeo.2011.10.013.

Martínez-Loriente, S., Gràcia, E., Bartolome, R., Sallarès, V., Connors, C., Perea, H., Lo Iacono, C., Klaeschen, D., Terrinha, P., Dañobeitia, J.J., and Zitellini, N., 2013, Active deformation in old oceanic lithosphere and significance for earthquake hazard: Seismic imaging of the Coral Patch Ridge area and neighboring abyssal plains (SW Iberian Margin): Geochemistry Geophysics Geosystems, v. 14, p. 2206–2231, doi:10.1002/ggge.20173.

Mazzini, A., Nermoen, A., Krotkiewski, M., Podladchikov, Y., Planke, S., and Svensen, H., 2009, Strike-slip faulting as a trigger mechanism for overpressure release through piercement structures. Implications for the Lusi mud volcano, Indonesia: Marine and Petroleum Geology, v. 26, p. 1751–1765, doi:10.1016/j.marpetgeo.2009.03.001.

Mottl, M.J., Wheat, C.G., and Monnin, C., 2000, Site 1023–1032: Data report: Trace elements in porewater, eastern flank of the Juan de Fuca Ridge: Proceedings Ocean Drilling Program, Scientific results, Volume 168: College Station, Texas, Ocean Drilling Program, p. 105–109.

Scholz, F., Hensen, C., Reitz, A., Romer, R.L., Liebetrau, V., Meixner, A., Weise, S.M., and Haeckel, M., 2009, Isotopic evidence ($^{87}Sr/^{86}Sr$, $\delta^{7}Li$) for alteration of the oceanic crust at deep-rooted mud volcanoes in the Gulf of Cadiz, NE Atlantic Ocean: Geochimica et Cosmochimica Acta, v. 73, p. 5444–5459, doi:10.1016/j.gca.2009.06.004.

Sibson, R.H., 1987, Earthquake rupturing as a mineralizing agent in hydrothermal systems: Geology, v. 15, p. 701–704, doi:10.1130/0091-7613(1987)15<701:ERAAMA>2.0.CO;2.

Stein, C.A., Stein, S., and Pelayo, A., 1995, Heat flow and hydrothermal circulation, *in* Humphris, S.E., et al., eds., Seafloor Hydrothermal Systems: Physical, Chemical, Biological, and Geological Interactions, Volume 91: Washington DC, American Geophysical Union, p. 425–445.

Sumner, R.H., and Westbrook, G.K., 2001, Mud diapirism in front of the Barbados accretionary wedge: the influence of fracture zones and North America - South America plate motions: Marine and Petroleum Geology, v. 18, p. 591–613, doi:10.1016/S0264-8172(01)00010-1.

Terrinha, P., et al., 2009, Morphotectonics and strain partitioning at the Iberian-Africa plate boundary from multibeam and seismic reflection data: Marine Geology, v. 267, p. 156–174, doi:10.1016/j.margeo.2009.09.012.

Viola, G., Andreoli, M., Ben-Avraham, Z., Stengel, I., and Reshef, M., 2005, Offshore mud volcanoes and onland faulting in southwestern Africa: neotectonic implications and constraints on the regional stress field: Earth and Planetary Science Letters, v. 231, p. 147–160, doi:10.1016/j.epsl.2004.12.001.

Von Damm, K.L., 1990, Seafloor hydrothermal activity: Black smoker chemistry and chimneys: Annual Review of Earth and Planetary Sciences, v. 18, p. 173–204, doi:10.1146/annurev.ea.18.050190.001133.

Von Herzen, R., 2004, Evidence for continuing hydrothermal circulation in old crust, *in* Davis, E.E., and Elderfield, H., eds., Hydrogeology of the Oceanic Lithosphere: Cambridge, UK, Cambridge University Press, p. 414–447.

Zitellini, N., et al., 2009, The quest for the Africa-Eurasia plate boundary west of the Strait of Gibraltar: Earth and Planetary Science Letters, v. 280, p. 13–50, doi:10.1016/j.epsl.2008.12.005.

Manuscript received 14 October 2014
Revised manuscript received 19 December 2014
Manuscript accepted 20 January 2015

Printed in USA

Geology, published online on 27 February 2015 as doi:10.1130/G36359.1

Geology

Strike-slip faults mediate the rise of crustal-derived fluids and mud volcanism in the deep sea

Christian Hensen, Florian Scholz, Marianne Nuzzo, Vasco Valadares, Eulàlia Gràcia, Pedro Terrinha, Volker Liebetrau, Norbert Kaul, Sonia Silva, Sara Martínez-Loriente, Rafael Bartolome, Elena Piñero, Vitor H. Magalhães, Mark Schmidt, Stephan M. Weise, Marina Cunha, Ana Hilario, Hector Perea, Lorenzo Rovelli and Klas Lackschewitz

Geology published online 27 February 2015;
doi: 10.1130/G36359.1

Notes

Tectonophysics 548–549 (2012) 1–21

Contents lists available at SciVerse ScienceDirect

Tectonophysics

journal homepage: www.elsevier.com/locate/tecto

Thrust–wrench interference between major active faults in the Gulf of Cadiz (Africa–Eurasia plate boundary, offshore SW Iberia): Tectonic implications from coupled analog and numerical modeling

F.M. Rosas [a,b,*], J.C. Duarte [a,b,d,1], M.C. Neves [a,c], P. Terrinha [a,d], S. Silva [a,b,d], L. Matias [a,e], E. Gràcia [f], R. Bartolome [f]

[a] Instituto Dom Luiz, Campo Grande, Ed. C1, Piso 2, 1749-016 Lisboa, Portugal
[b] Universidade de Lisboa, Faculdade de Ciências, Departamento de Geologia, Campo Grande, Ed. C6, Piso 4, 1749-016 Lisboa, Portugal
[c] Universidade do Algarve, 8000 Faro, Portugal
[d] LNEG, Unidade de Geologia Marinha, Estrada da Portela Zambujal-Alfragide Apartado 7586, 2720-866 Amadora, Portugal
[e] Universidade de Lisboa, Faculdade de Ciências, Departamento de Engenharia Geográfica, Geofísica e Energia, Campo Grande, Ed. C8, Piso 0, 1749-016 Lisboa, Portugal
[f] Unitat de Tecnologia Marina-CSIC, Centre Mediterrani d'Investigacions Marines i Ambientals, Pg. Marítim de la Barceloneta 37-49, 08003 Barcelona, Spain

ARTICLE INFO

Article history:
Received 4 October 2011
Received in revised form 13 April 2012
Accepted 20 April 2012
Available online 30 April 2012

Keywords:
Gulf of Cadiz
Thrust–wrench tectonics
Analog and numerical modeling
Fault interference
Multi-rupture seismic hazards
Lithospheric mantle seismicity

ABSTRACT

Analog and numerical modeling experiments were carried out to investigate the tectonic interference between intersecting major active strike–slip and thrust faults in the Gulf of Cadiz (Africa–Eurasia plate boundary, offshore SW Iberia). The obtained results show that newly mapped tectonic features located in the fault intersection area (corner zone) consist mostly in oblique (dextral-reverse) faults that accommodate significant strain partitioning. Modeling of this corner-zone faults show that they have endured some degree of rotation, displaying successive evolving geometries and kinematics. Numerical modeling results further show that an interbedded shallow soft layer, accounting for a regional (Late Miocene) gravitational "Chaotic" unit, could explain the mild bathymetric expression of the fault pattern in the corner-zone. Moreover, a recognized depth discrepancy, between the (upper crust) interference fault-pattern and the (lithospheric mantle) seismicity, is interpreted as a manifestation of similar thrust–wrench tectonic interference at different lithospheric depths. Accordingly, an intermediate lower crust–upper mantle aseismic (i.e. softened) depth-domain could be explained by pervasive alteration/serpentinization, prompted by fluid percolation through fault-related fractures associated with the newly revealed corner zone fault-network. Overall obtained results reinforce the relevance of a thrust–wrench multi-rupture seismic scenario as the main cause for the moderate seismicity (Mw<6.0) in the study area.

1. Introduction

The Gulf of Cadiz (Fig. 1A) has long been considered a key domain to unravel the complex tectonics of the Eurasia–Africa plate boundary (e.g. Duarte et al., 2011; Gràcia et al., 2003a,b; Gutscher et al., 2002, 2009a,b; Rosas et al., 2009; Sallarès et al., 2011; Sartori et al., 1994; Terrinha et al., 2003, 2009; Tortella et al., 1997; Zitellini et al., 2001, 2004, 2009). It corresponds to a specific segment of this boundary characterized by the interplay between the Iberia and Nubia subplates, connecting the (Atlantic) transform Gloria Fault, to the West, with the dextral transpressive Rif–Tell shear zone (Morel and Meghraoui, 1996) to the East of Straits of Gibraltar, and across the Betic–Rif orogenic arc.

In the Gulf of Cadiz domain, the Iberia–Nubia plate boundary has been considered of a diffuse nature (e.g. Medialdea et al., 2004; Sartori et al., 1994). Accordingly, present day WNW–ESE convergence between both plates at a ~4–5 mm/yr rate, (e.g. Fernandes et al., 2007; Nocquet and Calais, 2004; Serpelloni et al., 2007; Stich et al., 2006, gray line in the inset of Fig. 1B) is here accommodated by a considerable number of widespread and differently orientated active tectonic structures, mostly consisting of strike–slip and thrust faults (Fig. 1B). During the last decade, the acquisition and interpretation of geophysical data (e.g. reflection/refraction seismics and multi-beam swath bathymetry) led to the progressive discovery of several new morphotectonic features, resulting in the continuous improvement of the Gulf of Cadiz tectonic map (see Fig. 1B, Bartolome et al., accepted for publication; Duarte et al., 2009, 2010; Gràcia et al., 2003a,b; Rosas et al., 2009; Terrinha et al., 2003, 2009; Zitellini et al., 2004, 2009). Recently, based on a new wide-angle refraction seismic (WAS) profile (Fig. 1B), Sallarès et al. (2011) provided new insight on the nature of the crust across different morphotectonic domains in the central part of the Gulf of Cadiz, and

* Corresponding author at: Universidade de Lisboa, Faculdade de Ciências, Departamento de Geologia, Campo Grande, Ed. C6, Piso 4, 1749-016 Lisboa, Portugal. Tel.: +351 21 7500375; fax: +351 21 7500064.
E-mail address: frosas@fc.ul.pt (F.M. Rosas).
[1] Now at Monash University, VIC 3800, Melbourne, Australia.

0040-1951/$ – see front matter © 2012 Elsevier B.V. All rights reserved.
doi:10.1016/j.tecto.2012.04.013

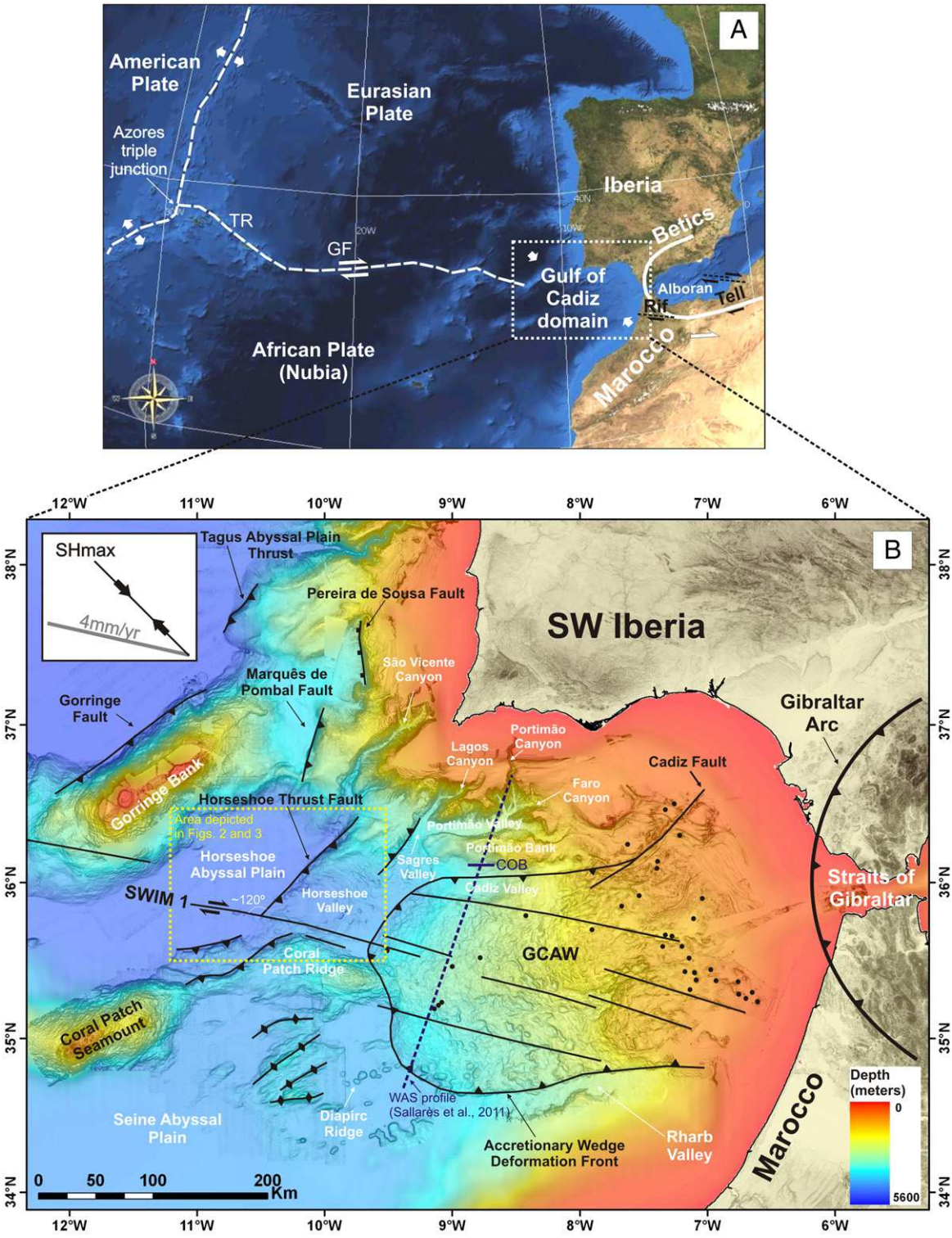
A
American Plate
Eurasian Plate
Azores triple junction
Iberia
TR
GF
Betics
Gulf of Cadiz domain
Alboran
Rif
Tell
African Plate (Nubia)
Marocco
B
SW Iberia
SHmax
4mm/yr
Tagus Abyssal Plain Thrust
Pereira de Sousa Fault
São Vicente Canyon
Marquês de Pombal Fault
Gorringe Fault
Gorringe Bank
Horseshoe Thrust Fault
Area depicted in Figs. 2 and 3
Horseshoe Abyssal Plain
SWIM 1
~120°
Horseshoe Valley
Coral Patch Ridge
Coral Patch Seamount
Seine Abyssal Plain
Diapirc Ridge
WAS profile (Sallarès et al., 2011)
Accretionary Wedge Deformation Front
Rharb Valley
Portimão Canyon
Lagos Canyon
Faro Canyon
Portimão Valley
Portimão Bank
COB
Sagres Valley
Cadiz Valley
Cadiz Fault
Gibraltar Arc
Straits of Gibraltar
GCAW
Depth (meters)
0
5600
0 50 100 200 Km
12°W
11°W
10°W
9°W
8°W
7°W
6°W
38°N
37°N
36°N
35°N
34°N
Thrust fault
Mud volcanoes
Dextral strike-slip faults (SWIM wrench system of Zitellini et al., 2009)
Normal fault
Antiform fold
Location of WAS profile of Sallarès et al. (2011)
COB: Continent-Ocean Boundary as proposed by Sallarès et al. (2011)

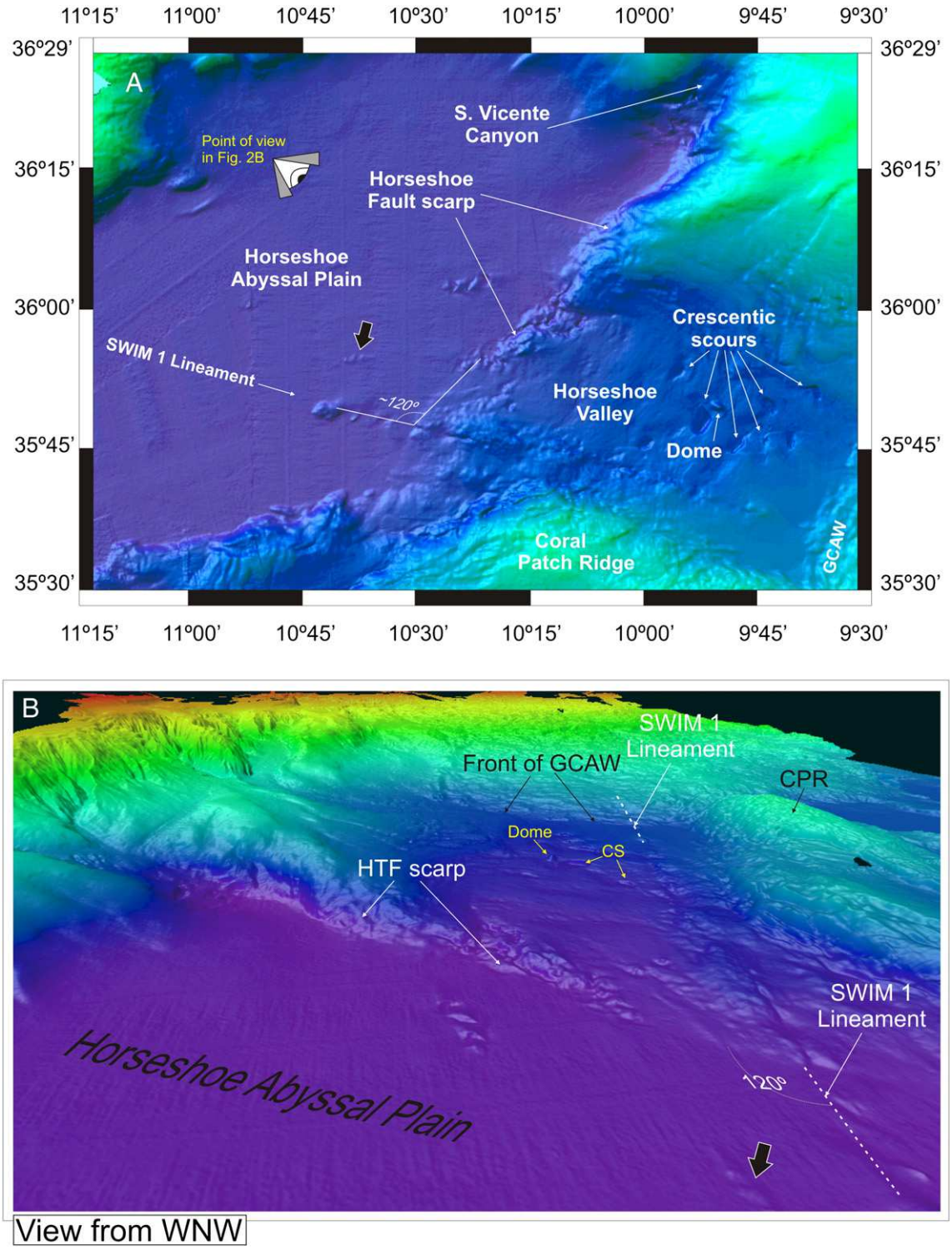

Fig. 2. (A) Detailed bathymetry and main morphological features in the study area (dashed-lined rectangle in Fig. 1B). (B) Perspective view (from WNW). HTF: Horseshoe Thrust Fault; GCAW: Gulf of Cadiz Accretionary Wedge; CS: Crescentic scours (Duarte et al., 2010); CPR: Coral Patch Ridge. Black arrow signals the location of the mild bathymetric perturbation associated to Corner fault 1 (CF1 in Figs. 3 and 5). Digital 3D bathymetry model (vertical exaggeration factor of 8) from SWIM dataset (Zitellini et al., 2009).

proposed the location of the lithospheric continent–ocean boundary (COB) at a distance of approximately 100 km from the Southern Iberian coast line (see COB in Fig. 1B).

The seismicity that has been recorded in the Gulf of Cadiz corresponds to a general scenario of moderate magnitude at shallow to intermediate depths (e.g. Borges et al., 2001; Buforn et al., 1995, 2004;

Fig. 1. (A) Location of the Gulf of Cadiz area in the general tectonic setting of the Euroasia (Iberia)–Africa (Nubia) plate boundary. TR: Terceira Ridge; GF: Gloria Fault. (B) Simplified tectonic map of the Gulf of Cadiz area (tectonic interpretation from Zitellini et al., 2009); Bathymetry from SWIM compilation of Zitellini et al. (2009) completed with GEBCO (2003). GCAW — Gulf of Cadiz Accretionary Wedge; Black dots correspond to the location of known mud volcanoes (e.g. Hensen et al., 2007). Inset in the upper left showing (in black) the average direction of the Maximum Horizontal Stresses — SHmax, and (in gray) the average direction of the ~4 mm/yr convergence rate between Nubia and Iberia (Fernandes et al., 2007; Nocquet and Calais, 2004; Stich et al., 2006). Blue dashed line marks the location of the WAS profile of Sallarès et al. (2011).

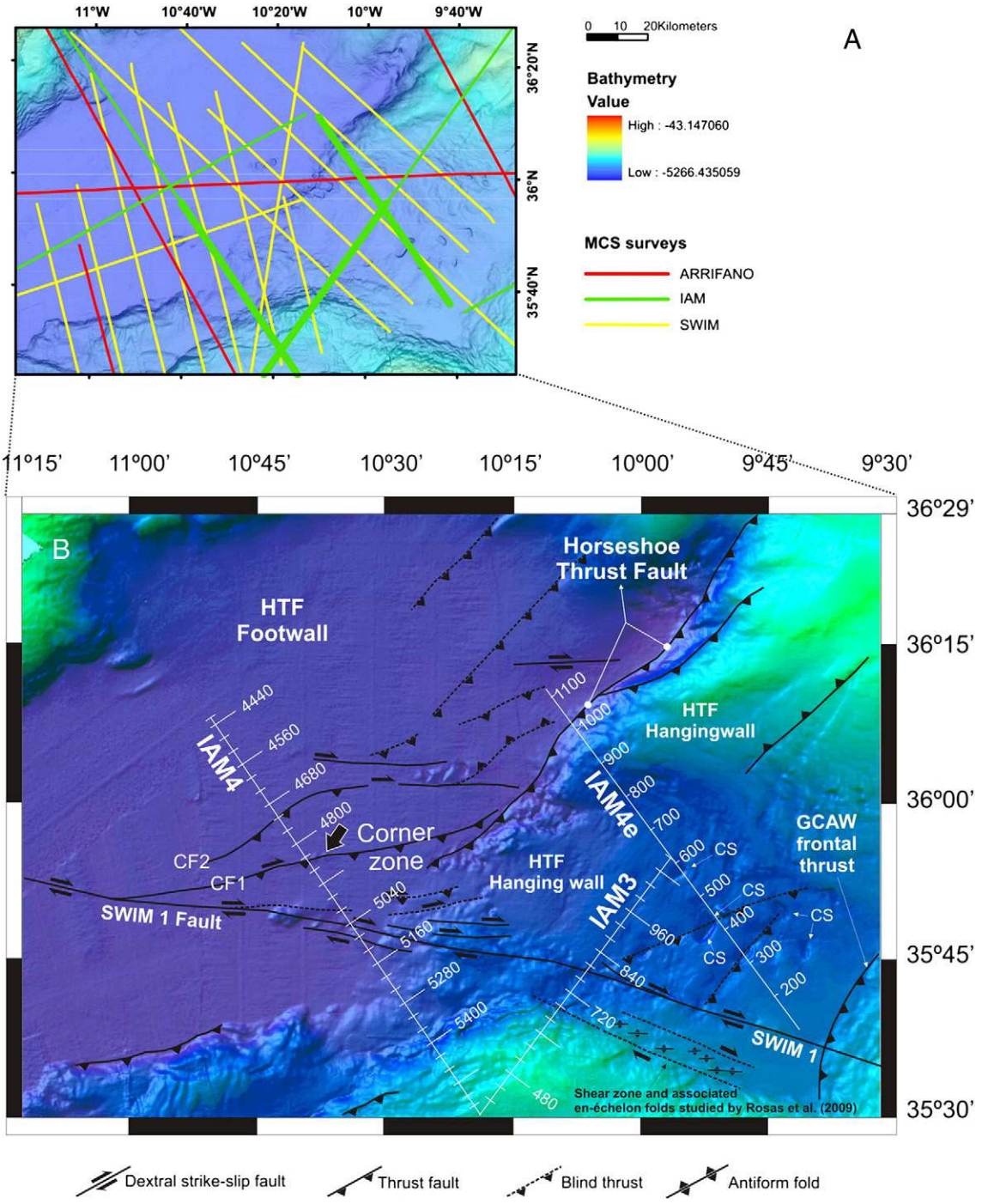

Fig. 3. (A) General seismic reflection dataset used as a basis for the new tectonic interpretation proposed for the corner zone study area (dashed-lined rectangle in Fig. 1B, ARRIFANO — Arco Rifano, IAM — Iberian Atlantic Margin, and SWIM — South West Iberian Margin surveys, Banda et al., 1995; Martinez-Loriente et al., 2008; Sartori et al., 1994; Tortella et al., 1997). Thick green lines correspond to the IAM4e and IAM4–IAM3 multi-channel seismic profiles shown in B and Figs. 4 and 5; (B) Newly proposed tectonic map of the study area, mostly corresponding to the (corner) zone of intersection between the SWIM 1 dextral strike–slip fault, and the Horseshoe Thrust Fault (HTF). CF1 and CF2: Corner faults (CS, GCAW and black arrow as in Fig. 2B).

Engdahl et al., 1998; Fukao, 1973; Grimison and Chen, 1986; Stich et al., 2005), in which, though, a direct correlation between earthquake location and known major tectonic structures is not straightforward. Large magnitude instrumental and historical events also occurred, such as the 28/02/1969 earthquake (Ms = 7.9), and the highly destructive 1755 Great Lisbon Earthquake (estimated magnitude between 8.5 and 8.8, e.g. Abe, 1979; Johnston, 1996; Solares and Arroyo, 2004), and associated tsunami (e.g. Baptista and Miranda, 2009; Baptista et al., 1998a,b; Terrinha et al., 2003; Zitellini et al., 2001). The recurrence interval of these great events (Mw > 8.0) has been estimated in 1800 years based on turbidite paleoseismology approach (Gràcia et al., 2010). In addition, a network of broadband OBS deployed in the area during a year, confirmed greater depths for low-magnitude local earthquakes (40–60 km, Geissler et al., 2010), highlighting the relevance of seismogenic mantle rheology and deep lithospheric structures, complementary to the known (i.e. mapped) shallower crustal faults. The seismic and tsunami hazard posed by the high-magnitude earthquakes continue to trigger the interest, and the need, to search for their seismogenic sources, and hence to better understand the tectonic evolution of the region.

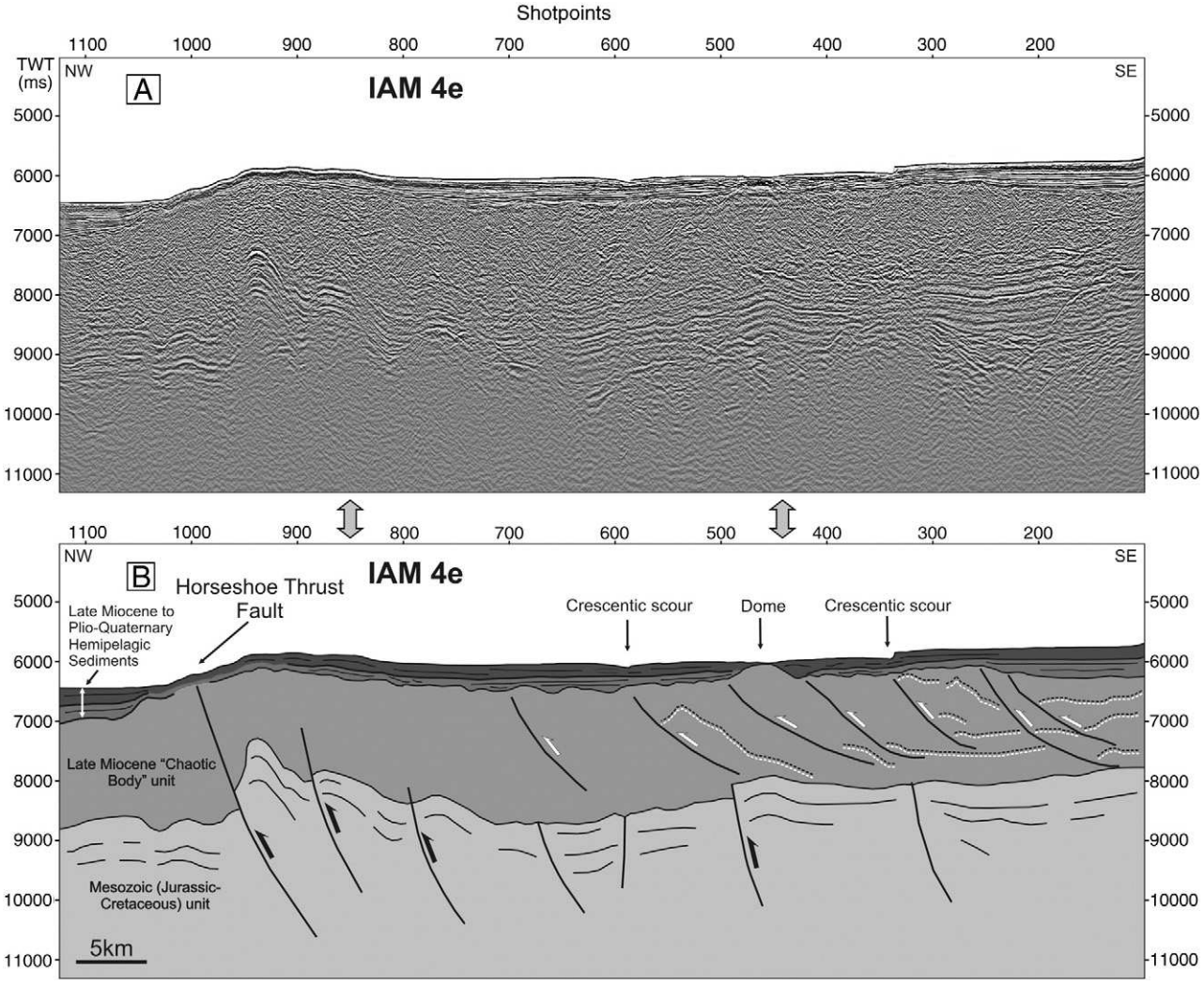

Fig. 4. (A) Multi-channel seismic profile IAM-4e (see Fig. 3 for location); and (B) correspondent seismostratigraphic and tectonic interpretation (adapted from Duarte et al., 2010). Thin black lines: seismic reflectors interpreted as stratigraphic horizons; Double-dashed black and white lines: intra-chaotic body reflections interpreted as decollement horizons and folded layered sediments.

1.1. Present work

In the study area, a new morphotectonic pattern is revealed in the zone of intersection (corner zone) between a main regional thrust, the so called Horseshoe Thrust Fault (Horseshoe Fault of Gràcia et al., 2003b), and a major dextral strike–slip fault, the SWIM 1 Fault (Zitellini et al., 2009), crossing each other and making an angle of ~120°/60° (HTF and SWIM 1in Figs. 1B, 2 and 3). The new corner zone tectonic structures, and their correspondent geometry and kinematics are here interpreted as resulting from regional, active, thrust–wrench tectonic interference. Based on the previously established regional seismostratigraphy, and on newly interpreted seismotectonic data, this assumption is tested through coupled analog, and 3D finite-element numerical modeling. Both modeling approaches assume (brittle) upper-crust mechanical interference. Obtained results are further compared with the natural example, and ensuing implications for the overall tectonic evolution of the Gulf of Cadiz are discussed.

2. Regional tectonic setting

In the Gulf of Cadiz tectonic map of Fig. 1B three main sets of major faults can be recognized: 1) The thrust front that bounds the so called Gulf of Cadiz Accretionary Wedge (GCAW, in the eastern half of the study area, Fig. 1B); 2) a set of NE–SW striking thrust-faults, preferably located to the west of the Horseshoe Valley (e.g. Horseshoe Thrust Fault, Marquês de Pombal Fault, Gorringe Fault, and Tagus Abyssal Plain Thrust); and 3) a set of WNW–ESE dextral strike–slip faults, corresponding to the SWIM wrench system, as defined by Zitellini et al. (2009).

The GCAW was interpreted as an accretionary wedge related with the eastwards dipping (roll back) subduction of an oceanic lithospheric slab beneath the Gibraltar arc (Gutscher, 2004; Gutscher et al., 2002). The same authors considered this subduction zone as the seismogenic source of the 1755 Great Lisbon Earthquake, although its present day activity is still intensively debated (Duarte et al., 2011; Gràcia et al., 2003a,b; Gutscher, 2004; Gutscher et al., 2002, 2009a,b; Terrinha et al., 2003, 2009; Zitellini et al., 2004, 2009).

The set of NE–SW thrusts includes the studied northwest-directed Horseshoe Thrust Fault (see Fig. 1B) that is considered one of the most significant structures in the Gulf of Cadiz, active since at least Tortonian times (~10 My, e.g. Gràcia et al., 2003a,b; Terrinha et al., 2009; Zitellini et al., 2004). This major thrust was previously proposed to share a common detachment with other NE–SW thrusts in the area, namely with the Marquês de Pombal Fault (MPF), with which it was also thought to represent an alternative source for the 1755 Great Lisbon Earthquake (Gràcia et al., 2003a,b; Terrinha et al., 2003, 2009). As a whole, these regional major thrusts (see Fig. 1B) were firstly hypothetically interpreted by Ribeiro et al. (1996) as

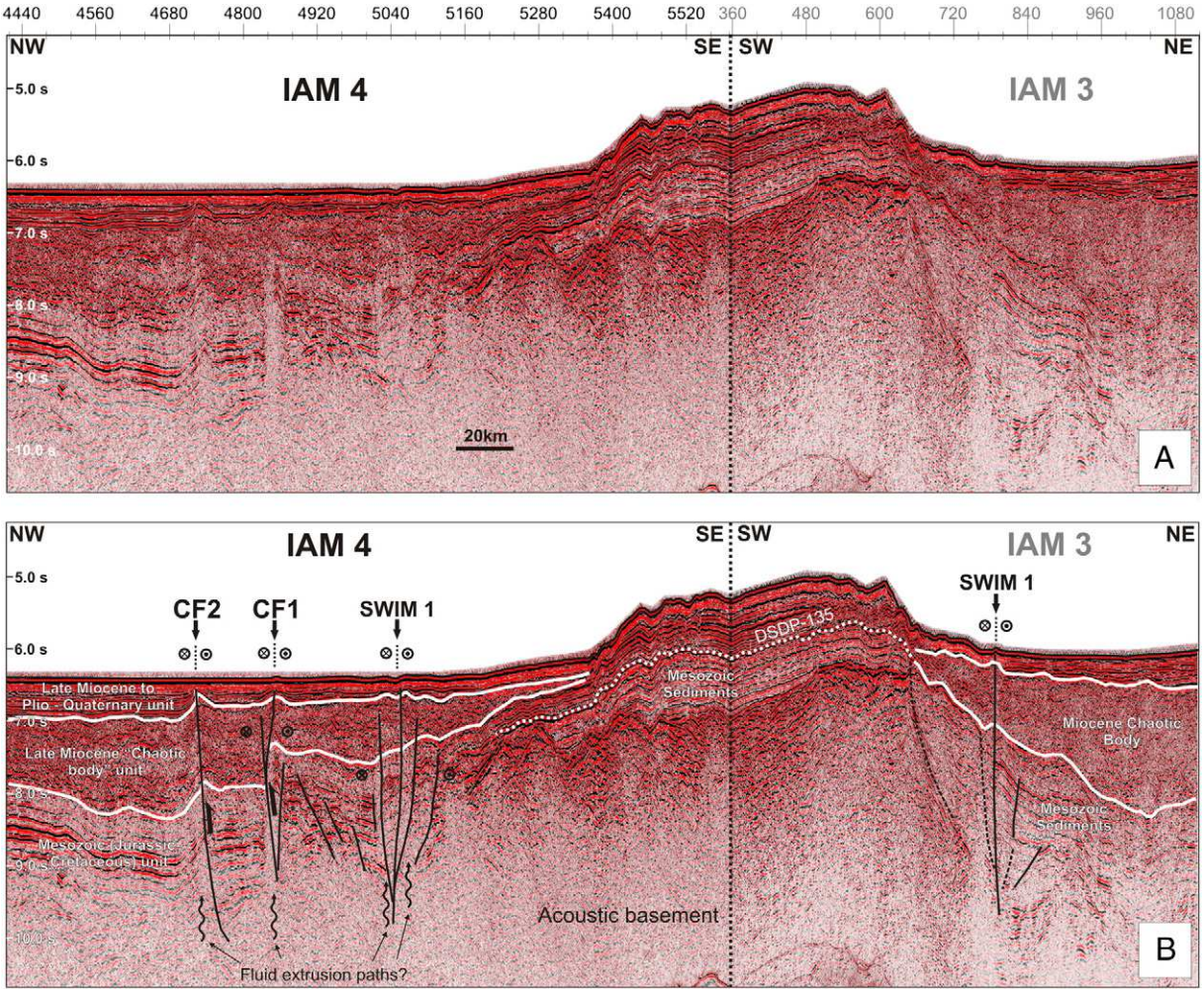

Fig. 5. (A) Multi-channel seismic profiles IAM4 and IAM3 (see Fig. 3 for location); and (B) correspondent seismostratigraphic and tectonic interpretation (modified after Rosas et al., 2009). DSDP-135 marks the seismostratigraphic top of the Mesozoic units.

early manifestations of the tectonic reactivation of the southwest Iberian margin, representing the onset of subduction initiation along this segment of the Atlantic passive margin. More recently, Terrinha et al. (2009) considered these same structures as part of an en-échelon 300 km long N–S trending fault system, extending between latitude ~35.5°N and 38°N. The same authors interpreted this system as the expression of a diachronic westwards and northwards migration of the deformation in the Gulf of Cadiz, from Late Miocene times to Present day. Accordingly, during this period of time active deformation would have propagated from the GCAW thrust front to the west (e.g. HTF and Gorringe Fault), and further to the north along the SW Iberian margin (e.g. MPF and Tagus Abyssal Plain Thrust). These same authors also argue for the present day existence of large scale strain partitioning in the Gulf of Cadiz, comprising not only the activity of the NE–SW thrust system, but also active dextral wrenching ascribed to the WNW–ESE SWIM system.

According to Zitellini et al. (2009) the SWIM system corresponds to a broad deformation band extending across the entire Gulf of Cadiz domain (along 600 km), essentially characterized by sets of major deep rooted, sub-vertical, dextral strike–slip faults (Bartolome et al., 2012). These SWIM faults (see Fig. 1B), which are thought to be active since at least ~1.8 My (Rosas et al., 2009), strike subparallel to the present day convergence direction between Nubia and Iberia (WNW–ESE, see gray line in the inset of Fig. 1B), and were interpreted as the precursor of a new (dextral) transcurrent plate boundary in the Gulf of Cadiz (Zitellini et al., 2009). Alternatively, Duarte et al. (2011) showed that the SWIM faults are more likely to correspond to the reactivation of the ancient Tethyan plate boundary.

In the study area the SWIM 1 Fault intersects the Horseshoe Thrust Fault (see Fig. 1B). Hence, some kind of tectonic interference between these two major active faults is expected to occur as a consequence.

2.1. Morphotectonic characterization of the study fault-systems

The area studied in detail in the present work is limited by the dash-lined rectangle in Fig. 1B, whose bathymetry and tectonic interpretation is depicted in Figs. 2 and 3, respectively. The newly proposed tectonic map of Fig. 3B corresponds mostly to the area of intersection between the Horseshoe Thrust and the SWIM 1 faults. This area was investigated through the detailed combined analysis of the available multibeam swath bathymetry (SWIM compilation, Zitellini et al., 2009), and numerous multi-channel seismic (MCS) reflection profiles. Sub-seafloor seismic interpretation has been essentially based on the SWIM-2006 high-resolution MCS cruise carried out on board the Spanish RV Hesperides (e.g. Bartolome et al., 2012; Gràcia et al., 2006; Martinez-Loriente et al., 2008) complemented with deeper penetration MCS profiles acquired during the IAM — Iberian Atlantic Margin, (e.g. Banda et al., 1995; Tortella et al., 1997) and ARRIFANO — Arco Rifano cruise (e.g. Sartori et al., 1994). A detailed morphological characterization of the NW Gulf of Cadiz domain, and its several different sub-domains, was recently presented by Terrinha et al. (2009). Consistently with their proposal, the main

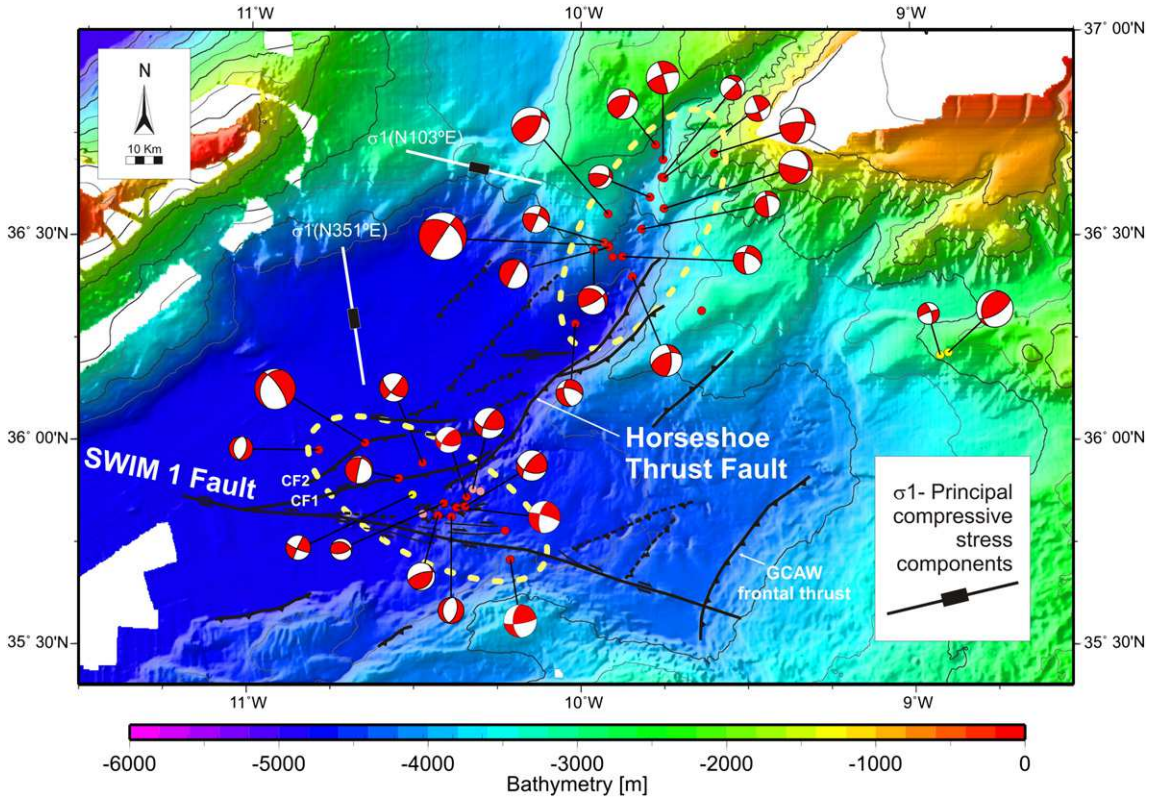

Fig. 6. Map of the newly proposed tectonic interpretation for the study area (as in Fig. 3B), showing the (dashed) elliptic outlines of low magnitude earthquake clusters and associated focal mechanisms reported by Geissler et al. (2010). Focal depths of <20 km (yellow dots), 40 to 55 km (red), and >55 km (pink) are indicated. Note the marked coincidence of the southern cluster with the intersection between the SWIM 1 and Horseshoe faults.CF1 and CF2: Corner faults. σ1: orientation of the main compressive stress components deduce from the focal mechanisms of each of the depicted clusters (adapted from Geissler et al., 2010).

large-scale bathymetric features in the study area are here interpreted as being tectonically controlled by the activity of the recognized major fault-systems (described below, see Figs. 2 and 3).

Based on the available seismic reflection dataset, a general seismostratigraphy was also previously established (e.g. Duarte et al., 2010; Sartori et al., 1994; Terrinha et al., 2009; Torelli et al., 1997; Tortella et al., 1997) comprising (Figs. 4 and 5): a) A basal Mesozoic (Jurassic–Cretaceous) unit (~2 s TWTT, two way travel time) corresponding to carbonate sediments; b) A Late Miocene gravitational "chaotic body" unit (~1.5 s TWTT) with a semi-chaotic seismic signature, previously interpreted as an olistostrome body or as a tectonic mélange (Iribarren et al., 2007; Terrinha et al., 2009; Torelli et al., 1997; Tortella et al., 1997); c) A top Late Miocene to Plio-Quaternary unit (~0.5 s TWTT), corresponding to a sequence of hemipelagic/turbidite sedimentary cover (Gràcia et al., 2010)..

Table 1
Analog modeling parameters and material properties.

Parameters and material properties	Quartz sand (model)	Natural prototype (upper crust)	Ratio: model/nature
Composition (%)	99.7% quartz	–	–
Grain shape	Well-rounded	–	–
Grain size (mm)	<0.30	–	–
Density (kg/m^{-3})	1300	2600	$\delta = 0.5$
Internal friction angle, ϕ (°)	~30	–	–
Coefficient of internal friction, μ_c	~0.6	0.6–0.85	–
Cohesion, c_0 (Pa)	Negligible	40×10^6	–
Gravity acceleration, g (m s^{-2})	9.81	9.81	$\gamma_g = 1$
Length, L (m)	0.01	2000	$\boldsymbol{\lambda = 5 \times 10^{-6}}$
Mass, M (Kg)	–	–	$\boldsymbol{\mu = 6.25 \times 10^{-17}}$

Scaled fundamental units are in **bold**.
A mean cohesion of $\mathbf{C_o = 40\ MPa}$ was assumed from the natural prototype (e.g. Hoshino et al., 1972; Weijermars et al., 1993).

2.1.1. The Horseshoe Thrust Fault

The NE–SW trending Horseshoe Thrust Fault scarp is clearly observed in the bathymetry (Fig. 2A and B), displaying a maximum height of ca. 1000 m in its north-easternmost segment, gradually vanishing towards the SW (Figs. 2 and 3). The SE part of the study area (mostly coinciding with the Horseshoe Valley at depths between 4200 m and 4800 m, see Fig. 2) is interpreted to correspond to the hanging wall of the NW directed HTF (e.g. Terrinha et al., 2009; Tortella et al., 1997; Zitellini et al., 2004), thus tectonically uplifted relatively to its footwall, which corresponds to the Horseshoe Abyssal Plain (HAP) in the NW half of the study area (at depths of >4800 m). In the IAM4e profile (Fig. 4), the HTF (around shotpoint 1000 in Fig. 4) is clearly imaged as a SE dipping, deep seated fault. It roots well into the Mesozoic unit, prolonging upwards across all the other overlying units, and breaching out at the seafloor surface, where the resulting prominent deformation is marked by an offset of ca. 420 m (~0.6 s TWTT in the IAM4e profile). The NW directed thrust kinematics is clearly shown by the geometry of the folds affecting the Mesozoic reflectors near the fault plane, and by the unambiguous offset of the surface marking the top of the Mesozoic unit (see Fig. 4). To the SE of the HTF other relatively minor thrusts affecting the basal Mesozoic unit were previously described (e.g. Duarte et al., 2010; Terrinha et al., 2009), although these only affect the base of the overlying Late Miocene chaotic body (see Fig. 4). The same authors also report some degree of tectonic imbrication within the Miocene chaotic body further to SE, only mildly perturbing the seafloor morphology.

2.1.2. The SWIM 1 Fault

The SWIM system was recently described by Zitellini et al. (2009) as corresponding to a set of WNW–ESE trending, vertical right-lateral strike–slip faults, characterized by a hundred-kilometer long linear bathymetric expression, ranging from the foot of the Gorringe Bank, in the West Gulf of Cadiz, across the HAP, the Horseshoe Valley and the GCAW, reaching its easternmost area near the Straits of Gibraltar (see Fig. 1B). The SWIM 1 Fault (Figs. 1–3) is crossed both by the IAM4 and the IAM3 seismic profiles (Fig. 5), where it can be observed to correspond to a deep-seated sub-vertical fault. It cuts across all the main seismostratigraphic units, occasionally breaching out, and rooting in the lower pre-Mesozoic (?) basement (at >9 km depth, Bartolome et al., accepted for publication). Some segments of the fault exhibit an overall geometry resembling flower-like structures (Fig. 5B), agreeing with the previously proposed transcurrent kinematics (e.g. Bartolome et al., accepted for publication; Duarte et al., 2009; Terrinha et al., 2009; Viola et al., 2005; Zitellini et al., 2009).

2.1.3. New interpretation of the tectonic corner zone

The SWIM 1 Fault intersects the Horseshoe thrust near its SW termination (Figs. 2 and 3). In the HAP, away from the HTF, the SWIM 1 lineament is not prominently recorded in the bathymetry. Nevertheless, the continuation of the correspondent basement strike–slip fault was thoroughly mapped farther to the west, up to the foothills of the Gorringe Bank flanking its south-western termination (see Figs. 1B and 3B, Bartolome et al., accepted for publication; Duarte et al., 2009; Terrinha et al., 2009). The available seismic dataset in this specific area (see Fig. 3A) leads to a newly interpreted tectonic configuration (see map of Fig. 3B) comprising a new set of faults (CF1 and CF2) located near the corner zone of intersection between the SWIM 1 strike–slip and the Horseshoe thrust. In the IAM4 profile (Fig. 5) it is possible to observe that these corner faults correspond to steep (southwards) dipping faults, rooting in the basement underneath the Mesozoic unit and cutting across the overlying ones, including the base of the Late Miocene to Plio-Quaternay top unit. In the case of CF1, the seafloor surface is only mildly perturbed (around SP 4840 in IAM4 profile, and black arrow in Figs. 2 and 3B), whereas CF2 lacks any kind of bathymetric expression. In the IAM4 profile a reverse-fault component of movement along both CF1 and CF2 faults is apparent, revealed namely by the offset of the upper limit of the Mesozoic unit across these faults that clearly denounces the upward movement of the respective SE fault blocks (see Fig. 5). Since the faults are very steep, a pure dip–slip thrusting movement is mechanically implausible in this situation. In contrast, oblique–slip faults, characterized by a predominantly dextral transcurrent kinematics and a minor SE-side up thrusting component, would fit the observed structural geometry.

Adding to this structural evidence, the recently proposed relocation of low to moderate magnitude earthquakes in the study area (Geissler et al., 2010), showed the existence of two clusters of seismic events near the northern and southern terminations of the HTF (Fig. 6, Geissler et al., 2010). The southern cluster coincides with the SWIM 1–HTF corner zone area, and exhibits a WNW–ESE general trend parallel to the SWIM 1 Fault. It should be noted that the great majority of these hypocenters are located at relatively high depths, between 40 and 55 km (red dots in Fig. 6), with only a few located out of this depth interval (see Fig. 6: focal depths<20 km — yellow dots; >55 km — pink dots). This shows that most of these earthquakes are probably located in the lithospheric mantle (Geissler et al., 2010; Sallarès et al., 2011), and thus cannot be directly linked to the faults imaged by the MCS profiles at upper crustal levels (maximum depths of ca. 6 km; see discussion below in Section 5). Nevertheless, the corresponding focal mechanism solutions reported in this corner zone domain show significant heterogeneity, possibly due to variable fault orientation, but generally accounting for dominant reverse and strike–slip faulting (Geissler et al., 2010).

These tectonic and seismic corner-zone manifestations are here suggested to have formed as the result of a particular type of thrust–wrench tectonic interference between the Horseshoe and the SWIM systems at different depths. This interference is here investigated and tested at upper crustal level through the analog and numerical modeling experiments presented below.

3. Analog modeling

Analog modeling experiments of separated wrench systems (e.g. Dooley and McClay, 1997; Le Guerroue and Cobbold, 2006; Mandl et al., 1977; McClay and Bonora, 2001; Richard et al., 1991; Schopfer and Steyrer, 2001) and thrust systems (e.g. Agarwal and Agrawal, 2002; Bonnet et al., 2007; Ellis et al., 2004; Gutscher et al., 1998a,b; Lallemand et al., 1994; Lohrmann et al., 2003; Malavieille, 1984, 2010; McClay et al., 2004; Mulugeta, 1988; Zhou et al., 2007) are common and well documented. Conversely, physical modeling dealing with the deformation caused by simultaneous thrusting and wrenching is less common, and generally focused on a variety of different specific aspects (e.g. Di Bucci et al., 2006, 2007; Diraison et al., 2000; Viola et al., 2004). Hence the present work, in which sand-box analog models were produced to better understand the deformation patterns resulting from thrust–wrench fault interference under the specific conditions of the study area.

3.1. Experimental method

3.1.1. Material properties and scaling

Experiments were done using dry quartz sand whose properties are summarized in Table 1. Sand is considered a Coulomb material deforming in a brittle way according to the Coulomb fracture criterion (e.g. Davis et al., 1983; Hubbert, 1937, 1951, Appendix A), and it has been extensively used in scaled model experiments simulating brittle deformation in the upper crust or other lithospheric competent levels. Assuming a brittle behavior for the modeled upper crust, the main material properties sustaining the dynamic similarity between this and the sand are the internal friction (μ_c) and the cohesion (c_0). The first is dimensionless, and approximately the same in both model and prototype (see Table 1), whereas the second has dimension of stress and must be scaled accordingly (Hubbert, 1937, and detailed explanation in Appendix A). Thus, for negligible inertial accelerations as in the present case, the model/prototype cohesion ratio (Σ) is ultimately dependent on the product of correspondent density (δ) and length (λ) ratios, which values are shown in Table 1 (see also Appendix A). It should be noted that since density ratio (δ) is generally close to 1 (between 0.5 and 0.7, e.g. Withjack et al., 2007) the strength of the materials expressed by Σ is scaled mostly through the length ratio (λ). Given the fact that in the present case $\lambda = 5\times10^{-6}$, and since cohesion for upper crustal rocks is clearly typically less than 50 MPa, it becomes immediately evident the utility of model materials with very low cohesion (<100 Pa), such as dry quartz sand, as analogs of upper crustal rocks. Since brittle deformation is time independent, scaling was achieved through considering model-prototype ratios for length (λ) and mass (μ) fundamental units alone (see Table 1).

3.1.2. Apparatus, initial stage and procedure

All the experiments were carried out in the 1000×600 mm Perspex deformation box depicted in Fig. 7. The box consists of two horizontal 10 mm thick basal plates (plates A and B in Fig. 7) that move relatively to each other along the X direction, simulating a right-lateral strike–slip (basement) fault. A thin metal sheet attached to the base of a backstop is moved by a stepping motor also along the X direction, sliding on top of both basal plates (Fig. 7A). The front of this metal sheet works as a velocity discontinuity (VD) making an angle of 60°/120° with the direction of the strike–slip fault (X direction). Two fixed lateral vertical walls confine the whole system. In

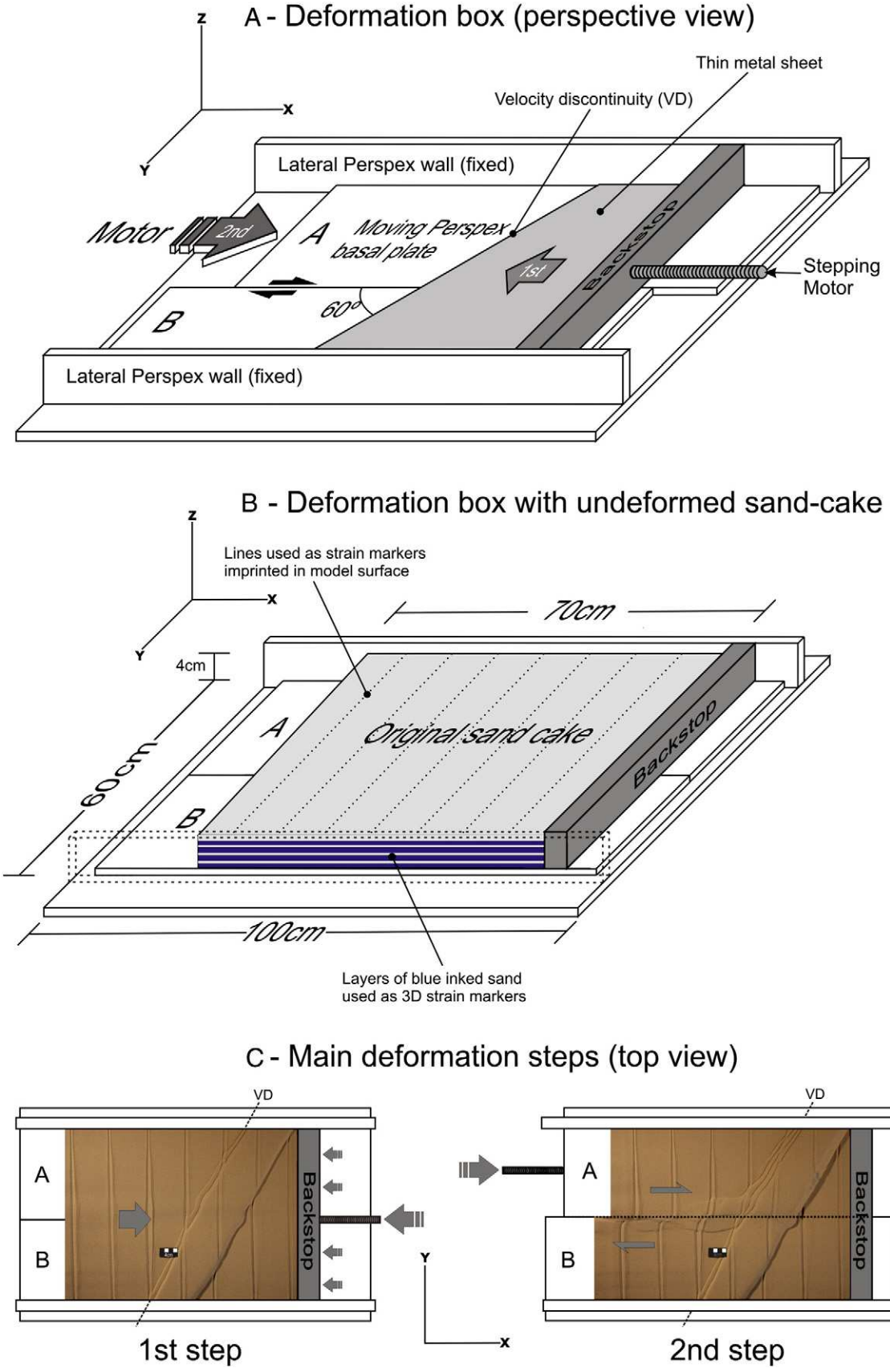

Fig. 7. Analog modeling experimental apparatus and setup. (A) Perspex deformation box. Arrows (1st and 2nd) indicate movement induced by stepping motors during the first and second experimental steps respectively. (B) Experimental initial stage depicting the sand cake prepared inside the Perspex box before the onset of deformation. (C) Top view of first and second experimental steps (see detail explanation in the text). VD — Velocity discontinuity. Notice Cartesian coordinate system (upper left).

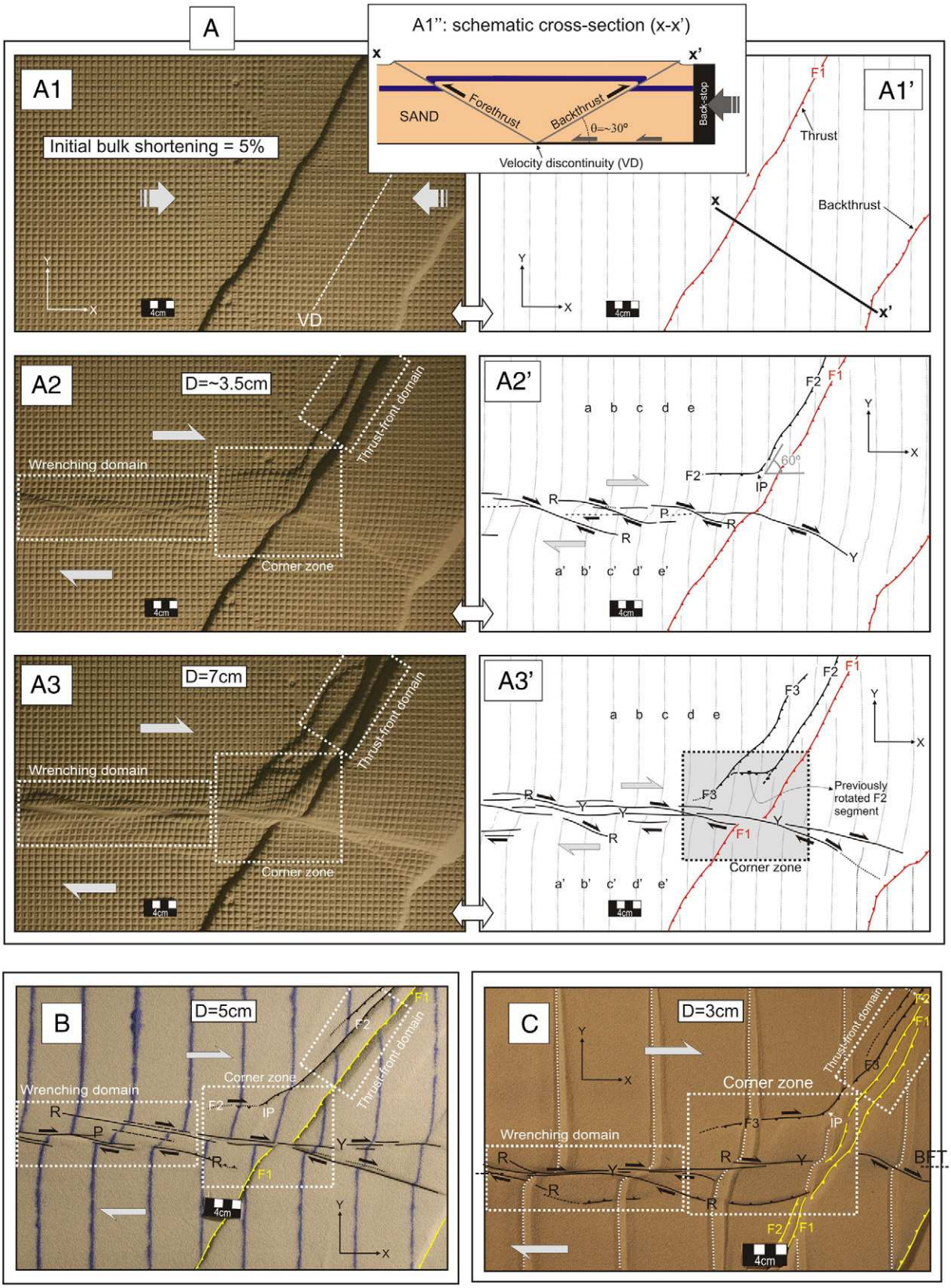

Fig. 8. Analog modeling results: top view photos and interpretation. All models are dynamically scaled relatively to the natural prototype (see Appendix A for details), length scale $\lambda = 1/200.000$. (A) Results for a considered sand-cake thickness of 5 cm (10 km). (A1–A1′) Experimental step 1 corresponding to initial bulk shortening (Inset A″: schematic cross-section). (A2, A3) Successive stages of experimental step 2, after basal-plate strike–slip displacement of 3.5 cm and 7 cm, respectively (horizontal displacement given by labeled a–a′ to e–e′ strain-marker lines). (B, C): Experimental results for sand-cake thickness of 4 and 3 cm (8 and 6 km, respectively), showing consistent corner zone deformation patterns (see text for further detailed explanation). VD: Trace of velocity discontinuity; D: Strike–slip displacement; F1–F3: Thrust faults (orange and yellow indicate faults originated during experimental step 1); R: Riedel-faults; Y: Y-faults (strike–slips); P: P-shears. Notice Cartesian coordinate system.

the initial stage, a layered sand cake was prepared inside the box on top of the intersection between the basal strike–slip fault and the velocity discontinuity (Fig. 7B). This was achieved by pouring batches of differently colored sand from a moving elongated funnel (with a width matching the one of the box), guarantying the leveling of its top surface. In most experiments the sand cake thickness was 3 cm (corresponding to 6 km in nature), although in several experiments thickness of 4 and 5 cm (8 and 10 km) were also used. Layering in the sand cake has no correspondence with any natural structures, and was used merely as a 3D strain marker, since at the end-stage of all the experiments the deformed sand cake was humidified, and several slices were serially cut along different chosen orientations. Likewise, parallel (or sometimes square) line grids were also imprinted on the top surface of the model to serve as (2D) passive strain markers.

In the present modeling the driving kinematics was conceived to correspond to the basal right-lateral strike–slip faulting, concurring with the natural example where the dextral SWIM faults are observed to strike subparallel to the present day convergence between Iberia and Nubia as shown by the reported geodetic data (e.g. Fernandes et al., 2007; Nocquet and Calais, 2004; Serpelloni et al., 2007; Stich et al., 2006, see gray line in the inset of Fig. 1B). It was assumed for all the experiments that when the SWIM fault system was active, a morphotectonic expression of the Horseshoe Thrust Fault already existed. This complies with the previously reported concept of counterclockwise rotation of the convergence direction between Iberia and Nubia subplates, from NW–SE in Late Miocene times, to Present day WNW–ESE (e.g. Duarte et al., 2011; Terrinha et al., 2009). Such rotation agrees with the notion of the NE–SW thrusting initiation being older than the WNW–ESE wrenching tectonic activity (Rosas et al., 2009; Terrinha et al., 2009; Zitellini et al., 2009). Furthermore, the interpretation of seismostratigraphic and tectonic overprint relationships, also shows the HTF to be active since at least Tortonian times (~10 My, e.g. Gràcia et al., 2003a,b; Terrinha et al., 2009; Zitellini et al., 2004), whereas the SWIM fault system only since ~1.8 My (Rosas et al., 2009; Terrinha et al., 2009). In accordance, all the experiments comprised the following two successive steps (see Fig. 7A and C):

1) A preliminary step that consisted in moving the backstop (and the attached thin metal sheet) along the X direction to the left, only until a few thrusts were observed to form breaching out at the top surface of the sand cake (Fig. 7C — step 1). This was done to produce an initial planar week anisotropy representing the original geometry of the HTF system, at an angle of 60/120° with the basal (SWIM) strike–slip direction.
2) A second step wherein the basal plates were moved relatively to each other (also along X), by pushing the farthest plate (basal plate A) to the right (Fig. 7C — step 2), producing a right-lateral movement along the vertical contact surface between both basal plates, simulating the SWIM 1 basement strike–slip fault.

During step 2, the central ("corner zone") domain of basal plate A was limited by two main kinematically active boundaries: one corresponding to the trace of the basal strike–slip fault, and the other to the velocity discontinuity (see Fig. 7A and C). Since the dextral strike–slip along the contact with plate B was accomplished by moving plate A to the right, the boundary between this plate and the over-sliding thin metal sheet (velocity discontinuity) corresponded to a convergent limit between the sand above basal plate A, and the sand sitting on top of the thin metal sheet (edged by the velocity discontinuity). Thus, the driving forces for deformation in the sand came from the relative movement between the sliding basal plates and the thin metal sheet, which were both in frictional contact with the overlying sand. As a result, during the second experimental step, the sand cake on top of the boundary between both basal plates endured dextral wrenching deformation, whereas simultaneously shortening accommodated by thrusting occurred in the sand above the velocity discontinuity. Stepping motors were used to move both the backstop and the basal plates at a constant velocity (~20 cm/h). The dimensions of the deformation box were sufficiently large to guarantee that the bulk of the model was not affected by boundary effects, and experiments were repeated several times to ensure the consistency of the obtained results. Besides photos of serially cut sections of the (end-stage) deformed models, top view photographs were also taken at regular time intervals as the experiments unfolded.

3.2. Experimental results

The main results are depicted in Figs. 8 and 9. In the experiments of Fig. 8A, B and C modeled crustal thickness was of 10, 8 and 6 km, respectively, scaled down to corresponding sand layer thickness of 5, 4 and 3 cm. This slight variation in the assumed crustal thickness was considered to comply with the inferences from the seismic reflection dataset. However, obtained results show that this did not have any significant influence on the experimentally obtained structural pattern (see below). During the first experimental step a pop-up structure always formed, bounded by a pair of opposite ~30° dipping (fore and back) thrusts, rooting in the velocity discontinuity (Fig. 8A1). During the second experimental step, different types of structures were simultaneously formed in the different areas of the model analyzed below.

3.2.1. Thrust-front and wrenching domains

In the area in front of the main thrust and relatively away from the corner zone (thrust-front domain depicted in Fig. 8), the incremental accumulation of shortening resulting from moving basal plate A to the right could no longer be exclusively accommodated by the original pair of thrusts (forethrust and backthrust) formed during experimental step1 (Fig. 8A1), and thus new forethrusts were successively formed (Fig. 8A2–A3 and B–C). As is classically the case in these type of experiments (e.g. Bonini et al., 2000; Koyi and Maillot, 2007; Lohrmann et al., 2003; Maillot and Koyi, 2006; Persson and Sokoutis, 2002) each new thrust rooted in the VD and accommodated a certain amount of shortening, before being transported along the backthrust fault plane when a newer forethrust was formed, leading to the end-term situation depicted in Fig. 9B (cross section 6).

Simultaneously, in the sand cake above the basal strike–slip fault (wrenching domain as defined in Fig. 8), the first formed structures were en-échelon Riedel faults (Riedel, 1929, R-faults in Fig. 8A2) orientated at low angles to the basement strike–slip direction (15° to 20° for the first increments of deformation). Between these, several P-faults also developed. Offset of parallel lines on model surface by R and P faults showed a synthetic (dextral) strike–slip component of movement along these structures. Further strike–slip increments (Fig. 8A3) originated Y-faults that formed parallel to the basement fault direction, cut the early R and P-faults, and also exhibited dextral strike–slip kinematics. As shear strain accumulated, the surface area between the R-faults rose significantly (compare the topography of Fig. 8A2 and A3) originating a deformation band parallel to the basement fault with a characteristic surface morphology, comprising several sub-parallel elongated bulges (see Fig. 8A3). Subsequent strike–slip increments mostly produced a continued reduction of the width of the previously formed deformation band, besides the amplification of its relief. In cross sections cut perpendicular to the deformation band (Fig. 9 — cross sections 1 and 2) the observed overall fault pattern corresponded to an upwards splaying from the basement fault, typically defining a flower structure. Within this, R-faults exhibited some degree of reverse component of movement, in line with an oblique (dextral-reverse) kinematics, although in the complete absence of any externally induced compression. These structures are typical of wrench fault systems, and confirm previous standard modeling results (e.g. Dooley and McClay, 1997; Le Guerroue and Cobbold, 2006; Mandl et al., 1977; McClay and Bonora, 2001; Richard et al., 1991; Schopfer and Steyrer, 2001; Viola et al., 2004). Specifically, the occurrence of oblique dextral-reverse kinematics along helicoidal R-faults in the absence of any externally induced

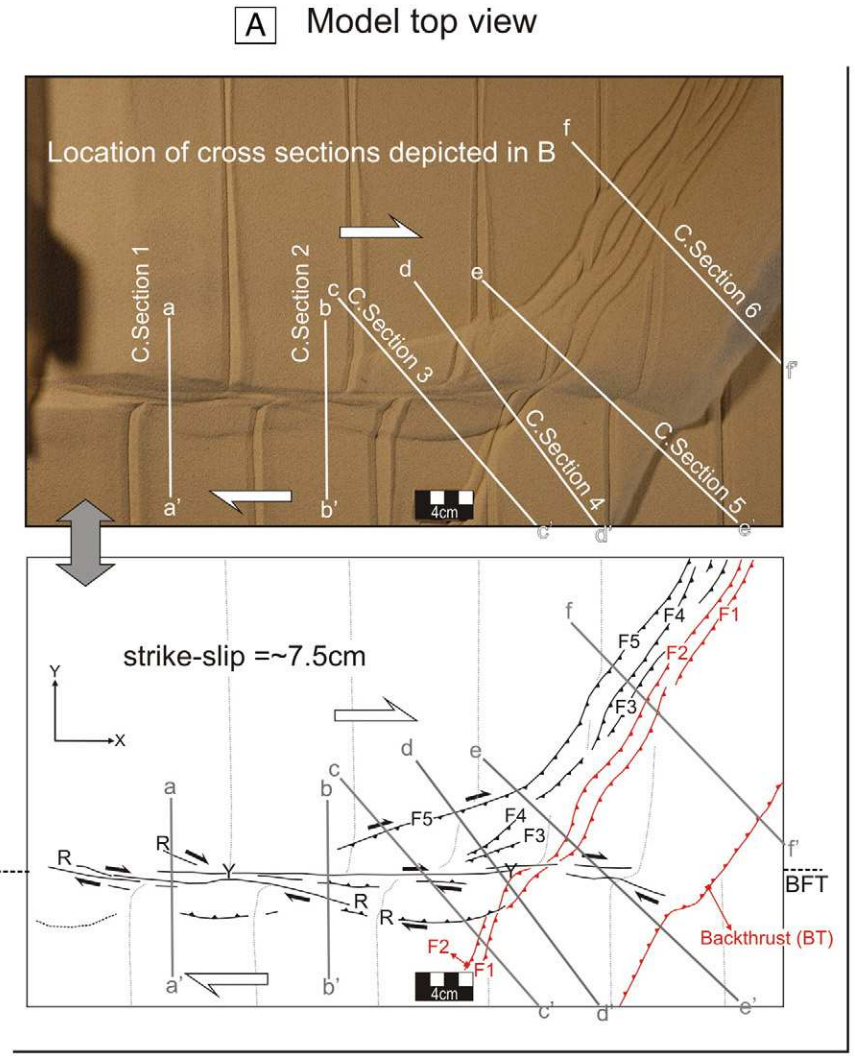
A Model top view
Location of cross sections depicted in B
C.Section 1
C.Section 2
C.Section 3
C.Section 4
C.Section 5
C.Section 6
4cm
strike-slip =~7.5cm
F1
F2
F3
F4
F5
BFT
Backthrust (BT)

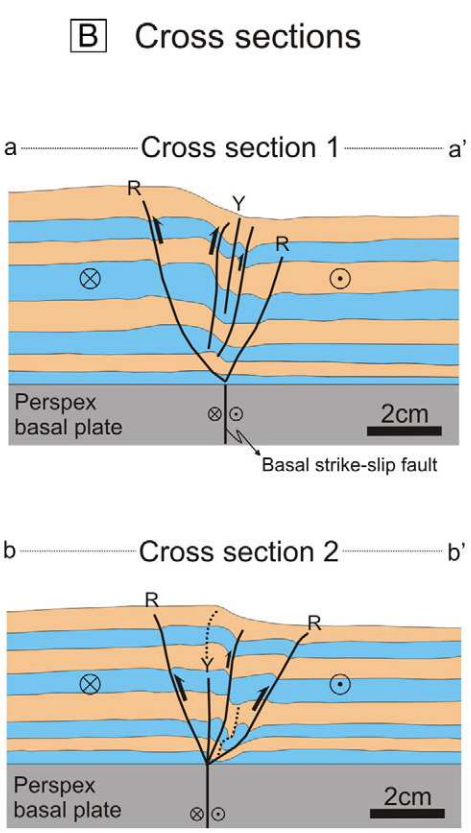
B Cross sections
Cross section 1
Perspex basal plate
2cm
Basal strike-slip fault
Cross section 2
Perspex basal plate
2cm

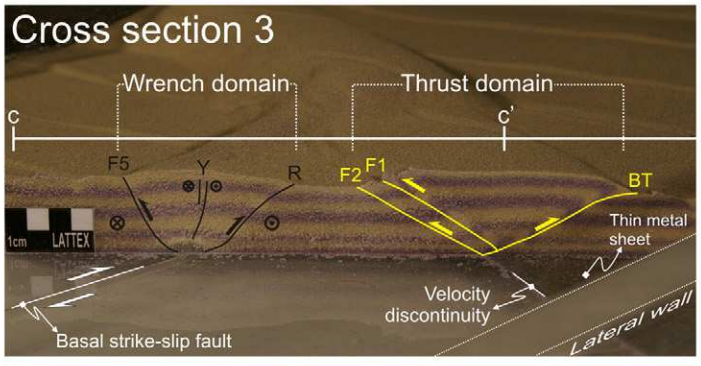
Cross section 3
Wrench domain
Thrust domain
BT
Thin metal sheet
Velocity discontinuity
Lateral wall
Basal strike-slip fault

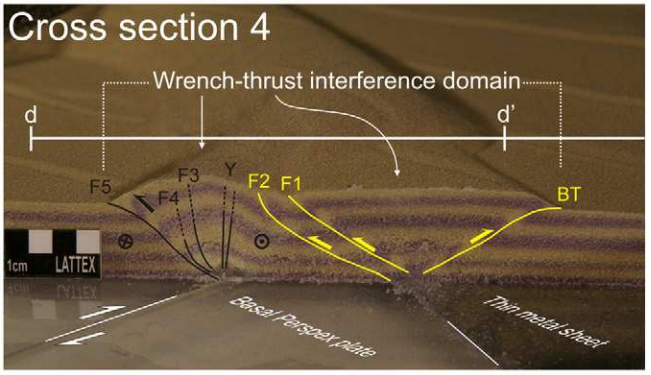
Cross section 4
Wrench-thrust interference domain
BT
Basal Perspex plate
Thin metal sheet

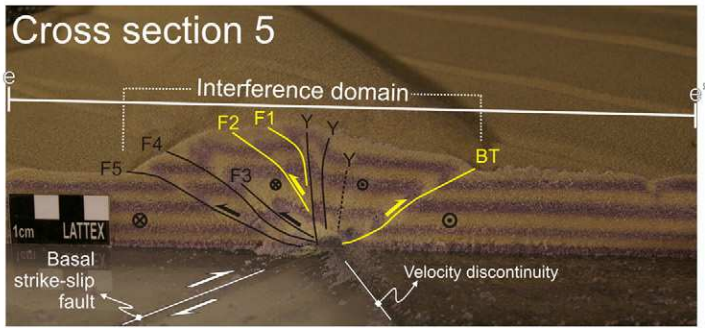
Cross section 5
Interference domain
BT
Basal strike-slip fault
Velocity discontinuity

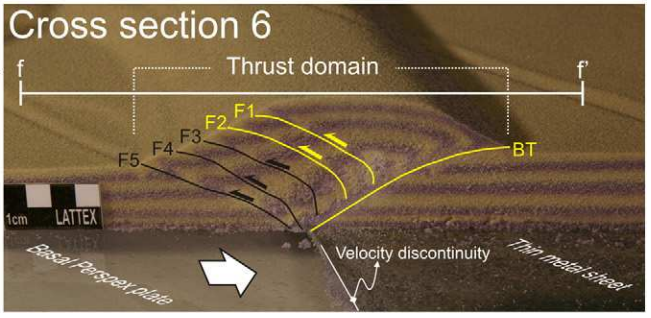
Cross section 6
Thrust domain
BT
Velocity discontinuity
Basal Perspex plate
Thin metal sheet

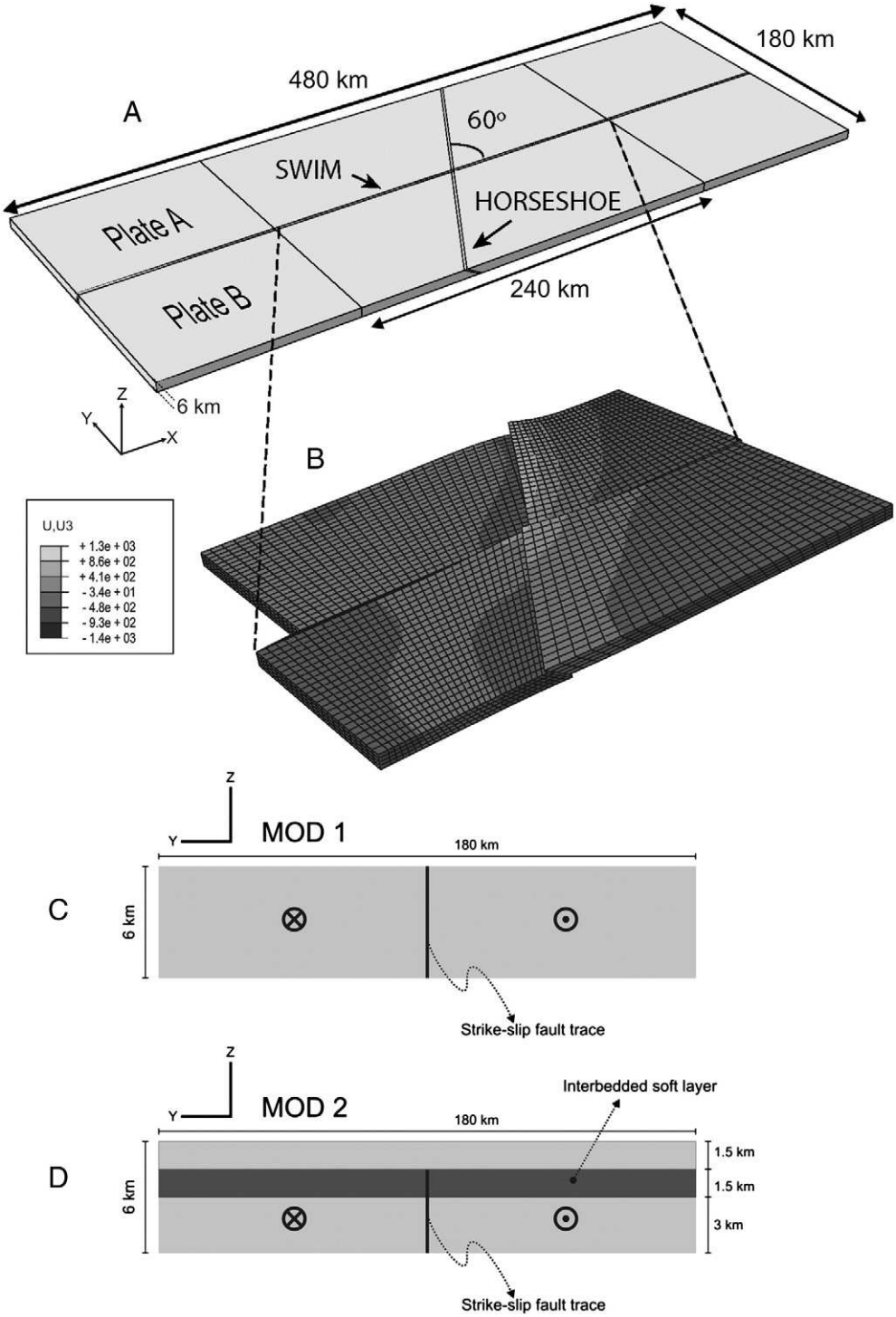

Fig. 10. (A) Geometry and boundary conditions of numerical model. Plate A moves to the right along the X direction. All other boundaries are fixed in the normal Y and Z directions. Gravity is balanced by an applied lithostatic pressure at the base of the model. Spring forces are also applied at the base to simulate isostasy. (B) Deformation of finite element grid and vertical displacement (U3) obtained for 10 km of applied shortening (MOD1). The results are displayed in the central 240 km region of the model. (C and D) Conceptual YZ sections illustrating model setup for MOD1 and MOD 2, respectively. In MOD2 a 1.5 km thick soft layer is placed at 1.5 km beneath the surface, with the strike–slip (SWIM) fault not defined above it.

compression, was previously explained as a result of 5–10% of dilatation in the sand, which is also thought to occur in a similar degree in brittle natural rocks (e.g. Dufréchou et al., 2011; Le Guerroue and Cobbold, 2006; Schopfer and Steyrer, 2001).

3.2.2. Corner zone

In the corner zone (as defined in Fig. 8), a lateral propagation of the thrust faults (F2, F3… Fn) into the wrenching domain was consistently observed, characterized by a rotation of these faults towards an

Fig. 9. (A) Analog modeling results: top view photo and interpretation of experimental step 2 (final stage): along strike displacement of ~7.5 cm (15 km). (B) Cross sections of sand model depicted in A. Cross sections 1 and 2: flower-structures orthogonal to the wrenching domain; cross sections 3 to 5: structure along sectioned planes successively closer to the intersection between the trace of the basal strike–slip and the velocity discontinuity; cross section 6: structure across the thrusting domain. F1, F2 and backthrust (BT) originated during experimental step 1 (structures in yellow and orange); F3 to F5, Riedel-faults (R) and Y-faults (Y) originated during experimental step 2 (structures in black). See text for further detailed explanation.

orientation sub-parallel to the basal strike – slip direction (i.e. X axis, e.g. F2 in Fig. 8A2 and B; F3 in Fig. 8C). This parallelization occurred from relatively early strike – slip increments, and displayed a clockwise rotation of about 60° around an inflection point (IP in Fig. 8A2, B and C). Offset of parallel strain marker lines along these rotated fault segments is consistent with a dextral strike – slip component of movement. In sections cut across the same structures (Fig. 9 — cross sections 3–5), it was apparent that these also maintained a thrusting component, consistently with general dextral-reverse oblique kinematics (e.g. F5 in cross sections 3 and 4 of Fig. 9). In some experiments, strain accommodation in the corner zone implied the formation of new forethrusts in front of previously rotated fault segments (e.g. F3 and F2 respectively in corner zone domain of Fig. 8A3), which as a result ceased to propagate and were passively thrusted in the hanging wall of the newer thrust-faults. Subsequently, these newer thrusts were themselves rotated also towards the basal strike–slip fault direction, mimicking the rotation of the previous ones. For further strike–slip increments, the early formed structures in the corner zone were overprinted by the later deformation and became eventually indistinguishable. As a result, only the younger outer (oblique) faults were observed in this domain (compare F5 outer thrust with F3 and F4 in Fig. 9A). The earlier (inner) thrusts tended to become more parallel to the strike–slip direction (i.e. they rotated more, e.g. F2 in Fig. 8A2, B and F3 in Fig. 8C) than those formed later, located more externally and generally displaying a more oblique direction (sub-perpendicular to the one bisecting the angle made by basal strike–slip and the velocity discontinuity — e.g. F5 in Fig. 9A). Along successive cross sections cut progressively closer to the intersection between the basal strike–slip and the velocity discontinuity (Fig. 9A and B — cross sections 3–5), it was possible to observe the variation of the interference between wrench-related and thrust-related structures.

In cross section 3 (Fig. 9B), wrench and thrust domains can still be separately identified. In the wrench domain, deformation bands were observed to be bounded, on the left, by a rotated segment of an outer thrust (F5, in Fig. 9A and B), and on the right by a Riedel fault. Both these structures showed some degree of dip–slip reverse movement, corresponding to dextral-reverse oblique faults bounding a transpressive pop-up, cut by Y-faults in its middle. The thrust domain along this same direction also corresponded to a (slightly asymmetric) pop-up structure, although in this case bounded by faults lacking any kind of strike–slip component of movement, formed during the first experimental step (faults in yellow in cross section 5 of Fig. 9B): on the left two forethrusts (F1 and F2), and on the right the original backthrust (BT).

Cross section 4 was cut closer to the intersection between the basal strike–slip fault and the velocity discontinuity (Fig. 9B — cross section 4). In this cross-section the right-bounding R-fault of the wrench domain was no longer observed, and instead the two original left-bounding faults of the thrust domain (F1 and F2) occurred immediately to the right of the Y-faults. It should be noted that to the left of these Y-faults, all the others (F3–F5) also accommodated some amount of dextral wrenching, consisting in rotated segments of original thrusts exhibiting oblique (dextral-reverse) kinematics. Conversely, to the right of the Y-faults, the (F1 and F2) thrusts lacked any kind of wrenching component.

Cross section 5 was cut through a direction containing the intersection between the trace of the basal strike–slip fault and the velocity discontinuity (Fig. 9B — cross section 5). Along this direction the separation between thrust and wrench domains was no longer straightforward. Instead a single interference domain was observed, comprising both original pure thrusts, formed during the first experimental step (F1, F2 and BT faults in yellow in Fig. 9B — cross section 5), and dextral strike–slip Y-faults as well as oblique dextral-reverse faults, formed during experimental step 2 (Y and F3–F5 faults in black in Fig. 9B — cross section 5). F1 and F2 were positioned to the left of Y-faults along this same cross-section, with the first steepening at depth towards the second, thus defining a tulip-like (positive) flower-structure geometry, consistent with overall (dextral) transpressional kinematics.

Table 2
Rheological properties of the finite element models.

	General properties			Specific material properties		
	ρ (kg/m^3)	E (GPa)	ν	φ	ψ	σ_y (MPa)
Crust (Drucker–Prager)	2900	70	0.25	27°	25°	350
Soft layer (Von-Mises)	2900	70	0.25	–	–	100
Thrust fault (cohesive material)	2900	70	0.25	G1 = 30 (GPa)	G2 = 30 (GPa)	–
Strike–slip fault (cohesive material)	2900	70	0.25	G1 = 10 (GPa)	G2 = 10 (GPa)	–

P = density, E = Young's modulus, ν = Poisson's ratio, φ = friction angle, ψ = dilation angle, σ_y = yield stress, G1 = G2 = cohesive stiffness.

4. Numerical modeling

Taking into account the same general rheological, geometrical and kinematical constraints described above for the SWIM 1–HTF tectonic system, wrench–thrust mechanical interference was simulated in a three-dimensional plate model using the ABAQUS/Standard software (ABAQUS, Inc. 2009). The main goal was to gain some quantitative insight regarding stress and strain distribution in the thrust–wrench corner zone, which could not be achieved by analog modeling alone. In accordance, the present numerical modeling assumed the same brittle (upper crustal) fault-interference conditions that were considered for the analog approach. This made it possible to compare both (analog and numerical) results, and to assess their degree of compatibility, i.e. to evaluate how well (if at all) the previously obtained structural pattern was matched by the new numerical output, confirming or dismissing a mechanical corner effect.

Additionally, the influence of an interbedded shallow soft layer in the mechanics of the interference at stake, as a possible cause of decoupled rheological behavior, was also considered. This was motivated by the known regional seismostratigraphy that includes the Late Miocene gravitational "chaotic body" unit (see Figs. 4 and 5). As referred above, this unit was previously interpreted as resulting from a mixture of olistostromes and tectonic mélanges (Iribarren et al., 2007; Terrinha et al., 2009; Torelli et al., 1997; Tortella et al., 1997), which could hypothetically determine a relatively less competent rheological behavior.

Since the studied major faults are only seismically imaged down to maximum depths of ca. 6 to 10 km, the performed numerical modeling did not consider their interference at lithospheric scale (accounting for depths of ca. 40–50 km). Instead, the main objective was to reproduce the same specific conditions assumed for the analog experiments, i.e. to focus on upper crust (brittle) fault-interference. It should be noted that a numerical modeling approach at lithospheric scale would specifically require the introduction of the ocean–continent transition and temperature dependent non-linear rheologies (e.g. Neves and Neves, 2009), which considering the main goal referred above was out of the scope of the present work.

4.1. Model setup

The basic model (MOD1) represents an upper crustal block covering an area of 480 × 180 km, with a thickness of 6 km (Fig. 10A and C). This thickness corresponds to the maximum depth imaged by the available reflection seismics (e.g. TWTT-depth conversion of IAM-4 line across the HAP by González et al., 1998; Jimenez-Munt et al., 2010). The obtained model results were drawn from a central 240 × 180 km subarea, to avoid boundary effects. Two planes of weakness, i.e. idealized

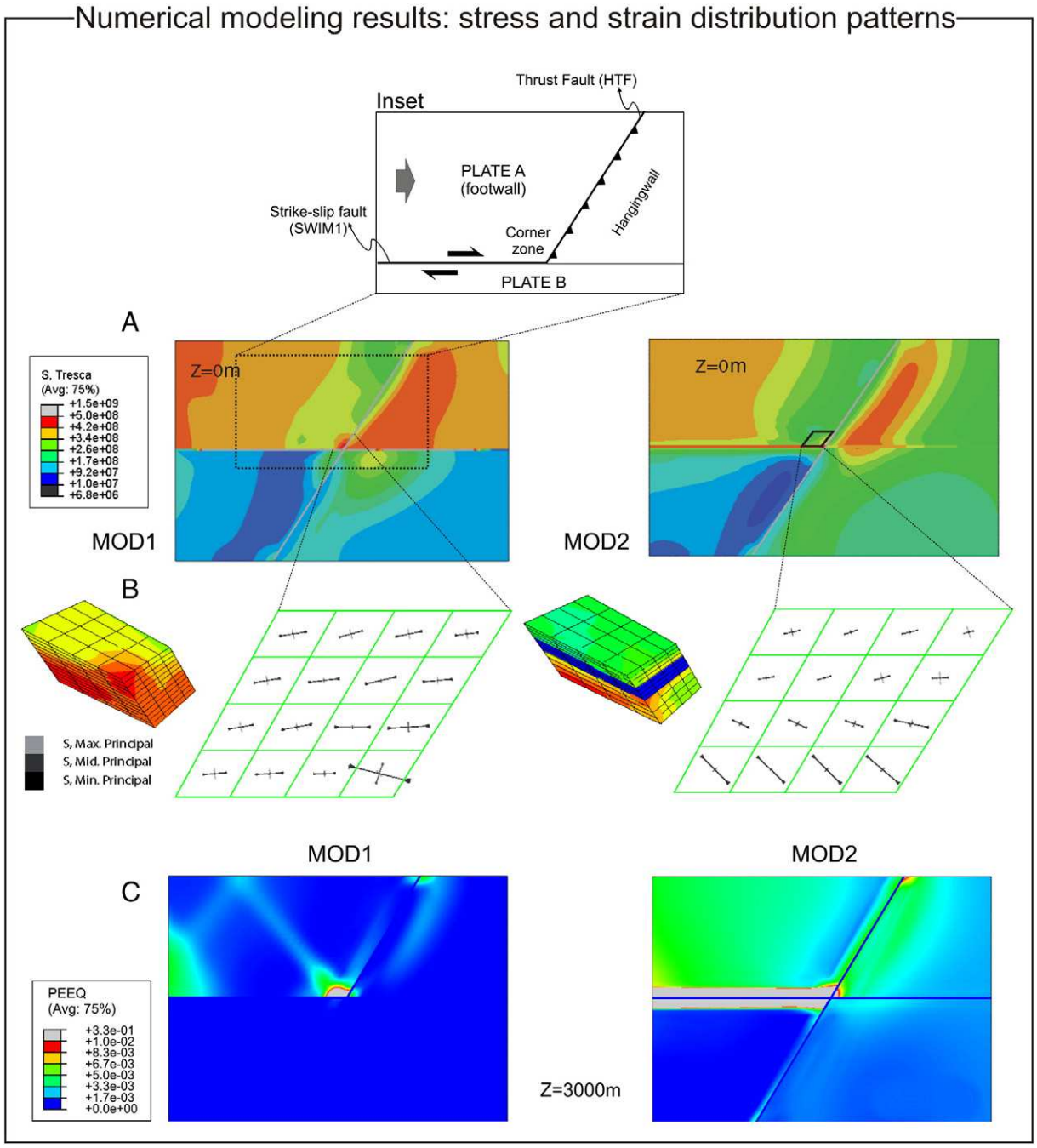

Fig. 11. (A) Maximum shear stress contours on a non-deformed frame (view from above of the central 240 × 180 km of the model) at the surface (z = 0 m) of MOD1 (left) and MOD2 (right). (B) Close-up in 3D of the area delimited by the parallelogram in A and top view of principal stress components at the thrust/strike–slip intersection. The horizontal grid resolution is ~4 km and there are 12 elements in the vertical dimension (4 elements per layer). (C) Accumulated plastic strain contours on a non-deformed frame (view from above of the central 240 × 180 km of the model). The strain pattern was analyzed in terms of the equivalent plastic strain, i.e. the total unrecoverable strain accumulated after the onset of yielding according to the Drucker–Prager criterion. Results for MOD1 and MOD2 shown for a depth of z = 3000 m (base of soft layer in MOD2).

faults, account for the Horseshoe thrust and SWIM 1 dextral strike–slip, dipping 30° and 90°, respectively, and intersecting each other with their surface traces making an angle of 120°/60° as in the natural example (see Figs. 2 and 3).

As referred above, the interpretation of the available seismic reflection dataset also supports the assumption of a ~1.5 km thick layer, corresponding to the hypothetically less competent Late Miocene "Chaotic body" unit (see Figs. 4 and 5), at approximately 1.5 km below the seafloor. This is simulated in the second set of models (MOD2) by an interbedded soft layer (Fig. 10D) with its top surface coinciding with the tip of the strike–slip fault that does not reach the model surface. This mimics the natural example wherein the SWIM 1 Fault shows little bathymetric expression (see Figs. 2 and 3), only mildly perturbing the top Late Miocene to Plio-Quaternary unit in a few locations, despite always undoubtedly cutting across the underlying Miocene gravitational "Chaotic body" unit (see Fig. 5).

4.1.1. Rheologic and fault parameters

Although ABAQUS is provided with many material behavior benchmarks, we needed to conduct a large number of systematic tests to select the material properties. The most challenging to be constrained were the material properties of the cohesive elements that constitute the faults, since they are commonly calibrated for small-scale fractures found in engineering problems, and not for large-scale geologic faults.

The adopted approach was to iteratively change the parameters until displacement and stress solutions compatible with the natural estimates and observations were found. The Drucker–Prager plasticity model was chosen to model the brittle crustal behavior. This was found to be numerically more stable than the Mohr–Coulomb model, which failed to converge at an earlier step in the analysis due to larger deformations. Since we were not interested in examining the details of the stress distribution within the soft layer, a simple Von-Mises plasticity model was chosen to model the soft layer in MOD2. A Von-Mises material provides a lower yield stress than the surrounding crustal material and simulates a decoupling layer.

The thrust and strike–slip faults are modeled as layers of cohesive elements. These are specifically designed for bonded interfaces where the interface thickness is negligibly small compared to other model dimensions. The constitutive response of the cohesive layer is defined in terms of an elastic traction versus separation law, i.e. there are three components of separation, one normal to the interface and two parallel to it. To prevent faults from opening or closing, the normal component (E) is much stiffer than the in-plane components (G1 and G2). The thrust fault cohesive stiffness, G1 = G2 = 30 GPa, is larger than the strike–slip fault cohesive stiffness, G1 = G2 = 10 GPa, following the Coulomb–Navier's law of fracture strength. All the material parameters are listed in Table 2.

4.1.2. Boundary conditions and procedure

The boundary conditions try to match those of the analog modeling experiments as closely as possible. Deformation is simulated by moving basal plate A to the right relatively to plate B (see Fig. 10A). Because there is some stiffness along the strike–slip fault, plate B is dragged by plate A towards the thrust fault. The maximum prescribed displacement along the X direction was 10 km, yielding a maximum shortening of 2%. Both basal plates are fixed in along the Y direction. Gravity ($g = 9.8\ m/s^2$) is applied as a body force. To counterbalance the weight of the overlying crust a lithostatic pressure is applied at the bottom of the model. Isostasy is simulated by applying spring forces at the bottom of the model with stiffness per unit area equal to $(\rho m - \rho w)g$ where $\rho m = 3300\ kg/m^3$ is the mantle density and $\rho w = 1000\ kg/m^3$ is the water density.

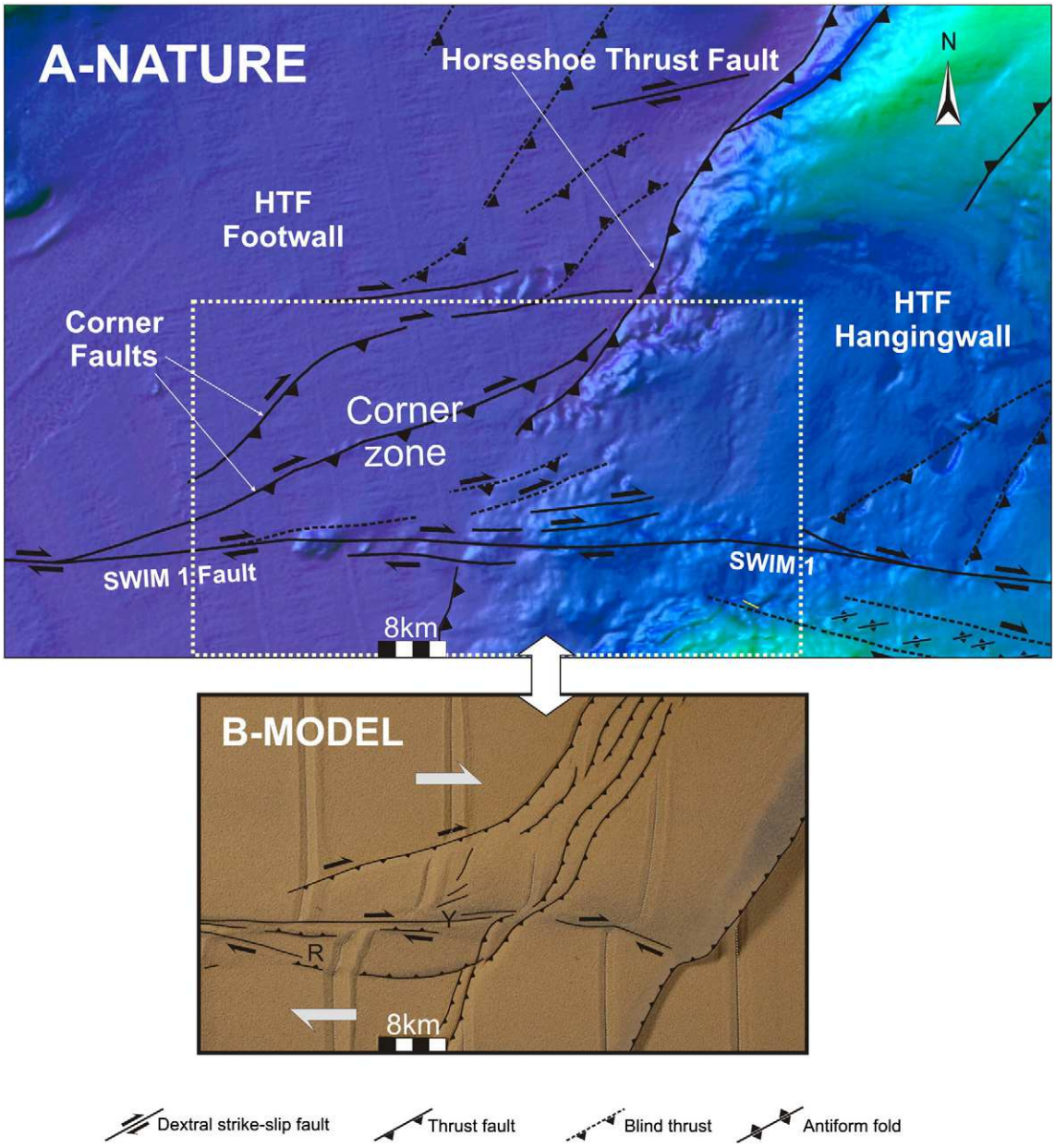

Fig. 12. Comparison of the natural morphotectonic pattern and the obtained analog modeling structural pattern.

4.2. Model results

4.2.1. Displacement pattern

Deformation of the basic model (MOD1) is illustrated by vertical displacement contours on a deformed grid (Fig. 10B), which shows that the rightwards push of basal plate A was accommodated by movement along both the thrust and strike–slip faults. Flexure of the plate also occurred in response to the topographical load caused by the fault offset, in agreement with the flexural theory of faulting (e.g. Bott, 1996). For 2% of shortening the maximum throw along the thrust fault was 1300 m (Fig. 10B).

4.2.2. Stress and strain distribution

Fig. 11A–C depicts the stress and strain distribution in the obtained numerical models. The relatively high concentration of stress in the corner zone of these models (Fig. 11A — MOD1) agrees with the results obtained in the analog experiments (see above). Likewise, the plot of principal stresses at model surface shows that the stress directions clearly rotate near this same corner zone (Fig. 11B — MOD1), and the maximum compressive stress magnitude increases by a factor of 1/3. Additionally, the obtained pattern of strain distribution also shows significant concentration in the MOD1 corner zone area (Fig. 11C — MOD1), confirming that this zone is where tectonic structures are preferably expected to develop and concentrate, in line with the predictions inferred from the analog results.

In contrast, some decrease of the overall state of stress was generally observed in MOD2 (Fig. 11A — MOD2). Between plates A and B stress was observed to concentrate at the model surface along a narrow band coinciding with the direction of the strike–slip fault, although this was not prescribed to affect the top 1.5 km thick model layer (see Fig. 10D). In addition, the maximum compressive stress orientation showed a constant obliquity (45°–50°) relative to the strike–slip direction, without any significant variations of magnitude or direction in the corner zone (Fig. 11B — MOD2). Complying with this stress distribution and with the existence of a shallow soft layer, higher amounts of strain were observed to diffusely affect the whole of this layer (Fig. 11C — MOD2), while some degree of strain concentration also occurred along the trace of the strike–slip fault.

5. Discussion

Both analog and numerical modeling results clearly show the importance of a *corner effect* expressed by the deformation pattern that is expected to develop in a brittle medium due to the mechanical interference between a dextral strike–slip fault and a thrust, intersecting each other at an angle of 120°/60°. Analog modeling provides a characterization of the resultant basic structural pattern, revealing its essential geometry and kinematics. Numerical modeling provides insights on the way stress and strain are distributed under the same conditions, and considers the effects of simple rheological variation accounting for a shallow interbedded soft layer within the same brittle medium.

5.1. Analog modeling output

The experimentally obtained structural pattern is mostly characterized by a concentration in the corner zone of (see Figs. 8 and 9): a) oblique (dextral-reverse) faults, with different evolving geometries and associated kinematics; and b) vertical (dextral) strike–slip Y-faults. While Y-faults tend to generally maintain their main geometry and kinematics as strain accumulates in the corner zone, oblique faults do not since they nucleate as segments of originally pure thrusts that progressively propagate and rotate from the thrust-front to the wrench domain (see Fig. 8). This propagation-rotation is matched by a corresponding change in kinematics; from pure (reverse dip–slip) thrusting, to oblique (transcurrent dominant) dextral-reverse faulting. Early formed faults undergo a greater amount of more abrupt rotation, with their planes being more promptly parallelized to the basal strike–slip direction (F2 in Fig. 8A2 and B, and F3 in Fig. 8C). As strain continues to accumulate in the corner zone, these same planes also become steeper (from an original dip of ~30°), and eventually subparallel to the Y-faults, preferably accommodating dextral strike–slip movement (see for instance in F3 and F4 in cross section 4 of Fig. 9B). Later (outer) faults in the corner zone endure relatively less displacement, and thus are less rotated and steepened, striking somewhat subperpendicularly to the bisector of the angle defined by the thrust-front and the wrenching domains (see for instance F5 in Fig. 9A and cross section 5).

These results show that in this particular structural setting faults genetically related either to the wrench or to the thrust system do not evolve independently. Active strike–slip faulting in the wrench domain simultaneously triggers reverse (dip–slip) faulting in the thrust domain, which subsequently evolves to reverse oblique–slip faulting towards the corner zone.

5.2. Numerical modeling output

The numerical modeling results also strengthen the working hypothesis of the existence of a thrust–wrench interference corner effect, in accordance with the structural pattern obtained in the analog experiments. Stress and strain contours obtained for MOD1 reveal a consistent concentration of both in the corner zone area (see Fig. 11A to C — MOD1). This agrees with the high concentration of faults that characterizes the corner zone in the analog models (see Figs. 8 and 9). Also, the rotation of the stress field and of the maximum compressive stress in the MOD1 corner zone (see Fig. 11B — MOD1) agrees with the described geometry and kinematics of early formed (inner) faults in the analog models, specifically with their steep planar attitude and dominant-transcurrent oblique kinematics (see F3 and F4 in Fig. 9A and cross section 4). In MOD2 strain diffusion in the soft (decoupled) layer (see Fig. 11C — MOD2) caused a decrease of the overall state of stress at the model surface, and hindered stress concentration in the corner zone (Fig. 11A and C — MOD2). The fact that the prescribed strike–slip fault in MOD2 does not breach out, explains the observed relative concentration of stress along a narrow band coincident with the direction of the underlying strike–slip fault (Fig. 11A — MOD2). This also complies with the observed constant obliquity of the maximum compressive stress relatively to that same strike–slip direction (Fig. 11B — MOD2).

5.3. Comparison with the natural example and tectonic implications

The obtained analog modeling results are consistent with the natural structural pattern revealed by the morphotectonic interpretation of the HAP corner zone area (Fig. 12). Similarities between model and natural example are given by the fault pattern, which contains structures with similar geometries and kinematics. Such model-prototype congruence shows that the observed natural tectonic pattern is the result of thrust–wrench interference between the SWIM 1 and Horseshoe faults.

The modeled interdependency between both these fault systems, agrees with a possible multi-rupture scenario involving coeval strike–slip faulting in the wrenching domain (SWIM system), reverse-faulting in the thrust domain (Horseshoe system), and sequentially induced oblique, dextral-reverse faulting in corner zone (SWIM 1–HTF intersection). Multi-rupture scenarios have been documented in other places involving dominant transcurrent continental fault-systems, in which main strike–slip earthquakes trigger thrust-related aftershocks, generally nucleating in restraining bends subsidiary of the main transcurrent system (e.g. Gobi–Altay Fault and San Andreas Fault, Bayarsayhan et al., 1996, Kurushin et al., 1997). Although also in continental domains, wrench–thrust interference faulting is likewise known to be associated to complex rupture, comprising triggering of thrust faulting only tens of seconds after strike–slip faulting (e.g. 1976 Tangshan earthquake,

Butler et al., 1979). In the Gulf of Cadiz, multi-rupture associated to some kind of interference between different faults (e.g. HTF, MPF and SWIM) has also been proposed by previous authors (e.g. Gràcia et al., 2003a,b; Terrinha et al., 2003, 2009; Zitellini et al., 2001). Specifically in the present case, and given the dimension of the faults at stake, rupture areas associated to the corresponding earthquakes could hardly justify the energy release implied by high magnitude events ($M>8.5$), such as the 1755 Great Lisbon Earthquake (Gutscher et al., 2009b). Nonetheless, the potential multi-rupture associated to the study thrust–wrench tectonic interference should be taken into consideration while addressing seismic hazards for low to moderate magnitude events ($Mw<6.0$).

In the study area, recent reports on the local seismicity corresponding to these low to moderate magnitude events (Geissler et al., 2010; Silva et al., 2010) showed a strong concentration in the SWIM1–HTF corner zone (see Fig. 6). However, as mentioned above, it is critical to note that these earthquakes are located at depths mostly comprised between 40 and 55 km, corresponding to the base of the seismogenic layer (within lithospheric mantle), whilst in the available MCS profiles corner faults are imaged at maximum depths of only ~6–10 km (e.g. CF1 and CF2 in Fig. 5). While strike–slip faults can easily be extrapolated vertically to great depths, major lithospheric thrust faults are expected to vary their dip as a function of depth and correspondent rheology, and thus a non-negligible horizontal offset between the fault traces and the earthquake epicenters should be expected. However, in the present case, epicenters are preferably concentrated merely ~14 and ~25 km to the SE of CF1 and CF2 faults, respectively (see Fig. 6). It is thus difficult to envisage a direct connection between these faults, imaged at upper crustal depths, and the reported seismicity originated at lithospheric mantle depths.

It is therefore more likely that the studied thrust–wrench interference corner effect recognized in the upper-crust could also exist at deeper lithospheric levels. According to this idea, a replication of similar tectonic interference patterns would occur at different depths, in different lithospheric layers with similar (competent) bulk rheologies, as a consequence of similar stress regimes. This is supported by the congruency between the variable orientation of the seismically imaged faults (at upper crustal depths), and the variation of planes deduced from focal mechanisms (at mantle lithospheric depths). These focal mechanisms were reported as somewhat heterogeneous by Geissler et al. (2010), although mostly compatible with reverse and strike–slip faulting. This agrees with the modeled thrust–wrench tectonic scenario as shown by the obtained interference structural pattern in the analog models, where corner zone faults assume evolving different geometries and kinematics ranging from pure thrust to pure strike–slip (see Figs. 8 and 9).

Geissler et al. (2010) also proposed a direction of principal stress components, based on the estimated average stress tensors consistent with the fault slip orientations from focal mechanisms. Accordingly, the maximum compressive stress rotates from an approximately E–W direction, near the northern termination of the HTF ($\sigma1$ — N103°E/26° strike/plunge, Fig. 6), to a more N–S direction in the corner zone ($\sigma1$ — N351°/12°, Fig. 6), roughly bisecting the angle between the SWIM 1 and the Horseshoe Thrust Fault. This rotation complies, not only with the corner zone rotation of the maximum compressive stress obtained for MOD1 numerical results (see Fig. 11B — MOD1), but also with the orientation of the characteristic oblique corner faults, observed both in the analog model and natural structural patterns (see Figs. 8, 9 and 12).

The idea that similar thrust–wrench tectonic interference can express itself in a decoupled manner at different (crustal and mantle) lithospheric depths, could explain the recurrently recognized spatial discrepancy in the Gulf of Cadiz between: (a) the mapped main tectonic structures, and (b) the dominant low to intermediate "background" seismicity ($Mw<6.0$), to which specific major faults are generally difficult to assign. This agrees with the conspicuous relative absence of earthquakes at lower crust–upper mantle depths (between ~15 and 40 km, see Fig. 6, Geissler et al., 2010; Silva et al., 2010), which could also be related to this fault interference pattern. In fact, the WAS data reported by Sallarès et al. (2011), although based on a profile located further to the east (see Fig. 1B), showed the existence of (oceanic) crust and upper mantle low velocities, which were interpreted by these authors as the result of alteration and serpentinization caused by fluid percolation through fault-related rock fractures. The authors specifically suggest that the SWIM faults, which in their WAS profile are also spatially coincident with low-marked velocity anomalies, probably play an important role in this rock alteration process. Thus, in the present study area, the newly discovered (corner zone) fault interference pattern could likewise powerfully assist abundant fluid percolation through a widespread network of fault-related rock fractures, promoting crustal alteration and mantle serpentinization possibly even in a more efficient and generalized way. This could explain the reported existence of earthquake only at mantle depths of >40 km (and <55 km, Geissler et al., 2010), where the reach of this softening alteration/serpentinization effect would tend to be attenuated.

It should be noted that in the Gulf of Cadiz this lower crustal–upper mantle fluid-related alteration effect, although generally reported as being associated to tectonic fault channeling, is also thought to be possible to occur more pervasively, in areas away from the main tectonic faults. Accordingly, lower upper-mantle velocities were described by Purdy (1975) and González et al. (1996) in the Horseshoe Abyssal Plain, similar to velocities reported in the Tagus Abyssal Plain as being related to mantle serpentinization in the local Ocean–Continental Transition Zone (Pinheiro et al., 1992).

Another point to consider is the location of the continent–ocean boundary in the present study area. The implied abrupt thickness and marked rheological contrast associated to such a boundary would exert a critical influence on depth nucleation of major tectonic structures, possibly including the ones associated to both the SWIM and the HTF systems. Future modeling work should thus consider the proposal of Sallarès et al. (2011) (see Fig. 1B), assuming for the study area the location of the COB at a distance of ~100 km from the southern Iberian coast line.

Rheology-controlled decoupling is also illustrated at a different scale in the upper crust by MOD2 numerical modeling results, which show that an interbedded soft layer can be responsible for a significant degree of strain diffusion and delocalization (Fig. 11C — MOD2), hindering the nucleation and upward propagation of faults, and thus inhibiting the morphological expression of the fault interference pattern in the corner zone. This could explain the poor bathymetric expression of the corner zone structural pattern in the HAP seafloor, caused by a soft-like rheological behavior of the Late Miocene gravitational "Chaotic Body" unit.

6. Conclusions

The following main conclusions are drawn:

a) The newly discovered tectonic pattern in the area of intersection (corner zone) between the SWIM 1 and the Horseshoe faults formed as the result of tectonic interference between active strike–slip and thrust faulting, respectively.
b) Modeling results show that in the corner zone domain a preferred concentration of stress and strain occurs (corner effect); the latter being mainly accommodated by reverse oblique faulting, with faults exhibiting different evolving geometries and kinematics as they endure some degree of rotation. A multi-rupture scenario within the active tectonic framework of the connected SWIM 1 and HTF systems can thus be envisaged, and should be carefully considered when assessing the seismic-related hazards of low to moderate seismicity ($Mw<6.0$) in the Gulf of Cadiz region.
c) In the SWIM 1–HTF corner zone the tectonic pattern is seismically imaged at upper crustal depths, whereas the local seismicity is reported to preferentially occur in the lithospheric mantle (Geissler et al., 2010). Nonetheless, faults and seismicity data are congruent in a

number of aspects (orientation of fault planes and planes deduced from focal mechanisms, fault kinematics and focal mechanisms, compatibility with similar stress field orientation). This suggests a possible occurrence of similar thrust–wrench tectonic interference at different lithospheric depth-levels with comparable (competent) rheologies. Accordingly, an intermediate lower crust–upper mantle aseismic depth domain could be explained by pervasive alteration/serpentinization, prompted by fluid percolation through fault-related fractures associated with the newly revealed corner zone (thrust–wrench) fault-network.

d) Numerical modeling results also illustrate the influence that rheological stratigraphy might exert on the nucleation and propagation of the corner zone fault pattern in the upper crust. Specifically, an interbedded soft layer is shown to inhibit the stress–strain corner zone concentration in the overlying competent layer. In accordance, the mild morphological (bathymetric) expression of the corner zone interference tectonic pattern in the HAP seafloor could eventually be explained by strain delocalization/diffusion, and consequent lack of fault propagation, induced by the presence of a rheologically soft Late Miocene gravitational "Chaotic" unit. Confirmation of such a possibility should be tested by future work assessing the relationship between the presence of this seismostratigraphic unit, and the attenuation of the bathymetric expression of the (seismically imaged) tectonic structures at stake. Likewise, future modeling on this issue should also take into account existent syn- and post-tectonic sedimentation rates, particularly in the HAP where these are expected to have a crucial influence on preserving/obliterating the bathymetric record of active tectonics (Gràcia et al., 2010; Lebreiro et al., 1997; Zitellini et al., 2009).

Acknowledgments

Experiments were performed in the Analogue Modeling Lab of Instituto Dom Luiz (IDL), a research Associate Laboratory funded by FCT. ALMOND — Multiscale modelling of deformation in the Gulf of Cadiz (PTDC/CTE-GIN/71862/2006). TOPOEUROPE/0001/2007-TOPOMED (Plate re-organization in the western Mediterranean: lithospheric causes and topographic consequences). Support by Landmark Graphics Corporation via the Landmark University Grant Program is acknowledged. The authors also acknowledge the support of the Spanish Ministry of Science and Innovation (MICINN) through National Projects SWIM (REN2002-11234E-MAR), EVENT (CGL2006-12861-C02-02), SHAKE (CGL2011-30005-C02-02), the European Science Foundation EuroMargins SWIM project (01-LEG-EMA09F) and the EU Program "Global Change and Ecosystems" contract no. 037110 (NEAREST). J.C. Duarte acknowledges a Ph.D. grant (SFRH/BD/31188/2006) from FCT and the support from the Australian Research Council through Discovery Grant DP110103387. F. Rosas and J. Duarte whish to thank Alexander (Sandy) Cruden and David Boutelier for a short visit to the Tectono-Physics Lab (University of Toronto), where the main ideas behind this paper first started to mature. We thank M. Gerbault and G. Viola for their constructive and thorough reviews of the manuscript.

Appendix A

Dry quartz sand is classically used to simulate the mechanical behavior of upper crustal rocks, since it deforms in a brittle way according to the Coulomb fracture criterion (e.g. Davis et al., 1983; Hubbert, 1937, 1951):

$$\tau_{ss} = \mu_c \sigma_n + c_0 \tag{1}$$

where τ_{ss} is the shear stress, μ_c is the coefficient of internal friction ($\mu_c = \tan\phi$, and $\phi =$ internal friction angle), σ_n is the normal stress, and c_0 is the cohesion of the material. According to the scale model theory (Hubbert, 1937), proper scaling is achieved when the ratios λ, τ and μ between model and natural prototype are independently established for the three fundamental units of length (L), time (T) and mass (M), respectively:

$$\lambda = \frac{L_{(m)}}{L_{(p)}}; \tau = \frac{T_{(m)}}{T_{(p)}}; \mu = \frac{M_{(m)}}{M_{(p)}} \tag{2}$$

where (m) stands for model and (p) for natural prototype. The Coulomb fracture criterion governs time independent deformation of brittle materials, since yield stress is insensitive to the rate of deformation provided that the inertial forces are negligible, as in the present case. Thus, τ ratio is redundant for the present scaling. Length ratio (λ) was chosen given the dimensions of the employed deformation apparatus (see Section 3.1.2 and Fig. 7A) as $\lambda = 5\times10^{-6}$. Of the two relevant material properties, coefficient of internal friction (μ_c) and cohesion (c_0), the first is dimensionless, and approximately the same in both model and prototype (see Table 1), whereas the second has dimension of stress and thus must be scaled accordingly (Hubbert, 1937):

$$\Sigma = \frac{c_{0(m)}}{c_{0(p)}} = \frac{\mu\gamma}{\lambda^2} \tag{3}$$

where Σ and γ are the model/prototype ratio for stress and for acceleration respectively. Since inertial forces are negligible when compared with gravity,

$$\gamma = \gamma_g = \frac{g_{(m)}}{g_{(p)}} = \frac{\lambda}{\tau^2} = 1 \tag{4}$$

where γ_g is the model/prototype gravity acceleration ratio. Thus, substituting $\gamma = 1$in Eq. (3) allows the following simplification:

$$\Sigma = \frac{c_{0(m)}}{c_{0(p)}} = \frac{\mu}{\lambda^2} = \frac{\mu\lambda}{\lambda^3} = \delta\lambda \tag{5}$$

where δ corresponds to the model/prototype density ratio. Substituting δ and λ in Eq. (5) by the respective values of Table 1, immediately allows the determination of the implied mass ratio $\mu = 6.25\times10^{-17}$.

References

Abe, K., 1979. Size of great earthquakes of 1837–1974 inferred from tsunami data. Journal of Geophysical Research 84 (NB4), 1561–1568.
Agarwal, K.K., Agrawal, G.K., 2002. Analogue sandbox models of thrust wedges with variable basal frictions. Gondwana Research 5 (3), 641–647.
Banda, E., Torné, M., I. A. M. Group, 1995. Iberia Atlantic Margin Group investigates deep structure of ocean margins. Eos Transactions, American Geophysical Union 76, 25–29.
Baptista, M.A., Miranda, J.M., 2009. Revision of the Portuguese catalog of tsunamis. Natural Hazards and Earth System Sciences 9 (1), 25–42.
Baptista, M.A., Heitor, S., Miranda, J.M., Miranda, P., Victor, L.M., 1998a. The 1755 Lisbon tsunami; evaluation of the tsunami parameters. Journal of Geodynamics 25 (1–2), 143–157.
Baptista, M.A., Miranda, P.M.A., Miranda, J.M., Victor, L.M., 1998b. Constrains on the source of the 1755 Lisbon tsunami inferred from numerical modelling of historical data on the source of the 1755 Lisbon tsunami. Journal of Geodynamics 25 (1–2), 159–174.
Bartolome, R., Gràcia, E., Stich, D., Martínez-Loriente, S., Klaeschen, D., Mancilla, F.L., Lo Iacono, C.I., Dañobeitia, J.J., Zitellini, N., 2012. Evidence for active strike–slip faulting along the Eurasia–Africa convergence zone: implications for seismic hazards on the SW Iberian Margin. Geology, G33107.1, http://dx.doi.org/10.1130/G33107.1.
Bayarsayhan, C., et al., 1996. 1957 Gobi–Altay, Mongolia, earthquake as a prototype for southern California's most devastating earthquake. Geology 24 (7), 579–582.
Bonini, M., Sokoutis, D., Mulugeta, G., Katrivanos, E., 2000. Modelling hanging wall accommodation above rigid thrust ramps. Journal of Structural Geology 22, 1165–1179.
Bonnet, C., Malavieille, J., Mosar, J., 2007. Interactions between tectonics, erosion, and sedimentation during the recent evolution of the Alpine orogen: analogue modeling insights. Tectonics 26, TC6016, http://dx.doi.org/10.1029/2006TC002048.
Borges, J.F., Fitas, A.J.S., Bezzeghoud, M., Teves-Costa, P., 2001. Seismotectonics of Portugal and its adjacent Atlantic area. Tectonophysics 331 (4), 373–387.
Bott, M.H.P., 1996. Flexure associated with planar faulting. Geophysical Journal International 126, F21–F24.
Buforn, E., Degaldeano, C.S., Udias, A., 1995. Seismotectonics of the Ibero-Maghrebian region. Tectonophysics 248 (3–4), 247–261.

Buforn, E., Bezzeghoud, M., Udias, A., Pro, C., 2004. Seismic sources on the Iberia–African plate boundary and their tectonic implications. Pure and Applied Geophysics 161 (3), 623–646.

Butler, R., Stewart, G.S., Kanamori, H., 1979. July 27, 1976 Tangshan, China earthquake — complex sequence of intraplate events. Bulletin of the Seismological Society of America 69 (1), 207–220.

Davis, D., Suppe, J., Dahlen, F.A., 1983. Mechanics of fold and thrust belts and accretionary wedges. Journal of Geophysical Research 88, 1153–1172.

Di Bucci, D., Ravaglia, A., Seno, S., Toscani, G., Fracassi, U., Valensise, G., 2006. Seismotectonics of the southern Apennines and Adriatic foreland: insights on active regional E–W shear zones from analogue modeling. Tectonics 25 (4).

Di Bucci, D., Ravaglia, A., Seno, S., Toscani, G., Fracassi, U., Valensise, G., 2007. Modes of fault reactivation from analogue modeling experiments: implications for the seismotectonics of the Southern Adriatic foreland (Italy). Quaternary International 171–72, 2–13.

Diraison, M., Cobbold, P.R., Gapais, D., Rossello, E.A., Le Corre, C., 2000. Cenozoic crustal thickening, wrenching and rifting in the foothills of the southernmost Andes. Tectonophysics 316 (1–2), 91–119.

Dooley, T., McClay, K., 1997. Analog modelling of pull-apart basins. AAPG Bulletin-American Association of Petroleum Geologists 81 (11), 1804–1826.

Duarte, J.C., Valadares, V., Terrinha, P., Rosas, F., Zitellini, N., Gràcia, E., 2009. Anatomy and tectonic significance of WNW–ESE and NE–SW lineaments at a transpressive plate boundary (Nubia–Iberia). Trabajos de Geologia 29, 237–241.

Duarte, J.C., Terrinha, P., Rosas, F.M., Valadares, V., Pinheiro, L.M., Matias, L., Magalhães, V., Roque, C., 2010. Crescent-shaped morphotectonic features in the Gulf of Cadiz (offshore SW Iberia). Marine Geology 271, 236–249.

Duarte, J.C., Rosas, F.M., Terrinha, P., Gutscher, M.-A., Malavieille, J., Silva, S., Matias, L., 2011. Thrust–wrench interference tectonics in the Gulf of Cadiz (Africa–Iberia plate boundary in the north-east Atlantic): insights from analog models. Marine Geology 289, 135–149.

Dufréchou, G., Odonne, F., Viola, G., 2011. Analogue models of second-order faults genetically linked to a circular strike–slip system. Journal of Structural Geology 33, 1193–1205.

Ellis, S., Schreurs, G., Panien, M., 2004. Comparisons between analogue and numerical models of thrust wedge development. Journal of Structural Geology 26 (9), 1659–1675.

Engdahl, R., van der Hilst, R., Buland, R., 1998. Global teleseismic earthquake relocation with improved traveltimes and procedures for depth determination. Bulletin of the Seismological Society of America 88, 722–743.

Fernandes, R.M.S., Miranda, J.M., Meijninger, B.M.L., Bos, M.S., Bastos, L., Ambrosius, B.A.C., Riva, R.E.M., 2007. Surface velocity field of the Ibero-Maghrebian segment of the Eurasia–Nubia plate boundary. Geophysical Journal International 169 (1), 315–324.

Fukao, Y., 1973. Thrust faulting at a lithospheric plate boundary Portugal earthquake of 1969. Earth and Planetary Science Letters 18 (2), 205–216.

Gebco, 2003. British Oceanographic Data Centre on behalf of IOC and IHO. GEBCO Digital Atlas.

Geissler, W.H., Matias, L., Stich, F., Carrilho, F., Jokat, W., Monna, S., IbenBrahim, A., Mancilla, F., Gutscher, M.-A., Sallarès, V., Zitellini, N., 2010. Focal mechanisms for sub-crustal earthquakes in the Gulf of Cadiz from a dense OBS deployment. Geophysical Research Letters 37, L18309.

González, A., Torné, M., Córdoba, D., Vidal, N., Matias, L.M., Diaz, J., 1996. Crustal thinning in the Southwestern Iberia margin. Geophysical Research Letters 23 (18), 2477–2480.

González, A., Córdoba, D., Vegas, R., Matias, L.M., 1998. Seismic crustal structure in the southwest of the Iberian Peninsula and the Gulf of Cadiz. Tectonophysics 296, 317–331.

Gràcia, E., Dañobeitia, J., Vergés, J., Bartolomé, R., 2003a. Crustal architecture and tectonic evolution of the Gulf of Cadiz (SW Iberian margin) at the convergence of the Eurasian and African plates. Tectonics 22 (4), 1033–1052.

Gràcia, E., Dañobeitia, J., Vergés, J., Team, P., 2003b. Mapping active faults offshore Portugal (36 degrees N–38 degrees N): implications for seismic hazard assessment along the southwest Iberian margin. Geology 31 (1), 83–86.

Gràcia, E., Bartolomé, R., Vizcaino, A., Terrinha, P., Lo Iacono, C., Dañobeitia, J.J., SWIM-06 cruise party, 2006. Earthquake and tsunami hazards in the Southwest Iberian Margin (SWIM): high-resolution imaging of active faults and paleoseismic signature at the external part of the Gulf of Cadiz. Proceedings of the 3rd EUROMARGINS Conference, Bologna (Italy), 4–7 October 2006.

Gràcia, E., Vizcaino, A., Escutia, C., Asioli, A., Rodés, A., Pallàs, R., Garcia-Orellana, J., Lebreiro, S., Goldfinger, C., 2010. Holocene earthquake record offshore Portugal (SW Iberia): testing turbidite paleoseismology in a slow-convergence margin. Quaternary Science Reviews 29, 1156–1172.

Grimison, N.L., Chen, W.-P., 1986. The Azores–Gibraltar plate boundary: focal mechanisms, depths of earthquakes, and their tectonic implications. Journal of Geophysical Research 91, 2029–2047.

Gutscher, M.A., 2004. What caused the Great Lisbon earthquake? Science 305 (5688), 1247–1248.

Gutscher, M.A., Kukowski, N., Malavieille, J., Lallemand, S., 1998a. Episodic imbricate thrusting and underthrusting: analog experiments and mechanical analysis applied to the Alaskan accretionary wedge. Journal of Geophysical Research 103, 10161–10176.

Gutscher, M.A., Kukowski, N., Malavieille, J., Lallemand, S., 1998b. Material transfer in accretionary wedges from analysis of a systematic series of analog experiments. Journal of Structural Geology 20, 407–416.

Gutscher, M.A., Malod, J., Rehault, J.P., Contrucci, I., Klingelhoefer, F., Mendes-Victor, L., Spakman, W., 2002. Evidence for active subduction beneath Gibraltar. Geology 30 (12), 1071–1074.

Gutscher, M.A., Dominguez, S., Westbrook, G.K., Gente, P., Babonneau, N., Mulder, T., Gonthier, E., Bartolome, R., Luis, J., Rosas, F., Terrinha, P., DELILA and DELSIS Scientific Teams, 2009a. Tectonic shortening and gravitational spreading in the Gulf of Cadiz accretionary wedge: observations from multi-beam bathymetry and seismic profiling. Marine and Petroleum Geology 26 (5), 647–659.

Gutscher, M.A., Dominguez, S., Westbrook, G.K., Leroy, P., 2009b. Deep structure, recent deformation and analog modelling of the Gulf of Cadiz accretionary wedge: implications for the 1755 Lisbon earthquake. Tectonophysics 475 (1), 85–97.

Hensen, C., Nuzzo, M., Hornibrook, E., Pinheiro, L.M., Bock, B., Magalhaes, V.H., Bruckmann, W., 2007. Sources of mud volcano fluids in the Gulf of Cadiz — indications for hydrothermally altered fluids. Geochimica et Cosmochimica Acta 71, 1232–1248.

Hoshino, K., Koide, H., Inami, K., Iwamura, S., Mitsui, S., 1972. Mechanical properties of Japanese Tertiary sedimentary rocks under high confining pressure. Geological Survey of Japan Report, 244.

Hubbert, M.K., 1937. Theory of scale models as applied to the study of geologic structures. Geological Society of America Bulletin 48, 1459–1520.

Hubbert, M.K., 1951. Mechanical basis for certain familiar geologic structures. Geological Society of America Bulletin 62, 355–372.

Iribarren, L., Vergés, J., Camurri, F., Fullea, J., Fernàndez, M., 2007. The structure of the Atlantic–Mediterranean transition zone from the Alboran Sea to the Horseshoe Abyssal Plain (Iberia–Africa plate boundary). Marine Geology 243, 97–119.

Jimenez-Munt, I., Fernandez, M., Verges, J., Afonso, J.C., Garcia-Castellanos, D., Fullea, J., 2010. Lithospheric structure of the Gorringe Bank: insights into its origin and tectonic evolution. Tectonics 29.

Johnston, A.C., 1996. Seismic moment assessment of earthquakes in stable continental regions .3. New Madrid 1811–1812, Charleston 1886 and Lisbon 1755. Geophysical Journal International 126 (2), 314–344.

Koyi, H., Maillot, B., 2007. Tectonic thickening of hanging-wall units over a ramp. Journal of Structural Geology 29, 924–932.

Kurushin, R.A., Bayasgalan, A., Lziybat, M., Enhtuvshin, B., Molnar, P., Bayarsayhan, Ch., Hudnut, K.W., Lin, J., 1997. The surface rupture of the 1957 Gobi-Altay, Mongolia, earthquake. Geological Society of America, Special Paper, 320.

Lallemand, S., Schnürle, P., Malavieille, J., 1994. Coulomb theory applied to accretionary and nonaccretionary wedges: possible causes for tectonic erosion and/or frontal accretion. Journal of Geophysical Research 99, 12033–12055.

Le Guerroue, E., Cobbold, P.R., 2006. Influence of erosion and sedimentation on strike–slip fault systems: insights from analogue models. Journal of Structural Geology 28 (3), 421–430.

Lebreiro, S.M., McCave, N.I., Weaver, P.E., 1997. Late Quaternary turbidite emplacement on the Horseshoe abyssal plain (Iberian margin). Journal of Sedimentary Research 67 (5), 856–870.

Lohrmann, J., Kukowski, N., Adam, J., Oncken, O., 2003. The impact of analogue material properties on the geometry, kinematics, and dynamics of convergent sand wedges. Journal of Structural Geology 25 (10), 1691–1711.

Maillot, B., Koyi, H., 2006. Thrust dip and refraction in fault-bend folds: analogue models and theoretical predictions. Journal of Structural Geology 28, 36–49.

Malavieille, J., 1984. Modélisation expérimentale des chevauchements imbriqués: application aux chaînes de montagnes. Bulletin de la Societe Geologique de France 26, 129–138.

Malavieille, J., 2010. Impact of erosion, sedimentation and structural heritage on the structure and kinematics of orogenic wedges : analog models and case studies. Geological Society of America, account GSA Today 20 (1), http://dx.doi.org/10.1130/GSATG48A.1.

Mandl, G., de Jong, L.N.J., Maltha, A., 1977. Shear zones in granular material; an experimental study of their structure and mechanical genesis. Rock Mechanics 9, 95–144.

Martinez-Loriente, S., Gràcia, E., Bartolomé, R., Sallarès, V., Dañobeitia, J.J., SWIM-06 Cruise Party, 2008. Pre-stack depth migration seismic imaging of the Coral Patch Ridge and adjacent Horseshoe and Seine Abyssal Plains (Gulf of Cadiz): tectonic implications. Trabajos de Geologia 30, 49–54 (ISSN:1886–4864).

McClay, K., Bonora, M., 2001. Analog models of restraining stepovers in strike–slip fault systems. AAPG Bulletin 85 (2), 233–260.

McClay, K.R., Whitehouse, P.S., Dooley, T., Richards, M., 2004. 3D evolution of fold and thrust belts formed by oblique convergence. Marine and Petroleum Geology 21, 857–877.

Medialdea, T., Vegas, R., Somoza, L., Vázquez, J.T., Maldonado, A., Díaz-del-Río, V., Maestro, A., Córdoba, D., Fernández-Puga, M.C., 2004. Structure and evolution of the "Olistostrome" complex of the Gibraltar Arc in the Gulf of Cadiz (eastern Central Atlantic): evidence from two long seismic cross-sections. Marine Geology 209 (1–4), 173–198.

Morel, J.L., Meghraoui, M., 1996. Goringe–Alboran–Tell tectonic zone: a transpression system along the Africa–Eurasia plate boundary. Geology 24 (8), 755–758.

Mulugeta, G., 1988. Modelling the geometry of Coulomb thrust wedges. Journal of Structural Geology 10, 847–859.

Neves, M.C., Neves, R.M., 2009. Flexure and seismicity across the ocean–continent transition in the Gulf of Cadiz. Journal of Geodynamics 47 (2–3), 119–129.

Nocquet, J.M., Calais, E., 2004. Geodetic measurements of crustal deformation in the Western Mediterranean and Europe. Pure and Applied Geophysics 161 (3), 661–681.

Persson, K., Sokoutis, D., 2002. Analogue models of orogenic wedges controlled by erosion. Tectonophysics 356, 323–336.

Pinheiro, L.M., Whitmarsh, R.B., Miles, P.R., 1992. The ocean–continent boundary off the western continental margin of Iberia — II. Crust structure in the Tagus Abyssal Plain. Geophysical Journal International 109, 106–124.

Purdy, G.M., 1975. The eastern end of the Azores–Gibraltar plate boundary. Geophysical Journal of the Royal Astronomical Society 43, 973–1000.

Ribeiro, A., Cabral, J., Baptista, R., Matias, L., 1996. Stress pattern in Portugal mainland and the adjacent Atlantic region, West Iberia. Tectonics 15 (2), 641–659.

Richard, P., Mocquet, B., Cobbold, P.R., 1991. Experiments on simultaneous faulting and folding above a basement wrench fault. Tectonophysics 188 (1–2), 133–141.
Riedel, W., 1929. Zur Mechanik geologischer Brucherscheinungen. Zentralblatt für Mineralogie, Geologie und Paläontologie 1929B, 354–368.
Rosas, F.M., Duarte, J.C., Terrinha, P., Valadares, V., Matias, L., 2009. Morphotectonic characterization of major bathymetric lineaments in Gulf of Cadiz (Africa–Iberia plate boundary): insights from analogue modelling experiments. Marine Geology 261 (1–4), 33–47.
Sallarès, V., Gailler, A., Gutscher, M.-A., Graindorge, D., Bartolomé, R., Gràcia, E., Díaz, J., Dañobeitia, J.J., Zitellini, N., 2011. Seismic evidence for the presence of Jurassic oceanic crust in the central Gulf of Cadiz (SW Iberian margin). Earth and Planetary Science Letters 311, 112–123.
Sartori, R., Torelli, L., Zitellini, N., Peis, D., Lodolo, E., 1994. Eastern segment of the Azores–Gibraltar Line (central-eastern Atlantic) — an oceanic plate boundary with diffuse compressional deformation. Geology 22 (6), 555–558.
Schopfer, M.P.J., Steyrer, H.P., 2001. Experimental modeling of strike–slip faults and the self-similar behavior. In: Koyi, H.A., Mancktelow, N.S. (Eds.), Tectonic Modelling: A Volume in Honor of Hans Ramberg Geological Society of America Memoir, 193, pp. 21–27.
Serpelloni, E., Vannucci, G., Pondrelli, S., Argnani, A., Casula, G., Anzidei, M., Baldi, P., Gasperini, P., 2007. Kinematics of the western Africa–Eurasia plate boundary from focal mechanisms and GPS data. Geophysical Journal International 169 (3), 1180–1200.
Silva, S., Romsdorf, M., Matias, L., Geissler, W.H., Terrinha, P., Carrilho, F., 2010. Characterization of the seismicity in the Gulf of Cadiz based on eleven month monitoring by the NEAREST OBS network. Geophysical Research Abstracts (EGU General Assembly) 12, 11554.
Solares, J.M.M., Arroyo, A.L., 2004. The great historical 1755 earthquake. Effects and damage in Spain. Journal of Seismology 8 (2), 275–294.
Stich, D., Mancilla, F.D., Morales, J., 2005. Crust–mantle coupling in the Gulf of Cadiz (SW-Iberia). Geophysical Research Letters 32 (13).
Stich, D., Serpelloni, E., Mancilla, F.D., Morales, J., 2006. Kinematics of the Iberia–Maghreb plate contact from seismic moment tensors and GPS observations. Tectonophysics 426 (3–4), 295–317.
Terrinha, P., Pinheiro, L.M., Henriet, J.P., Matias, L., Ivanov, M.K., Monteiro, J.H., Akhmetzhanov, A., Volkonskaya, A., Cunha, T., Shaskin, P., Rovere, M., 2003. Tsunamigenic–seismogenic structures, neotectonics, sedimentary processes and slope instability on the southwest Portuguese Margin. Marine Geology 195 (1–4), 55–73.
Terrinha, P., Matias, L., Vicente, J., Duarte, J., Luis, J., Pinheiro, L., Lourenço, N., Diez, S., Rosas, F., Magalhães, V., Valadares, V., Zitellini, N., Roque, C., Victor, L.M., Team, M.A.T.E.S.P.R.O., 2009. Morphotectonics and strain partitioning at the Iberia–Africa plate boundary from multibeam and seismic reflection data. Marine Geology 267 (3–4), 156–174.
Torelli, L., Sartori, R., Zitellini, N., 1997. The giant chaotic body in the Atlantic Ocean off Gibraltar: new results from a deep seismic reflection survey. Marine and Petroleum Geology 14 (2), 125–138.
Tortella, D., Torné, M., Pérez-Estáun, A., 1997. Geodynamic evolution of the eastern segment of the Azores–Gibraltar Zone: the Gorringe Bank and the Gulf of Cadiz region. Marine Geophysical Researches 19, 211–230.
Viola, G., Odonne, F., Mancktelow, N., 2004. Analogue modelling of reverse fault reactivation in strike–slip and transpressive regimes: application to the Giudicarie fault system, Italian eastern Alps. Journal of Structural Geology 36, 401–418.
Viola, G., Andreoli, M., Ben Avraham, Z., Stengel, I., Reshef, M., 2005. Offshore mud volcanoes and onland faulting in southwestern Africa: neotectonic implications and constraints on the regional stress field. Earth and Planetary Science Letters 231, 147–160.
Weijermars, R., Jackson, M.P.A., Vendeville, B., 1993. Rheological and tectonic modeling of salt provinces. Tectonophysics 217, 143–174.
Withjack, M.O., Schlische, R.W., Henza, A.A., 2007. Scaled experimental models of extension: dry sand vs.wet clay. Houston Geological Society Bulletin 49 (8), 31–49.
Zhou, J., Xu, F., Wei, C., Li, G., Yu, F., Tong, H., 2007. Shortening of analogue models with contractive substrata: insights into the origin of purely landward-vergent thrusting wedge along the Cascadia subduction zone and the deformation evolution of Himalayan–Tibetan orogen. Earth and Planetary Science Letters 260, 313–327.
Zitellini, N., Mendes, L.A., Cordoba, D., Danobeitia, J., Nicolich, R., Pellis, G., Ribeiro, A., Sartori, R., Torelli, L., Bartolomé, R., Bortoluzzi, G., Calafato, A., Carrilho, F., Casoni, L., Chierici, F., Corela, C., Correggiari, A., Della Vedova, B., Gràcia, E., Jornet, P., Landuzzi, M., Ligi, M., Magagnoli, A., Marozzi, G., Matias, L., Penitenti, D., Rodriguez, P., Rovere, M., Terrinha, P., Vigliotti, L., Zahinos Ruiz, A., 2001. Source of 1755 Lisbon earthquake and tsunami investigated. Eos Transactions, American Geophysical Union 82 (26), 290–291.
Zitellini, N., Rovere, M., Terrinha, P., Chierici, F., Matias, L., Bigsets Team, 2004. Neogene through Quaternary tectonic reactivation of SW Iberian passive margin. Pure and Applied Geophysics 161 (3), 565–587.
Zitellini, N., Gràcia, E., Matias, L., Terrinha, P., Abreu, M.A., DeAlteriis, G., Henriet, J.P., Dañobeitia, J.J., Masson, D.G., Mulder, T., Ramella, R., Somoza, L., Diez, S., 2009. The quest for the Africa–Eurasia plate boundary west of the Strait of Gibraltar. Earth and Planetary Science Letters 280 (1–4), 13–50.

Marine Geology 289 (2011) 135–149

Contents lists available at SciVerse ScienceDirect

Marine Geology

journal homepage: www.elsevier.com/locate/margeo

Thrust–wrench interference tectonics in the Gulf of Cadiz (Africa–Iberia plate boundary in the North-East Atlantic): Insights from analog models

João C. Duarte [a,b,c,*], Filipe M. Rosas [a,b], Pedro Terrinha [b,c], Marc-André Gutscher [d], Jacques Malavieille [e], Sónia Silva [a,b,c], Luis Matias [f]

[a] Instituto Dom Luiz, Campo Grande, Ed. C1, Piso 2, 1749-016 Lisboa, Portugal
[b] Universidade de Lisboa, Faculdade de Ciências, Departamento de Geologia, Campo Grande, Ed. C6, Piso 4, 1749-016 Lisboa, Portugal
[c] LNEG, Unidade de Geologia Marinha, Estrada da Portela Zambujal-Alfragide Apartado 7586, 2720-866 Amadora, Portugal
[d] Université Européene de Bretagne, Brest, IUEM, Domaines Océaniques, UMR6538 CNRS, Univ. Brest, France
[e] Université Montpellier 2, CNRS UMR 5243, Géosciences Montpellier, 34095 Montpellier Cedex 5, France
[f] Universidade de Lisboa, Faculdade de Ciências, Departamento de Engenharia Geográfica, Geofísica e Energia, Campo Grande, Ed. C8, Piso 0, 1749-016 Lisboa, Portugal

ARTICLE INFO

Article history:
Received 28 July 2010
Received in revised form 21 September 2011
Accepted 22 September 2011
Available online 8 October 2011

Communicated by D.J.W. Piper

Keywords:
SWIM wrench system
Gulf of Cadiz Accretionary Wedge (GCAW)
thrust–wrench interference
analog modeling
Tethyan-related plate boundary

ABSTRACT

In the Gulf of Cadiz key segment of the Africa–Iberia plate boundary (North-East Atlantic ocean), three main different modes of tectonic interference between a recently identified wrench system (SWIM) and the Gulf of Cadiz Accretionary Wedge (GCAW) were tested through analog sand-box modeling: a) An active accretionary wedge on top of a pre-existent inactive basement fault; b) An active strike-slip fault cutting a previously formed, inactive, accretionary wedge; and c) Simultaneous activity of both the accretionary wedge and the strike-slip fault. The results we obtained and the comparison with the natural deformation pattern favor a tectonic evolution comprising two main steps: i) the formation of the Gulf of Cadiz Accretionary Wedge on top of inactive, Tethyan-related, basement faults (Middle Miocene to ~1.8 Ma); ii) subsequent reactivation of these basement faults with dextral strike-slip motion (~1.8 Ma to present) simultaneously with continued tectonic accretion in the GCAW. These results exclude the possibility of ongoing active SWIM wrench system cross-cutting an inactive GCAW structure. Our results also support a new interpretation of the SWIM wrench system as fundamentally resulting from strike-slip reactivation of an old (Tethyan-related) plate boundary.

1. Introduction

The Gulf of Cadiz is situated in the North-East Atlantic Ocean, west of the Gibraltar Straits, offshore SW Iberia and NW Morocco (Fig. 1). This zone marks the transition between the Mediterranean Alpine Collision Belt and the Atlantic Azores–Gibraltar Fracture Zone (AGFZ; see Fig. 1) and corresponds to a segment of the Africa–Eurasia plate boundary previously described as tectonically diffuse (e.g. Sartori et al., 1994; Medialdea et al., 2004). Accordingly, a variety of tectonic structures with different orientations, corresponding mostly to W–NW directed thrusts and WNW–ESE dextral strike-slip faults (Fig. 1B), are thought to accommodate a WNW–ESE present convergence between Eurasia (Iberia sub-plate) and Africa (Nubia sub-plate) at a rate of ca. 4–5 mm/year (Argus et al., 1989; DeMets et al., 1994; Sella et al., 2002; Calais et al., 2003; Fernandes et al., 2003; Fernandes, 2004; Nocquet and Calais, 2004; Fernandes et al., 2007).

The seismicity of this domain has been characterized as moderate, although several high magnitude historical and instrumental earthquakes are known (e.g. Ms = 7.9 28/02/1969 and Mw = 6.0, 12/02/2007 earthquakes respectively, Fukao, 1973 and Stich et al., 2006, 2007). Among these, the 1755 Great Lisbon Earthquake (estimated magnitude of 8.5 to 8.7; Abe, 1979; Johnston, 1996; Martinez-Solares and López Arroyo, 2004) triggered a devastating tsunami and destroyed the Portuguese capital (Baptista et al., 1998; Zitellini et al., 2001; Martinez-Solares and López Arroyo, 2004). Despite recent mapping updates of the main tectonic structures of this region based on the interpretation of a great variety of newly acquired data (e.g. multi-beam swath bathymetry, reflection and refraction seismics, geodetic; Johnston, 1996; González et al., 1996; Zitellini et al., 2001; Gutscher et al., 2002, 2009a,b; Baptista et al., 2003; Gràcia et al., 2003a,b; Mulder et al., 2003; Zitellini et al., 2004; Rosas et al., 2009; Terrinha et al., 2009; Zitellini et al., 2009), the precise location of the seismogenic/tsunamigenic source of 1755 major event is still the subject of ongoing debate (e.g. Baptista et al., 1998; Buforn et al., 1988; Zitellini et al., 2001; Gràcia et al., 2003a,b; Terrinha et al., 2003; Gutscher, 2004; Gutscher, 2006; Terrinha et al., 2009).

In the tectonic map of Fig. 1B three main sets of structures are immediately recognized: a) several NE–SW striking, westward directed

* Corresponding author at: School of Geosciences, Monash University, Building 28, Clayton Campus, Wellington Road, Clayton, Melbourne, VIC 3800, Australia. Tel.: +61 3 99020062.
E-mail addresses: joao.duarte@monash.edu, joao.moedas@gmail.com (J.C. Duarte).

0025-3227/$ – see front matter © 2011 Elsevier B.V. All rights reserved.
doi:10.1016/j.margeo.2011.09.014

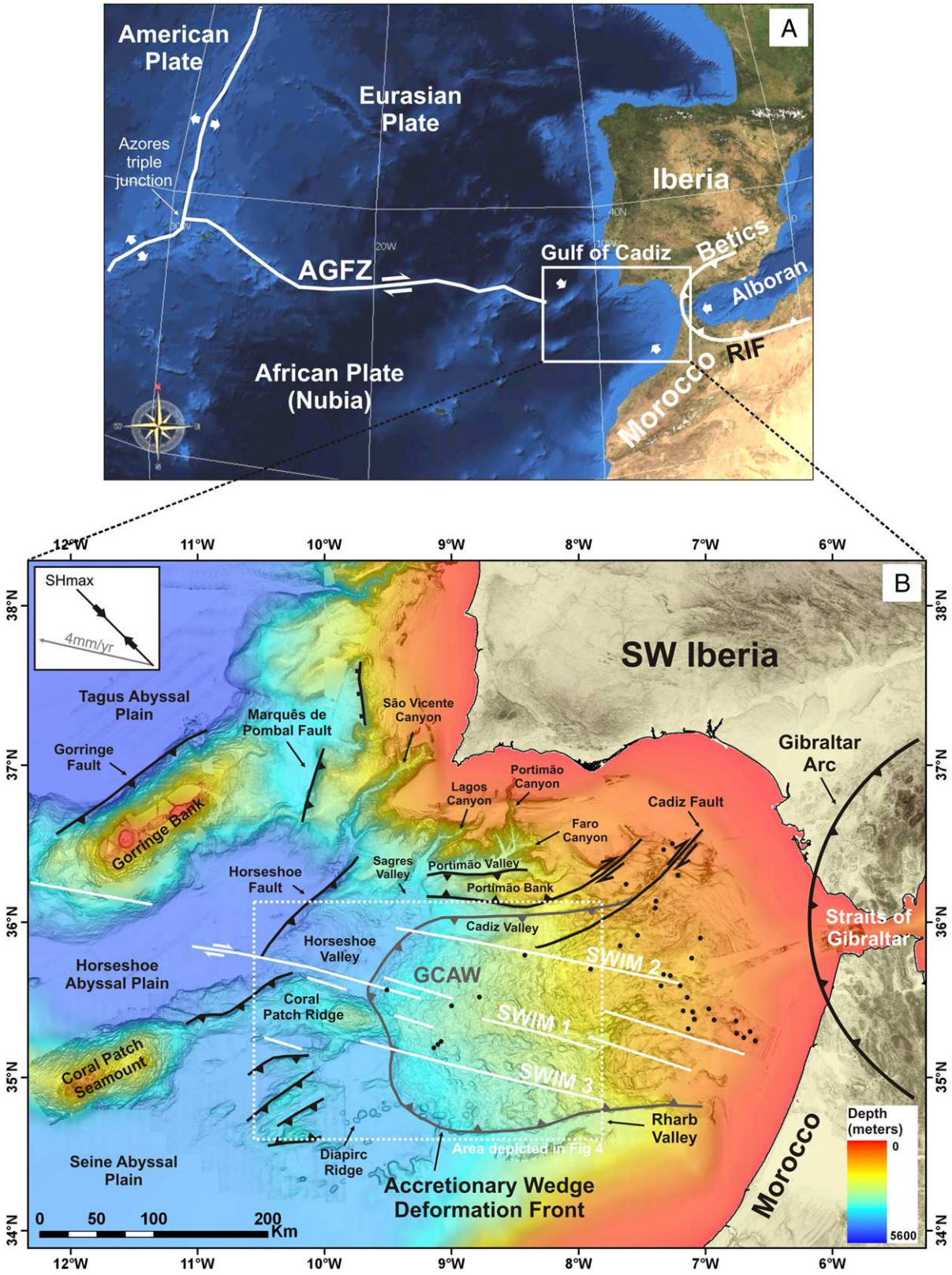

Fig. 1. (A) Location of the Gulf of Cadiz area in the general tectonic setting of the Eurasia (Iberia)–Africa (Nubia) plate boundary. AGFZ — Açores–Gibraltar Fracture Zone; (B) Simplified tectonic map of the Gulf of Cadiz area. Gulf of Cadiz Accretionary Wedge (GCAW) — dark gray outline; SWIM wrench system according to Zitellini et al. (2009) — white lines. Black dots correspond to the location of known mud volcanoes (e.g. Hensen et al., 2007).
Panel B is adapted from Duarte et al. (2009), Terrinha et al. (2009), Zitellini et al. (2009) and Duarte et al. (2010); bathymetry from the SWIM compilation; Zitellini et al., 2009.

thrust faults (e.g. Gorringe, Horseshoe and Marquês de Pombal faults); b) major WNW–ESE striking dextral strike-slip faults (the SWIM faults) and c) a major thrust bounding the so called Gulf of Cadiz Accretionary Wedge (GCAW frontal thrust). Structures of the first set have previously been described as active and, individually (e.g. Gorringe fault), or together (Marques de Pombal and Horseshoe

faults), successively considered and dismissed as possible seismogenic/tsunamigenic sources of the 1755 Great Lisbon Earthquake (e.g. Buforn et al., 1988; Baptista et al., 1998; Zitellini et al., 2001; Terrinha et al., 2009). The other two sets of tectonic structures support the following two fundamental ideas for the interpretation of the Gulf of Cadiz tectonic framework (Gutscher et al., 2002; Zitellini et al., 2009):

- Gutscher et al. (2002), building on previously reported similar ideas (e.g. Royden, 1993 and Lonergan and White, 1997), considered the tectonic evolution of this plate boundary as being dominated by active (roll back) subduction of a retreating east-dipping lithospheric slab, presently positioned beneath the Gibraltar Arc (Fig. 1B). Accordingly, associated synthetic accretion of sediments is also reported to occur, represented by the Gulf of Cadiz Accretionary Wedge (GCAW, Fig. 1B), in which several imbricated west-directed active thrusts accommodate on-going shortening.
- Zitellini et al. (2009) argued for the existence of a broad transpressive deformation band, comprising a set of WNW–ESE striking, subvertical, dextral strike-slip faults (SWIM faults in Fig. 1B), which as a whole extend for more than 600 km, from the eastern part of the Gulf of Cadiz to the southern limit of the Gorringe bank. These faults are interpreted by the cited authors as lithospheric faults, and in view of that the SWIM fault system was proposed to mark a newly formed plate boundary connecting the AGFZ to the Rif Mountain belt in northern Morocco.

It should be noted that Zitellini et al. (2009) considered the dextral transcurrent SWIM faults in the Gulf of Cadiz as presently active, and cutting the GCAW thrusts, whose activity is considered to be negligible since late Miocene times. Conversely, Gutscher et al. (2002) considered the GCAW thrusts as still active, and as referred above related with present on-going subduction beneath the Gibraltar arc.

In the present work, we test the above assumptions using analog modeling sand-box experiments to model the interference between the two major tectonic systems in the Gulf of Cadiz, i.e. SWIM dextral wrenching and GCAW thrusting, assuming three main different possibilities:

1) The GCAW is presently active and the SWIM faults are thought to correspond to inactive basement faults, inherited from a previous tectonic evolution;
2) The SWIM faults are thought to correspond to major, presently active, dextral strike-slips, cutting a previously formed inactive GCAW;
3) Both tectonic systems are presently active.

Thorough comparison of the obtained results with the observed natural morphotectonic pattern is carried out for each of the above cases. Accordingly, resulting tectonic implications for the local and whole scale evolution of this segment of the Eurasia–Africa plate boundary are evaluated and explored.

2. Morphotectonic characterization of the study area

The morphology of the Gulf of Cadiz is largely controlled by the main tectonic processes in the area: the thrusting accommodating the GCAW accretion and the wrenching associated to the SWIM fault system. The high-resolution bathymetry of the GCAW shows a west dipping U-shaped body (Figs. 1B and 2A) that extends for more than 250 km from about longitude 7°W to 9°30′W, with depths ranging from 200 to 4300 m. It narrows slightly to the west with a width varying from 160 to 140 km (see Figs. 1B and 2A). Its wrinkled surface morphology is shaped not only by thrust-related slope breaks and associated folds, which define a large scale stepping morphology, but is also the result of the different combined manifestations of gravitational and fluid escape processes (e.g. “raft-tectonics” type features, sub-circular collapse depressions, mud volcanoes, salt diapirs; Mulder et al., 2003; Pinheiro et al., 2003; Gutscher et al., 2009b; Terrinha et al., 2009; Zitellini et al., 2009). From a structural point of view, the accretionary wedge corresponds to an eastward thickening pile of westward thrust sediments (Fig. 2B and C), reaching a maximum thickness of ca. 15 km near the Gibraltar Straits (Thiebot and Gutscher, 2006; Gutscher et al., 2009a). The thrusts root in a common sub-horizontal to gently east dipping decollement layer, exhibiting an overall geometry complying with on-going eastward subduction beneath the Gibraltar Arc (Gutscher et al., 2002). During the last 5 Ma, the E–W convergence rate implied in such a subduction is thought to have diminished from ca. 2 cm/year to 0.5 cm/year (Gutscher et al., 2009a), with a consequent decrease in the activity of the wedge thrusts during this time span. Accordingly, the same authors argue that the present internal deformation is preferentially accommodated by small increments of local reactivation of inherited blind thrusts, being more homogeneously distributed over the entire wedge, rather than concentrated on newly formed major frontal thrusts.

The morphologic expression of the SWIM faults corresponds to a continuous alignment of seafloor crests and troughs, sometimes exhibiting an en-échelon geometrical disposition, and commonly punctuated by active mud volcanoes within the domain of the accretionary wedge (see Fig. 1B; Duarte et al., 2009; Terrinha et al., 2009; Zitellini et al., 2009). This overall linear morphology is more prominent both close to the northern part of the GCAW front and in the Horseshoe Valley, where lineaments can be followed almost continuously for more than 200 km (e.g. SWIM 1 in Figs. 1B and 3A). The available reflection seismic dataset in the study area shows that SWIM faults correspond to aligned arrays of deep-rooted faults, often breaching out through the present seafloor sediments and showing extensive evidence for associated fluid migration (e.g. seismic blanking along fluid extrusion paths in Fig. 3B and C; Rosas et al., 2009; Terrinha et al., 2009). From the inspection of the IAM 4 and 3 seismic profiles in Fig. 3, it is apparent that the SWIM faults are aligned along basement pre-existent (Mesozoic) faults (dashed black lines in Fig. 3; see also Duarte et al., 2009 and Terrinha et al., 2009). Analog modeling of sets of en-échelon folds formed in soft-cover sediments overlying some of the SWIM basement dextral strike-slips (Rosas et al., 2009) yielded an age for their activity of ca. 1.8 Ma.

2.1. The SWIM–GCAW interference area

The critical area to understand the interference between the SWIM strike-slips and the GCAW is close to its deformation front (Fig. 4A). Along this front, from north to south, three interference sub-areas were thoroughly analyzed (B to D in Fig. 4). The SWIM 2 fault intersects a northern segment of the GCAW front (Fig. 4B) in the vicinity of the Sagres Valley, at an angle of about 40°. Within the thrust wedge to the east, the morphological expression of the SWIM 2 is well marked by a slightly arched trough that splays in the same direction. Conversely, in the Sagres Valley it is almost indiscernible due to the widespread presence of scours and slumps, and it is only detectable by the presence of a gentle slope break. In this area no offset of the wedge deformation front is observed, instead only a small wrinkled WNW–ESE elongate bulge can be detected in the bathymetry of the frontal GCAW (see Fig. 4B). The SWIM 1 fault exhibits a clear morphological expression in the Horseshoe Valley, intersecting the wedge deformation front just to the north of the Coral Patch Ridge, at an angle of about 70° (Fig. 4C). Its continuation to the east is less visible, although punctuated by mud volcanoes. Similarly to what was described for the SWIM 2 fault, there is no bathymetric evidence for the offset of the wedge front by the SWIM 1 fault. The SWIM 3 fault cuts along the southern flank of the Coral Patch Ridge with a strong morphological imprint (Fig. 4D), corresponding to a

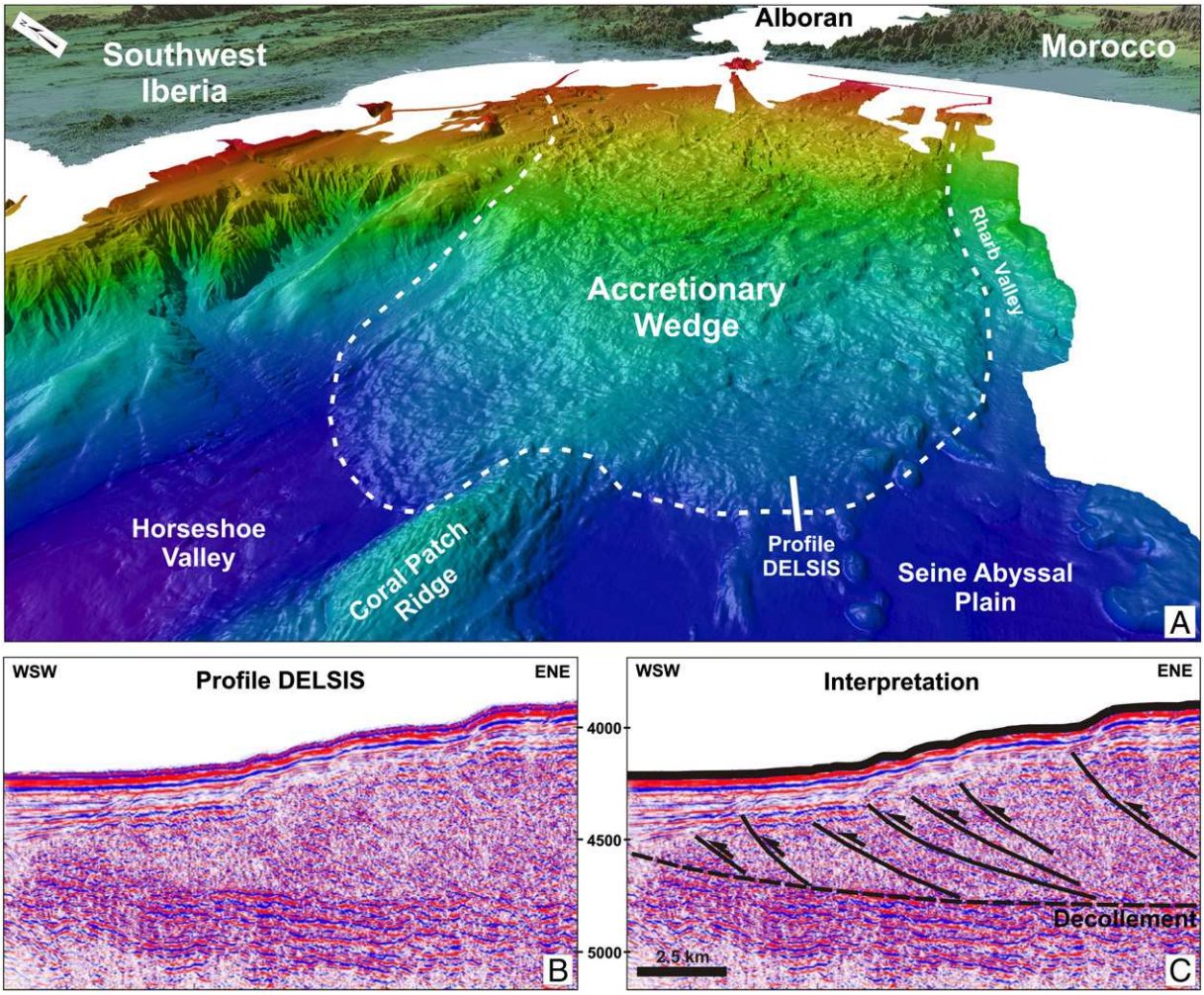

Fig. 2. (A) Perspective view (from southwest) of the Gulf of Cadiz Accretionary Wedge surface and adjacent areas; (B) Delsis Multichannel seismic profile across the accretionary wedge deformation front (see A for location) and (C) respective interpretation.

lineament marked by several elongated WNW–ESE ridges, troughs and slope breaks. To the east, this lineament crosses a small portion of the Seine Abyssal Plain and intersects the accretionary wedge deformation front, at an angle of about 80°. In this location the wedge front is marked by a slight embayment. On the wedge surface to the north of the fault and parallel to it, an elongated protuberance is also unmistakably observed, limited by two descending slope breaks and vanishing progressively toward the east. As in the two cases described above, the observed morphology does not account for any kind of fault offset overprint relationships.

3. Analog modeling

Our objective is to test several simple chronological possibilities of mechanical interference between a strike-slip fault and a thrust wedge front, under model conditions comparable to the ones governing the SWIM–GCAW tectonic interference. Three main experiments were carried out to investigate the different deformation patterns resulting from: a) A thrust wedge developed on top of an inactive basement (strike-slip) fault; b) An active dextral strike-slip fault affecting an inactive thrust wedge; c) The simultaneous alternate activity of a thrust wedge front and a dextral strike-slip fault. Experiments were performed to respect the general, simplified, geometry, kinematics and rheology ascribed to the natural strike-slip (SWIM) system and to the (GCAW) thrust wedge. However, analog modeling with dry granular materials cannot reproduce all the complex processes (e.g. fluid overpressure and expulsion, sedimentary deposition, and local gravitational instabilities) which occur in submarine environments. Nevertheless, the regional kinematic and relative timing caused by the local tectonic driving forces and the ensuing structural evolution can be well investigated.

3.1. Experimental method

3.1.1. Material properties and scaling

The material used as an analog of the GCAW sedimentary rocks was dry quartz sand, whose properties are summarized in Table 1. Sand is considered a Coulomb material deforming in a brittle way according to the Coulomb fracture criterion (e.g. Hubbert, 1937, 1951; Davis et al., 1983, Appendix A), and it has been extensively used in scaled model experiments simulating similar brittle deformation in the upper crust (e.g. Mandl et al., 1977; Mulugeta, 1988; Casas et al., 2001; Marques and Cobbold, 2002).

The present models were properly scaled according to the scale model theory of Hubbert (1937). The assumed model — prototype ratios are presented in Table 1, and the detailed procedure of scaling is specified in Appendix A.

3.1.2. Apparatus and initial stage

Experiments were done using a rectangular 100 cm × 60 cm Perspex deformation rig, comprising two laterally juxtaposed basal plates and a moving backstop (Fig. 5A). In the initial stage of the

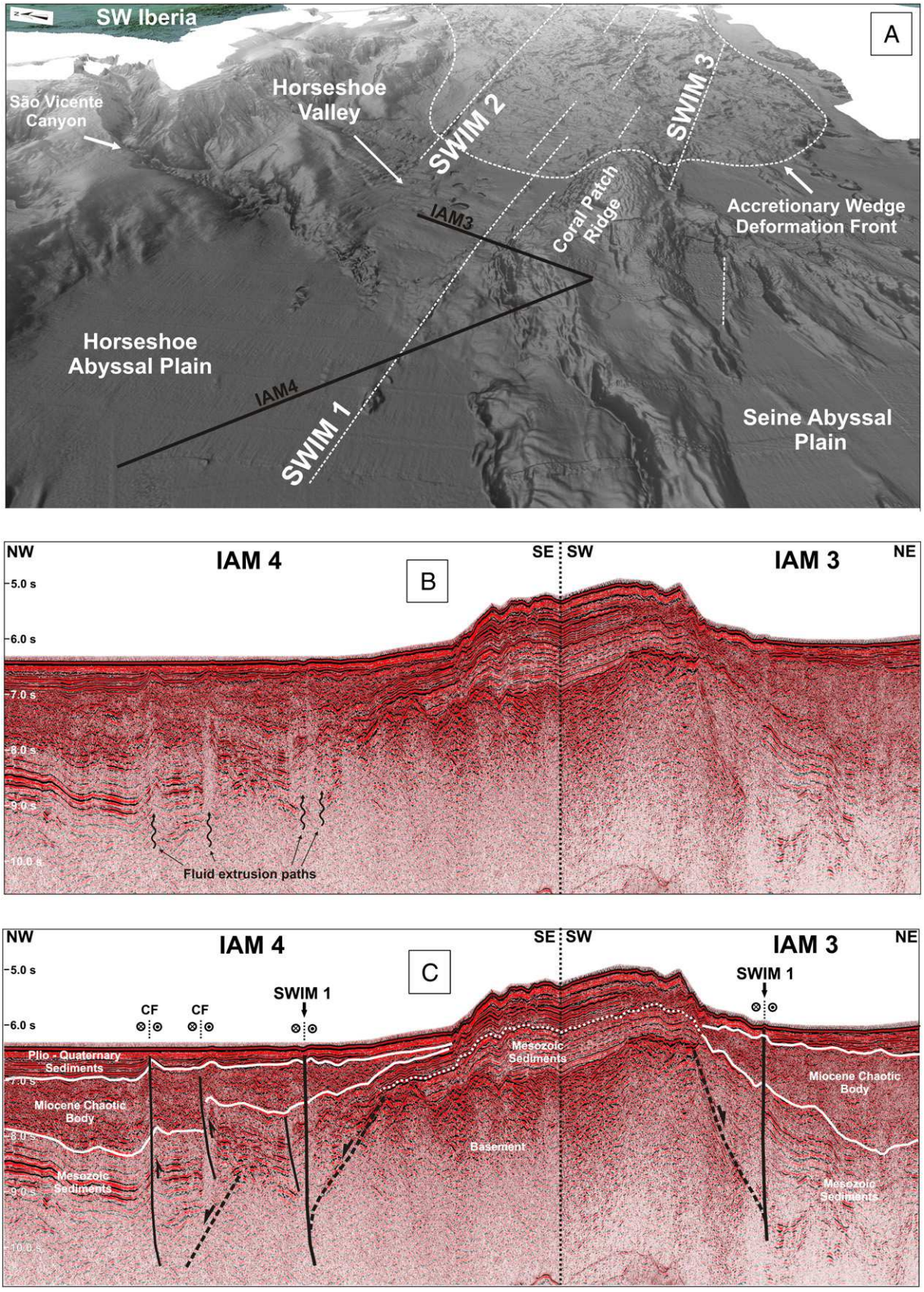

Fig. 3. (A) Perspective view (from southwest) of the SWIM lineaments; (B) Multichannel seismic profiles IAM-4 and IAM-3 crosscutting SWIM fault 1 and (C), and respective interpretation; note the Mesozoic rift-related faults (black dashed lines). CF — Oblique dextral-reverse faults (Corner Faults of Rosas et al., submitted for publication). See location in A.

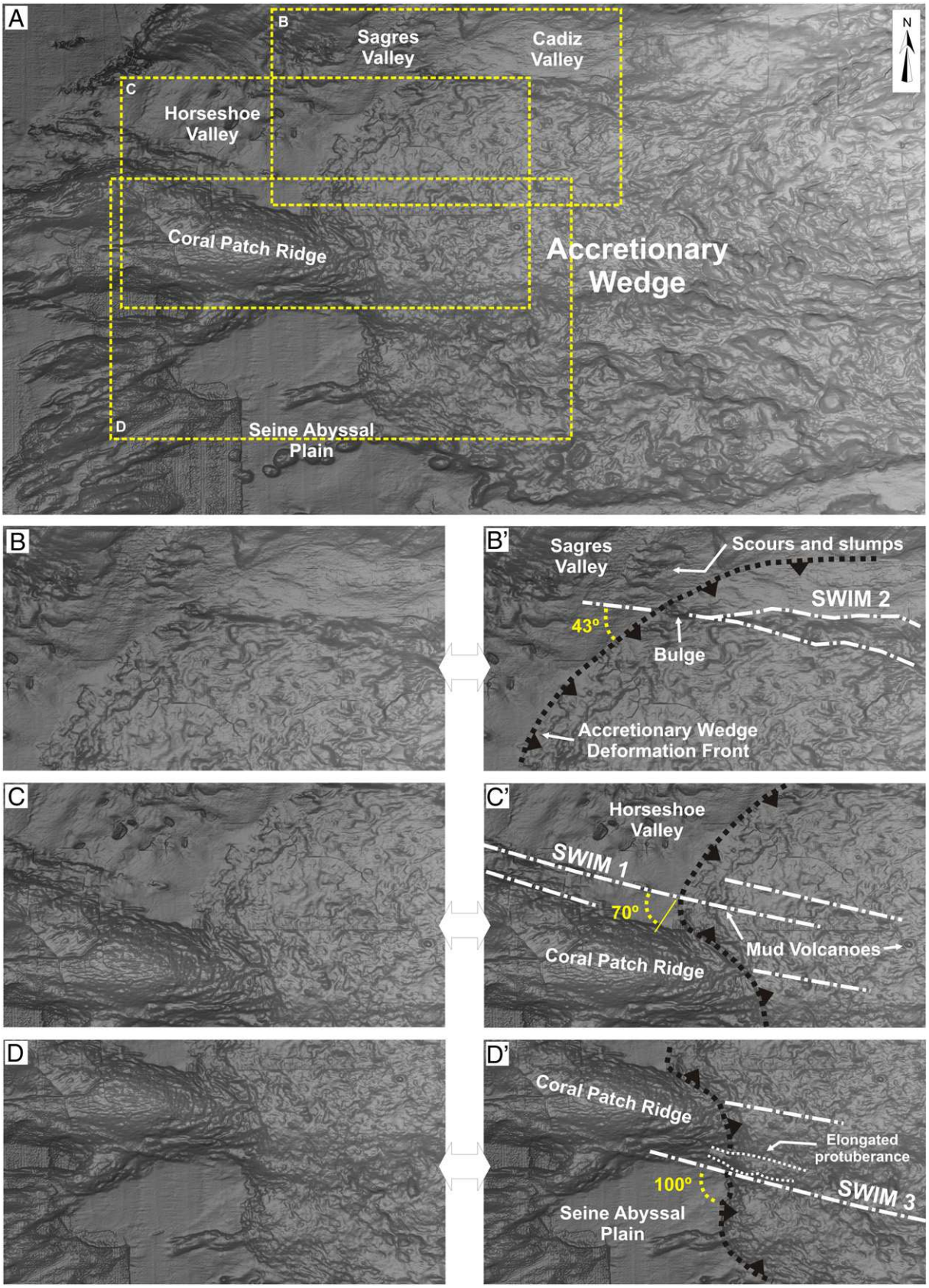

Fig. 4. General (A) and detailed (B, C and D) bathymetric imaging and respective morphotectonic interpretation (B′, C′, and D′) of the interference area between the accretionary wedge deformation front and the SWIM 1, 2 and 3 strike-slip faults. Note the absence of offset overprint relationships.

Table 1
Parameters and material properties. Note: Scaled fundamental units are in bold. A mean cohesion of $c_0 = 40$ MPa was assumed from the natural prototype (e.g. Hoshino et al., 1972; Weijermars et al., 1993).

Parameters and material properties	Quartz sand (model)	Natural prototype	Ratio: model/nature
Composition (%)	99.7% quartz	–	–
Grain shape	Well-rounded	–	–
Grain size (mm)	<0.30	–	–
Density (kg m^{-3})	1300	2600	$\delta = 0.5$
Internal friction angle, ϕ (°)	~30	–	–
Coefficient of internal friction, μ_c	~0.6	0.6–0.85	–
Cohesion, c_0 (Pa)	Negligible	40×10^6	–
Gravity acceleration, g (ms^{-2})	9.81	9.81	$\gamma_g = 1$
Length, L (m)	0.01	5000	$\boldsymbol{\lambda = 2 \times 10^{-6}}$
Mass, M (kg)	–	–	$\boldsymbol{\mu = 4 \times 10^{-18}}$

experiments, 1 cm thick layered sand cake was built on top of the basal rigid plates by pouring batches of differently colored sand from a moving elongated funnel, guaranteeing the leveling of its top surface. The basal plates in the model move laterally relatively to each other, and account for the natural basement beneath the thrust wedge decollement (see Fig. 2C). The vertical contact plane between these plates complies with the dominant WNW–ESE orientation of the SWIM 1 fault system (see Figs. 1 and 4). The model sand cake corresponds to the overlying cover sediments, in which accretion is simulated by pushing against it a backstop that slides on top of both basal plates. The backstop lacks any kind of correspondence with any natural feature, and was exclusively used to produce a classical model thrust wedge. Likewise the (~0.2 cm thick) layering in the sand cake has also no correspondence with any natural structures, and was used merely as a 3D passive strain marker. In all experiments the dimensions of the deformation rig were sufficiently large to guarantee that the bulk of the model was not affected by boundary conditions. The experiments were repeated several times to ensure the reproducibility of the obtained results. Top view photographs were taken at regular time intervals. The final stage of the model was humidified and serially sectioned for three-dimensional analysis.

3.1.3. Procedure

Three main experiments were carried out to study three basic possibilities of mechanical interference between a strike-slip basement fault and a thrust wedge:

1) Active thrust wedge and inactive basement fault: the backstop was initially pushed against the sand-cake, on top of the two immobile basal plates.
2) Active basement fault and inactive thrust wedge: after a thrust wedge was previously formed in the sand, the basal plates were dextrally moved relatively to each other.
3) Active basement fault and active thrust wedge: the reactivation of a previously formed thrust wedge was successively alternated with the right-lateral movement between the basal plates.

3.2. Experimental results

3.2.1. Experiment 1: active thrust wedge and inactive basement fault

Up until ~30% of shortening a thrust wedge was classically obtained, through the forward propagation of regularly spaced thrusts, as a result of moving the backstop to the left (see Figs. 5B and 6A). For a shortening of 31% (Fig. 6A) the front of the accretionary wedge developed an embayment coinciding with the direction of the inactive basement fault (yellow dashed line in Fig. 6A). For a shortening of 38% a new thrust (n + 1 in Fig. 6B) was formed exclusively to the north of that basement discontinuity. Only when the shortening reached 39%, did the equivalent new thrust form to the south, resulting in a misleading left-lateral offset geometry (yellow arrows in Fig. 6C), in spite of the total absence of relative movement between the two basal rigid plates. For a shortening of 48% this false offset in front of the newer thrust disappeared (Fig. 6D). In the wedge lower area a linear southeastward splaying, slightly anastomosing, deformation pattern (white lines in Fig. 6D) was progressively developed as shortening accumulated and new outward thrusts successively formed.

3.2.2. Experiment 2: active basement fault and inactive thrust wedge

After 48% of shortening the basement strike-slip fault was activated with dextral movement (Fig. 7) When the horizontal displacement between the basal plates reached only 0.2 cm, a thin elongated bulge formed coinciding with the basement strike-slip direction (Fig. 7A). At this stage no offset of the thrust wedge was observed. A further right-lateral displacement of 0.6 cm between the basal plates clearly offset the thrust wedge, preferably affecting its frontal outer thrust (Fig. 7B). For a displacement of 1.3 cm the strike-slip fault seemingly propagated inward, but only across the following three thrusts (Fig. 7C–D). The resultant model deformation pattern always showed the preferential offset of the frontal thin part of the accretionary wedge, relative to its innermost domains that remained unaffected.

3.2.3. Experiment 3: active basement fault and active thrust wedge

After the formation of a thrust wedge due to 47% of shortening, a right-lateral displacement of 1 cm was applied to the basal plates (Fig. 8A). As a result, a linear bulge formed in the sand foreland,

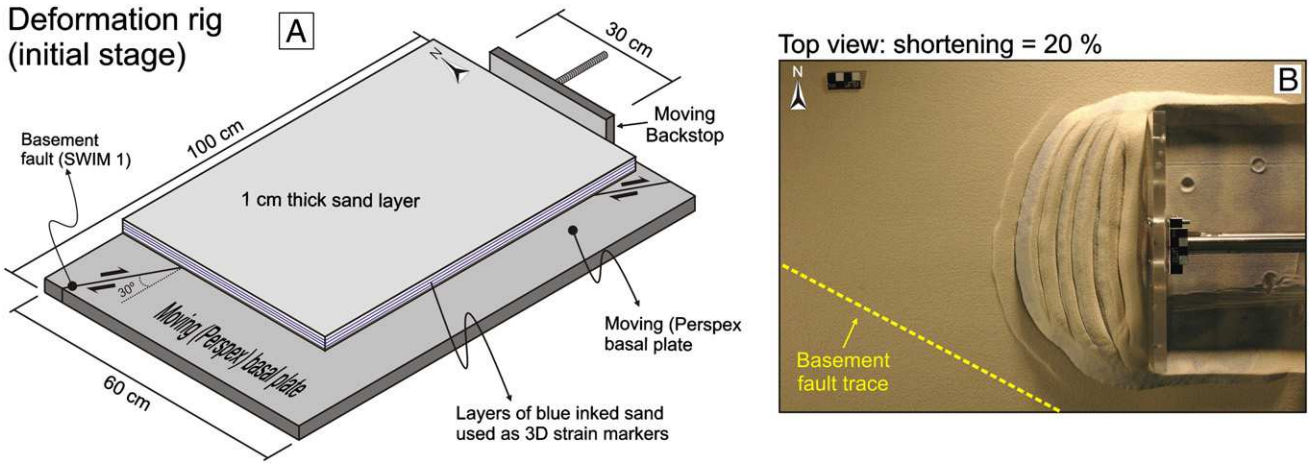

Fig. 5. (A) — Sketch of experimental apparatus and model set-up at initial stage. (B) Model top view after 20% of shortening.

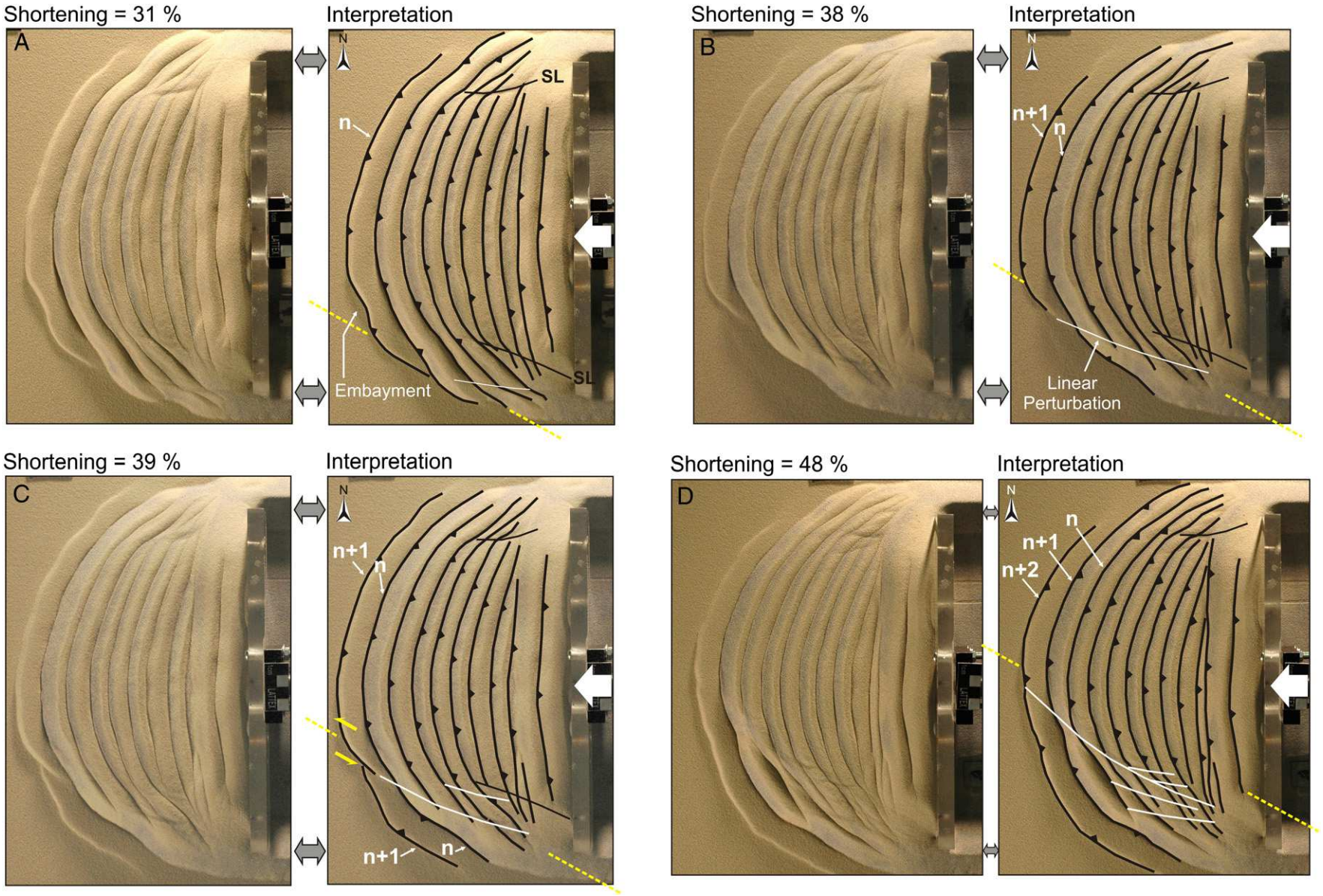

Fig. 6. Results of experiment 1: active thrust wedge and inactive basement fault. A, B, C and D — Model top view after 31, 38, 39 and 48% of shortening, respectively. Yellow dashed line — direction of basement (inactive) fault; white arrow — direction of shortening; yellow half arrows — apparent left-lateral offset; white lines mark the inner splaying geometry of the wedge surface perturbation; n, n + 1, …n + n refer to the relative chronology of thrust propagation in B, C and D. SL (thin black lines) — slip lines (Note that the slip lines are a byproduct of boundary conditions due to backstop finite length).

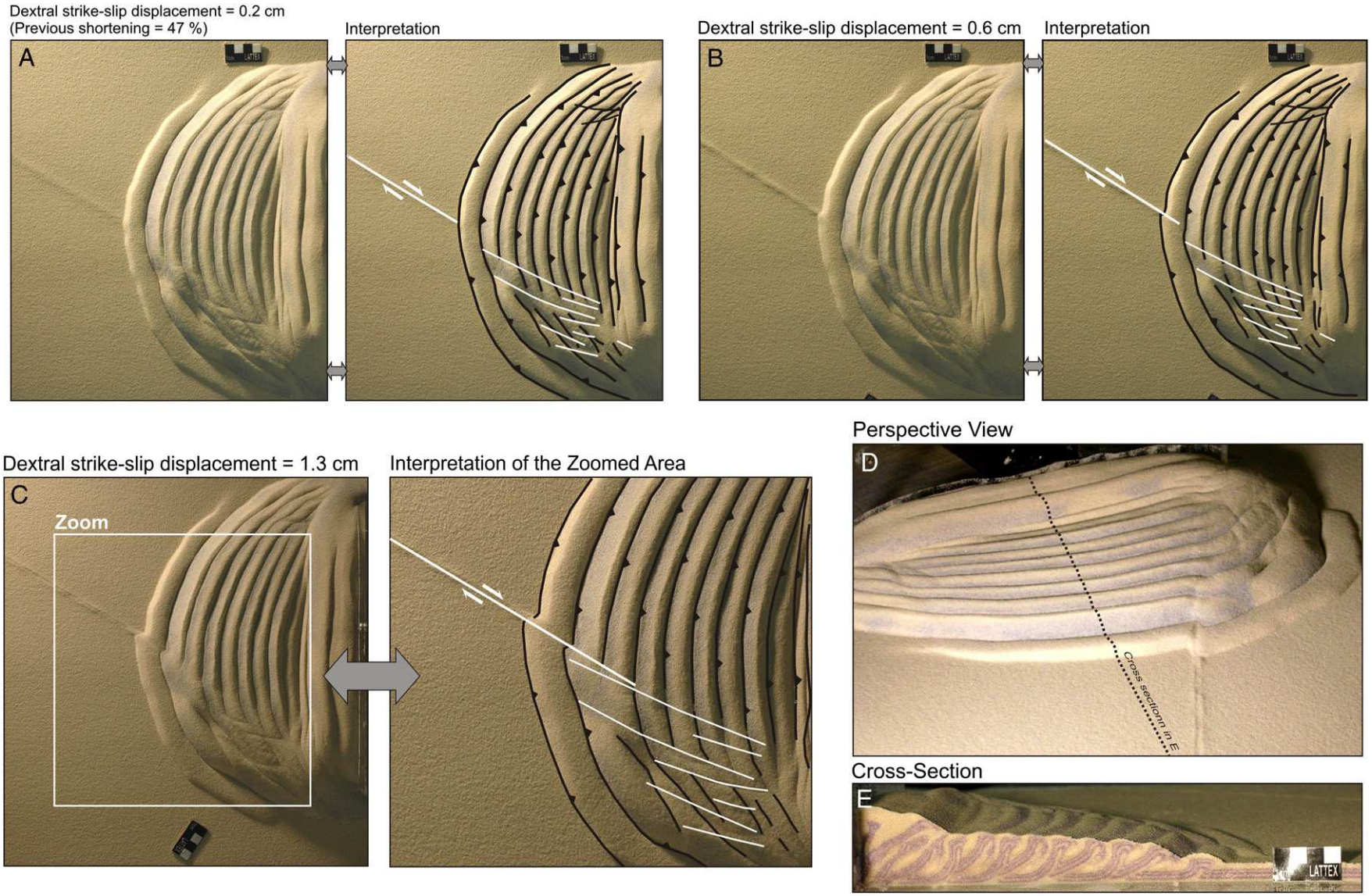

Fig. 7. Results of experiment 2: active basement fault and inactive thrust wedge. A, B and C — Model top view after 0.2, 0.6 and 1.3 cm of right-lateral strike-slip displacement, respectively. D — Perspective view of the deformation stage illustrated in C. E — Orthogonal cross section of the thrusted wedge (see location in D). White half arrows indicate right-lateral offset.

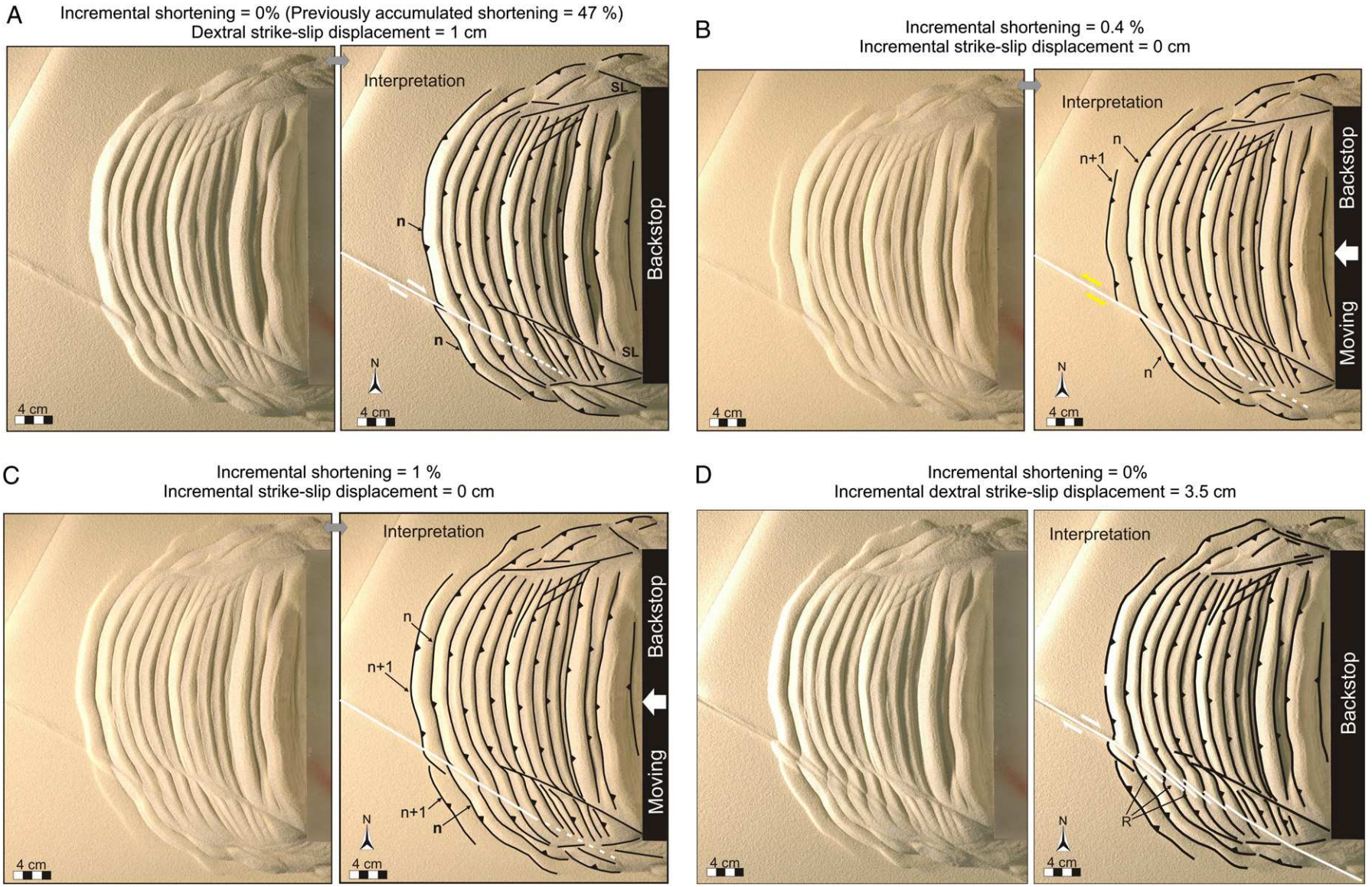

Fig. 8. Results of experiment 3: active basement fault and active thrust wedge. A, B, C and D — Model top view after different increments of shortening and dextral strike-slip displacements; n, n + 1, …n + n refer to the relative chronology of thrust propagation; white line — dextral strike-slip fault trace (R — en-échelon Riedels). White half arrows — dextral offset; yellow half arrows — false left-lateral offset of the frontal wedge thrust.

along the strike-slip direction, cutting across the thrust wedge and offsetting its front. Similarly to experiment 2, the amount of right-lateral displacement diminished toward the thicker inner part of the wedge. Subsequently, another 0.4% of incremental shortening was applied to the model (Fig. 8B). As a result, a new frontal thrust formed, but only to the north of the strike-slip fault. The resultant geometry mimics a false left-lateral offset of the outer frontal thrust (apparent as n + 1 in Fig. 8B), although careful consideration of the propagation chronology of the thrusts revealed a true dextral offset (affecting thrust n in Fig. 8B), complying with the underlying basement fault kinematics. Further 1% of applied shortening (Fig. 8C) produced the new thrust (n + 1) also to the south of the strike-slip fault, erasing the previously formed false offset. Another 3.5 cm of dextral strike-slip displacement was additionally applied to the basal plates (Fig. 8D), and as a consequence, the wedge front was once more kinematically truly dextrally offset. Riedel faults formed on the wedge surface displaying a clear en-échelon spatial disposition, and interfering with the preexistent stepping morphology associated with the thrust stacking. Finally, after another 2.6% of shortening (Fig. 9), reaching a total accumulated amount of 51%, the frontal wedge offset was once again almost completely attenuated, although the total accumulated basal strike-slip displacement was of 4.5 cm (corresponding to 22.5 km). It should be noted that the previously formed linear en-échelon pattern was preserved in the wedge surface, including in its innermost domain.

4. Discussion

Experiment 1 shows that an active thrust wedge forming in cover sediments above an inactive basement fault records the resultant mechanical interference in the form of a linear, inner splaying, perturbation of the wedge morphological surface (white lines in Fig. 6C–D). This formed as the result of the successive thrust propagation across the basement anisotropy, which behaved as a mechanical obstacle for the lateral propagation of the frontal thrust. Since this basement anisotropy remains stationary relatively to an external reference frame, and the thrust front propagates forward (to the left), the resultant interference area between both these features migrates from the lower periphery of the thrust front to its central domain (compare the position of the linear perturbation pattern in Fig. 6A to D). Comparison with the natural example shows that the observed inner splaying lineaments in the GCAW (see SWIM 1 in Fig. 1B and SWIM 2 in Fig. 4B), could have originated simply as a consequence of preexisting inactive basement faults. This agrees with the fact that these lineaments are observed in the inner thicker part of the natural thrust wedge, in the complete absence of offset of its thinner frontal part.

Experiment 2 shows that an active basement strike-slip fault affecting an overlying preexistent thrust-wedge, must produce a clear offset of its thinner front, even for minor increments of strike-slip basal displacement (1.3 cm corresponding to 6.5 km). This offset vanishes rapidly toward the inner thicker parts of the wedge, affecting almost exclusively the outer frontal thrusts. Comparison with the natural example shows that if the GCAW is presently inactive, and cut by active dextral strike-slip (SWIM) faults, then unambiguous offset of the GCAW front has to exist, which is clearly not the case (see Figs. 1B, 2 and 4).

Experiment 3 shows that if both the basal strike-slip fault and the thrust wedge are active, with alternating incremental fault slips, then the resultant interference deformation pattern can be the cyclic repetition of the following three possibilities: a) true right-lateral offset of the thrust wedge front (see Fig. 8A and D); b) false left-lateral offset of the thrust wedge front (see Fig. 8B, similar to experiment 1 see Fig. 6C); c) no offset of the thrust wedge front (see Figs. 8C and 9). It should be noted that the absence of thrust wedge offset does not imply an absence of basement strike-slip displacement, which quite on the contrary is continually increasing. However, the alternation with the incremental shortening that drives the successive forward thrust propagation cyclically erases the offset of the frontal thrust wedge. Differently, the resultant linear en-échelon interference pattern tends to be increasingly well marked, including in the innermost domains of the thrust wedge (compare the lineament in the Figs. 8A and 9). Similarly to experiment 1, the intermediate experimental stage in which a false left-lateral offset originates (see Fig. 8B), is here interpreted as the result of a delayed propagation of the newer outer thrust across the strike-slip fault, which in accordance seemingly behaves as a mechanical obstacle to such propagation.

In view of these results, and considering the fact that in the natural example the GCAW front is not offset across any of the mapped SWIM faults, one of the two following tectonic scenarios is possible: a) either the GCAW is active, and forming over a basement anisotropy (inactive SWIM fault?); or b) both the GCAW and the SWIM faults are active. The possibility of an inactive GCAW being cut by active dextral

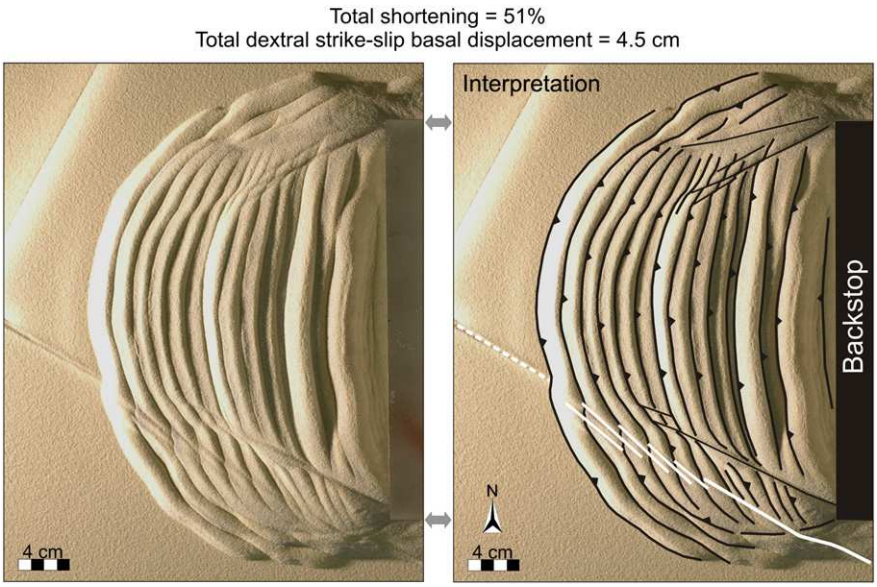

Fig. 9. Final stage of experiment 3: active basement fault and active thrust wedge (continuation). Model top view after 51% of shortening and 4.5 cm of dextral strike-slip displacement. Note the practical absence of corresponding offset in the frontal thrust wedge.

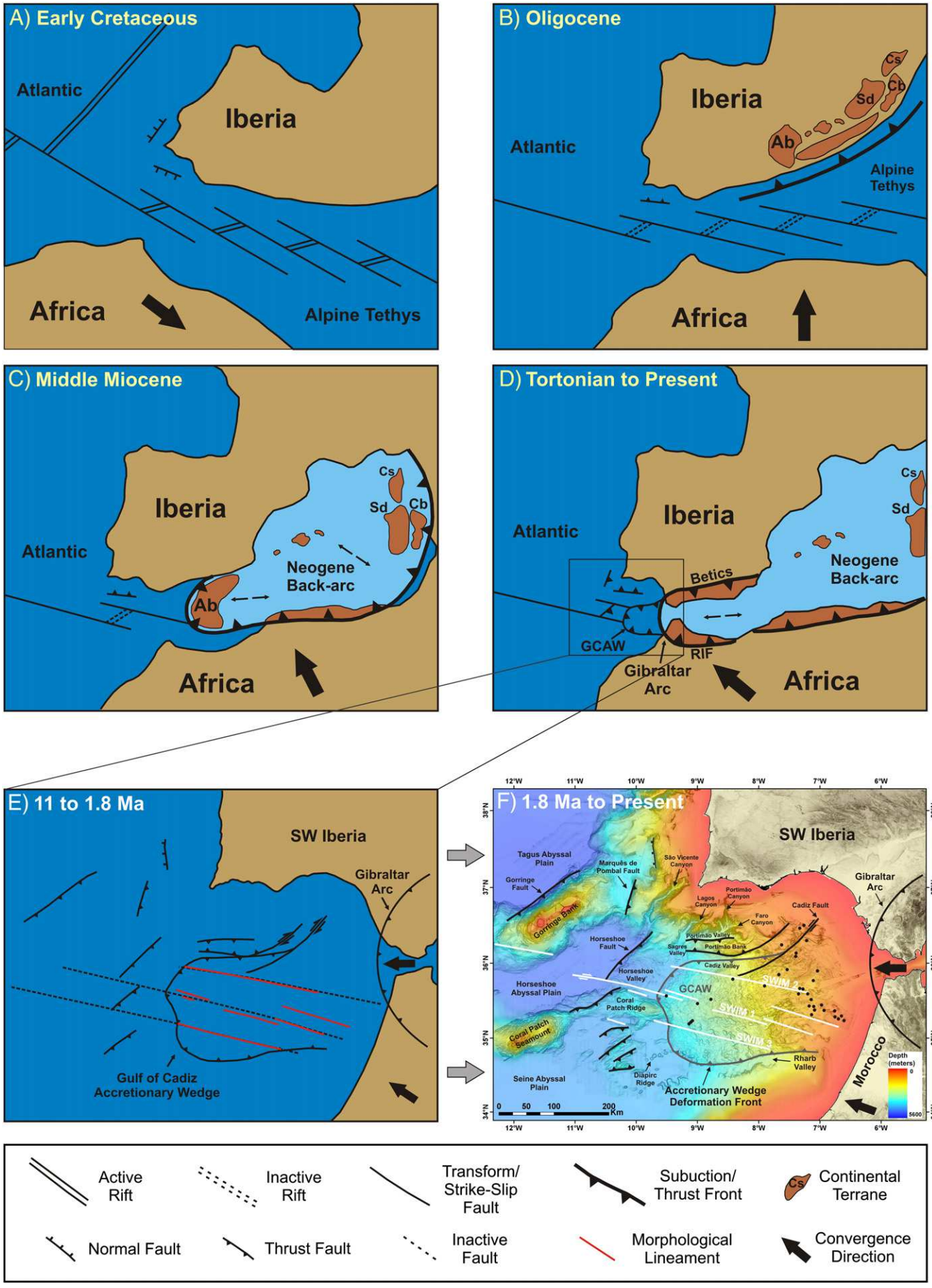
A) Early Cretaceous
Atlantic
Iberia
Africa
Alpine Tethys
B) Oligocene
Iberia
Atlantic
Cs
Sd
Cb
Ab
Alpine Tethys
Africa
C) Middle Miocene
Iberia
Atlantic
Cs
Sd
Cb
Neogene Back-arc
Ab
Africa
D) Tortonian to Present
Iberia
Atlantic
Cs
Sd
Neogene Back-arc
Betics
GCAW
RIF
Gibraltar Arc
Africa
E) 11 to 1.8 Ma
SW Iberia
Gibraltar Arc
Gulf of Cadiz Accretionary Wedge
F) 1.8 Ma to Present
SW Iberia
Tagus Abyssal Plain
Marquês de Pombal Fault
São Vicente Canyon
Gorringe Fault
Gorringe Bank
Portimão Canyon
Lagos Canyon
Gibraltar Arc
Cadiz Fault
Faro Canyon
Horseshoe Fault
Portimão Valley
Sagres Valley
Portimão Bank
Cadiz Valley
Horseshoe Valley
Horseshoe Abyssal Plain
GCAW
SWIM 2
Coral Patch Ridge
SWIM 1
Coral Patch Seamount
SWIM 3
Rharb Valley
Morocco
Depth (meters)
0
5600
Seine Abyssal Plain
Diapiric Ridge
Accretionary Wedge Deformation Front
0 50 100 200 Km
12°W
11°W
10°W
9°W
8°W
7°W
6°W
38°N
37°N
36°N
35°N
34°N
Active Rift
Inactive Rift
Transform/ Strike-Slip Fault
Subuction/ Thrust Front
Cs
Continental Terrane
Normal Fault
Thrust Fault
Inactive Fault
Morphological Lineament
Convergence Direction

strike-slip SWIM faults is clearly ruled out by the present experimental results.

4.1. Tectonic implications

The west Mediterranean tectonic evolution comprised the Mesozoic opening of the Tethys Ocean (Fig. 10A; e.g. Maldonado et al., 1999; Gutscher et al., 2002; Stampfli et al., 2002; Gràcia et al., 2003a; Jiménez-Munt et al., 2010). This would account for a basement tectonic anisotropy, hypothetically, either consisting in previous transform faults, or in rift-related normal faults (Fig. 10A and B). In view of the presented experimental results, the accretionary wedge (GCAW) is here interpreted to have formed on top of such basement faults (present day SWIM faults) as a consequence of roll-back subduction beneath Gibraltar. During this period (Middle Miocene to ~1.8 Ma?, Fig. 10C to E) these faults were probably inactive, although capable of originating a linear-like perturbation in the GCAW surface morphology (experiment 1). At the same time, the main regional convergence direction between Iberia and Africa gradually suffered a counterclockwise rotation, shifting from N–S (Fig. 10B) to near WNW–ESE (Fig. 10E). Such reorientation is interpreted to have triggered (since at least ~1.8 Ma) a dextral strike-slip reactivation of the basement (SWIM) faults (Fig. 10F), during a period in which the subduction driving the GCAW growth was still active (experiment 3), although slowing down (Gutscher et al., 2009a). It should be noted that this rotation of the main convergence direction also agrees with the general strain partitioning tectonic scenario previously proposed by Terrinha et al. (2009), according to which besides dextral strike slip faulting along near E–W orientated faults, northwest directed thrusts also occur along NE–SW orientated tectonic structures (e.g. Horseshoe, Marquês de Pombal and Gorringe Faults in Fig. 1B).

Other indirect evidence supporting present simultaneous activity of SWIM and GCAW includes the fact that not only all known mud volcanoes in the Gulf of Cadiz are located on top of the accretionary wedge, but also the circumstance that most of the deep mud volcanoes are symptomatically aligned and coincident with the SWIM faults (Fig. 1A). This suggests that the fluid migration and escape may be simultaneously controlled by the activity of both structures. If that is in fact the case, then the mud volcanoes could be preferentially located at the intersection between the SWIM strike-slip and the GCAW thrust faults, with such loci providing good pathways for the fluid to ascend (Pinheiro et al., 2003, 2005; Duarte et al., 2005; Rosas et al., 2009; Terrinha et al., 2009; Zitellini et al., 2009).

5. Conclusions

1. In view of the presented experimental results, the observed morphotectonic pattern of the frontal GCAW area is compatible with:
   i) The development of the GCAW on top of inactive, previously formed, basement faults (present day SWIM fault system).
   ii) The simultaneously (alternating) activity of the GCAW thrusting with the activity of the SWIM-related dextral strike-slip faults.

Conversely, the comparison of the same experimental results with the natural example unambiguously excludes the possibility of active strike-slip faulting (SWIM system) affecting an inactive preexistent GCAW, implying that if the SWIM fault system is active then the GCAW must also be presently active.

2. The main tectonic implications of the above conclusions comprise an initial (Middle Miocene to ~1.8 Ma) accretion of the GCAW sediments on top of preexistent Tethyan rift-related faults, preceding strike-slip reactivation of these faults (SWIM system), simultaneously with decreasing GCAW activity (~1.8 Ma to present), as a function of counterclockwise rotation of the main Iberia–Nubia convergence direction.
3. The modeling and morphological observations favor the interpretation of the SWIM fault system as the strike-slip reactivation of pre-existent basement faults. This suggests that the SWIM plate boundary proposed by Zitellini et al. (2009) may in fact correspond to the local reactivation of the older Tethyan plate boundary.

Acknowledgments

This work was sponsored by ALMOND (Multiscale modeling of deformation in the Gulf of Cadiz, PTDC/CTE-GIN/71862/2006), EURO-MARGINS SWIM (Earthquake and Tsunami hazards of active faults at the South-West Iberian Margin: deep structure, high-resolution imaging and paleo-seismic signature, REN2002-11234-EMAR, 01-LEC-EMA09F), TOPOEUROPE/0001/2007-TOPOMED (Plate re-organization in the western Mediterranean: lithospheric causes and topographic consequences) and NEAREST (Integrated observations from NEAR shore sourcES of Tsunamis: toward an early warning system, ESF Euro-Margins Program, contract no. 01-LEC-EMA09F and from EU Specific Programme "Integrating and Strengthening the European Research Area", Sub-Priority 1.1.6.3, "Global Change and Ecosystems", contract no. 037110) projects. Experiments were performed in the Analog Modeling Laboratory of IDL. J. Duarte and S. Silva thank FCT for the PhD grants SFRH/BD/31188/2006 and SFRH/BD/46227/2008, respectively. The support by Landmark Graphics Corporation via the Landmark University Grant Program and NASA WorldWind is also acknowledged. We specially thank Stephane Dominguez (University of Montpellier), Sandy Cruden and David Boutelier (Monash University) and Vasco Valadares (LNEG) for insightful discussions. Ruth Keppler, Ana Costa, André Blanco and Liliana D'Almeida are acknowledged for their help in the lab.

Appendix A

The material used as an analog of the upper crust sedimentary rocks was dry quartz sand, which is considered a Coulomb material deforming in a brittle way according to the Coulomb fracture criterion (e.g. Hubbert, 1937, 1951; Davis et al., 1983):

$$\tau_{ss} = \mu_c \sigma_n + c_0 \quad (1)$$

where τ_{ss} is the shear stress, μ_c is the coefficient of internal friction ($\mu_c = \tan\phi$, and ϕ = internal friction angle), σ_n is the normal stress, and c_0 is the cohesion of the material. According to the scale model theory (Hubbert, 1937), proper scaling is achieved when the ratios between model and natural prototype are independently established for the three fundamental units of length (λ), time (τ) and mass (μ):

$$\lambda = \frac{L_{(m)}}{L_{(p)}}; \tau = \frac{T_{(m)}}{T_{(p)}}; \mu = \frac{M_{(m)}}{M_{(p)}} \quad (2)$$

where L = length, T = time and M = mass, and (m) stands for model and (p) for natural prototype. The Coulomb fracture criterion governs

Fig. 10. Tectonic model: summarized, schematic representation of the main chronologic events leading to the formation of the present day main tectonic features in the Gulf of Cadiz. Ab — Alboran; Cb — Calabria; Cs — Corsica; Sd — Sardinia. See detailed explanation in the text.
Stages A to D are adapted from Rosenbaum et al. (2002) and Rosenbaum and Lister (2004); and complemented with Maldonado et al. (1999), Michard et al. (2002), Gràcia et al. (2003a) and Terrinha et al. (2009).

time independent deformation of brittle materials like sedimentary upper crustal rocks, since yield stress is insensitive to the rate of deformation provided that the inertial forces are negligible, as in the present case. This means that τ ratio is not needed for scaling in this situation. Length ratio (λ) was chosen given the maximum dimensions of the deformation apparatus used in the experiments (see Section 3), and was conveniently established as $\lambda = 2\times10^{-6}$. In the present case, of the two relevant material properties, coefficient of internal friction (μ_c) and cohesion (c_0), the first is dimensionless, and approximately the same in both model and prototype, whereas the second has dimension of stress and thus must be scaled accordingly (Hubbert, 1937):

$$\Sigma = \frac{c_{0(m)}}{c_{0(p)}} = \frac{\mu\gamma}{\lambda^2} \tag{3}$$

where Σ and γ are the model/prototype ratio for stress and for acceleration respectively. Since inertial forces are negligible when compared with gravity,

$$\gamma = \gamma_g = \frac{g_{(m)}}{g_{(p)}} = \frac{\lambda}{\tau^2} = 1 \tag{4}$$

where γ_g is the model/prototype gravity acceleration ratio. Thus, substituting $\gamma = 1$ in Eq. (3) allows the following simplification:

$$\Sigma = \frac{c_{0(m)}}{c_{0(p)}} = \frac{\mu}{\lambda^2} = \frac{\mu\lambda}{\lambda^3} = \delta\lambda \tag{5}$$

where δ corresponds to the model/prototype density ratio. Substituting δ and λ in Eq. (5) by the respective values in Table 1, immediately allows the determination of the implied mass ratio $= 4\times10^{-18}$. It should also be noted that since δ is generally close to one (between 0.5 and 0.7, e.g. Withjack et al., 2007) the strength of the materials expressed by Σ is scaled with the length (λ). Given the fact that in the present case $\lambda = 2\times10^{-6}$ and since cohesion for upper crustal rocks is clearly typically less than 50 MPa, it becomes immediately evident the utility of model materials with very low cohesion (<100 Pa), such as dry quartz sand, as analogs of upper crustal rocks.

References

Abe, K., 1979. Size of great earthquakes of 1837–1974 inferred from tsunami data. Journal of Geophysical Research 84 (NB4), 1561–1568.

Argus, D.F., Gordon, R.G., DeMets, C., Stein, S., 1989. Closure of the Africa–Eurasia–North America plate motion circuit and tectonics of the Gloria Fault. Journal of Geophysical Research B, Solid Earth and Planets 24, 5585–5602. doi:10.1016/j.marpetgeo.2007.11.008.

Baptista, M.A., Heitor, S., Miranda, J.M., Miranda, P.M.A., Mendes Victor, L., 1998. The 1755 Lisbon tsunami; evaluation of the tsunami parameters. Journal of Geodynamics 25 (1–2), 143–157.

Baptista, M.A., Miranda, J.M., Chierici, F., Zitellin, N., 2003. New study of the 1755 earthquake source based on multi-channel seismic survey data and tsunami modeling. Natural Hazards and Earth System Sciences 3, 333–340.

Buforn, E., Udias, A., Colombas, M.A., 1988. Seismicity, source mechanisms and tectonics of the Azores–Gibraltar plate boundary. Tectonophysics 152 (1–2), 89–118.

Calais, E., DeMets, C., Nocquet, J.-M., 2003. Evidence for a post-3.16-Ma change in Nubia–Eurasia–North America plate motions? Earth and Planetary Science Letters 216, 81–92.

Casas, A.M., Gapais, D., Nalpas, T., Besnard, K., Román-Berdiel, K., 2001. Analogue models of transpressive systems. Journal of Structural Geology 23, 733–743.

Davis, D., Suppe, J., Dahlen, F.A., 1983. Mechanics of fold and thrust belts and accretionary wedges. Journal of Geophysical Research 88, 1153–1172.

DeMets, C., Gordon, R.G., Argus, D.F., Stein, S., 1994. Effect of recent revisions to the geomagnetic reversal time scale on estimates of current plate motions. Geophysical Research Letters 21 (5), 2191–2194.

Duarte, J.C., Rosas, F., Pinheiro, L.M., Matias, L.M., Carvalho, A.M., Terrinha, P., Ivanov, M., 2005. Interpretation of Recent Sedimentary and Tectonic Structures Off SW Iberia from Multibeam Bathymetry, Seismic Reflection and Experimental Modelling. Geophysical Research Abstracts, 7. European Geosciences Union, p. 07867 (2005).

Duarte, J.C., Valadares, V., Terrinha, P., Rosas, F., Zitellini, N., Gràcia, E., 2009. Anatomy and tectonic significance of WNW–ESE and NE–SW lineaments at a transpressive plate boundary (Nubia–Iberia). Trabajos de Geologia 29, 237–241.

Duarte, J.C., Terrinha, P., Rosas, F.M., Valadares, V., Pinheiro, L.M., Matias, L., Magalhães, V., Roque, C., 2010. Crescent-shaped morphotectonic features in the Gulf of Cadiz (offshore SW Iberia). Marine Geology 271, 236–249.

Fernandes, R.M.S., 2004. Present-day Kinematics at the Azores–Gibraltar Plate Boundary as Derived from GPS Observations. Delft University Press, The Netherlands.

Fernandes, R.M.S., Ambrosius, B.A.C., Noomen, R., Bastos, L., Wortel, M.J.R., Spakman, W., Govers, R., 2003. The relative motion between Africa and Eurasia as derived from ITRF 2000 and GPS data. Geophysical Research Letters 30 (16), 1828.

Fernandes, R.M.S., Miranda, J.M., Meijninger, R.M.L., Bos, M.S., Noomen, R., Bastos, L., Ambrosius, B.A.C., Riva, R.E.M., 2007. Surface velocity field of the IberoMaghrebian segment of the Eurasia–Nubia plate boundary. Geophysical Journal International 169, 315–324.

Fukao, Y., 1973. Thrust faulting at a lithospheric plate boundary, The Portugal earthquake of 1969. Earth and Planetary Science Letters 18, 205–216.

González, A., Torné, M., Córdoba, D., Vidal, N., Matias, L.M., Díaz, J., 1996. Crustal thinning in the southwestern Iberia margin. Geophysical Research Letters 23 (18), 2477–2480.

Gràcia, E., Dañobeitia, J., Vergés, J., Bartolomé, R., 2003a. Crustal architecture and tectonic evolution of the Gulf of Cadiz, SW Iberia, at the convergence of the Eurasian and African plates. Tectonics 22 (4), 1033.

Gràcia, E., Dañobeitia, J., Vergés, J., PARSIFAL Team, 2003b. Mapping active faults offshore Portugal (36 degrees N–38 degrees N); implications for seismic hazard assessment along the Southwest Iberian margin. Geology 31 (1), 83–86.

Gutscher, M.A., 2004. What caused the Great Lisbon earthquake? Science 305 (5688), 1247–1248.

Gutscher, M.-A., 2006. The great Lisbon earthquake and tsunami of 1755: lessons from the recent Sumatra earthquakes and possible link to Plato's Atlantis. European Review 14 (2), 181–191.

Gutscher, M.-A., Malod, J., Rehault, J.-P., Contrucci, I., Klingelhoefer, F., Spakman, W., Mendes-Victor, L., 2002. Evidence for active subduction beneath Gibraltar. Geology 30 (12), 1071–1074.

Gutscher, M.-A., Dominguez, S., Westbrook, G.K., Leroy, P., 2009a. Deep structure, recent deformation and analog modeling of the Gulf of Cadiz accretionary wedge: implications for the 1755 Lisbon earthquake. Tectonophysics 475, 85–97.

Gutscher, M.-A., Dominguez, S., Westbrook, G.K., Gente, P., Babonneau, N., Mulder, T., Gonthier, E., Bartolome, R., Luis, J., Rosas, F., Pedro, T., Delila and DelSis Scientific Teams, 2009b. Tectonic shortening and gravitational spreading in the Gulf of Cadiz accretionary wedge: observations from multi-beam bathymetry and seismic profiling. Marine and Petroleum Geology 26, 647–659.

Hoshino, K., Koide, H., Inami, K., Iwamura, S., Mitsui, S., 1972. Mechanical properties of Japanese Tertiary sedimentary rocks under high confining pressure. Geological Survey of Japan Report 244.

Hubbert, M.K., 1937. Theory of scale models as applied to the study of geologic structures. Geological Society of America Bulletin 48, 1459–1520.

Hubbert, M.K., 1951. Mechanical basis for certain familiar geologic structures. Geological Society of America Bulletin 62, 355–372.

Jiménez-Munt, I., Fernàndez, M., Vergés, J., Afonso, J.C., Garcia-Castellanos, D., Fullea, J., 2010. The lithospheric structure of the Gorringe Bank: insights into its origin and tectonic evolution. Tectonics 29, TC5019. doi:10.1029/2009TC002458.

Johnston, A., 1996. Seismic moment assessment of earthquakes in stable continental regions: III. New Madrid, 1811–1812, Charleston 1886 and Lisbon 1755. Geophysical Journal International 126, 314–344.

Lonergan, L., White, N., 1997. Origin of the Betic–Rif mountain belt. Tectonics 16, 504–522.

Maldonado, A., Somoza, L., Pallarés, L., 1999. The Betic orogen and the Iberian–African boundary in the Gulf of Cadiz: geological evolution (central North Atlantic). Marine Geology 155 (1–2), 9–43.

Mandl, G., de Jong, L.N.J., Maltha, A., 1977. Shear zones in granular material; an experimental study of their structure and mechanical genesis. Rock Mechanics 9, 95–144.

Marques, F.O., Cobbold, P.R., 2002. Topography as a major factor in the development of arcuate thrust belts: insights from sandbox experiments. Tectonophysics 348, 247–268.

Martinez-Solares, J.M., López Arroyo, A., 2004. The great historical 1755 earthquake: effects and damage in Spain. Journal of Seismology 8, 275–294.

Medialdea, T., Vegas, R., Somoza, L., Vázquez, J.T., Maldonado, A., Díaz-del-Río, V., Maestro, A., Córdoba, D., Fernández-Puga, M.C., 2004. Structure and evolution of the "Olistostrome" complex of the Gibraltar Arc in the Gulf of Cádiz (eastern Central Atlantic): evidence from two long seismic cross-sections. Marine Geology 209, 173–198.

Michard, A., Chalouan, A., Feinberg, H., Goffé, B., Montigny, R., 2002. How does the Alpine belt end between Spain and Moroco? Bulletin de la Societe Geologique de France 173 (1), 3–15.

Mulder, T., Voisset, M., Lecroart, P., Le Drezen, E., Gonthier, E., Cadisar Shipboard Party, 2003. The Gulf of Cadiz: an unstable giant contouritic levee. Geo-Marine Letters 23, 7–18.

Mulugeta, G., 1988. Modelling the geometry of Coulomb thrust wedges. Journal of Structural Geology 10, 847–859.

Nocquet, J.M., Calais, E., 2004. Geodetic measurements of crustal deformation in the western Mediterranean and Europe. Pure and Applied Geophysics 161 (3), 661–681.

Pinheiro, L., Ivanov, M.K., Sautkin, A., Akhmanov, G., Magalhães, V., Volkonskaya, A., Monteiro, J.H., Somoza, L., Gardner, J., Hamouni, N., Cunha, M.R., 2003. Mud volcanism in the Gulf of Cadiz: results from the TTR-10 cruise. Marine Geology 195, 131–151.

Pinheiro, L.M., Comas, M., Magalhães, V., Carvalho, A., Moedas, J., Aguado, B., Somoza, L., Gardner, J., Ivanov, M., 2005. Structural control on hydrocarbon-rich fluid venting

in the Gulf of Cadiz: new insights from the TTR-14 and MATESPRO cruises. Geophysical Research Abstracts 7, 10386.
Rosas, F.M., Duarte, J.C., Terrinha, P., Valadares, V., Matias, L., 2009. Morphotectonic characterization of major bathymetric lineaments in NW Gulf of Cadiz (Africa–Iberia plate boundary): insights from analogue modelling experiments. Marine Geology 261, 33–47.
Rosas, F.M., Duarte, J.C., Neves, M.C., Terrinha, P., Silva, S., Matias, L.., submitted for publication. Thrust–wrench interference between major active faults in the Gulf of Cadiz (Africa–Eurasia plate boundary, offshore SW Iberia): tectonic implications from analogue and numerical modeling. Tectonophysics.
Rosenbaum, G., Lister, G.S., 2004. Formation of arcuate orogenic belts in the western Mediterranean region. In: Sussman, A.J., Weil, A.B. (Eds.), Orogenic Curvature: Integrating Paleomagnetic and Structural Analyses: Boulder, Colorado: Geological Society of America Special Paper, 383, pp. 41–56.
Rosenbaum, G., Lister, G.S., Duboz, C., 2002. Reconstruction of the tectonic evolution of the western Mediterranean since the Oligocene. In: Rosenbaum, G., Lister, G.S. (Eds.), Reconstruction of the evolution of the Alpine-Himalayan. Orogen: Journal of the Virtual Explorer, 8, pp. 107–126.
Royden, L.H., 1993. Evolution of retreating subduction boundaries formed during continental collision. Tectonics 12, 629–638.
Sartori, R., Torelli, L., Zitellini, N., Peis, D., Lodolo, E., 1994. Eastern segment of the Azores–Gibraltar line (central-eastern Atlantic): an oceanic plate boundary with diffuse compressional deformation. Geology 22, 555–558.
Sella, G.F., Dixon, T.H., Mao, A., 2002. REVEL; a model for recent plate velocities from space geodesy. Journal of Geophysical Research 107 (B4), 17.
Stampfli, G.M., Borel, G.D., Marchant, R., Mosar, J., 2002. Western Alps geological constraints on western Tethyan reconstructions. In: Rosenbaum, G., Lister, G.S. (Eds.), 2002. Reconstruction of the Evolution of the Alpine-Himalayan Orogen: Journal of the Virtual Explorer, 8, pp. 77–106.
Stich, D., Serpelloni, E., Mancilla, F.-L., Morales, J., 2006. Kinematics of the Iberia-Maghreb plate contact from seismic moment tensors and GPS observations. Tectonophysics 426, 295–317.
Stich, D., Mancilla, F., de, L., Pondrelli, S., Morales, J., 2007. Source analysis of the February 12th 2007, Mw 6.0 Horseshoe earthquake: implications for the 1755 Lisbon earthquake. Geophysical Research Letters 34, 12.
Terrinha, P., Pinheiro, L.M., Henriet, J.P., Matias, L., Ivanov, M.K., Monteiro, J.H., Akhmetzhanov, A., Volkonskaya, A., Cunha, T., Shaskin, P., Rovere, M., 2003. Tsunamigenic–seismogenic structures, neotectonics, sedimentary processes and slope instability on the southwest Portuguese Margin. Marine Geology 195 (1–4), 55–73.
Terrinha, P., Matias, L., Vicente, J.C., Duarte, J., Luís, J., Pinheiro, L., Lourenço, N., Diez, S., Rosas, F.M., Magalhães, V., Valadares, V., Zitellini, N., Mendes-Víctor, L., MATESPRO Team, 2009. Morphotectonics and strain partitioning at the Iberia–Africa plate boundary from multibeam and seismic reflection data. Marine Geology 267, 156–174.
Thiebot, E., Gutscher, M.-A., 2006. The Gibraltar Arc seismogenic zone (part 1): constraints on a shallow east dipping fault plane source for the 1755 Lisbon earthquake provided by seismic data, gravity and thermal modeling. Tectonophysics 426, 135–152.
Weijermars, R., Jackson, M.P.A., Vendeville, B., 1993. Rheological and tectonic modeling of salt provinces. Tectonophysics 217, 143–174.
Withjack, M.O., Schlische, R.W., Henza, A.A., 2007. Scaled experimental models of extension: dry sand vs. wet clay. Houston Geological Society Bulletin 49 (8), 31–49.
Zitellini, N., Mendes, L.A., Cordoba, D., Danobeitia, J., Nicolich, R., Pellis, G., Ribeiro, A., Sartori, R., Torelli, L., Bartolomé, R., Bortoluzzi, G., Calafato, A., Carrilho, F., Casoni, L., Chierici, F., Corela, C., Correggiari, A., Della Vedova, B., Gràcia, E., Jornet, P., Landuzzi, M., Ligi, M., Magagnoli, A., Marozzi, G., Matias, L., Penitenti, D., Rodriguez, P., Rovere, M., Terrinha, P., Vigliotti, L., Zahinos Ruiz, A., 2001. Source of 1755 Lisbon earthquake and tsunami investigated. EOS Transactions, American Geophysical Union 82 (26), 290–291.
Zitellini, N., Rovere, M., Terrinha, P., Chierici, F., Matias, L., Bigsets Team, 2004. Neogene through quaternary tectonic reactivation of SW Iberian passive margin. Pure and Applied Geophysics 161 (3), 565–587.
Zitellini, N., Gracia, E., Matias, L., Terrinha, P., Abreu, M.A., DeAlteriis, G., Henriet, J.P., Dañobeitia, J.J., Masson, D.G., Mulder, T., Ramella, R., Somoza, L., Diez, S., 2009. The quest for the Africa–Eurasia plate boundary west of the Strait of Gibraltar. Earth and Planetary Science Letters 280 (1–4), 13–50.